

UNIVERZITA PALACKÉHO OLOMOUC

Přírodovědecká fakulta



**Nanostrukturální polovodiče: komplikovaná příprava a
popis rekombinačních procesů vykoupené výjimečnými
vlastnostmi**

Habilitační práce

Praha 2024

2024

RNDr. Pavel Galář, Ph.D.

Prohlašuji, že jsem habilitační práci vypracoval samostatně a uvedl jsem všechny použité podklady a literaturu.

V Praze, 27. 12. 2024

Poděkování

Na vzniku této práce se podílela celá řada výjimečných lidí, kteří mě v průběhu let vědecky inspirovali, podporovali, motivovali a spolupracovali se mnou. Mezi nejvýznamnější z nich patří mí kolegové z MFF, doc. M. Kozák a Dr. A. Fučíková, spolupracovníci z VŠCHT, zejména doc. V. Scholtz, a má současná vedoucí z FZÚ, K. Kůsová. Zvláštní poděkování si zaslouží také můj doktorand, Ing. F. Matějka, se kterým jsem realizoval značnou část nedávných vědeckých projektů.

Velký dík patří i mé ženě Michaele, která mi byla ve všech mých aktivitách oporou, stála mi po boku a v mnoha ohledech mě inspirovala. Nemohu opomenout ani mou nedávno narozenou dceru Terezku, jejíž blížící se příchod na svět významně přispěl k mé motivaci dokončit habilitační práci v co nejkratším termínu.

Vám všem, stejně jako těm, které zde nejmenuji, patří mé srdečné poděkování za vaši podporu, spolupráci a inspiraci.

Obsah

Úvod	5
Předmluva autora	7
1. Polovodičové nanomateriály.....	8
1.1 Vlastnosti polovodičů.....	8
1.2 Původ výjimečných vlastností nanomateriálů.....	14
1.3 Křemíkové kvantové tečky.....	27
1.4 Perovskitové struktury a jeho hybridy.....	33
1.5 Nanokrystalický diamant.....	42
2. Syntéza křemíkových nanostruktur.....	49
2.1 Nanostruktury vytvořené pomocí netermálního plazmatu.....	49
2.2 Kvantové tečky s různou dominantní facetou	52
3. Povrchově modifikované křemíkové kvantové tečky.....	57
3.1 Terminace kvantových teček plazmaticky aktivovanou vodou.....	57
3.2 Vliv povrchové úpravy na rekombinační procesy excitovaných nosičů náboje.....	60
4. Studium rekombinačních a transportních procesů v perovskitovém nanohybridu	66
5. Chování excitovaných nosičů v nanodiamantových hybridech	71
5.1 Vliv nediamondové fáze na rekombinační procesy v nanokrystalickém diamantu...	71
5.2 Separace excitovaných nosičů v rámci hybridu nanodiamond/vodivý polymer.....	74
Reference	77
Přiložené publikace.....	89

Úvod

Polovodivé materiály byly jedním z hlavních tahounů průmyslového a vědeckého rozvoje minulého století a jejich význam přetrval i do toho současného. Technologie na bázi křemíku dominují mnoha tradičním odvětvím v elektronice, optoelektronice a fotovoltaice, zatímco binární, ternární a dokonce i organické polovodiče získaly značnou popularitu v pokročilých aplikacích zahrnujících světelné zdroje (LED/OLED), detekci světla, medicínu a energetiku (uskladnění energie). I přes tyto úspěchy nejsou možnosti polovodivých materiálů nekonečné. Postupující technologický vývoj klade na polovodiče stále vyšší požadavky, které není snadné uspokojit, čímž tyto materiály začínají narážet na limity svého využití. Mezi nejnaléhavější nároky patří nejen široká laditelnost fyzikálních vlastností, ale také ustavičně rostoucí důraz na nízkou ekologickou zátěž jejich přípravy i recyklace a nízkou toxicitu použitých prvků. Jednou z možných cest, jak dále rozšiřovat spektrum vlastností současných polovodičů, je přechod k jejich nanostrukturálním formám. Snižením rozměrů objektů pod 1/1000 tloušťky vlasu (~ 50 nm) dojde ke zvýšení vlivu povrchu materiálu na jeho vlastnosti a při dalším snižování (<10 nm) se přidají i efekty spojené s přítomností kvantově-rozměrového jevu. Kombinací těchto efektů je možné zásadním způsobem měnit vlastnosti látek, a tím rozšiřovat pole jejich využití. Zmíněný aplikační potenciál je však vykoupen mnoha překážkami, které musí být nejprve zdolány.

Velkou výzvou bývá samotná příprava nanomateriálů. Metody, které by dovedly vytvořit kvalitní nanostruktury o dostatečném množství a za konkurenceschopnou cenu, jsou ojedinělé. Doposud známé postupy přípravy většinou splňují jeden, případně dva zmíněné požadavky. Další překážkou je hledání metod efektivní a cílené úpravy jejich povrchů, a to především z důvodů vysoké reaktivity povrchu nanomateriálů. Komplikace nastávají nejen u vytváření nanomateriálů, ale i při studiu a popisu jejich chování. Kombinací objemových vlastností, kvantových jevů a všudypřítomných defektů získávají nanomateriály vlastnosti, které často nelze snadno odhadnout ze známé teorie. Především se to týká relaxačních, rekombinačních a transportních procesů excitovaných nosičů, které určují optické a elektrické vlastnosti těchto látek. I přes všechny tyto výzvy výzkum polovodivých nanomateriálů dynamicky probíhá a přináší mnoho zajímavých aplikačních výstupů. Pomineme-li běžné aplikace využívající např. nanostrukturální oxid titaničitý (kosmetika, voděodolné povrchy atd.), aplikace nanomateriálů již vedla k rozvoji světelných kolektorů, nanomedicíny, bio-

zobrazování, zvyšování kapacity Li-iontových baterií, dokonce i k mnoha ekologicky zaměřeným technologiím (např. čištění vody či ovzduší).

Předkládaná habilitační práce prezentuje dosavadní vědecký výstup žadatele, který se syntéze, vývoji a charakterizaci různých polovodičových nanostruktur systematicky věnuje. Práce jmenovitě prezentuje výsledky získané při studiu tří následujících nanostruktur:

- křemíkové kvantové tečky,
- polykrytalický diamant,
- halogenidové perovskity.

Primárně práce obsahuje výsledky žadatele získané při studiu křemíkových kvantových teček. Tyto objekty jsou v současné době jedním z hlavních hráčů na poli kovalentních polovodičových nanostruktur, protože jsou složeny z běžného prvku, který je netoxický, biokompatibilní, a navíc může vykazovat vysokou efektivitu konverze světla či vázání lithia. Práce prezentuje nejen vývoj nových metod jeho přípravy a povrchové terminace, ale i výzkum jeho vlastností a aplikací.

Druhým studovaným materiélem je také kovalentní polovodičová nanostruktura, a to polykrytalický diamant. Diamant je i přes široký zakázaný pás (5,6 eV) díky svým všudypřítomným příměsím považován za polovodič, který je biokompatibilní, netoxický, chemicky odolný a vykazuje zajímavé vodivé, optické a mechanické vlastnosti. Jeho monokrytalická forma je však extrémně finančně náročná na přípravu, a proto se výzkum tohoto materiálu zaměřil na jeho polykrytalickou alternativu, která je složena z nanokrystalů oddělených nediamondovou uhlíkovou fází. Využití nanokrytalického diamantu je závislé na dostatečném zmapování vlivu rozhraní a nediamondové fáze na rekombinační procesy excitovaných nosičů, čemuž se věnuje výzkum předkladatele.

Posledním prezentovaným materiélem je hybridní nanostruktura složená z binárních kvantových teček PbS vložených do nosné matrice halogenidových perovskitů. Perovskity jsou komplexní organo/anorganické materiály, které vykazují výborné absorpcní i vodivostní vlastnosti, díky čemuž jsou velmi perspektivní jako fotovoltaický materiál nebo nosný materiál pro transfer nosičů náboje do nanočástic s vysokým kvantovým výtěžkem. Práce prezentuje výsledky studia transportních procesů nosičů náboje ve zmíněné hybridní struktuře.

Předmluva autora

Přestože přítomnost osobního úvodu není u habitačních prací obvyklá, dovolím si na tomto místě prezentovat několik osobních poznámek/poznatků. Při jedné diskuzi na téma habitační práce mi jeden známý český fyzik řekl, že by měla představovat přehled dosavadního akademického života navrhovatele, a tak se k jejímu psaní přistoupil. Sám svůj akademický život vnímám jako minci se dvěma stranami – vědeckou a pedagogickou.

Má vědecká kariéra je spojena s přípravou, modifikací a studiem vlastností kvantových teček a nanomateriálů obecně. Z mé zkušenosti vědecká práce s těmito drobnými strukturami připomíná kompletování virtuálních skládaček, kdy jednotlivé dílky často do sebe nezapadají, i když by měly, a jejich tvar či obsah nelze snadno odhadnout pomocí známých teorií. Přesto věřím, že výsledné obrázky, které jsme v rámci publikací vytvořili, dávají smysl. Ať už se jedná o modely transportních mechanizmů v perovskitových hybridech, předpokládanou strukturu nediamondové fáze v nanodiamondech, nebo o přípravu, modifikaci a popis chování emise křemíkových kvantových teček. Doufám, že navzdory některým nedokonalým okrajům mohou naše výsledky sloužit jako dílky ve větších skládačkách jiných vědeckých skupin.

Předkládaná práce neobsahuje jen rozbor vědeckých článků, ale i rešeršní část, jejíž obsah je významně poznamenán mou pedagogickou stránkou. Namísto stručného teoretického přehledu, jak bývá zvykem, jsem se rozhodl přehledně seskupit informace, které mi o nanomateriálech přijdou důležité a významně ovlivnily můj pohled na práci s nimi. V této části se snažím mimo jiné ukázat, jaké vlastnosti objemových látek jsou přechodem k nanostrukturám ovlivněny, proč tomu tak je a od jaké velikosti se tyto změny projevují. Rovněž se věnuji tomu, jak nahlížet na kvantové tečky a nanostruktury obecně. Na základě svých zkušeností vnímám kvantové tečky nikoliv jako krystalické kuličky s rozšířeným zakázaným pásem, ani jako molekule podobné struktury s diskrétními energetickými hladinami, jak jsou někdy popisovány. Jde o struktury na rozhraní diskrétního a spojitého světa, které kombinují vlastnosti obou. Navíc jsou ovlivněny deformovanými vazbami vlastních atomů i vlivem atomů cizích na jejich povrchu. Pro tematické ucelení rešerše je tato část doplněna o krátký úvod do teorie pevných látek. Věřím, že erudovaní čtenáři tuto podkapitolu s grácií přeskočí, neboť je určena spíše méně zkušenému publiku, které by ji mohlo využít ke vzdělávacím účelům. Z tohoto důvodu jsem se také rozhodl práci napsat v českém jazyce.

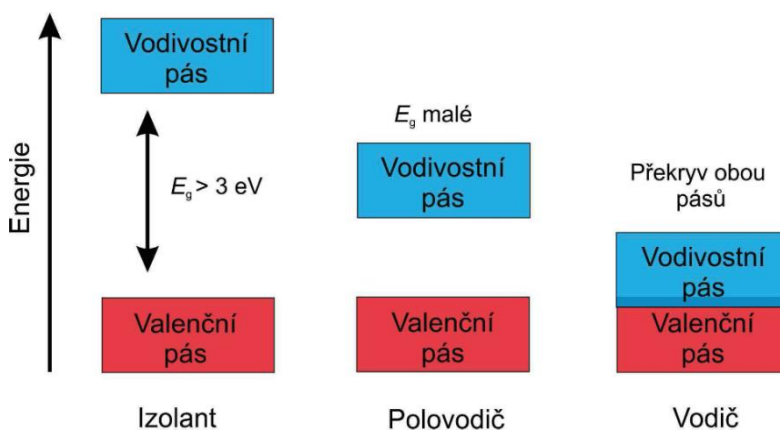
S úctou

Pavel Galář

1.Polovodičové nanomateriály

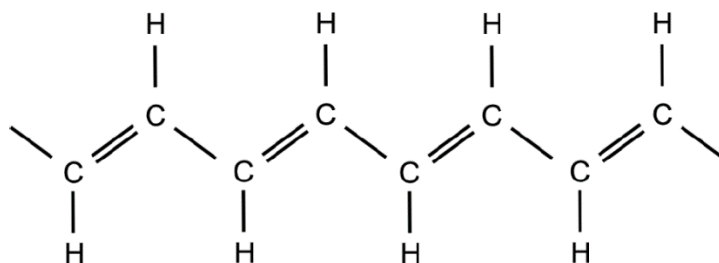
1.1. Vlastnosti polovodičů

Pro ucelenosť prezentovaného tématu budou v rámci této kapitoly zavedeny základní pojmy spojené s anorganickými a organickými polovodiči. Zaměříme se na zavedení hlavních rekombinačních procesů, jejich vlivu na základní optické a elektrické vlastnosti polovodičů, stejně jako vlivu defektů a neuspořádanosti. Popis nebude vyčerpávají, ale bude zaměřen na navazující teorii a výzkum prezentovaný v předkládané práci. Jako polovodiče označujeme materiály, jejichž hodnota specifické vodivosti spadá do intervalu hodnot od $10^{-8} \text{ S}\cdot\text{m}^{-1}$ do $10^6 \text{ S}\cdot\text{m}^{-1}$. Rozdíl mezi polovodiči, vodiči a izolátory se dá ovšem definovat i pomocí energetické pásové struktury těchto látek. Na základě Blochovi teorie, definující periodický průběh el. potenciálu, jsou elektronové stavy v uspořádaných látkách rozděleny do tzv. pásů. Tyto pásy jsou odděleny oblastmi energií, kterých elektrony nemohou nabývat (**Obrázek 1**). Mezi nejdůležitější pásy patří tzv. vodivostní a valenční pás. Za běžných podmínek je u homogenních látek vodivostní pás téměř prázdný a vodivostní téměř plný. Elektrony ve valenčním pásu jsou pevně vázány k atomům a nepřispívají k el. vodivosti látky, což neplatí o dírách, kvazičásticích spojených s volným stavem v tomto pásu, a o volných elektronech ve vodivostním pásu. V jednoduchosti tedy můžeme říci, že míra vodivosti látek je dána schopností elektronů přeskočit do vodivostního pásu. Pokud je šířka energetické bariéry mezi maximem valenčního a minimem vodivostního pásu (tzv. zakázaný pás, E_g , z angl. Energy gap) větší než $\sim 3 \text{ eV}$, označujeme látku jako izolant (teplná excitace je obtížná). V opačném případě je považujeme za polovodiče. Specifická situace nastává u vodičů, kde dochází dána schopností elektronů přeskočit do el. vodivostního pásu.



Obrázek 1. Energetická (pásová) struktura izolantu, polovodiče a vodiče.

Mezi čistými prvky příliš polovodičů bohužel nenajdeme (tzv. elementární polovodiče). Tuto vlastnost vykazují jen prvky z IV. skupiny a z praktického hlediska se dá efektivně využít pouze křemík ($E_g = 1,1$ eV) a germanium ($E_g = 0,66$ eV). Ostatní prvky z dané skupiny mají příliš úzký zakázaný pás pro polovodivé aplikace. Za polovodič se však považuje i uhlík v diamantové formě, přestože šířka jeho zakázaného pásu je rovna 5,5 eV. Diamant totiž vždy obsahuje příměsi, které zvyšují jeho vodivost. Z aplikačního hlediska je množství těchto polovodičů však nedostatečné, především proto, že nelze snadno měnit šířku ani charakter jejich zakázaného pásu (přímý/nepřímý viz dále) nebo mřížkovou konstantu a tím i mnoho jejich vlastností. Proto byly vytvořena nová třída polovodičů, obsahujících v krystalické mřížce dva nebo i více různých prvků. Mezi nejběžnější patří binární polovodiče kombinující atomy z III. a V., případně II. a VI. skupiny (PbS, GaN, GaAs, InAs, ZnO, TiO₂, ZnS atd.). Polovodiče obsahující více atomů označujeme jako multinární (AlGaAs, HgCdTe, Ag₂ZnSnS₄, Cu₂ZnGeS₄ atd.). Jejich příprava je však náročná nejen technicky, ale i finančně, což omezuje jejich aplikační rozsah. Pro úplnost je dobré zmínit, že polovodivé vlastnosti vykazují nejen anorganické, ale i organické látky, které jsou v drtivé většině případů dobrými izolátory. Nutnou podmínkou pro získání polovodivých vlastností u organických látek je periodické střídání π - a σ -vazeb, a to buď v blocích nebo ve formě polymeru. Mezi typické zástupce polovodivých organických látek patří vodivé polymery, které mohou dosahovat vodivosti až 10^3 S·m⁻¹ (**Obrázek 2**).



Obrázek 2. Struktura vodivého polymeru polyacetylénu.

Stavy v zakázaném pásu polovodičů

Výše zmíněný pohled na energetickou strukturu látek byl do značné míry zjednodušený. Očekával totiž splnění Blochova přiblížení předpokládající periodický průběh potenciální energie v poli jader. Tímto zjednodušením je zanedbána vícečásticová interakci nosičů náboje prostřednictvím Coulombické síly a jejich interakce s vibrací mříže. Látky také nejsou ideální a často obsahují různé defekty či nemusí platit dalekodosahové uspořádání, což nastává u

amorfních, polykryystalických, organických vodivých polymerů či nanostrukturálních látek. Všechny tyto vlivy vedou k modifikaci energetického spektra, a především ke vzniku energetických stavů v zakázaném pásu, což významně ovlivňuje a komplikuje popis rekombinačních a vodivostních procesů v látce, a tím i jejich optických a elektrických vlastností. Díky úzkému zakázanému pásu jsou na přítomnost těchto stavů nejcitlivější právě polovodiče.

Energetické stavy v zakázaném pásu způsobené porušením dalekodosahového uspořádání označujeme jako lokalizované (též pastové), protože nosiče v nich mají nízkou pohyblivost, dokud nejsou excitovány do vodivostního (elektrony) nebo valenčního pásu (díry). Mezi tyto lokalizované stavy patří například defekty mříže, ke kterým se řadí dopanty a jiné příměsi, vakance, dislokace nebo různé stavy spojené s povrchem (cílené terminace, kývavé vazby atd.). S růstem neuspořádanosti v polovodičích dochází k *rozmažání* hran zakázaného pásu a vzniku tzv. výběžkových stavů (z angl. tail states), jejichž hustota exponenciálně klesá od hrany valenčního/vodivostního do zakázaného pásu. Z terminologického hlediska je dobré zmínit, že u velmi neuspořádaných látek (amorfní) z principu nemá cenu mluvit o hrani valenčního a vodivostního pásu (porušení periodicity potenciálu), přestože energetická struktura látky zůstává v obecných rysech zachována. Jejich role je nahrazována tzv. pohyblivostní hranou. Nosiče nad touto hranou se považují za volné, pod touto hranou za lokalizované. U vodivých polymerů a kvantových teček také dochází k modifikaci výše zmíněné terminologie. Jelikož tyto objekty svou velikostí připomínají velkou molekulu, vodivostní pás u nich bývá označován jako nejnižší neobsazený molekulární orbital (tzv. LUMO) a valenční jako nejvyšší obsazený molekulární orbital (tzv. HOMO).

Přítomností vícečásticové interakce nosičů náboje a jejich interakcí s vibrací mřížky vznikají v látce entity, které označujeme jako kvazičástice. Jím příslušící energetické stavy taktéž spadají do zakázaného pásu. Mezi nejběžnější kvazičástice ovlivňující vlastnosti anorganických či organických polovodičů patří excitony, polarony a solitonky. Excitonky jsou složeny z elektronu a díry navzájem vázaných Coulombickou interakcí. Mohou být pohyblivé nebo vázané na místo v látce (defekt). Mezi nejdůležitější parametry excitonu patří vzdálenost elektronu a díry (tzv. Bohrův poloměr a_x) a jeho vazebná energie. Oba tyto parametry jsou spojeny s velikostí Coulombické síly mezi elektronem a dírou, která je ovlivněna především relativní permitivitou látky. Velikost a_x se u polovodičů pohybuje v rozsahu $\sim 2 - 50$ nm (ZnS, respektive PbSe).^{1,2} Podle vazebné energie dělíme excitony na tzv. Wannier-Mottovi (v řádu $\sim 0,01$ eV) nebo Frenkelovy excitony ($\sim 0,1 - 1$ eV). Druhé zmíněné se však u polovodičů téměř nevyskytují (pouze krystalické organické molekuly). Díky své nízké vazebné energii Wannier-

Mottovi excitony za běžných teplot rychle disociují (tepelná energie za pokojové teploty $\sim 0,025$ eV). To se však mění přechodem k nanostrukturám (rozměr objektu blízký nebo nižší než a_x), kdy stabilita excitonů výrazně roste, což se dá představit jako stlačování excitonu, čímž se zvyšuje jeho vazebná energie. Polarony tvoří vázaný stav mezi nosičem náboje a vibrací mřížky (fononem). Vznikají v látkách, kde dochází k silné Coulombické interakci mezi excitovanými nosiči a atomy mříže (polární polovodiče, CdS, ZnSe atd.). Podle znaménka náboje na nosiči je dělíme na pozitivní a negativní. Jejich přítomnost je zásadní především u polovodivých organických látek, kde je naopak zdrojem jejich vodivosti (viz dále). S růstem koncentrace polaronů mohou vznikat stabilnější kvazičástice bipolarony (spojení dvou polaronů). Význam i těchto kvazičástic roste přechodem směrem k nanostrukturním formám polovodičů (především 2D). Solitony jsou specifické kvazičástice, protože dle teorie se jedná o vlnu, která se šíří polovodičem a nese náboj. Tato vlna má sebezesilující vlastnosti, takže během jejího šíření nedochází ke snižování její amplitudy ani její deformaci. Jejich výskyt se omezuje především na prostorově omezené vodivé polymery.

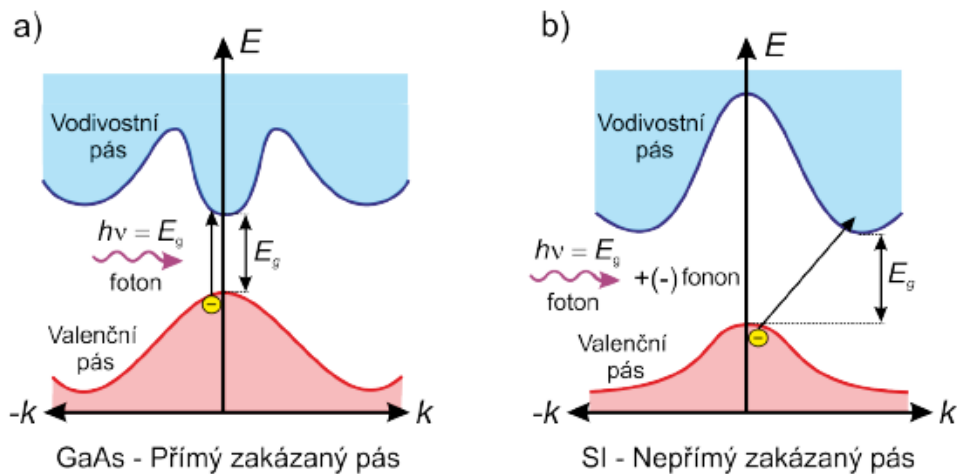
Rekombinační procesy v polovodičích a jejich optické vlastnosti

Mechanické a některé chemické vlastnosti polovodičů jsou určeny především jejich strukturou (síla a charakter vazeb, mřížka atd.). Optické a elektrické vlastnosti jsou naproti tomu silně závislé na již zmíněné pásové struktuře polovodičů. Důležitá není jen velikost zakázaného pásu, ale i to, zda se jedná o polovodiče s přímým nebo nepřímým zakázaným pásem. Vzdálenost mezi maximem zakázaného a minimem vodivostního pásu není pro všechny elektronové stavy na hraně zakázaného pásu stejná, ale je závislá na hybnosti elektronu v daném stavu. Tato závislost se zobrazuje v tzv. k -prostoru (prostor definovaný energií elektronů a jejich hybností, respektive vlnovým číslem k). Pokud odpovídá minimum vodivostního pásu a maximum valenčního pásu stejně hodnotě vlnového čísla (leží v k -prostoru nad sebou), jedná se o polovodič s přímým zakázaným pásem (většina binárních polovodičů, **Obr. 3a**). V opačném případě se jedná o polovodič se zakázaným pásem nepřímým (elementární polovodiče, **Obr. 3b**). Forma zakázaného pásu zásadním způsobem ovlivňuje rekombinační vlastnosti látky, tedy proces návratu excitovaných nosičů do původních stavů. Po excitaci totiž vybuzené elektrony termalizují (emitují fonony a tím se propadají vodivostním pásem) do volného stavu s nejnižší možnou energií, což bývá dno vodivostního pásu. Díry naopak směřují na vrchol valenčního pásu. Vybuzené elektrony a díry se následně rekombinují přes zakázaný pás a tím se vrací do původního stavu před excitací. Rekombinační přechod musí splňovat zákon zachování energie

(ZZE) i hybnosti (ZZH). U přímých polovodičů je ZZH splněn automaticky a ZZE je splněn vyzářením fotonu o rozdílu energie excitovaného elektronu a díry (zářivá rekombinace) nebo pomocí nezářivé rekombinace, kdy elektron odevzdá energii jinou cestou, například přes stavy v zakázaném pásu.³ Jev, při kterém látka generuje světlo tímto mechanismem, označujeme jako luminiscence. Spektrum rekombinačních procesů je široké, ale v jednoduchosti se dají dělit podle počtu entit, které se jich účastní na Augerovské (3 entity), bimolekulární (2 entity) a monomolekulární. U nepřímých polovodičů nemůže zářivá rekombinace proběhnout tak snadno, protože pro splnění ZZH musí být současně emitován fonon. Nepřímé polovodiče jsou tedy špatnými zdroji světla, což omezuje jejich aplikační potenciál. Efektivita luminiscence je zásadní vlastnost každého polovodiče a je kvantifikována tzv. kvantovým výtěžkem (z angl. quantum yield, QY), která je dána poměrem mezi množstvím vyzářené a absorbované energie:

$$QY = \frac{E_{vyz}}{E_{abs}} \cdot 100 \% \quad (1)$$

U některých polovodivých materiálů se tato hodnota blíží až 100 % (PbS), u křemíku (nepřímý polovodič) dosahuje hodnot okolo 0,001 %.



Obrázek 3. Energetická závislost elektronových stavů na jejich vlnovém čísle pro a) přímé polovodiče, b) nepřímé polovodiče. Na schématech je znázorněn princip excitace elektronu.

Elektrické vlastnosti polovodičů

Mezi základní elektrické vlastnosti látek patří dielektrická permitivita ϵ_r (relativní permitivita), elektrická měrná (specifická) vodivost G (σ) a difuzní délka (koeficient) nosičů $L(D)$. První jmenovaný parametr určuje míru zeslabení elektrického pole v dané látce a tím mnoho jevů spojených s interakcí s elektrickým polem (například i hodnotu indexu lomu), zatímco druhá

určuje schopnost látky vést elektrický proud jakožto reakci na přiložené elektrické napětí. Obecně je specifická vodivost definovaná jako:

$$\sigma = \sum_i \mu_i q_i n_i, \quad (2)$$

kde μ značí pohyblivost nosiče, q je elektrický náboj na nosiči (násobek elementárního náboje) a n je hustota nosičů. Poslední zmíněné fyz. veličiny L , resp. D určují střední vzdálenost, resp. rychlosť difuze nosičů, tedy kam se excitovaný nosič dostane za střední dobu života, resp. jak rychle. Tyto parametry jsou úzce spojeny s pohyblivostí nosičů. U anorganických objemových polovodičů je vedení elektrického proudu realizováno pohybem elektronů a děr. Velikost vodivosti je závislá na koncentraci těchto volných nosičů náboje, která u čistých (intrinských) polovodičů nebývá vysoká. Jejich vodivost se zvyšuje tzv. dopováním (extrinské polovodiče), kdy je atom polovodiče nahrazen jiným atomem, který do látky dodá volný elektron (donor) nebo díru (akceptor). U elementárních polovodičů se jedná o prvky ze skupiny III. (dodávají díru, polovodiče typu p) a skupiny V. (dodají volný elektron, polovodiče typu n). Obdobně můžeme dopovat i binární a jiné polovodiče. Mechanismus zvyšování vodivosti zde však není tak jednoduchý, protože jeden prvek může být donor i akceptor podle toho, jaký atom v krystalické mřížce nahradí.⁴ U organických polovodičů je princip vodivosti ještě komplikovanější. K zvýšení vodivosti je nutné provést disociaci π vazeb. Toho může být docíleno pomocí světla nebo přímým vstřikováním náboje, ale nejčastěji dopováním organického polovodiče, kdy je například pomocí přítomnosti oxidačního činidla ve formě halového prvku odveden jeden elektron z π vazby. Vodivost výsledné organické látky je poté realizována pomocí polaronů, bipolaronů nebo solitonů.

Přítomnost defektů a kvazičástic nekomplikuje pouze popis absorpčních/rekombinačních jevů,³ ale i pohyblivosti nosičů náboje a jejich koncentrace. To vede k projevům i jiných vodivostních mechanismů než standardní elektron děrové vodivosti (pásová vodivost), která je typická pro uspořádané polovodiče. U neideálních polovodičů se může projevovat přeskok mezi lokalizovanými stavami (z angl. hopping transport), kdy je transport nosičů náboje realizován přeskokem tepelně aktivovaných nosičů mezi těmito stavami. Pokud je vzdálenost lokalizovaných stavů konstantní, tak je specifická vodivost popsána tzv. Arheniovou rovnicí (**rov. 3a**). V opačném případně mluvíme o přeskocích na proměnnou vzdálenost (z angl. variable range hopping – VRH, **rov. 3b**). VRH byl popsán Mottem a je velmi běžným mechanismem vodivosti u neuspořádaných (amorfních) polovodičů a vodivých polymerů, kde

dochází k transportu polaronů.⁵ Teplotní závislost obou vodivostních mechanismů lze popsát dle následujících vztahů:

$$\sigma_{Arh} = \sigma_0 \exp\left(-\frac{\Delta E_a}{k_b T}\right), \quad \sigma_{VRH} = \sigma_0 \exp\left(-\left(\frac{T_0}{T}\right)^{\frac{1}{d+1}}\right), \quad (3a, 3b)$$

kde ΔE_a je aktivační energie přeskoku, T je termodynamická teplota, k_b Boltzmanova konstanta, σ_0 měrná vodivost při nekonečné teplotě, T_0 Mottova teplota vázaná na daný materiál a d dimenze polovodiče (1-3). Mimo tyto vodivostní mechanismy se u neuspořádaných polovodičů může projevovat excitonová vodivost, která je obdobou předešlého mechanismu, kdy ovšem musí nejprve dojít k disociaci excitonů v látce. Poslední běžným transportním procesem je kvantově-mechanické tunelování projevující se v polykrystalických látkách (krystalické zóny oddělené amorfni složkou) nebo souboru blízkých nanostruktur (shluhy nanočástic, kvantové vrstvy atd.).

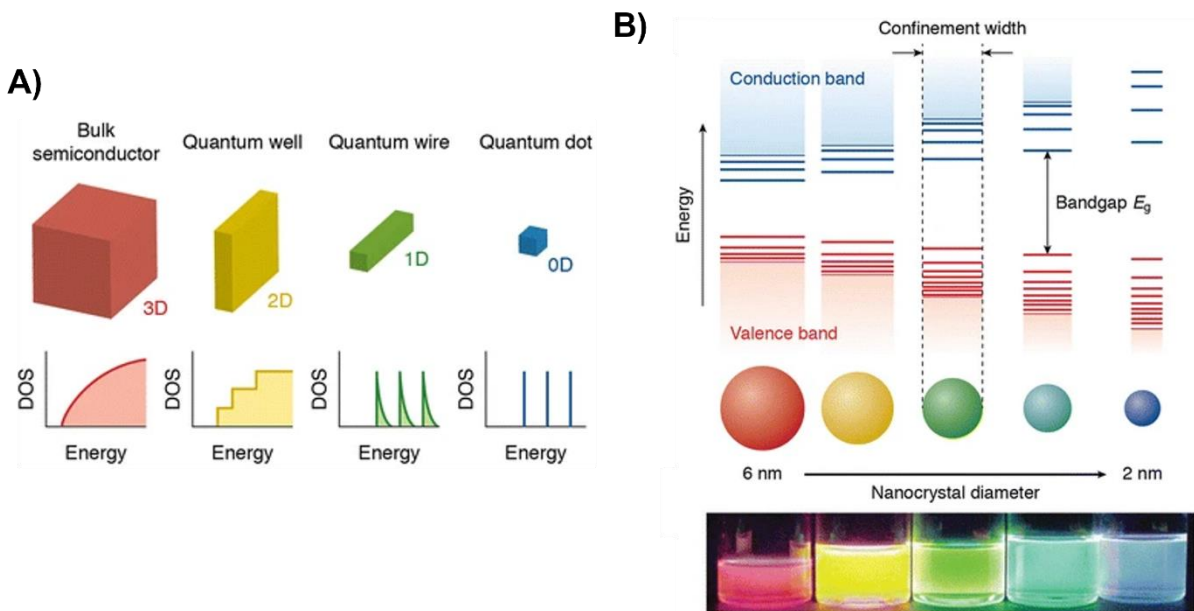
1.2. Původ výjimečných vlastností nanomateriálů

I přes širokou aplikovatelnost různých polovodičů stále narážíme na hranice jejich vlastností. Příkladem je velmi omezená možnost ladění velikosti jejich zakázaného pásu, hustoty stavů nebo preferovaných rekombinačních procesů. Tyto překážky lze obejít přechodem k jejich nanostrukturním formám. Snížením rozměrů totiž často dochází nejen k vylepšování stávajících vlastností polovodičů mimo hranice běžné pro jejich objemové formy, ale dokonce jim můžeme přidat vlastnosti, které předtím neměly. Typickým příkladem je vysoký QY u polovodičů s nepřímým zakázaným pásem nebo vysoká reaktivita u látek, které jsou ve své objemové formě stabilní.^{6, 7} Tyto modifikace jsou způsobeny především přítomností dvou efektů: kvantově-rozměrový jev (z angl. quantum confinement effect) a zvýšený vliv povrchu k objemu nanostruktur. V této kapitole se proto podrobně zaměříme na popis vlastností polovodičových nanostruktur. Ukážeme podstatu obou výše zmíněných jevů a jejich vliv na energetickou distribuci elektronových stavů, relaxační a rekombinační procesy a s tím spojené optické vlastnosti nanočástic. Částečně ukážeme i jiné než optické vlastnosti nanomateriálů a popíšeme jejich původ.

Vliv kvantově-rozměrového jevu na energetické stavy v nanostrukturách

Snižováním rozměrů materiálů pod hodnotu Bohrova poloměru excitonu a_x dochází k růstu vlivu tzv. kvantově-rozměrového jevu. Tento efekt se projevuje ve dvou směrech: a) dochází

ke změně hustoty energetických stavů v látce a b) dochází k růstu šířky zakázaného pásu (tzv. otevírání zakázaného pásu).¹ Přestože oba jevy pozorujeme ve všech látkách, nejvýznamněji ovlivňují vlastnosti právě polovodičů. Kvantově-rozměrový jev totiž při snižování velikosti látky nejprve mění vlastnosti okrajů energetických pásů, kde se nachází nosiče, které na rozdíl od vodičů a izolátorů do značné míry definují optické a elektrické vlastnosti právě polovodičů. U kovů a izolátorů se projevují až s výraznějším snížením velikosti.¹



Obrázek 4. a) Rozdělení hustoty stavů v různých nanostrukturálních látkách, b) Změna hustoty stavů v kvantové tečce v závislosti na snižování jejich rozměrů. Uvedena je i reálná luminiscence daných nanočástic (licence obrázků CC BY, majitel práv Springer Nature).³

Energetická závislost hustoty stavů nanostruktur $g(E)$ je závislá na tom, v kolika směrech je látka prostorově omezena. Omezíme-li ji v jednom směru, dojde k přechodu od klasické závislosti hustoty stavů $g(E) \sim E^{1/2}$ ke schodovitému rozdělení (**Obr. 4a**). Tyto nanostruktury označujeme jako kvantové jámy (2D struktury). Sítě kvantových jam vytváří tzv. supermrížky a bývají realizovány jako tenké vrstvy binárních a/nebo ternárních polovodičů. Mezi významné aplikace těchto struktur patří zdroje světla (LED, lasery), fotodetektory nebo i fotovoltaika a jiné, kde se využívá především tunelování nosičů ve směru kvantového omezení.⁸ Látky prostorově omezené ve dvou směrech označujeme jako kvantové drátky (1D struktury). Jejich energetické spektrum již není spojité, ale roste skokově z nulové hodnoty s pozvolným dozvíváním (**Obr. 4a**). U těchto struktur bývá využíváno jejich specifických vodivostních vlastností v jediném neomezeném směru. Kvantové dráty se využívají také ke studiu jevů spojených s nanovodivostí. 1D struktury mohou být jak anorganického,⁹ tak organického

původu. Ty organické bývají ve formě nanotrubiček (vodivé polymery, uhlík).¹⁰ Objekty omezené ve všech směrech označujeme jako nanočástice, případně kvantové tečky (0D, z angl. quantum dots - QDs). U nich dochází k přechodu od původně spojitého energetického spektra až k diskrétnímu. Navíc se snižujícími rozměry roste jejich zakázaný pás a dochází ke stabilizaci excitonů, což významně ovlivňuje jejich absorpční i luminiscenční vlastnosti (**Obr. 4b**).

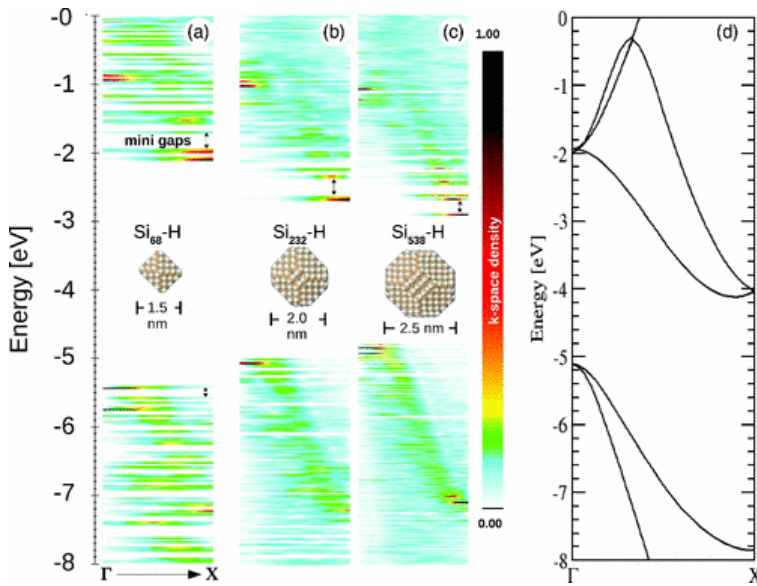
Mezi základní fyzikální představy vysvětlující vliv kvantově-rozměrového jevu patří Heisenbergův princip neurčitosti:

$$\Delta x \Delta p_x \geq \frac{\hbar}{2}, \quad (4)$$

kde Δx a Δp_x popisuje neurčitost polohy a hybnosti částice a \hbar je redukovaná Planckova konstanta. V objemové látce je volný elektron dostatečně delokalizovaný, aby existovala jen malá neurčitost jeho hybnosti. V omezeném prostoru však dochází k růstu neurčitosti hybnosti a tím rozmazání elektronu v k -prostoru. Výsledné energetické stavы elektronů pak mohou být považovány za superpozici stavů v k -prostoru objemového materiálu.¹¹ Stabilizace excitonů (růst vazebné energie) je možné odůvodnit stlačením jejich rozměrů v kvantové tečce, což zesílí vzájemnou Coulombickou interakci mezi dírou a elektronem.

Tolik základní teorie nanomateriálů, nicméně přechod látky z objemové formy k nanostruktúře není zdaleka tak jednoduchý, jak bývá prezentováno (**obr. 4b**). V širokém rozsahu velikostí i nad Bohrův poloměr se jedná o kombinaci vlastností obou forem materiálů. Přesněji se to pokusíme vysvětlit na příkladu kvantových teček. V prvé řadě je nutno říci, že vytváření diskrétních energetických stavů v kvantových tečkách se projevuje až v tzv. režimu silného kvantově-rozměrového jevu, který nastává, pokud je jejich poloměr R v intervalu hodnot $\sim 1 \text{ nm} < R < a_x$. Kvantové tečky o poloměru menším než 1 nm jsou již složeny z tak malého množství atomů, že u nich nemá cenu hovořit o prostorovém uspořádání. U kvantových teček s mírně větším R než $4a_x$ se projevuje režim slabého kvantově-rozměrového jevu. Za téhoto podmínek kvantově-rozměrový jev způsobuje pouze kvantování kinetické energie pohybu těžiště excitonů. Přechodovou oblast definovanou na intervalu poloměrů $a_x < R < 4a_x$ označujeme jako režim středního kvantově-rozměrového jevu.¹² Jak již její název napovídá, už v tomto intervalu začíná docházet ke komplexnějším efektům spojeným s kvantově-rozměrovým jevem, jako je například otevřání zakázaného pásu. Pro představu, u křemíkových kvantových teček vykazujících $a_x = 4,2 \text{ nm}$ se modrý posuv luminiscenčního spektra, který je typický projeven otevřání zakázaného pásu, projevuje od průměru okolo 12 nm.¹³ Nicméně

ani v oblasti silného kvantově-rozměrového jevu nedojde nárazově k diskretizaci energetických stavů v kvantové tečce, ale spíše k pozvolnému přechodu od objemové hustoty s postupným otevíráním zakázaného pásu. Realitě tedy mnohem více odpovídá obr. 5a, který ukazuje simulaci stavů v křemíkových nanočásticích o průměru 1,5 – 2,5 nm, což je významně pod hranicí a_x pro křemík. Z obrázku je patrné, že i přes vznik diskrétních oblastí v energetickém spektru kvantových teček odpovídá rozložení hustoty stavů závislosti pozorované v jejich objemové formě.

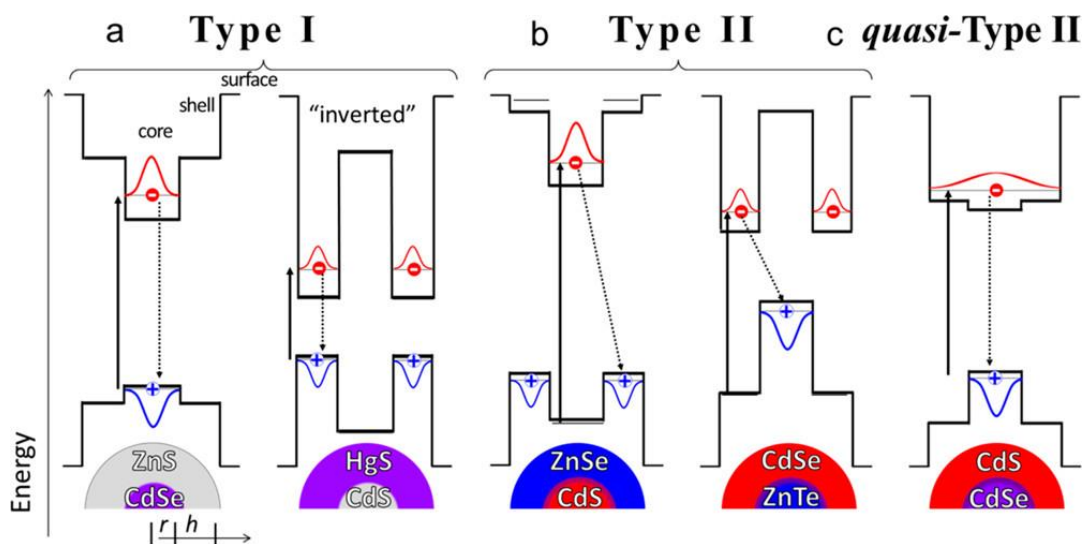


Obrázek 5. DFT simulace (z angl. density functional theory) hustoty stavů valenčního a vodivostního pásu v k -prostoru pro různé velikosti křemíkových kvantových teček. Simulace je srovnána s energetickým rozdělením stavů vodivostního a valenčního pásu v k -prostoru objemového křemíku (použito se svolením majitele práv John Wiley and Sons).¹⁴

Vliv povrchu na energetické stavy v nanostrukturách

Energetické stavy a vlastnosti kvantových teček obecně jsou významně ovlivněny nejen svou velikostí, ale i povrchem, který bývá tvořen až desítkami procent všech atomů.¹⁵ Povrchové atomy totiž z důvodů nedostatku *vhodných sousedů* nemají možnost vytvářet vhodně orientované vazby, a tak vznikají silně deformované vazby. Tento efekt pozorovaný i u běžných povrchů je významně zesílen zakřivením povrchu teček. Takto namáhané vazby mají na rozdíl od objemových vazeb výrazně nižší disociační energii, což zvyšuje jejich reaktivnost. Povrch teček proto přirozeně obsahuje vysoké množství různých strukturních defektů (pasti, nesdílené elektronové orbitaly, kývavé vazby atd.). Mnoho druhů kvantových teček je z tohoto důvodu

také silně náchylných k oxidaci.¹⁶ Toto vše mění energetickou strukturu nanočástice, především skrz vznik lokalizovaných stavů v zakázaném pásu, nicméně deformace vazeb může ovlivňovat i charakter původních energetických pásů v tečce, a tím pádem i její optické a elektrické vlastnosti.¹⁷ Z toho důvodu se povrch kvantových teček upravuje ať už za účelem snížení počtu defektů a jejich stabilizaci, nebo se cílenou úpravou ladí jejich vlastnosti.



Obrázek 6. Typy tzv. jádro/slupka polovodičových heterostruktur. U každého typu je zobrazeno i prostorové rozložení pravděpodobnosti výskytu jednotlivých nosičů (použito se svolením majitele práv ACS Publishing).¹⁸

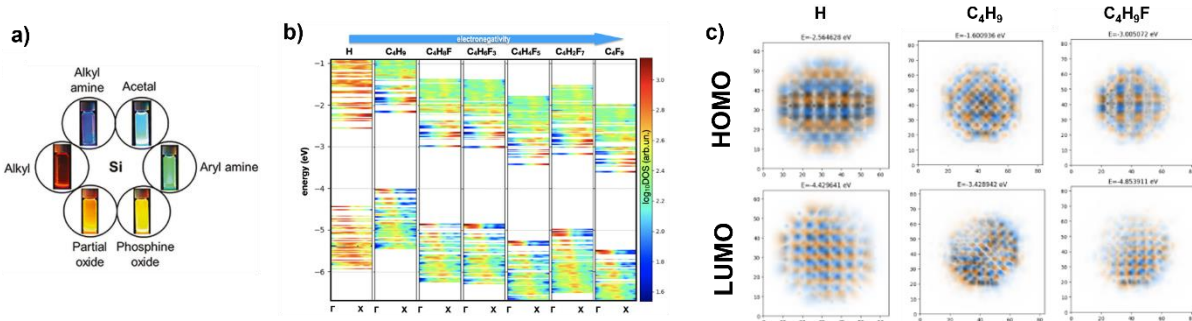
Prvním způsobem úpravy povrchu kvantových teček (terminace/pasivace) je vytvoření tzv. jádro/slupka hybridní struktury (z anglicky core/shell, někdy značeno jako core@shell). Jádrem se rozumí pasivovaná tečka a slupka je tvořena tenkou vrstvou polovodiče o obdobné mřížkové konstantě a různé velikosti zakázaného pásu (**Obr. 6**). Podobného efektu se dá případně docílit i zabudováním tečky do matrice.¹⁹ Vytvoření struktury jádro/slupka nevede jen k efektivní pasivaci povrchových stavů, ale na základě kombinace velikostí zakázaného pásu obou polovodičů můžeme měnit prostorovou lokalizaci excitovaných nosičů (**Obr. 6**). Mezi nejběžnější typy této hybridních struktur patří tzv. Typ I a II. První jmenovaná struktura lokalizuje nosiče v jádře struktury, což zvyšuje efektivitu zářivé rekombinace (zdroje světla). Druhý typ má přesně opačný efekt a může být použit například k transportu excitovaných nosičů. Jako metoda přípravy jádro/slupka struktury je považována i přirozená oxidace některých polovodičů (například Si/SiO₂), která také vede k pasivaci jejich povrchu. Oxidová slupka bývá tlustá maximálně několik málo atomárních vrstev, které poté brání další oxidaci jádra.¹⁶

Nanočástice bývají terminovány také tzv. ligandem, což může být prvek, funkční skupina nebo i komplikovaná organická molekula. Cílem této terminace bývá nejen pasivovat lokalizované stavy na povrchu. Chemické složení ligantu ovlivňuje schopnost sekundární terminace či následné zabudování tečky do matrice a mění i dispergovatelnost teček v roztocích, jelikož mění rozložení elektrického náboje na povrchu tečky a tím i její elektrokinetický potenciál v různých roztocích.²⁰ Ligand může mít také několik funkčních vlastností. Může sloužit k efektivnímu přenosu energie z tečky nebo jako barevná značka. Kvalita terminace je dána nejen chemickým složením ligantu, ale i jeho velikostí. Z prostorových důvodů nelze všechny povrchové vazby terminovat velkou organickou molekulou. Svůj vliv při efektivitě terminace hraje i velikost nanočástice. Obecně platí, že čím menší tečka, tím je větší zakřivení povrchu, a lze tedy povrch snadněji terminovat. Vlastnosti povrchu jsou navíc často ovlivněny i různými facetami kvantových teček.^{15, 21}

Samostatnou kapitolu při terminaci ligandem tvoří jeho vliv na vnitřní energetické stavu teček, které jsou již tak pozměněny kvantově-rozměrovým jevem. Nejsilněji ovlivnitelné jsou v tomto směru polovodivé tečky obsahující kovalentní vazby, u kterých se projevuje vysoká míra sdílení elektronů v jádře tečky (Si, Ge).²²⁻²⁵ Modelovým systémem pro studii úpravy povrchu jsou křemíkové kvantové tečky. Ty jsou složeny nejen z kovalentních vazeb, ale po své syntéze bývají často terminovány vodíkem, jehož elektronegativita je blízká křemíku (2,2 pro vodík vs. 1,9 pro křemík). Rozložení energetických stavů v tečce tedy vodíková terminace ovlivňuje jen minimálně. U křemíkových teček byl pozorován posun luminiscenční spektra napříč téměř celým viditelným intervalom jen na základě rozdílné terminace povrchu (**Obr. 7a**).^{23, 25} Vlnové funkce elektronů z povrchových atomů o výrazně odlišné elektronegativitě než má křemík totiž snadno penetrují dovnitř nanočástice, a tím mění prostorové rozložení elektronových vlnových funkcí v tečce a tím i energetických stavů (**Obr. 7b,c**). Zde je dobré zdůraznit, že se stále jedná o luminiscenci pocházející z jádra teček, a ne příměsovou luminiscenci. To bylo prokázáno nejen měřením dob doznívání luminiscence, ale i simulacemi rozložení energetických stavů a rekombinačních procesů (**Obr. 7b,c**). Více si o vlivu povrchu na optické vlastnosti kvantových teček řekneme v kap. 1.3.

V této podkapitole bylo ukázáno, jak významně a komplexně ovlivňuje velikost a povrchová chemie energetické stavu kvantových teček. Výčet daných jevů není úplný, jelikož svůj vliv má i okolí či shluky nanočastic. Výsledné optické a elektrické vlastnosti jsou však dány nejen hustotou energetických stavů, ale i efektivitou přechodů nosičů mezi těmito stavů, a tedy efektivitou různých relaxačních a rekombinačních procesů excitovaných nosičů. Jejich

klasifikace a kvantifikace hraje často zásadní roli v pochopení chování nanomateriálů, což bude obsahem následující podkapitoly.



Obrázek 7. a) Fotoluminiscence křemíkových kvantových teček o různé terminaci (licence obrázku CC BY-NC-ND, majitel práv Walter de Gruyter GmbH)²³. DFT simulace b) energetické závislosti logaritmu hustoty elektronových stavů a c) prostorové rozložení HOMO a LUMO stavů křemíkové kvantové tečky (řez x-z rovinou; použito se svolením majitele práv ACS Publishing).²⁶

Dynamiky excitovaných nosičů v nanostrukturách

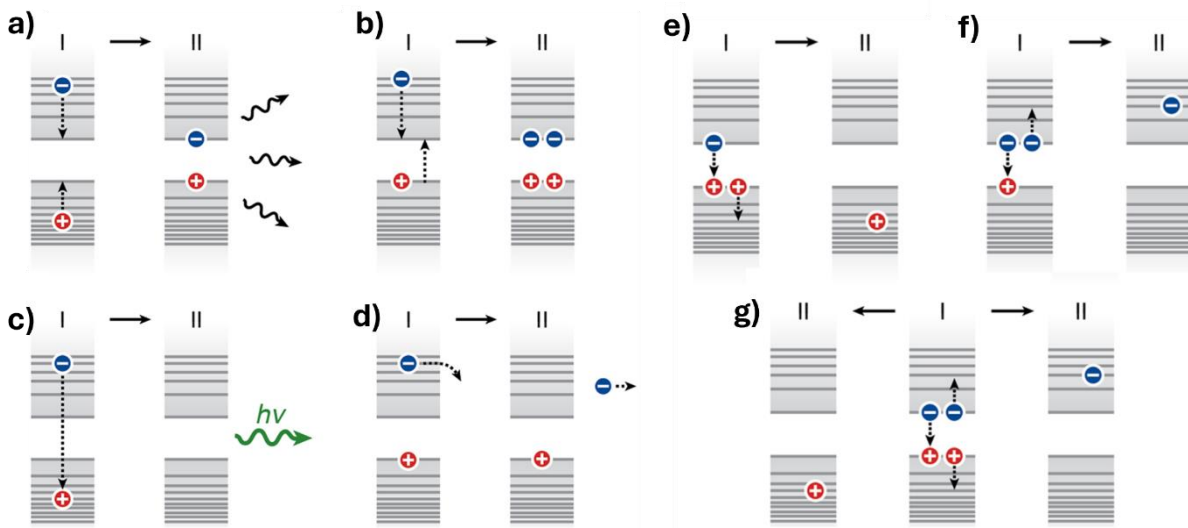
Dynamikou excitovaných nosičů rozumíme děje, které nastávají od jeho excitace až po jeho návrat do stabilního stavu. Přestože excitovaný nosič může přejít do původního stavu pomocí jednoho děje, v kvantových tečkách k tomu většinou musí provést hned několik různých po sobě následujících přechodů. Škála těchto dějů je rozmanitá a sahá od termalizace (relaxace za současného vyzáření fononu), záhytu na lokalizovaných stavech, transportu/transferu do ligandu či jiné nanočástice, zářivé mezipásové rekombinace až po Augerovské procesy.³ Následnost jednotlivých dějů není jednoznačně dána, excitovaný nosič má v určitém stavu možnost vykonat několik různých paralelních přechodů. Pravděpodobnost těchto přechodů je charakterizována koeficientem míry (rychlosti) daného přechodu k . Čím větší je rychlosť přechodu, tím efektivnější přechod je, a tím pravděpodobněji se touto cestou bude excitovaný nosič ubírat. Parametr k se běžně využívá při teoretickém popisu vnitřních procesů excitovaných nosičů. Z praktického hlediska se ovšem pro dynamiky přechodů častěji využívá jeho převrácení hodnota τ , která v jednoduchosti popisuje průměrnou dobu, za kterou daný přechod proběhne. Návaznost přechodů a jejich efektivita hraje zásadní roli pro vlastnosti objektů jako je QY, absorpční průřez, celková doba doznívání, transportní vlastnosti látky atd., jak si ukážeme v následující podkapitole.²⁷ Jednotlivé přechodové děje probíhají ve velmi širokém časovém intervalu od desítek fs až po minuty (hodnoty dob života τ). Pro snadnější

orientaci v těchto dějích si je rozdělíme a popíšeme v jim typických časových oknech, a to od nejrychlejší, po ty nejpomalejší.

Ultrarychlé procesy (10 fs – 10 ps). Po excitaci dochází mezi elektronem a dírou k vzájemným elastickým srážkám, než je mezi nimi nastoleno Fermi-Diracovo rozdělení pro vysoké energie (~ 10 fs).²⁸ Tyto nosiče následně termalizují (chladnou) do nejnižšího možného stavu v daném pásu přes emisi fononů (HOMO/LUMO u kvantových teček), což za běžných podmínek probíhá v časovém horizontu mezi od 100 fs do 10 ps (**Obr. 8a**). Existuje hned několik jevů zpomalujících termalizaci. Mezi nejběžnější patří tzv. efekt hrdla láhve (z angl. phonon bottleneck).²⁸ V jednoduchosti se jedná o situaci, kdy se výrazně zpomalí efektivita generace optických fononů, a tím rychlosť termalizace. K tomu může dojít, pokud generace fononů výrazně převýší jejich doznívání, čímž se zvýší efektivita jejich reabsorpce elektronem. Tento jev je nejčastěji u objemových látek vyvolán příliš vysokou koncentrací excitovaných nosičů, je však zesilován přítomností jádro/slupka struktury či obecně vlivem kvantově-rozměrového jevu. Pro pozorování tohoto jevu jsou vhodné především některé jádro/slupka kvantové tečky struktury Typu I a II.^{29, 30} Kromě termalizace může docházet i k jiným ultrarychlým procesům excitovaných nosičů. Jejich efektivita však bývá výrazně nižší a pro jejich pozorování je nutné zpomalení termalizace. Pokud mají excitované nosiče dvojnásobnou energii zakázaného pásu, může dojít k bi- nebo multi-excitonové excitaci, kdy excitované nosiče předají část své energie jinému elektron-děrovému páru (**Obr. 8b**).³¹ Nosiče mohou také přímo zářivě rekombinovat (**Obr. 8c**).^{32, 33} V neposlední řadě může excitovaný nosič daný materiál opustit, pak mluvíme o transferu horkého nosiče, k němuž dochází například mezi shlukem kvantových teček či v rámci nanohybridu (**Obr. 8d**).^{34, 35}

Procesy předcházející zářivé rekombinaci – subnanosekundové procesy (<1000 ps). Do této skupiny patří téměř výhradně procesy Augerovské. Jedná se o tři a více molekulární děje, kdy ve většině případů dojde k nezářivé rekombinaci elektron-děrového páru za současného předání energie jinému nosiči nebo excitonu. Ve výjimečných případech může dojít k zářivé Augerovské rekombinaci.³⁶ U objemových látek je k dosažení dobré efektivity těchto procesů nutná velmi silná excitace, a tak nebývají tolik významné.^{37, 38} To se však mění přechodem ke kvantovým tečkám, a to ze dvou důvodů. Prvním je výrazné omezení prostoru excitonů, a tím zesílení Coulombické interakce mezi nosiči náboje. Druhým je fakt, že některé Augerovské přechody jsou zakázané z důvodů nezachování celkové hybnosti. Kvůli výrazné lokalizaci nosičů v kvantových tečkách, a tím spojeným rozmažáním jejich hybnosti, dochází k zvýšení efektivity i těchto přechodů.³⁹ Mezi nejběžnější Augerovské procesy v nanomateriálech patří rekombinace excitonu s předáním energie jinému excitovanému nosiči

(Obr. 8e-f). Této interakci se někdy říká trionová (mezi 3 nosiči).³⁸ Méně často dochází k předání energie lokalizovanému nosiči (v zakázaném pásu). Při multiexcitonové excitaci může energie rekombinujících nosičů přejít na jiný exciton (**Obr. 8g**). Časový horizont těchto procesů je silně závislý na materiálu a míře prostorového omezení, běžně se pohybuje do 1000 ps.^{3, 31} Jelikož se jedná o nezářivé přechody, pro většinu nanomateriálových aplikací je nutno jejich přítomnost omezit. Jednou z možností je zvýšit velikost kvantových teček, což ovšem ovlivní jejich jiné vlastnosti. Další možností je zvolit vhodnou jádro/slupka strukturu, která vede ke snížení prostorového překryvu excitovaných nosičů nebo k dielektrickému stínění mezi nosiči.^{40, 41}



Obrázek 8. Schématické znázornění relaxační a rekombinační procesy excitovaných nosičů v látce. a) – d) Termalizační procesy excitovaných nosičů. e) – g) Augerovské procesy excitovaných nosičů (licence obrázků CC BY, majitel práv Springer Nature).³

Zářivá rekombinace a další procesy termalizovaných nosičů (1 ns – 1 ms). Po překročení 1 ns od excitace dochází u většiny látek k aktivaci hlavních kanálů zářivé rekombinace excitovaných nosičů. Tím nejdůležitějším je spontánní zářivá rekombinace (též spontánní emise), která je u drtivé většiny nanočástic hlavním zdrojem emitovaných fotonů. Tento proces probíhá nejčastěji mezi delokalizovanými excitovanými nosiči na dnech energetických pásů, případně HOMO/LUMO či diskrétních stavech kvantových teček. Další možností je spontánní zářivý přechod s lokalizovaným stavem či zářivým přechodem s dopantem/ligandem s vysokým kvantovým výtěžkem (například Mn či Tb ionty). První jmenovaný však většinou přispívá k nezářivým přechodům, a tedy snižuje efektivitu zářivé rekombinace, druhý jmenovaný se dá spíše brát jako rekombinace na příměsi než uvnitř

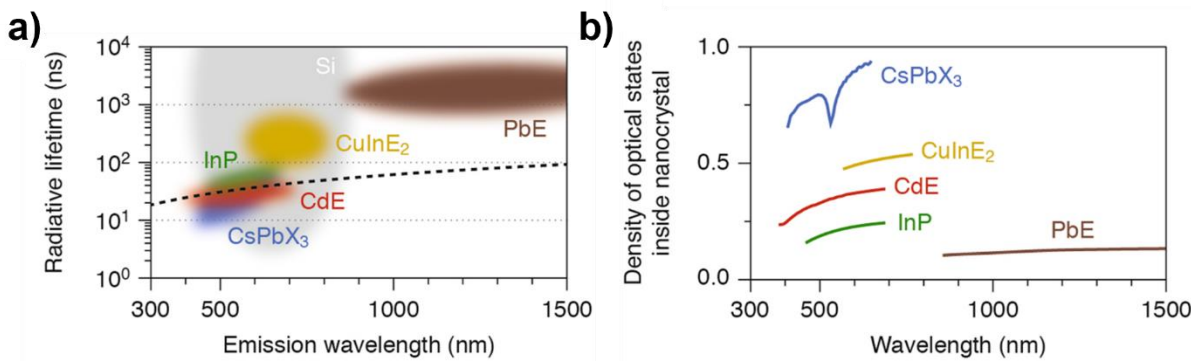
nanočástice. Vlastnosti emitovaného záření (doba doznívání luminiscence, pozice a tvar spektra, intenzita) jsou dány mírou překryvu vlnových funkcí excitovaných nosičů a velikostí zakázaného pásu. Dají se tedy zásadně ovlivnit nejen velikostí, tvarem, použitým materiélem, povrchovou úpravou, ale i složením jádro/splášť struktury či okolním mediem, například u koloidních teček. Typickým příkladem je míra zářivých přechodů k_r u delokalizovaných nosičů, která se dá v jednoduchosti vyjádřit následujícím vztahem:⁴²

$$k_r = \frac{C\rho K}{\lambda}, \quad (5)$$

kde λ je vlnová délka emitovaného záření, C je materiálový parametr látky závislý především na jejích elektrických vlastnostech, ρ definuje hustotu stavů a K je kvadrát překryvového integrálu rekombinujících nosičů. Většina těchto parametrů se dá ladit změnou některé z výše zmíněných vlastností tečky.

Přehlednou summaraci zářivých dob života τ_r a hustot stavů na vlnové délce emise pro různé polovodičové kvantové tečky můžeme najít na **Obr. 9a,b**. Kromě vlivu složení na zmíněné vlastnosti můžeme na prvním z grafů také dobře vidět rozdíl mezi kvantovými tečkami polovodičů s přímým a nepřímým zakázaným pásem. Zatímco rozptyl hodnot zářivých dob života u polovodičů s přímým zakázaným pásem je okolo 1 rádu a jen výjimečně přesahuje 1 μ s, u křemíku je situace jiná. Nanočástice křemíku totiž vykazují dva typy zářivých přechodů, tzv. S (z angl. slow) a F (z angl. fast) pás. Prvním je přechod přímý, který je dán rozmazáním excitovaných nosičů v k -prostoru (ns časové okno), těmto přechodům je přisuzována zelená a oranžová část spektra (F-pás). Druhým spontánním rekombinačním přechodem je rekombinace excitonů přes nepřímý pás. Jelikož se jedná o přechod s asistencí emise fononu, probíhá výrazně pomaleji (μ s časové okno, S-pás). Tomuto přechodu je přisuzována emise fotonů ve spektrální oblasti od oranžové až do infračervené spektrální oblasti.²⁵

Obdobně jako v tom předešlém, i v tomto časovém okně může probíhat hned několik nezářivých procesů spojených především se záchytem na pasti, Augerovskými procesy atd.⁴³ Přestože mechanismy záhytu nosičů jsou dlouhodobě studovány, jejich přesný popis není doposud znám. V jednoduchosti se očekává, že jsou spojeny s nesatuřovanými vazbami na povrchu (kývavé vazby). Tento efekt potvrzují i pozorování, kdy dodatečná terminace nanočastic či navázání ligandu vedlo k výraznému zvýšení QY nanočastic.^{13, 22, 25, 44}



Obrázek 9. a) Spektrální závislost doby života zářivého přechodu ($1/k_r$) pro vybrané polovodičové kvantové tečky. b) Spektrální závislost hustoty stavů v kvantových tečkách prezentovaných v a) (licence obrázků CC BY, majitel práv Springer Nature).³

Pomalé procesy na kvantových strukturách (1 ms – 10tky min). V časovém horizontu přesahujícím dobu života excitonů byla pozorována celá řada procesů vedoucích ke změně dynamik rekombinace excitovaných nosičů. Ve své podstatě nejde o nové rekombinační procesy, ale děje, které at' už vratně nebo nevratně mění rekombinační vlastnosti nanočástic. Mezi nejběžnější nevratné změny patří různé fotochemické či fotooxidační procesy, které vedou k permanentním spektrálním změnám luminiscence.^{45, 46} Z fyzikálního hlediska jsou však mnohem zajímavější procesy vratné. Na nanočásticích jich bylo pozorováno hned několik, jako je například efekt intermitence, někdy familiárně označován jako blikání⁴⁷, zpožděná emise,^{48, 49} spektrální difuse,^{50, 51} a další procesy, jež vedou ke snižování (z angl. photodimming) či zvyšování (z angl. photobrightening) intenzity luminiscence.

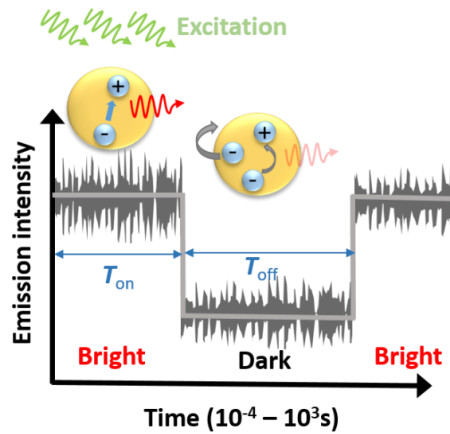
Pro bližší popis některých z těchto jevů je nutné zavést termíny jasná (z angl. bright) a temná (z angl. dark) nanočástice. Jako jasnou označujeme kvantovou tečku, u níž míra dominantního zářivého rekombinačního procesu je výrazně vyšší než u procesů nezářivých, jejich kvantová účinnost se poté blíží 100 %. Pokud naopak dominují nezářivé rekombinační procesy, a tedy QY tečky se blíží 0 %, mluvíme o temné tečce.⁵² Ve výjimečných případech byly pozorovány i kvantové tečky s QY mezi těmito hodnotami, které bývají označovány jako šedé (z angl. grey). Interpretace takového chování není snadná a bývá spojena se změnou chování nanočástice v čase nebo přítomností navzájem kompetitivních zářivých a nezářivých přechodů o blízké době života.^{53, 54}

Intermitence je jev, při kterém dochází k náhodným změnám vyzařovacích vlastností na časovém horizontu od milisekund do minut. Tento efekt je znám po více než 25 let a byl pozorován na jednotlivých polovodivých kvantových tečkách (ve shlucích zaniká),

organických nanostrukturách nebo i v organických barvivech.^{47, 55, 56} Přestože byly na tečkách pozorovány různé formy blikání, ve své nejjednodušší formě může být tento jev popsán jako náhodné přepínání teček mezi jasnou a temnou formou. Nejčastěji bývá blikání analyzováno pomocí pravděpodobnostní distribuce (P_{on}/P_{off}) času v jasné (T_{on}) a temné (T_{off}) formě.⁵⁷ Bylo zjištěno, že histogramy hodnot T_{on}/T_{off} pozorované na tečkách velmi často následují mocninou závislost (PLD, z angl. power-law distribution) s exponenciálním odříznutím ve vysokých časech ve tvaru:

$$PLD(t) = t^{-\alpha} e^{-\frac{t}{T}}, \quad (7)$$

kde α nabývá hodnot od 1 do 2. Snaha o vysvětlení procesů stojících za intermitencí patří k významným bodům studia kvantových teček, protože by mohlo vést k omezení temných stavů a tím zvýšení QY nanočástic. Velký důraz je kladen na odhalení fyzikální podstaty efektu zodpovědného za mocninné rozdělení přepínání.⁵⁸ Bylo prokázáno, že zásadní roli hraje například povrch nanočástic. Dostatečně tlustý plášť či určitý ligand efekt intermitence potlačí. K potlačení dojde také ve shluku okolo 10 nanočástic a více.^{47, 59} Kvantové tečky mohou také vykazovat přepínání do šedých stavů⁴⁷. Očekává se, že blikání je spojené s nabíjením povrchu nanočástic, jelikož bylo ukázáno, že ionizace povrchu pomocí Augerovy rekombinace nebo tunelování excitovaného nosiče do povrchové pasti vede k přechodu do temného stavu tečky (Obr. 10).⁶⁰ Nabíjení povrchu bylo také interpretováno pomocí difuzí kontrolovaném elektronovém transferu.⁶¹



Obrázek 10. Schéma přepínání tečky mezi jasným a temným stavem pomocí Augerovy rekombinace.

Další jmenovaný jev, spektrální difuze, je spojen s náhodnou fluktuací maxima luminiscenčního spektra teček v řádu několika nanometrů.⁵⁰ Jelikož tyto změny probíhají

v obdobných časových intervalech jako blikání, očekává se, že i tento jev je spojen s intermitencí. Odložená emise se projevuje prodloužením doby zářivé rekombinace excitovaných nosičů.⁴⁹ Je pravděpodobně spojena s náhodným uvolněním nosiče z pasti.

Kvantový výtěžek souboru kvantových teček

Se znalostí relaxačních a rekombinačních procesů na kvantových tečkách se můžeme podívat na postup určování výše zmíněných významných parametrů, a to kvantový výtěžek a míra rekombinačních procesů. Kromě již zmíněné definice (**rov. 1**) bývá QY definován pomocí parametrů dynamik excitovaných nosičů jako:²⁵

$$QY = \frac{k_r}{k_r + k_{nr}} = \frac{\tau_{PL}}{\tau_r}, \quad \text{kde } \frac{1}{\tau_{PL}} = \frac{1}{\tau_r} + \frac{1}{\tau_{nr}}, \quad (8)$$

kde k_r je míra zářivého přechodu, k_{nr} celková míra všech nezářivých přechodů, τ_r doba života zářivého přechodu, τ_{nr} celková doba nezářivých přechodů a τ_{PL} doba doznívání luminiscence. Zanedbáme-li efektivitu vyvázání světla a efekt reabsorpce, tyto vztahy by platily s vysokou přesností u většiny homogenních objemových látek a u homogenních souborů navzájem neinteragujících nanočástic. Obecně ale pro kvantové tečky neplatí. Zářivé a nezářivé procesy prezentované v rov. (8) jsou totiž spojeny s vnitřními dynamikami v samotné nanočástici. Přesněji proto bývá veličina definovaná rov. (8) označovaná jako vnitřní kvantový výtěžek – iQY. Jeho hodnota by odpovídala QY, pokud by tečky nebyly ovlivněny tzv. vnějšími ztrátami. Efektivitu zářivých přechodů totiž může snížit vzájemná interakce nanočástic, vliv okolního prostředí, reabsorpce na jiných tečkách, efektivita vyvázání světla ze souboru teček či dynamicky se měnící zářivé schopnosti nanočástic (např. blikání). Tyto jevy snižují efektivitu generace světla a tím hodnotu QY. V souboru teček mohou být přítomny také temné kvantové tečky, které sice fotony absorbují, ale neemitují, čímž také snižují celkový QY. Výsledný kvantový výtěžek by byl tedy dán jako iQY vynásobený koeficientem zahrnujícím všechny vnější uvedené ztráty a přítomnost temných teček.

Tím se dostáváme k další možné definici QY pro kvantové tečky. Obecně se očekává, že u každé nanočástice významně převládá míra zářivé nebo nezářivé rekombinace. Každá nanočástice má tedy iQY velmi blízko buď 100 %, nebo naopak 0 % (jasné a temné tečky). V koloidní disperzi (tečky vzájemně neinteragují) by výsledný QY daného souboru byl dán poměrem množství obou typů častic. V opačném případě by byl snížen o vliv jejich vzájemné interakce. Ani v tomto případě by však u reálného souboru nanočástic nebyl popis jejich QY tak snadný z důvodů možné přítomnosti šedých teček.^{53, 62} Z předešlého popisu je patrné, že

přesné určení vnitřních mechanismů ovlivňujících QY souboru nanočástic bývá v praxi velmi obtížné a často vede k nutnosti úpravy souborů nanočástic a využití komplexních metod, jako je například Purcellův efekt. Přesný popis těchto postupů je mimo rozsah práce a je k nalezení v přiložené literatuře.^{62, 63}

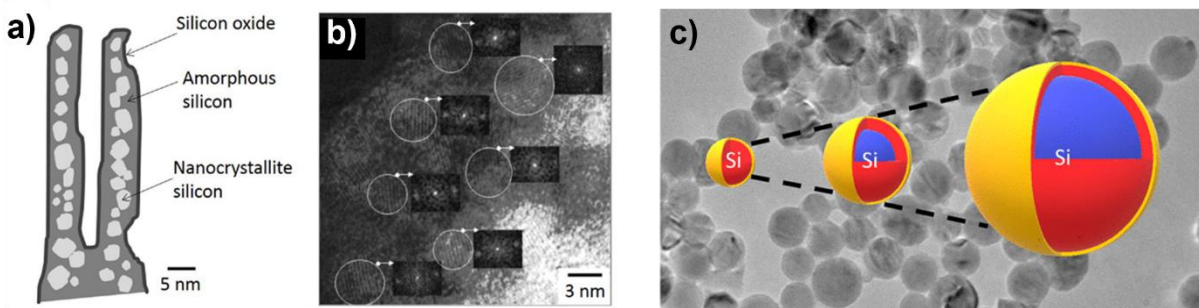
1.3. Křemíkové kvantové tečky

Křemíkové kvantové tečky patří mezi nejběžnější kvantové struktury s kovalentní vazbou a jedny z nejvíce využívaných kvantových teček vůbec. Jejich výzkum je spojen hned s několika zásadními vědeckými i aplikačními milníky. Přestože se nejednalo o první objevené a připravené polovodičové kvantové tečky, ty se datují do 80. let minulého století,⁶⁴ objev křemíkových nanostruktur vykazujících efektivní fotoluminiscenci byl významný vzhledem k poznávání zákonitostí nanosvěta (Canham 1990).⁶⁵ Ve svých počátcích byly zářivé křemíkové nanostruktury označovány jako kvantové drátky, protože vznikly elektrochemickým leptáním křemíkových destiček kyselinou fluorovodíkovou (HF), což mělo vést k vytváření korálovité křemíkové struktury. Hlubší rozbor však prokázal, že intenzivní luminiscence pochází z kvantových teček, které jsou uzavřeny ve slupkách složených z SiO₂ a amorfního křemíku tvořících strukturu korálu. Tento materiál začal být nazýván nanoporézním křemíkem (**Obr. 11a,b**). Dá se říct, že objev nanoporézního křemíku přepsal učebnice fyziky, protože do té doby nebyla pozorována efektivní zářivá rekombinace u nepřímých polovodičů. Následné teoretické studie ukázaly, že luminiscence křemíkových kvantových teček (SiQDs) je spojena s excitonovou rekombinací, jejichž stabilita roste vlivem kvantově-rozměrového jevu. Tato rekombinace, nevyžadující asistenci fononu, je možná kvůli rozmařání hybnosti nosičů v *k*-prostoru.^{66, 67} Na základě studia vlastností SiQDs bylo také předpovězeno, že změna velikosti zakázaného pásu na jejich velikosti, označovaná jako rozměrová energie (z angl. confinement energy), je dána vztahem:

$$E_c \sim \frac{1}{D^x}, \quad (9)$$

kde *D* je velikost kvantové tečky a *x* je parametr o hodnotě v rozmezí 1 – 2. Tento předpoklad se ukázal jako správný a dodnes dochází pouze k zpřesňování hodnot parametru *x*. Dále bylo ukázáno, že s rostoucí velikostí *E_c* nedochází u SiQDs pouze k modrému posuvu luminiscenčních spekter, ale i růstu efektivity zářivé excitonové rekombinace, kdy se tento proces stává v tečkách dominantním rekombinačním kanálem již od hodnoty *E_c* = 0,7 eV.⁶⁷ Aktuální pozorovaný rozsah hodnoty *E_c* spadá do intervalu 0 – 2,1 eV (zakázaný pás ~ 3,2

eV).⁶⁸ Velmi podrobný popis vlivu velikosti na rozložení energetických stavů ve vodíkem terminovaných křemíkových tečkách byl již zmíněn v předešlé kapitole.¹⁴



Obrázek 11. a) Schéma struktury porézního křemíku, b) TEM snímek porézního křemíku s vyznačenými křemíkovými tečkami (licence obrázků CC BY, majitel práv Frontiers Media),⁶⁹ c) schéma struktury SiQDs v závislosti na její velikosti (žlutá – plášt, červená – pod povrch, modrá – krystalické jádro; použito se svolením majitele práv American Chemical Society).⁷⁰

Ruku v ruce s růstem poznání fyzikálních vlastností a vnitřních procesů SiQDs roste i znalost jeho struktury, která se zdá být netriviální. Z důvodů silné deformace křemíkových vazeb v blízkosti povrchu teček se očekává, že jsou tyto nanostruktury pravděpodobně složeny z 3 vrstev: čistý povrch, pod povrch a jádro. Pomineme-li atomovou vrstvu povrchu, tak atomy pod ním nejsou schopny udržet diamantovou krystalickou mřížku typickou pro křemík, ale dochází k její deformaci. Tato zóna následně více připomíná amorfní křemík než ten krystalický. SiQDs tedy více odpovídají jádro/slupka struktuře složené z krystalického/amorfního křemíku. Tloušťka amorfní vrstvy kromě velikosti jádra ovlivňuje i optické vlastnosti teček.⁷¹ Přítomnost popsáne třísložkové struktury se u SiQDs očekává pro velikosti 9 nm a méně (**Obr. 11c**).⁷⁰

Obdobně jako u jiných kovalentních kvantových teček má na vlastnosti těch křemíkových zásadní vliv i jejich povrch. To se u SiQDs projevovalo od úplného počátku, a to prostřednictvím oxidace, která u nich probíhá velmi snadno a vede k modrému posuvu luminiscenčního spektra⁶⁵. Tento jev se vysvětluje na bázi oxidací iniciované snižováním velikosti kvantové tečky, ale také na změně rozložení energetických stavů v tečce¹⁴. Oxidová terminace ovšem také ovlivňuje kvantový-rozměrový jev. Očekává se, že u nanočástic menších jak 3 nm začne růst efekt záchrny excitonů na oxidovaném povrchu, a tím přestávají být závislé na velikosti nanočástice, což vysvětluje saturaci emisní energie na oxidovaných SiQDs okolo 2,1 eV⁷². Oxidace ukřemíkových teček je navíc velmi komplikovaný jev. Pro její iniciaci stačí již několik sekund v kyslíkové atmosféře. Kyslík nejprve způsobí disociaci Si-Si vazeb, mezi

které se sám naváže⁷³. Tomuto procesu se říká páteřová oxidace (z angl. backbone). Následně dochází ke vzniku různých suboxidů se současnou oxidací i vodíkových vazeb, které jsou u nově připravených Si nanočastic běžně přítomné, až dojde k vytvoření stabilní SiO₂ slupky o tloušťce mírně pod 1 nm⁷⁴. Další oxidace přes tuto slupku je nepravděpodobná, protože následná difusní oxidace probíhá u křemíku velmi pomalu a jen při vysokých teplotách (1 °A/s při 1000 °C)⁷⁵. Tato terminace je proto velmi agresivní a stabilní. Pro přípravu jiných typů terminací je nutné používat Si tečky, které nepřišly do kontaktu s kyslíkem. Bylo prokázáno, že atomy spojené s povrchovou terminací silně interagují s jádrem nanočástice a ovlivňují energetické rozložení stavů. Míra vlivu povrchu je závislá na rozdílu elektronegativit křemíku a povrchového atomu. Povrch ovšem nemění rekombinační mechanismus excitonů, který je spojen s jádrem. Může ho pouze urychlovat/zpomalovat a ovlivňovat velikost zakázaného pásu v širokém rozsahu (**Obr. 7a**)^{14,76}. Mezi nejběžnější patří terminace dusíkem, halovým prvkem či pomocí různých uhlíkových funkčních skupin (alkyly, amidy, alkoxy atd.)²⁴. Mezi těmito terminacemi stojí za vyzdvihnutí studie sledující vliv metylace SiQDs teček, kde bylo prokázáno, že přítomnost těchto drobných molekul vyvolává transformaci nepřímého zakázaného pásu na přímý. Toho je docíleno kombinací efektů spojených s kvantově-rozměrovým jevem a vlivem vysokého pnutí na povrchu teček.⁷⁷ Vliv povrchového tlaku na energetické stavy v kvantových tečkách Si byl prokázán již dříve.⁷⁶

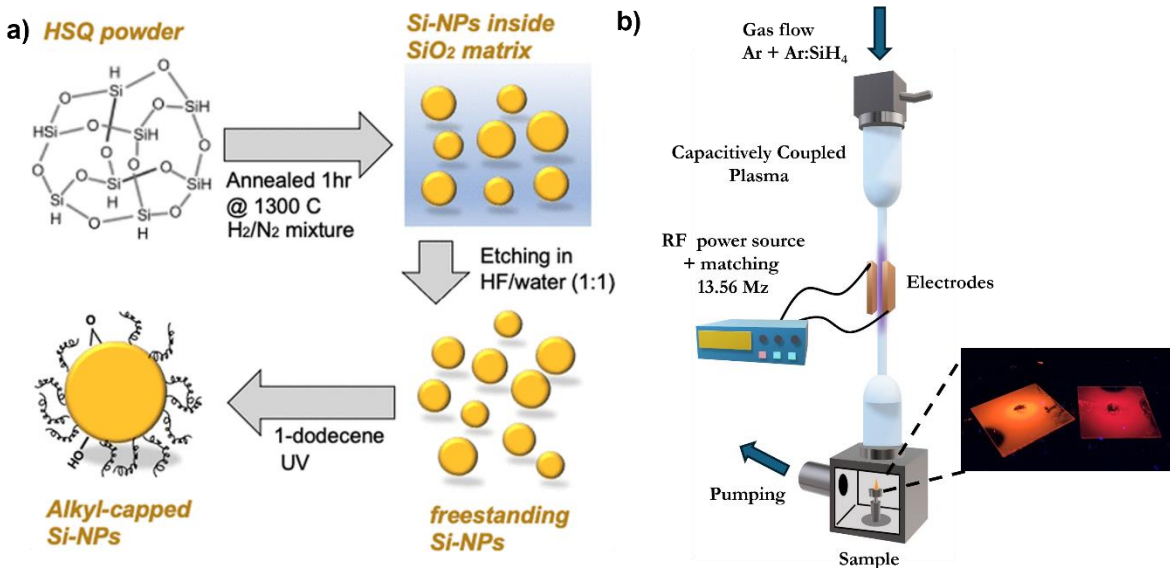
Mezi další významné vlastnosti křemíkových kvantových teček, které rozšiřují záběr jejich aplikačních možností, je nejen jejich nízká toxicita, což není u nanostruktur díky jejich silné povrchové reaktivnosti a složení (např. PbS, CdSe, InAs, GaAs, atd.) pravidlem, ale především biodegradabilita⁷⁸. Bylo prokázáno, že lidské tělo dovede SiQDs odbourat přes kyselinu ortokřemičitou - Si(OH)₄.⁷⁹ Je dobré zmínit, že ani výzkum křemíkových teček se neobešel bez určitých kontroverzí. V roce 2000 byla publikována studie prokazující optický zisk na těchto nanostrukturách⁸⁰. To by otevřelo cestu vytvoření křemíkových laserů, což by mohlo mít zásadní vliv na jeho optoelektronické aplikace, a především na přípravy fotonové výpočetní techniky. Závěry zmíněné studie však byly po živé diskuzi na základě nezapočítání vlivu vlnovodních vlastností použitého materiálu vyvráceny.⁸¹

Studiem rekombinačních procesů v SiQDs, a to především hledáním zákonitostí spojených s pomalou složkou luminiscence se zabývá i výzkum předkladatele.^{54,82} Současně je jeho autorská činnost zaměřena i na zpřesňování pohledu na komplexní strukturu těchto kvantových objektů.⁸³

Metody přípravy a povrchové úpravy křemíkových kvantových teček

Jednou z hlavních výzev při výzkumu nanomateriálů není pouze rozklíčování vlivu různých parametrů na jejich vlastnosti a dynamiky elektronových dějů, ale často také vytvoření vhodných metod jejich přípravy a povrchové úpravy, které by bylo možné používat efektivně, snadno, rychle, ekologicky a ideálně ve velkém rozsahu.

První objevenou metodou přípravy kvantových teček bylo již zmíněné elektrochemické leptání krystalických křemíkových destiček. Tato metoda je ovšem nejen zdlouhavá (\sim dny/v řádu dnů), ale také drahá a její výtěžnost malá.⁶⁵ U kovalentních kvantových teček nelze použít chemická syntéza z roztoků, která je široce využívána u binárních kvantových struktur.⁸⁴ Kovalentní vazba mezi křemíky je totiž příliš silná, což je demonstrováno například vysokou teplotou tání křemíku (\sim 1415 °C) nebo jeho objemovou energetickou hustotou (\sim 75,5 kJ/cm³), která je 2,5krát vyšší než u benzínu. Přestože bylo publikováno několik postupů ukazujících na možné postupy přípravy teček z roztoků, validita daných metod byla často rychle vyvrácena.⁸⁵,⁸⁶ Během let však bylo představeno hned několik alternativních postupů využívajících např. laserovou ablaci křemíkových destiček či oxidaci Zintlových solí (Me_ySi_x, Me = Na, K, Mg) za pomoci mikrovlnného záření.⁸⁷ Ve větším měřítku jsou využívány pouze dvě metody, a to termální disproporcionace křemíkových oxidů a syntéza pomocí netermálního plazmatu. První jmenovaná metoda je založena na žíhání křemíkových oxidů za současného vzniku SiQDs. Přebytečný materiál je následně odleptán pomocí HF (**Obr. 12a**). Přestože metoda vykazuje dobrých výsledků za využití amorfního křemíku i SiO₂, nejlepších výtěžností je dosahováno na HSQ (z angl. hydrogen silsesquioxane), který je ovšem nejdražší ze zmíněných vstupních materiálů.⁸⁸ Druhá metoda využívá tzv. křemíkové polymerizace plynného prekurzoru (běžně SiH₄) iniciované netermálním plazmatem.⁸⁹ V jednoduchosti se dá říci, že v plazmatu dochází k disociaci molekul SiH₄, vzniklé SiH₃ radikály spolu následně vytváří Si-Si vazby (**Obr. 12b**). Tímto postupem podobajícím se polymerizaci organických látek dochází k růstu křemíkových zárodků, které se následně sdružují a krystalizují. Obě metody jsou schopny připravit kvalitní vodíkem terminované SiQDs v uspokojivém množství (\sim 100 mg/hod), a to dokonce relativně udržitelnou cestou (ekologicky i ekonomicky). Výhodou prvního postupu je jeho přímočarost, druhého zase vysoká variabilita, kdy změnou koncentrace pracovního plynu či výkonu plazmatu je možno široce ladit strukturní i povrchové vlastnosti vzniklých nanočástic. Touto metodou také vznikly SiQDs s doposud nejvyšší prokázanou hodnotou QY dosažené bez sekundární povrchové terminace (50-60 %).⁹⁰

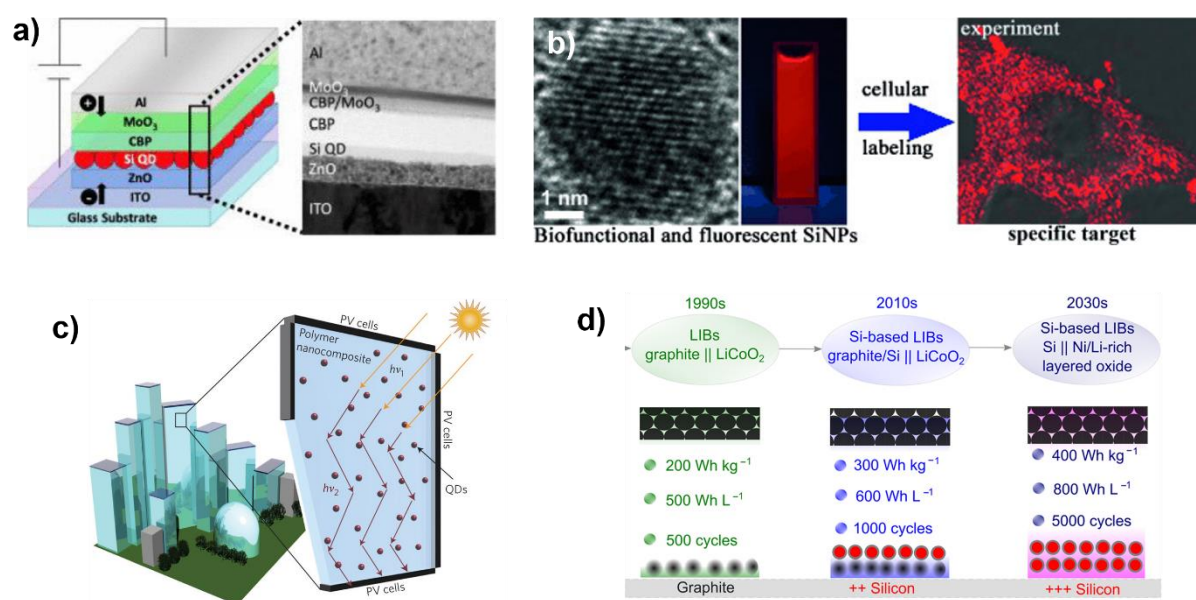


Obrázek 12. a) Schéma přípravy křemíkových kvantových teček metodou termální disproporcionace HSQ (použito se svolením majitele práv American Chemical Society),⁸⁸ b) schéma aparatury na přípravu Si teček využívající netermálního plazmatu.

Mezi nejběžnější povrchové úpravy křemíkových teček patří oxidace. Ta probíhá okamžitě při kontaktu s nově připravenou vodíkem terminovanou tečkou a vede ke stabilní pasivaci. Saturace nedokonalých povrchových stavů navíc často vede ke zvýšení QY teček. Oxidace lze však dosáhnout i kontrolovaně - typickým příkladem je oxidace pomocí vysokotlaké páry, která vede ke vzniku kvantových teček o QY ~ 60 %.⁹¹ Nejběžnější cílenou terminační technikou u těchto nanostruktur je hydrosilylace. Jedná se o postup, kdy dojde k navázání molekuly zakončené dvojnou vazbou na povrchu nanočástice. Celý proces je spojen s rozevřením dvojné vazby, která na povrchu tečky nahradí jeden vodík. Tato reakce může být iniciovaná tepelně, přítomností radikalizátoru nebo světelně, a bývá nejčastěji využívána k terminaci organickou funkční skupinou.⁹²⁻⁹⁴ SiQDs mohou být terminovány i běžnou chemickou cestou z roztorku. Takto dochází například k terminaci halovým prvkem. Tyto vazby jsou reaktivnější než původní terminace, a proto se používají k další úpravě, například pro následnou alkylaci.⁹⁵ K povrchové úpravě se však dá využít i samotný proces přípravy nanočástic pomocí netermálního plazmatu. Přidáním dodatečného plynu do koncové části plazmatu (tzv. afterglow), případně s využitím dvoufázového plazmatického reaktoru, se dá dosáhnout nejen úpravy povrchu, ale i přípravy jádro/plášť křemíkové struktury.^{96, 97} Autorský výzkum předkladatele se zabývá i vývojem postupů přípravy a povrchové terminace SiQDs. Především na poli dvoustupňových reaktorů a úpravy povrchu nanočástic pomocí plazmaticky aktivovaných kapalin.⁹⁷⁻¹⁰⁰

Aplikace kvantových teček

Díky kombinaci výše zmíněných vlastností vykazují SiQDs široký aplikační potenciál. Vzhledem k svým emisním vlastnostem se dají využít ke zlepšení kvality vyzařování LED (tzv. Si-QLED, **Obr. 13a**),¹⁰¹ zvýšení efektivity konverze standardních křemíkových solárních panelů¹⁰² či ke konstrukci v současnosti velmi diskutovaných solárních koncentrátorů.¹⁰³ Poslední jmenovaná aplikace je založena na přípravě světlo propustných skel, které budou obsahovat okem nepostřehnutelnou koncentraci kvantových teček. Ty budou pohlcovat UV záření a generovat viditelné světlo, které je pomocí vlnovodných vlastností skla vedeno do svých okrajů (rámů). Zde mají být umístěny tenké solární panely, které světelnou energii přivedou na elektrickou (**Obr. 13c**).



Obrázek 13. a) Struktura LED využívající SiQDs (použito se svolením majitele práv American Chemical Society)¹⁰¹, b) snímek HeLa buněk obsahující SiQDs pořízení konfokálním mikroskopem (použito se svolením majitele práv John Wiley and Sons),¹⁰⁴ c) schématické znázornění solárního kolektoru využívajícího SiQDs (licence obrázku CC BY, majitel práv Springer Nature),¹⁰³ d) znázornění historické a očekávané evoluce Li-ion technologie zahrnující významné začlenění křemíku v nanostrukturální formě (licence obrázku CC BY, majitel práv Springer Nature).¹⁰⁵

V kombinaci s dobrou biologickou kompatibilitou, fotostabilitou a nízkou toxicitou se SiQDs efektivně využívají i jako značky pro biologické zobrazování (**Obr. 13b**).^{68, 104, 106} Svůj potenciál mají také jako fototerapeutické materiály, biologické senzory či nosiče léčiv v technologii cíleného směrování léčiv.¹⁰⁷ Nanokřemík má významný potenciál v Li-ion

technologií. Křemík totiž vykazuje unikátní hodnotu gravimetrické kapacity ~ 4200 mAh/g, což určuje množství uskladnitelné elektrické energie při lithiaci. Tato hodnota převyšuje v současné době běžně využívaný elektrodový materiál, uhlík, řádově 10krát. V Li-ion technologii se v současnosti křemík nepoužívá, jelikož při lithiaci zvětšuje svůj objem o téměř 300 %, což vede k destrukci elektrody. SiQDs a nanostruktury jsou však obecně schopny tlaky spojené s touto expanzí lépe snášet. Začlenění Si nanostruktur do Li-ion technologie vede k výraznému zlepšování jejich kapacit (**Obr. 13d**).¹⁰⁵ Očekávanou aplikací nanokřemíku je také energetika založená na vodíku. Křemík je schopen povrchově vázat velké množství vodíku a uvolňovat jej za podmínek, které jsou laditelné přípravou.^{108, 109} Pro podrobnější diskuzi a další aplikace kvantových křemíkových teček bych odkázal na následující přehledové publikace.^{68, 87, 91, 110}

1.4 Perovskitové struktury a jeho hybridy

Jako perovskity jsou označovány materiály s krystalickou strukturou splňující chemický vzorec ABX_3 , kde A a B jsou kationy a X aniont. Perovskity obsahující halogenidový aniont jsou v současné době jedny z nejvíce studovaných materiálů. Tento výjimečný zájem je motivován jejich téměř ideálními vlastnostmi pro konverzi světelné a elektrické energie. Za necelých 15 let jejich výzkumu byla efektivita solárních panelů (PCE) založených na perovskitech zvýšena na cca 26 %, což mírně převyšuje současnou křemíkovou technologii.¹¹¹ Na druhou stranu však perovskity vykazují problémy se stabilitou a silnou degradací vnějšími vlivy jako je UV záření či přítomnost vody nebo kyslíku. Právě snaha o vyřešení těchto nedostatků, která by mohla vést k revoluci v hned několika aplikačních směrech, způsobuje zájem o perovskity, jenž je demonstrován tisíci vědeckými články na toto téma ročně.¹¹²

V rámci následující kapitoly se budeme věnovat popisu základních vlastností objemové formy perovskitů včetně zmíněných nedostatků. Vzhledem k zaměření experimentální práce předkladatele se následně zaměříme na detailnější popis a využití nízkodimenzionálních a hybridních perovskitových struktur využívajících kvantové tečky. Shrnutí metod přípravy perovskitů, které jsou v podstatě omezeny na relativně snadnou syntézu z roztoků, a jejich aplikací, zahrnující převážně fotovoltaiku, světelné detektory, detektory rentgenového záření a zdroje světla, lze najít v mnoha přehledových pracích¹¹²⁻¹¹⁴ a v souhrnu budou zmíněny spíše okrajově.

Vlastnosti objemových halogenidových perovskitů

Přírodní perovskity využívají jako aniontu kyslíku (např. CaTiO_3 , BaTiO_3 , BiFeO_3), a přestože vykazují feromagnetické a piezoelektrické vlastnosti, nenašly zásadního technického či průmyslového uplatnění. Jako aplikačně velmi zajímavé se však ukázaly být uměle připravené halogenidové PS (dále jen PS). Jejich krystaly jsou tvořeny halogenidovým aniontem ($X = \text{I}^-$, Cl^- – a Br^-) a kationem bivalentního kovu na pozici B (nejčastěji Pb^+) tvořící anorganickou osmistěnnou strukturu (BX_6).¹¹⁵ Ta spolu s kationem v pozici A vytváří krystalickou mřížku celého PS (**Obr. 14a**). Přestože to není pravidlem, nejčastěji se jedná o mřížku kubickou. Jako A kationt se využívá malá organická molekula (např. CH_3NH_3^+ – MAA nebo $\text{HC}(\text{NH}_2)_2^+$ – FAA).

Základem výjimečných vlastností PS je především přítomnost BX_6 struktury. Použijeme-li k dalšímu popisu zdaleka nejběžnější PS MAPbI_3 , je maximum jeho valenčního i dno vodivostního pásu tvořeno antivazebními orbitaly olova (6s) a jádu (5p) (**Obr. 14a**).¹¹² Díky tomu vykazují PS hned několik významných elektrických a optických intrinsických vlastností:¹¹⁴

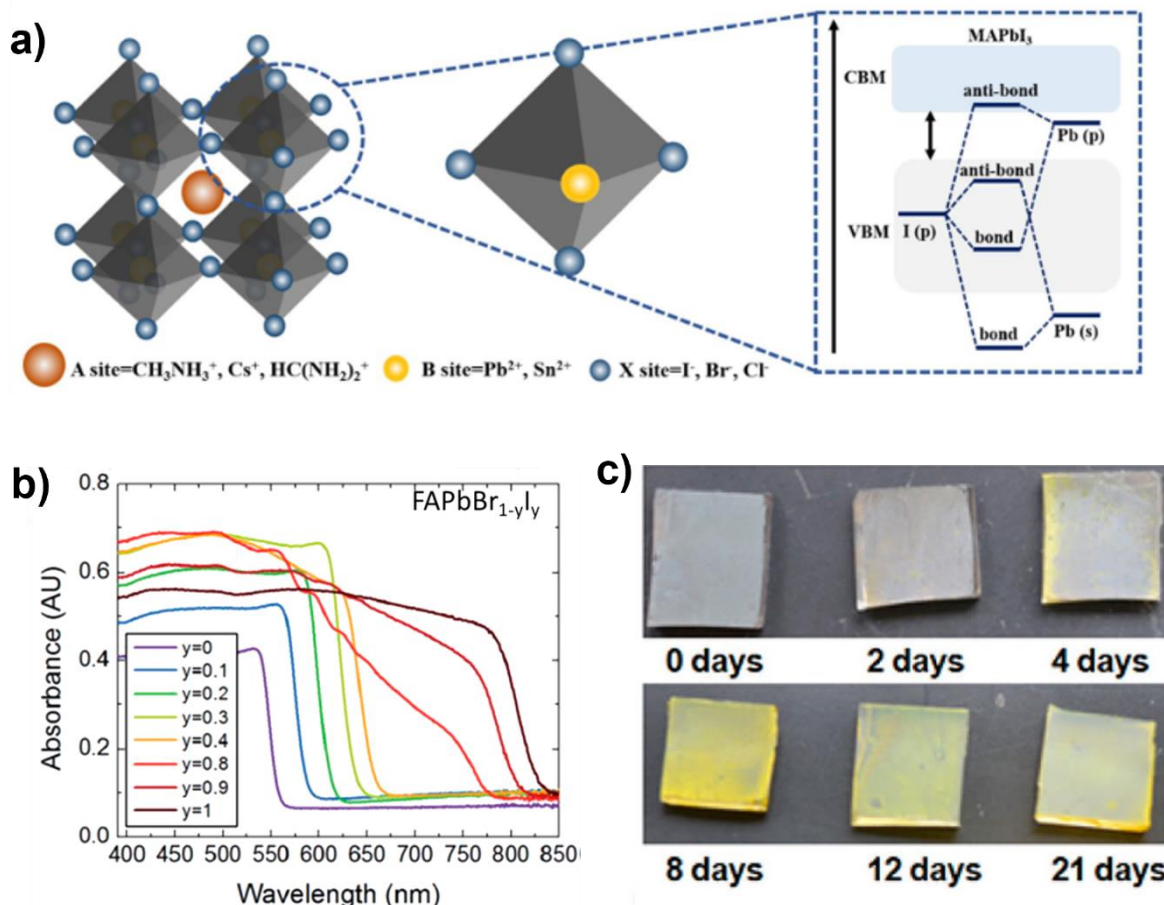
a) Popsaná energetickou struktura vede k vzniku přímého zakázaného pásu a přítomnosti volného elektronového páru olova, což způsobuje efektivní absorpci světla PS ve viditelném intervalu.

b) Odstraněním jednoho z iontů mřížky dochází k vytvoření defektu uvnitř nebo blízko okraje valenčního či vodivostního pásu (dáno energetickou strukturou pásu). Tyto pasti tedy významně neovlivňují chování excitovaných nosičů, což vede k toleranci PS k přítomnosti defektů.

c) Antivazebná interakce projevující se u PS má za následek nízkou hodnotu efektivní hmotnosti elektronů i děr ($0,23m_0$, respektive $0,29m_0$), a tedy vysoké mobilitě obou nosičů ($\sim 10 \text{ cm}^2\text{V}^{-1}\text{s}^{-1}$).

Vysoká tolerance k defektům a vysoká mobilita nosičů způsobuje, že PS vykazují velmi dlouhou difuzní délku u obou nosičů náboje – až $1 \text{ }\mu\text{m}$ v polykrystalické a $100 \text{ }\mu\text{m}$ v monokrystalické formě. Velikost zakázaného pásu je navíc snadno laditelná výměnou halogenu napříč téměř celým viditelným intervalom (přechodem k lehčím halovým prvkům se rozšiřuje zakázaný pás, **Obr. 14b**).¹¹⁶ Z uvedených vlastností by se mohlo zdát, že vliv kationtu A na chování PS je minimální. Přestože tato složka nezasahuje do formování stavů okolo zakázaného pásu, její význam není zanedbatelný. Hraje totiž významnou roli ve stabilitě PS prostřednictvím kompenzace náboje ve struktuře BX_6 , která je silně založena na elektrické

interakci. Kationt A také na základě své velikosti může vyvolávat kontrakci nebo expanzi anorganické mříže, což mění optické vlastnosti celého PS¹¹⁷.



Obrázek 14. a) Krystalická struktura PS MAPbI₃ a složení jeho molekulárních orbitalů (použito se svolením majitele práv The Royal Society of Chemistry),¹¹⁵ b) absorpční spektra FAPb(Br_{1-y}I_y) (použito se svolením majitele práv the Royal Society of Chemistry)¹¹⁶ c) degradace MAPbI₃ za běžných podmínek na vzduchu během 21 dnů (licence obrázku CC BY, majitel práv Springer Nature).¹¹⁸

I přes zmíněné výjimečné vlastnosti je aplikační rozmach PS zpomalován hned několika překážkami. Jedná se především o nedostatečnou stabilitu těchto látek a jejich degradaci při kontaktu se vzduchem, vodou a UV zářením^{112, 119}. Tento nedostatek je způsoben slabou iontovou mříží a přítomností nestabilních komponent využívajících vodíkovou nebo Van der Waalsovu interakci. Méně závažnou překážkou, i když často skloňovanou, je toxicita olova, které tvoří velmi významnou a složitě nahraditelnou složku běžných PS¹²⁰. Blíže se podíváme na parametry ovlivňující stabilitu PS a nejběžnější mechanismy jejich degradace:

Stabilita. Iontová struktura běžných PS bohužel není dlouhodobě stabilní a po nějakém čase dochází k jejímu rozpadu pomocí procesů iontové migrace, generace defektů, segregace

fáze a tvorbou různých jiných forem poruch mřížky (často v řádu týdnů, **Obr. 14c**).¹¹⁸ Míra zmíněných procesů je úzce spojena s hodnotou tzv. Goldschmidtova tolerančního faktoru t , která je definována jako:

$$t = \frac{r_A + r_X}{\sqrt{2}(r_B + r_X)}, \quad (10)$$

kde r jsou poloměry jednotlivých iontů PS. U organických molekul je tato hodnota složitě určitelná a většinou dochází k jejímu odhadu na základě empirických dat. Bylo zjištěno, že jen PS nabývající hodnotu t v intervalu 0,8 – 1 vykazují za pokojových teplot strukturu s výše popsanými významnými vlastnostmi (ostatní PS se laicky označují jako neperovskitové struktury). Do tohoto intervalu patří PS s kubickou nebo tetragonální krystalickou mřížkou. Navíc bylo zjištěno, že rychlosť vnitřních degradačních procesů výrazně roste s přibližováním hodnoty t k okrajům stabilního intervalu.¹¹² Hledání vhodného složení PS, který by vykazoval optimální hodnotu tolerančního faktoru, proto patří mezi významné kroky při přípravě PS.

Vlivy okolí. Běžné PS struktury jsou velmi citlivé na přítomnost vody. Ta totiž iniciuje rozklad anorganické mřížky PS.¹¹⁹ V případě MAPbI₃ dochází k rozkladu PbI₆ na PbI₂. To vede k typickému žloutnutí struktury, která je jinak díky efektivní absorpci ve viditelné oblasti velmi tmavá. Na základě tohoto jevu se také často nejen degradované, ale i halogenidové neperovskitové struktury označují jako žlutá PS fáze. Vodou indukovaná degradace PS je navíc zesílena případnou přítomností UV záření. Rozpad struktury na PbI₂ však může být iniciován i samotným UV zářením, i když s výrazně pomalejším tempem. Neprítelem PS je také kyslík, jeho molekula se může snadno zachytit na povrchu struktury a získat z PS přebytečný elektron. Vzniklý superoxid následně reaguje s PS za vzniku PbI₂ a vody.¹¹⁹ Stabilizace PS vzhledem ke světlem iniciovaným degradačním procesům je zásadní pro případné fotovoltaické aplikace těchto struktur.

Současný vývoj PS je směrován především k optimalizaci jejich elektrických a optických vlastností, omezení projevů zmíněných destruktivních jevů a nahradě toxickeho olova. Pomineme-li enkapsulaci a podobné povrchové úpravy omezující vliv okolí a přechod k nanostrukturním formám PS, kterým bude věnována následující podkapitola, zůstává hned několik postupů, jak tyto nedostatky odstranit. Většina je spojena s nahradou tradičních složek PS nebo vytvářením složitějších PS podobných struktur. Ty nejperspektivnější cesty rozebereme důkladněji:

Alternace A kationtu. Na základě teorie by nejlepší elektrické a optické vlastnosti měl vykazovat PS obsahující molekulu FA. Díky své velikosti však PS obsahující FA vykazují

vysoké hodnoty tolerančního faktoru mnohdy přesahující 1. Za běžných podmínek jsou tedy silně nestabilní, rychle degradují a jejich využití je omezené.¹²¹ Jako zajímavá cesta ke snížení vlivu okolních podmínek se ukázalo být použití anorganických kationtů, a to především Cs.¹²² Jeho přítomnost sice zvyšuje odolnost vůči vodě, ale relativně malá velikost těchto atomů (vzhledem k MA) významně snižuje toleranční faktor, a tím celkovou stabilitu PS (*t* faktor okolo 0,8). V současné době se zdá být efektivní využití kombinace kationtů. U těchto komplexních PS dochází během přípravy k míchání více kationtů v různých poměrech tak, aby se nejen využilo jejich pozitivních vlivů na výslednou strukturu, ale nastavila se i vhodná hodnota tolerančního faktoru. Nejvíce se v tomto směru využívá kombinací FA, MA, Cs, ale i Rb. Tyto struktury sice vykazují lepší míru stability a odolnosti vůči vnějším vlivům ve srovnání se standardním MAPbI₃, ale stále nedosahují jeho elektrických vlastností a jejich příprava je také výrazně náročnější.^{121, 123}

Alternace B kationtu. Dlouhodobým cílem výzkumu PS je také nahrazení olova za jiný bivalentní prvek při zachování elektrických vlastností struktury. Bylo testováno využití Ge²⁺, Ca²⁺, Mn²⁺, Fe²⁺ a dalších prvků, ale nejlepším kandidátem se ukázal být Sn²⁺. Cín má totiž obdobnou jak elektronovou konfiguraci, tak i iontový poloměr jako olovo. Teoreticky by PCE cínových PS mohla přesahovat 33 %¹²⁴. V praxi se to však nepotvrdilo, jelikož cín v PS snadno vytváří vakantní stavy a Sn⁴⁺ ionty. SnI₂ struktura navíc snadno reaguje s organickým kationtem, což vede k nízké pohyblivosti nosičů a špatné stabilitě PS¹²⁰. Mezi alternativní postupy nahrazení olova patří vytváření dvojitých PS či perovskitu podobných struktur využívajících jako B kationy dvojici prvků (např. AgBi). Žádná z těchto struktur však nevykazuje PCE převyšující 15 %¹²⁵.

Smíšené perovskity. Jak bylo zmíněno, šířku zakázaného pásu a obecně optické vlastnosti PS lze měnit použitím různého halogenidu. Jako velmi efektivní se ovšem ukázala být i příprava tzv. smíšených PS. Ty jsou složeny hned z několika různých A kationtů (až 4 různé současně) a halogenidů (většinou dva různé). Tyto struktury jsou obtížně připravitelné, ale vhodným poměrem všech složek u nich lze nejen spojité ladit velikost zakázaného pásu v téém celém viditelném intervalu (anionty), ale i zvyšovat stabilitu (ladění *t* faktoru) a odolnost vůči vnějším vlivům (cationty)^{112, 126}.

Nanostruktturní halogenidové perovskity

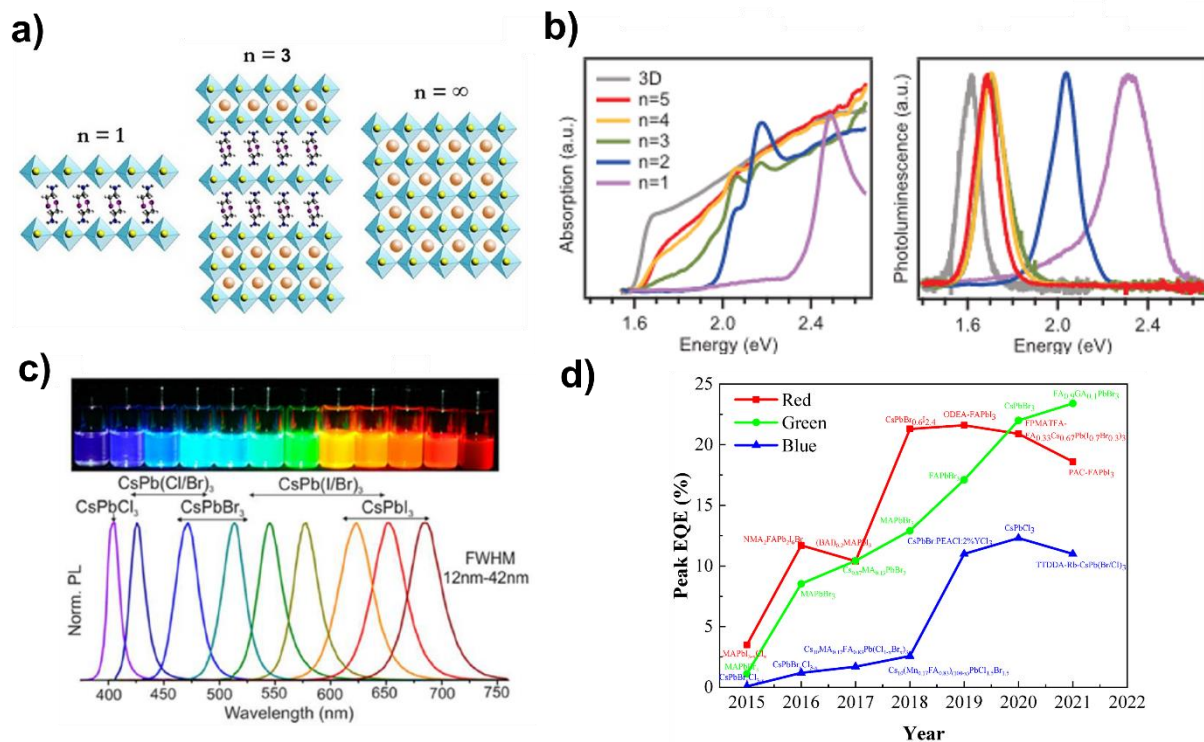
Významným krokem k ladění vlastností a zvyšování odolnosti PS se ukázalo využití jejich nízkodimenzionálních struktur. Přestože se v praxi využívá hned několik typů těchto struktur, zde se podíláme na dvě nejdůležitější: nanovrstvy – kvantové jámy (2D struktury) a kvantové tečky (0D) struktury.

PS nanovrstvy jsou typicky připravované ve formě sendvičové struktury, kdy vždy n vrstev anorganické mřížky PS je odděleno tzv. separátorem (zangl. spacer). Tím bývá nejčastěji větší organická molekula (např. butilamonium, BA).¹²⁷ Schématické znázornění takové struktury je uvedeno na **Obr. 15a**. Parametr n následně slouží ke klasifikaci 2D struktur, protože v mnoha ohledech reflektuje jeho výsledné chování. PS nanovrstvy vykazují hned několik zajímavých vlastností. V prvé řadě se ukázalo, že jsou mnohem odolnější na degradaci způsobenou vlhkostí.¹¹² Separátor totiž slouží jako přirozená ochranná vrstva PS. Tento efekt je ještě zesílen, pokud má separátor hydrofobní vlastnosti. Působením separátoru navíc dochází ke stabilizaci vrstev, které by podle tolerančního faktoru byly velmi náchylné na degradaci (okolo 0,8 nebo 1).¹²⁸ Pro optické a elektrické vlastnosti nanovrstev je naopak zásadní vliv kvantově-rozměrového jevu a dielektrického-rozměrového jevu. První jmenovaný významně ovlivňuje rozložení energetický stavů, rozšiřuje zakázaný pás a zvyšuje stabilitu excitonů na základě počtu oddelených vrstev, a tedy velikosti omezeného prostoru (čím nižší n , tím vyšší vliv kvantového omezení, **Obr. 15b**).¹²⁹ Excitonová vazebná energie je u objemových PS nižší než tepelná energie fononů za běžné teploty. Dochází tedy k jejich efektivní disociaci v časovém intervalu \sim fs až ps. To neplatí u nízkodimenzionálních struktur. Stabilita excitonů je navíc zvýšena i přítomností dielektrického-rozměrového jevu, který je spojen se skokovou změnou permitivity mezi separátorem a PS, což zvyšuje sílu Coulombické interakce mezi nosiči tvořícími exciton. Výsledná vazebná energie excitonů se tím může zvýšit z původních \sim 10 meV až na \sim 300 meV.^{128, 130} Důsledkem těchto změn je nejen získání nové cesty, jak ladit šířku zakázaného pásu PS, ale i významné snížení mobility nosičů, a naopak zesílení efektivity excitonové luminiscence. Aplikační potenciál PS nanovrstev tedy leží především v generaci světla, atď už ve formě LED nebo LD.^{114, 115}

Své uplatnění našly i struktury stojící na hranici 2D a 3D PS, tzv 2D/3D vrstvy, někdy též nazývané jako PS se smíšenou dimenzí. V podstatě se jedná o 2D PS s velmi velkým parametrem n (desítky). 2D/3D vrstvy vykazují elektrické a optické vlastnosti objemového PS, ale občasná přítomnost oddělovacích vrstev zlepšuje jeho odolnost proti vodní degradaci a vylepšuje i PCE, pravděpodobně díky zvýšení stability struktury.¹³¹ Touto tématikou se zabývá i jedna publikace předkladatele.¹³²

Zajímavé vlastnosti vykazují i PS kvantové tečky a nanokrystaly obecně. Bylo prokázáno, že snížením rozměrů dochází k významnému zvýšení stability PS prostřednictvím vysoké povrchové energie a změně povrchového napětí.¹³³ To umožňuje využití plně anorganických PS, které vykazují vyšší odolnost proti vnějším vlivům (např. CsPbI₃), ale

jejichž toleranční faktor by byl za běžných okolností mimo stabilní interval. PS QDs navíc vykazují velmi efektivní fotoluminiscenci ($\text{QY} \sim 50 - 90\%$),^{134, 135} což je dáno vysokou efektivitou absorpce světla, přítomností kvantově-rozměrového jevu zvyšujícího vazebnou energii excitonů a nízkou koncentrací defektů.¹³⁶ Pozice emisního spektra je navíc snadno laditelná přes celý viditelný interval, a to především vhodnou kombinací halogenidů (Obr. 15c).¹³⁴ Optické vlastnosti jsou však ovlivnitelné velikostí a povrchovou terminací, jako u všech běžných QDs. PS QDs našly uplatnění nejen jako efektivní zdroje světla (QLEDs), ale využívají se i v hybridních PS strukturách, jak bude kázáno v následující kapitole. Detaily o jejich vlastnostech, aplikacích a metodách přípravy je možno získat v následujících publikacích.^{135, 137}



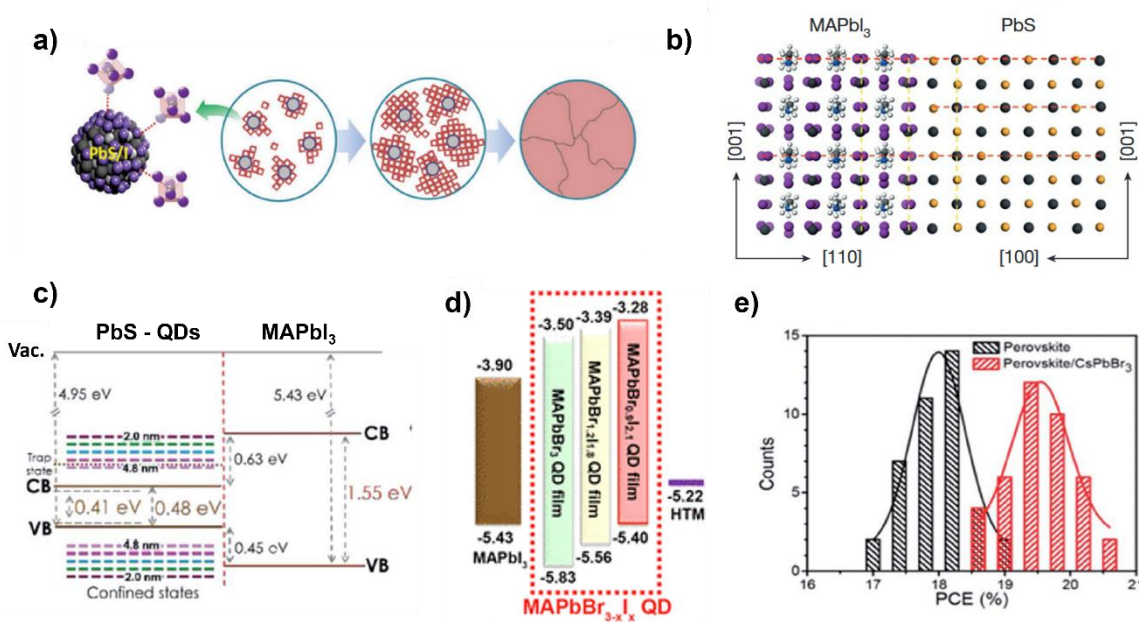
Obrázek 15. a) Schématické znázornění struktury 2D PS o různém parametru n (použito se svolením majitele práv John Wiley and Sons),¹³⁸ b) absorpční a luminiscenční spektra 2D PS $(\text{BA})_2(\text{MA})_{n-1}\text{Pb}_n\text{I}_{3n+1}$ o různém parametru n (použito se svolením majitele práv AAAS)¹²⁹, c) fotoluminiscenční spektra PS QDs obsahujících různou koncentraci halogenidů (použito se svolením majitele práv ACS Publications),¹³⁴ d) vývoj účinnosti QLED založených na PS QDs v rámci posledních let (licence obrázku CC BY, majitel práv MDPI journals).¹³⁵

Perovskitové hybridní struktury

Výjimečné vlastnosti PS našly uplatnění i v kombinaci s jinou látkou. Mezi nejperspektivnější PS hybrydy patří struktury typu částice-v-matrici (z angl. dot-in-matrix), které jsou složeny z QDs a 3D PS. Nejčastěji se jedná o QDs olovnatých chalkogenidů (heterogenní hybrydy) nebo samotných PS QDs (homogenní hybrydy). Spojení těchto materiálů má mnoho výhod.¹³⁹ V prvé řadě zlepšuje strukturní a povrchové vlastnosti obou komponent. Při přípravě PS vrstev máme obecně jen slabou kontrolu nad samotnou syntézou, její kontrola probíhá volbou rozpouštědla, poměrem ingrediencí, určením teploty přípravy nebo substrátu. Bylo ukázáno, že QDs mohou v této fázi hrát efektivní roli krystalizačních zrn, kdy výsledná matrice vykazuje vyšší krystalinitu a menší množství strukturních i morfologických defektů (**Obr. 16a**).¹⁴⁰ Jak PS QDs, tak většina olovnatých chalkogenidů (např. PbS) vykazují s PS velmi dobrou shodu ve struktuře krystalické mřížky (shoda mezi vzdálenostmi atomárních rovin je $\sim 0,1\text{\AA}$), což umožňuje snadnou integraci nanočastic a vytvoření rozhraní o velmi slabém pnutí a minimální koncentraci defektních stavů¹⁴¹. Velmi dobré podmínky na rozhraní těchto dvou materiálů byly prokázány i pomocí DFT simulací. Výsledky studie deklarovaly téměř ideální shodu (110) facety PbS s (110) facetou od běžných PS. Energie spojená s formováním rozhraní těchto dvou materiálů vykazuje zanedbatelné hodnoty pod 10 meV/ \AA (**Obr. 16b**).^{141, 142} Navíc bylo prokázáno, že přítomnost QDs zvyšuje celkovou odolnost matrice na degradační procesy spojené s přítomností vody i iontové migrace.¹⁴² Tento efekt je výraznější při použití chalkogenidových QDs. Vytváření PS/QDs hybridních struktur nevede pouze k růstu kvality PS, ale je výhodné i pro samotné QDs, jejichž vlastnosti jsou často degradovány vysokou koncentrací povrchových defektů. Bylo prokázáno, že v PS matrici dochází k jejich efektivní povrchové pasivaci.¹³⁹

Elektrické a optické vlastnosti hybridu jsou silně závislé na energetické struktuře obou složek. Ve své podstatě se totiž jedná o strukturu jádro/slupka (QDs/PS). Hybrid z elektrického hlediska tedy může vytvářet struktury typu I nebo II (**Obr. 6**).¹¹² Ve specifických případech dochází i k tvorbě reverzních typů I, kdy QDs vykazuje výrazně vyšší velikost zakázaného pásu než PS matrice. Ve strukturách typu I leží zakázaný pás QDs v červené nebo infračervené oblasti, na rozdíl od širšího zakázaného pásu PS. Jako světelný absorbér zde poté slouží PS matrice. Excitované nosiče jsou následně transportovány do QDs, kde zářivě rekombinují prostřednictvím stabilních excitonů.^{143, 144} Pokud se dá hybridní struktura charakterizovat jako Typ II, případně reverzní Typ I, slouží nanočasticce jako absorbér světla a donor excitovaných nosičů, případně jako efektivní elektronový nebo děrový transportní materiál. Schéma energetické struktury hybridu PbS/MAPbI₃ je zachycen na **Obr. 16c**. U této struktury dochází

změnou velikosti QDs k přechodu od Typu I na Typ II.¹⁴⁵ Hraniční velikost je odhadnuta na hodnotu okolo 2,9 nm. Naproti tomu na **Obr. 16d** je zachycen reverzní Typ I, kdy QDs jsou tvořeny PS a jejich energetická struktura je laděna změnou koncentrace halogenidů.¹⁴⁶ Za této situace bude PS QDs sloužit nejen jako zdroj excitovaných nosičů, ale také jako efektivní děrový transportní materiál. Vzhledem k očekávané funkci hybridu jsou nanočástice v matrici rozloženy buď homogenně, nebo se vytváří jejich vrstva na okraji matrice (slouží k extrakci nosičů do elektrod u fotovoltaických aplikací).¹⁴²



Obrázek 16. a) Nukleace a růst PS krystalu za přítomnosti PbS QDs terminovaného MAI (použito se svolením majitele práv The Royal Society of Chemistry),¹⁴⁰ b) model PbS a MAPbI₃ krystalové struktury a jejich rozhraní z roviny X-Z (jednotlivé facety jsou vyznačeny; použito se svolením majitele práv Springer Nature),¹⁴¹ c) vypočtené energetické schéma 3D PS MaPbI₃ s PbS QDs o velikosti od 4,8 do 1,9 nm (použito se svolením majitele práv ACS Publication),¹⁴⁵ d) energetické schéma PS QDs MAPbBr_{3-x}I_x a MAPbI₃, znázorněna je i poloha děrového transportního materiálu (použito se svolením majitele práv ACS Publication),¹⁴⁶ e) histogram PCE čtyřiceti solárních panelů vytvořených s a bez přítomnosti CsPbBr₃ QDs (použito se svolením majitele práv ACS Publication).¹⁴⁷

Na základě popsaných transportních procesů slouží hybridy vykazující Typ I jako efektivní zdroje světla v celém viditelném intervalu.^{144, 148} Bylo prokázáno, že díky dlouhé difuzní délce PS a vysoké kvalitě matrice je v těchto strukturách transportováno do QDs až 80 % excitovaných nosičů, což vede k velmi vysoké vnější kvantové účinnosti těchto hybridů

> 20 %.^{139, 149} Struktury Typu II a reverzní Typ I mohou sloužit jako efektivní fotodetektory, ale především se využívají jako fotovoltaické materiály.¹³⁶ Kombinací dobrých strukturních vlastností matrice, vyšších odolností na degradaci, efektivnější extrakcí excitovaných nosičů a často rozšířenému absorpčnímu spektrálnímu intervalu, vedoucímu k vyšším proudům na krátko,¹⁴⁶ vykazují PS/QDs solární panely nejen vyšší hodnoty PCE než čisté 3D PS, ale i vysokou stabilitu (**Obr. 16e**).^{139, 147}

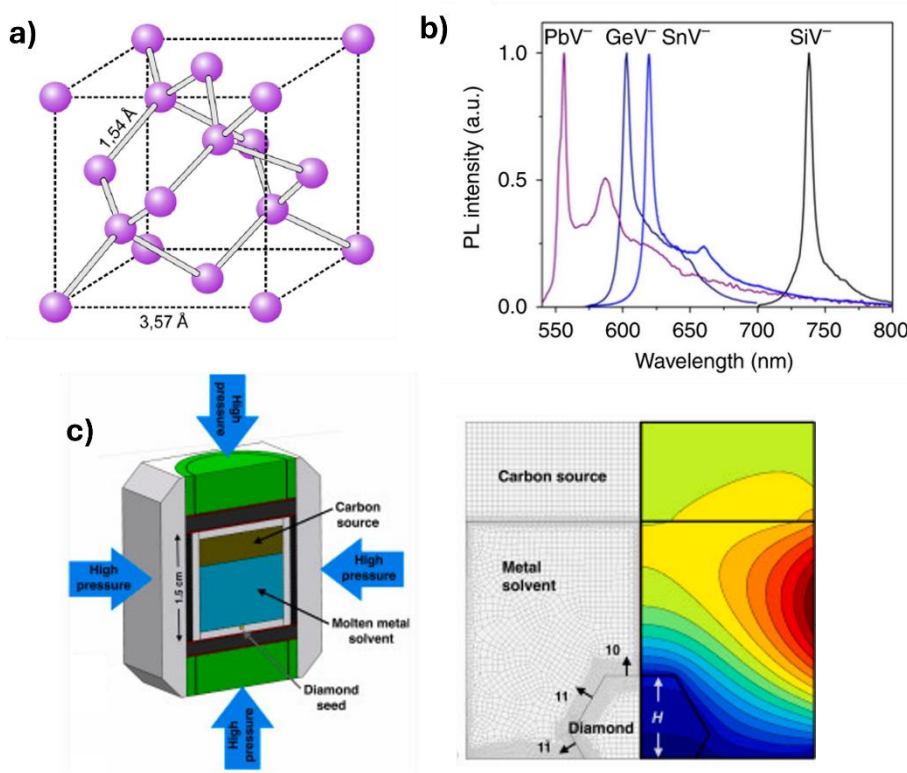
Z popisu fungování PS hybridů je zřejmé, že zásadní roli zde hrají transportní a rekombinační vlastnosti nosičů na rozhraní PS a QDs, případně rozhraní těchto materiálů a extrakčních materiálů. K tomu je nutný důkladný popis těchto mechanismů, čemuž se bude věnovat několik publikací autora uvedených v praktické části habilitační práce.^{19, 150}

1.5. Nanokrystalický diamant

Diamant je jedním z nejzajímavějších nerostů na naší planetě. Je nejen velmi vzácný, ale vykazuje i mnoho výjimečných fyzikálních vlastností. Oba zmíněné fakty jsou spojeny s jeho mikroskopickou strukturou. Diamant je totiž složen z atomů uhlíku uspořádaných do dvojtě plošně centrované kubické mřížky (**Obr. 17a**). Atomy uhlíku v této struktuře vykazují tzv. sp³ hybridizaci, kdy jsou jednotlivé atomy propojeny pouze jednoduchými a velmi pevnými kovalentními σ vazbami (vazebná energie ~7,36 eV).¹⁵¹ Toto uspořádání vede k vytvoření velmi těsné, kompaktní a pevné struktuře, což je nejen zdrojem zmíněných vlastností, ale i extrémních podmínek pro jeho vznik a tím pádem i malého výskytu. Pro zajímavost, uhlík je nejmenší atom, který je schopen vytvářet zmíněnou krystalickou strukturu. Obdobně jako u křemíku, diamant nelze uměle připravit chemickou cestou z roztoku, přesto to není nemožné. V praxi se využívá dvou typů metod jeho syntézy, jedny kopírují přirozené podmínky jeho vzniku v přírodě (vytvoření vysokých tlaků a teplot), ale se zvýšenou rychlostí konverze uhlíků v nediamondové fázi (HPHT nebo detonační metoda, **Obr. 17c**), druhé celý diamant sestavují po atomech pomocí depozice z plynné fáze (například CVD), více přiložené odkazy.¹⁵²⁻¹⁵⁵

Výčet zajímavých vlastností diamantu by byl rozsáhlý, zde zmíníme jen ty nejdůležitější. Diamant vykazuje nejvyšší objemovou hustotu atomů mezi všemi látkami ($1,77 \cdot 10^{23} \text{ cm}^{-3}$). Jedná se o nerost s nejvyšší tvrdostí a Youngovým modulem pružnosti. Díky své kompatibilitě je ideálním médiem pro šíření fononů. Vykazuje nejvyšší rychlosť šíření zvuku ($v_s = 18 \text{ km} \cdot \text{s}^{-1}$) a tepelnou vodivost ($21,9 \text{ W} \cdot \text{cm}^{-1} \cdot \text{K}^{-1}$), která je jen pro představu asi 10x vyšší než u hliníku. Vykazuje i velmi vysokou pohyblivost obou nosičů náboje (3000 – 4000 $\text{cm}^2 \cdot \text{V}^{-1} \cdot \text{s}^{-1}$)^{152, 156}. Silné kovalentní vazby vedou i k vysoké chemické odolnosti diamantu, navíc díky přítomnosti uhlíku je biokompatibilní a netoxický.

Z energetického hlediska vykazuje diamant nepřímý zakázaný pás o hodnotě 5,47 eV (přímý přechod ~7 eV).¹⁵⁶ V čistém stavu je tedy průhledný a dobrý izolátor. V tomto stavu se však ani v přírodě, ani po své syntetické přípravě nevyskytuje. Jeho elektrické a optické vlastnosti jsou tak do značné míry závislé na míře defektů, které obsahuje. Ty vznikají nejen během přípravy, ale mohou být i dodatečně vytvořeny. Nejčastěji se jedná o poruchu mřížce (např. vakance, dislokace a atomy v intersticiální poloze) nebo příměsi v substitučních polohách.^{157, 158} S přihlédnutím na kompaktní diamantovou strukturu však není mnoho atomů, co mohly být jako příměsi použity. V podstatě se jedná jen o bór, dusík, fosfor a křemík, kdy pouze první 3 jmenovaní fungují jako dopanty.



Obrázek 17. a) Struktura diamantové mřížky,¹⁵⁹ b) fotoluminiscenční spektra vybraných barevných center v diamantu (použito se svolením majitele práv Springer Nature),¹⁶⁰ c) princip růstu monokrystalického diamantu pomocí metody HPHT - v levé části obrázku je znázorněn reaktor a složení použité směsi, poloha zárodečného diamantu je vyznačena, v pravé části je vidět růst diamantu a tepelná mapa v reaktoru (použito se svolením majitele práv Elsevier).¹⁵⁵

Díky naprosté běžné kontaminaci diamantu uvedenými prvky je diamant na základě své vodivosti často považován za polovodič. Zmíněné defekty navíc mohou být zdrojem absorpce a emise světla ve viditelné oblasti. Na základě lokálnímu charakteru v mříži jsou opticky aktivní

defekty označovány jako centra. Významná jsou především tzv. barevná centra vyznačující se zrcadlovou symetrií absorpčního a luminiscenčního spektra kolem tzv. nulfuronové čáry.¹⁶⁰ Zmíněné spektrální závislosti navíc vykazují Gaussovský charakter. Přestože bylo identifikováno téměř 100 takových center, mezi nejběžnější barevná centra řadíme N-V (dusíkový atom a vakance) a Si-V komplexy (**Obr. 17b**).^{161, 162} Ty mohou být nejen zdrojem přesně spektrálně lokalizované a efektivní luminiscence, ale díky kontrole fotonové emise těchto center mají potenciál být využity ke kvantovému počítání či kryptografii.¹⁶⁰

Výčet diamantových kvalit ukončíme zmíněním jedné jeho neočekávané schopnosti. I přes své izolační vlastnosti totiž vykazuje efektivní povrchovou vodivost. Tento jev je vysvětlován pomocí tzv. povrchovým transportní dopování, kdy elektrony z diamantu tunelují do volných stavů v povrchové vrstvičce vody, což následně vede k vytvoření ochuzené vrstvy pod povrchem diamantu vykazující silnou děrovou vodivost.¹⁵⁶ Podmínkou vzniku povrchové vodivosti je nutná povrchová terminace vodíkem a přítomnost vzduchu a vody. Tento jev však není pro diamant unikátní, ale vyskytuje se i u GaN a ZnO.

Přestože rozsah potenciálních diamantových aplikací je široký a sahá od mechaniky, tribologie, optoelektroniky až po biomedicínu, jeho reálné využití je silně omezené cenou. Nejen přírodní, ale i syntetický monokrystalický diamant je velmi nákladný. Přestože vývoj jeho přípravy velmi postoupil, a to především prostřednictvím zmíněné chemické depozice z plynné fáze (CVD), v praxi se využívají především různé formy diamantu polykrytalického.¹⁵⁷

Polykrytalický diamant

Hledání cest, jak využít vlastnosti diamantů v rámci akceptovatelných nákladů, bylo vždy velmi impaktovaným tématem. Nakonec se ukázalo, že tuto možnost nabízí tzv. polykrytalické diamantové struktury (PCD). Tyto materiály je totiž možno připravit výrazně snadněji, a tím pádem i levněji než jejich objemové alternativy (lze vytvořit na libovolný substrát, větší variabilita podmínek přípravy atd.) a současně si zachovávají mnohé výjimečné vlastnosti monokrystalického diamantu.¹⁵⁴ Ze strukturního hlediska jsou PCD složeny z diamantových krystalů (monokrystalických zrn) o velikosti od 5 nm do jednotek μm . Zrna mohou vytvářet spojité povrhy, pak mluvíme o diamantových filmech, nebo mohou být samostatné (prášky). Pro lepší orientaci se na základě velikosti zrn PCD dále dělí na ultra-nanokrytalické (UNCD, do 20 nm), nanokrytalické (NCD, do 100 nm) a mikrokrytalické diamanty (MCD) (**Obr. 18a**).¹⁶³ Prostor mezi zrny je vyplněn tzv. uhlíkovou nediamantovou fází, její popis a význam bude uveden v následujícím textu. Za povšimnutí stojí, že se tyto

materiály volně v přírodě téměř nevyskytují. K jejich vzniku by muselo dojít k dramatickému narušení podmínek pro růst diamantů, například při zemětřesení.

Pro správné pochopení vlastností PCD je nutné vzít v potaz jejich mikroskopickou strukturu. Ta je totiž složena z diamantových zrn o výše definovaných vlastnostech, jejich rozhraní a nediamantové fáze mezi nimi. Rozhraní v prvé řadě přirozeně naruší šíření tepla (rozptyl fononů) a výrazně snižuje pohyblivost excitovaných nosičů náboje. Na povrchu zrn se také nachází intrinsické a extrinsické defekty. Mezi intrinsické defekty patří poruchy spojené s narušením dalekodosahového usporádání uhlíku, jako jsou kývavé vazby, deformované uhlíkové vazby či atomy uhlíku v sp^2 fázi. Do extrinsických defektů řadíme příměsi, které se během přípravy nedostatečně integrovaly do zrn, povrchové terminace a uhlík v sp^2 hybridizaci, který běžně vyplňuje prostor mezi zrny a může se nacházet v amorfní fázi nebo v lokálních vodivých klastrech.¹⁶⁴ Mezi zrny se také pravděpodobně nachází malé množství amorfního uhlíku v sp^3 fázi. Poslední dva defekty bývají souhrnně označovány jako uhlík v nediamantové fázi.¹⁶⁵ Vliv rozhraní a také koncentrace uhlíku v nediamantové fázi významně roste s klesající velikostí zrn. Poměr sp^2 a sp^3 uhlíku v PCD se standardně kvantifikuje pomocí tzv. faktoru kvality f_q , který je počítán z intenzity Ramanova signálu od uhlíku z obou fází. Jelikož velikost zrn u NCD a UNCD obvykle vykazuje velikost pod 50 nm, je na místě diskutovat i případný vliv kvantově-rozměrového jevu. Bohrův poloměr uhlíku je však velmi malý, odpovídá $a_B = 1,58$ nm. Vlivy kvantového omezení se u zmíněných struktur projevují velmi omezeně.¹⁵⁷

Jak zmíněné strukturní modifikace ovlivňují vlastnosti PCD? Bylo prokázáno, že přechodem k PCD není narušena biokompatibilita, nízká toxicita a i do značné míry chemická odolnost diamantu. Některé typy PCD dokonce vykazují lepší mechanické vlastnosti (Youngův modul pružnosti a tvrdost) než jejich objemové alternativy, což je dáno sníženým šířením dislokací mezi zrny.¹⁵² Zhoršení tepelné vodivosti závisí na velikosti zrn a snížení této fyzikální vlastnosti se škáluje od jednotek procent až po 3 řády pro některé typy UNCD.¹⁶⁶ Na základě těchto vlastností se polykrystalické diamantové prášky využívají jako aditivum olejů ke snížení koncentrace sedimentů a opotřebení kovových částí obecně, jako abraziva a leštící media. PCD filmy se využívají jako mechanická a chemická ochrana v medicíně (kloubní náhrady) či libovolných kovů (chirurgické nástroje atd.).^{156, 167}

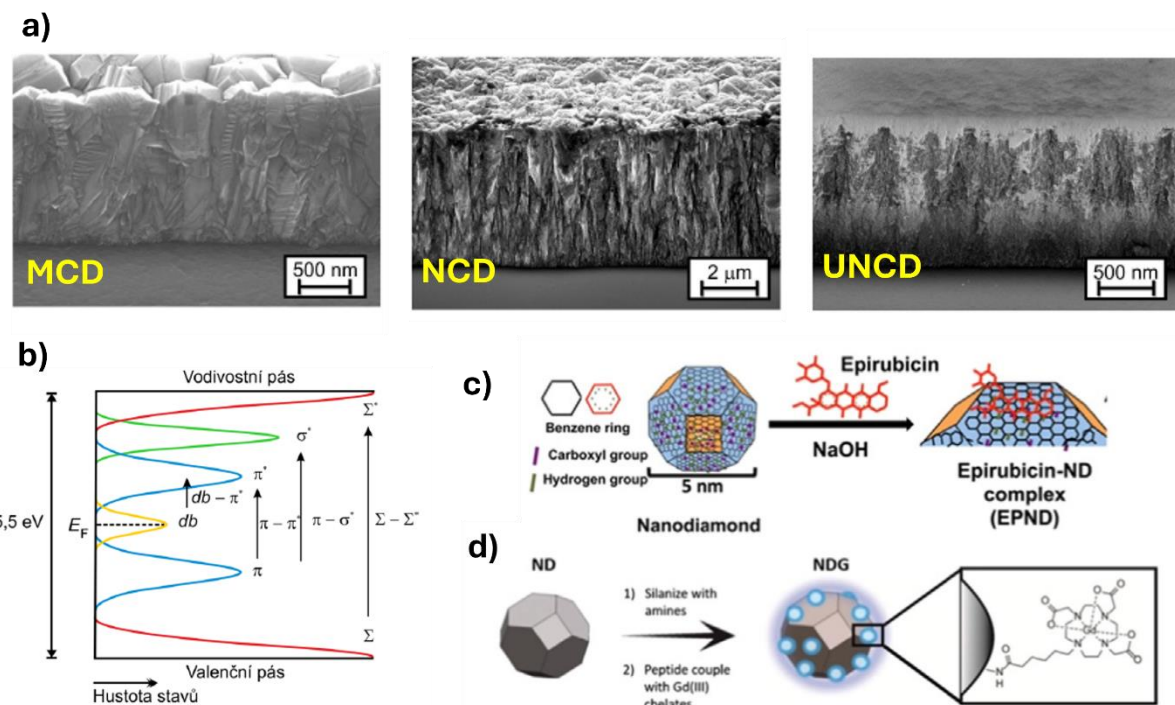
Složitější situace nastává s popisem a interpretací elektrických a optických vlastností PCD. Ty totiž nejsou ovlivněny pouze samotnou přítomností rozhraní zrn, ale především chemickým složením jejich povrchu a také uhlíkem nacházejícím se mezi zrny. PCD obecně vykazuje výrazně vyšší měrnou vodivost než jeho objemová alternativa (nárůst z $\sim 10^{-17}$ na $10^{-10} \text{ S}\cdot\text{m}^{-1}$), a to i přes nižší pohyblivost nosičů.¹⁶⁸ Tento efekt je spojen především s

přítomností slabě vázaných elektronů v π stavech od uhlíků v sp^2 fázi.¹⁶³ Obtížné je i dopování PCD vzorků, protože oba typy dopantů (bór a dusík) se během přípravy snadno zachycují na hranicích zrn a ne v jejich objemu. Bylo však ukázáno, že přítomnost dusíku během přípravy PCD i tak zvyšuje vodivost filmů.¹⁶⁴ Nejedná se však o standardní dopovací mechanismus. Z dosud neúplně zřejmých důvodů totiž přidání dusíku do pracovního plynu zvyšuje koncentraci nediamantové fáze ve výsledném filmu. Mechanismus vodivosti v PCD stále není detailně popsán, nejčastěji však bývá spojován s přeskoky s proměnným rozsahem (z angl. Variable range hopping – VRH).¹⁶⁹

Optické vlastnosti PCD můžeme nejlépe demonstrovat na základě jejich očekávaného energetického schématu (**Obr. 18b**). Přítomnost sp^2 uhlíkové fáze je prezentována přítomností obsazeného π a prázdného π^* stavu (modrá barva). Šířka těchto pásů se pohybuje okolo 1 eV a vzdálenost maxim $\sim 2,5 - 3,5$ eV. Růst koncentrace nediamantové fáze by se měl projevovat rozšiřováním a přibližováním obou pásů. Vlivem neuspořádanosti a deformací uhlíků v sp^3 fázi dochází ke vzniku chvostových stavů kolem hranic zakázaného pásu (červená barva). Stavy spojené s přítomností kývavých vazeb se očekávají kolem Fermiho meze (žlutá barva) a stavy spojené s uhlíkem v sp^3 fázi nacházející se mimo zrna jsou charakterizovány pásem σ^* (zelená barva). Na existenci posledních dvou stavů však prozatím nepanuje u odborné veřejnosti shoda.

Díky přítomnosti stavů v zakázaném pásu vykazuje PCD silnou absorpci od ~ 1 eV až do hranice zakázaného pásu (přechody vyznačeny v **Obr. 18b**). Stavy v zakázaném pásu jsou navíc zdrojem širokospektrální luminiscence ve viditelné oblasti, která doplňuje emisi od barevných center. Bylo prokázáno, že efektivita této luminiscence je ovlivněna okolními podmínkami (teplota, tlak, složení atmosféry) i podmínkami přípravy PCD (pravděpodobně variace struktury sp^2).^{152, 169} Očekává se, že zdrojem této emise je především rekombinace mezi π stavů. Systematická studie dynamik rekombinačních procesů excitovaných nosičů v PCD, která by pomohla upřesnit charakter relaxačních a rekombinačních procesů excitovaných nosičů, a tím i vliv struktury na optické a elektrické vlastnosti PCD, stále chybí. Dospod totiž bylo zrealizováno pouze několik časově rozlišených studií chování excitovaných nosičů, které ukazují na vícesložkové doznívání (v horizontu desítek a stovek ps) či možné doznívání luminiscence v závislosti na použitém PCD a vlastnostech excitace.¹⁷⁰⁻¹⁷² Rozšířením a doplněním poznání v tomto směru je věnována část vědecké aktivity předkladatele¹⁷³. Přesnější poznání vnitřní struktury a její vliv na vlastnosti PCD je mimo jiné zásadní pro její další aplikovatelnost a cílenou přípravu povrchů pro specifické aplikace. Ty jsou na základě elektrických a optických vlastností dosud omezeny na mikro/nano elektromechanické

systémy (MEMS/NEMS), Schottkyho bariérové diody, detekce plynů či vysokoenergetického záření.^{156, 157, 174}



Obrázek 18. a) SEM snímky polykrystalického diamantu: MCD, NCD a UNCD (použito se svolením majitele práv Optica Publishing group),¹⁷³ b) energetické schéma polykrystalického diamantu,¹⁵⁹ c) využití UNCD prášku jako nosiče chemoterapeutika (použito se svolením majitele práv ACS Publications),¹⁷⁵ d) využití UNCD prášku jako kontrastní látka v medicíně (použito se svolením majitele práv ACS Publications).¹⁷⁶

Nanodiamantové hybridy

Vývoj technologie přípravy polykrystalického diamantu vede k dynamickému snižování ceny a růstu kvality připravených filmů/prášků. S tím jde ruku v ruce i rozvoj nových využití tohoto materiálu, a to především do stále pokročilejších aplikací. Mezi nejzajímavější současné aplikace patří především bioelektronika a medicína.^{153, 177-179} Bioelektronická zařízení jsou typická vytvářením hybridu (kompozitu) anorganického substrátu a organické aktivní vrstvy. Výhodou organických vrstev je jejich citlivost, levnější a ekologičtější příprava a potenciál být využité *in vivo*. U téhoto zařízení se však klade velký důraz na vlastnosti substrátů. Ty musí být schopny efektivního přenosu signálu z aktivní vrstvy, kvalitního uchycení organické složky a ideálně vykazovat nízkou degradaci a toxicitu při použití *in vivo*. První dvě podmínky dobře splňuje zlato či křemík, všechny očekávané požadavky splňuje diamant. Ten je navíc schopen s organickou aktivní vrstvou vytvářet silné uhlíkové kovalentní vrstvy. Mezi nejběžnější bioelektronická zařízení patří biotranzistory, bio MEMS či biosenzory.^{156, 178, 180}

Díky dobré biokompatibilitě si polykrystalický diamant začíná nacházet místo i v pokročilých medicínských aplikacích mimo již známé ochranné povrchy či bioelektronická zařízení. Jedním z takových je technologie cíleného směrování léčiv. Nanodiamantový prášek se totiž ukázal být velmi kvalitním nosičem léčiva (**Obr. 18c,d**).¹⁷⁷ Podle současných výsledků nejsou UNCD toxicke pro organismus a jsou schopny transportu léčiva, jak prokázaly například prvotní experimenty s chemoterapeutikem doxorubicin hydrochlorid (DOX).¹⁸¹ Díky uhlíkové struktuře se také PCD terminované kyslíkem ukázaly být vhodnými substráty pro kultivaci buněk.¹⁸²

Jednou z hlavních překážek v rozvoji těchto technologií je vysoká chemická odolnost diamantu, a v případě bioelektroniky i nedostatečná znalost mechanismů dynamik nosičů náboje na rozhraní obou složek hybridu. Zatímco první zmíněná překážka se daří úspěšně zvládat cílenou terminací povrchu diamantu vodíkem, kyslíkem nebo fluorem (především pomocí vystavení diamantového povrchu příslušnému plazmatu),^{179, 183} druhá tématika je stále nedostatečně zmapovaná. I tomuto tématu se věnuje další prezentovaná publikace předkladatele. Přesněji je daná publikace věnována studiu transportních a rekombinačních mechanismů nosičů náboje na rozhraní nanohybridu vodivého polymeru a PCD, který má potenciál být efektivně využitelný ve fotovoltaice a bioelektronice.¹⁸⁴

2. Syntéza křemíkových nanostruktur

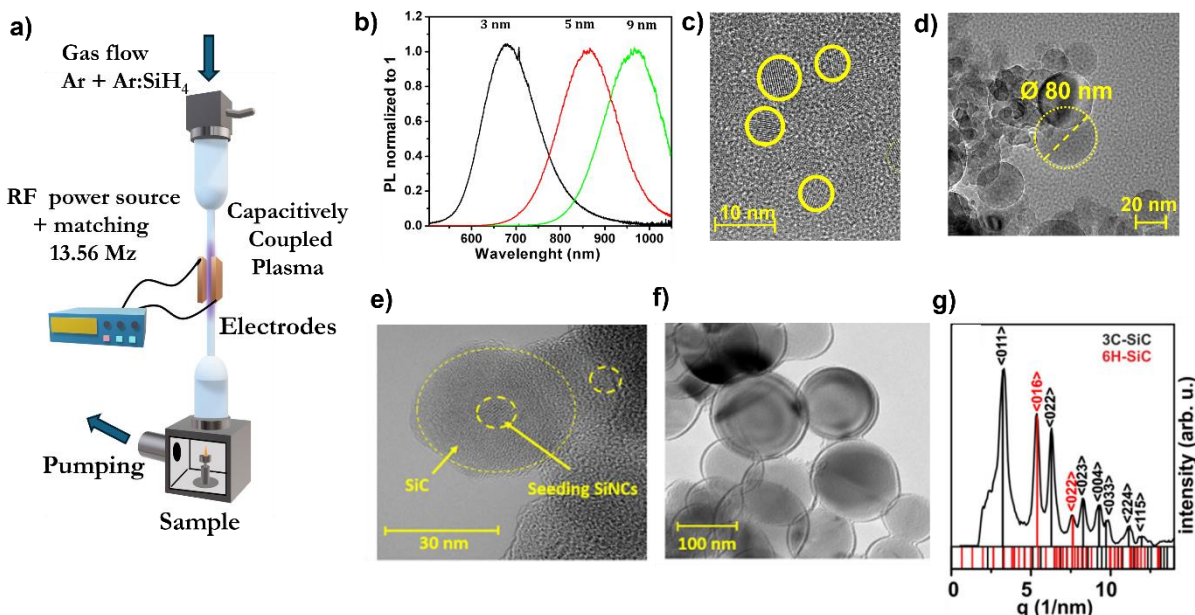
2.1 Křemíkové nanostruktury připravené pomocí netermálního plazmatu

Předešlý výzkum naší vědecké skupiny ukázal potenciál SiQDs nejen jako vhodného materiálu pro studium kvantových efektů v polovodičích, ale také aplikačně zajímavého materiálu pro optoelektronické a fotovoltaické aplikace.⁷⁷ Bohužel tehdejší metoda přípravy využívající elektrochemického leptání nebyla schopna vytvořit dostatečné množství SiQDs a také neumožňovala snadno a kontrolovaně ladit jejich strukturní vlastnosti. Z toho důvodu jsme vybudovali systém pro přípravu SiQDs pomocí nízkotlakého netermálního plazmatu využívajícího radiofrekvenčního zdroje (RF). Z konstrukční stránky jsme při jeho tvorbě adaptovali systém využívaný jedním z průkopníků této technologie prof. Kortshagena a upravili ho pro naše potřeby (**Obr. 19a**).⁸⁹ Systém využívá silanu jako zdrojového plynu křemíku a argonu jako plynu nosného. Přesný popis našeho systémů je možné najít v přiložené publikaci.⁹⁷ Optimalizací experimentálních parametrů jsme byli schopni cíleně a opakovatelně připravit nejen amorfní křemíkové nanočástice, ale i krystalické QDs o velikosti od 2,5 nm do 20 nm a to s výtěžkem okolo 50 mg/hodina. QDs o velikosti od 2,5 – 8 nm vykazovaly excitonovou luminiscenci na světelném intervalu od 600–1050 nm, hodnoty QY v rozmezí od 0,1 do 1 % (vodíkem terminované, **Obr. 19b,c**). Po oxidaci okolní atmosférou došlo ke zvýšení QY do maximální hodnoty 7 %. Mimo standardně udávané parametry ovlivňující výsledek syntézy, mezi které se počítá: a) koncentrace silanu, b) rychlosť průtoku plynu výbojem, běžně charakterizovaná dobou průletu částice výbojem (z angl. residence time) a c) výkon RF zdroje, jsme odhalili i další publikacně opomíjené parametry. Jedná se například o: a) tvar elektrod, který určoval homogenitu a délku výboje v závislosti na výkonu zdroje. U nás byly testovány prstencové, deskové a nedávno i elektrody ve tvaru dvojitě spirály.¹⁸⁵ b) Tvar reaktoru. V našich podmírkách nebylo zprvu možno vytvořit kvalitní SiQDs s reaktorem o běžně udávaném vnitřním průměru $d = 23$ mm. Vytvořili jsme proto reaktor se zúženou střední částí ($d = 7$ mm). Díky tomu došlo ke zvýšení homogeneity a energie výboje v dané oblasti bez přítomnosti nechtěného přehřívání elektrod a dalších parazitních jevů spojených s přílišným výkonem. c) Tlak a tlakový gradient v reaktoru ovlivňující četnost srážek iontů v plazmatu a d) množství vodíku v pracovním plynu. Vodík je přirozenou součástí silanu (SiH₄), takže je automaticky přítomný v pracovní směsi. Nicméně, bylo ukázáno, že zvýšení jeho koncentrace dodatečným přidáním čistého vodíku vede nejen k mírnému snížení velikosti SiQDs, ale také změně jeho

povrchové chemie, projevující se změnou poměr $*\text{SiH}_x$ hydridových vazeb na povrchu (viz dále).^{83, 186}

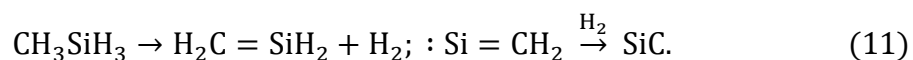
Přestože nám adaptace této technologie umožnila vytvářet amorfní křemíkové nanočástice a SiQDs s laditelnou velikostí v dostatečném množství, jednostupňový průtokový reaktor neumožnuje měnit povrchovou terminaci nanočástic (mimo tu vodíkovou), zvýšit jejich velikost nad 20 nm a také vytvářet komplexní struktury typu jádro/slupka. Za tímto účelem došlo k zavedení dvou dvoustupňových systémů. Jeden byl vytvořen a druhý vznikl úpravou staršího systému. První stupeň byl u obou systémů složen z reaktoru prezentovaného na **Obr. 19a** a druhý tvořil: a) průtokových reaktor téměř identický s prvním a b) komora s objemovým netermálním RF plazmatem.

První námi navržená dvoustupňová průtoková aparatura je určena k rychlé povrchové úpravě nanočastic křemíku a také dodatečnému růstu zárodečných zrn z prvního stupně. Cílem je nejen příprava a-Si/c-Si struktur (amorfni/krytalické), ale také růst větších krytalických nanočastic, a to dodáním dalšího silanu přímo do výboje v druhém stupni. Obě zmíněné nanostruktury mají velký potenciál například v Li-Ion technologii. V současné době jsme již schopni vytvářet nanočasticice do velikosti 80 nm. Data a postupy prozatím nebyly publikovány (**Obr. 19d**).



Obrázek 19. a) Schéma experimentální aparatury na přípravu křemíkových nanostruktur pomocí netermálního plazmatu. b) Normovaná fotoluminiscenční spektra SiQDs o vybraných velikostech. c) HRTEM SiQDs o velikosti ~ 6 nm. d) TEM Si nanočastic připravených pomocí dvoustupňové přípravy. e) a f) TEM Si/SiC nanostruktur. g) SAED analýza Si/SiC nanostruktury (použito se svolením majitele práv John Wiley and Sons).⁹⁷

Druhý zmíněný systém byl úspěšně použit k povrchové terminaci SiQDs uhlíkovými funkčními skupinami¹⁸⁶ a také na přípravu křemíkových nano-heterostruktur typu jádro/slupka.⁹⁷ Významně úspěšná byla především příprava Si/SiC nanostruktury jádro/slupka. Nanostrukturní formy karbidu křemíku jsou totiž aplikačně velmi zajímavé, a to díky jejich nevšedním elektrickým a optickým vlastnostem, jejich příprava je ovšem velmi obtížná. Teplota tání SiC totiž přesahuje 2700°C a jedním z mála postupů přípravy nano SiC je implementace karbotermické redukce SiO₂ uhlíkem za teplot okolo 1500°C s redukcí velikostí jednotlivých krystalických zrn,¹⁸⁷ případně elektrochemické leptání SiC waferu.¹⁸⁸ Existuje i několik prací ukazujících možný způsob syntézy SiC pomocí netermálního plazmatu, a to především přímou syntézou z tetramethyl silanu. Výstupem těchto snažení byly amorfni nanočástice SiC o velikosti 10 nm,¹⁸⁹ případně QDs o průměru okolo 5 nm.¹⁹⁰ Na rozdíl od těchto postupů jsme ukázali, že pomocí dvoustupňové syntézy jsme schopni připravit téměř ideálně sféricky symetrické krystalické Si/SiC nanočástice o velikostech od 50 – 150 nm (**Obr. 19e,f**).⁹⁷ Přesný postup přípravy nanočastic zahrnoval syntézu krystalických SiQDs v prvním stupni reaktoru (zárodečná zrno) a jejich následnou několika minutovou interakci s plazmatem ve stupni druhém. Plazma ve druhém stupni bylo tvořeno methylsilanem (MMT) a použitý výkon byl 5x slabší než ve stupni prvním. Za této situace nedocházelo k propojování zárodečných zrn, ale pouze k růstu SiC slupky. Strukturní vlastnosti nanočastic byly ověřeny pomocí HRTEM a elektronové difracce (SAED), která prokázala, že se jedná o 3C-SiC polymorf (**Obr. 19g**). Chemické složení slupky potvrdila i charakterizace povrchu pomocí infračervené spektroskopie (FTIR) a detekce, pro tento typ materiálu typické, oranžové fotoluminiscenční odezvy. Testováno bylo i možné přidání MMS do prvního stupně syntézy, případně přímá příprava SiC pomocí čistého MMS v prvním stupni reaktoru. Za těchto podmínek buď žádné nanočástice nevznikly nebo vznikl amorfni SiC. Použití drobného Si zrna je tedy zásadní pro vznik sférických krystalických Si/SiC nanočastic. Přestože existuje několik chemických cest pro přípravu SiC z plynu, vzhledem k podmínkám v reaktoru je nejpravděpodobnější, že k růstu SiC na Si zárodku dochází podle následujícího schématu využívajícího reakce přes Si=CH₂:¹⁹¹



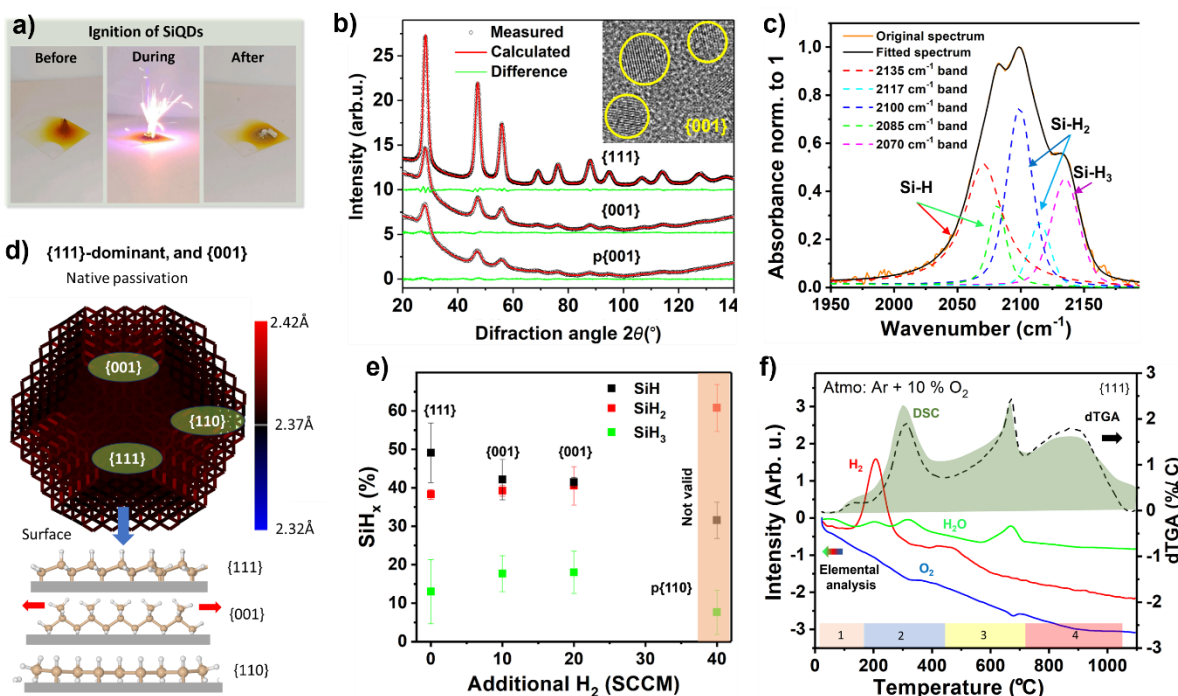
Námi objevený postup přípravy těchto sférických krystalických nano-heterostruktur byl opakovatelný a struktury by mohly být snadno využitelné v různých vysokoteplotních aplikacích.

2.2 Křemíkové kvantové tečky s různou dominantní facetou

Během sestavovaní databáze procedur na tvorbu SiQDs pomocí jednostupňové aparatury jsme narazili na následující tendence. Při přidávání dodatečného vodíku do syntetizační směsi jsme byli schopni připravit SiQDs o velmi podobné velikosti, ovšem odlišném složení povrchových ${}^*\text{SiH}_x$ hydridů. Jelikož SiQDs připravené netermálním plazmatem vykazují téměř výhradně sférický tvar, a navíc křemík krystalizuje jen do plošně centrované kubické mřížky, tak by zmíněná změna povrchové chemie měla být spojena s restrukturalizací povrchových atomů, které by následně prioritně vytvářely jiné křemíkové hydridy. Tato pozorování byla zajímavá i vzhledem k faktu, že přesná struktura povrchu a jádra SiQDs je stále velmi diskutovaným tématem.⁷⁰ Byla proto vytvořena sada vzorků, při jejichž přípravě bylo postupně zvyšováno množství dodatečného vodíku, a to v rozmezí od 0 do 40 SCCM. Překročení horního limitu vedlo k amorfizaci nanostruktur. Struktura SiQDs byla charakterizována pomocí Ramanovské spektroskopie, HRTEM, SAXS a XRD. Tyto metody ověřily krystalický charakter teček a určily jejich velikost, která mírně rostla s ubývajícím množstvím vodíku v rozmezí od 4,5 do 6 nm (**Obr. 20b**). Byla provedena detailní analýza FTIR spekter vzorků a určeny poměry ${}^*\text{SiH}_x$ hydridů na jejich povrchu. Určení zastoupení ${}^*\text{SiH}_x$ hydridů se standardně zjišťuje z poměru ${}^*\text{SiH}_x$ píků v intervalu 2000 – 2200 cm^{-1} ($\nu({}^*\text{Si–H}_x)$ stretching mode, **Obr. 20c).**¹⁹² Bylo prokázáno, že vzorek připravený bez přidaného vodíku obsahuje nejvyšší koncentraci ${}^*\text{SiH}$ a nejnižší ${}^*\text{SiH}_3$ hydridů, vzorky připravené s 10 – 30 SCCM vykazovaly téměř identické složení povrchu s vyšším poměrem ${}^*\text{SiH}_{2-3}$ (**Obr. 20e**). U posledního vzorku nebyla analýza průkazná. Jeho povrch již pravděpodobně vykazoval snížení míry uspořádání, což vedlo ke snížení profilování píků a vysoké chybě analýzy. Ta ukazovala na vysoké koncentrace ${}^*\text{SiH}_2$ vazeb, což je v rozporu s absencí pásu na 695 cm^{-1} , který odpovídá vibraci ${}^*\text{Si–H}_2$ (wagging mode). Na základě struktury FTIR spektra mimo sledovaný interval 2000 – 2200 cm^{-1} by měl být povrch posledního vzorku spíše dominován ${}^*\text{Si–H}$ vazbami.

Tyto výsledky byly následně srovnány s modely povrchů SiQDs vytvořenými prof. Königem.¹⁵ Ten pouhým odříznutím části kubické struktury křemíku vytvořil *hranaté* nanočástice s ideální facetou {111}, {001} a {110}. Jeho studie ukázala, že přechodem od první jmenované struktury k poslední výrazně roste jejich volná povrchová energie (angl. free surface energy – SFE) a to o 0,2 eV/atom mezi facetami. Navíc se mění i poměr povrchových hydridů. Trend změny složení křemíkových hydridů na povrchu našich QDs s přidáváním dodatečného vodíku významně koreloval se změnou chemického složení výše uvedených modelových objektů při přechodu od {111} k {110}. Na rozdíl od našich výsledků však prezentované

modelové struktury obsahují pouze zanedbatelné množství $*\text{SiH}_3$ nezávisle na facetě. Zastoupení tohoto hydridu na povrchu našich SiQDs se pohybovalo okolo 10 – 15 % napříč vzorky. Jelikož však naše SiQDs vytváří sférické struktury, není možné, aby jejich reálný povrch plně odpovídal prezentovanému modelu. Ve spolupráci s prof. Königem byl tedy vytvořen nový, realističtější model kvazisférické SiQD. Ten vychází i z práce B. Jariwala, který očekává, že povrch SiQDs je tvořen větším počtem facet navzájem tvořících menší terasy.¹⁹² Povrchová struktura takového objektu je následně téměř nerozlišitelná od čistě sférického tvaru. Přestože takto vytvořené kvazičástice obsahují různé facety, jeden typ facet je vždy nejvíce exponován, a tak určuje (dominuje) charakter povrchu.



Obrázek 20. a) Demonstrační výkres výplně H-SiQDs. b) SAXS analýza SiQDs s dominantními facetami $\{111\}$, $\{001\}$ a $p\{110\}$. V řezu je HRTEM snímek SiQDs s dominantními facetami $\{001\}$. c) Ukázka analýzy složení křemíkových hydridů na povrchu SiQDs dominantní- $\{111\}$ pomocí FTIR spekter v intervalu $2000 - 2200 \text{ cm}^{-1}$. Model povrchu SiQDs pomocí simulace klasického silouzvěho pole. e) Složení hydridů na povrchu SiQDs s dominantními facetami $\{111\}$, $\{001\}$ a $p\{110\}$ za použití analýzy z c). f) Porovnání TGA, dTGA (diferenciální TGA) a elementární analýzy H_2 , H_2O a O_2 na SiQDs s dominantními facetami $\{111\}$ v 10% kyslíkové atmosféře (použito se svolením majitele práv ACS Publications).⁸³

Na základě těchto poznatků jsme zavedli termín tzv. kvantové tečky s dominantními facetami, kterým označujeme mnohostennou kvazisférickou částici s jednou převládající

facetou. Modely takových objektů pro dominantní- $\{111\}$, $\{001\}$, $\{110\}$ vykazovaly obdobné trendy složení hydridů, jako ve zjednodušeném modelu, ovšem s výrazně vyšším zastoupení $^{*}\text{SiH}_3$ na přechodech mezi facetami, což odpovídá měřením na našich plazmaticky připravených SiQDs. Očekáváme proto, že SiQDs připravené bez použití vodíku mají podobný povrch jako QDs dominantní- $\{111\}$, SiQDs připravené s přidáním 10 – 30 SCCM odpovídají QDs s dominantní- $\{001\}$ a SiQDs připravené s 40 SCCM mají obdobnou strukturu jako dominantní- $\{110\}$. Pro ucelenosť popisu je dobré zmínit, že na základě FTIR analýz očekáváme u vzorků připravených s 40 SCCM přidaného vodíku mírný amorfí charakter povrchu. V textu proto tyto vzorky označujeme jako SiQDs dominantní-p $\{110\}$ (partly). Možnost ladit složení povrchových facet SiQDs pomocí přidaného vodíku souhlasí i s očekávaným vlivem přidaného vodíku na syntetizační mechanismy SiQDs. Tvar vznikajících kvazisférických mnohostěnů je totiž spojen s minimalizací lokálního pnutí mezi atomy, které pochází z deformace délky vazeb a úhlu mezi nimi. Vezme-li v potaz, že atomární vodík v plazmatu je schopen leptat vznikajících nanočástic, a navíc ovlivňovat efektivitu přenosu energie z iontů argonu do nanočastic, jeho přítomnost může měnit podmínky pro vznik zmíněných mnohostěnů a tím typ dominantní facety. Pro ověření očekávaného vlivu vodíku byl také vytvořen model kvazisférické částice pomocí simulace klasického silového pole. Na tomto modelu bylo studováno, jak velké pnutí v SiQDs by vytvořilo nahrazení jedné atomové vrstvy křemíkových atomů hydridem $^{*}\text{SiH}_3$. Tento postup měl simuloval leptání povrchu ve vodíkovém plazmatu (**Obr. 20d**). Zatímco u dominantní- $\{111\}$ struktury byl výsledný vliv minimální, u SiQDs s dominantní- $\{110\}$ vyvolala popsána změna značné pnutí a tím výrazně snižovala tepelnou stabilitu povrchu.

Zda naše vzorky opravdu vykazují vlastnosti SiQDs s dominantními facetami jsme se rozhodli ověřit studiem jejich termálních vlastností. Jako vzorový jev jsme si vybrali tzv. nízkoteplotní vznícení. Bylo prokázáno, že nanostrukturální křemík terminovaný vodíkem má tendence se vznítit za relativně nízkých teplot. Tato teplota se napříč strukturami výrazně lišila a sahala od 200 do 700 °C.^{108, 193} Nejnižší teplota vznícení byla pozorována u amorfního křemíku a SiQDs. Přestože se očekává výrazný vliv povrchového vodíku, podstata tohoto jevu nebyla nikdy jednoznačně vysvětlena. Především je matoucí fakt, že při teplotách okolo 200°C by nemělo docházet k dehydrogenaci povrchu a dehydrogenační teplota by neměla měnit svou hodnotu v takovém rozsahu. U našich vzorků bylo zjištěno, že i ony vykazují nízkoteplotní vznícení, a to v rozsahu iniciovačních teplot od 220 °C do 150 °C při přechodu od vzorků s dominantní facetou $\{111\}$ k p $\{110\}$ (**Obr. 20a**). Nejnižší teplotu vznícení tak neměl vzorek s nejvyšší koncentrací $^{*}\text{Si-H}_{2-3}$ vazeb (SiQDs s dominantní- $\{001\}$), které by měly být

nejsnadnějším zdrojem vodíku (nižší disociační energie než ${}^3\text{Si-H}$), ale vzorek s nejvyšší hodnotou SFE. Pro získání detailnějších informací o termálních vlastnostech našich vzorků jsme provedli jejich charakterizaci za současného využití termogravimetrické analýzy (TGA), diferenciální snímací kalorimetrie (DSC) a hmotnostní spektroskopie na teplotním intervalu 25 – 1100°C. Pro určení vlivu kyslíku při těchto experimentech byla daná měření provedena jak pod ochrannou atmosférou, tak i za přítomnosti 10% kyslíku v argonu (**Obr. 20f**). Měření odhalila hned několik významných termických procesů, které ukazují na růst tepelné nestability SiQDs s růstem očekávané SFE a také potvrdila shodu poměrového rozložení hydridů mezi našimi vzorky a teoretickým složením povrchu SiQDs s dominantní facetou. Detaily měření jsou k nalezení v přiložené publikaci.⁸³ Zde shrneme jen hlavní pozorování: a) bylo zjištěno, že teplota vznícení je velmi blízká s náběhovou teplotou (z angl. onset temperature) pro páteřní oxidaci křemíku (z angl. backbone oxidation) a náběhovou teplotou dehydrogenace ${}^3\text{Si-H}_{2-3}$. Ta je ovšem až o téměř 100°C nižší než by se očekávalo na základě běžné udávané disociační energie dané vazby. Na základě získaných dat a faktu, že nanostrukturální křemík vykazuje velmi nízkou tepelnou vodivost (0,1 W/mK), což je 1000x méně než u objemového křemíku a 3x více než u vzduchu, jsme navrhli následující vysvětlení níztoteplotního vznícení SiQDs. Exotermní oxidace povrchových Si-Si vazeb pravděpodobně na povrchu SiQDs vytváří přehřátá místa, která kumulují tepelnou energii. Díky přehřátým místům následně dehydrogenace z ${}^3\text{SiH}_{2-3}$ probíhá při nižších teplotách, než by odpovídalo její disociační energii, a to vede při dostatečném množství okolního kyslíku k řetězové oxidační reakci a shoření celé nanočástice. Tento efekt je zesílen, pokud se jedná o SiQDs s vysokou SFE, jelikož s růstem SFE jsme pozorovali snižování onset teplot pro páteřní oxidaci i dehydrogenaci SiH_{2-3} vazeb.⁸³ b) Růstem SFE nebyla ovlivněna teplota dehydrogenace z monohydridů, ale docházelo ke snižování teploty vyvolávající difuzní oxidaci SiQDs. c) Množství uvolněného vodíku v teplotních intervalech, kde očekáváme dehydrogenaci z ${}^3\text{Si-H}_{2/3}$ a ${}^3\text{Si-H}$, odpovídalo předpovězenému složení povrchu jednotlivých SiQDs s dominantní facetou (model a FTIR měření). d) Podařilo se nám také objasnit výrazný nárust uvolněné energie pozorovaný při teplotách okolo 700°C, který byl u SiQDs detekován jinými autory a byl interpretován jako dodatečná krystalizace častic.¹⁹⁴ Při této teplotě jsme totiž naměřili i uvolnění většího množství vody a úbytek kyslíku v okolní atmosféře. Je obecně známo, že SiQDs mohou během oxidace vytvářet mezi sebou pevnou vazbu přes kyslíkové atomy, což je důvodem obtížné dispergace oxidovaných SiQDs aglomerátů. S největší pravděpodobností při zmíněné teplotě dochází k praskání těchto vazeb a tím i aglomerátů SiQDs, za současného nárazového uvolnění vodíku z dutin mezi SiQDs. Tento

vodík poté rychle reaguje s kyslíkem za vzniku vody a uvolnění energie. Toto chování nebylo pozorováno při termální charakterizaci pod inertní atmosférou.

Na základě tohoto výzkumu jsme ukázali, že úpravou podmínek přípravy nanočástic netermálním plazmatem je možno připravit SiQDs o různé SFE. Povrchovou strukturu těchto SiQDs je možno s dobrou přesností popsat pomocí tzv. dominantních facet, což rozšiřuje současné poznání o povrchu SiQDs. Přípravou teček o různé SFE můžeme měnit nejen jejich povrchovou reaktivitu, ale i složení Si hydridů a tím je optimalizovat pro odlišné aplikace.

Publikace autora zabývající se tímto tématem:

- 1) Galář, P., et al. *Engineering the thermal and energy-storage properties of quantum dots using surface free energy*. *ACS Nano*, 2024: Accepted.
- 2) Galář, P., et al., *Highly spherical SiC nanoparticles grown in nonthermal plasma*. *Plasma Proc. Polym.*, 2022, 19, 1 – 10; 0.1002/ppap.202100127
- 3) Müller, M., Galář, P., et al., *Synthesis and surface modification of light emitting silicon nanoparticles using non-thermal plasma techniques*. *Eur. Phys. J. Appl. Phys.*, 2020. **89**(2): p. 20401, 10.1051/epjap/2020190263
- 4) Dworschak, M., Kohlmann, N., Matějka, F., Galář, P. et al., *Silicon nanocrystal synthesis with the atmospheric plasma source HelixJet*. *Plasma Proc. Polym.*, 2023; 10.1002/ppap.20220 0129

3. Povrchově modifikované křemíkové kvantové tečky

3.1 Terminace kvantových teček plazmaticky aktivovanou vodou

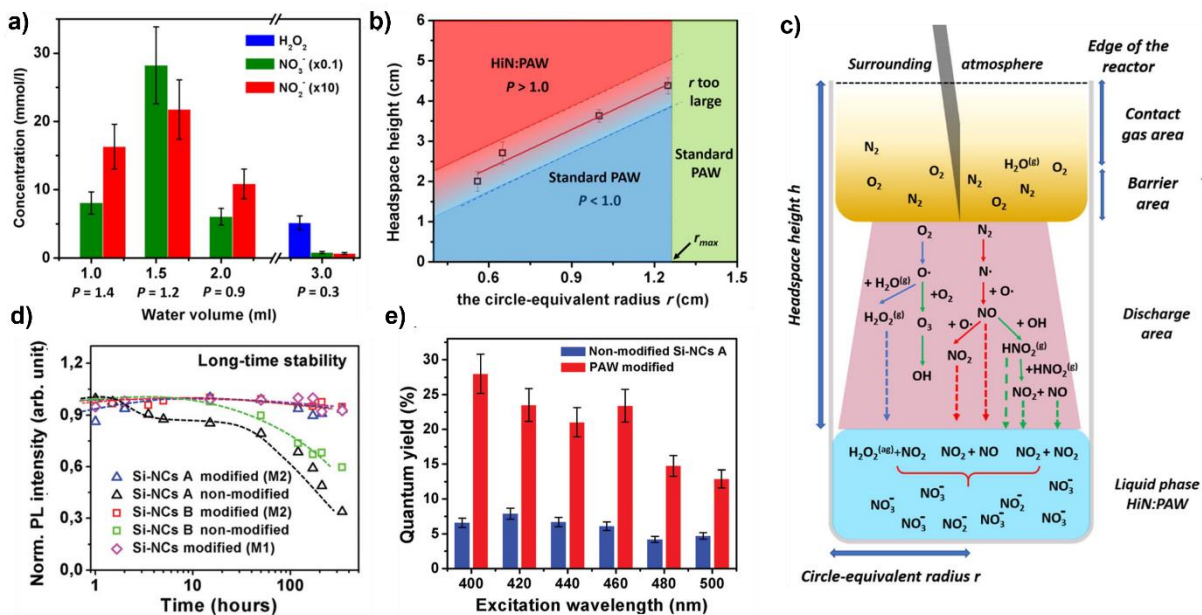
Netermální plazma je využitelné nejen k přípravě křemíkových nanočástic, ale má mnoho další aplikací. Jednou z nich je příprava tzv. plazmou aktivovaných kapalin (PAL, z angl. plasma-activated liquid).^{195, 196} Interakce plazmatu s kapalinou vede k vzniku roztoku o vysoké hustotě různých reaktivních entit, jejich složení je závislé na vlastnostech plazmatu, prostředí, v němž plazma hoří a samozřejmě použitému roztoku. Drtivá většina všech vědeckých prací na toto téma se věnuje plazmou aktivované vodě – PAW, která je užívána k dezinfekci, ničení plísni, či ochraně potravin.¹⁹⁷ Mezi hlavní stabilní reaktivní entity v PAW patří ionty NO_2^- , NO_3^- a molekulární H_2O_2 . Existuje však i hrstka průkopnických prací, které částečně úspěšně ukázaly možné využití reaktivního prostředí PAW k povrchové terminaci SiQDs založené na dusíkových reaktivních entitách.¹⁹⁸ Překážkou k dalšímu rozvoji této snadné, ekologické a levné techniky povrchové úpravy nanomateriálů je především přítomnost H_2O_2 , který nejen že narušuje vznikající dusíkovou terminaci, ale v případě křemíku i strukturu nanočástice samotné. Pro efektivní využití PAW k terminaci povrchu SiQDs jsme tedy museli nejprve vytvořit postup pro přípravu tohoto média s vysokým obsahem NO_x^- bez přítomnosti H_2O_2 .

Za tímto účelem jsme vytvořili plazmatický systém založený na přechodové jiskře, jakožto výboji, který je schopen generovat PAW o vysokém obsahu NO_x^- . Následně jsme studovali vliv konstrukce elektrodového systému, vlastnostech výboje, konstrukce reaktoru obsahujícího aktivovanou vodu a okolní atmosféry na chemické složení výsledné PAW.^{98, 99} Bylo zjištěno, že všechny zmíněné parametry mění poměr mezi NO_x^- a H_2O_2 , ovšem překvapivě nejzásadnější roli hraje geometrie reaktoru (**Obr. 21a**). Přesněji poměr jeho šířky a vzdálenosti volné hladiny PAW od okraje reaktoru, definující bariéru mezi hladinou PAW a okolní atmosférou. Z empirických dat jsme definovali tzv. bariérový parametr P :⁹⁹

$$P = \frac{h - 0,3823}{3,225 r}, \quad (12)$$

kde h je vzdálenost volné hladiny od okraje reaktoru a r je kruhový ekvivalent poloměru reaktoru. V případě, že parametr $P > 1$ docházelo u našeho systémů ke generaci PAW o minimální koncentraci H_2O_2 . Naopak koncentrace NO_x^- překračovala všechna dosud publikovaná data o více než jeden řád (**Obr. 21b**). Nejlepších výsledků bylo dosaženo při nastavení, kdy $P = 1,2$ (**Obr. 21a**). Koncentrace NO_3^- a NO_2^- byla za těchto podmínek rovna

~ 300 mmol/l, respektive 2 mmol/l. Rov. (12) platí pro reaktor s libovolným r nepřekračujícím hraniční hodnotu r_{\max} . Větší reaktory generovaly standardní PAW s vysokým obsahem H_2O_2 bez ohledu na hodnotu jakéhokoliv dalšího parametru. Vodu aktivovanou výše popsaným postupem jsme označovali jako HiN:PAW (z angl. high in nitrogen).



Obrázek 21. a) Koncentrace hlavních reaktivních entit v PAW aktivovaných pomocí přechodové jiskry za podmínek různých hodnot parametru P . b) Sumarizace podmínek spojených s použitým reaktorem vedoucích ke generaci HiN:PAW na rozdíl od standardní PAW. c) Schématické znázornění hlavních reakčních cest při generaci HiN:PAW (licence obrázků a, b, c CC BY, majitel práv IOP Publishing).⁹⁹ d) Stabilita intenzity PL O-SiQDs za běžných podmínek a pomocí HiN:PAW ve vodě. e) Srovnání QY O-SiQDs a terminovaných pomocí HiN:PAW na různých vlnových délkách (obrázky d, e použity se svolením majitele práv The Royal Society of Chemistry).⁹⁸

Za účelem vysvětlit vliv parametru P na vznik HiN:PAW, jsme provedli měření dynamik emisních spekter výbojů a složení aktivovaných vod za podmínek vykazujících různou hodnotu P . Bylo prokázáno, že složení spekter výbojů za všech sledovaných situací je v první fázi hoření výboje téměř identické a složené z molekulární emise plynů obsažených ve vzduchu ($t < 10$ min). U reaktorů vykazujících $P > 1$ však postupně dochází k zesilování atomární emise od H, O a N. Se změnou charakteru výboje z molekulárního na atomární docházelo také k redukci koncentrace H_2O_2 , která byla v první fázi přítomna ve všech aktivovaných kapalinách a růstu koncentrace NO_x^- . Na základě těchto výsledků jsme identifikovali 3 hlavní reakční cesty, ke kterým dochází v našich reaktorech (**Obr. 21c**). První (PAW1) je založena na generaci

kyslíkových radikálů za vzniku H_2O_2 . Druhá a třetí cesta (PAW2 a PAW3) je spojena s generací NO a NO_2 za přispění dusíkových radikálů. Tyto produkty následně ve vodě reagují za vzniku NO_x^- . H_2O_2 se ve vodě spotřebovává při reakci s NO_2 za vzniku NO_3^- . Nutnými podmínkami pro přípravu HiN:PAW se tedy ukázalo být: a) dosažení vysoké koncentrace dusíkových radikálů ve výboji, b) přítomnost vodních par a c) minimální množství kyslíku v prostoru výboje. Jelikož disociační energie N_2 je výrazně vyšší než O_2 (9,8 eV, respektive 5,2 eV) ke splnění první podmínky je nutné použít výboje o značné energii a současně zajistit atmosféru, která umožní postupný nárůst koncentrace dusíkových radikálů nad mez, kdy v reaktoru převládne reakční cesta PAW2 a PAW3 nad kyslíkovou (PAW1). Tím začne v aktivované vodě dominovat vznik NO_x^- , které následně spotřebují vznikající H_2O_2 v kapalině. Tímto požadavkem do reakce vstupuje hodnota parametru P (**Obr. 21c**). V situaci kdy $P > 1$ je hladina vody v reaktoru dostatečně daleko od jeho okraje, a dochází ke vzniku částečně uzavřené atmosféry („bariéry“), která blokuje výměnu plynů s okolím a tím dovolí nárůstu dusíkových radikálů. Prostor nad hladinou však stále umožňuje pozvolný přísun nespotřebované atmosféry. Detailní popis tohoto mechanismu a chemických reakcí vedoucích ke generaci HiN:PAW je uveden v přiložených publikacích.^{98, 99}

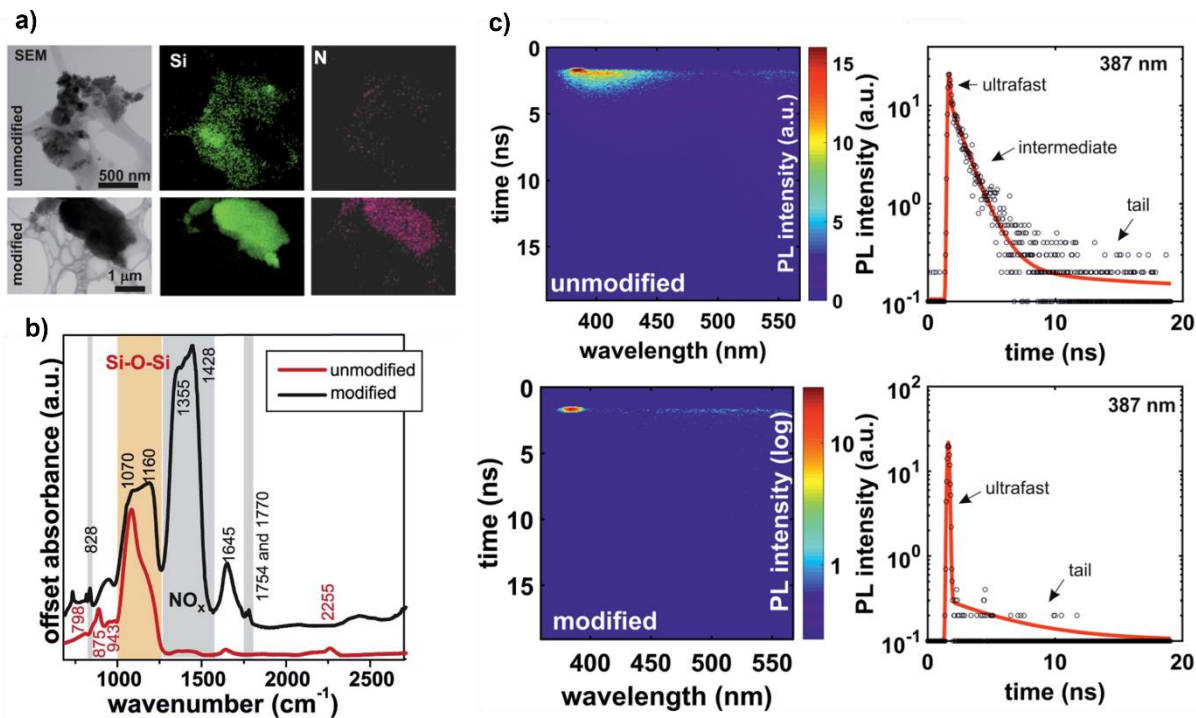
Následně jsme studovali možnosti povrchové úpravy SiQDs pomocí HiN:PAW.⁹⁸ Standardní povrchové úpravy založené na hydrosilyaci vyžadují plně vodíkem terminovaný povrch a trvají až nižší desítky hodin.⁹³ Naproti tomu povrchové a fyzikální vlastnosti SiQDs vykazovaly při interakci s HiN:PAW změny téměř okamžitě a to v případě jak H-SiQDs, tak i oxidovaných SiQDs. Saturace pozorovaných změn bylo dosaženo po ~ 30 min.⁹⁸ Interakcí s HiN:PAW docházelo k růstu QY SiQDs, posuvu emisního spektra do červené oblasti a zvýšení jejich dispergovatelnosti ve vodě. Například u O-SiQDs byla tímto postupem zvýšena jejich QY z 6 % na 25 % a bylo pozorováno zpomalení doznívání PL o 30 % (**Obr. 21e**). FTIR analýza prokázala přítomnost dusíkových komplexů na povrchu modifikovaných SiQDs. Tyto změny byly navíc stabilní po dobu minimálně několika týdnů, což není u SiQDs běžné. Dlouhodobým působením vody totiž standardní O-SiQDs degradují v horizontu dnů (**Obr. 21d**). Bylo také ukázáno, že pro vytvoření povrchové terminace dusíkovými komplexy není nutná přítomnost SiQDs ve vodě během její aktivace, ale je možné tečky smíchat s již aktivovanou vodou. Lepších výsledků je ovšem dosaženo prvním zmíněným postupem. To je dáno existencí reaktivních entit s krátkou dobou života (radikálů), které pomáhají k vytvoření kvalitní povrchové terminace a v předem připravené HiN:PAW nejsou přítomny. Pomocí DFT simulace, kdy jsme předpokládali nahrazení 50 % původní -OH povrchové terminace SiQDs za -O- NO_2 , bylo prokázáno, že tato úprava vede k vzniku nových energetických stavů kolem

zakázaného pásu, což zvyšuje míru zářivého přechodu excitovaných nosičů 2,5 – 5krát. Tyto hodnoty odpovídají pozorovanému zvýšení QY. Uvedená terminační procedura byla testována i na jiných polovodičových nanočásticích, a to jmenovitě ZnO a MgO. U obou typů nanočastic byla pomocí FTIR prokázána úspěšná povrchová úprava pomocí dusíkových komplexů a zlepšení jejich fotoluminiscenčních vlastností.

V rámci našeho výzkumu jsme tedy vyvinuly postup, jak vytvořit plazmaticky aktivovanou vodu s minimálním obsahem H_2O_2 a rekordním obsahem NO_x^- .⁹⁸ Toto medium bylo následně úspěšně použito na vytvoření povrchové terminace různých SiQDs, která byla nejen stabilní a vytvořena za velmi krátký čas, ale vedla i ke zlepšení hned několika pro QDs významných fyzikálních a chemických vlastností. Systém potřebný k vytvoření HiN:PAW je navíc jednoduchý, levný (do 10tis. Kč), na rozdíl od jiných metod využívá pouze běžnou vodu a výsledné produkty nejsou škodlivé. Tento postup povrchové úpravy nanočastic byl navíc naší skupinou patentován.¹⁰⁰

3.2 Vliv povrchové úpravy na rekombinační procesy excitovaných nosičů náboje

Postupu povrchové terminace SiQDs pomocí HiN:PAW jsme také využili k rozšiřování poznání o rekombinačních procesech na SiQDs.⁸² SiQDs totiž mimo běžně pozorovanou excitonovou luminiscenci (též označována jako pomalá/mikrosekundová či červená složka), může vykazovat i PL odezvu v modrém spektrálním intervalu. Tato luminiscence vykazuje výrazně rychlejší dobu života, a to v nanosekundové časové škále (též označována jako modrá nebo rychlá/nanosekundová složka). Její původ není jednoznačně určen, ale bývá spojován s přímým přechodem netermalizovaných elektronů přes $\Gamma_{15} - \Gamma'_{25}$ stavy křemíku, defekty na povrchu, příměsi, či zářivými stavy v SiO_2 pasivaci.^{199, 200} Při studiu modré PL složky SiQDs bylo mimo jiné ukázáno, že pozitivní vliv na její intenzitu má přítomnost dusíku během přípravy teček nebo jejich pasivace.²⁰¹ V rozporu s těmito závěry jsme povrchovou úpravou plazmaticky připravených SiQDs pomocí HiN:PAW vznik modré složky luminiscence nepozorovali.⁹⁸ Pro ověření vlivu dusíkových komplexů na PL SiQDs jsme vytvořili sérii teček, které byly syntetizovány pomocí elektrochemického leptání, nechali je přirozeně zoxidovat a následně provedli jejich povrchovou úpravu prostřednicvím HiN:PAW. Na rozdíl od prvních zmiňovaných totiž O-SiQDs připravené elektrochemickou cestou modrou složku luminiscence přirozeně vykazují.⁸² Přestože elementární i povrchové charakterizace prokázaly efektivní navázání dusíkových komplexů na jejich povrch (**Obr. 22a,b**), ani v tomto případě jsme nepozorovali zesílení modré složky PL, ale naopak její výrazné potlačení. Vlastnosti modré



Obrázek 22. a) SEM a elementární analýza elektrochemicky připravených O-SiQDs před a po terminaci HiN:PAW (unmodified/modified). b) Srovnání FTIR charakterizace vzorků z a). Hlavní peaky jsou vyznačeny. c) 2D mapa spektrální a časové závislosti doznívání PL na vzorcích z a) získané pomocí rozmítací kamery a detailní analýza dynamiky PL na vlnové délce 387 nm. PL bylo excitováno pulzy o časové šířce 150 fs, frekvenci 1 kHz a vlnové délce 343 nm (použito se svolením majitele práv The Royal Society of Chemistry).⁸²

složky luminiscence elektrochemických O-SiQDs byly proto před i po modifikaci detailněji studovány pomocí časově rozlišené laserové spektroskopie využívající rozmítací kamery (**Obr. 22c**). Doznívání PL nemodifikovaných O-SiQDs vykazovalo třísložkový charakter. První dvě měly mono-exponenciální časovou závislost o časových konstantách $\tau_1 \sim 40$ ps a $\tau_2 \sim 1,2$ ns. Poslední složka byla dobře approximovatelná napnutou (z angl. stretched) exponenciální funkcí ($\tau_3 \sim 10$ ns). Modifikace pomocí HiN:PAW sice neovlivnila první složku doznívání, druhou složku však plně potlačila a třetí intenzitně zeslabila ~ 5 krát. Jelikož spektrální poloha první složky byla korelována s excitační vlnovou délkou, byla ztotožněna s Ramanovským signálem a nejedná se tedy o PL signál ze vzorků. S přihlédnutím k výše prezentovaným simulacím energetického spektra SiQDs modifikovaných pomocí HiN:PAW je druhá složka doznívání luminiscence pravděpodobně spojena s defekty v SiO₂ obalu.⁹⁸ Poslední složka by poté měla odpovídat zářivým procesům nosičů v jádře nanočástic a jedná se o přímou rekombinaci netermalizovaných nosičů náboje. Povrchová terminace totiž nenaváže

na povrch pouze dusíkové komplexy, ale vede i ke zlepšení kyslíkové pasivace SiQDs. To potlačí PL generovanou z povrchových defektů a současně způsobí urychlení termalizace excitovaných nosičů a tím snížení intenzity poslední složky PL. Náš výzkum tedy ukázal, že ne všechny dusíkové terminace musí vést k růstu efektivity modré luminiscence na SiQDs, ale mohou ji i potlačovat. V našem případně hrálo větší roli zvyšování kvality povrchové oxidované pasivace SiQDs v přítomnosti HiN:PAW než vliv dusíkových komplexů.

V rámci našeho výzkumu jsme provedli i komplexní studium dynamik červené složky luminiscence různě připravených a terminovaných SiQDs za účelem osvětlení parametrů ovlivňující jejich vnitřní (iQY) a vnější (QY) kvantový výtěžek.⁵⁴ Je obecně přijímáno, že zdrojem červené složky luminiscence je rekombinace excitonů v jádru teček. Stále však nejsou jednoznačně objasněny mechanismy ovlivňující časový průběh jejich dynamik PL a vztah mezi iQY a QY souborů teček (**Obr. 23a**). Nejednotný není ani postup approximace časového doznívání červené složky PL. Nejčastěji bývá využíváno více exponenciálních funkcí nebo napnuté exponenciální funkce, která má funkční předpis:²⁰²

$$I(t, \lambda) = I_0(\lambda) e^{\left(\frac{-t}{\tau_{SE}(\lambda)}\right)^{\beta(\lambda)}}, \quad (13)$$

kde τ_{SE} a β značí časovou konstantu napnuté exponenciály, respektive disperzní parametr. Odchylka těchto doznívání od mono-exponenciální dynamiky typické pro binární kvantové tečky bývá interpretována na základě drobné variance dob života různých teček nebo přítomností kompetitivního chování zářivých a nezářivých rekombinačních procesů na SiQDs.²⁰³ V tom světle můžeme τ_{SE} chápat jako průměrnou dobu života nanočástic v souboru a β je spojeno s velikostí intervalu těchto dob. Díky svým zkušenostem s přípravou plazmatických/elektrochemických SiQDs o různé velikosti a povrchové úpravě máme dobré podmínky pro komplexní studium chování doznívání červené PL na velmi širokém souboru vzorků o různých vlastnostech. Tento soubor byl navíc doplněn i o SiQDs připravené termální disproporcionací HSQ, které byly připraveny spolupracující skupinou (prof. Ceroni, Italy). Většina použitých vzorků měla přirozenou kyslíkovou povrchovou pasivaci a některé byly terminovány uhlíkovým ligandem pomocí standardního hydrosilylačního postupu. U všech těchto vzorků bylo provedeno měření doznívání luminiscence (**Obr. 23a**). K jejich vyhodnocení jsme využili novou metodu založenou na výpočtu tzv. průměrné doby života – τ_{AV} (**Obr. 23b**).²⁷ Výhodou tohoto postupu je nezávislost výpočtu τ_{AV} na zvoleném matematickém modelu pro approximaci doznívání a také přiřazení danému doznívání pouze jeden parametr, který jej charakterizuje, což zvýší přesnost jeho výpočtu. Parametry komplikovanějších fitů

jsou totiž často vzájemně závislé. Předpis pro výpočet spektrální průměrné doby života τ_{AV} je roven:

$$\tau_{AV}(\lambda) = \frac{\int_0^\infty tI(t, \lambda)dt}{\int_0^\infty I(t, \lambda)dt}. \quad (14)$$

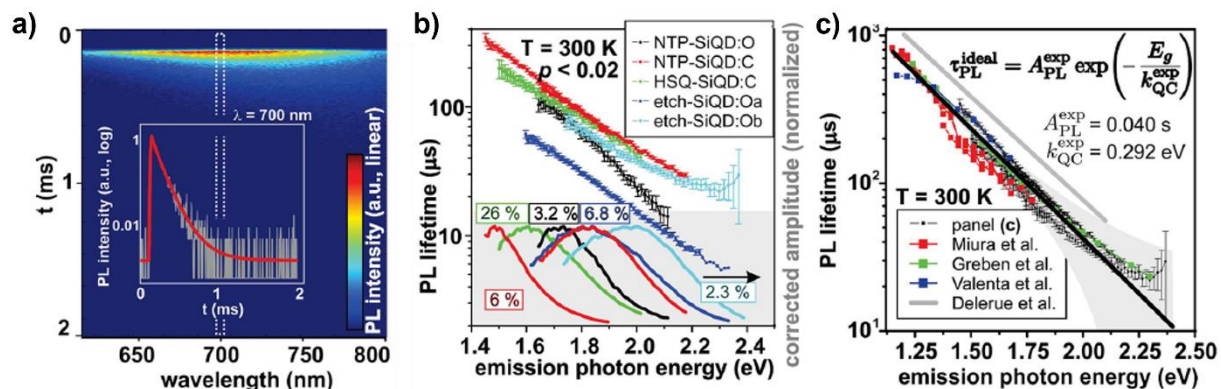
Tato závislost byla následně převedena do formy τ_{AV} (eV). Studiem doznívání našich vzorků následně vyplynulo, že $\tau_{AV}(E)$ mono-exponenciální charakter ve tvaru:⁵⁴

$$\tau_{AV}(E) = A_{PL} e^{\frac{-E}{k_{QC}}}, \quad (15)$$

kde E udává energii fotonů v eV, výraz $1/k_{QC}$ charakterizuje sílu kvantově-rozměrového jevu, respektive jeho vliv na zářivou dobu života excitovaných nosičů. Význam offset parametru A_{PL} bude vysvětlen později. Analyzovaná doznívání nevykazovala pouze společnou závislost dle předpisu (15), ale měly téměř identické hodnoty parametrů k_{QC} a A_{PL} (**Obr. 23b**). Pro srovnání byly metodou výpočtu průměrné doby života vyhodnoceny i PL doznívání SiQDs vykazující čistě zářivý charakter ($iQY \sim 100\%$), které byly publikovány jinými skupinami.²⁷,²⁰³. Výsledné závislosti τ_{AV} (eV) byly téměř identické s našimi vzorky (**Obr. 23c**). Jelikož τ_{AV} (eV) v sobě zahrnuje vliv zářivých i nezářivých rekombinačních procesů, tak jediné vysvětlení pozorované shody je, že i většina našich SiQDs vykazuje plně zářivý charakter. U těchto vzorků bylo následně provedeno měření QY (celkového kvantového výtěžku souboru teček) metodou využívající integrační koule. Vzorky vykazovaly QY od 2 do 26 %. Rozdíl mezi hodnotou iQY a QY lze interpretovat následujícím způsobem: každý vzorek obsahuje SiQDs, na kterých plně převládá buď nezářivý nebo zářivý rekombinační kanál. Kvantová tečka poté vykazuje buď $iQY \sim 100\%$ (jasná kvantová tečka) nebo $iQY \sim 0\%$ (temná kvantová tečka). Jelikož temné SiQDs neemitují PL, tak jejich přítomnost neovlivňuje výsledek výpočtu τ_{AV} . I ony však absorbují dopadající světlo, takže se jejich přítomnost projeví v hodnotě QY souboru SiQDs. Pokud budeme uvažovat přítomnost pouze jasných a temných teček a očekáváme stejný účinný průřez obou entit, pak hodnota QY přímo reflektuje poměr mezi temnými a jasnými tečkami. Tento poměr je vypočítán a diskutován v naší publikaci.⁵⁴ Otázkou pouze zůstává, proč se průběh τ_{AV} (eV) dvou vzorků lišil od všech ostatních (plazmatické O-SiQDs a leptané O-SiQDs). Na vině je pravděpodobně fakt, že vzorky neobsahují jen temné a jasné tečky. Pokud na tečce jednoznačně nepřevládá jeden typ rekombinace, ale jejich efektivita je blízká, může iQY nabývat libovolných hodnot od 0 do 100 %. Mluvíme pak o tzv. šedých kvantových

tečkách. Velikost iQY je poté přirozeně spojena hodnotou parametru A_{PL} , která může být použita k hrubému odhadu velikosti iQY teček v daném vzorku, více viz publikace.⁵⁴

Výše zmíněnou analýzou našich vzorků bylo zjištěno, že na rozdíl od O-SiQDs hydrosilyované vzorky připravené libovolnou metodou vykazují iQY $\sim 100\%$. Přirozeně oxidované vzorky naopak často vykazují přítomnost šedých teček, což je pravděpodobně dánou nehomogenitou jejich povrchové terminace a přítomností pastových povrchových stavů. Naše výsledky jednoznačně neodhalily, zda hydrosilylace může převádět temné tečky na světlé nebo jen zlepšuje iQY u šedých nanočástic. Tečky připravené metodou bottom-up mohou mít defekty přímo v jádře nanočástice, což u metod top-down (elektrochemické leptání) není tak pravděpodobné. Povrchová úprava tedy nemusí být vždy schopna ovlivnit nezářivé rekombinační procesy dominující v temných tečkách. Tato práce ukázala potenciál analýzy doznívání PL SiQDs pomocí výpočtu τ_{AV} (eV). Zmíněný proces vyhodnocení PL je schopen nejen studovat složitě měřitelný iQY kvantových teček v souboru, ale i odhalit přítomnost šedých kvantových teček, což je jinak experimentálně velmi složitý úkol. Komplexnější diskuze vztahu mezi τ_{AV} a fitovacími parametry napnuté exponenciály, spolu s detailním rozborem studovaných vzorků a jejich vlastnosti je k nazelení v přiložené publikaci.⁵⁴



Obrázek 23. a) Ukázka závislosti doznívání intenzity PL na vlnové délce detekovaná rozmitací kamerou na vzorovém SiQDs. b) Spektrální průběh červené složky PL vzorků (spodní část) a jím příslušné závislosti τ_{AV} (eV). c) Srovnání spektrálního průběhu τ_{AV} našich vybraných vzorků a měřených na jasných SiQDs publikovaných jinými skupinami (použito se svolením majitele práv ACS Publications).⁵⁴

Nejvýznamnější publikace autora zabývající se tímto tématem:

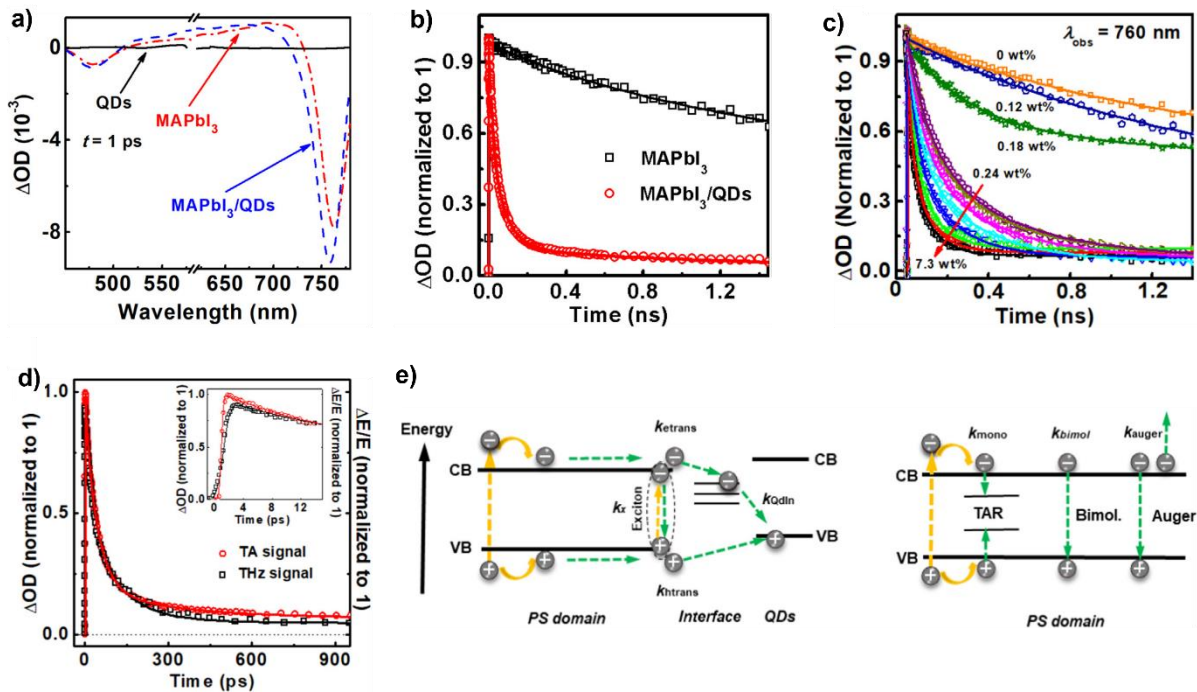
- 1) Galář, P., et al., Non-thermal pulsed plasma activated water: environmentally friendly way for efficient surface modification of semiconductor nanoparticles. *Green Chem.*, 2021. 23(2): p. 898-911. 10.1039/D0GC02619K2
- 2) Galář, P., et al., The red and blue luminescence in silicon nanocrystals with an oxidized, nitrogen-containing shell. *Faraday Discuss.*, 2020. 222(0): p. 240-257, 10.1039/C9FD00092E
- 3) Matějka, F., Galář, P., et al., Mechanisms leading to plasma activated water high in nitrogen oxides. *Physica Scripta*, 2023. 98(4): p. 045619, 10.1088/1402-4896/acc48e
- 4) Galář, P., et al., A METHOD FOR SURFACE MODIFICATION OF SEMICONDUCTOR NANOPARTICLES USING NON-THERMAL PLASMA ACTIVATED WATER AND PRODUCT THEREOF, European patent n. EP3796366, 30. 10. 2024
- 5) Popelář, T., Galář, P., et al., Universal Radiative Lifetimes in the Long-Lived Luminescence of Si Quantum Dots. *The Journal of Physical Chemistry C*, 2023. 127(41): p. 20426-20437, 10.1021/acs.jpcc.3c05423

4. Rekombinační a transportní procesy v perovskitovém nanohybridu

Halogenidové perovskity (PS) patří v současné době k jedněm z nejintenzivněji studovaných a rozvíjejících se pokročilých materiálů. To je dáno nejen jejich snadnou přípravou, ale především excellentními vlastnostmi na poli konverze světelné a elektrické energie.^{111, 117} Studiu rekombinačních a vodivostních procesů v objemových PS byla věnována plejáda publikací.^{204, 205} Nicméně překvapivě omezené jsou práce popisující procesy excitovaných nosičů v jednom z nejjazímacovějších hybridů na zmíněném materiálu, a to PS obohacených o polovodičové kvantové tečky. Přitom spojení absorpčních a vodivostních vlastností PS a efektivní zářivé rekombinace lokalizovaných nosičů na QD je možno využít v aplikacích zaměřených na světelnou generaci, fotodetekci a při vhodné energetické a strukturní konfiguraci i ke zvýšení efektivity PS fotovoltaických zařízení.

V rámci našeho výzkumu jsme se zaměřili na detailní mapování procesů excitovaných nosičů náboje ve zmíněných hybridech. Pro usnadnění interpretace pozorovaných jevů jsme náš hybrid vytvořili z jednoho z nejlépe prostudovaných PS (MAPbI_3) a standardních polovodičových kvantových teček (PbS), které byly pro zvýšení lokalizace nosičů navíc dodatečně potaženy slupkou z CdS . Velikost kvantových teček byla 3 nm (0,3 nm slupka).¹⁹ Připraveny byly vzorky s různou koncentrací QDs kvantifikovanou pomocí hmotnostního procenta (w%) v rozmezí od 0 do 7,3 %. Dynamiky excitovaných nosičů jsme studovali několika komplementárními metodami. Využili jsme: a) ultrarychlou spektroskopickou metodu přechodné absorpcie (z angl. transient absorption - TA), která je schopna s časovým rozlišením < 1 ps studovat dynamiky excitovaných nosičů v různých stavech; b) ultrarychlou terahertzovou spektroskopii (THz), která se srovnatelným časovým rozlišením sleduje změnu fotovodivosti vzorku. Spojením výstupů obou metod můžeme získat komplexní vhled do procesů spojených s transportem, transferem, záchytem nebo rekombinací excitovaných nosičů. Tyto metody byly navíc doplněny c) zábleskovou fotolýzou, která dává informaci o hodnotě přechodné absorpcie v dlouhých časových intervalech > 1 ns, a tím doplňuje celkový obraz studovaných rekombinačních procesů i o ty s pomalou dynamikou. Jelikož TA signál z QDs v hybridi byl zanedbatelný, pro studium rekombinace nosičů na tečkách byla použita d) časově integrovaná luminiscenční spektroskopie. Pro získání co možná nejkomplexnějšího pohledu na studované dynamiky byla měření TA realizována s použitím různých excitačních vlnových délek, čímž jsme mohli srovnat chování nosičů s různou hodnotou excitační energie, a také za použití různých excitačních intenzit, což přineslo informace o zastoupení

monomolekulárních, bimolekulárních a Augerovských procesů. Obdobná měření byla provedena i pomocí THz spektroskopie.



Obrázek 24. a) TA spektra čistého MAPbI₃ a MAPbI₃/QDs ($w\% = 6.3\%$) excitovaná pulzy o vlnové délce 600 nm a skenovaná bílým světlem se zpožděním 1 ps. b) Doznívání TA obou vzorků na vlnové délce 760 nm. c) Doznívání TA MAPbI₃/QDs vzorků o různých koncentracích QDs na vlnové délce 760 nm. d) Srovnání doznívání TA a fotovodivosti na 760 nm ($w\% = 6.3\%$). e) Schémata kinetických procesů realizovaných v čistém MAPbI₃ a MAPbI₃/QDs (použito se svolením majitele práv Elsevier).¹⁹

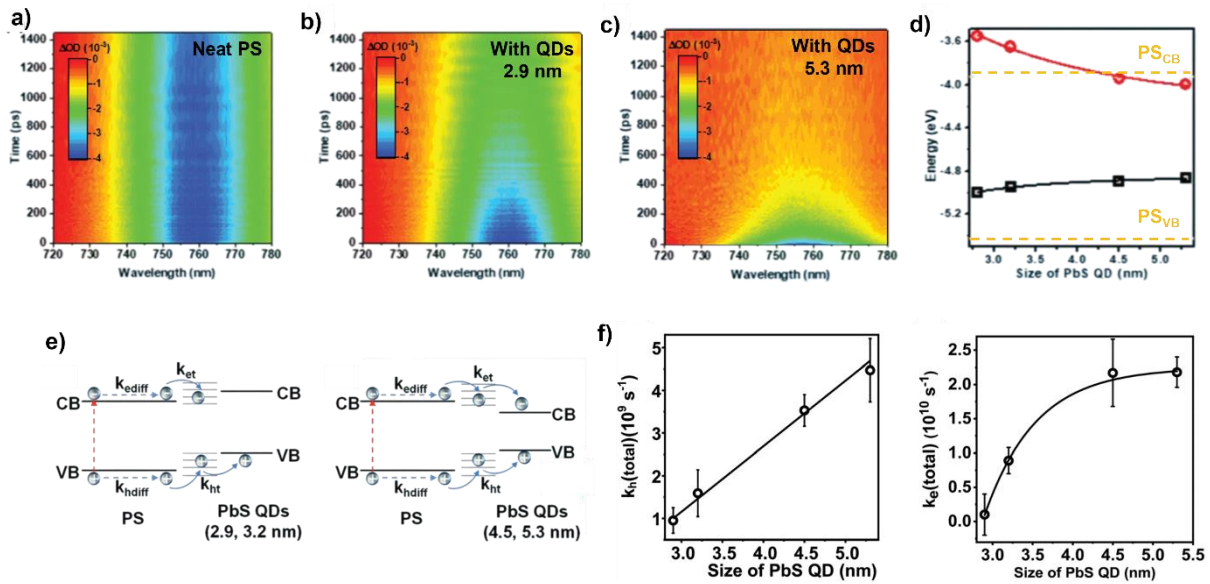
Měření TA na MAPbI₃ bez přítomnosti QDs vykazovala typický spektrální průběh složený ze dvou negativních pásů spojených se saturací absorpce okolo 480 a 760 nm a pozitivního pásu indukované absorpce na volných excitovaných nosičích 520 – 700 nm (**Obr. 24a**). Detailně analyzována byla doznívání hlavního negativního pásu s maximem okolo 760 nm, který je spojen se saturací absorpce v blízkosti zakázaného pásu. Dynamika TA tohoto pásu byla pozvolná a na sledovaném časovém intervalu sahajícím do 1,4 ns klesla intenzita signálu na ~ 70 % počáteční hodnoty (**Obr. 24b**). Velmi podobné chování bylo pozorováno i na vzorcích MAPbI₃/QDs s $w\%$ od 0 do 0,18 % (**Obr. 24c**). Vzorky s vyšší koncentrací QDs sice vykazovaly s čistým PS téměř shodné počáteční TA spektrum, což ukazuje na to, že měřený signál TA je dominován nosiči generovanými v perovskitové matrici, ale doznívání signálu hlavního negativního pásu bylo mnohem rychlejší a u nejkoncentrovanějších vzorků dosahovalo až 90% snížení intenzity na prvních 200 ps (**Obr. 24a,b,c**). Obdobných dynamik

bylo dosaženo i při měření vzorků pomocí THz spektroskopie (**Obr. 24d**). Dynamiky fotovodivosti tedy byly dány pouze změnou koncentrace excitovaných nosičů, a ne jejich pohyblivosti. Získané dynamiky byly následně analyzovány pomocí kinetického modelu běžně aplikovaného ke studiu procesů na čistém PS, který jsme modifikovali o procesy spojené s transportem/transferem nosičů z PS do QDs.¹⁹ Na základě výsledků z těchto modelů a znalosti energetického schématu MAPbI₃/PbS@CdS jsme byly schopni naměřená data interpretovat a došli jsme k následujícímu zjištění o chování nosičů ve studovaném hybridu.

Každý vzorek by se dal pomyslně rozdělit do dvou oblastí. Excitované nosiče z první oblasti nebyly ovlivněny přítomností teček a rekombinovaly dle standardních procesů pro čistý PS (**Obr. 24e**). Nosiče v druhé oblasti se díky vysoké difuzní vzdálenosti dostaly k nejbližší QD, kde docházelo k transferu děr do valenčního pásu tečky a elektronů do stavů na rozhraní PS a QD (**Obr. 24e**). Takto zachycené nosiče následně vzájemně zářivě rekombinovaly s dlouhou časovou konstantou, což dokazují měření fotoluminiscence. Spektrální pozice detekované luminiscence totiž odpovídá energetické vzdálenosti valenčního pásu PbS a pastových stavů na rozhraní. Netradičně pro PS struktury bylo na našich vzorcích detekováno i malé množství rychle rekombinujících excitonů (ps časový interval), které pravděpodobně vznikly na defektech na rozhraních PS a QDs. Velikost obou popsaných oblastí byla závislá na koncentraci QDs. Velikost druhé oblasti pro vzorky s w% nad 0,18 % se pohybovala od 85 do 92 %. Z našich měření plyne, že od koncentrace QDs o w% 0,18 % výše bylo více než 85 % nosičů excitovaných v PS efektivně svedeno do QDs. Koncentrace teček navíc ovlivňovala i hodnotu koeficientu míry transferu excitovaných nosičů (k_{etrans} a k_{htrans}), která se s růstem koncentrace zvyšovala od původních 0,13 až po $4,6 \cdot 10^{10} \text{ s}^{-1}$ pro díry a od 0,002 až po $1,2 \cdot 10^{10} \text{ s}^{-1}$ pro elektrony. Tyto parametry zahrnují jak difuzi nosičů k rozhraní, tak samotný přeskok. Koncentrace excitonů taktéž rostla s koncentrací QDs a u nejkoncentrovanějšího vzorku dosahovala 7 % všech excitovaných nosičů.

Mezi zajímavé závěry patří i 4krát vysší efektivita transferu děr do valenčního pásu PbS než záchyt elektronů na rozhraní. Jelikož mobilita děr a elektronů je u tohoto PS téměř stejná, je tento rozdíl dán především koncentrací pastových stavů na rozhraní obou složek hybridu.¹⁹ Současně se také ukázalo, že vzorky s vyšší koncentrací QDs vykazují nižší hodnotu difuzní vzdálenosti, která byla až 10krát nižší než tomu je u čistého perovskitu (~ 40 nm). To ukazuje na nižší kvalitu PS matrice v rámci hybridu, což jde proti běžně publikovaným výsledkům, kdy se QDs o obdobné mřížkové konstantě cíleně používají ke zvýšení kvality PS krystalů.¹³⁶ Nicméně, náš výzkum nejen ukázal vysokou efektivitu transferu excitovaných nosičů z PS do QDs v rámci hybridu, ale především detailně zmapoval rekombinační procesy v rámci hybridu

MAPbI₃/PbS@CdS. Demonstrované výsledky, a především navržené a úspěšně otestované kinetické modely, mohou být použity při snaze snížit koncentraci defektů na rozhraní složek hybridu či při zavádění jiných optimalizačních postupů.



Obrázek 25. 2D časová a spektrální závislost TA signálu: a) čistého PS MAPbI₃, b) MAPBI₃/QDs o velikosti 2,9 nm a c) MAPBI₃/QDs o velikosti 5,3 nm. d) Vývoj energie valenčního a vodivostního pásu PbS v závislosti na velikosti tečky, srovnáný s pozicí těchto pásů v čistém MAPbI₃. e) Schéma kinetických procesů realizovaných u MAPbI₃/QDs využívajících QDs o různých velikostech. f) Závislost velikosti celkového koeficientu míry transferu dér (k_h) a elektronů (k_e) z PS do QDs na velikosti QDs (neočištěný o difuzi k rozhraní; použito se svolením majitele práv The Royal Society of Chemistry).¹⁵⁰

V dalším kroku výzkumu hybridů PS/QDs jsme se pokusili odhalit vliv velikosti QDs, a tedy reaktivnosti povrchu a vzájemné polohy energetických hladin obou složek hybridu, na chování excitovaných nosičů.¹⁵⁰ Za účelem zjednodušení popisu energetických stavů, a také snížení množství defektů na rozhraní složek hybridů, jsme tentokrát do MAPbI₃ zabudovali čisté PbS QDs o velikosti 2,9, 3,2, 4,5 a 5,3 nm. PbS má totiž vzhledem k MAPbI₃ bližší hodnotu mřížkové konstanty než CdS. U dvou nejmenších skupin teček by měla pozice vodivostního pásu PbS ležet nad vodivostním pásem MAPbI₃ a u zbylých QDs by měla být vzájemná poloha vodivostních pásů opačná. Valenční pás PbS je vždy nad tímto pásem v perovskitu (**Obr. 25d**). Množství QDs o různé velikosti bylo v každém hybridu nastaveno tak, aby jejich vzdálenost v PS matrici byla u všech vzorků stejná, a tím se minimalizoval vlivy vzdáleností, kterou musí excitované nosiče difundovat k tečce. Všechny vzorky byly charakterizovány obdobným způsobem jako v minulé práci, tedy především pomocí TA a THz

ultrarychlé spektroskopie. Studován byl i vliv velikosti excitační vlnové délky a intenzity. Výsledné dynamiky byly vyhodnoceny matematickým modelem z předešlé práce.

Výsledky měření ukázala výrazné zrychlování doznívání TA i THz signálu s rostoucí velikostí QDs, a tím zvyšování rychlosti transportu/transferu elektronů a děr do QDs (**Obr. 25a,b,c**). Byl navržen kinetický model, který předpokládá transfer děr z PS matrice do valenční hladiny PS přes povrchové stav a elektronový transfer QDs do povrchových stavů nebo dokonce vodivostní hladiny PbS (**Obr. 25d,e**). Se znalostí průměrné vzdálenosti QDs v PS matrici a mobility nosičů díky THz měření bylo v tomto případě možno vypočítat nejen celkové koeficienty transportu elektronů a děr (**Obr. 25f**) pro jednotlivé vzorky, ale dokonce z těchto parametrů odečíst dobu nutnou k difuzi nosičů směrem k tečce, a získat tak pouze čistou konstantu transferu elektronů, respektive děr do QDs či rozhraní hybridu. U děr hodnota očištěné konstanty transferu rostla téměř lineárně s velikostí QDs a zmíněný koeficient dosahoval hodnot od $1,04 \cdot 10^9 \text{ s}^{-1}$ do $7,81 \cdot 10^9 \text{ s}^{-1}$. U elektronů byl nárůst efektivity transferu ještě výraznější. Pro nejmenší QDs, kdy docházelo k transferu elektronů do pastových stavů na rozhraní, se konstanta míry transferu pohybovala od $0,11 \cdot 10^{10} \text{ s}^{-1}$ do $1,56 \cdot 10^{10} \text{ s}^{-1}$. Pro větší QDs, kdy elektrony mohly být přeneseny i od valenčního pásu teček, byl přechod rychlejší než časové rozlišení měření (< 70 fs). Výrazně pomalejší přechod děr do valenčního pásu PbS než u elektronů do vodivostního pásu je pravděpodobně dán nízkou koncentrací povrchový stavů, které slouží jako moderátor transferu. Předkládaný výzkum tedy demonstruje vliv nejen velikosti QDs, a tím hodnoty zakázaného pásu, ale také koncentrace defektů na rozhraní složek hybridů na efektivitu rekombinačních/transportních procesů nosičů excitovaných v PS matrici.

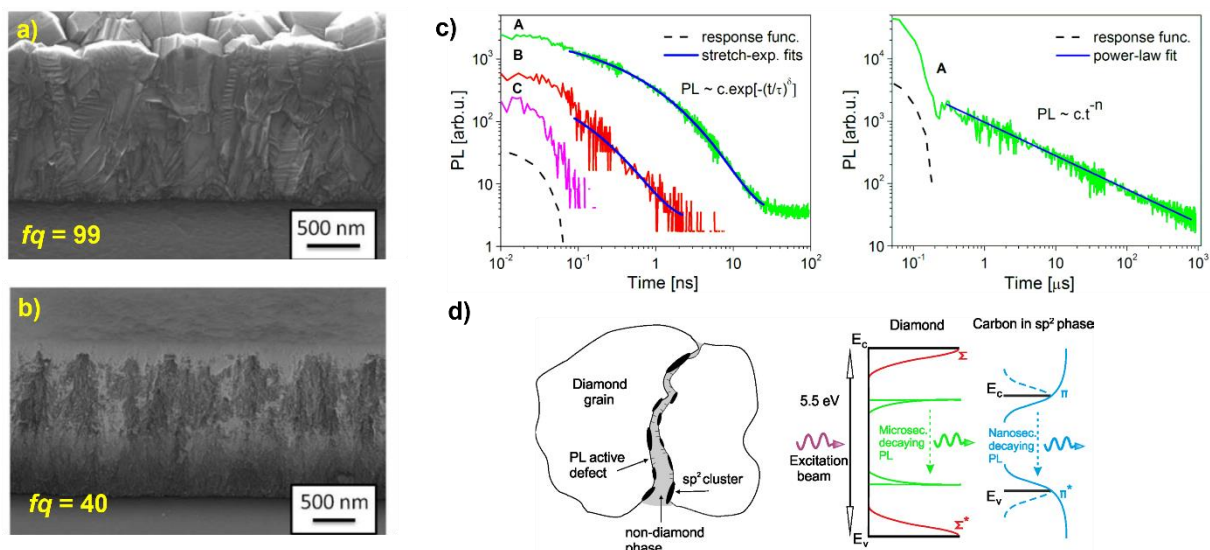
Nejvýznamnější publikace autora zabývající se tímto tématem:

- 1) Galar, P., et al., **Perovskite-quantum dots interface: Deciphering its ultrafast charge carrier dynamics.** *Nano Energy*, 2018. 49: p. 471-480. 0.1016/j.nanoen.2018.04.069.
- 2) Piatkowski, P., Masi, S., Galář, P., et al., **Deciphering the role of quantum dot size in the ultrafast charge carrier dynamics at the perovskite–quantum dot interface.** *Journal of Materials Chemistry C*, 2020. 8(42): p. 14834, 10.1039/D0TC03835K

5. Chování excitovaných nosičů v nanodiamantových hybridech

5.1 Vliv nediamondové fáze na rekombinační procesy v nanokrystalickém diamantu

Nanokrystalický diamant (NCD) v sobě kombinuje unikátní vlastnosti objemového diamantu s možností snadnější a ekonomičtější přípravy, než tomu je u jeho objemové alternativy. Rozsah aplikací těchto materiálů sahá od opto-elektroniky, senzoriky až po biologii a medicínu.^{156, 177} Pro mnohé z těchto aplikací je nutné vytvářet hybridy NCD s organickými látkami, nejčastěji makromolekulami nebo vodivými polymery.^{206, 207} Přestože příprava těchto hybridů je v dnešní době již relativně běžnou záležitostí, stále není zřejmé, jakým způsobem probíhá transport/transfer excitovaných nosičů na rozhraní složek těchto hybridů. Překázkou k objasnění podstaty zmíněných procesů nejsou pouze obtíže spojené s charakterizací a interpretací dynamik nosičů na rozhraní obou složek, ale i fakt, že stále nepanuje shoda na přesné podstatě rekombinačních procesů excitovaných nosičů v samotném NCD. Především není jasný vliv množství nediamondové fáze a rozhraní zrn na tyto procesy.¹⁵²



Obrázek 26. SEM snímky NCD filmu s a) $f_q = 99$ a b) $f_q = 40$. c) Doznívání PL vzorků s $f_q = 99$ (označeno jako A), 59 (B) a 40 (C) na nanosekundové a mikrosekundové časové škále. PL byla excitována fs pulzy o excitační vlnové délce 400 nm. Doznívání jsou approximována napnutou exponenciálou, respektive mocninnou funkcí. d) Model struktury NCD filmu o vysokém f_q a příslušné energetické schéma zobrazující procesy zodpovědné za mikrosekundovou a nanosekundovou luminiscenci (použito se svolením majitele práv Optica Publishing Group).¹⁷³

Naše snaha o objasnění podstaty dynamik excitovaných nosičů na rozhraní NCD/organická látka tedy musela být rozdělena do dvou kroků. V prvním kroku jsme se zaměřili na studium procesů excitovaných nosičů v samotném NCD.¹⁷³ Za tímto účelem byly připraveny tři různé NCD filmy, jejichž faktor kvality (f_q) měl hodnotu 99, 59 a 40. Parametr f_q charakterizuje poměr mezi diamantovou a nediamantovou složkou v NCD a jeho hodnota sahající od 0 (jen nediamantová fáze) do 100 (čistý diamant) se určuje analýzou Ramanova signálu NCD. Po strukturní analýze (**Obr. 26a,b**) byly filmy charakterizovány pomocí časově rozlišené luminiscenční spektroskopie s využitím rozmítací kamery za použití excitace nepřesahující zakázaný pás diamantu ($\lambda = 400$ nm). Měření odhalila, že vzorky se liší nejen časově integrovaným PL spektrem, ale především dynamikou doznívání luminiscence (**Obr. 26c**). Vzorek s nejvyšším f_q vykazoval přítomnost dvou nezávislých rekombinačních procesů. První proces se odehrával na nanosekundovém časovém intervalu, jeho dynamiku bylo možno dobře approximovat napnutou exponenciálou (viz rov. 13) a jemu příslušící integrované spektrum se rozprostíralo v intervalu 350 – 600 nm. Jak bylo řečeno v předešlé kapitole, doznívání charakterizované napnutou exponenciálou bývá interpretováno pomocí zářivé rekombinace na více zdrojích, které vykazují mono-exponenciální doznívání s mírně se lišící dobou života. Druhý proces byl výrazně pomalejší, nacházel se v mikrosekundovém časovém okně, vykazoval dynamiku odpovídající mocninné funkci a příslušné integrované spektrum se nacházelo v intervalu 400 – 750 nm. Funkční předpis pro mocninné doznívání je dán vztahem:

$$I(t) = At^{-n}. \quad (16)$$

Tento typ doznívání se často projevuje v neuspořádaných či amorfních systémech, kde důležitou roli hraje separace nosičů. Případně se jedná o rekombinaci na náhodně rozložených pasťových stavech. Hodnota exponentu n je poté úzce spojena s rekombinačním procesem zodpovědným za pozorovanou dynamiku. Doznívání vykazující hodnotu $n < 1$ bývá spojeno s tunelováním nosičů mezi pastmi a rekombinačními centry. Při hodnotě $n > 1,5$ bývá rekombinace nosičů dána přeskoky mezi lokalizovanými stavami nebo difuzí nosičů.^{208, 209} V našem případě hodnota parametru n rostla s klesající vlnovou délkou a pohybovala se od 0,45 do 0,8. Zbylé dva filmy vykazovaly rádově nižší intenzitu luminiscence. To bylo dáno nejen absencí mikrosekundového doznívání, ale i urychlením dynamik nanosekundové rekombinace s poklesem hodnoty f_q .

Pro získání komplexnějšího pohledu na chování obou rekombinačních procesů bylo následně provedeno měření doznívání PL u filmu s nejvyšším f_q v závislosti na teplotě (15 – 300 K) a tlaku okolní atmosféry. Studován byl i vliv excitační intenzity a vlnové délky (použito

$\lambda = 325$ nm a 200 nm). Zatímco chování mikrosekundové složky PL nebylo změnou teploty ani tlaku nijak ovlivněno, nanosekundová složka vykazovala výrazné urychlení doznívání a nárůst intenzity PL po ohřátí filmu nad 200 K. Intenzita PL této složky byla zvýšena i přechodem z atmosférického tlaku do vakua. Měření s rostoucí excitační intenzitou prokázalo lineární nárůst intenzity PL nanosekundové složky a relativně rychlou saturaci složky mikrosekundové, což ukazuje na omezenou koncentraci stavů zodpovědných za pomalejší z nich. PL odezva obou složek byla navíc velmi citlivá na přechod k excitaci přes zakázaný pás diamantu ($\lambda = 200$ nm). Poměr mezi celkovou intenzitou nanosekundové a mikrosekundové PL složky se při této excitaci zvýšil $\sim 60x$ ve prospěch druhé jmenované.

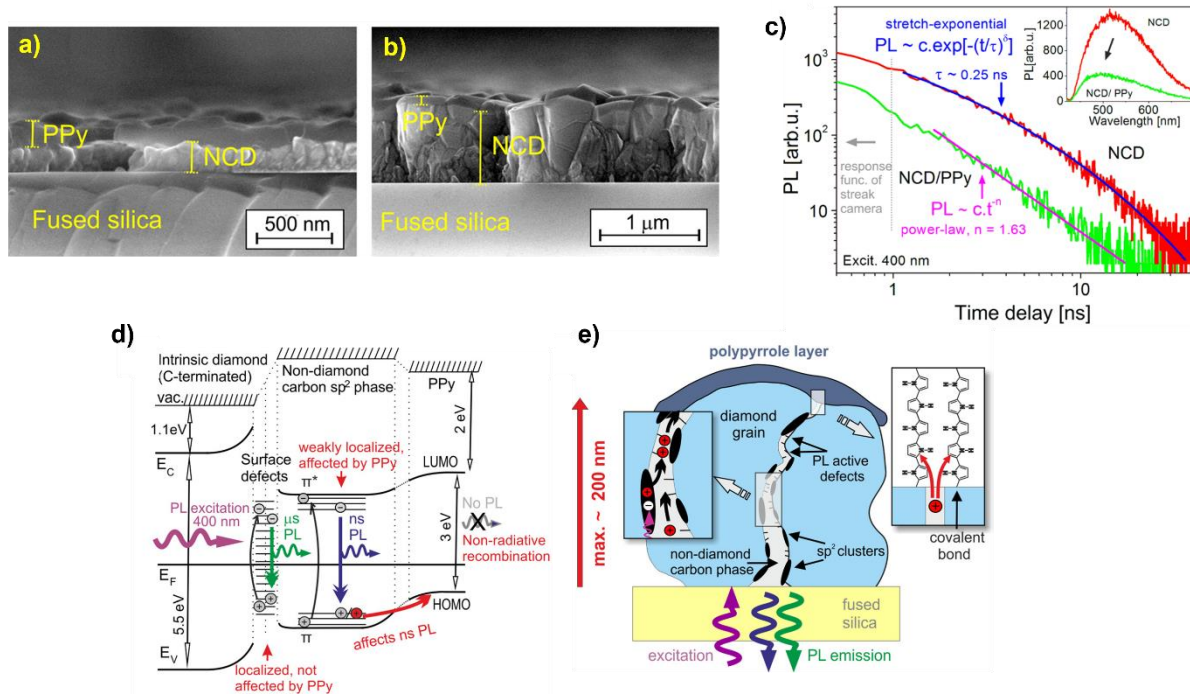
Na základě těchto výsledků jsme navrhli model energetických stavů a vnitřní struktury NCD vysvětlující rekombinační procesy excitovaných nosičů u filmů s vysokou a nízkou hodnotou f_q . Filmy s vysokým f_q bývají složeny z velkých diamantových zrn, které jsou obaleny menším množstvím nediamantové fáze (**Obr. 26d**). Očekáváme, že mikrosekundová složka doznívání je spojena s past'ovými stavy na hranicích zrn, což souhlasí nejen s mocninnou dynamikou PL, ale i s nízkou citlivostí na okolní tlak a teplotu, saturací PL s rostoucí excitační intenzitou, nebo i výrazným zesílením intenzity přechodem k excitaci nad zakázaný pás (**Obr. 26d**). Tyto past'ové stavy jsou totiž dostupné volným nosičům z diamantu, které vznikají excitací nad zakázaným pásem diamantu. Naopak nanosekundová dynamika PL se dá vysvětlit jako rekombinace nosičů mezi $\pi-\pi^*$ stavy uhlíku v sp^2 fázi. Aby nedocházelo k rychlé prostorové separaci těchto nosičů, musí být dané stavy prostorově lokalizované. To by odpovídalo přítomnosti sp^2 klastrů mezi diamantovými zrny, jejichž existence byla předpovězena.²¹⁰ Chování nosičů v těchto stavech souhlasí s pozorovanými měřeními, a to včetně spektrální pozice PL, tepelné aktivace po překročení teploty 200 K i dynamik PL odpovídajícím napnuté exponenciále. Dá se totiž očekávat, že klastry budou mít různou velikost i tvar, což bude spojeno s variací míry lokalizace excitovaných nosičů napříč klastry a tím i dob života zmíněných nosičů. U vzorků z nižší f_q dochází k nárůstu nediamantové fáze a snížení velikosti diamantových zrn. To je pravděpodobně spojeno s růstem velikosti klastrů a jejich možnému propojování, což by snížilo lokalizaci excitovaných nosičů spojených s klastry, a vedlo k urychlení rekombinace mezi $\pi-\pi^*$ stavy uhlíku v sp^2 fázi. Strukturní změny spojené se snížením f_q vedou také k pasivaci povrchových pastí zodpovědných za mikrosekundovou složku PL, případně k vytvoření nových nezářivých rekombinačních kanálů, a tím potlačení této emise.

5.2 Separace excitovaných nosičů v rámci hybridu nanodiamant/vodivý polymer

V druhém kroku jsme připravili dva NCD filmy o téměř identickém parametru $f_{q\bar{q}}$ (97 a 95).¹⁸⁴ Vzorky o vysokém $f_{q\bar{q}}$ jsme pro studium separačních procesů hybridu zvolili z důvodů možnosti studovat vliv organické složky na obě složky PL, a také z čistě aplikačního hlediska. Právě tyto typy filmů jsou totiž v pokročilých aplikacích více využívány z důvodů vyšší propustnosti světla.¹⁵⁶ Oba NCD filmy se lišily svou tloušťkou, kdy první vzorek vykazoval tloušťku 170 nm a druhý 920 nm. Na části obou vodíkem terminovaných NCD filmů byla následně metodou elektrochemického napojování (z angl. electrochemical grafting) deponována vrstva vodivého polymeru polypyrrolu (PPy). Tato metoda umožňuje vytvořit kovalentní vazbu mezi atomy uhlíku polymeru a NCD, a tím nastavit podmínky na efektivní interakci mezi složkami hybridu. Tlušťka PPy vrstev byla u obou filmů srovnatelná a měla hodnotu okolo 150 nm (**Obr. 27a,b**). Oba hybrydy byly charakterizovány pomocí časově rozlišené luminiscenční spektroskopie za obdobných podmínek jako samostatné NCD filmy z prvního kroku výzkumu. Na tomto místě je dobré zdůraznit, že NCD film byl excitován a PL byla detekována na opačné straně, než byla deponována PPy vrstva. PPy sám sice nevykazuje téměř žádnou PL odezvu, ale silně absorbuje světlo ve viditelném intervalu. Současně bylo také zjištěno, že intenzita obou složek PL NCD u obou hybridů klesla po depozici PPy minimálně 2,5krát. Jelikož se tento efekt vyskytuje u všech provedených měření, není pravděpodobně dán změnou rekombinačních procesů, ale je čistě optického charakteru. Může se jednat např. o změnu odrazivosti či omezení rozptylu na odvráceném rozhraní NCD. Tento předpoklad byl ověřen nakápnutím oleje či nanesením chemicky připraveného PPy, který nemá potenciál vytvořit kovalentní vazbu s NCD, na čisté části NCD filmů. V obou případech došlo ke snížení PL intenzity NCD, aniž bychom pozorovali ovlivnění dynamik obou složek PL. Změna intenzity PL byla navíc reverzibilní a po odstranění PPy vrstvy se vrátila na velmi podobnou hodnotu, jakou vykazovala odhalená část NCD filmu. V dalším textu jsou tedy diskutovány jen efekty vedoucí ke snížení PL intenzity nad výše zmíněnou hodnotu (označováno jako dodatečné snížení PL) a změně dynamik doznívání PL po depozici PPy.

U tenčího z NCD filmů přítomnost kovalentně vázaného PPy způsobila dodatečné snížení intenzity PL (~ 2krát) nanosekundové složky a transformaci její dynamiky z napnuté exponenciály na mocninnou funkci s koeficientem $n = 1,63$ (**Obr. 27c**). Obdobné chování bylo pozorováno pro excitaci pod i přes zakázaný pás diamantu. Naproti tomu dynamika mikrosekundové složky PL NCD nevykazovala žádné změny po depozici PPy. Pouze bylo pozorováno dodatečné snížení intenzity PL této složky při přechodu od excitace na 400 nm

k 200 nm (~ 3 krát). V případě tlustšího NCD hybridu nebyl pozorován žádný vliv přítomnosti PPy nad rámec zmíněného plošného snížení PL intenzity.



Obrázek 27. SEM snímky NCD/PPy hybridů o tloušťce NCD vrstvy a) 170 nm a b) 920 nm. c) Srovnání doznívání PL v nanosekundovém časovém okně čistého NCD a NCD/PPy pro vzorek a). Použitá excitační vlnová délka pulzů byla 400 nm. Prezentovaná doznívání jsou proložena napnutou exponenciálou a mocninnou funkcí. Přiložena jsou i příslušná integrovaná PL spektra. d) Energetické a e) strukturní schéma hybridu NCD/PPy demonstrující procesy zodpovědné za separaci excitovaných nosičů na rozhraní složek hybridu, a tím změnu doznívání nanosekundové složky PL (použito se svolením majitele práv AIP Publishing).¹⁸⁴

Pro interpretaci těchto výsledků jsme vyšli z energetického a strukturního modelu NCD, který jsme navrhli v prvním kroku výzkumu a modifikovali ho stavu spojenými s přítomností PPy (Obr. 27d,e). Nejprve jsme se zaměřili na tenčí z obou hybridů. Jelikož u tohoto vzorku nedošlo depozici polymeru ke změně dynamiky mikrosekundového doznívání PL, kovalentně navázané PPy pravděpodobně nemá vliv na nosiče zachycené v povrchových pastových stavech diamantových zrn. Na druhou stranu, výrazné snížení intenzity této složky PL po přechodu k excitaci přes zakázaný pás naznačuje, že je PPy schopno ovlivňovat dynamiku volných nosičů náboje v diamantové fázi, které po depozici PPy nekončily ve zmíněných povrchových stavech zrn. Změna dynamiky nanosekundové složky PL NCD po depozici PPy je s největší pravděpodobností dána separací děr excitovaných v nediamantové fázi mezi zrnami. Přítomnost PPy na povrchu NCD může díky energetické poloze valenčního pásu PPy vést

k vytvoření vnitřního elektrického pole, které způsobuje drift děr excitovaných uvnitř dobře vodivé nediamantové fáze mezi diamantovými zrny směrem k PPy vrstvě. Tento proces vytváří dodatečný nezářivý kanál pro nosiče, které by v opačném případě zářivě rekombinovaly mezi $\pi-\pi^*$ stavy uhlíku v sp^2 fázi. Toto tvrzení je v souladu nejen s očekávaným energetickým schématem hybridu, snížením intenzity této složky po depozici PPy, ale i mocninnou dynamikou doznívání s hodnotou exponentu n nad 1,5, který naznačuje difuzní/driftovou separaci nosičů. Jelikož popsané změny dynamik nebyly pozorovány u silnějšího NCD a ani u tenčího NCD, kdy PPy bylo pouze nakápnuto, dá se očekávat, že zásadní pro separaci děr je nejen kovalentní navázání PPy, ale i jeho vzdálenost od pozorovaného povrchu. Na základě našich měření odhadujeme, že PPy je schopno ovlivnit nosiče excitované maximálně do hloubky 200 – 300 nm NCD. Předkládaný výzkum nejen prokázal schopnost kovalentně navázaného PPy separovat nosiče excitované v nediamantové fázi NCD, ale i ovlivnit dynamiky volných nosičů excitovaných v diamantových zrnech, což by mohlo mít uplatnění jak v optoelektronice, tak i senzorice.

Nejvýznamnější publikace autora zabývající se tímto tématem:

- 1) Galář, P., et al., Influence of non-diamond carbon phase on recombination mechanisms of photoexcited charge carriers in microcrystalline and nanocrystalline diamond studied by time resolved photoluminescence spectroscopy. *Optical Materials Express*, 2014. 4(4): p. 624-637. 10.1364/OME.4.000624
- 2) Galář, P., et al., Electrochemically grafted polypyrrole changes photoluminescence of electronic states inside nanocrystalline diamond. *Journal of Applied Physics*, 2014. 116(22). 10.1063/1.4903937.

6. Reference

- (1) Alivisatos, A. P. Perspectives on the Physical Chemistry of Semiconductor Nanocrystals. *J. Phys. Chem.* **1996**, *100* (31), 13226-13239. DOI: 10.1021/jp9535506.
- (2) Moreels, I.; Lambert, K.; De Muynck, D.; Vanhaecke, F.; Poelman, D.; Martins, J. C.; Allan, G.; Hens, Z. Composition and Size-Dependent Extinction Coefficient of Colloidal PbSe Quantum Dots. *Chem. Mater.* **2007**, *19* (25), 6101-6106. DOI: 10.1021/cm071410q.
- (3) Rabouw, F. T.; de Mello Donega, C. Excited-State Dynamics in Colloidal Semiconductor Nanocrystals. *Top. Curr. Chem.* **2016**, *374* (5), 58. DOI: 10.1007/s41061-016-0060-0.
- (4) Sahu, A.; Kang, M. S.; Kompch, A.; Notthoff, C.; Wills, A. W.; Deng, D.; Winterer, M.; Frisbie, C. D.; Norris, D. J. Electronic Impurity Doping in CdSe Nanocrystals. *Nano Lett.* **2012**, *12* (5), 2587-2594. DOI: 10.1021/nl300880g.
- (5) Hill, R. M. Variable-range hopping. *Phys. Stat. Sol. (a)* **1976**, *34* (2), 601-613. DOI: <https://doi.org/10.1002/pssa.2210340223>.
- (6) Cullis, A. G.; Canham, L. T. VISIBLE-LIGHT EMISSION DUE TO QUANTUM SIZE EFFECTS IN HIGHLY POROUS CRYSTALLINE SILICON. *NATURE* **1991**, *353* (6342), 335-338. DOI: 10.1038/353335a0.
- (7) Xu, L.; Liang, H.-W.; Yang, Y.; Yu, S.-H. Stability and Reactivity: Positive and Negative Aspects for Nanoparticle Processing. *Chem. Rev.* **2018**, *118* (7), 3209-3250. DOI: 10.1021/acs.chemrev.7b00208.
- (8) Hunsperger, R. G. Quantum-Well Devices. In *Integrated Optics: Theory and Technology*, Hunsperger, R. G. Ed.; Springer Berlin Heidelberg, 2002; pp 325-348.
- (9) Yan, R.; Gargas, D.; Yang, P. Nanowire photonics. *Nature Photonics* **2009**, *3* (10), 569-576. DOI: 10.1038/nphoton.2009.184.
- (10) Hu, F.; Yan, B.; Sun, G.; Xu, J.; Gu, Y.; Lin, S.; Zhang, S.; Liu, B.; Chen, S. Conductive Polymer Nanotubes for Electrochromic Applications. *ACS Appl. Nano Mater.* **2019**, *2* (5), 3154-3160. DOI: 10.1021/acsnm.9b00472.
- (11) Gaponenko, S., & Demir, H. Quantum confinement effects in semiconductors. In *Applied Nanophotonics*, Demir, H. V., Gaponenko, S. V. Eds.; Cambridge University Press, 2018; pp 52-91.
- (12) Pelant, I.; Valenta, J. Luminescence Spectroscopy of Semiconductors. Oxford University Press, 2012.
- (13) Mazzaro, R.; Romano, F.; Ceroni, P. Long-lived luminescence of silicon nanocrystals: from principles to applications. *Phys. Chem. Chem. Phys.* **2017**, *19* (39), 26507-26526, 10.1039/C7CP05208A. DOI: 10.1039/C7CP05208A.
- (14) Hapala, P.; Kůsová, K.; Pelant, I.; Jelínek, P. Theoretical analysis of electronic band structure of 2- to 3-nm Si nanocrystals. *Phys. Rev. B* **2013**, *87* (19), 195420. DOI: 10.1103/PhysRevB.87.195420.
- (15) König, D. Number series of atoms, interatomic bonds and interface bonds defining zinc-blende nanocrystals as function of size, shape and surface orientation: Analytic tools to interpret solid state spectroscopy data. *AIP Adv.* **2016**, *6* (8). DOI: 10.1063/1.4960994 (acccessed 9/5/2023).
- (16) Winters, B. J.; Holm, J.; Roberts, J. T. Thermal processing and native oxidation of silicon nanoparticles. *J. Nanoparticle Res.* **2011**, *13* (10), 5473. DOI: 10.1007/s11051-011-0535-4.
- (17) Kůsová, K.; Ondič, L.; Klimešová, E.; Herynková, K.; Pelant, I.; Daniš, S.; Valenta, J.; Gallart, M.; Ziegler, M.; Hönerlage, B.; et al. Luminescence of free-standing versus matrix-embedded oxide-passivated silicon nanocrystals: The role of matrix-induced strain. *Appl. Phys. Lett.* **2012**, *101* (14). DOI: 10.1063/1.4756696 (acccessed 8/6/2024).
- (18) Pietryga, J. M.; Park, Y.-S.; Lim, J.; Fidler, A. F.; Bae, W. K.; Brovelli, S.; Klimov, V. I. Spectroscopic and Device Aspects of Nanocrystal Quantum Dots. *Chem. Rev.* **2016**, *116* (18), 10513-10622. DOI: 10.1021/acs.chemrev.6b00169.
- (19) Galar, P.; Piatkowski, P.; Ngo, T. T.; Gutiérrez, M.; Mora-Seró, I.; Douhal, A. Perovskite-quantum dots interface: Deciphering its ultrafast charge carrier dynamics. *Nano Energy* **2018**, *49*, 471-480. DOI: <https://doi.org/10.1016/j.nanoen.2018.04.069>.
- (20) Singh, R.; Srinivas, S. P.; Kumawat, M.; Daima, H. K. Ligand-based surface engineering of nanomaterials: Trends, challenges, and biomedical perspectives. *OpenNano* **2024**, *15*, 100194. DOI: <https://doi.org/10.1016/j.onano.2023.100194>.

- (21) Kim, M.; Choi, M.; Choi, S.; Jeong, S. Semiconductor Nanocrystals: Unveiling the Chemistry behind Different Facets. *Accounts of Chemical Research* **2023**, *56* (13), 1756-1765. DOI: 10.1021/acs.accounts.3c00123.
- (22) Dohnalová, K.; Kůsová, K. Optical Properties of Si Nanocrystals Enhanced by Ligands. In *Silicon Photonics IV: Innovative Frontiers*, Lockwood, D. J., Pavesi, L. Eds.; Springer International Publishing, 2021; pp 3-65.
- (23) Li, Q.; Jin, R. Photoluminescence from colloidal silicon nanoparticles: significant effect of surface. *Nanotechnol. Rev.* **2017**, *6* (6), 601-612. DOI: doi:10.1515/ntrev-2017-0145 (acccesed 2023-09-06).
- (24) Milliken, S.; Thiessen, A. N.; Cheong, I. T.; O'Connor, K. M.; Li, Z.; Hooper, R. W.; Robidillo, C. J. T.; Veinot, J. G. C. “Turning the dials”: controlling synthesis, structure, composition, and surface chemistry to tailor silicon nanoparticle properties. *Nanoscale* **2021**, *13* (39), 16379-16404, 10.1039/D1NR04701A. DOI: 10.1039/D1NR04701A.
- (25) K. Kůsová, K. D. Organically capped silicon nanocrystal. In *Silicon Nanomaterials Sourcebook Low-Dimensional Structures Nanopow*, Sattler, K. D. Ed.; CRC Press, 2017; p 32.
- (26) Dohnalová, K.; Hapala, P.; Kůsová, K.; Infante, I. Electronic Structure Engineering Achieved via Organic Ligands in Silicon Nanocrystals. *Chem. Mater.* **2020**, *32* (15), 6326-6337. DOI: 10.1021/acs.chemmater.0c00443.
- (27) Greben, M.; Khoroshyy, P.; Sychugov, I.; Valenta, J. Non-exponential decay kinetics: correct assessment and description illustrated by slow luminescence of Si nanostructures. *Appl. Spectrosc. Rev.* **2019**, *54* (9), 758-801. DOI: 10.1080/05704928.2018.1517263.
- (28) Zhang, Y.; Conibeer, G.; Liu, S.; Zhang, J.; Guillemoles, J.-F. Review of the mechanisms for the phonon bottleneck effect in III-V semiconductors and their application for efficient hot carrier solar cells. *Prog. Photovolt. Res. Appl.* **2022**, *30* (6), 581-596. DOI: <https://doi.org/10.1002/pip.3557>.
- (29) Rosenwaks, Y.; Hanna, M. C.; Levi, D. H.; Szmyd, D. M.; Ahrenkiel, R. K.; Nozik, A. J. Hot-carrier cooling in GaAs: Quantum wells versus bulk. *Phys. Rev. B* **1993**, *48* (19), 14675-14678. DOI: 10.1103/PhysRevB.48.14675.
- (30) Hirst, L. C.; Yakes, M. K.; Affouda, C. A.; Bailey, C. G.; Tischler, J. G.; Esmaelpour, H.; Whiteside, V. R.; Sellers, I. R.; Lumb, M. P.; Forbes, D. V.; et al. Hot-carrier effects in type II heterostructures. In *2015 IEEE 42nd Photovoltaic Specialist Conference (PVSC)*, 14-19 June 2015, 2015; pp 1-3. DOI: 10.1109/PVSC.2015.7356231.
- (31) Klimov, V. I.; McGuire, J. A.; Schaller, R. D.; Rupasov, V. I. Scaling of multiexciton lifetimes in semiconductor nanocrystals. *Phys. Rev. B* **2008**, *77* (19), 195324. DOI: 10.1103/PhysRevB.77.195324.
- (32) Papagiorgis, P.; Manoli, A.; Michael, S.; Bernasconi, C.; Bodnarchuk, M. I.; Kovalenko, M. V.; Othonos, A.; Itskos, G. Unraveling the Radiative Pathways of Hot Carriers upon Intense Photoexcitation of Lead Halide Perovskite Nanocrystals. *ACS Nano* **2019**, *13* (5), 5799-5809. DOI: 10.1021/acsnano.9b01398.
- (33) Shah, J.; Leite, R. C. C. Radiative Recombination from Photoexcited Hot Carriers in GaAs. *Phys Rev. Lett.* **1969**, *22* (24), 1304-1307. DOI: 10.1103/PhysRevLett.22.1304.
- (34) Li, M.; Bhaumik, S.; Goh, T. W.; Kumar, M. S.; Yantara, N.; Grätzel, M.; Mhaisalkar, S.; Mathews, N.; Sum, T. C. Slow cooling and highly efficient extraction of hot carriers in colloidal perovskite nanocrystals. *Nature Comm.* **2017**, *8* (1), 14350. DOI: 10.1038/ncomms14350.
- (35) Tisdale, W. A.; Williams, K. J.; Timp, B. A.; Norris, D. J.; Aydil, E. S.; Zhu, X.-Y. Hot-Electron Transfer from Semiconductor Nanocrystals. *Science* **2010**, *328* (5985), 1543-1547. DOI: doi:10.1126/science.1185509.
- (36) Löbl, M. C.; Spinnler, C.; Javadi, A.; Zhai, L.; Nguyen, G. N.; Ritzmann, J.; Midolo, L.; Lodahl, P.; Wieck, A. D.; Ludwig, A.; et al. Radiative Auger process in the single-photon limit. *Nature Nanotechnol.* **2020**, *15* (7), 558-562. DOI: 10.1038/s41565-020-0697-2.
- (37) Carmele, A. Auger processes in a single quantum dot. *Nature Nanotechnol.* **2020**, *15* (7), 513-515. DOI: 10.1038/s41565-020-0691-8.
- (38) Kurzmann, A.; Ludwig, A.; Wieck, A. D.; Lorke, A.; Geller, M. Auger Recombination in Self-Assembled Quantum Dots: Quenching and Broadening of the Charged Exciton Transition. *Nano Lett.* **2016**, *16* (5), 3367-3372. DOI: 10.1021/acs.nanolett.6b01082.
- (39) Climente, J. I.; Movilla, J. L.; Planelles, J. Auger Recombination Suppression in Nanocrystals with Asymmetric Electron-Hole Confinement. *Small* **2012**, *8* (5), 754-759. DOI: <https://doi.org/10.1002/smll.201101740>.

- (40) He, Y.; Hu, S.; Han, T.; Chen, X.; Yu, Y.; Li, T.; Zhu, W.; Ouyang, G. Suppression of the Auger Recombination Process in CdSe/CdS Core/Shell Nanocrystals. *ACS Omega* **2019**, *4* (5), 9198-9203. DOI: 10.1021/acsomega.9b00926 From NLM.
- (41) Hou, X.; Kang, J.; Qin, H.; Chen, X.; Ma, J.; Zhou, J.; Chen, L.; Wang, L.; Wang, L.-W.; Peng, X. Engineering Auger recombination in colloidal quantum dots via dielectric screening. *Nature Comm.* **2019**, *10* (1), 1750. DOI: 10.1038/s41467-019-09737-2.
- (42) Efros, A. L.; Rosen, M.; Kuno, M.; Nirmal, M.; Norris, D. J.; Bawendi, M. Band-edge exciton in quantum dots of semiconductors with a degenerate valence band: Dark and bright exciton states. *Phys. Rev. B* **1996**, *54* (7), 4843-4856. DOI: 10.1103/PhysRevB.54.4843.
- (43) Tsui, E. Y.; Carroll, G. M.; Miller, B.; Marchioro, A.; Gamelin, D. R. Extremely Slow Spontaneous Electron Trapping in Photodoped n-Type CdSe Nanocrystals. *Chem. Mater.* **2017**, *29* (8), 3754-3762. DOI: 10.1021/acs.chemmater.7b00839.
- (44) Ding, Y.; Sugaya, M.; Liu, Q.; Zhou, S.; Nozaki, T. Oxygen passivation of silicon nanocrystals: Influences on trap states, electron mobility, and hybrid solar cell performance. *Nano Energy* **2014**, *10*, 322-328. DOI: <https://doi.org/10.1016/j.nanoen.2014.09.031>.
- (45) Sark, W. v.; Frederix, P. L. T. M.; Heuvel, D. J. V. d.; Gerritsen, H. C.; Lingen, J. N. J. v.; Donegá, C. d. M.; Meijerink, A. Photooxidation and Photobleaching of Single CdSe/ZnS Quantum Dots Probed by Room-Temperature Time-Resolved Spectroscopy. *J. Phys. Chem. B* **2001**, *105*, 8281-8284.
- (46) Dzhagan, V.; Stroyuk, O.; Raievska, O.; Isaieva, O.; Kapush, O.; Selyshchev, O.; Yukhymchuk, V.; Valakh, M.; Zahn, D. R. T. Photoinduced Enhancement of Photoluminescence of Colloidal II-VI Nanocrystals in Polymer Matrices. *Nanomater.* **2020**, *10* (12), 2565.
- (47) Galland, C.; Ghosh, Y.; Steinbrück, A.; Sykora, M.; Hollingsworth, J. A.; Klimov, V. I.; Htoon, H. Two types of luminescence blinking revealed by spectroelectrochemistry of single quantum dots. *Nature* **2011**, *479* (7372), 203-207. DOI: 10.1038/nature10569.
- (48) He, S.; Han, Y.; Guo, J.; Wu, K. Long-Lived Delayed Emission from CsPbBr₃ Perovskite Nanocrystals for Enhanced Photochemical Reactivity. *ACS Energy Lett.* **2021**, *6* (8), 2786-2791. DOI: 10.1021/acsenergylett.1c01291.
- (49) Hinterding, S. O. M.; Vonk, S. J. W.; van Harten, E. J.; Rabouw, F. T. Dynamics of Intermittent Delayed Emission in Single CdSe/CdS Quantum Dots. *J. Phys. Chem. Lett.* **2020**, *11* (12), 4755-4761. DOI: 10.1021/acs.jpclett.0c01250.
- (50) Gómez, D. E.; van Embden, J.; Mulvaney, P. Spectral diffusion of single semiconductor nanocrystals: The influence of the dielectric environment. *Appl. Phys. Lett.* **2006**, *88* (15). DOI: 10.1063/1.2193967 (acccesed 9/17/2023).
- (51) Sharma, D. K.; Hirata, S.; Bujak, L.; Biju, V.; Kameyama, T.; Kishi, M.; Torimoto, T.; Vacha, M. Single-particle spectroscopy of I–III–VI semiconductor nanocrystals: spectral diffusion and suppression of blinking by two-color excitation. *Nanoscale* **2016**, *8* (28), 13687-13694, 10.1039/C6NR03950B. DOI: 10.1039/C6NR03950B.
- (52) Osborne, M. A.; Lee, S. F. Quantum Dot Photoluminescence Activation and Decay: Dark, Bright, and Reversible Populations in ZnS-Capped CdSe Nanocrystals. *ACS Nano* **2011**, *5* (10), 8295-8304. DOI: 10.1021/nn202994w.
- (53) Spinicelli, P.; Buil, S.; Quélin, X.; Mahler, B.; Dubertret, B.; Hermier, J. P. Bright and Grey States in CdSe-CdS Nanocrystals Exhibiting Strongly Reduced Blinking. *Phys Rev. Lett.* **2009**, *102* (13), 136801. DOI: 10.1103/PhysRevLett.102.136801.
- (54) Popelář, T.; Galář, P.; Matějka, F.; Morselli, G.; Ceroni, P.; Kůsová, K. Universal Radiative Lifetimes in the Long-Lived Luminescence of Si Quantum Dots. *J. Phys. Chem. C* **2023**, *127* (41), 20426-20437. DOI: 10.1021/acs.jpcc.3c05423.
- (55) Nirmal, M.; Dabbousi, B. O.; Bawendi, M. G.; Macklin, J. J.; Trautman, J. K.; Harris, T. D.; Brus, L. E. Fluorescence intermittency in single cadmium selenide nanocrystals. *Nature* **1996**, *383* (6603), 802-804. DOI: 10.1038/383802a0.
- (56) Frantsuzov, P.; Kuno, M.; Jankó, B.; Marcus, R. A. Universal emission intermittency in quantum dots, nanorods and nanowires. *Nature Phys.* **2008**, *4* (7), 519-522. DOI: 10.1038/nphys1001.
- (57) Kůsová, K.; Pelant, I.; Humpolíčková, J.; Hof, M. Comprehensive description of blinking-dynamics regimes in single direct-band-gap silicon nanocrystals. *Phys. Rev. B* **2016**, *93* (3), 035412. DOI: 10.1103/PhysRevB.93.035412.

- (58) Kuno, M.; Fromm, D. P.; Hamann, H. F.; Gallagher, A.; Nesbitt, D. J. Nonexponential “blinking” kinetics of single CdSe quantum dots: A universal power law behavior. *J. Chem. Phys.* **2000**, *112* (7), 3117-3120. DOI: 10.1063/1.480896 (accessed 9/17/2023).
- (59) Wang, S.; Querner, C.; Fischbein, M. D.; Willis, L.; Novikov, D. S.; Crouch, C. H.; Drndic, M. Blinking Statistics Correlated with Nanoparticle Number. *Nano Lett.* **2008**, *8* (11), 4020-4026. DOI: 10.1021/nl802696f.
- (60) Kuno, M.; Fromm, D. P.; Johnson, S. T.; Gallagher, A.; Nesbitt, D. J. Modeling distributed kinetics in isolated semiconductor quantum dots. *Phys. Rev. B* **2003**, *67* (12), 125304. DOI: 10.1103/PhysRevB.67.125304.
- (61) Efros, A. L.; Nesbitt, D. J. Origin and control of blinking in quantum dots. *Nature Nanotechnol.* **2016**, *11* (8), 661-671. DOI: 10.1038/nnano.2016.140.
- (62) Valenta, J.; Greben, M.; Dyakov, S. A.; Gippius, N. A.; Hiller, D.; Gutsch, S.; Zacharias, M. Nearly perfect near-infrared luminescence efficiency of Si nanocrystals: A comprehensive quantum yield study employing the Purcell effect. *Sci Rep* **2019**, *9* (1), 11214. DOI: 10.1038/s41598-019-47825-x From NLM.
- (63) Valenta, J. Determination of absolute quantum yields of luminescing nanomaterials over a broad spectral range: from the integrating sphere theory to the correct methodology. *Nanosci. Methods* **2014**, *3* (1), 11-27. DOI: 10.1080/21642311.2014.884288.
- (64) Efros, A. L.; Brus, L. E. Nanocrystal Quantum Dots: From Discovery to Modern Development. *ACS Nano* **2021**, *15* (4), 6192-6210. DOI: 10.1021/acsnano.1c01399.
- (65) Canham, L. T. Silicon quantum wire array fabrication by electrochemical and chemical dissolution of wafers. *Appl. Phys. Lett.* **1990**, *57* (10), 1046-1048. DOI: 10.1063/1.103561 (accessed 8/8/2024).
- (66) Hybertsen, M. S. Absorption and emission of light in nanoscale silicon structures. *Phys Rev. Lett.* **1994**, *72* (10), 1514-1517. DOI: 10.1103/PhysRevLett.72.1514.
- (67) Kovalev, D.; Heckler, H.; Ben-Chorin, M.; Polisski, G.; Schwartzkopff, M.; Koch, F. Breakdown of the \$k\\$-Conservation Rule in Si Nanocrystals. *Phys Rev. Lett.* **1998**, *81* (13), 2803-2806. DOI: 10.1103/PhysRevLett.81.2803.
- (68) Montalti, M.; Cantelli, A.; Battistelli, G. Nanodiamonds and silicon quantum dots: ultrastable and biocompatible luminescent nanoprobes for long-term bioimaging. *Chem. Soc. Rev.* **2015**, *44* (14), 4853-4921, 10.1039/C4CS00486H. DOI: 10.1039/C4CS00486H.
- (69) Hernandez-Montelongo, J.; Muñoz-Noval, A.; García-Ruiz, J. P.; Torres-Costa, V.; Martin-Palma, R. J.; Manso-Silvan, M. Nanostructured porous silicon: The winding road from photonics to cell scaffolds. A review. *Front. bioeng. biotechnol.* **2015**, *3*, Review. DOI: 10.3389/fbioe.2015.00060.
- (70) Thiessen, A. N.; Ha, M.; Hooper, R. W.; Yu, H.; Oliynyk, A. O.; Veinot, J. G. C.; Michaelis, V. K. Silicon Nanoparticles: Are They Crystalline from the Core to the Surface? *Chem. Mater.* **2019**, *31* (3), 678-688. DOI: 10.1021/acs.chemmater.8b03074.
- (71) Cheong, I. T.; Yang Szepesvari, L.; Ni, C.; Butler, C.; O'Connor, K. M.; Hooper, R.; Meldrum, A.; Veinot, J. G. C. Not all silicon quantum dots are equal: photostability of silicon quantum dots with and without a thick amorphous shell. *Nanoscale* **2024**, *16* (2), 592-603, 10.1039/D3NR04478E. DOI: 10.1039/D3NR04478E.
- (72) Wolkin, M. V.; Jorne, J.; Fauchet, P. M.; Allan, G.; Delerue, C. Electronic States and Luminescence in Porous Silicon Quantum Dots: The Role of Oxygen. *Phys Rev. Lett.* **1999**, *82* (1), 197-200. DOI: 10.1103/PhysRevLett.82.197.
- (73) Bashouti, M. Y.; Sardashti, K.; Ristein, J.; Christiansen, S. H. Early stages of oxide growth in H-terminated silicon nanowires: determination of kinetic behavior and activation energy. *Phys. Chem. Chem. Phys.* **2012**, *14* (34), 11877-11881, 10.1039/C2CP41709J. DOI: 10.1039/C2CP41709J.
- (74) Cvirkovich, L.; Waldhör, D.; El-Sayed, A.-M.; Jech, M.; Wilhelmer, C.; Grasser, T. Dynamic modeling of Si(100) thermal oxidation: Oxidation mechanisms and realistic amorphous interface generation. *Appl. Surf. Sci.* **2023**, *610*, 155378. DOI: <https://doi.org/10.1016/j.apsusc.2022.155378>.
- (75) Kovalev, D.; Timoshenko, V. Y.; Künzner, N.; Gross, E.; Koch, F. Strong Explosive Interaction of Hydrogenated Porous Silicon with Oxygen at Cryogenic Temperatures. *Phys Rev. Lett.* **2001**, *87* (6), 068301. DOI: 10.1103/PhysRevLett.87.068301.
- (76) Carroll, G. M.; Limpens, R.; Neale, N. R. Tuning Confinement in Colloidal Silicon Nanocrystals with Saturated Surface Ligands. *Nano Lett.* **2018**, *18* (5), 3118-3124. DOI: 10.1021/acs.nanolett.8b00680.

- (77) Kůsová, K.; Hapala, P.; Valenta, J.; Jelínek, P.; Cibulka, O.; Ondič, L.; Pelant, I. Direct Bandgap Silicon: Tensile-Strained Silicon Nanocrystals. *Adv. Mater. Interfaces* **2014**, *1* (2), 1300042. DOI: <https://doi.org/10.1002/admi.201300042>.
- (78) Fucikova, A.; Valenta, J.; Pelant, I.; Kalbacova, M. H.; Broz, A.; Rezek, B.; Kromka, A.; Bakaeva, Z. Silicon nanocrystals and nanodiamonds in live cells: photoluminescence characteristics, cytotoxicity and interaction with cell cytoskeleton. *RSC Adv.* **2014**, *4* (20), 10334-10342, 10.1039/C3RA47574C. DOI: 10.1039/C3RA47574C.
- (79) Park, J.-H.; Gu, L.; von Maltzahn, G.; Ruoslahti, E.; Bhatia, S. N.; Sailor, M. J. Biodegradable luminescent porous silicon nanoparticles for in vivo applications. *Nature Mater.* **2009**, *8* (4), 331-336. DOI: 10.1038/nmat2398.
- (80) Pavesi, L.; Dal Negro, L.; Mazzoleni, C.; Franzò, G.; Priolo, F. Optical gain in silicon nanocrystals. *Nature* **2000**, *408* (6811), 440-444. DOI: 10.1038/35044012 From NLM.
- (81) Valenta, J.; Pelant, I.; Linnros, J. Waveguiding effects in the measurement of optical gain in a layer of Si nanocrystals. *Appl. Phys. Lett.* **2002**, *81* (8), 1396-1398. DOI: 10.1063/1.1502195 (acccesed 8/9/2024).
- (82) Galář, P.; Popelář, T.; Khun, J.; Matulková, I.; Němec, I.; Newell, K. D.; Michalcová, A.; Scholtz, V.; Kůsová, K. The red and blue luminescence in silicon nanocrystals with an oxidized, nitrogen-containing shell. *Faraday Discuss.* **2020**, *222* (0), 240-257, 10.1039/C9FD00092E. DOI: 10.1039/C9FD00092E.
- (83) Galar, P. K., J. Král, R. Matějka, F. Zemenová, P. Dopita, M. Hapala, P. Konig, D. Vrbka, P. Kusova, K. Engineering the thermal and energy-storage properties of quantum dots using surface free energy. *ACS Nano* **2024**, Accepted.
- (84) Peng, M.; Liu, Y.; Li, F.; Hong, X.; Liu, Y.; Wen, Z.; Liu, Z.; Ma, W.; Sun, X. Room-Temperature Direct Synthesis of PbSe Quantum Dot Inks for High-Detectivity Near-Infrared Photodetectors. *ACS Appl. Mater. Interfaces* **2021**, *13* (43), 51198-51204. DOI: 10.1021/acsami.1c13723.
- (85) Wilbrink, Jonathan L.; Huang, C.-C.; Dohnalova, K.; Paulusse, J. M. J. Critical assessment of wet-chemical oxidation synthesis of silicon quantum dots. *Faraday Discuss.* **2020**, *222* (0), 149-165, 10.1039/C9FD00099B. DOI: 10.1039/C9FD00099B.
- (86) Oliinyk, B. V.; Korytko, D.; Lysenko, V.; Alekseev, S. Are Fluorescent Silicon Nanoparticles Formed in a One-Pot Aqueous Synthesis? *Chem. Mater.* **2019**, *31* (18), 7167-7172. DOI: 10.1021/acs.chemmater.9b01067.
- (87) Morozova, S.; Alikina, M.; Vinogradov, A.; Pagliaro, M. Silicon Quantum Dots: Synthesis, Encapsulation, and Application in Light-Emitting Diodes. *Front. Chem.* **2020**, *8*, Mini Review. DOI: 10.3389/fchem.2020.00191.
- (88) Hessel, C. M.; Henderson, E. J.; Veinot, J. G. C. Hydrogen Silsesquioxane: A Molecular Precursor for Nanocrystalline Si–SiO₂ Composites and Freestanding Hydride-Surface-Terminated Silicon Nanoparticles. *Chem. Mater.* **2006**, *18* (26), 6139-6146. DOI: 10.1021/cm0602803.
- (89) Kortshagen, U. R.; Sankaran, R. M.; Pereira, R. N.; Girshick, S. L.; Wu, J. J.; Aydil, E. S. Nonthermal Plasma Synthesis of Nanocrystals: Fundamental Principles, Materials, and Applications. *Chem. Rev.* **2016**, *116* (18), 11061-11127. DOI: 10.1021/acs.chemrev.6b00039.
- (90) Jurbergs, D.; Rogojina, E.; Mangolini, L.; Kortshagen, U. Silicon nanocrystals with ensemble quantum yields exceeding 60%. *Appl. Phys. Lett.* **2006**, *88* (23). DOI: 10.1063/1.2210788 (acccesed 8/9/2024).
- (91) Canham, L. Introductory lecture: origins and applications of efficient visible photoluminescence from silicon-based nanostructures. *Faraday Discuss.* **2020**, *222* (0), 10-81, 10.1039/D0FD00018C. DOI: 10.1039/D0FD00018C.
- (92) Yu, Y.; Fan, G.; Fermi, A.; Mazzaro, R.; Morandi, V.; Ceroni, P.; Smilgies, D.-M.; Korgel, B. A. Size-Dependent Photoluminescence Efficiency of Silicon Nanocrystal Quantum Dots. *J. Phys. Chem. C* **2017**, *121* (41), 23240-23248. DOI: 10.1021/acs.jpcc.7b08054.
- (93) Koh, T. T.; Huang, T.; Schwan, J.; Xia, P.; Roberts, S. T.; Mangolini, L.; Tang, Ming L. Low temperature radical initiated hydrosilylation of silicon quantum dots. *Faraday Discuss.* **2020**, *222* (0), 190-200, 10.1039/C9FD00144A. DOI: 10.1039/C9FD00144A.
- (94) Hua, F.; Swihart, M. T.; Ruckenstein, E. Efficient Surface Grafting of Luminescent Silicon Quantum Dots by Photoinitiated Hydrosilylation. *Langmuir* **2005**, *21* (13), 6054-6062. DOI: 10.1021/la0509394.

- (95) Dasog, M.; Bader, K.; Veinot, J. G. C. Influence of Halides on the Optical Properties of Silicon Quantum Dots. *Chem. Mater.* **2015**, 27 (4), 1153-1156. DOI: 10.1021/acs.chemmater.5b00115.
- (96) Anthony, R. J.; Rowe, D. J.; Stein, M.; Yang, J.; Kortshagen, U. Routes to Achieving High Quantum Yield Luminescence from Gas-Phase-Produced Silicon Nanocrystals. *Adv. Funct. Mater.* **2011**, 21 (21), 4042-4046. DOI: <https://doi.org/10.1002/adfm.201100784>.
- (97) Galář, P.; Stuchlík, J.; Müller, M.; Kočka, J.; Kůsová, K. Highly spherical SiC nanoparticles grown in nonthermal plasma. *Plasma Process. Polym.* **2022**, 19 (2), 2100127. DOI: <https://doi.org/10.1002/ppap.202100127>.
- (98) Galář, P.; Khun, J.; Fučíková, A.; Dohnalová, K.; Popelář, T.; Matulková, I.; Valenta, J.; Scholtz, V.; Kůsová, K. Non-thermal pulsed plasma activated water: environmentally friendly way for efficient surface modification of semiconductor nanoparticles. *Green Chem.* **2021**, 23 (2), 898-911, 10.1039/D0GC02619K. DOI: 10.1039/D0GC02619K.
- (99) Matějka, F.; Galář, P.; Khun, J.; Scholtz, V.; Kůsová, K. Mechanisms leading to plasma activated water high in nitrogen oxides. *Phys. Scripta* **2023**, 98 (4), 045619. DOI: 10.1088/1402-4896/acc48e.
- (100) Galář, P.; Kůsová, K.; Fučíková, A.; Khun, J. A METHOD FOR SURFACE MODIFICATION OF SEMICONDUCTOR NANOPARTICLES USING NON-THERMAL PLASMA ACTIVATED WATER AND PRODUCT THEREOF. Czech Republic 2024.
- (101) Yamada, H.; Saitoh, N.; Ghosh, B.; Masuda, Y.; Yoshizawa, N.; Shirahata, N. Improved Brightness and Color Tunability of Solution-Processed Silicon Quantum Dot Light-Emitting Diodes. *J. Phys. Chem. C* **2020**, 124 (42), 23333-23342. DOI: 10.1021/acs.jpcc.0c06672.
- (102) Higuera-Valenzuela, H. J.; Ramos-Carrazco, A.; García-Gutierrez, R.; Romo-García, F.; Rangel, R.; Contreras, O. E.; Berman-Mendoza, D. Efficiency enhancement of silicon solar cells by silicon quantum dots embedded in ZnO films as down-shifting coating. *J. Mater. Sci.: Mater. Electron.* **2020**, 31 (22), 20561-20570. DOI: 10.1007/s10854-020-04576-0.
- (103) Meinardi, F.; Ehrenberg, S.; Dhamo, L.; Carulli, F.; Mauri, M.; Bruni, F.; Simonutti, R.; Kortshagen, U.; Brovelli, S. Highly efficient luminescent solar concentrators based on earth-abundant indirect-bandgap silicon quantum dots. *Nature Photonics* **2017**, 11 (3), 177-185. DOI: 10.1038/nphoton.2017.5.
- (104) Zhong, Y.; Peng, F.; Wei, X.; Zhou, Y.; Wang, J.; Jiang, X.; Su, Y.; Su, S.; Lee, S.-T.; He, Y. Microwave-Assisted Synthesis of Biofunctional and Fluorescent Silicon Nanoparticles Using Proteins as Hydrophilic Ligands. *Angew. Chem., Int. Ed.* **2012**, 51 (34), 8485-8489. DOI: <https://doi.org/10.1002/anie.201202085>.
- (105) Eshetu, G. G.; Zhang, H.; Judez, X.; Adenusi, H.; Armand, M.; Passerini, S.; Figgemeier, E. Production of high-energy Li-ion batteries comprising silicon-containing anodes and insertion-type cathodes. *Nature Comm.* **2021**, 12 (1), 5459. DOI: 10.1038/s41467-021-25334-8.
- (106) Li, Z.; Sun, Q.; Zhu, Y.; Tan, B.; Xu, Z. P.; Dou, S. X. Ultra-small fluorescent inorganic nanoparticles for bioimaging. *J. Mater. Chem. B* **2014**, 2 (19), 2793-2818, 10.1039/C3TB21760D. DOI: 10.1039/C3TB21760D.
- (107) Marcelo, G. A.; Montpeyo, D.; Novio, F.; Ruiz-Molina, D.; Lorenzo, J.; Oliveira, E. Luminescent silicon-based nanocarrier for drug delivery in colorectal cancer cells. *Dyes Pigments* **2020**, 181, 108393. DOI: <https://doi.org/10.1016/j.dyepig.2020.108393>.
- (108) Huang, S.; Parimi, V. S.; Deng, S.; Lingamneni, S.; Zheng, X. Facile Thermal and Optical Ignition of Silicon Nanoparticles and Micron Particles. *Nano Lett.* **2017**, 17 (10), 5925-5930. DOI: 10.1021/acs.nanolett.7b01754.
- (109) Neiner, D.; Kauzlarich, S. M. Hydrogen-Capped Silicon Nanoparticles as a Potential Hydrogen Storage Material: Synthesis, Characterization, and Hydrogen Release. *Chem. Mater.* **2010**, 22 (2), 487-493. DOI: 10.1021/cm903054s.
- (110) Beri, D. Silicon quantum dots: surface matter, what next? *Mater. Adv.* **2023**, 4 (16), 3380-3398, 10.1039/D2MA00984F. DOI: 10.1039/D2MA00984F.
- (111) Sharif, R.; Khalid, A.; Ahmad, S. W.; Rehman, A.; Qutab, H. G.; Akhtar, H. H.; Mahmood, K.; Afzal, S.; Saleem, F. A comprehensive review of the current progresses and material advances in perovskite solar cells. *Nanoscale Adv.* **2023**, 5 (15), 3803-3833, 10.1039/D3NA00319A. DOI: 10.1039/D3NA00319A.
- (112) Jena, A. K.; Kulkarni, A.; Miyasaka, T. Halide Perovskite Photovoltaics: Background, Status, and Future Prospects. *Chem. Rev.* **2019**, 119 (5), 3036-3103. DOI: 10.1021/acs.chemrev.8b00539.

- (113) He, X.; Deng, Y.; Ouyang, D.; Zhang, N.; Wang, J.; Murthy, A. A.; Spanopoulos, I.; Islam, S. M.; Tu, Q.; Xing, G.; et al. Recent Development of Halide Perovskite Materials and Devices for Ionizing Radiation Detection. *Chem. Rev.* **2023**, *123* (4), 1207-1261. DOI: 10.1021/acs.chemrev.2c00404.
- (114) Dong, H.; Ran, C.; Gao, W.; Li, M.; Xia, Y.; Huang, W. Metal Halide Perovskite for next-generation optoelectronics: progresses and prospects. *eLight* **2023**, *3* (1), 3. DOI: 10.1186/s43593-022-00033-z.
- (115) Chen, K.; Schünemann, S.; Song, S.; Tüysüz, H. Structural effects on optoelectronic properties of halide perovskites. *Chem. Soc. Rev.* **2018**, *47* (18), 7045-7077, 10.1039/C8CS00212F. DOI: 10.1039/C8CS00212F.
- (116) Eperon, G. E.; Stranks, S. D.; Menelaou, C.; Johnston, M. B.; Herz, L. M.; Snaith, H. J. Formamidinium lead trihalide: a broadly tunable perovskite for efficient planar heterojunction solar cells. *Energy Environ. Sci.* **2014**, *7* (3), 982-988, 10.1039/C3EE43822H. DOI: 10.1039/C3EE43822H.
- (117) Chen, Q.; De Marco, N.; Yang, Y.; Song, T.-B.; Chen, C.-C.; Zhao, H.; Hong, Z.; Zhou, H.; Yang, Y. Under the spotlight: The organic-inorganic hybrid halide perovskite for optoelectronic applications. *Nano Today* **2015**, *10* (3), 355-396. DOI: <https://doi.org/10.1016/j.nantod.2015.04.009>.
- (118) Ahn, N.; Kwak, K.; Jang, M. S.; Yoon, H.; Lee, B. Y.; Lee, J.-K.; Pikhitsa, P. V.; Byun, J.; Choi, M. Trapped charge-driven degradation of perovskite solar cells. *Nature Comm.* **2016**, *7* (1), 13422. DOI: 10.1038/ncomms13422.
- (119) Zhuang, J.; Wang, J.; Yan, F. Review on Chemical Stability of Lead Halide Perovskite Solar Cells. *Nano-Micro Letters* **2023**, *15* (1), 84. DOI: 10.1007/s40820-023-01046-0.
- (120) Hao, F.; Stoumpos, C. C.; Cao, D. H.; Chang, R. P. H.; Kanatzidis, M. G. Lead-free solid-state organic-inorganic halide perovskite solar cells. *Nature Photonics* **2014**, *8* (6), 489-494. DOI: 10.1038/nphoton.2014.82.
- (121) Li, Z.; Yang, M.; Park, J.-S.; Wei, S.-H.; Berry, J. J.; Zhu, K. Stabilizing Perovskite Structures by Tuning Tolerance Factor: Formation of Formamidinium and Cesium Lead Iodide Solid-State Alloys. *Chem. Mater.* **2016**, *28* (1), 284-292. DOI: 10.1021/acs.chemmater.5b04107.
- (122) Zhou, W.; Zhao, Y.; Zhou, X.; Fu, R.; Li, Q.; Zhao, Y.; Liu, K.; Yu, D.; Zhao, Q. Light-Independent Ionic Transport in Inorganic Perovskite and Ultrastable Cs-Based Perovskite Solar Cells. *J. Phys. Chem. Lett.* **2017**, *8* (17), 4122-4128. DOI: 10.1021/acs.jpclett.7b01851.
- (123) Yi, C.; Luo, J.; Meloni, S.; Boziki, A.; Ashari-Astani, N.; Grätzel, C.; Zakeeruddin, S. M.; Röthlisberger, U.; Grätzel, M. Entropic stabilization of mixed A-cation ABX₃ metal halide perovskites for high performance perovskite solar cells. *Energy Environ. Sci.* **2016**, *9* (2), 656-662, 10.1039/C5EE03255E. DOI: 10.1039/C5EE03255E.
- (124) Dupré, O.; Vaillon, R.; Green, M. A. Physics of the temperature coefficients of solar cells. *Sol. Energy Mater.* **2015**, *140*, 92-100. DOI: <https://doi.org/10.1016/j.solmat.2015.03.025>.
- (125) Yu, W.; Zou, Y.; Wang, H.; Qi, S.; Wu, C.; Guo, X.; Liu, Y.; Chen, Z.; Qu, B.; Xiao, L. Breaking the bottleneck of lead-free perovskite solar cells through dimensionality modulation. *Chem. Soc. Rev.* **2024**, *53* (4), 1769-1788, 10.1039/D3CS00728F. DOI: 10.1039/D3CS00728F.
- (126) Yang, W. S.; Park, B.-W.; Jung, E. H.; Jeon, N. J.; Kim, Y. C.; Lee, D. U.; Shin, S. S.; Seo, J.; Kim, E. K.; Noh, J. H.; et al. Iodide management in formamidinium-lead-halide-based perovskite layers for efficient solar cells. *Science* **2017**, *356* (6345), 1376-1379. DOI: doi:10.1126/science.aan2301.
- (127) Chen, J.; Zhou, Y.; Fu, Y.; Pan, J.; Mohammed, O. F.; Bakr, O. M. Oriented Halide Perovskite Nanostructures and Thin Films for Optoelectronics. *Chem. Rev.* **2021**, *121* (20), 12112-12180. DOI: 10.1021/acs.chemrev.1c00181.
- (128) Straus, D. B.; Kagan, C. R. Electrons, Excitons, and Phonons in Two-Dimensional Hybrid Perovskites: Connecting Structural, Optical, and Electronic Properties. *J. Phys. Chem. Lett.* **2018**, *9* (6), 1434-1447. DOI: 10.1021/acs.jpclett.8b00201.
- (129) Blancon, J.-C.; Tsai, H.; Nie, W.; Stoumpos, C. C.; Pedesseau, L.; Katan, C.; Kepenekian, M.; Soe, C. M. M.; Appavoo, K.; Sfeir, M. Y.; et al. Extremely efficient internal exciton dissociation through edge states in layered 2D perovskites. *Science* **2017**, *355* (6331), 1288-1292. DOI: doi:10.1126/science.aal4211.
- (130) Hong, X.; Ishihara, T.; Nurmikko, A. V. Dielectric confinement effect on excitons in PbI_3 -based layered semiconductors. *Phys. Rev. B* **1992**, *45* (12), 6961-6964. DOI: 10.1103/PhysRevB.45.6961.

- (131) Lu, J.; Jiang, L.; Li, W.; Li, F.; Pai, N. K.; Scully, A. D.; Tsai, C.-M.; Bach, U.; Simonov, A. N.; Cheng, Y.-B.; et al. Diammonium and Monoammonium Mixed-Organic-Cation Perovskites for High Performance Solar Cells with Improved Stability. *Adv. Energy Mater.* **2017**, *7* (18), 1700444. DOI: <https://doi.org/10.1002/aenm.201700444>.
- (132) Rodríguez-Romero, J.; Clasen Hames, B.; Galar, P.; Fakharuddin, A.; Suarez, I.; Schmidt-Mende, L.; Martínez-Pastor, J. P.; Douhal, A.; Mora-Seró, I.; Barea, E. M. Tuning optical/electrical properties of 2D/3D perovskite by the inclusion of aromatic cation. *Phys. Chem. Chem. Phys.* **2018**, *20* (48), 30189-30199, 10.1039/C8CP06418K. DOI: 10.1039/C8CP06418K.
- (133) Kovalenko, M. V.; Protesescu, L.; Bodnarchuk, M. I. Properties and potential optoelectronic applications of lead halide perovskite nanocrystals. *Science* **2017**, *358* (6364), 745-750. DOI: doi:10.1126/science.aam7093.
- (134) Protesescu, L.; Yakunin, S.; Bodnarchuk, M. I.; Krieg, F.; Caputo, R.; Hendon, C. H.; Yang, R. X.; Walsh, A.; Kovalenko, M. V. Nanocrystals of Cesium Lead Halide Perovskites (CsPbX_3 , X = Cl, Br, and I): Novel Optoelectronic Materials Showing Bright Emission with Wide Color Gamut. *Nano Lett.* **2015**, *15* (6), 3692-3696. DOI: 10.1021/nl5048779.
- (135) Ren, X.; Zhang, X.; Xie, H.; Cai, J.; Wang, C.; Chen, E.; Xu, S.; Ye, Y.; Sun, J.; Yan, Q.; et al. Perovskite Quantum Dots for Emerging Displays: Recent Progress and Perspectives. *Nanomater.* **2022**, *12* (13), 2243.
- (136) Huang, K.; Liu, J.; Yuan, J.; Zhao, W.; Zhao, K.; Zhou, Z. Perovskite-quantum dot hybrid solar cells: a multi-win strategy for high performance and stability. *J. Mater. Chem. A* **2023**, *11* (9), 4487-4509, 10.1039/D2TA09434G. DOI: 10.1039/D2TA09434G.
- (137) Sanehira, E. M.; Marshall, A. R.; Christians, J. A.; Harvey, S. P.; Ciesielski, P. N.; Wheeler, L. M.; Schulz, P.; Lin, L. Y.; Beard, M. C.; Luther, J. M. Enhanced mobility CsPbI_{3} quantum dot arrays for record-efficiency, high-voltage photovoltaic cells. *Science Adv.* **2017**, *3* (10), eaao4204. DOI: doi:10.1126/sciadv.aao4204.
- (138) Koh, T. M.; Shanmugam, V.; Schlipf, J.; Oesinghaus, L.; Müller-Buschbaum, P.; Ramakrishnan, N.; Swamy, V.; Mathews, N.; Boix, P. P.; Mhaisalkar, S. G. Nanostructuring Mixed-Dimensional Perovskites: A Route Toward Tunable, Efficient Photovoltaics. *Adv. Mater.* **2016**, *28* (19), 3653-3661. DOI: <https://doi.org/10.1002/adma.201506141>.
- (139) Rakshit, S.; Piatkowski, P.; Mora-Seró, I.; Douhal, A. Combining Perovskites and Quantum Dots: Synthesis, Characterization, and Applications in Solar Cells, LEDs, and Photodetectors. *Adv. Opt. Mater.* **2022**, *10* (14), 2102566. DOI: <https://doi.org/10.1002/adom.202102566>.
- (140) Li, S.-S.; Chang, C.-H.; Wang, Y.-C.; Lin, C.-W.; Wang, D.-Y.; Lin, J.-C.; Chen, C.-C.; Sheu, H.-S.; Chia, H.-C.; Wu, W.-R.; et al. Intermixing-seeded growth for high-performance planar heterojunction perovskite solar cells assisted by precursor-capped nanoparticles. *Energy Environ. Sci.* **2016**, *9* (4), 1282-1289, 10.1039/C5EE03229F. DOI: 10.1039/C5EE03229F.
- (141) Ning, Z.; Gong, X.; Comin, R.; Walters, G.; Fan, F.; Voznyy, O.; Yassitepe, E.; Buin, A.; Hoogland, S.; Sargent, E. H. Quantum-dot-in-perovskite solids. *Nature* **2015**, *523* (7560), 324-328. DOI: 10.1038/nature14563.
- (142) Yan, D.; Liu, M.; Li, Z.; Hou, B. Colloidal quantum dots and metal halide perovskite hybridization for solar cell stability and performance enhancement. *J. Mater. Chem. A* **2021**, *9* (28), 15522-15541, 10.1039/D1TA02214H. DOI: 10.1039/D1TA02214H.
- (143) Gao, L.; Quan, L. N.; García de Arquer, F. P.; Zhao, Y.; Munir, R.; Proppe, A.; Quintero-Bermudez, R.; Zou, C.; Yang, Z.; Saidaminov, M. I.; et al. Efficient near-infrared light-emitting diodes based on quantum dots in layered perovskite. *Nature Photonics* **2020**, *14* (4), 227-233. DOI: 10.1038/s41566-019-0577-1.
- (144) Gong, X.; Yang, Z.; Walters, G.; Comin, R.; Ning, Z.; Beauregard, E.; Adinolfi, V.; Voznyy, O.; Sargent, E. H. Highly efficient quantum dot near-infrared light-emitting diodes. *Nature Photonics* **2016**, *10* (4), 253-257. DOI: 10.1038/nphoton.2016.11.
- (145) Gaulding, E. A.; Chen, X.; Yang, Y.; Harvey, S. P.; To, B.; Kim, Y.-H.; Beard, M. C.; Sercel, P. C.; Luther, J. M. Embedding PbS Quantum Dots (QDs) in Pb-Halide Perovskite Matrices: QD Surface Chemistry and Antisolvent Effects on QD Dispersion and Confinement Properties. *ACS mater. lett.* **2020**, *2* (11), 1464-1472. DOI: 10.1021/acsmaterialslett.0c00302.

- (146) Cha, M.; Da, P.; Wang, J.; Wang, W.; Chen, Z.; Xiu, F.; Zheng, G.; Wang, Z.-S. Enhancing Perovskite Solar Cell Performance by Interface Engineering Using CH₃NH₃PbBr_{0.9}I_{2.1} Quantum Dots. *J. Am. Chem. Soc.* **2016**, *138* (27), 8581-8587. DOI: 10.1021/jacs.6b04519.
- (147) Zai, H.; Zhu, C.; Xie, H.; Zhao, Y.; Shi, C.; Chen, Z.; Ke, X.; Sui, M.; Chen, C.; Hu, J.; et al. Congeneric Incorporation of CsPbBr₃ Nanocrystals in a Hybrid Perovskite Heterojunction for Photovoltaic Efficiency Enhancement. *ACS Energy Lett.* **2018**, *3* (1), 30-38. DOI: 10.1021/acsenergylett.7b00925.
- (148) Yang, Z.; Voznyy, O.; Walters, G.; Fan, J. Z.; Liu, M.; Kinge, S.; Hoogland, S.; Sargent, E. H. Quantum Dots in Two-Dimensional Perovskite Matrices for Efficient Near-Infrared Light Emission. *ACS Photonics* **2017**, *4* (4), 830-836. DOI: 10.1021/acspophotonics.6b00865.
- (149) Tavakoli, M. M.; Dastjerdi, H. T.; Prochowicz, D.; Yadav, P.; Tavakoli, R.; Saliba, M.; Fan, Z. Highly efficient and stable inverted perovskite solar cells using down-shifting quantum dots as a light management layer and moisture-assisted film growth. *J. Mater. Chem. A* **2019**, *7* (24), 14753-14760, 10.1039/C9TA03131F. DOI: 10.1039/C9TA03131F.
- (150) Piatkowski, P.; Masi, S.; Galar, P.; Gutiérrez, M.; Ngo, T. T.; Mora-Seró, I.; Douhal, A. Deciphering the role of quantum dot size in the ultrafast charge carrier dynamics at the perovskite–quantum dot interface. *J. Mater. Chem. C* **2020**, *8* (42), 14834-14844, 10.1039/D0TC03835K. DOI: 10.1039/D0TC03835K.
- (151) Collins, A. T. Synthetic diamond: Emerging CVD science and technology. Edited by Karl E. Spear and John P. Dismukes, Wiley, Chichester, UK 1994, XV, 663 pp., hardcover, £74.00, ISBN 0-471-53589-3. *Chem. Vap. Depos.* **1995**, *1* (1), 33-33. DOI: <https://doi.org/10.1002/cvde.19950010109>.
- (152) Williams, O. A. Nanocrystalline diamond. *Diam. Relat. Mater.* **2011**, *20* (5), 621-640. DOI: <https://doi.org/10.1016/j.diamond.2011.02.015>.
- (153) Qin, J.-X.; Yang, X.-G.; Lv, C.-F.; Li, Y.-Z.; Liu, K.-K.; Zang, J.-H.; Yang, X.; Dong, L.; Shan, C.-X. Nanodiamonds: Synthesis, properties, and applications in nanomedicine. *Mater. Des.* **2021**, *210*, 110091. DOI: <https://doi.org/10.1016/j.matdes.2021.110091>.
- (154) Zhang, J.; Wang, J.; Zhang, G.; Huo, Z.; Huang, Z.; Wu, L. A review of diamond synthesis, modification technology, and cutting tool application in ultra-precision machining. *Mater. Des.* **2024**, *237*, 112577. DOI: <https://doi.org/10.1016/j.matdes.2023.112577>.
- (155) Dossa, S. S.; Ponomarev, I.; Feigelson, B. N.; Hainke, M.; Kranert, C.; Friedrich, J.; Derby, J. J. Analysis of the High-Pressure High-Temperature (HPHT) growth of single crystal diamond. *J. Cryst. Growth* **2023**, *609*, 127150. DOI: <https://doi.org/10.1016/j.jcrysgr.2023.127150>.
- (156) Auciello, O.; Aslam, D. M. Review on advances in microcrystalline, nanocrystalline and ultrananocrystalline diamond films-based micro/nano-electromechanical systems technologies. *J. Mater. Sci.* **2021**, *56* (12), 7171-7230. DOI: 10.1007/s10853-020-05699-9.
- (157) Koizumi, S. N., Ch. Nesládek, M. *Physics and Applications of CVD Diamond*; Wiley-VCH, 2008.
- (158) Jelezko, F.; Wrachtrup, J. Single defect centres in diamond: A review. *Phys. Stat. Sol. (a)* **2006**, *203* (13), 3207-3225. DOI: <https://doi.org/10.1002/pssa.200671403>.
- (159) Galar, P. *Ultrarychlá laserová spektroskopie hybridních nanosystémů, dizertační práce*; Matematicky fyzikální fakulta UK, 2016.
- (160) Bradac, C.; Gao, W.; Forneris, J.; Trusheim, M. E.; Aharonovich, I. Quantum nanophotonics with group IV defects in diamond. *Nature Comm.* **2019**, *10* (1), 5625. DOI: 10.1038/s41467-019-13332-w.
- (161) Stehlik, S.; Varga, M.; Stenclova, P.; Ondic, L.; Ledinsky, M.; Pangrac, J.; Vanek, O.; Lipov, J.; Kromka, A.; Rezek, B. Ultrathin Nanocrystalline Diamond Films with Silicon Vacancy Color Centers via Seeding by 2 nm Detonation Nanodiamonds. *ACS Appl. Mater. Interfaces.* **2017**, *9* (44), 38842-38853. DOI: 10.1021/acsami.7b14436.
- (162) Zaitsev, A., M. *Optical Properties of Diamond: A Data Handbook*; Springer 2001.
- (163) Kebinski, P.; Phillipot, S. R.; Wolf, D.; Gleiter, H. On the nature of grain boundaries in nanocrystalline diamond. *Nanostructured Mater.* **1999**, *12* (1), 339-344. DOI: [https://doi.org/10.1016/S0965-9773\(99\)00130-0](https://doi.org/10.1016/S0965-9773(99)00130-0).
- (164) Musale, D. V.; Sainkar, S. R.; Kshirsagar, S. T. Raman, photoluminescence and morphological studies of Si- and N-doped diamond films grown on Si(100) substrate by hot-filament chemical vapor deposition technique. *Diam. Relat. Mater.* **2002**, *11* (1), 75-86. DOI: [https://doi.org/10.1016/S0925-9635\(01\)00521-0](https://doi.org/10.1016/S0925-9635(01)00521-0).

- (165) Kozakov, A. T.; Kochur, A. G.; Kumar, N.; Panda, K.; Nikolskii, A. V.; Sidashov, A. V. Determination of sp₂ and sp₃ phase fractions on the surface of diamond films from C1s, valence band X-ray photoelectron spectra and CKVV X-ray-excited Auger spectra. *Appl. Surf. Sci.* **2021**, *536*, 147807. DOI: <https://doi.org/10.1016/j.apsusc.2020.147807>.
- (166) Balandin, A. A. Thermal properties of graphene and nanostructured carbon materials. *Nature Mater.* **2011**, *10* (8), 569-581. DOI: 10.1038/nmat3064.
- (167) Li, G.; Rahim, M. Z.; Pan, W.; Wen, C.; Ding, S. The manufacturing and the application of polycrystalline diamond tools – A comprehensive review. *J. Manuf. Process.* **2020**, *56*, 400-416. DOI: <https://doi.org/10.1016/j.jmapro.2020.05.010>.
- (168) Nebel, C. E. Electronic properties of CVD diamond. *Semicond. Sci. Technol.* **2003**, *18* (3), S1. DOI: 10.1088/0268-1242/18/3/301.
- (169) Achatz, P.; Garrido, J. A.; Williams, O. A.; Bruno, P.; Gruen, D. M.; Kromka, A.; Steinmüller, D.; Stutzmann, M. Structural, optical, and electronic properties of nanocrystalline and ultrananocrystalline diamond thin films. *Phys. Stat. Sol. (a)* **2007**, *204* (9), 2874-2880. DOI: <https://doi.org/10.1002/pssa.200776337>.
- (170) Dzurňák, B.; Trojánek, F.; Preclíková, J.; Kromka, A.; Rezek, B.; Malý, P. Ultrafast photoluminescence spectroscopy of H- and O-terminated nanocrystalline diamond films. *Diam. Relat. Mater.* **2011**, *20* (8), 1155-1159. DOI: <https://doi.org/10.1016/j.diamond.2011.06.025>.
- (171) Zhao, F. L.; Gong, Z.; Liang, S. D.; Xu, N. S.; Deng, S. Z.; Chen, J.; Wang, H. Z. Ultrafast optical emission of nanodiamond induced by laser excitation. *Appl. Phys. Lett.* **2004**, *85* (6), 914-916. DOI: 10.1063/1.1777803 (acccessed 9/15/2024).
- (172) Zukerstein, M.; Trojánek, F.; Koutenský, P.; Varga, M.; Kromka, A.; Kozák, M.; Malý, P. Sub-picosecond electron dynamics in polycrystalline diamond films. *Diam. Relat. Mater.* **2020**, *108*, 107935. DOI: <https://doi.org/10.1016/j.diamond.2020.107935>.
- (173) Galář, P.; Dzurňák, B.; Varga, M.; Marton, M.; Kromka, A.; Malý, P. Influence of non-diamond carbon phase on recombination mechanisms of photoexcited charge carriers in microcrystalline and nanocrystalline diamond studied by time resolved photoluminescence spectroscopy. *Opt. Mater. Express* **2014**, *4* (4), 624-637. DOI: 10.1364/OME.4.000624.
- (174) Mochalin, V. N.; Shenderova, O.; Ho, D.; Gogotsi, Y. The properties and applications of nanodiamonds. *Nature Nanotechnol.* **2012**, *7* (1), 11-23. DOI: 10.1038/nnano.2011.209.
- (175) Wang, X.; Low, X. C.; Hou, W.; Abdullah, L. N.; Toh, T. B.; Mohd Abdul Rashid, M.; Ho, D.; Chow, E. K.-H. Epirubicin-Adsorbed Nanodiamonds Kill Chemoresistant Hepatic Cancer Stem Cells. *ACS Nano* **2014**, *8* (12), 12151-12166. DOI: 10.1021/nn503491e.
- (176) Rammohan, N.; MacRenaris, K. W.; Moore, L. K.; Parigi, G.; Mastarone, D. J.; Manus, L. M.; Lilley, L. M.; Preslar, A. T.; Waters, E. A.; Filicko, A.; et al. Nanodiamond–Gadolinium(III) Aggregates for Tracking Cancer Growth In Vivo at High Field. *Nano Lett.* **2016**, *16* (12), 7551-7564. DOI: 10.1021/acs.nanolett.6b03378.
- (177) Xu, J.; Chow, E. K.-H. Biomedical applications of nanodiamonds: From drug-delivery to diagnostics. *SLAS Technol.* **2023**, *28* (4), 214-222. DOI: <https://doi.org/10.1016/j.slast.2023.03.007>.
- (178) Tomagra, G.; Peroni, G.; Aprà, P.; Bonino, V.; Campostrini, M.; Carabelli, V.; Collà Ruvolo, C.; Lo Giudice, A.; Guidorzi, L.; Mino, L.; et al. Diamond-based sensors for in vitro cellular radiobiology: Simultaneous detection of cell exocytic activity and ionizing radiation. *Biosens. Bioelectron.* **2023**, *220*, 114876. DOI: <https://doi.org/10.1016/j.bios.2022.114876>.
- (179) Barzegar Amiri Olia, M.; Donnelly, P. S.; Hollenberg, L. C. L.; Mulvaney, P.; Simpson, D. A. Advances in the Surface Functionalization of Nanodiamonds for Biological Applications: A Review. *ACS Appl. Nano Mater.* **2021**, *4* (10), 9985-10005. DOI: 10.1021/acsnanm.1c02698.
- (180) Manai, R.; Scorsone, E.; Rousseau, L.; Ghassemi, F.; Possas Abreu, M.; Lissorgues, G.; Tremillon, N.; Ginisty, H.; Arnault, J. C.; Tuccori, E.; et al. Grafting odorant binding proteins on diamond bio-MEMS. *Biosens. Bioelectron.* **2014**, *60*, 311-317. DOI: <https://doi.org/10.1016/j.bios.2014.04.020>.
- (181) Qin, S.-R.; Zhao, Q.; Cheng, Z.-G.; Zhang, D.-X.; Zhang, K.-K.; Su, L.-X.; Fan, H.-J.; Wang, Y.-H.; Shan, C.-X. Rare earth-functionalized nanodiamonds for dual-modal imaging and drug delivery. *Diam. Relat. Mater.* **2019**, *91*, 173-182. DOI: <https://doi.org/10.1016/j.diamond.2018.11.015>.
- (182) Bacakova, L.; Grausova, L.; Vacik, J.; Fraczek, A.; Blazewicz, S.; Kromka, A.; Vanecek, M.; Svorcik, V. Improved adhesion and growth of human osteoblast-like MG 63 cells on biomaterials

- modified with carbon nanoparticles. *Diam. Relat. Mater.* **2007**, *16* (12), 2133-2140. DOI: <https://doi.org/10.1016/j.diamond.2007.07.015>.
- (183) Salvadori, M. C.; Araújo, W. W. R.; Teixeira, F. S.; Cattani, M.; Pasquarelli, A.; Oks, E. M.; Brown, I. G. Termination of diamond surfaces with hydrogen, oxygen and fluorine using a small, simple plasma gun. *Diam. Relat. Mater.* **2010**, *19* (4), 324-328. DOI: <https://doi.org/10.1016/j.diamond.2010.01.002>.
- (184) Galář, P.; Čermák, J.; Malý, P.; Kromka, A.; Rezek, B. Electrochemically grafted polypyrrole changes photoluminescence of electronic states inside nanocrystalline diamond. *J. Appl. Phys.* **2014**, *116* (22). DOI: 10.1063/1.4903937 (accessed 9/15/2024).
- (185) Dworschak, M.; Kohlmann, N.; Matějka, F.; Galář, P.; Kienle, L.; Schäfer, J.; Benedikt, J. Silicon nanocrystal synthesis with the atmospheric plasma source HelixJet. *Plasma Process. Polym.* **2023**, *20* (2), 2200129. DOI: <https://doi.org/10.1002/ppap.202200129>.
- (186) Müller, M.; Galář, P.; Stuchlík, J.; Kočka, J.; Kupka, J.; Kůsová, K. Synthesis and surface modification of light emitting silicon nanoparticles using non-thermal plasma techniques★. *Eur. Phys. J. Appl. Phys.* **2020**, *89* (2), 20401.
- (187) Meng, G. W.; Cui, Z.; Zhang, L. D.; Philipp, F. Growth and characterization of nanostructured β-SiC via carbothermal reduction of SiO₂ xerogels containing carbon nanoparticles. *J. Cryst. Growth* **2000**, *209* (4), 801-806. DOI: [https://doi.org/10.1016/S0022-0248\(99\)00435-2](https://doi.org/10.1016/S0022-0248(99)00435-2).
- (188) Wu, X. L.; Fan, J. Y.; Qiu, T.; Yang, X.; Siu, G. G.; Chu, P. K. Experimental Evidence for the Quantum Confinement Effect in 3\$C\$-SiC Nanocrystallites. *Phys Rev. Lett.* **2005**, *94* (2), 026102. DOI: 10.1103/PhysRevLett.94.026102.
- (189) Lin, H.; Gerbec, J. A.; Sushchikh, M.; McFarland, E. W. Synthesis of amorphous silicon carbide nanoparticles in a low temperature low pressure plasma reactor. *Nanotechnol.* **2008**, *19* (32), 325601. DOI: 10.1088/0957-4484/19/32/325601.
- (190) Chaukulkar, R. P.; de Peuter, K.; Ghodes, J. A.; Pylypenko, S.; Cloud, J. E.; Yang, Y.; Stradins, P.; Agarwal, S. Single-step non-thermal plasma synthesis of 3C-SiC nanoparticles. *Mater. Res. Express* **2015**, *2* (1), 015019. DOI: 10.1088/2053-1591/2/1/015019.
- (191) Sawrey, B. A.; O'Neal, H. E.; Ring, M. A.; Coffey Jr., D. The gas-phase decomposition of methylsilane. Part I. Mechanism of decomposition under shock-tube conditions. *Int. J. Chem. Kinet.* **1984**, *16* (1), 7-21. DOI: <https://doi.org/10.1002/kin.550160104>.
- (192) Jariwala, B. N.; Kramer, N. J.; Petcu, M. C.; Bobela, D. C.; Sanden, M. C. M. v. d.; Stradins, P.; Ciobanu, C. V.; Agarwal, S. Surface Hydride Composition of Plasma-Synthesized Si Nanoparticles. *J. Phys. Chem. C* **2011**, *115* (42), 20375-20379. DOI: 10.1021/jp2028005.
- (193) Xu, F.; Nava, G.; Biswas, P.; Dulalia, I.; Wang, H.; Alibay, Z.; Gale, M.; Kline, D. J.; Wagner, B.; Mangolini, L.; et al. Energetic characteristics of hydrogenated amorphous silicon nanoparticles. *Chem. Eng. J.* **2022**, *430*, 133140. DOI: <https://doi.org/10.1016/j.cej.2021.133140>.
- (194) Rath, C.; Farjas, J.; Roura, P.; Kail, F.; i Cabarrocas, P. R.; Bertran, E. Thermally Induced Structural Transformations on Polymorphous Silicon. *J. Mater. Sci. Res.* **2005**, *20* (9), 2562-2567. DOI: 10.1557/jmr.2005.0322.
- (195) Bruggeman, P. J.; Kushner, M. J.; Locke, B. R.; Gardeniers, J. G. E.; Graham, W. G.; Graves, D. B.; Hofman-Caris, R. C. H. M.; Maric, D.; Reid, J. P.; Ceriani, E.; et al. Plasma–liquid interactions: a review and roadmap. *Plasma Sources Sci. Technol.* **2016**, *25* (5), 053002. DOI: 10.1088/0963-0252/25/5/053002.
- (196) Kovačević, V. V.; Sretenović, G. B.; Obradović, B. M.; Kuraica, M. M. Low-temperature plasmas in contact with liquids—a review of recent progress and challenges. *J. Phys. D: Appl. Phys.* **2022**, *55* (47), 473002. DOI: 10.1088/1361-6463/ac8a56.
- (197) Zhou, R.; Zhou, R.; Wang, P.; Xian, Y.; Mai-Prochnow, A.; Lu, X.; Cullen, P. J.; Ostrikov, K.; Bazaka, K. Plasma-activated water: generation, origin of reactive species and biological applications. *J. Phys. D: Appl. Phys.* **2020**, *53* (30), 303001. DOI: 10.1088/1361-6463/ab81cf.
- (198) Mariotti, D.; Švrček, V.; Hamilton, J. W. J.; Schmidt, M.; Kondo, M. Silicon Nanocrystals in Liquid Media: Optical Properties and Surface Stabilization by Microplasma-Induced Non-Equilibrium Liquid Chemistry. *Adv. Funct. Mater.* **2012**, *22* (5), 954-964. DOI: <https://doi.org/10.1002/adfm.201102120>.
- (199) de Boer, W. D.; Timmerman, D.; Dohnalová, K.; Yassievich, I. N.; Zhang, H.; Buma, W. J.; Gregorkiewicz, T. Red spectral shift and enhanced quantum efficiency in phonon-free

- photoluminescence from silicon nanocrystals. *Nat Nanotechnol* **2010**, *5* (12), 878-884. DOI: 10.1038/nnano.2010.236 From NLM.
- (200) Bruhn, B.; Brenny, B. J. M.; Dekker, S.; Doğan, I.; Schall, P.; Dohnalová, K. Multi-chromatic silicon nanocrystals. *Light sci. appl.* **2017**, *6* (6), e17007-e17007. DOI: 10.1038/lsa.2017.7.
- (201) Dasog, M.; De los Reyes, G. B.; Titova, L. V.; Hegmann, F. A.; Veinot, J. G. C. Size vs Surface: Tuning the Photoluminescence of Freestanding Silicon Nanocrystals Across the Visible Spectrum via Surface Groups. *ACS Nano* **2014**, *8* (9), 9636-9648. DOI: 10.1021/nn504109a.
- (202) Linnros, J.; Lalic, N.; Galeckas, A.; Grivickas, V. Analysis of the stretched exponential photoluminescence decay from nanometer-sized silicon crystals in SiO₂. *J. Appl. Phys.* **1999**, *86* (11), 6128-6134. DOI: 10.1063/1.371663 (acccessed 10/26/2024).
- (203) Sangghaleh, F.; Sychugov, I.; Yang, Z.; Veinot, J. G. C.; Linnros, J. Near-Unity Internal Quantum Efficiency of Luminescent Silicon Nanocrystals with Ligand Passivation. *ACS Nano* **2015**, *9* (7), 7097-7104. DOI: 10.1021/acsnano.5b01717.
- (204) Sum, T. C.; Mathews, N.; Xing, G.; Lim, S. S.; Chong, W. K.; Giovanni, D.; Dewi, H. A. Spectral Features and Charge Dynamics of Lead Halide Perovskites: Origins and Interpretations. *Accounts of Chemical Research* **2016**, *49* (2), 294-302. DOI: 10.1021/acs.accounts.5b00433.
- (205) Hutter, E. M.; Eperon, G. E.; Stranks, S. D.; Savenije, T. J. Charge Carriers in Planar and Meso-Structured Organic-Inorganic Perovskites: Mobilities, Lifetimes, and Concentrations of Trap States. *J. Phys. Chem. Lett.* **2015**, *6* (15), 3082-3090. DOI: 10.1021/acs.jpclett.5b01361.
- (206) Strobel, P.; Riedel, M.; Ristein, J.; Ley, L. Surface transfer doping of diamond. *Nature* **2004**, *430* (6998), 439-441. DOI: 10.1038/nature02751.
- (207) Rezek, B.; Čermák, J.; Kromka, A.; Ledinský, M.; Hubík, P.; Mareš, J. J.; Purkrt, A.; Cimrová, V.; Fejfar, A.; Kočka, J. Synthesis, structure, and opto-electronic properties of organic-based nanoscale heterojunctions. *Nanoscale Res. Lett.* **2011**, *6* (1), 238. DOI: 10.1186/1556-276X-6-238.
- (208) Huntley, D. J. An explanation of the power-law decay of luminescence. *J. Phys. Condens. Matter.* **2006**, *18* (4), 1359. DOI: 10.1088/0953-8984/18/4/020.
- (209) Jonscher, A. K.; Polignac, A. d. The time dependence of luminescence in solids. *J. Phys C: Solid State Phys.* **1984**, *17* (35), 6493. DOI: 10.1088/0022-3719/17/35/018.
- (210) Robertson, J. Gap states in diamond-like amorphous carbon. *Philos. Mag. B* **1997**, *76* (3), 335-350. DOI: 10.1080/01418639708241098.

Engineering the Thermal and Energy-Storage Properties in Quantum Dots Using Dominant Faceting: The Case Study of Silicon

Pavel Galář, Jakub Kopenec, Robert Král, Filip Matejka, Petra Zemenová, Milan Dopita, Prokop Hapala, Dirk König, Pavel Vrbka, and Katerina Kušová*



Cite This: <https://doi.org/10.1021/acsnano.4c11376>



Read Online

ACCESS |

Metrics & More

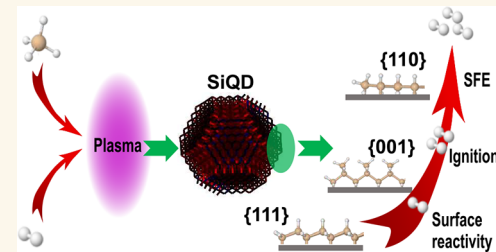
Article Recommendations

Supporting Information

ABSTRACT: The storage and release of energy is an economic cornerstone. In quantum dots (QDs), energy storage is mostly governed by their surfaces, in particular by surface chemistry and faceting. The impact of surface free energy (SFE) through surface faceting has already been studied in QDs. Here, we introduce dominant faceting representing the structural order of the surface. In particular, we propose that realistic QDs attain complicated polyhedral quasi-spherical shapes while keeping the dominance of a certain type of facet. The type of dominant facet determines the rates of surface-related processes. Therefore, by connecting dominant faceting with SFE, trends analogical to bulk material are kept despite the lack of evident microscopic shape control.

To demonstrate the applicability of dominant faceting, we synthesize the sets of silicon QDs with sizes around 5 nm and classify them based on increasing SFE of the corresponding analytic geometrical models, using a detailed surface chemistry analysis. Total energies released during oxidation of the synthesized QDs reach the theoretical limit, unlike in the reference, "large" (>100 nm) silicon nanoparticles, which release about 15% less energy. Next, we perform a comprehensive experimental study of dehydrogenation and thermal oxidation of the synthesized QDs in the temperature range of 25–1100 °C, identifying SFE as the key factor determining their thermal stability and surface reactivity. In particular, four distinctive stages of energy release were observed with onset temperatures ranging between 140 and 250 °C, ≈500 and 650–700 °C, respectively, for the SFE-differing samples. Finally, the thermal oxidation of the synthesized QDs is completed at lower temperatures with increasing SFE, decreasing from 1065 to 970 °C and being > 150 °C lower in QDs than in larger reference nanoparticles. Therefore, despite a rich mixture of features, our description based on linking dominant faceting with SFE allows us to fully explain all the observed trends, demonstrating both the potential of SFE-based engineering of energy-storage properties in QDs and the prospects of silicon QDs as an energy-storage material.

KEYWORDS: quantum dots, dominant faceting, thermal oxidation, energy storage, surface free energy, silicon, ignition



INTRODUCTION

Diversification of ways to produce, store and reuse energy is an important task which will to a large degree influence future advancements in technology and society. Many ways to store energy so that it could be used later are being explored,^{1,2} including improvements of existing Li-ion batteries, generation of hydrogen in combination with the fuel cell technology, ground thermal storage, capacitors, flywheel energy storage, and many more. In addition to energy storage, closely related energetic materials including thermites, which rely on highly controlled release of energy, also deserve close attention.³ Similar to other applications, the specific properties of quantum dots (QDs) or nanostructured materials in general are employed,^{4,5} as these materials allow for tuning of a wide

range of their physical and chemical properties, thus tailoring them for a specific application.

Key properties to tune the behavior of QDs are their size,⁴⁵ surface ligands or shell and the degree of structural order in⁴⁶ their core. A degree of freedom which is much less explored⁴⁷ here is the surface free energy (SFE), or in other words, the⁴⁸ excess energy that the surface has compared to the bulk of the⁴⁹ material. The surface of any QD must have undergone surface⁵⁰

Received: August 18, 2024

Revised: December 2, 2024

Accepted: December 10, 2024

51 reconstruction to minimize its total energy, exposing different
 52 surface facets. While QDs with varied surface facets differ in
 53 SFE and thus in their stability, they also favor certain types of
 54 chemical reactions, as such chemical reactions proceed on
 55 surfaces with different orientations at substantially different
 56 rates. In ligand-passivated QDs, different surface facets also
 57 support different types of ligands, as due to geometrical
 58 constraints, each surface atom is bonded to a given number of
 59 neighboring atoms, which leaves a certain number of bond(s)
 60 exposed.⁶ Thus, SFE is an important parameter for tailoring
 61 surface reactivity and possibly other properties of QDs.

62 Generally speaking, surface faceting is known to impact
 63 stability.^{7,8} As such, tuning of SFE is not an unexplored topic
 64 even in QDs. In the past, chemical or physical properties of
 65 QDs synthesized using wet-chemistry methods were linked to
 66 the geometry of model QDs. For example, in II–VI QDs, a
 67 clear connection between surface geometry and surface traps
 68 has been reported based on calculations.⁹ In lead chalcogenide
 69 PbS QDs, a size-related threshold between mixed {111} and
 70 {100} faceting and exclusive {111} faceting has been identified
 71 as the root cause of size-dependent air stability, as the {100}
 72 facets are more prone to oxidation.¹⁰ The synthesis of
 73 exclusively {111} faceted tetrahedral InP QDs imparted optical
 74 properties different from their spherical counterparts.^{11,12}

75 An ideal material for the study of the influence of SFE on the
 76 energetic and energy-storage properties of QDs is silicon.
 77 There are many reasons for this choice: (i) Crystalline silicon
 78 has a relatively high melting point (≈ 1415 °C), due to the
 79 strong covalent bonds between its atoms, implying large
 80 volumetric energy density of $75.5\text{ kJ}\cdot\text{cm}^{-3}$, which is about 2.5
 81 \times higher than gasoline. The corresponding gravimetric energy
 82 density is $32.4\text{ kJ}\cdot\text{g}^{-1}$.¹³ (ii) Unlike other semiconductor
 83 materials, it crystallizes only in a single type of face-centered
 84 diamond cubic structure. Its crystalline structure is highly
 85 stable in a wide range of temperatures and even under
 86 pressure.¹⁴ Therefore, any observed change in behavior of this
 87 material can be assigned to the influence of the surface;
 88 potential changes in the crystalline structure can be excluded as
 89 long as the material stays crystalline. (iii) Bulk Si itself is
 90 unsuitable as a carrier of energy, because the rupture of Si–Si
 91 bonds requires high temperatures,¹⁵ and oxidation is limited by
 92 the extremely slow diffusion of oxygen through the surface

93 SiO_2 layer (1 \AA s at 1000 °C).¹⁶ Fortunately, the high surface
 94 reactivity of nanostructured Si overcomes these limita-
 95 tions.^{16–19} (iv) The direct chemical toxicity of silicon and
 96 SiO_2 are low, even in the form of QDs,²⁰ and its abundance in
 97 the Earth's crust is extremely high,²¹ providing strong
 98 motivation for using silicon as resource-efficient environ-
 99 mentally friendly energy-storage material. (v) Even if SiQDs
 100 are not yet readily commercially available, they can be obtained
 101 in sufficient amounts and their structural properties can be
 102 widely tuned if they are synthesized in nonthermal plasma.^{4,22}

103 The highly covalent nature of SiQDs brings about several
 104 challenges when compared to the more traditionally studied
 105 QD materials. The reported shapes of SiQDs are, with only a
 106 few exceptions,^{23–25} almost exclusively spherical^{26,27} and the
 107 tendency of SiQDs to form purely faceted structures might be
 108 severely limited. Moreover, covalent Si QDs require higher
 109 energies for their formation and therefore cannot be fabricated
 110 using wet-chemistry approaches typical for other QDs.
 111 Consequently, the methods of synthesis of SiQDs do not yet
 112 reach the same high levels of elaborate control and precise

shape tuning of macroscopic amounts as in more traditional
 113 QD materials.
 114

Nevertheless, hints as to the possible immense influence of
 115 SFE in nanostructured silicon can be found in the literature,
 116 with the most obvious one being the low-temperature ignition
 117 phenomenon. In nanoporous silicon, spontaneous combustion
 118 was reported even at the temperature range as low as 4.2 – 90 K
 119 under special conditions,¹⁶ if condensed or liquid oxygen filled
 120 the pores of H-terminated porous Si. Other ignition temper-
 121 atures for nanosized Si were reported to be higher, above 600
 122 °C,³ but still well below the temperatures typical for effective
 123 combustion by in-diffusion of oxygen on a large scale. These
 124 findings suggest that dehydrogenation and/or oxidation of
 125 nanostructured silicon is widely tunable if suitable conditions
 126 are applied.
 127

In this article, we introduce the term of dominant faceting,
 128 which refers to the SFE-governed tunability of surface
 129 properties without evident microscopic shape control. The
 130 apparent contradiction of facet tuning without shape control is
 131 achieved through highly polyhedral, quasi-spherical shape of the
 132 nanoparticles, in which a certain facet still spatially dominates
 133 the surface. Thus, dominant faceting signifies that the trends
 134 inferred based on simple bulk geometrical models and SFE are
 135 also observed in QDs “on average”, that is if the QDs are
 136 experimentally studied as a macroscopic ensemble. This
 137 approach is in contrast to, and in a way a generalization of,
 138 the published reports on the tuning of properties of chemically
 139 synthesized QDs using the faceting of their surface. In order to
 140 show how surface properties and dominant faceting influence
 141 SiQDs, we focus on the ignition of Si nanoparticles fabricated
 142 by standard protocols and explain the observed phenomena
 143 using a detailed study of the dehydrogenation and thermal
 144 oxidation of surface bonds in SiQDs. In these sets of
 145 experiments, we identify SFE as a key factor determining the
 146 stability and surface reactivity of the synthesized material. In
 147 addition to the introduction of dominant faceting, our results
 148 thus provide a detailed guide to the tuning of energy-storage
 149 and thermal properties of SiQDs and explore their potential as
 150 an energy-storage material.
 151

RESULTS AND DISCUSSION

Ignition Properties of Si Nanoparticles. In order to
 153 efficiently tune the degree of structural order of the surface, Si
 154 nanoparticles for this study were synthesized in nonthermal
 155 plasma, see Table 1 and Supporting Information Section S2.1
 156 t1 for details. Each sample was collected on a $150\text{-}\mu\text{m}$ -thick glass
 157 slide in the form of a cone-shape pile of lightly packed powder
 158 in the amounts of approximately 5 mg per synthesis
 159

Table 1. List of the Most Important Properties of the Studied Samples and Preparation Conditions (Using 1% Silane in Argon at 80-SCCM Flow Rate as the Carrier Gas)^a

label	power (W)	hydrogen flow (sccm)	fresh/aged	nominal size (nm)
amorphous 1	30	0	✗	2–6, irregular
amorphous 2	90	0–100	✗	2–6, irregular
SiQDs	150	0	✓	≈ 5 –6
{111}	150	10–30	✓	≈ 5 –6
{001}	150	40	✓	≈ 4 –5
p{110}	150	commercial	✗	170
c-SiNCs				

^aThe fresh/aged column shows which of the samples were studied as the two separate fresh/aged varieties (✓), and which were not (✗).

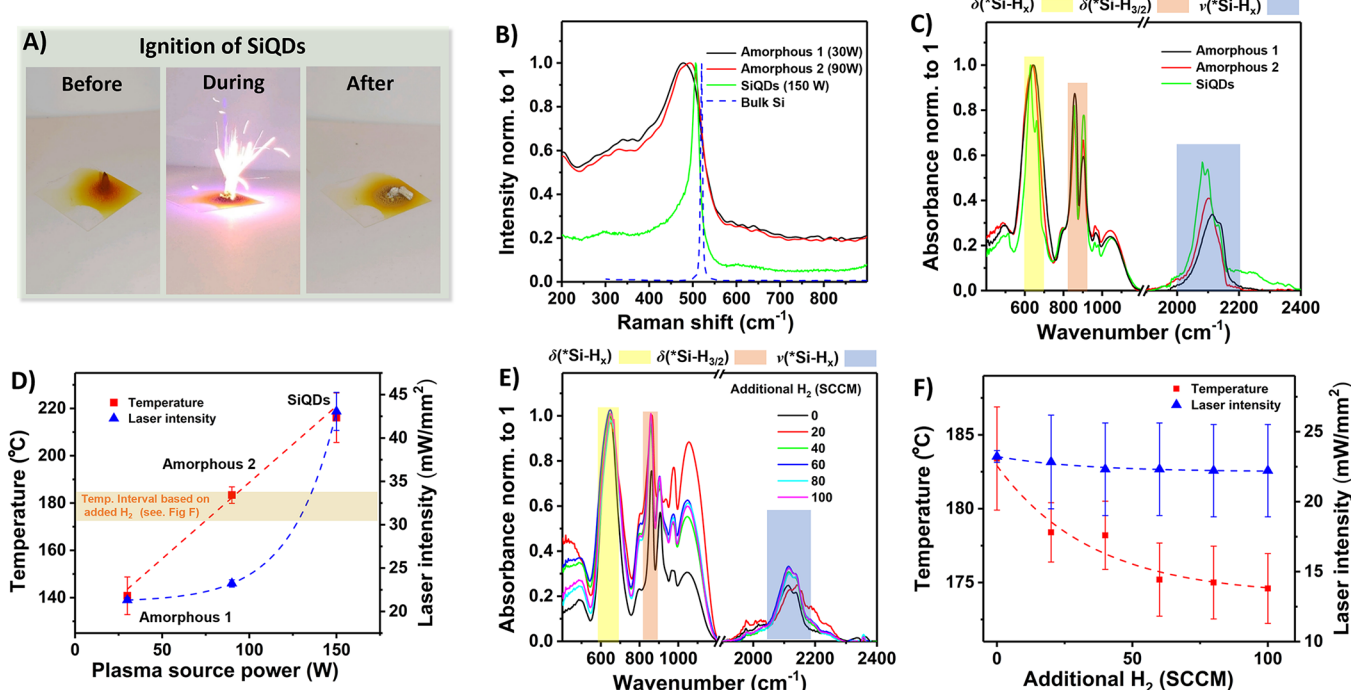


Figure 1. (a) Ambient-light photographs of synthesized SiQDs as deposited, ignited with a laser pointer (405 nm, 50 mW) and after combustion (from left to right). The change in color from beige-orange to white marks the complete oxidation of silicon into silicon dioxide. See a [Supplementary Video File](#) for an example of light-initiated ignition. (b) Raman spectra of Si nanoparticles fabricated with different outputs on the source, influencing the degree of structural order. Raman spectrum of bulk silicon is included for comparison as the dashed blue curve. (c) FTIR spectra showing Si–H bonds on the surface of Si nanoparticles from panel (b). (d) Ignition conditions of Si nanoparticles from panel (b). The samples were ignited on a hot plate or using a laser pointer. The dashed curves serve merely as the guides for the eye. (e) FTIR spectra of Si nanoparticles synthesized at 90 W (amorphous 2 in panel (b)) under varying flow of H₂, effectively etching the surface of Si nanoparticles during the synthesis. (f) Ignition conditions of Si nanoparticles from panel (e). The dashed curves serve merely as the guides for the eye, and error bars are standard deviations.

(depending on the type of sample). Based on a simple estimate, the porosity (the volume fraction of air) in our samples¹⁹ is 0.77. An example of a synthesized sample is shown in Figure 1a in the leftmost photograph. In some of the synthesized samples, we observed spontaneous combustion when the sample was transferred out of the reactor and exposed to ambient conditions (not shown). The combustion of synthesized SiQDs under controlled conditions is shown in a [Supplementary Video File](#) and in Figure 1a. The change in the ambient-lightning color of the SiQD powder before and after the combustion from deep beige/orange to white signifies a highly efficient oxidation of the starting mostly Si-based material to SiO₂, which was accompanied by the energy release in the form of a small explosion.

To explore the combustion conditions in more detail, we fabricated three types of samples with varying input power of the source during synthesis. Power on the source predominantly tunes the structural order of atoms in the nanoparticle core, since the core crystallizes only if sufficient energy is available.^{28,29} Possibly, also the size of the produced nanoparticles can be influenced. The structural change from amorphous nanoparticles to SiQDs is documented in Figure 1b, where, at the highest power setting, the corresponding Raman spectra change from the broad peak assigned to amorphous Si to a sharper line at $\approx 510\text{ cm}^{-1}$, typical for the optical phonon in quantum-confined Si.^{28,30} The produced set of amorphous and crystalline Si nanoparticles was further characterized using FTIR measurements presented in Figure 1c. The synthesized material is

mostly hydride terminated, showing only trace amounts of 189 surface oxidation as the broad peaks at $\approx 1045\text{ cm}^{-1}$ assigned 190 to the antisymmetric stretches of Si–O–Si.^{31–33} The typical 191 2000–2200 cm⁻¹ region marked as $\nu(\text{*Si–H}_x)$ whereby *Si 192 stands for silicon on the surface of an Si nanoparticle, is 193 clearly associated with the *Si–H_x stretching modes,^{26,34–39} 194 namely with $\nu(\text{Si–H})$ at 2080 cm⁻¹, $\nu(\text{Si–H}_2)$ at 2098 cm⁻¹ 195 and $\nu(\text{Si–H}_3)$ 2133 cm⁻¹. Furthermore, the region between 196 600–700 cm⁻¹ marked as $\delta(\text{*Si–H}_x)$ is characteristic of *Si– 197 H bending and/or *Si–H₂ wagging modes.^{35,40} However, the 198 assignment of the doublet marked as $\delta(\text{*Si–H}_{3/2})$ at 905 and 199 857 cm⁻¹ is less clear. Based on literature data, it can represent 200 the degenerate and symmetric deformation modes of silicon 201 trihydrides *Si–H₃, respectively, even though also silicon 202 dihydrides can be present in this region.³⁴ Unlike the two other 203 features, this doublet appears only in plasma-synthesized Si 204 nanoparticles,^{3,34,36,41} whereas in SiQDs prepared by electro- 205 chemical etching or by thermal annealing of Si-rich SiO₂, only 206 a single peak at $\approx 900\text{ cm}^{-1}$ appears.^{35,39,40,42} Thus, we believe 207 that the spectral shape of the 900 cm⁻¹ region is, for reasons 208 currently unbeknownst, linked to the applied synthesis method 209 rather than to the structural properties of the sample. One 210 possibility is that one of the peaks in the doublet is not directly 211 connected to the surface of Si nanoparticles, but rather 212 represents the interconnecting material.²¹³

Interestingly, the structural change from fully amorphous to 214 structurally ordered material evidenced by Raman measure- 215 ments in Figure 1b is also reflected on the surface of the 216 nanoparticles, as confirmed by FTIR measurements. The FTIR 217

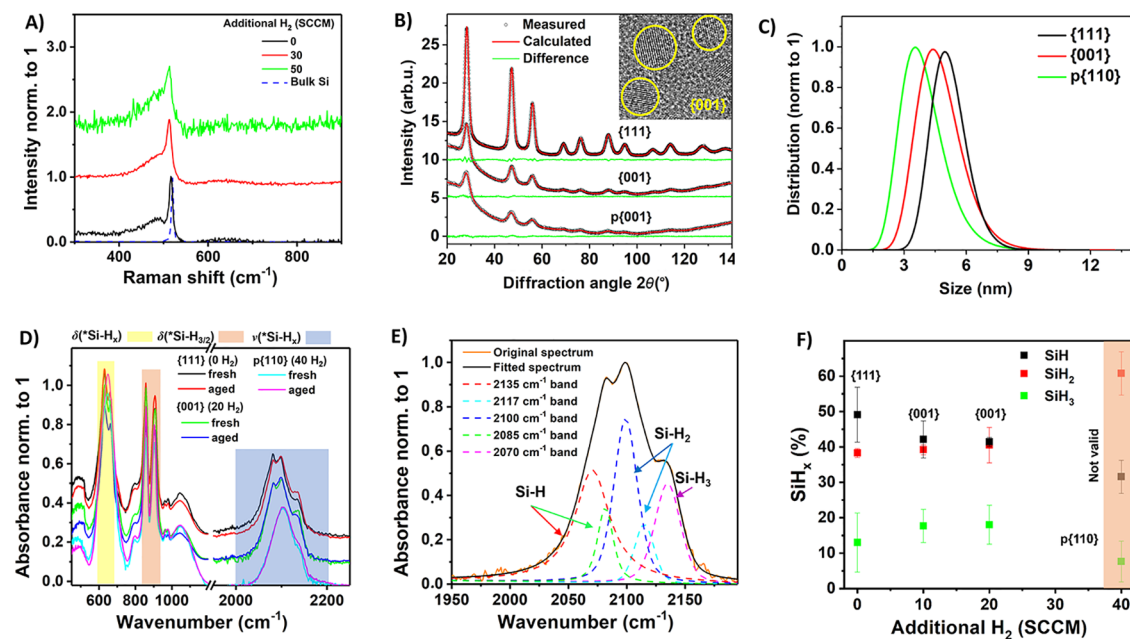


Figure 2. (a) Raman spectra of SiQDs synthesized under varying hydrogen dilution. (b) Measured (black circles), calculated (red line), and difference (green line) X-ray diffraction patterns of investigated samples (please note that a smaller amount of {001} and p{110} sample was used due to technical reasons). (c) Particle size distributions of the investigated samples determined from SAXS measurements, the corresponding fits are shown in Figure S5. (d) FTIR spectra of structurally ordered SiQDs with varying hydrogen dilution. Samples marked as “fresh” were characterized shortly after the synthesis, samples marked as “aged” were characterized after about a 14-day storage in a nitrogen-filled glovebox. Full FTIR spectra are shown in Figure S7. (e) Example of the deconvolution of the spectral structure $\nu(\text{Si}-\text{H}_x)$ into the individual components for the 20 sccm SiQD sample. (f) Ratio of silicon mono-, di- and trihydrides on the surface of SiQDs from panel (d) determined using the deconvolution shown in panel (e). “Fresh” and “aged” samples are treated simultaneously since no difference was detected in their FTIR spectra. The error bars correspond to standard deviations. The FTIR spectra of the p{110} sample are no longer well-resolved due to a lower degree of structural order on the surface, which invalidates the deconvolution analysis in that sample.

218 stretching-mode region at 2000–2200 cm^{-1} and the
219 deformation modes at 600–700 cm^{-1} (Figure 1c) exhibit a
220 systematic change from broader smooth peaks in the
221 amorphous nanoparticles to sharper lines and a more structured
222 shape in the structurally ordered SiQD sample. Narrowing of
223 peaks in a crystalline SiQD is to be expected, since the more
224 ordered character of the QD core also causes higher ordering
225 of the surface of the QD, resulting in better-defined vibrations
226 of surface hydrides. The narrowing effect in the SiQD sample
227 is evident especially in the deformation-mode $\delta(\text{Si}-\text{H})$
228 spectral region, where a clearly resolved doublet appears at
229 630 and 661 cm^{-1} , together with a hint of a side shoulder at
230 695 cm^{-1} . Here, the 630/661 cm^{-1} doublet is likely to
231 originate in $\text{Si}-\text{H}$ bending deformations and the side
232 shoulder at 695 cm^{-1} is due to $\text{Si}-\text{H}_2$ wagging vibrations.
233 A very similar spectral shape of the corresponding FTIR peak
234 is typically observed also in fully crystalline SiQDs in porous-
235 silicon layers.^{35,40} Unlike these spectral regions, the 905/857
236 cm^{-1} doublet stays resolved in all the samples regardless of
237 their degree of structural order. This absence of spectral
238 change is likely connected to the unclear assignment of this
239 spectral structure as discussed above. Therefore, this structure
240 will not be further discussed in the text. Notwithstanding, our
241 experiments clearly demonstrate that the structural ordering of
242 SiQDs is strongly reflected also in their surface-bond
243 vibrations.

244 Next, we studied the ignitions conditions for the amorphous
245 Si nanoparticles and SiQDs from Figure 1b,c. The samples
246 were ignited as deposited on the glass slide. The glass slides
247 were either placed on a hot plate and slowly heated up, or they

were irradiated with a 405 nm (50 mW) laser pointer with
248 increasing the intensity of the laser pointer and the conditions
249 required for ignition were recorded. The results are presented
250 in Figure 1d. An important observation here is that the ignition
251 temperature is relatively low, in the range of 150–200 °C,
252 which is even below the dissociation temperatures of higher
253 hydrides on silicon, as shown later in Figure 1b. Moreover, this
254 is a much lower temperature than that reported when
255 amorphous Si nanoparticles were used as an additive to
256 lower ignition temperature in an Si/KClO₄ nanocomposite.³

As the next step, we wanted to test if and how much the
258 ignition properties of Si nanoparticles can be influenced by the
259 surface. Thus, we synthesized “amorphous 2” Si nanoparticles
260 close to the amorphous/structurally ordered threshold, but
261 using a varying H₂ dilution in the synthesis gas. Diluting the
262 synthesis gas with H₂ induces an etching-like process in the
263 plasma and thus can change the composition of surface
264 hydrides.³⁴ The FTIR spectra of these Si nanoparticles in
265 Figure 1e show very little difference with increasing H₂
266 dilution, demonstrating that due to the amorphous nature of
267 these nanoparticles, potential changes in the overall
268 composition of the surface hydrides are small. However, the
269 subsequent study of the ignition conditions presented in Figure
270 1f reveals a systematic trend of decreasing ignition temperature
271 and light intensity with increasing H₂ dilution. This direction
272 of the trend is intuitively expected, as nanoparticles with more
273 disturbed surfaces due to the additional hydrogen in the
274 synthesis process are likely to be less stable. However,
275 quantitatively speaking, the corresponding changes are modest,

277 about 5% at most, corroborating the nearly identical FTIR
278 spectra.

279 Thus, even though the properties of the surface have a clear
280 potential to be used to tune the thermal properties of
281 nanoparticles, amorphous nanoparticles do not seem to be the
282 ideal candidate. Therefore, a more thorough study of the
283 surface composition and thermal properties was conducted
284 using structurally ordered QDs.

285 **Structural and Surface Characterization of SiQDs.**
286 Therefore, we synthesized a set of highly structurally ordered
287 Si nanoparticles with varying H₂ flow in the synthesis gas and
288 characterized both their structure and surface chemistry. Then,
289 to address the suitability of Si nanoparticles for energy-storage
290 applications, we measured the energy density released by these
291 nanoparticles during oxidation.

292 However, one possible interpretation of the low-temperature
293 ignition mechanism in the sample of Si nanoparticles we
294 reported in Figure 1 is the release of energy caused by the
295 contact of hydrogen trapped in the microvoids within the pile
296 of Si nanoparticles with atmospheric oxygen. Thus, the
297 experiments presented in this section were performed on
298 “fresh” and “aged” samples. In “fresh” SiQDs, the measure-
299 ments were conducted relatively shortly (24 h at maximum)
300 after the synthesis with minimized exposure to atmospheric
301 oxygen. Samples referred to as “aged” were kept approximately
302 14 days in a nitrogen-filled glovebox to significantly decrease
303 the potential hydrogen trapped in microvoids. Thus, the
304 differentiation between the “fresh” and “aged” samples will
305 reveal the influence of both potentially trapped hydrogen and
306 storage time on the studied SiQDs.

307 In analogy to the experiments from Figure 1, the character of
308 the surface of structurally ordered SiQDs is affected by
309 hydrogen flow in the synthesis gas. The influence of hydrogen
310 flow was first probed using Raman spectra of SiQDs, as
311 presented in Figure 2a. Clearly, if hydrogen flow is kept under
312 50 sccm, the synthesized nanoparticles are highly structurally
313 ordered, as evidenced by the relatively narrow Raman line at
314 $\approx 514\text{--}519\text{ cm}^{-1}$. Therefore, in order to focus on structurally
315 ordered SiQDs, hydrogen flow during the synthesis of SiQDs
316 was varied in the 0–40-sccm range.

317 X-ray diffraction (XRD) measurements were used to obtain
318 more detailed structural and microstructural information about
319 SiQDs synthesized under varying hydrogen flow. Measured
320 XRD patterns fitted using the whole powder pattern fitting
321 procedure, specifically the Rietveld method using the MStruct
322 software,⁴³ are shown in Figure 2b. XRD confirmed that the
323 investigated samples consist of a single crystalline phase,
324 namely cubic Si (space group *Fd*3*m*). The significant
325 broadening of the diffraction profiles in comparison to bulk
326 Si clearly confirms nanocrystalline nature of the investigated
327 samples. The refined lattice parameters presented in Table 2
328 are only slightly smaller (0.2–0.5%) than the tabulated data for
329 coarse-grained, defect-free standard Si powder. The size of
330 coherently diffracting domains was modeled using a log-normal
331 distribution and mean sizes are listed in Table 2.

332 The distribution of sizes was determined using small-angle
333 X-ray scattering (SAXS) by fitting using the model of spherical
334 particles with the sticky hard sphere structure factor^{44,45}
335 assuming the log-normal distribution. Refined normalized log-
336 normal distributions of particle diameters are shown in Figure
337 2c. Additionally, the sizes were also characterized using high-
338 resolution transmission electron microscopy (HRTEM), as
339 shown in Figure S6. Mean sizes derived using these two

Table 2. List of Mean Diameters of the Investigated Samples Determined Using Different Methods, and $\frac{\text{FWHM}}{2}$ Is Used as the Error to Characterize the Width of the Distribution^a

SiQD sample	SAXS	HRTEM	XRD	<i>a</i> (Å)
{111}	5.5 ± 1.0	6.2 ± 0.5 ^b	4.0 ± 0.2	5.4258 ± 0.0014
{001}	4.6 ± 1.2	5.5 ± 0.7	3.2 ± 0.3	5.4269 ± 0.0007
p{110}	4.0 ± 1.5	4.0 ± 0.7	2.4 ± 0.3	5.4282 ± 0.0002

^aThe last column lists lattice constants *a* derived from XRD characterizations (NIST Si standard reference material: *a* = 5.43102 Å). ^bThe HRTEM-derived distribution of the {111} sample indicates the presence of smaller sizes of (4.8 ± 0.4) nm making up approximately 15% of QDs.

methods are listed in Table 2. Clearly, the SAXS- and 340 HRTEM-derived sizes are in good agreement. There is a 341 significant overlap between the distributions of sizes of the 342 individual samples, which can be quantified using the 343 Bhattacharyya coefficient of the correponding normal dis- 344 tributions as 0.75 and 0.88 for the first and second, and second 345 and third sample, respectively. Thus, even though the mean 346 sizes decrease from about 5.5 to 4 nm with increasing 347 hydrogen flow, this difference is not large considering the 348 significant overlap of the distributions. 349

Mean sizes were also determined from XRD measurements, 350 yielding smaller values than the SAXS- and HRTEM-based 351 distribution. This difference is a consequence of the applied 352 method, since XRD detects only the signal from the volume 353 diffracting with a high degree of coherence, which is evident 354 from the high certainty of the derived lattice constants in Table 355 2. Thus, in contrast to XRD, HRTEM and SAXS also include 356 the reconstructed surface. This effect has been observed in the 357 past and was attributed to an amorphous shell.⁴⁶ However, in 358 our case, the surface of the investigated samples has a higher 359 degree of structural order when compared to a purely 360 amorphous layer, as will be shown below. Notably, in addition 361 to the good agreement between the size distributions obtained 362 by different methods, our measurements confirm the absence 363 of potential larger nanoparticles, which could influence the 364 results of further experiments.⁴⁷ Both the SAXS and XRD 365 techniques probe macroscopic amounts of SiQDs, ensuring 366 that the derived distributions represent the whole sample. 367 Combining the macroscopic characterization with probing of 368 the whole core of QDs, SAXS is the method of choice for the 369 accurate determination of size distributions, while HRTEM 370 guarantees the accuracy of the absolute size measurements 371 obtained.⁴⁸ 372

The Fourier-transform infrared spectroscopy (FTIR) 373 characterization of the surface of SiQDs synthesized under 374 varying hydrogen flow is shown in Figure 2d. First, there is 375 only the negligible difference between the “fresh” and “aged” 376 varieties of the samples, including a low level of oxidation 377 evidenced by the weak $\approx 1045\text{ cm}^{-1}$ Si—O—Si peak. Thus, we 378 can conclude that medium-term storage time in nitrogen 379 atmosphere at room temperature does not affect the surface of 380 the synthesized SiQDs to a notable degree. Furthermore, the 381 SiQDs synthesized in the 0–30-sccm H₂ flow keep a very 382 similar well-resolved spectral structure in both the $\delta(^*\text{Si}-\text{H}_x)$ 383 bending-deformation spectral region at 600–700 cm^{-1} and at 384 the $\nu(^*\text{Si}-\text{H}_x)$ stretching-mode region at 2000–2200 cm^{-1} , 385 except for a somewhat different ratio of the mono-, di- and 386 trihydrides.^{26,37} Following the well-established methodology 387

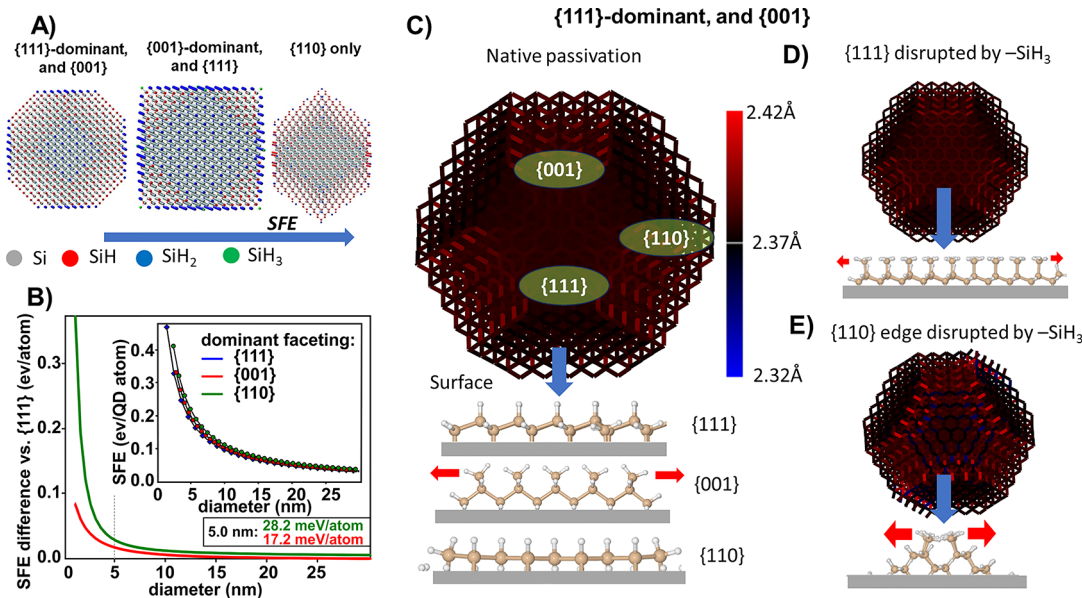


Figure 3. (a) Idealized geometric models of SiQDs cut off from a perfect crystal so that certain types of crystalline facets on the surface are exposed. The color coding highlights the different ratios of silicon hydrides in such structures. Adapted after⁶ (CC BY license). (b) Difference in SFE Δ SFE relative to the {111}-dominant faceted QD type with the lowest SFE values. The inset shows absolute values from which Δ SFE was derived, see text for details. (c) Example of a geometry of a 5 nm natively H-passivated SiQD with {111} dominant faceting relaxed by the classical force field. The color of the bonds indicates the difference of bond length from the bulk lattice constant, illustrating passivation-induced strain. The bottom of the panel shows native bonding of hydride surface groups on different facets. (d) Geometry from panel (c) was disrupted by the incorporation of *SiH₃ groups, simulating the extreme situation, where exactly half a layer of Si atoms was etched away by hydrogen plasma. Only minor strain is induced. The bottom of the panel shows hydride bonding on the disrupted {111} facet. (e) Geometry from panel (c), where Si–Si bonds at the {110}-like edge are broken and replaced by hydrogen to simulate the plasma etching, leading to *SiH₃ groups. Significant strain is induced. The bottom of the panel shows hydride bonding on the disrupted {110}-like edge.

presented in,²⁶ we deconvoluted the $\nu(*\text{Si}-\text{H}_x)$ stretching-mode region into the individual components, as outlined in Figure 2e.

The results of the surface-hydride analysis are presented in Figure 2f. This analysis confirms that Si trihydrides are the least common ones and that there is a roughly 1:1 ratio of dihydrides and monohydrides on the surface of SiQDs. However, a clear step-like change is detected with the addition of hydrogen flow to the synthesis, when the relative ratio of surface monohydrides drops in the 10-sccm sample but stays the same for the 20-sccm sample. However, in the 40-sccm sample, a clear change of the shape of the FTIR spectrum occurs: the typical structure at the bending-deformation spectral region at 600–700 cm⁻¹ disappears and the peak slightly shifts, see Figure 2d. Moreover, the lines in the 2000–2200 cm⁻¹ stretching-mode range broaden and merge. Whereas the typical fwhm of the fitted lines is 25 cm⁻¹ in the 0–30-sccm samples, apart from the first line wider probably as a result of fitting of the minuscule tail at 2000 cm⁻¹, fitted peaks reach the fwhm of 40 cm⁻¹ and are much less proportionate in the 40-sccm sample. Overall, the broader FTIR peaks and change in spectral shape prohibit the automatic application of the same deconvolution approach, as the surface of this SiQDs clearly reverts to a less-ordered state despite the structurally ordered core confirmed by Raman spectroscopy. Even though the changes observed in the 2000 cm⁻¹ spectral region used for the surface-hydride analysis are small, repeatability of the obtained results ensures that our approach is valid.

To summarize, the structural characterization presented in Figure 2a–c proves that the SiQD samples studied here are,

given the state-of-the-art synthesis protocols in this material, as similar as possible in their internal structure, whereas their surface properties can be tuned (Figure 2d–f) by changing hydrogen flow in the plasma during synthesis. The three different types of QDs support a different composition of surface hydrides and also likely a structurally less ordered state in the sample with the highest hydrogen flow. Also, no detectable differences were found between the “fresh” and “aged” varieties of the sample, implying that no trapped hydrogen is present in the porous sample and that storage time in a nitrogen-filled glovebox before the measurement does not influence the surface properties.

Dominant Faceting. The quantitative and qualitative interpretation of FTIR spectra can be combined using models of SiQDs. In general, models of SiQDs can be computationally constructed with the structures being optimized to attain the lowest total energy state simulating surface reconstructions, but such calculations are extremely computationally costly and have so far been performed only for smaller QDs.⁴⁹ However, as a first approximation, we can use a simple purely geometrical model of ideally crystalline SiQDs constructed by being cut off from a perfect crystal and exposing certain facets,⁶ see Figure 3a. Clearly, a certain type of facet prevails on the surface of these QD models, which we refer to as dominant faceting. The SFE area densities of the relevant facet orientations are $D_{\text{SFE}}^{(111)} = 1.23 \text{ J/m}^2$, $D_{\text{SFE}}^{(001)} = 1.36 \text{ J/m}^2$, and $D_{\text{SFE}}^{(110)} = 1.43 \text{ J/m}^2$.⁵⁰ Using the analytic framework of⁶ we can derive the surface area per facet orientation for all three Si QD types as a function of their size, see Section S1 in Supporting Information. The multiplication of the above SFE density

values with such specifically oriented surface areas yields the total SFE per SiQD. The nominal unit for such SFEs at hand would be femto-Joule (fJ) which is somewhat difficult to relate to general forces in the nanoscale range such as van der Waals or Casimir–Polder forces. Therefore, we relate the SFE to the number of Si atoms forming the respective QD, and convert the energy units from fJ to electronvolt per atom. This way, we obtain an SFE value per QD atom which can readily be related to general nanoscale forces.

For the three Si QD topologies from Figure 3a, we show the SFE values in the inset of Figure 3b. For comparing different QD geometries, we need the difference in SFE (ΔSFE) relative to a baseline given by the QD type with the lowest SFE values, see Section S1 for details. This QD type is presented by the quatodecahedral Si QD with {111}-dominated faceting, see Figure 3b. For QD sizes of around 5 nm as featured in our work, we obtain a total SFE per QD of $\text{SFE}_{q,111} \approx 0.18 \text{ eV/QD atom}$ for the {111}-dominated geometry, of $\text{SFE}_{q,001} \approx 0.20 \text{ eV/QD atom}$ for the {001}-dominated geometry, and of $\text{SFE}_{q,110} \approx 0.22 \text{ eV/QD atom}$ for the {110}-dominated geometry. Due to the selectivity of chemical reactions, each type of facet supports a certain type of hydride configuration as becomes apparent from geometrical boundary conditions, see Figure 3.

First, these SiQD models show a very low proportion of trihydrides, which appear only at the “apexes”. The low proportion of trihydrides is corroborated by our experiments, even though the measured proportions are higher than what would be expected from the idealized geometry. This finding can be interpreted to the end that the increased amount of detected $^*\text{SiH}_3$ accounts for a non-negligible structural disturbance on SiQD surfaces, forming small terraces with numerous edges and atomic steps.²⁶ Second, as demonstrated by the analytic QD description in,⁶ a model QD with dominant {111} faceting is terminated dominantly with monohydrides, but dihydrides are still non-negligible. The ideal dominantly {001} faceted QD contains roughly a balanced proportion of mono- and dihydrides, while exclusive {110} faceting leads to a very high proportion of monohydrides on the surface. Importantly, the very same pattern of the evolution of the composition of hydrides occurs in our synthesized SiQDs. In the sample synthesized without any hydrogen flow, mono-hydrides are dominant according to Figure 2f and the 2080 cm^{-1} FTIR line corresponding to hydrogen on Si{111} in bulk is the strongest. In the samples synthesized with up to 30 sccm hydrogen flow, mono- and dihydrides are roughly balanced, similarly to the ideal geometrical model with dominant {001} faceting. The single broader band at $\approx 2100 \text{ cm}^{-1}$ in the 40-sccm sample, where the mathematical deconvolution is no longer valid, most likely corresponds to the vibrational bands of monohydrides on several orientations of crystalline Si surfaces, possibly with the dominance of Si{110}.^{51,52} The interpretation of an increased proportion of monohydrides incurred by H_2 etching in plasma in the 40-sccm sample is supported by the disappearance of its $^*\text{Si}-\text{H}_2$ shoulder line at 695 cm^{-1} at this sample.

Thus, even though the variability in the composition of surface hydrides has been reported in the past,^{26,51} we provide a physical interpretation of this phenomenon. The additional H_2 flow in plasma, causing “etching” of the surface of SiQDs and/or influencing the transfer of kinetic energy from Ar ions during the collisions with the forming particles, leads to different dominant faceting of the synthesized QDs, evolving as

{111} → {001} → {110} with increasing H_2 flow in the synthesis gas. Our samples will be labeled using this notation, see Table 1, apart from the 40-sccm sample, which will be referred to as p{110}, where p stands for partial faceting due to the likely more disordered nature of its surface.

This classification based on dominant faceting does not imply that each of the synthesized SiQDs in the particular sample has the shape shown in Figure 3a. Since the synthesis is a highly nonequilibrium process, the forming nanoparticles typically do not reach ideal faceted crystal structures. During the formation process, apexes and edges are the least stable parts, most accessible to potential cleavage. Therefore, the surface is likely made up by a larger number of facets, forming smaller terraces.²⁶ Such a multifaceted nanoparticle, albeit assuming embedding in an SiO_2 matrix in their case, was constructed theoretically by Hadjisavvas et al.⁵³ Their calculation produced a 5 nm SiQD with 42 facets of three types. In our experimental study, we propose an analogous situation: we argue that a realistic QD, unlike the idealized models from Figure 3a, typically has a larger number of facets, with edges and apexes possibly eroded.²⁴ Such a complicated polyhedral shape is basically indistinguishable from a spherical one using classical HRTEM imaging, let alone for a macroscopic number of QDs. However, a certain type of the exposed surface is dominant. We propose that, when experimentally probing a macroscopic set of QDs, the preference for a certain type of surface, or dominant faceting, is the key property regardless of the spatial distribution of these facets on the surface of the QD. Thus, a set of SiQDs with one type of dominant faceting will exhibit an average characteristics in analogy to the corresponding bulk material, e.g. in its thermal properties.

During the formation of a nanoparticle, the details of the quasi-spherical polyhedral shape are a result of the local minimization of strain energy originating in bond-length and bond-angle distortions. A thorough analysis of the synthesis process and atomistic details of the surface of realistic particles are beyond the scope of the current article. Nevertheless, it is fairly certain that the limited reaction time, energy, and varying volume flux density of the SiQD precursor SiH_4 in the nonthermal plasma results in different SiQD geometries, of which many are “frozen” in a premature stage by the limited time-energy integral during their formation. To gain some insight into the relation between crystalline facets, surface passivation and the formation of the nanoparticles in hydrogen-enriched plasma, we calculated local strain of Si–Si bonds induced by the presence of different hydrides for three limiting model situations using the classical force field simulations based on FireCore.⁵⁴ First, a {111}-dominantly faceted SiQD with the diameter comparable to the QDs we synthesize was constructed (see Figure 3c). In addition to {111} facets, this model also has {001} facets to mimic the observed spherical shape. The edges between the {111} and {001} facets are structurally equivalent to {110} facets. Already in this natively passivated model, the less stable {001} facets are slightly tensile-strained by the steric repulsion of the natively passivating $^*\text{SiH}_2$ groups, whereas the {111} facets are completely bulk-like. To simulate hydrogen “etching”, this geometrical model was disrupted by removing the topmost Si atoms and artificially repassivating the bonds with $^*\text{SiH}_3$ groups. When such disruption was applied to the {111} facet, see Figure 3d, the passivating $^*\text{SiH}_3$ groups sterically fit rather well and produce only minor strain, comparable to or

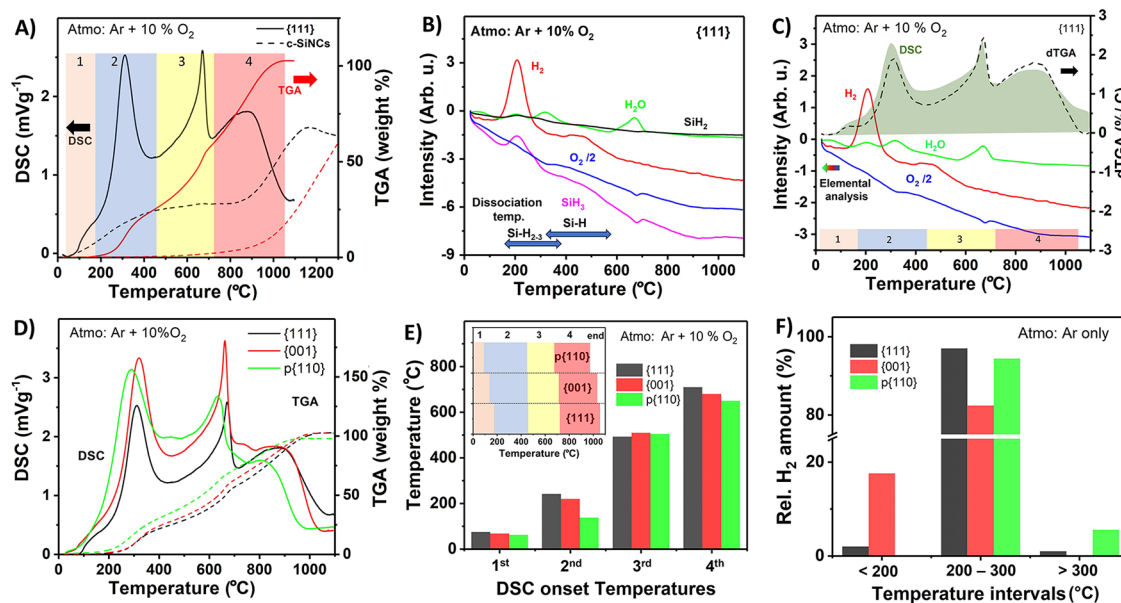


Figure 4. Characterization of the thermal properties of SiQDs by simultaneous measurements of differential scanning calorimetry (DSC), thermogravimetric analysis (TGA), and mass spectrometry (MS). (a) DSC and TGA measurements of SiQD-{111} (solid curves) and commercial Si nanocrystals (170 nm, the dashed curves). The studied temperature range is divided into four zones based on the prevailing effects responsible for the release of energy. (b) Elemental analysis of selected species released/consumed during the annealing of SiQD-{111}. Ranges of reported dissociation temperatures for *Si-H_x species are also included.^{3,26,38,55,56} (c) Combination of the DSC and MS curves from panels (a) and (b) plotted in one graph to facilitate the comparison. These curves are complemented with a derivative of the TGA curve (dTGA) from panel (a). (d) Comparison of the DSC and TGA curves of the three studied SiQD samples. (e) DSC-based onset temperatures marking the onset of energy release in the four zones identified in panel (a) for the three studied SiQD samples. The inset directly compares the TGA-derived temperature ranges marking different oxidation processes, corresponding to the individual zones in the studied samples. (f) Origin of released hydrogen for the three studied samples. The analyses presented in all panels were performed in an oxidizing (10% O₂/Ar) atmosphere, with the exception of panel (f), which reports released hydrogen under an inert atmosphere (pure Ar), where the presence of oxygen cannot interfere with its detection.

even smaller than that in natively *SiH₂-passivated {001} facets. We do not expect the presence of *SiH₃ groups at {001} facets as the removal of an Si layer at this facet recovers the *SiH₂-passivated {001} surface (just rotated by 90°). However, the disruption of the {110}-like edge produces sterically hindered *SiH₃, see Figure 3e, which face each other due to the geometry of the underlying crystal lattice, causing significant tensile strain to nearby Si–Si bonds. In realistic nanowires, this local strain would make these bonds more reactive and prone to further etching and can even lead to reorganization of the surface. Thus, we put forward a hypothesis that the local strain, especially at the {110} edges, leads to the lower thermal stability and increased reactivity of hydrogen-“etched” SiQDs as well as to the observed nonideal quasi-spherical shape.

The different dominant faceting is associated with increasing surface energy $E_{\{xyz\}}$, with $E_{\{111\}} < E_{\{001\}} < E_{\{110\}}$ ^{6,50} and with increased local strain on the facets. Therefore, we predict that the presence of H₂ in the synthesis gas leads to SiQDs structures with higher SFE and thus lower thermal stability. The first piece of evidence supporting the lower thermal stability of higher-SFE samples is the measurement of ignition temperature of the SiQD samples shown in Figure S8. These measurements clearly indicate that lower-SFE samples are systematically ignited at lower temperatures. The lower thermal stability is also supported by the analytic SFE calculations above which clearly show a maximum SFE for the {110} facets. Therefore, SiQDs with an increased fraction of {110} facets become thermally less stable and are prime

candidates for a pyrophoric reaction in air at the minimum possible temperature.

In the theoretical study by Hadjisavvas et al.,⁵³ the {001} interface was found to be the most stable one because they consider a system of SiQDs embedded in surface-bonded oxide. Here, we focus on free-standing hydrogen-terminated SiQDs. As hydrogen termination is known to influence the electronic properties of SiQDs to only a very small extent,⁴⁹ the stability trend we propose in our system reflects the purely structural SFE of silicon surfaces.⁵⁰ Thus, the term of dominant faceting we introduce here, using the case study of hydrogen-terminated SiQDs, can be generalized to other systems. In ligand-terminated QDs, a prevalent type of crystallographic surface in a highly polyhedral, quasi-spherical QD can be linked to the composition of the surface ligands as in our case. In more complicated systems, the difference in interfacial energy corresponding to individual facets will be minimized, but the quasi-spherical shape with dominant faceting can still prevail.

Energy Density. For assessing the energy density of our synthesized SiQDs, we carried out calorimetric measurements in pure oxygen, see Figure S9. The calorimetric measurements were performed separately for the “fresh” and “aged” varieties of the samples, but no statistically significant differences were observed. Thus, the “fresh” and “aged” varieties of samples were grouped together. (One exception was the p{110}-fresh SiQD sample, which burnt when introduced to the calorimetric chamber and therefore could not be characterized.) The measured values of released energy (32.0–32.6 kJ/g) are equal to the theoretical limit of the gravimetric energy density in

634 silicon, confirming that all the silicon present in the sample is
635 indeed surface-oxidized, as has already been suggested by the
636 clear white color of the Si nanoparticles after combustion in
637 **Figure 1a**. As a comparison, we also performed calorimetric
638 measurements of commercial Si nanocrystals with the diameter
639 of about 170 nm, which, in contrast to SiQDs, burnt only
640 incompletely and their released energy was lower by about
641 15%, see **Figure S9**. Thus, reaching the theoretical limit of
642 released energy in SiQDs was made possible by the nanometer-
643 sized nature of the sample with its high surface-to-volume
644 ratio.⁶

645 The calorimetric measurements of oxidized, as opposed to
646 hydrogen-terminated, SiQD-{111} sample showed a modest
647 decrease in released energy to 30.5 kJ/g. The decrease is easily
648 understandable because in an oxidized SiQD sample, the
649 oxidized surface bonds cannot release any energy. Using a
650 simple estimate based on a geometrical model,⁶ about $\frac{1}{5}$ of
651 bonds in a 5 nm SiQD are interfacial and the energy contained
652 in the “surface” Si–H bonds makes up about 3–5% of
653 the energy originating in the “volume” Si–Si bonds, depending
654 on dominant faceting. In accordance with this estimate, the
655 energy density of the H-terminated samples is by about five
656 percent larger than that of the oxidized sample. This estimate
657 also indicates that the relative differences of the gravimetric
658 density based on varying dominant faceting and different
659 content of hydrogen are very small, in the range of 1–2%,
660 again in accordance with **Figure S9**. Thus, in our set of
661 samples, nearly the same amount of energy is released during
662 oxidation, regardless of dominant faceting and the composition
663 of surface hydrides. However, as a result of the highest density
664 of surface bonds,⁶ the relatively highest amount of Si–H-
665 originating energy (5%) should be present in the {001}-
666 dominated sample. Again, **Figure S9** suggests the very same
667 tendency, even though the difference is close to the
668 experimental error. Also, the {001} facets chemisorb the
669 highest amount of hydrogen, whereby it is also plausible that
670 such H atoms initiate the oxidation process in SiQDs.

671 **Thermal Properties of SiQDs.** In order to understand the
672 phenomena responsible for the flammability of SiQDs
673 presented in **Figure 1** and to verify if the dominant faceting
674 introduced in **Figure 2f** and SFE influence the thermal
675 properties of SiQDs, we performed simultaneous differential
676 scanning calorimetry (DSC) measurements, thermogravimetric
677 analysis (TGA) and mass spectrometry (MS). As no detectable
678 differences between the “fresh” and “aged” varieties of the
679 samples were found, the storage time before measurement was
680 disregarded as a potential parameter and the “fresh” and “aged”
681 varieties were no longer distinguished. These measurements
682 were conducted in the temperature range from 25 to 1100 °C
683 (unless specified otherwise) in both, 10% O₂/Ar atmosphere,
684 referred to as “oxidizing”, and pure Ar atmosphere, referred to
685 as “inert”. As samples, we used the three types of SiQDs and
686 the commercial SiNCs listed in **Table 1**.

687 Prior to the discussion of the SiQD samples, it is important
688 to discuss the effects present in a typical commercial
689 nanostructured Si (c-SiNCs, diameter 170 nm), which does
690 not exhibit low-temperature ignition and is surface-oxidized. Its
691 behavior during annealing under oxidizing atmosphere is
692 shown in **Figure 4a** by the dashed curves. The slowly increasing
693 DSC curve with two visible broad bands with onset
694 temperatures of 80 and 830 °C confirms a slow gradual
695 release of energy during annealing. Moreover, the increase of

696 the TGA curve implies that the c-SiNCs sample gains weight.
697 Initially, the increase of mass is only by about 6 (w/w)% in the
698 temperature range 300–800 °C, and the subsequent significant
699 rise continues to 1350 °C, reaching 64 (w/w)%. This sample is
700 not fully oxidized after the annealing. MS measurements did
701 not detect any signal related to any monitored compounds or
702 fragments except for the ongoing consumption of oxygen (see
703 **Figure S10**). Thus, as the sample underwent the initial surface
704 oxidation, the only two effects observed in c-SiNCs during
705 annealing are connected with (i) the slightly exothermic
706 structural rearrangements of surface oxide at temperatures
707 <800 °C and (ii) the diffusive oxidation of the Si core at high
708 temperatures (800–1350 °C). This interpretation is further
709 validated by the thermal characterization of surface-etched
710 partially hydrogen-terminated commercial Si nanocrystals (H-
711 c-SiNCs). The corresponding DSC and TGA curves are shown
712 in **Figure S11** and the MS curves are presented in **Figure S10**.
713 During annealing, the DSC and TGA curves of H-c-SiNCs
714 followed a similar trend as the one observed in oxidized c-
715 SiNCs under oxidizing atmosphere. Virtually no effects in the
716 whole 25–1000 °C temperature range under inert atmosphere.
717 One subtle difference is a hint of an exothermic effect in the
718 DSC curve starting at around 250–300 °C, see **Figure S11a**,
719 which is likely connected with the surface dehydrogenation
720 and oxidation of this sample. Moreover, the diffusive oxidation
721 effect clearly starts and finishes at lower temperature for the
722 partially oxidized nanocrystals (H-c-SiNCs), which is due to the
723 thicker oxide shell in c-SiNCs, which represents a higher
724 barrier for the oxidation process. These results corroborate the
725 well-known stability of silicon structures, in which the bulk of
726 the material is susceptible only to diffusive oxidation at high
727 temperatures.^{15,16} Clearly, this stability persists even at
728 relatively small sizes of the nanostructures of about 170 nm.
729

In contrast to simple nanostructured Si, SiQDs show a much
730 wider variety of processes during the annealing process. As
731 illustrated in **Figure 4a** for the SiQD-{111} sample, the studied
732 temperature range can be divided into four different zones.
733 The onset temperatures of the weight-gaining processes
734 (oxidation) in the TGA curve mark the end points of the
735 intervals: Zone 1 ranges from 25 to approximately 180 °C with
736 no increase in weight of the sample, followed by Zone 2 from
737 180 to 450 °C with 25 (w/w)%, then followed by Zone 3
738 between 450 and 720 °C with a 35 (w/w)% increase and,
739 finally, Zone 4 from 720 to 1050 °C with a 44 (w/w)%
740 increase. After heating, the SiQD sample is fully oxidized, as
741 corroborated by the change in its ambient-lightning color from
742 beige-orange to white, see **Figure S12**. The total relative weight
743 increase during the heating process reaches 104 (w/w)%,
744 which is slightly lower than the theoretical value of 114 (w/
745 w)% in an ideal sample made up solely by silicon atoms
746 undergoing complete oxidation. As a reference, TGA measure-
747 ments of the SiQD-{111} sample under inert atmosphere
748 showed only minor changes, see **Figure S11d**, namely a small
749 decrease of about 1 (w/w)% in the interval from 235 to 500
750 °C, which can be explained by the release of hydrogen, and a
751 slow continuous relative weight rise of about 2 (w/w)% up to
752 1100 °C (**Figure S13a**), which likely results from weak
753 oxidation caused by either adsorbed water or trapped oxygen,
754 or tentatively impurities in the carrier Ar gas (**Figure S13c**). On
755 the whole, there is a marked difference in the DSC curves
756 between commercial nanoparticles and SiQDs under oxidizing
757 atmosphere. This difference results from a variety of processes,
758 which will be explained in detail in the following paragraphs.
759

The summary of DSC/TGA/MS results is shown in Figure 4. First, we focus on a representative SiQD-{111} sample as Figure 4a,b compares their DSC/TGA and MS curves with those of c-SiNCs. Figure 4c then shows the DSC/MS curves for the representative SiQD sample for comparative purposes and plots the derivative of TGA (dTGA). This derivative highlights the portions of the TGA curve where changes occur. Thus, the good correspondence between the DSC and the dTGA curves in Figure 4c demonstrates that the detected exothermic processes are connected with the increase of sample weight (through oxidation). Next, the influence of SFE on the surface reactivity of SiQDs, in particular the dehydrogenation and thermal oxidation of their surface, is discussed separately, see Figure 4d–f. The processes are described using two types of temperature labeling: TGA-based temperature intervals, marking the individual oxidation-related zones, and DSC onset temperatures, which indicate the temperatures at which the release of energy starts. Please note that we opted to classify the zones based on oxidation processes, which do not include dehydrogenation. The latter process is therefore not in close alignment with the chosen boundaries of the zones (see Figure 5).

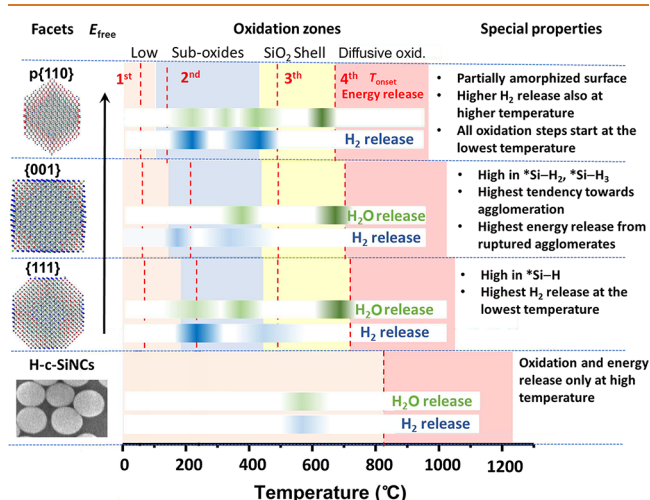


Figure 5. Schematic summary of the observed trends in SiQDs compared to commercial partially hydrogen terminated c-SiNCs, serving as a guide for tuning energy storage properties and its release. The different TGA-based oxidation zones are shown by different colors, the energy-release DSC onset temperatures are shown as the red dashed lines. Temperature ranges in which hydrogen is released are indicated by the dark blue stripes. Detection of water, most of which originate from released hydrogen reacting with oxygen before detection, is marked by the green stripes. The detection of solely water in the 600–700 °C range in the SiQD samples comes from hydrogen released from ruptured agglomerates. The main properties of the individual samples are listed. Please note that the H-c-SiNC sample also very likely undergoes a small degree of oxidation around 600 °C, where released hydrogen is detected. However, due to a much smaller relative surface-to-volume ratio in these large nanoparticles, the oxidation effects are difficult to detect.

with onset temperature at 79 °C ($T_{\text{max}} = 130$ °C). As is evident from the measurements under inert atmosphere, a small amount of hydrogen (onset temperature 70 °C) is released in this temperature range, see Figure S13c. Very likely, some hydrogen is released also under oxidizing atmosphere, and it is partially transformed into water before detection while oxygen is consumed, see Figure 4b. The release of hydrogen in Zone 1 is unlikely to originate in the thermal breaking of Si–H_x bonds, since the temperature is too low.^{3,26,38,55,56} Therefore, the process responsible for the exothermic event occurring in Zone 1 is the relaxation of surface and structural defects,⁵⁵ and or, alternatively, the out-diffusion of H₂ from interstitial sites within the SiQD lattice.

Zone 2 (Backbond Oxidation, Hot Spots, and Dehydrogenation). A wide range of effects occurs in Zone 2 in the temperature range of 180–450 °C in SiQD-{111} under oxidizing atmosphere: there is a weight gain related to oxidation (Figure 4a, TGA), which is highly exothermic (Figure 4a, DSC) and accompanied by the release of hydrogen, small amounts of SiH₂ and SiH₃ radicals and even water (Figure 4b). At the start Zone 2, backbond oxidation, proceeding primarily through the breakage of the bonds between surface Si atoms, starts to play an important role.^{56,57} However, unexpectedly high amounts of released hydrogen were detected at sample temperatures even below 200 °C, see the MS H₂ curve in Figure 4b. Typically, higher surface hydrides *Si–H_{2/3} dehydrogenate in the 200–400 °C temperature range in nanocrystalline silicon, whereas stronger monohydrides *Si–H dehydrogenate at even higher temperatures at 400–600 °C, see Figure 4b.^{3,26,38,55,56} Please note that the difference in dissociation temperatures results from activation energies of the dissociation processes, which can substantially vary in surface hydrides with different compositions and even on different surfaces.^{58,59} The breakage of Si–H bonds in higher hydrides observed here can be explained by the formation of hot-spots within the sample locally at higher temperature as a result of the poor heat conductivity of SiQDs in powder form.⁶⁰ The subsequent exothermic reaction, evident in the DSC curve with the onset at about 240 °C ($T_{\text{max}} = 309$ °C) most likely accelerates the process of H release by out-diffusion. It results also in the dehydrogenation of the stronger Si–H bonds in monohydrides, as most hydrogen including that in the monohydrides is released within Zone 2, see the MS H₂ curve in Figure 4b. In addition to H₂, the detected water also signifies the release of hydrogen under oxidizing atmosphere, as hydrogen can be partially converted to water before detection. The same measurements carried out under inert atmosphere (Figure S13b) are helpful in revealing the structural changes in the absence of oxidation. Here, the dehydrogenation occurs in a somewhat wider temperature range and its slower progression results from a smaller influence of hot-spots due to the absence of oxidation as an additional exothermic effect promoting H release in any form. The dehydrogenation under inert atmosphere lacking the oxidation-related acceleration is evidenced by the MS H₂ peak with onset at 150 °C and a side shoulder with onset at 330 °C (Figure S13c). These two peaks are likely connected to the dehydrogenation of higher hydrides and monohydrides, respectively, based on the relative strengths of the two types of bonds.^{3,26,38,55,56} Virtually no water and about twice as much hydrogen is detected under inert atmosphere as compared to the oxidizing ambient because released hydrogen cannot be effectively transformed to water before detection.

Zone 1 (Relaxation of Surface and Structural Defects). The changes occurring in Zone 1 in the temperature range 25–180 °C in SiQD-{111} under oxidizing atmosphere are not connected with any weight gain, as is clear from the TGA curve in Figure 4a,c, thus, no oxidation takes place. However, the DSC curve (Figure 4a) features a weak exothermic event

The amount of energy released under the two atmospheres is comparable up to about 240 °C, above which oxidation leads to a more rapid energy release under oxidizing atmosphere. Similarly, the Si–H_{2/3} species are also not detected under inert atmosphere, implying that their release is driven by surface oxidation. Thus, we clearly show that the co-occurrence of oxidation and dehydrogenation is the driving factor for the highly exothermic processes in Zone 2, being responsible for the sharp DSC peak absent in other types of nanostructured silicon or under inert atmosphere.

Zone 3 (Residual Dehydrogenation and Rupture of Agglomerates). At the beginning of Zone 3, which extends between 450 and 720 °C in the SiQD-{111} sample under oxidizing atmosphere, oxidation progresses through the transformation of separate suboxide fragments into a compact layer, just a few atomic monolayers thick,^{38,56,61} as evidenced by the weight gain (Figure 4a, TGA) and the ongoing consumption of oxygen (Figure 4b). Furthermore, dehydrogenation of the residual monohydride species not yet dehydrogenated due to hot-spots proceeds, as confirmed by the MS H₂ peak (Figure 4b) and by the broader peak with a gradual increase and onset temperature of 485 °C in the DSC curve (Figure 4a). In addition, the DSC curve shows a sharp and strongly exothermic effect with maximum at 672 °C and a temperature range of 630–700 °C. This effect was observed in the past,^{3,55} and was attributed to the crystallization of Si nanoparticles⁵⁵ or to diffusive oxidation.³ We disagree with both these interpretations because (i) our SiQDs are already crystalline, (ii) the energy release in the temperature range from 630 to 700 °C significantly exceeds the amount to be expected from a mere relaxation of Si atoms from a disordered into a more ordered phase, and (iii) diffusive oxidation proceeds at later stages of the heating process, as shown below. A peculiar feature of this process is the detection of high amounts of water and the consumption of oxygen with no detectable release of hydrogen at 675 °C (Figure 4b). Clearly, at temperatures above 600 °C the sample should be free of hydrogen and water. Therefore, we ascribe this effect to the rupture of agglomerates of SiQDs. Si nanocrystals are known to form agglomerates and aggregates strongly bonded via the growing surface oxide, starting at the very early stages of oxidation.⁶² Going through Zone 2, SiQDs first oxidize and agglomerate, which results in the sealing of microvoids in between SiQDs. Then, the dehydrogenation of silicon hydrides occurs throughout Zones 2 and 3. After reaching a critical temperature of 630 °C, the agglomerates are no longer stable as a result of high temperature and the overall stage of oxidation. Therefore, the agglomerates rupture, the remaining trapped hydrogen is released and is detected as water after it was oxidized. Moreover, the exposition of the as of yet unoxidized SiQD surfaces results in oxidation (see the peak in the TGA curve in Figure 4a), which is rapid and highly exothermic. Our interpretation is corroborated by measurements under inert atmosphere, where neither the exothermic DSC effect (Figure S13b) nor the detection of higher amounts of hydrogen or water (Figure S13c) occur, because the absence of oxidation did not lead to the formation of agglomerates. Thus, the driving factor behind the second sharp exothermic effect observed during the thermal oxidation of SiQDs is the rupture of oxide-bonded agglomerates and the subsequent oxidation of the newly exposed surfaces. In a nutshell, Zone 3 could be described by thermal cracking with subsequent oxidation of the exposed Si surfaces.

Zone 4 (Diffusive Oxidation). In the last Zone 4, extending between 720 and 1050 °C in the SiQD-{111} sample under oxidizing atmosphere, the oxidation of silicon in SiQDs is completed via diffusive oxidation. This interpretation is confirmed by the continuous rise in TGA, the peak in the DSC signal with onset temperature at 707 °C and $T_{\max} = 892$ °C (Figure 4a), the absence of any effects under inert atmosphere (Figure S13) and the continuous consumption of oxygen (Figure 4b). The rupture of agglomerates occurring in the preceding zone facilitates the diffusion of oxygen to the cores of SiQDs and contributes to the completion of the oxidation process at lower temperatures.

Changes in Thermal Properties with Dominant Faceting. The overall TGA-derived weight gain is very similar regardless of dominant faceting, signifying that the difference in the amount of surface-bonded hydrogen in the three types of samples under study is not significant, at least in terms of its relative weight. The differences in the three samples will be discussed for the individual zones separately.

Zone 1. The main difference observed in the other two samples with higher SFE during the surface and defect relaxation stage is the lower DSC onset temperature (around 50 °C, see Figure 4d,e), implying that the energy release begins at lower temperatures. Moreover, in agreement with the increased percentage of less stable higher surface hydrides as shown in Figure 2f, the {001} sample, in contrast to {111}, releases much more hydrogen before reaching Zone 2, see Figure 4f. This effect is especially apparent in the MS curves under inert atmosphere (Figure S14).

Zone 2. Within the backbond oxidation and dehydrogenation stage, both the samples with higher SFE released about 30% more energy than {111}, see Figure 4d. The dehydrogenation process at ≈ 200 °C differ considerably on a per-sample basis, see Figure S14. The least amount of hydrogen is released by the medium-SFE sample {001}, because its much more profound dehydrogenation had occurred already in Zone 1. Also, the side shoulder of the MS H₂ peak attributed to the dehydrogenation of surface monohydrides is the least evident in the {001} sample, which has the lowest proportion of surface monohydrides, see Figure 2f. The DSC onset temperature of Zone 2 gradually shifts to lower temperatures (Figure 4e) with increasing SFE down to roughly 100 °C at p{110}. This downshift correlates well with the expected lower stability of the higher-SFE samples.

Zone 3. In the zone characteristic for residual dehydrogenation and rupture of agglomerates, there are detectable differences in the initial dehydrogenation stage. In good agreement with the composition of surface hydrides (Figure 4d), no hydrogen is released by the {001} sample which has a higher proportion of less stable higher hydrides. On the other hand, the MS H₂ peak of the p{110} sample predominantly terminated by monohydrides (Figure S14f) still has a detectable tail here, see Figure 4f. The onset temperatures of Zone 3 are almost the same for all three samples, see Figure 4e, because the outermost atomic shells of the QDs, which have already been covered with a monolayer of oxide, are not as sensitive to the silicon surface bonds and dominant faceting as in the initial stage of oxidation. After exceeding 650 °C and the rupture of agglomerates, the most energy is released by the medium-SFE sample {001}, which is a consequence of its most complex composition of surface hydrides getting decomposed. This decomposition causes its highest propensity to agglomerate.

976 **Zone 4.** The only significant difference between the three
977 samples in the diffusive-oxidation zone is the lowering of both
978 the TGA and the DSC onset temperature and the lowering of
979 the temperature when the oxidation is finished (Figure 4d).
980 This effect results from (i) a lower stability of the higher-SFE
981 QDs and/or (ii) a somewhat smaller size of the more surface-
982 etched, higher-SFE QDs.

983 We therefore, despite the complicated trends observed
984 during the thermal oxidation of SiQDs, successfully explained
985 the evolution of the DSC/TGA/MS curves in all the SiQD
986 samples based on the existing knowledge of oxidation and
987 dehydrogenation in nanostructured silicon. The key factors
988 driving the processes are differences in SFE and the closely
989 related differences in the composition of surface hydrides. Our
990 description successfully explains even the observed hydrogen
991 released in the highest-SFE partially structurally disordered
992 SiQD-p{110} at relatively higher temperatures when compared
993 to the other two types of samples, which would not be an effect
994 intuitively expected. Thus, these results underline the
995 importance of SFE and dominant faceting in the properties
996 of QDs.

997 **Dominant Faceting versus Size Dependence.** In
998 principle, the differences in surface reactivity could be caused
999 by the slightly different size distributions of the synthesized
1000 nanoparticles (see Figure 2c). There are several arguments
1001 against this interpretation. A preliminary assessment of the
1002 extent to which the size and dominant faceting influence SFE
1003 can be based on our calculations from Figure 3b using mean
1004 sizes of the individual samples. This analysis shows that, for an
1005 ≈ 5 nm QD, the changes in SFE induced by these two factors
1006 are at least comparable ($\approx 20 - 30 \frac{\text{meV}}{\text{QD atom}}$). However, surface
1007 reactivity experiments probe the whole size distributions rather
1008 than just the mean sizes. Thus, the overlap of the distributions
1009 of 0.75 and 0.88 as characterized by the Bhattacharyya
1010 coefficient reduces the impact of size even further. Moreover, a
1011 closer look at the HRTEM-derived histograms in Figure S6
1012 reveals that the size distribution of the {111}-dominantly
1013 faceted sample could be slightly bimodal, which is an
1014 additional factor contributing to the overlap of the first two
1015 distributions. Importantly, the inherent connection between
1016 size and SFE is strictly *monotonous*, see Figure 3b. In contrast
1017 to a monotonous trend, in our experiments, the {001}-
1018 dominantly faceted middle-SFE (and medium-sized) sample
1019 exhibits a detectably nonmonotonously different dynamics of
1020 the dehydrogenation process, clearly determined by its
1021 dominant faceting rather than size-induced SFE changes, see
1022 Figure 4f. Therefore, our experiments justify the proposed
1023 assignment of dominant faceting as an important factor in
1024 surface reactivity.

1025 **Tuning of Thermal Oxidation in Silicon Quantum
1026 Dots.** The trends observed during the thermal oxidation
1027 process are schematically summarized in Figure 5. This scheme
1028 clearly shows how higher SFE leads to the lowering of the end
1029 points of the TGA-based temperature intervals for the
1030 individual stages of thermal oxidation. The exception to the
1031 rule here is, quite intuitively, the Zone-3 growth of a thicker
1032 SiO₂ shell on an already oxidized surface. Moreover, the DSC-
1033 based onset temperatures also decrease with increasing SFE
1034 with the exception of Zone-3 residual dehydrogenation.
1035 However, the subsequent agglomerate-rupture-related energy
1036 release is finished at lower temperatures in higher-SFE samples.

The release of hydrogen is then influenced by both the SFE 1037
and the composition of surface hydrides. 1038

An interesting feature observed in Zone 1 is the relatively 1039
high amount of released energy, especially considering DSC 1040
measurements under inert atmosphere, see Figure S11c, where 1041
no energy can be released from hydrogen. Therefore, we 1042
attribute the energy released in this temperature range to the 1043
structural reorganization of the surface. In general, structural 1044
relaxation in a similar temperature region was described mostly 1045
in glassy systems.⁶³ However, an analogic phenomenon can 1046
occur in Si (or other) QDs. The exothermic structural 1047
relaxation results from the increased fluidity or mobility of 1048
atoms due to the increase of free volume, which is the 1049
difference of an average volume per molecule/atom in the 1050
liquid and its van der Waals volume. 1051

Figure 5 provides a guide for the tuning of the thermal 1052
properties of SiQDs via dominant faceting. Clearly, ignition 1053
temperatures as low as 150 °C are attainable in SiQDs if 1054
desired. However, if need be, the energy release in the Zone-2 1055
temperature range can be bypassed by performing slow natural 1056
oxidation under ambient conditions. In such an oxidized 1057
sample, major energy release would come from the Zone-3 1058
rupture of agglomerates at much higher temperatures >600 °C. 1059
This scenario very likely occurred, perhaps inadvertently, in the 1060
study of the combustion of amorphous Si nanoparticles,³ 1061
where, similarly to our measurements, the DSC curves of H- 1062
terminated Si nanoparticles showed a major peak at low 1063
temperatures around 200 °C. However, ignition of a 1064
nanoparticle-based composite happened at much higher 1065
temperatures (>700 °C). This discrepancy is likely to have 1066
been caused by a thin layer of oxide on silicon nanoparticles in 1067
the combustion experiments, formed during the ultrasonica- 1068
tion step when the nanocomposites were prepared. It appears 1069
that in their³ combustion experiments, the silicon nano- 1070
particles were no longer H-terminated and the ignition was 1071
initiated by the hydrogen released after the rupture of the 1072
agglomerates. This example illustrates how, using a combina- 1073
tion of SFE and surface chemistry, the ignition temperature of 1074
Si nanoparticles can be tuned from temperatures as low as 150 1075
°C to >700 °C. 1076

Apart from ignition-related properties useful for energetic 1077
applications,³ Figure 5 also hints toward the possibility of using 1078
SiQDs for hydrogen storage since hydrogen release can be 1079
achieved under various conditions. Even though our findings 1080
represent fundamental characteristics of this material, the main 1081
motivation driving this research is the potential of having 1082
resource-efficient²¹ material with inherently low toxicity²⁰ 1083
since silicon is the second most abundant element in the 1084
Earth's crust and a trace element in humans. Unlike other 1085
traditional energy-storage materials, silicon is so biocompatible 1086
that high-quality SiQDs can even be synthesized using rice 1087
husks, which is agricultural waste, as the source of silicon.⁶⁴ 1088
Naturally, countless other issues need to be resolved before a 1089
potential production roll-out, including the reversibility of the 1090
oxidation reaction leading to highly stable products. Whereas 1091
complete oxidation including the Zone-4 diffusive stage is very 1092
likely irreversible because the QDs are destroyed, the 1093
reversibility of the surface backbond oxidation is currently 1094
being tackled in silicon-air batteries.²¹ Interestingly, plasma 1095
synthesis of silicon nanoparticles itself has already been 1096
commercialized. Slightly larger silicon nanoparticles (~12 1097
nm) formulated into a screen printable ink are already available 1098
as a selective emitter layer in silicon solar cells by Innovalight 1099

1100 Corporation.⁶⁵ Besides, the utilization of silicon is considered
1101 in Li-based batteries,^{66,67} partially because Si nanoparticles and
1102 QDs can accommodate expansion.⁶⁸

1103 While thermal oxidation was chosen as the studied process
1104 here because SiQDs are highly prone to oxidation and readily
1105 oxidize when exposed an environment containing oxygen
1106 species, it is also possible to tune the energy-storage properties
1107 by changing the reactive environment. However, such a study
1108 is beyond the scope of this article.

1109 **Mechanism of Ignition.** The combined measurements
1110 allow us to identify the processes responsible for the relatively
1111 low-temperature ignition of Si nanoparticles reported in
1112 Figures 1 and S8. The initially proposed possibility of the
1113 combustion being linked to trapped hydrogen was proven
1114 wrong by experiments using the “fresh” and “aged” varieties of
1115 samples. These experiments demonstrate that the amount of
1116 trapped, not chemically bonded hydrogen is negligible. Thus,
1117 the low-temperature combustion is linked almost exclusively to
1118 the highly exothermic hot-spot-driven processes occurring at
1119 the beginning of Zone 2. Several factors influence the observed
1120 ignition process. First, in general, SiQDs are known to have
1121 low thermal conductivity.⁶⁹ Based on calculations presented
1122 in,¹⁹ the effective thermal conductivity k_{eff} of our samples
1123 (porosity 0.77) is roughly $0.1 \frac{\text{W}}{\text{m}\cdot\text{K}}$, which is much closer to air (1124
 $k_{\text{air}} \approx 0.03 - 0.04 \frac{\text{W}}{\text{m}\cdot\text{K}}$ at $30-200^\circ\text{C}$) than to silicon (1125
 $k_{\text{Si}} \approx 100 \frac{\text{W}}{\text{m}\cdot\text{K}}$ at $30-200^\circ\text{C}$). These conditions favor the
1126 backbond-oxidation-driven formation of hot-spots locally at
1127 much higher temperatures, as locally, temperatures around 400°C
1128 can be reached solely as a result of absorption of light.⁷⁰
1129 Such temperatures are well within the temperature range of the
1130 typical dehydrogenation of silicon hydride bonds, see Figure
1131 4b. Next, the oxidation of hydrogen in contact with air results
1132 in a gaseous reaction product diffusing away (vs SiO_2 staying
1133 put as a solid), and a considerable amount of thermal energy is
1134 being passed on to neighboring Si atoms as a result of
1135 dehydrogenation. Thus, the released hydrogen provides
1136 sufficient energy to drive further dehydrogenation and, finally,
1137 also the diffusive oxidation of the whole volume of the sample.
1138 The ignition temperature is lower in amorphous nano-
1139 particles, see Figure 1d, as, in accordance with the trends
1140 reported in Figure 5, the thermal oxidation processes start
1141 earlier in less structurally ordered nanoparticles. In addition,
1142 amorphous Si nanoparticles can store and thus also release
1143 higher amounts of H when heated. Since H is much more
1144 reactive in bonding with oxygen as compared to Si, a catalytic
1145 Si oxidation due to local heat transfer from H undergoing an
1146 oxyhydrogen reaction lowers the combustion temperature of
1147 amorphous Si nanoparticles.

1148 On the contrary, when the combustion process is initiated
1149 by light absorption rather than by heating, light is absorbed
1150 primarily by nanoparticles, which are insulated from one
1151 another by air. Here, the key factor driving the combustion
1152 process is the dissipation of heat from the nanoparticles to the
1153 surrounding air. Therefore, this process is unlikely to be
1154 strongly dependent on the degree of structural order, instead, a
1155 difference between fully amorphous and structurally ordered
1156 nanoparticles can be expected. This expectation is confirmed
1157 by the trends observed in Figure 1d,f.

1158 No ignition analogous to that described in Figure 1 was
1159 observed in the DSC experiments. The lack of this effect can
1160 be caused by (i) a lower oxygen content in the oxidizing

1161 atmosphere during the DSC/TGA/MS measurements and (ii) 1162 faster heating rates in the ignition experiments, which lead to 1163 more pronounced hot-spots and (iii) the pumping present in 1164 the DSC/TGA/MS measurements, which causes the outflow 1165 of the reaction byproduct from the reactor so that it could be 1166 analyzed.

1167 **Other Considerations.** As a result, surface properties, 1168 thermal properties and the overall stability of SiQDs can be 1169 tuned by SFE. In this regard, synthesis in nonthermal plasma 1170 could be the ideal method for SFE tuning. The two other most 1171 frequent competitive methods capable of producing SiQDs are 1172 electrochemical etching⁷¹ and thermal annealing of Si-rich 1173 silicon-oxide matrices.^{72,73} During electrochemical etching, 1174 SiQDs are “extracted” from an initially ideally crystalline wafer 1175 with a defined crystalline orientation through an HF-based wet 1176 electrolytic etching process. In the thermal annealing approach, 1177 a silicon-rich glass with a suitable composition undergoes 1178 thermal annealing at high temperatures $>1000^\circ\text{C}$, which 1179 induces the diffusion of silicon atoms, leading to the formation 1180 of QDs. Then, the oxide matrix is removed by HF etching.¹¹⁸⁰ Neither of these methods seems promising in tuning the 1181 surface properties of the produced QDs: etching of a 1182 monocrystal in a predefined crystalline direction is unlikely 1183 to lead to QDs with varying surface faceting and the degrees of 1184 freedom of the migration of ions inside a solid amorphous 1185 matrix is in principle significantly limited by the matrix itself.¹¹⁸⁶ Thus, while dominant faceting in SiQDs can be tuned, it is 1187 possible that only some methods can provide such tuning 1188 abilities, with the synthesis in nonthermal plasma being an 1189 ideal candidate.¹¹⁹⁰

1191 One more interesting observation we want to discuss 1192 pertains to the highest-SFE sample SiQD-p{110}. Based on 1193 FTIR spectroscopy, we argue that the surface of this sample 1194 seems less ordered than in the other SiQD samples studied 1195 here, most likely as a result of the highest SFE. However, it still 1196 contains a high proportion of surface monohydrides and its 1197 surface geometry is analogous to a {110} faceted Si surface. A 1198 model of an SiQD being a heterostructure comprising a 1199 structurally ordered core and an “amorphized Si shell” has 1200 been proposed in SiQDs fabricated by thermal annealing.^{46,73}
1201 Here, we prefer to use the term “degree of structural order” 1202 rather than the bulk-based dichotomy of crystalline vs 1203 amorphous materials, as the question of crystalline order in 1204 QDs is more complex.⁷⁴ Moreover, we believe that the 1205 difference in the size distribution as determined from 1206 coherently diffracting domains in XRD and using HRTEM⁴⁶ 1207 reflects the layer in a QD affected by surface reconstruction, 1208 which does not necessarily need to be amorphous. This 1209 quantity is closely related to the degree of structural order of 1210 the surface which we describe using SFE. Leaving this issue 1211 aside, the obvious question which comes to mind is, if and how 1212 much the proposed amorphized shell is linked to the HF- 1213 etching step of the fabrication process in the thermally 1214 annealed SiQDs. It is entirely plausible that the interaction of 1215 the surface of synthesized QDs, whatever its initial structural 1216 properties might be, with a highly corrosive agent might 1217 change the initial surface structure to a less ordered state. For 1218 planar Si surfaces such as crystalline Si wafers, such increased 1219 disorder reveals itself by an increased surface roughness. Thus, 1220 the structural properties of the surface, as discussed here and 1221 in^{73,75} can be highly dependent on the fabrication method and 1222 sample history. However, at this point, we leave this hypothesis 1223 unproven, pointing to further research efforts.¹²²³

1224 CONCLUSIONS

1225 We introduced the concept of dominant faceting as macro-
1226 scopically detectable preferential structural order of the surface
1227 of QDs, present even without evident shape control on the
1228 microscopic scale. Dominant faceting describes a state in which
1229 a certain type of facet dominates at the surface of highly
1230 polyhedral quasi-spherical QD, determining the QD's surface
1231 reactivity regardless of the concrete spatial distribution of the
1232 facets on the surface. We tentatively propose that local strain
1233 induced by surface atoms on the facets is responsible for the
1234 changes in reactivity, as supported by classical force field
1235 simulations. Furthermore, we showed that dominant faceting
1236 can be applied to tune the thermodynamical properties of
1237 QDs, such as their stability or surface reactivity, using SiQDs as
1238 a case-study material. In particular, we derived analytical
1239 expressions for surface free energy for three model geometries
1240 of SiQDs differing in dominant faceting. Next, we established a
1241 link between the measured surface properties of synthesized
1242 SiQDs with the surface free energy of the idealized SiQD
1243 models and show that this association successfully predicts the
1244 lowering of onset temperatures of different exothermic
1245 processes during thermal oxidation. We discussed that SFE
1246 tuning can potentially be dependent on the fabrication
1247 method, with synthesis in nonthermal plasma being able to
1248 attain a wide range of SFE in SiQDs. Moreover, the energy
1249 released during thermal oxidation was shown to be very close
1250 to theoretical limits, confirming that full oxidation of all the
1251 contained silicon material is achieved. This finding underpins
1252 the potential of silicon as an energy-storage material. Next,
1253 using combined DSC, TGA and MS measurements, we
1254 identified the processes responsible for the release of energy
1255 during thermal oxidation of SiQDs. Here, especially the release
1256 of surface-bonded hydrogen was shown to be tunable in a wide
1257 range of temperatures by surface properties. In addition to
1258 introducing dominant faceting, our experiments provide a
1259 detailed guide for using SiQDs as an energy-storage or thermal
1260 material, by showing that both low-temperature ignition (\approx
1261 200 °C) and higher-temperature energy release (\approx 650 °C)
1262 can be obtained by tuning their SFE.

1263 METHODS

1264 This section lists only a brief overview of the applied methods, see
1265 Supporting Information for a more detailed description.

1266 **Synthesis of Nanoparticles.** SiQDs were synthesized using a
1267 noncommercial flow-through reactor in nonthermal plasma and
1268 collected onto glass covers for microscopy. Synthesis parameters for
1269 the individual samples are listed in Table 1. The commercial oxidized
1270 Si nanoparticles (c-SiNCs) were purchased from PlasmaChem
1271 GmbH. The partially hydrogen-terminated commercial Si nano-
1272 particles (H-c-SiNCs) were etched using HF.

1273 **Study of Ignition Conditions.** In the heat-initiated ignition, the
1274 sample was placed on a hot plate on top of an aluminum foil and
1275 temperature was increased stepwise from 50 °C until ignition. The
1276 light-initiated ignition was realized using a standard 405 nm laser
1277 pointer. The measurements were repeated several times to obtain
1278 standard deviation of the ignition temperature.

1279 **Structural and Chemical Characterization.** X-ray diffraction
1280 (XRD) measurements were performed on a Rigaku SmartLab
1281 diffractometer equipped with a 9 kW rotating anode Cu source
1282 (wavelength $K_{\alpha 1} \lambda = 0.154056$ nm) in a semi focusing Bragg–
1283 Brentano geometry. Diffracted intensity was counted by a 2D hybrid
1284 pixel single photon counting HyPix3000 detector.

1285 The ordered mesoporous structure was determined from small-
1286 angle X-ray scattering (SAXS) using Xenocs Xeuss 2.0 SAXS
1287 instrument equipped with the Mo K_{α} ($\lambda = 0.07107$ nm) radiation

X-ray microfocus sources, toroidal X-ray mirror and scatter-less slits 1288
producing collimating parallel beam point focus, and a Pilatus 200k 1289
(Dectris) hybrid pixel single-photon counting detector. 1290

High-resolution transmission electron microscopy (HRTEM) 1291
measurements were carried out using EFTEM Jeol 2200 FS operated 1292
at 200 kV. Surface of HRTEM analyzed SiQDs was dodecyl 1293
terminated using the thermal hydrosilylation method. The acquired 1294
HRTEM images were analyzed manually. 1295

The Fourier-transform infrared (FTIR) absorption analysis was 1296
realized using Nicolet iS50 FT-IR microscope (Thermo Scientific). 1297
The measurements were performed in the attenuated total reflectance 1298
regime using a monocrystalline diamond crystal. The Raman spectra 1299
measurements were realized using microspectrometer Renishaw inVia 1300
Reflex equipped with a HeCd continuous laser (Kimmon Dual 1301
Wavelength HeCd) using the excitation wavelength of 442 nm. We 1302
cannot rule out that some of the observed shifts in the 520 cm^{-1} are 1303
caused by sample heating. 1304

Determination of the Ratios of Surface Hydrides. Based on 1305
published analysis,²⁶ we used one peak for the SiH_3 surface stretching 1306
mode (2140 cm^{-1}), two peak for the stretching modes of SiH_2 (2100 cm^{-1} 1307
and 2117 cm^{-1}) and two peak for the stretching modes of SiH (2070 1308
and 2085 cm^{-1}). The ratio of the integrated peaks was used to 1309
determine the surface hydride composition. Each data point of SiH_x 1310
composition represents at least six independent measurements. 1311

Classical Force Field Simulations of Strain. The classical force 1312
field simulations were conducted with homemade code FireCore.⁵⁴ 1313

Calorimetry. The gravimetric energy density was determined 1314
using a commercial Combustion compensated jacket calorimeter Parr, 1315
Model 1351, (Parr Instr. Comp., Moline, IL, USA), equipped with an 1316
oxygen bomb Parr 1108. 1317

DSC/TGA/MS. All samples were measured by nonisothermal DSC- 1318
TG analysis using the Setaram Themys 2400 simultaneous thermal 1319
analyzer, which was coupled by a quartz capillary with the Pfeiffer 1320
Vacuum OmniStarTM GSD320 mass spectrometer. Data from all 1321
performed analyses (DSC-TGA-MS) were processed by the Calisto 1322
Processing software. Each experiment was repeated 2–3 × for every 1323
sample, repeated experiments led to very similar trends. 1324

ASSOCIATED CONTENT

SI Supporting Information

The Supporting Information is available free of charge at 1327
<https://pubs.acs.org/doi/10.1021/acsnano.4c11376>. 1328

Derivation of the absolute SFE as a function of QD 1329
faceting and size, details of the applied methods, 1330
additional MS/DSC/TGA and other analyses, and 1331
photographs of samples (PDF) 1332

Example of light-initiated ignition (MP4) 1333

AUTHOR INFORMATION

Corresponding Author

Katerína Kušová – Institute of Physics of the CAS, 162 00 Prague 1336
Prague 6, Czechia; orcid.org/0000-0002-8545-5965; 1337
Email: kusova@fzu.cz 1338

Authors

Pavel Galář – Institute of Physics of the CAS, 162 00 Prague 1340
6, Czechia; orcid.org/0000-0003-2220-2976 1341

Jakub Kopenc – Institute of Physics of the CAS, 162 00 Prague 1342
Prague 6, Czechia; orcid.org/0009-0004-0469-0018 1343

Robert Král – Institute of Physics of the CAS, 162 00 Prague 1344
6, Czechia; orcid.org/0000-0002-4519-6030 1345

Filip Matějka – Institute of Physics of the CAS, 162 00 Prague 1346
6, Czechia; orcid.org/0000-0003-3291-2242 1347

Petra Zemenová – Institute of Physics of the CAS, 162 00 Prague 1348
Prague 6, Czechia; orcid.org/0000-0002-6739-9832 1349

1350 Milan Dopita — Faculty of Mathematics and Physics, Charles
1351 University, 121 16 Praha 2, Czechia;  orcid.org/0000-
1352 0003-4485-5265

1353 Prokop Hapala — Institute of Physics of the CAS, 162 00
1354 Prague 6, Czechia;  orcid.org/0000-0003-4807-0326

1355 Dirk König — Integrated Materials Design Lab and
1356 Department of Applied Mathematics, Research School of
1357 Physics, The Australian National University, Canberra, ACT
1358 2601, Australia; Institute of Semiconductor Electronics
1359 (IHT), RWTH Aachen University, 52074 Aachen,
1360 Germany;  orcid.org/0000-0001-5485-9142

1361 Pavel Vrbka — University of Chemistry and Technology, 166
1362 28 Praha 6, Czechia;  orcid.org/0000-0003-2251-1445

1363 Complete contact information is available at:
1364 <https://pubs.acs.org/10.1021/acsnano.4c11376>

1365 Author Contributions

1366 P.G. suggested the idea of studying ignition conditions in
1367 SiQDs, made the complex interpretation of TGA/DSC data,
1368 and significantly participated in drafting and revising the
1369 manuscript. J.K. characterized the ignition conditions and
1370 synthesized some of the studied samples. R.K. analyzed and
1371 oversaw the TGA/DSC measurements. F.M. carried out the
1372 FTIR characterization, built the synthesis setup, and
1373 synthesized some of the studied samples. P.Z. carried out the
1374 TGA/DSC measurements. P.V. carried out and analyzed the
1375 calorimetry measurements. M.D. carried out and interpreted
1376 the XRD measurements. P.H. made the classical force field
1377 simulations and drafted and revised the corresponding part of
1378 the manuscript. D.K. derived the analytic description of SFE
1379 evolution for the three different SiQD topologies used in this
1380 work and participated in the thermodynamic analysis of SiQD
1381 ignition and oxidation. D.K. participated in drafting and
1382 revising the manuscript. K.K. supervised the collaboration,
1383 developed the idea of dominant faceting, drafted the outline of
1384 the manuscript, and significantly participated in drafting and
1385 revising the manuscript. All authors agreed on the text of the
1386 manuscript.

1387 Notes

1388 The authors declare no competing financial interest.

1389 ACKNOWLEDGMENTS

1390 P.G., J.K., F.M., and K.K. acknowledge the Czech Science
1391 Foundation project GACR 23-05784S. R.K. and P.Z. were
1392 supported by OP JAC financed by ESIF and MEYS SENDISO
1393 (CZ.02.01.01/00/22_008/0004596). We acknowledge the
1394 CzechNanoLab research infrastructure supported by the
1395 MEYS (LM2023051, Raman measurements). D.K. acknowl-
1396 edges funding by the 2018 Theodore-von Kármán Fellowship
1397 awarded by RWTH Aachen University. The authors thank Ing.
1398 J. Červenka for introducing the idea of DSC/TGA measure-
1399 ments and Ass. Prof. Alena Michalcová for performing the
1400 HRTEM measurements.

1401 REFERENCES

- 1402 (1) Koohi-Fayegh, S.; Rosen, M. A. A review of energy storage types,
1403 applications and recent developments. *J. Energy Storage* **2020**, *27*,
1404 No. 101047.
- 1405 (2) Bassyouni, Z.; Allagui, A.; Abou Ziki, J. D. Microsized
1406 Electrochemical Energy Storage Devices and Their Fabrication
1407 Techniques For Portable Applications. *Adv. Mater. Technol.* **2023**, *8*,
1408 No. 2200459.
- (3) Xu, F.; Nava, G.; Biswas, P.; Dulalia, I.; Wang, H.; Alibay, Z.; Gale, M.; Kline, D. J.; Wagner, B.; Mangolini, L.; Zachariah, M. R. Energetic characteristics of hydrogenated amorphous silicon nano-particles. *Chem. Eng. J.* **2022**, *430*, No. 133140.
- (4) Kovalenko, M. V.; Manna, L.; Cabot, A.; Hens, Z.; Talapin, D. V.; Kagan, C. R.; Klimov, V. I.; Rogach, A. L.; Reiss, P.; Milliron, D. J.; Guyot-Sionnest, P.; Konstantatos, G.; Parak, W. J.; Heyeon, T.; Korgel, B. A.; Murray, C. B.; Heiss, W. Prospects of Nanoscience with Nanocrystals. *ACS Nano* **2015**, *9*, 1012–1057.
- (5) Mizutani, T.; Ohta, H.; Ueda, T.; Kashiwagi, T.; Fukuda, T.; Shiobara, T.; Saitow, K.-I. Mechanochemically Tailored Silicon Particles for Efficient H₂ Production: Entropy and Enthalpy Engineering. *ACS Sustain. Chem. Eng.* **2023**, *11*, 11769–11780.
- (6) König, D. Number series of atoms, interatomic bonds and interface bonds defining zinc-blende nanocrystals as function of size, shape and surface orientation: Analytic tools to interpret solid state spectroscopy data. *AIP Adv.* **2016**, *6*, No. 085306.
- (7) Wang, K.; Zhang, Z.; Ding, Y.; Cheng, S.; Xiao, B.; Sui, M.; Yan, P. Surface Facet Dependent Cycling Stability of Layered Cathodes. *Adv. Funct. Mater.* **2023**, *33*, No. 2302023.
- (8) Ma, C.; Eickemeyer, F. T.; Lee, S.-H.; Kang, D.-H.; Kwon, S. J.; Grätzel, M.; Park, N.-G. Unveiling facet-dependent degradation and facet engineering for stable perovskite solar cells. *Science* **2023**, *379*, 173–178.
- (9) Houtepen, A. J.; Hens, Z.; Owen, J. S.; Infante, I. On the Origin of Surface Traps in Colloidal II–VI Semiconductor Nanocrystals. *Chem. Mater.* **2017**, *29*, 752–761.
- (10) Choi, H.; Ko, J.-H.; Kim, Y.-H.; Jeong, S. Steric-Hindrance-Driven Shape Transition in PbS Quantum Dots: Understanding Size-Dependent Stability. *J. Am. Chem. Soc.* **2013**, *135*, 5278–5281.
- (11) Kim, K.; Yoo, D.; Choi, H.; Tamang, S.; Ko, J.-H.; Kim, S.; Kim, Y.-H.; Jeong, S. Halide-Amine Co-Passivated Indium Phosphide Colloidal Quantum Dots in Tetrahedral Shape. *Angew. Chem., Int. Ed.* **2016**, *55*, 3714–3718.
- (12) Kim, Y.; Choi, H.; Lee, Y.; Koh, W.-K.; Cho, E.; Kim, T.; Kim, H.; Kim, Y.-H.; Jeong, H. Y.; Jeong, S. Tailored growth of single-crystalline InP tetrapods. *Nat. Commun.* **2021**, *12*, 4454.
- (13) Comet, M.; Martin, C.; Schnell, F.; Spitzer, D. Nanothermites: A short Review. Factsheet for Experimenters, Present and Future Challenges. *Propellants Explos. Pyrotech.* **2019**, *44*, 18–36.
- (14) Hannah, D. C.; Yang, J.; Podsiadlo, P.; Chan, M. K. Y.; Demortière, A.; Gosztola, D. J.; Prakapenka, V. B.; Schatz, G. C.; Kortshagen, U.; Schaller, R. D. On the Origin of Photoluminescence in Silicon Nanocrystals: Pressure-Dependent Structural and Optical Studies. *Nano Lett.* **2012**, *12*, 4200–4205.
- (15) Deal, B. E.; Grove, A. S. General Relationship for the Thermal Oxidation of Silicon. *J. Appl. Phys.* **2004**, *36*, 3770–3778.
- (16) Kovalev, D.; Timoshenko, V. Y.; Künzner, N.; Gross, E.; Koch, F. Strong Explosive Interaction of Hydrogenated Porous Silicon with Oxygen at Cryogenic Temperatures. *Phys. Rev. Lett.* **2001**, *87*, No. 068301.
- (17) Koch, E.-C.; Clément, D. Special Materials in Pyrotechnics: VI. Silicon—An Old Fuel with New Perspectives. *Propellants Explos. Pyrotech.* **2007**, *32*, 205–212.
- (18) Adams, S. K.; Piekiel, N. W.; Ervin, M. H.; Morris, C. J. Silicon quantum dots for energetic material applications. *Appl. Phys. Lett.* **2018**, *112*, 233108.
- (19) Huang, S.; Parimi, V. S.; Deng, S.; Lingamneni, S.; Zheng, X. Facile Thermal and Optical Ignition of Silicon Nanoparticles and Micron Particles. *Nano Lett.* **2017**, *17*, 5925–5930.
- (20) Ranjbar-Navazi, Z.; Omidi, Y.; Eskandani, M.; Davaran, S. Cadmium-free quantum dot-based theranostics. *TrAC Trend Anal. Chem.* **2019**, *118*, 386–400.
- (21) Weinrich, H.; Durmus, Y. E.; Tempel, H.; Kungl, H.; Eichel, R.-A. Silicon and Iron as Resource-Efficient Anode Materials for Ambient-Temperature Metal-Air Batteries: A Review. *Materials* **2019**, *12*, 2134.
- (22) Kortshagen, U. R.; Sankaran, R. M.; Pereira, R. N.; Girshick, S. L.; Wu, J. J.; Aydil, E. S. Nonthermal Plasma Synthesis of

- 1478 Nanocrystals: Fundamental Principles, Materials, and Applications. *1479 Chem. Rev.* **2016**, *116*, 11061–11127.
- 1480 (23) Ishikawa, Y.; Shibata, N.; Fukatsu, S. Fabrication of highly 1481 oriented Si:SiO₂ nanoparticles using low energy oxygen ion 1482 implantation during Si molecular beam epitaxy. *Appl. Phys. Lett.* 1483 **1996**, *68*, 2249–2251.
- 1484 (24) Oda, S.; Nishiguchi, K. Nanocrystalline silicon quantum dots 1485 prepared by VHF plasma enhanced chemical vapor deposition. *J. Phys.* 1486 *IV* **2001**, *11*, Pr3-1065.
- 1487 (25) Bapat, A.; Gatti, M.; Ding, Y.-P.; Campbell, S. A.; Kortshagen, 1488 U. A plasma process for the synthesis of cubic-shaped silicon 1489 nanocrystals for nanoelectronic devices. *J. Phys. D: Appl. Phys.* **2007**, 1490 *40*, 2247.
- 1491 (26) Jariwala, B. N.; Kramer, N. J.; Petcu, M. C.; Bobela, D. C.; 1492 Sanden, M. C. M. v. d.; Stradins, P.; Ciobanu, C. V.; Agarwal, S. 1493 Surface Hydride Composition of Plasma-Synthesized Si Nano- 1494 particles. *J. Phys. Chem. C* **2011**, *115*, 20375–20379.
- 1495 (27) Panthani, M. G.; Hessel, C. M.; Reid, D.; Casillas, G.; José- 1496 Yacamán, M.; Korgel, B. A. Graphene-Supported High-Resolution 1497 TEM and STEM Imaging of Silicon Nanocrystals and their Capping 1498 Ligands. *J. Phys. Chem. C* **2012**, *116*, 22463–22468.
- 1499 (28) Anthony, R.; Kortshagen, U. Photoluminescence quantum 1500 yields of amorphous and crystalline silicon nanoparticles. *Phys. Rev. B* 1501 **2009**, *80*, No. 115407.
- 1502 (29) Kramer, N. J.; Anthony, R. J.; Mamunuru, M.; Aydil, E. S.; 1503 Kortshagen, U. R. Plasma-induced crystallization of silicon nano- 1504 particles. *J. Phys. D: Appl. Phys.* **2014**, *47*, No. 075202.
- 1505 (30) Hernández, S.; Martínez, A.; Pellegrino, P.; Lebour, Y.; Garrido, 1506 B.; Jordana, E.; Fedeli, J. M. Silicon nanocluster crystallization in SiO_x 1507 films studied by Raman scattering. *J. Appl. Phys.* **2008**, *104*, 1508 No. 044304.
- 1509 (31) Kirk, C. T. Quantitative Analysis of the Effect of Disorder- 1510 Induced Mode Coupling on Infrared Absorption in Silica. *Phys. Rev. B* 1511 **1988**, *38*, 1255–1273.
- 1512 (32) Gardelis, S.; Nassiopoulou, A. G.; Mahdouani, M.; Bourguiga, 1513 R.; Jaziri, S. Enhancement and Red Shift of Photoluminescence of 1514 Fresh Porous Si under Prolonged Laser Irradiation or Ageing: Role of 1515 Surface Vibration Modes. *Physica E* **2009**, *41*, 986–989.
- 1516 (33) Mawhinney, D. B.; Glass, J. A., Jr.; Yates, J. T., Jr FTIR Study of 1517 the Oxidation of Porous Silicon. *J. Phys. Chem. B* **1997**, *101*, 1202– 1518 1206.
- 1519 (34) Marra, D. C.; Edelberg, E. A.; Naone, R. L.; Aydil, E. S. Silicon 1520 hydride composition of plasma-deposited hydrogenated amorphous 1521 and nanocrystalline silicon films and surfaces. *J. Vac. Sci. Technol. A* 1522 **1998**, *16*, 3199–3210.
- 1523 (35) Stewart, M. P.; Buriak, J. M. New Approaches toward the 1524 Formation of Silicon–Carbon Bonds on Porous Silicon. *Comm. Inorg.* 1525 *Chem.* **2002**, *23*, 179–203.
- 1526 (36) Holm, J.; Roberts, J. T. Thermal Oxidation of 6 nm Aerosolized 1527 Silicon Nanoparticles: Size and Surface Chemistry Changes. *Langmuir* 1528 **2007**, *23*, 11217–11224.
- 1529 (37) Carroll, G. M.; Limpens, R.; Neale, N. R. Tuning Confinement 1530 in Colloidal Silicon Nanocrystals with Saturated Surface Ligands. 1531 *Nano Lett.* **2018**, *18*, 3118–3124.
- 1532 (38) Winters, B. J.; Holm, J.; Roberts, J. T. Thermal processing and 1533 native oxidation of silicon nanoparticles. *J. Nanopart. Res.* **2011**, *13*, 1534 5473–5484.
- 1535 (39) Rivolo, P.; Geobaldo, F.; Rocchia, M.; Amato, G.; Rossi, A. M.; 1536 Garrone, E. Joint FTIR and TPD study of hydrogen desorption from 1537 p⁺-type porous silicon. *phys. stat. solidi (a)* **2003**, *197*, 217–221.
- 1538 (40) Ogata, Y.; Niki, H.; Sakka, T.; Iwasaki, M. Hydrogen in Porous 1539 Silicon: Vibrational Analysis of SiH_x Species. *J. Electrochem. Soc.* **1995**, 1540 *142*, 195.
- 1541 (41) Mangolini, L.; Kortshagen, U. Plasma-Assisted Synthesis of 1542 Silicon Nanocrystal Inks. *Adv. Mater.* **2007**, *19*, 2513–2519.
- 1543 (42) Henderson, E. J.; Kelly, J. A.; Veinot, J. G. C. Influence of 1544 HSiO_{1.5} Sol-Gel Polymer Structure and Composition on the Size and 1545 Luminescent Properties of Silicon Nanocrystals. *Chem. Mater.* **2009**, 1546 *21*, 5426–5434.
- (43) Matej, Z.; Kadlecová, A.; Janeček, M.; Matějová, L.; Dopita, M.; Kužel, R. Refining bimodal microstructure of materials with MSTRUCT. *Powder Diffr.* **2014**, *29*, S35–S41.
- (44) Baxter, R. J. Percus-Yevick Equation for Hard Spheres with Surface Adhesion. *J. Chem. Phys.* **1968**, *49*, 2770–2774.
- (45) Doucet, M.; Cho, J. H.; Alina, G.; Attala, Z.; Bakker, J.; Bouwman, W.; Bourne, R.; Butler, P.; Cadwallader-Jones, I.; Campbell, K.; Cooper-Benun, T.; Durniak, C.; Forster, L.; Gilbert, P.; Gonzalez, M.; Heenan, R.; Jackson, A.; King, S.; Kienzle, P.; Krzywon, J. et al. *SasView, version 5.0.5, Zenodo*, 2022.
- (46) Thiessen, A. N.; Ha, M.; Hooper, R. W.; Yu, H.; Oliynyk, A. O.; Veinot, J. G.; Michaelis, V. K. Silicon Nanoparticles: Are They Crystalline from the Core to the Surface? *Chem. Mater.* **2019**, *31*, 678–688.
- (47) Zajac, V.; Němec, H.; Kadlec, C.; Kůsová, K.; Pelant, I.; Kužel, P. THz photoconductivity in light-emitting surface-oxidized Si nanocrystals: the role of large particles. *New J. Phys.* **2014**, *16*, No. 093013.
- (48) Stehlík, S.; Mermoux, M.; Schummer, B.; Vanek, O.; Kolarova, K.; Stenclova, P.; Vlk, A.; Ledinsky, M.; Pfeifer, R.; Romanyuk, O.; Gordeev, I.; Roussel-Dherbey, F.; Nemecova, Z.; Henych, J.; Bezdička, P.; Kromka, A.; Rezek, B. Size Effects on Surface Chemistry and Raman Spectra of Sub-5 nm Oxidized High-Pressure High-Temperature and Detonation Nanodiamonds. *J. Phys. Chem. C* **2021**, *125*, 5647–5669.
- (49) Dohnalová, K.; Hapala, P.; Kůsová, K.; Infante, I. Electronic Structure Engineering Achieved via Organic Ligands in Silicon Nanocrystals. *Chem. Mater.* **2020**, *32*, 6326–6337.
- (50) Eaglesham, D. J.; White, A. E.; Feldman, L. C.; Moriya, N.; Jacobson, D. C. Equilibrium shape of Si. *Phys. Rev. Lett.* **1993**, *70*, 1643–1646.
- (51) Marra, D. C.; Edelberg, E. A.; Naone, R. L.; Aydil, E. S. Effect of H₂ dilution on the surface composition of plasma-deposited silicon films from SiH₄. *Appl. Surf. Sci.* **1998**, *133*, 148–151.
- (52) Shinohara, M.; Hara, K.; Takami, Y.; Takaki, Y.; Matsuda, Y.; Fujiyama, H. Infrared Spectroscopic Study on a Reaction of Hydrogen Plasma with Si(110) surface. *Trans. Mater. Res. Soc. Jpn.* **2011**, *36*, 491–494.
- (53) Hadjisavvas, G.; Remediakis, I. N.; Kelires, P. C. Shape and faceting of Si nanocrystals embedded in a-SiO₂: A Monte Carlo study. *Phys. Rev. B* **2006**, *74*, No. 165419.
- (54) Hapala, P.; Kočí, M.; Nicolini, P. *ProkopHapala/FireCore*; GitHub, 2024.
- (55) Rath, C.; Farjas, J.; Roura, P.; Kail, F.; Roca i Cabarrocas, P.; Bertran, E. Thermally Induced Structural Transformations on Polymorphous Silicon. *J. Mater. Res.* **2005**, *20*, 2562–2567.
- (56) Bashouti, M. Y.; Sardashti, K.; Ristein, J.; Christiansen, S. H. Early stages of oxide growth in H-terminated silicon nanowires: determination of kinetic behavior and activation energy. *Phys. Chem. Chem. Phys.* **2012**, *14*, 11877–11881.
- (57) Sailor, M. J.; Lee, E. J. Surface Chemistry of Luminescent Silicon Nanocrystallites. *Adv. Mater.* **1997**, *9*, 783–793.
- (58) Gupta, P.; Colvin, V. L.; George, S. M. Hydrogen desorption kinetics from monohydride and dihydride species on silicon surfaces. *Phys. Rev. B* **1988**, *37*, 8234–8243.
- (59) Gai, Y.; Yi, D.; Ding, Y.; Wang, S.; Qian, G.; Liang, Z. First-Principles Study of the Effect of Surface Heteroatoms on Silane Dissociation. *J. Phys. Chem. C* **2023**, *127*, 20979–20986.
- (60) Ohkura, Y.; Weisse, J. M.; Cai, L.; Zheng, X. Flash Ignition of Freestanding Porous Silicon Films: Effects of Film Thickness and Porosity. *Nano Lett.* **2013**, *13*, 5528–5533.
- (61) Yang, D.-Q.; Meunier, M.; Sacher, E. Room temperature air oxidation of nanostructured Si thin films with varying porosities as studied by X-ray photoelectron spectroscopy. *J. Appl. Phys.* **2006**, *99*, No. 084315.
- (62) Hofmeister, H.; Ködderitzsch, P. Nanosized silicon particles by inert gas arc evaporation. *Nanostruct. Mater.* **1999**, *12*, 203–206.

- 1614 (63) Slipenyuk, A.; Eckert, J. Correlation between enthalpy change
1615 and free volume reduction during structural relaxation of
1616 $Zr_{55}Cu_{30}Al_{10}Ni_5$ metallic glass. *Scripta Materialia* **2004**, *50*, 39–44.
- 1617 (64) Terada, S.; Xin, Y.; Saitow, K.-I. Cost-Effective Synthesis of
1618 Silicon Quantum Dots. *Chem. Mater.* **2020**, *32*, 8382–8392.
- 1619 (65) Antoniadis, H. Silicon Ink high efficiency solar cells. In *34th*
1620 *IEEE Photovoltaic Specialists Conference (PVSC)*; IEEE, 2009; pp.
1621 2091–2095.
- 1622 (66) Khan, M.; Yan, S.; Ali, M.; Mahmood, F.; Zheng, Y.; Li, G.; Liu,
1623 J.; Song, X.; Wang, Y. Innovative Solutions for High-Performance
1624 Silicon Anodes in Lithium-Ion Batteries: Overcoming Challenges and
1625 Real-World Applications. *Nano-Micro Lett.* **2024**, *16*, 179.
- 1626 (67) Li, J.; Su, H.; Liu, Y.; Zhong, Y.; Wang, X.; Tu, J. Li Alloys in
1627 All Solid-State Lithium Batteries: A Review of Fundamentals and
1628 Applications. *Electrochem. Energy Rev.* **2024**, *7*, 18.
- 1629 (68) Klimešová, E.; Kůsová, K.; Vacík, J.; Holý, V.; Pelant, I. Tuning
1630 luminescence properties of silicon nanocrystals by lithium doping. *J.*
1631 *Appl. Phys.* **2012**, *112*, No. 064322.
- 1632 (69) Wang, Z.; Alaniz, J. E.; Jang, W.; Garay, J. E.; Dames, C.
1633 Thermal Conductivity of Nanocrystalline Silicon: Importance of
1634 Grain Size and Frequency-Dependent Mean Free Paths. *Nano Lett.*
1635 **2011**, *11*, 2206–2213.
- 1636 (70) Huang, J.; Li, Q.; Shao, Z. Fabricating highly luminescent solid
1637 hybrids based on silicon nanoparticles: a simple, versatile and green
1638 method. *Nanoscale* **2018**, *10*, 10250–10255.
- 1639 (71) Dohnalová, K.; Ondič, L.; Kůsová, K.; Pelant, I.; Rehspringer, J.
1640 L.; Mafouana, R.-R. White-Emitting Oxidized Silicon Nanocrystals:
1641 Discontinuity in Spectral Development with Reducing Size. *J. Appl.*
1642 *Phys.* **2010**, *107*, No. 053102.
- 1643 (72) Hessel, C. M.; Henderson, E. J.; Veinot, J. G. C. Hydrogen
1644 Silsesquioxane: A Molecular Precursor for Nanocrystalline Si-SiO₂
1645 Composites and Freestanding Hydride-Surface-Terminated Silicon
1646 Nanoparticles. *Chem. Mater.* **2006**, *18*, 6139–6146.
- 1647 (73) Milliken, S.; Thiessen, A. N.; Cheong, I. T.; O'Connor, K. M.;
1648 Li, Z.; Hooper, R. W.; Robidillo, C. J. T.; Veinot, J. G. C. Turning the
1649 dials": controlling synthesis, structure, composition, and surface
1650 chemistry to tailor silicon nanoparticle properties. *Nanoscale* **2021**, *13*,
1651 16379–16404.
- 1652 (74) Kůsová, K. Silicon Nanocrystals: From Indirect to Direct
1653 Bandgap. *Phys. Stat. solidi (a)* **2018**, *215*, No. 1700718.
- 1654 (75) Thiessen, A. N.; Zhang, L.; Oliynyk, A. O.; Yu, H.; O'Connor,
1655 K. M.; Meldrum, A.; Veinot, J. G. C. A Tale of Seemingly "Identical"
1656 Silicon Quantum Dot Families: Structural Insight into Silicon
1657 Quantum Dot Photoluminescence. *Chem. Mater.* **2020**, *32*, 6838–
1658 6846.

Highly spherical SiC nanoparticles grown in nonthermal plasma

Pavel Galář | Jiří Stuchlík | Martin Müller | Jan Kočka | Katerina Kůsová

Department of Thin Films and Nanostructures, Institute of Physics Czech Academy of Sciences, Prague, Czechia

Correspondence

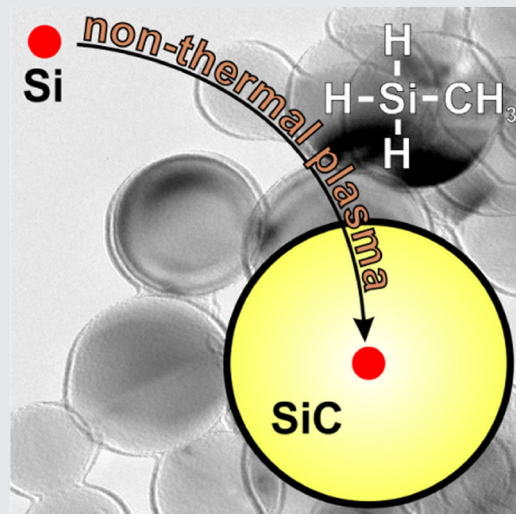
Katerina Kůsová, Department of Thin Films and Nanostructures, Institute of Physics Czech Academy of Sciences, Cukrovarnická 10, 16200 Prague, Czechia.
 Email: kusova@fzu.cz

Funding information

Grantová Agentura České Republiky, Grant/Award Number: 18-05552S; Czech Ministry of Education, Youth and Sports, Grant/Award Number: SOLID21 CZ.02.1.01/0.0/0.0/16_019/0000760

Abstract

Silicon carbide (SiC) nanoparticles have excellent properties and varied possible applications. However, the synthesis of this material usually requires high temperatures due to its high melting point (2730°C). In this study, we report on a synthesis of highly spherical SiC nanocrystals (50–150 nm) using nonthermal plasma, a method not yet widely employed for the synthesis of SiC, but generally very suitable for high-melting-point materials. We perform the synthesis in a two-stage reactor, where Si nanocrystals are synthesized in the first stage and these are used as growth seeds for SiC in the second stage. The Si nanocrystals remain inside the SiC nanoparticles after the synthesis. The produced SiC nanocrystals exhibit yellow-orange naked-eye-visible photoluminescence.



KEY WORDS

nanoparticles, nonthermal plasma, SiC, synthesis

1 | INTRODUCTION

Silicon carbide (SiC), in a bulk or nanostructured form, is a material with unique properties in terms of mechanical hardness and fracture toughness, high chemical stability, high charge carrier mobility, and good thermal transport properties. These favorable properties predestine this material to a very varied usage, ranging from the early abrasive agents to more advanced applications for example in high-power electronics^[1] or in quantum computing.^[2]

Moreover, as a result of the inherently low toxicity and biodegradability of SiC, this material can be advantageous also as a novel anode material in lithium batteries,^[3] for bioimaging (see e.g., Reference [4] and references therein) or even as an immunomodulatory agent.^[5]

The synthesis of bulk crystalline SiC typically requires very high temperatures. Commercially, crystalline SiC is produced via the carbothermic reduction (>1500°C) of quartz sand (SiO₂) by carbon using the same raw materials.^[6] Nanoparticles (NPs) can then be

manufactured from SiC bulk wafers using electrochemical etching, leading to sub-10-nm NPs exhibiting the quantum confinement effect.^[7] This process seemingly avoids the high-temperature stage, but clearly leads to a substantial material loss. Other, more resource-efficient procedures yielding submicron-sized SiC particles include, for example, the microwave sintering of pressed pellets of waste crystalline silicon (1450°C),^[8] an NP analogy of the traditional bulk synthesis via the carburization of SiO₂ NPs (1450°C)^[9] or other materials,^[10] the addition of metal agents such as magnesium during the synthesis (600–700°C),^[11] various types of chemical vapor depositions from tetramethylsilane or methylchlorosilane precursors (>1000°C)^[12,13] or thermal plasmas (>600°C).^[14] SiC NPs can also be synthesized by chemical vapor deposition from Si NPs (1000°C)^[3] and new preparation routes are constantly being reported.^[15,16]

However, the application of highly nonequilibrium nonthermal plasma to the growth of SiC NPs has been investigated only scarcely so far despite its clear potential for the synthesis of nanocrystals of materials with high melting points.^[17] Specifically, carbon-rich amorphous SiC with sizes <10 nm were produced by the decomposition of tetramethylsilane in a gas phase flow reactor induced by low-temperature microwave plasma^[18] and atmospheric pressure microplasmas were also applied to synthesize SiC NPs from tetramethylsilane.^[19–21] Small, 5-nm 3C-SiC NPs were synthesized by the in-flight carburization in C₂H₂/Ar of crystalline Si NPs formed upstream in a tubular flow reactor.^[6] Last, hollow ~20-nm SiC NPs were obtained via a two-step tandem process wherein silicon NPs produced in a nonthermal plasma reactor were carburized in a second methane stage.^[22]

In contrast to the above techniques, we show that it is possible to synthesize 3C-SiC NPs (average size 100 nm) with a carbon-rich surface layer using monomethylsilane (MMS) plasma if upstream-synthesized Si nanocrystals are used as seeds. This procedure does not proceed through the traditional carburization reaction and the Si seeds remain inside the formed SiC NPs after the synthesis. The resulting SiC nanocrystals can be prepared in the form of a thin film, or they can be dispersed in a liquid. The structural and chemical properties of the resulting SiC NPs are confirmed by high-resolution transmission electron microscopy (HRTEM), Fourier-transform Infrared (FTIR), and the selected area electron diffraction (SAED) studies and the produced material exhibits naked-eye observable photoluminescence at about 620 nm.

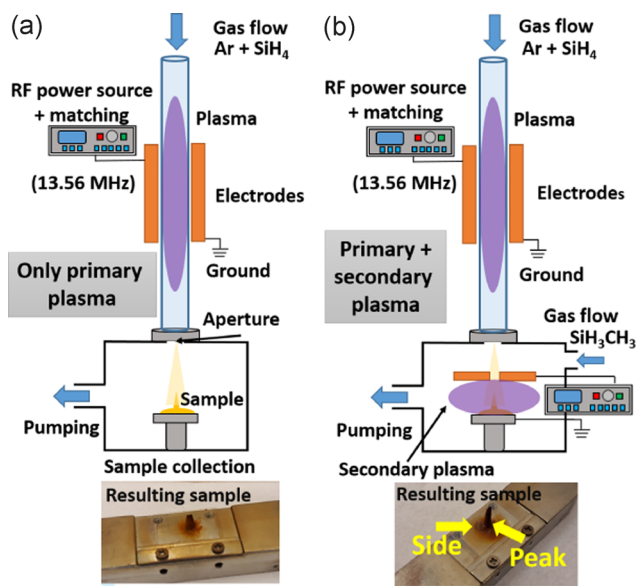


FIGURE 1 Schemes of the apparatus containing a first (glass tube) and a second stage (vacuum chamber) supplemented by the images of the resulting samples. (a) Preparation of the seeding Si nanocrystals and (b) preparation of the silicon carbide nanocrystals. The main conical part (Peak) and the thin side layer (Side) of the sample are highlighted

2 | EXPERIMENTAL

2.1 | The nonthermal plasma system

The syntheses were carried out in a two-stage low-pressure flow-through nonthermal plasma reactor.^[23] The setup is schematically shown in Figure 1. The first stage was made up of a glass tube with an inner diameter of 7 mm. In this glass tube, capacitively coupled plasma was generated using a radiofrequency (RF) power source RFG-600W by Coaxial Power Systems operating at the frequency of 13.56 MHz, coupled to the high-efficiency automatic matching network AMN-600 (Coaxial Power Systems). The plasma region in the glass tube was powered (in contrast to the ring electrodes in Reference [23]) by two rectangular copper electrodes with a size of 3 × 9 cm². The electrodes were placed parallel to the glass tube with the distance slightly exceeding 10 mm so they almost touched the glass tube walls. One of the electrodes was grounded while the other one was powered by the RF generator. The second stage was a standard vacuum chamber, separated from the first stage by an aperture and evacuated by the same vacuum pump system. The second chamber served for the collection of the sample (Figure 1a), but it also enabled the ignition of a second nonthermal plasma using a 13.56-MHz RF

generator (Thamway T161-5068A) coupled to an FM-AM signal generator SG 5155 and a manual T020-5068A matchbox. The plasma in the second stage was generated almost in the whole volume of the chamber and reached the substrate for sample collection (Figure 1b). The second stage had a separate gas mixture input. The collection substrates were kept at room temperature.

2.1.1 | Silane synthesis only

The synthesis was performed from a mixture of 1 sccm of silane as a precursor gas mixed in 150 sccm of argon as a carrier gas in the first stage. The pressure inside the tube rose up to 500 Pa. The power of the RF generator was set to 120 W, which made the plasma region as long as 20 cm. On the basis of these parameters, the estimated residence time of the forming NPs in the plasma was about 15 ms. The synthesized NPs were carried by the gas flow through the aperture to the second chamber where the pressure was approximately one-fifth of that in the glass tube. The sample was collected on a glass substrate placed 10 cm below the aperture in a form of dry powder (Figure 1a). No additional gas or plasma was present in the second stage. Because of the initial gas flow and the pressure gradient between both the stages, the powder formed a compact cone surrounded by a fine layer. The synthesis time was 2 min and the amount of the SiNCs sample ranged from 2 to 3 mg.

2.1.2 | MMS synthesis only/ MMS + silane only

The flow of the MMS was also 1 sccm. In the case of the gas mixture, 0.5 sccm of each gas was used. The remaining experimental conditions were the same as in the case of the silane-only synthesis. A 2-min run of the “MMS synthesis only” experiment provided about 1 mg of powder.

2.1.3 | MMS plasma

In addition to the silane-only synthesis, a small amount of MMS with a flow of 0.7 sccm was introduced to the second-stage vacuum chamber (Figure 1b) where the sample was collected. The second-stage MMS plasma was ignited simultaneously with the first-stage plasma using an RF generator power in the range of 5–25 W. The carrier gas with the synthesized Si nanocrystals flowed through a second plasma stage before the sample collection on the glass substrate. The total pressure of the primary-stage gas

mixed with MMS in the second stage was 100 Pa. The synthesis duration was 2 min, afterward, the primary plasma together with the precursor gas was switched off, and the sample was treated by MMS plasma for up to 10 min.

2.2 | Material analysis

The morphology of the samples was studied using HRTEM and field-effect scanning electron microscopy. The HRTEM images were obtained using Jeol 2200 FS (200 kV). Holey carbon 300 mesh copper grids were used as the support for the NPs. The images of SAED were analyzed using the CrysTBox software^[24] with cell parameters taken from Reference [25]. The SEM images were collected using MAIA3 (TESCAN) with the acceleration voltage of 10 kV and the magnification of $\times 100$ k. The chemical composition of the samples was studied using energy-dispersive spectroscopy (EDS) and FTIR absorption spectroscopy. The EDS was collected using the Bruker Quantax 200 with the 610 XFlash detector with an acceleration voltage of 15 kV. The FTIR analysis was realized in the attenuated total reflectance (ATR) mode using Nicolet iS50 (Thermo Fisher Scientific). The spectra were collected within the range of 400–4000 cm^{-1} , the spectral resolution was 4 cm^{-1} . The data were collected using a DTGS (deuterated triglycine sulfate) detector. The ATR system was equipped with a diamond crystal (Type IIa), the angle of incidence was set to 45°. The use of the diamond substrate caused the presence of low substrate-originating signal within the 2000–2300 cm^{-1} region. A KBr crystal was used as a beam splitter. The powder sample was deposited on the diamond crystal using a pressure tip, which was placed at the same position for every measurement. As the IR signal in the range of 600–2300 cm^{-1} was interpreted only relatively, the data were not corrected for the optical properties of the diamond crystal.

2.3 | Photoluminescence (PL) measurements

Steady-state PL spectra were collected using imaging spectrograph Shamrock 300i (Andor; Oxford Instruments) coupled with an EMCCD camera (Newton 971; Andor, Oxford Instruments). The PL spectra were excited by a continuous-wave HeCd laser at 325 nm. The laser beam intensity was about 3.5 mW. In order to minimize the effect of possible sample inhomogeneities and to avoid potential laser-induced modification of the sample, the nanocrystals were characterized dispersed in toluene (UV/IR Grade, >99.8%, Rotisolv; Carl Roth) in a quartz

cuvette. The dispersion was homogenized in a standard laboratory ultrasonic bath for 20 min before the PL measurements. All collected spectra were corrected for the spectral sensitivity of the whole system. Even though the PL measurements were not absolute, they were always normalized for the absorption of the laser beam in the sample and, therefore, the PL intensity of the individual PL spectra is fully comparable among the individual samples with the margin of error of about 10%.

The PL spectra from Figure 5a were plotted in the “physically correct” axis of photon energies, including the intensity-axis transformation term ($I(\text{eV}) = I(\text{nm})\lambda^2(\text{nm})$).^[26] The spectra were fitted with two Gaussians for the sample treated for 2 min (MMS plasma 2 min), which exhibits two peaks, and one Gaussian for the rest of the samples. The extracted peak positions in eV were then recalculated back into nanometers for easier comparison. Please note that, contrary to intuition, broad PL spectra do exhibit different positions of maxima when plotted in photon energies or wavelengths as a result of the intensity transformation term^[26] and the apparent difference in peak position in Figure 5a and Table 3 is not erroneous. The peak center values from the wavelength-dependent plots are preferred in the text to ease the comparison with other standard wavelength-plotted results.

3 | RESULTS

The performed syntheses and control experiments are summarized in Table 1 and will be discussed in more detail in the following text.

3.1 | MMS as the primary stage precursor gas (MMS synthesis only)

First, we employed a system based on a low-pressure glass-tube flow-through nonthermal reactor, as described in detail in Section 2.1 and shown in Figure 1a. To synthesize SiC

NPs, we use the MMS gas $\text{CH}_3 - \text{SiH}_3$ as a prospective source of a stoichiometric ratio of the silicon and carbon species. The synthesis used 1 sccm of MMS in 150 sccm of argon. The structural (HRTEM) and chemical (FTIR) analyses of the resulting sample are presented in Figures 2a and 3a. The HRTEM characterization points to the presence of irregular structures in the produced sample with a few spherical structures without a clear presence of crystals. The FTIR spectra are dominated by a broad band located at about 830 cm^{-1} . This spectral region is typical of Si-C bonds;^[27] however, the fact that the band is broad and featureless implies that the resulting structure is amorphous.^[27] Thus, this simple nonthermal plasma synthesis produces SiC NPs, but these are not crystalline.

3.2 | Silane in the primary stage precursor gas (silane synthesis only)

Reactors such as the one described in Section 3.1 are typically used for the nonthermal plasma synthesis of the nanocrystals of silicon.^[17,23,28] To confirm the operation of the system, we used it to synthesize silicon nanocrystals using 1 sccm of silane as a precursor gas mixed in 150 sccm of argon as a carrier gas. The resulting powder forms a conical deposit on the collection substrate (Figure 1a). HRTEM analysis of the produced sample in Figure 2b clearly shows the presence of crystalline particles with sizes of about 8 nm (a larger field of view is shown in Figure S1, a more detailed image of the crystalline NPs in Figure S2). Moreover, the FTIR spectrum in Figure 3b is composed of bands typical for the as-prepared nonthermal plasma nanocrystals,^[28] confirming the originally hydrogen-terminated and subsequently oxidized surface. In particular, the spectrum is dominated by peaks related to the Si-H bonds at 627 and 665 cm^{-1} , Si-H₂ bonds at 856 and 903 cm^{-1} , and Si-O-Si bonds at 1060 cm^{-1} bands, a broad band containing the contributions of various Si-Hx species ranging from 2060 to 2150 cm^{-1} and a weak peak of Si-OH at 962 cm^{-1} .

TABLE 1 Summary of the performed syntheses and their main parameters (source of silicon atoms and the power of RF generated)

Label	First stage	Second stage	Outcome
MMS synthesis only	MMS, 120 W	Sample collection	Amorphous SiC
Silane synthesis only	Silane, 120 W	Sample collection	Si nanocrystals (8 nm)
MMS plasma (side/peak)	Silane, 120 W	MMS, 25 W	SiC nanocrystals (50–150 nm)
MMS gas	Silane, 120 W	MMS, discharge off	Si nanocrystals (8 nm)
Silane + MMS	Silane + MMS, 120 W	Sample collection	Nonstructured powder, carbon clusters

Structural properties of the resulting nanoparticle are also presented.

Abbreviations: MMS, monomethylsilane; RF, radiofrequency; SiC, silicon carbide.

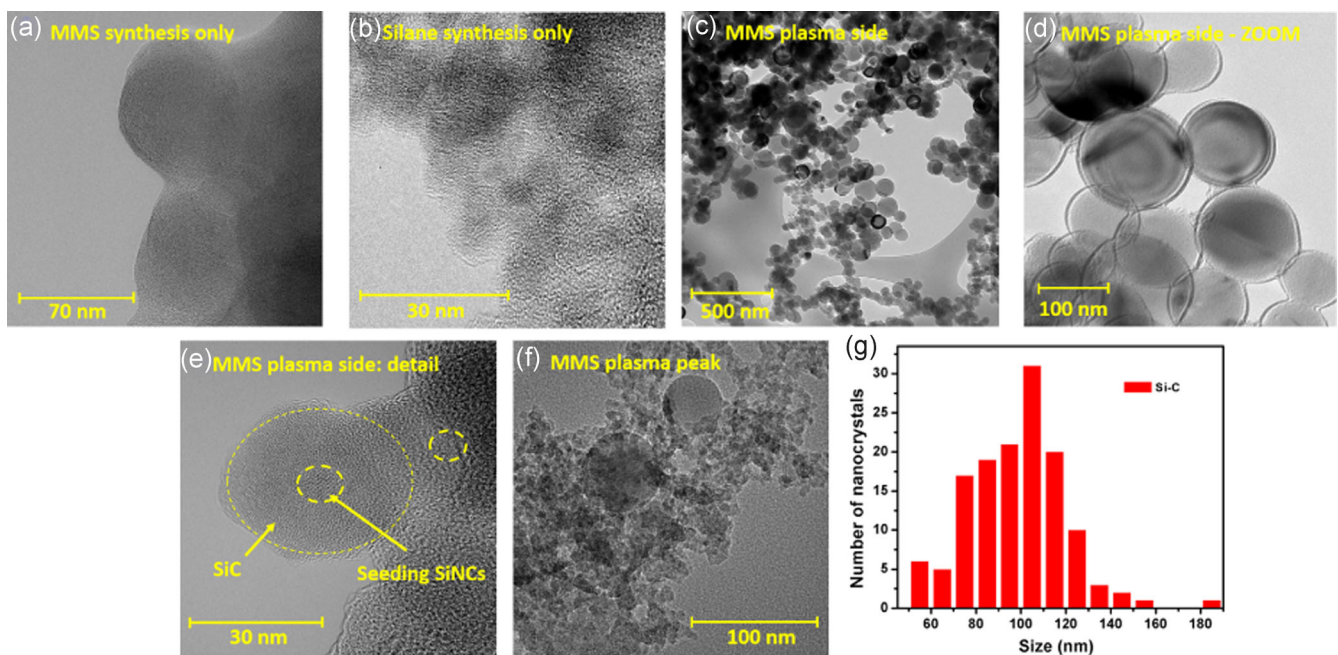


FIGURE 2 (a-f) Transmission electron microscopy (TEM) images of the products of the performed syntheses, synthesis conditions for the individual panels are listed in Table 1. (e) A higher-resolution detail of panel (c), which displays an SiC nanocrystal small enough for the inner Si nanocrystal to be visualized. (g) A histogram of the sizes of the formed SiC nanoparticles based on TEM measurements of approximately 150 nanoparticles

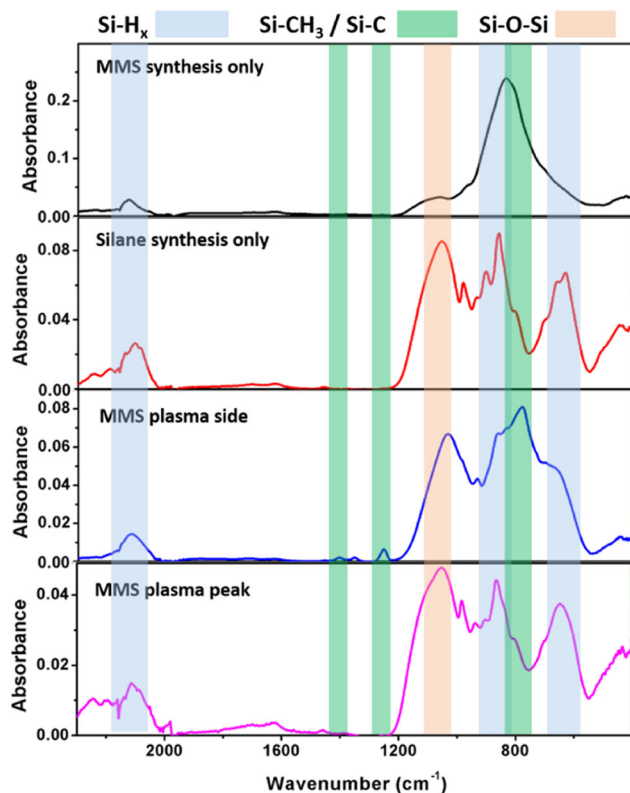


FIGURE 3 Fourier transform infrared analysis of the synthesis products. The synthesis conditions for the individual panels are listed in Table 1 (the “MMS plasma” samples were treated in MMS for 10 minutes)

TABLE 2 Assignment of the Fourier-transform infrared peaks from Figure 3, including the references

Peak (cm ⁻¹)	Interpretation	Reference
627	Si-H bend	[29]
665	Si-H wagg	[29]
770–790	Si-C	[30]
802	Si-O	[31,32]
830	Si-C amorph	[27]
856	Si-H ₂ wagg	[32–34]
903	Si-H ₂ stretch	[29,34,35]
930	Si-C	[36]
962	Si-OH	[27]
980	Si-O-Si	[27]
1030	Si-O-C	[37,38]
1062	Si-O-Si	[31,33]
1250	Si-CH ₃	[30,37,39]
1344	CH ₃	[27]
1392	Si-CH ₃	[37,39]
2080	Si-H	[35,40]
2101	Si-H ₂	[35,40]
2138	Si-H ₃	[35,40]
2242	–O _y Si–H _x	[32,33]

(see also Table 2 for the assignment of the peaks and the corresponding references).

The crystalline nature of the sample was confirmed using selected-area electron diffraction (SAED) measurements presented in Figure 4a. The diffraction rings are typical diffraction patterns of an ensemble of very

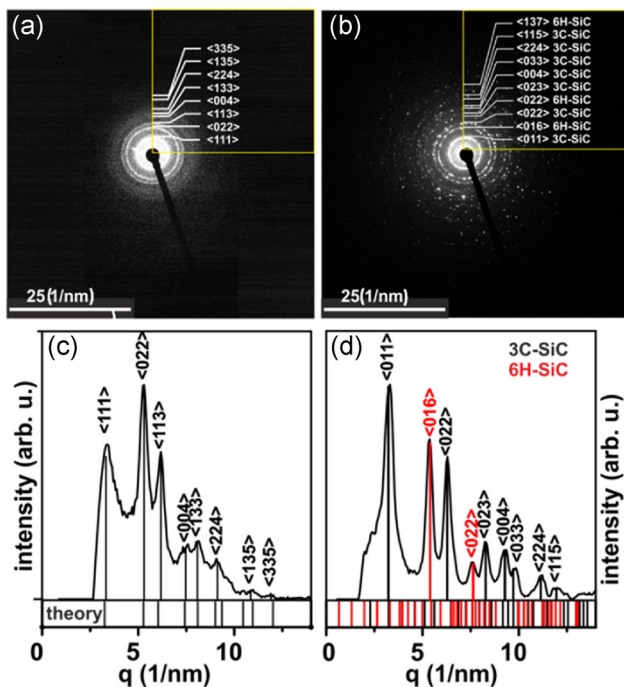


FIGURE 4 Selected area electron diffraction pattern of (a) the “silane synthesis only” and (b) the “monomethylsilane plasma side” samples. (c,d) Radially averaged plots with indexed peaks. The bottom parts of the two panels present the theoretical positions of peaks of the corresponding bulk materials

small, randomly oriented NPs and their positions can be indexed based on the structure of crystalline Si, as evidenced in Figure 4c. Moreover, the crystalline silicon NPs exhibit a broad PL band located at around 930 nm (see Figure 5a) which is a characteristic of this size of silicon nanocrystal.^[41] There was no difference between the part of the sample inside the central cone of the deposit and in the fine layer surrounding it, implying that the whole sample is composed of Si nanocrystals.

3.3 | MMS plasma in the second stage, SiNCs as seeds (MMS plasma)

After the unsuccessful attempt at the direct nonthermal plasma synthesis of crystalline SiC NPs in Section 3.1, we used Si nanocrystals as seeds. The vacuum chamber stage of the reactor was used only for the collection of the sample in the preceding experiments. In this experiment, as presented in Figure 1b, the vacuum chamber was utilized as a second stage, for a mild MMS plasma treatment of the Si nanocrystals synthesized in the first-stage flow-through glass tube using the conditions of the “silane only” experiment. The natural conical shape of the sample deposit (see the photo in Figure 1b) allows for a simple reference of the influence of the second-stage plasma treatment. The powder in the bulk of the central “heap” is protected from the MMS plasma treatment, therefore a lesser effect is expected, whereas the fine layer surrounding the conical structure will be exposed to the MMS plasma homogeneously, resulting in a more profound influence. Therefore, these two parts were

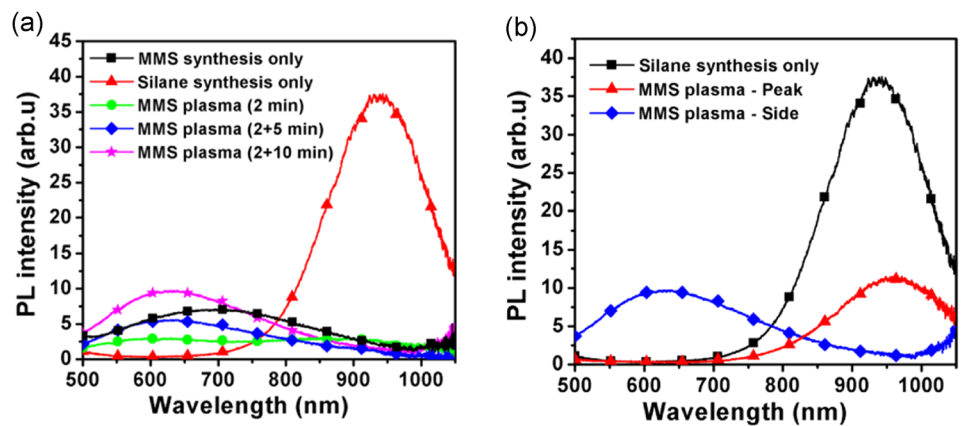


FIGURE 5 The PL spectra of the products of the syntheses. The syntheses conditions for the individual curves are listed in Table 1. The “MMS plasma” samples in (a) were taken from the “side” part and treated in MMS plasma for 2 min with an additional after-treatment for 5 and 10 min, as listed in parentheses. The “MMS plasma” sample shown in (b) was treated for (2 + 10 min). The PL was excited by continuous beam excitation at 325 nm with the intensity of 3.5 mW, the produced powder was dispersed in toluene. The spectra were corrected for the spectral sensitivity of the system

characterized separately and will be referred to as “peak” and “side,” respectively. The difference in the effect of the secondary plasma on these two parts of the sample was evident even by a simple naked-eye observation when the “side” layer of the sample changed its ambient lighting color from brown to sage green.

HRTEM analysis of the “MMS plasma” sample in the “side” layer showed that the MMS plasma led to a growth of relatively large NPs (Figure 2c,d), with sizes ranging from approximately 50 to 150 nm and surprisingly regular spherical shape. The corresponding size histogram is presented in Figure 2g. Furthermore, the Si nanocrystals did not disappear during the growth of the spheres, but they stayed in the center of the shell material (Figure 2e). While the part of the sample from the “side” fine layer around the peak was composed nearly entirely of these spheres, only a few such spheres were detected in the volume of the central “peak” part (Figure 2f). The structural difference between the two regions of the sample is also evident from a larger electron-microscopy image (Figure S1B,C), where the presence of the spheres in the “side” sample leads to a “fluffier,” more cauliflower-like structure.

As shown in Figure 3c,d, the “MMS plasma” sample showed a reduction of the FTIR bands connected with the surface of Si nanocrystals, namely lowered Si–H_x-related bonds and the total quenching of Si–OH. On the contrary, an increase in the signal related to Si–C at 770–790 (LO) and 930 cm⁻¹ (TO), Si–CH₃ at 1250 and 1390 cm⁻¹, CH₃ at 1344 cm⁻¹ was detected. In contrast to the “MMS synthesis only” sample, the LO SiC band is structured and its splitting into two bands at 780 and 830 cm⁻¹ could be indicative of a small-size crystalline SiC structure.^[10] Thus, the synthesized spheres are mostly made up of SiC. The predominantly SiC composition of the “side” sample is confirmed also by EDS elemental analysis (Figure S3), where the carbon content increases in the “side” sample even when compared to the “peak” sample. The shift of the Si–O–Si FTIR broad band in the “silane synthesis only” experiment toward lower wavenumbers in the “MMS plasma” synthesis can then be interpreted as the formation of Si–O–C bonds, commonly observed at around 1030 cm⁻¹. This band, together with the Si–CH₃ bonds, is most likely responsible for a thin amorphous structure surrounding the synthesized SiC NPs evident in HRTEM images (Figure 2d).

The crystalline nature of the synthesized SiC NPs was confirmed by SEAD measurements, see Figure 4b. The circularly arranged dots are a typical pattern for an ensemble of larger, randomly oriented crystalline NPs. The radially averaged profile of the SAED pattern (Figure 4d) can be indexed to the diffraction lines of the β (3C)

polytype of SiC, mainly due to the $\langle 004 \rangle$ and $\langle 033 \rangle$ diffraction peaks, which are present in a region with no lines in the α (6H, 4H, 2H) polytypes (see the theoretical positions of the lines included as a bottom panel in Figure 4b). However, the addition of the 6H-SiC polytype to the analysis improved the fitted positions of two identified peaks (see Figure 4d), and therefore, the presence of this phase cannot be excluded. On the contrary, the diffraction lines of the 4H-SiC polytype clearly did not match the measured diffraction pattern.

The growth of the SiC nanocrystals also alters the original PL of the Si nanocrystal seeds: the original Si-originating PL peak is quenched, while a new PL peak located at approximately 620 nm appears, see Figure 5. To identify the origin of the rising PL peak, the PL spectra were fitted with Gaussian curves. The results of this analysis are summarized in Table 3. First, the secondary MMS plasma treatment, which was on only for the duration of the primary silane plasma (2 min) led to a PL spectrum containing both the PL peaks (see Figure S4). Whereas the Si-originating IR peak slightly blueshifts in comparison with the “silane only” sample, the newly arising PL peak stays roughly at the same position and increases in intensity with the prolongation of the MMS treatment (2 + 5 and 2 + 10 min). This gradual increase without a change in position is one indicator that the new visible PL peak comes from the growing SiC NPs. Moreover, the visible SiC-originating PL is broader than the Si-originating IR one (about 2 \times), further corroborating the different origins of the two peaks. The tendency toward broader peak widths during the shortest MMS treatment (2 min) then suggests that in its initial stages, the MMS treatment causes a higher degree of disorder in the material. Also, as expected, the MMS plasma affected only the PL of the “side” part of the sample (Figure 5b, please note that the PL is measured in

TABLE 3 Analysis of the data from Figure 5a

MMS	Center (eV)	Center (nm)	Intensity (a.u.)	Width (meV)
Silane only	1.306 ± 0.001	~950	13.4 ± 0.1	104 ± 1
2 min	1.346 ± 0.003	~920	0.69 ± 0.09	170 ± 8
	1.842 ± 0.042	~673	1.28 ± 0.13	430 ± 40
(2 + 5) min	1.827 ± 0.003	~678	2.16 ± 0.02	362 ± 3
(2 + 10) min	1.85 ± 0.001	~670	3.55 ± 0.01	348 ± 1

Note: The PL spectra plotted in photon energies were fitted with Gaussians and the peak centers (the column Center [eV]), widths (the column Width [meV]), and areas (the column Intensity [a.u.]) were extracted. The listed errors are 95% confidence bands of the fits. The fitted peak position is recalculated into nanometers for easier comparison (the column Center [nm]). The recalculation of the spectrum into photon energies naturally leads to shifted positions of peaks.^[26]

the form of a dispersion of SiC nanocrystals, and therefore the bulk of the “peak” part is probed by this measurement).

The significant reduction of the Si-seed-originating IR PL peak in the “MMS plasma” sample is an additional confirmation of the growth of SiC nanocrystals, as the thick SiC layer of the NP effectively screens off the laser excitation signal from the Si seed. First, comparing the bulk absorption coefficients of Si and SiC as the basic characterization of the material absorption cross-section ($\alpha_{325\text{nm}}^{\text{Si}} = 1.2 \times 10^6 \text{ cm}^{-1} = 0.12 \text{ nm}^{-1}$, $\alpha_{325\text{nm}}^{\text{3C-SiC}} = 3.7 \times 10^4 \text{ cm}^{-1} = 3.7 \times 10^{-4} \text{ nm}^{-1}$ ^[42]) confirms that silicon generally absorbs excitation much more efficiently ($\alpha_{325\text{nm}}^{\text{Si}} \approx 320\alpha_{325\text{nm}}^{\text{3C-SiC}}$) as a result of the very wide direct bandgap of SiC (6 eV). However, in contrast to bulk materials, the absorption cross-section in NPs is volume-weighted.^[43] The Si:SiC volume ratio in a 100-nm SiC NP with an 8-nm Si seed is 1:2000. Factoring the volume weighting into the solely material-based absorption reverses the absorption ratio ($\alpha_{325\text{nm}}^{\text{Si(8nm)}} \approx 1/6\alpha_{325\text{nm}}^{\text{3C-SiC(92nm)}}$). Last, considering a simple one-dimensional approximation of the 8-nm Si seed being in the middle of 100-nm SiC and the bulk absorption coefficients, the integration of the Lambert–Beer’s law produces another factor of only 10% of the excitation being absorbed in the Si seed. Combined together, these factors give the estimate of at most 2% of the excitation light being absorbed in Si. Consequently, the signal emitted by the seeding Si nanocrystals has to be lowered accordingly.

SiC is a material with a fundamental indirect bandgap of 2.36 eV (525 nm) at room temperature.^[44] The sizes of the synthesized SiC nanocrystals are clearly far too large to impart a quantum confinement effect (the Bohr radius for 3C-SiC is 2.0 nm^[19]) and the observed SiC PL thus, in agreement with Table 3, cannot be tuned by the size of the nanocrystal. Being situated inside the bandgap,^[19] the observed PL is surface-induced. A hint toward the origin of the observed PL is given by the position of the observed peak, which is typical of the 3C-SiC polytype with Si–O bonds.^[4,10,45] This red PL is in contrast to the PL of the “MMS only” sample with a broad band centered at longer wavelengths (700 nm), which very likely originates in amorphous SiC (a broad band at 650 nm) and/or carbon clusters (750 nm).^[45]

3.4 | Control experiments

In addition to the above-described syntheses, we performed two control experiments to verify that the “MMS plasma” conditions are ideal for the synthesis of spherical SiC NPs. As confirmed by the FTIR and PL

measurements presented in Figures S5 and S6, neither the treatment of the Si nanocrystal seeds in nonionized MMS plasma nor the synthesis carried out using both silane and MMS as the primary gas yield SiC NPs. The former synthesis results in Si nanocrystals with a worse surface passivation layer for PL, while the latter yields most probably carbon clusters.

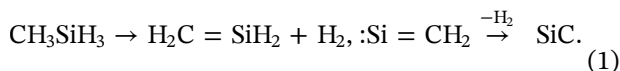
4 | DISCUSSION

Both the first-stage and the second-stage plasma were switched on at the same time and, therefore, during the synthesis, the Si seeds were potentially affected by the MMS plasma in two ways: (i) during the flight through the second-stage vacuum chamber and (ii) after being deposited on the substrate. The effect of the duration of the exposition of the “MMS plasma” sample to the MMS plasma documented in Figure 5 has two important implications. First, the growth of the SiC nanocrystals clearly does not proceed during the flight of the sample through the MMS plasma (which is a very short time interval, units of ms), but during the following treatment on the substrate after the collection of the sample. Second, the plasma cannot effectively penetrate the compact cone and only the upper layer of the cone is affected by the MMS plasma. Thus, our synthesis method is well suited for the production of a thin layer of SiC nanocrystals.

A very interesting aspect of the proposed synthesis is the fact that the Si nanocrystals remain inside the SiC NPs after the synthesis. Usually, the growth of SiC proceeds via the carburization of crystalline Si into SiC, which is how small 3C-SiC nanocrystals^[6] or larger hollow SiC nanocrystals^[22] were formed. In our synthesis, the Si nanocrystals clearly act as seeds, in parallel to the seeded growth of nanodiamond layers.^[46] However, as is evident from Table 3, the Si-originating PL undergoes a blueshift in the initial stages of the MMS treatment. This observation suggests that the seeding Si nanocrystals decrease their size to a small extent. The shift (as deduced from the wavelength-intensity plots) from about^[41] 8 to 7 nm, indicating that the outer part of the Si nanocrystal is consumed in the initial stage of SiC growth.

Factors that contribute to the possibility of the seed mode of growth are the high reactivity of the surface Si–H bonds of the Si seeds and the relatively mild conditions in the nonthermal MMS plasma where most of the energy is provided by highly mobile electrons. Moreover, we chose a chemically relatively simple MMS gas as a prospective source of Si and C in roughly stoichiometric ratio. In contrast to our approach, for

example, the study producing hollow SiC NPs^[22] employed Si nanocrystals as the source of silicon and methane as the source of carbon. Moreover, a study of the reactions pathways of the more commonly used tetramethylsilane precursor^[12] confirms that a wide variety of reaction pathways are possible in tetramethylsilane due to isomerization steps. MMS, on the contrary, constitutes only one of the branches in this pathway scheme, which leads directly to SiC via the Si=CH₂ species^[12,47]:



Thus, the use of the MMS gas prevents the formation of other, competing phases, resulting in the growth of perfectly spherical 3C–SiC nanospheres with amorphous, carbon-rich shell.

5 | CONCLUSION

We report on a two-stage nonthermal plasma synthesis of highly spherical 3C–SiC nanocrystals (50–150 nm). In the synthesis, Si nanocrystals synthesized in the first stage in a silane plasma are deposited onto a substrate in the form of a thin layer and undergo nonthermal plasma treatment in MMS. During this treatment, Si nanocrystals act as seeds for the growth of highly spherical SiC nanocrystals.

ACKNOWLEDGMENTS

The authors thank Asst. Prof. Alena Michalcová for the electron-microscopy images. The Czech Science Foundation funding (Grant no. 18-05552S) and the Operational Programme Research, Development, and Education financed by European Structural and Investment Funds and the Czech Ministry of Education, Youth and Sports (Project no. SOLID21 CZ.02.1.01/0.0/0.0/16_019/0000760) are also gratefully acknowledged.

DATA AVAILABILITY STATEMENT

The data that support the findings of this study are available from the corresponding author upon reasonable request.

REFERENCES

- [1] C. R. Eddy, D. K. Gaskill, *Science* **2009**, *324*, 1398. <https://Science.Scienmag.org/content/324/5933/1398>
- [2] V. A. Soltamov, A. A. Soltamova, P. G. Baranov, I. I. Proskuryakov, *Phys. Rev. Lett.* **2012**, *108*, 226402. <https://doi.org/10.1103/PhysRevLett.108.226402>
- [3] T. Sri Devi Kumari, D. Jeyakumar, T. Prem Kumar, *RSC Adv.* **2013**, *3*, 15028. <https://doi.org/10.1039/C3RA40798E>
- [4] F. Chen, E. R. Zhao, T. Hu, Y. Shi, D. J. Sirbuly, J. V. Jokerst, *Nanoscale Adv.* **2019**, *1*, 3514. <https://doi.org/10.1039/C9NA00237E>
- [5] T. Bělinová, I. Machová, D. Beke, A. Fučíková, A. Gali, Z. Humlová, J. Valenta, M. Hubálek Kalbáčová, *Nanomaterials* **2020**, *10*, 573. <https://doi.org/10.3390/nano10030573>
- [6] R. P. Chaukulkar, K. de Peuter, J. A. Ghodes, S. Pylypenko, J. E. Cloud, Y. Yang, P. Stradins, S. Agarwal, *Mater. Res. Express* **2015**, *2*, 015019. <https://doi.org/10.1088/2053-1591/2/1/015019>
- [7] X. L. Wu, J. Y. Fan, T. Qiu, X. Yang, G. G. Siu, P. K. Chu, *Phys. Rev. Lett.* **2005**, *94*, 026102. <https://doi.org/10.1103/PhysRevLett.94.026102>
- [8] M. Zhao, M. Johnson, W. He, G. Li, C. Zhao, J. Huang, H. Zhu, *Powder Technol.* **2017**, *322*, 290. <https://doi.org/10.1016/j.powtec.2017.09.024>
- [9] G. Meng, Z. Cui, L. Zhang, F. Phillip, *J. Cryst. Growth* **2000**, *209*, 801. <https://www.sciencedirect.com/science/article/pii/S0022024899004352>
- [10] K. J. Kim, S. Lee, J. H. Lee, M.-H. Roh, K.-Y. Lim, Y.-W. Kim, *J. Am. Ceram. Soc.* **2009**, *92*, 424. <https://doi.org/10.1111/j.1551-2916.2008.02913.x>
- [11] M. Dasog, L. F. Smith, T. K. Purkait, J. G. C. Veinot, *Chem. Commun.* **2013**, *49*, 7004. <https://doi.org/10.1039/C3CC43625J>
- [12] X. Liu, J. Zhang, A. Vazquez, D. Wang, S. Li, *Phys. Chem. Chem. Phys.* **2018**, *20*, 18782. <https://doi.org/10.1039/C8CP02626B>
- [13] X. Yang, F. Zhang, Y. You, M. Guo, Y. Zhong, P. Wang, J. Lin, Z. Zhu, L. Zhu, *J. Eur. Ceram. Soc.* **2019**, *39*, 4495. <https://www.sciencedirect.com/science/article/pii/S0955221919305096>
- [14] S.-M. Oh, M. Cappelli, D.-W. Park, *Korean J. Chem. Eng.* **2002**, *19*, 903. <https://doi.org/10.1007/BF02706987>
- [15] G. Károlyházy, D. Beke, D. Zalka, S. Lenk, O. Krafcsik, K. Kamarás, Á. Gali, *Nanomaterials* **2020**, *10*, 538. <https://doi.org/10.3390/nano10030538>
- [16] S. Li, J. Zhou, H. He, Z. Peng, S. Chatterjee, F. Liang, *J. Fluoresc.* **2020**, *30*, 151. <https://doi.org/10.1007/s10895-019-02480-3>
- [17] U. R. Kortshagen, R. M. Sankaran, R. N. Pereira, S. L. Girshick, J. J. Wu, E. S. Aydil, *Chem. Rev.* **2016**, *116*, 11061. <https://doi.org/10.1021/acs.chemrev.6b00039>
- [18] H. Lin, J. A. Gerbec, M. Sushchikh, E. W. McFarland, *Nanotechnology* **2008**, *19*, 325601. <https://doi.org/10.1088/0957-4484/19/32/325601>
- [19] S. Askari, A. UlHaq, M. Macias-Montero, I. Levchenko, F. Yu, W. Zhou, K. K. Ostrikov, P. Maguire, V. Svrcek, D. Mariotti, *Nanoscale* **2016**, *8*, 17141. <https://doi.org/10.1039/C6NR03702J>
- [20] J. McKenna, J. Patel, S. Mitra, N. Soin, V. Svrcek, P. Maguire, D. Mariotti, *Eur. Phys. J. Appl. Phys.* **2011**, *56*, 24020. <https://doi.org/10.1051/epjap/2011110203>
- [21] A. U. Haq, P. Lucke, J. Benedikt, P. Maguire, D. Mariotti, *Plasma Processes Polym.* **2020**, *17*, 1900243. <https://doi.org/10.1002/ppap.201900243>
- [22] D. Coleman, T. Lopez, O. Yasar-Inceoglu, L. Mangolini, *J. Appl. Phys.* **2015**, *117*, 193301. <https://doi.org/10.1063/1.4919918>

- [23] M. Müller, P. Galář, J. Stuchlík, J. Kočka, J. Kupka, K. Kůsová, *Eur. Phys. J. Appl. Phys.* **2020**, *89*, 20401. <https://doi.org/10.1051/epjap/2020190263>
- [24] M. Klinder, *Crystbox—Crystallographic Toolbox*, Institute of Physics of the Czech Academy of Sciences, Prague, Czechia **2015**.
- [25] The Springer Materials website. <https://materials.springer.com>, (accessed: June 2021).
- [26] Y. Wang, P. Townsend, *J. Lumin.* **2013**, *142*, 202. <http://www.sciencedirect.com/science/article/pii/S0022231313001920>
- [27] E. L. H. Thomas, S. Mandal, Ashek-I-Ahmed, J. E. Macdonald, T. G. Dane, J. Rawle, C.-L. Cheng, O. A. Williams, *ACS Omega* **2017**, *2*, 6715. <https://doi.org/10.1021/acsomega.7b00866>
- [28] O. Yasar-Inceoglu, T. Lopez, E. Farshihagro, L. Mangolini, *Nanotechnology* **2012**, *23*, 255604. <https://doi.org/10.1088/0957-4484/23/25/255604>
- [29] P. Kumar, P. Huber, *J. Phys. D: Appl. Phys.* **2007**, *40*, 2864. <https://doi.org/10.1088/0022-3727/40/9/030>
- [30] L. M. Johnson, L. Gao, C. W. Shields IV, M. Smith, K. Efimenko, K. G. Cushing, J. Genzer, G. P. Lopez, *J. Nanobiotechnol.* **2013**, *11*, 22. <https://doi.org/10.1186/1477-3155-11-22>
- [31] C. T. Kirk, *Phys. Rev. B* **1988**, *38*, 1255. <https://doi.org/10.1103/PhysRevB.38.1255>
- [32] S. Gardelis, A. G. Nassiopoulou, M. Mahdouani, R. Bourguiga, S. Jaziri, *Physica E* **2009**, *41*, 986. <http://doi.org/10.1016/j.physe.2008.08.021>
- [33] D. B. Mawhinney, J. A. Glass Jr., J. T. Yates Jr., *J. Phys. Chem. B* **1997**, *101*, 1202. <https://doi.org/10.1021/jp963322r>
- [34] D. Kar, D. Das, *J. Mater. Chem. A* **2013**, *1*, 14744. <https://doi.org/10.1039/C3TA12878D>
- [35] D. Xu, L. Sun, H. Li, L. Zhang, G. Guo, X. Zhao, L. Gui, *New J. Chem.* **2003**, *27*, 300. <https://doi.org/10.1039/B204359A>
- [36] W. Li, Q. Jia, D. Yang, X. Liu, *Materials* **2018**, *11*, 766. <https://doi.org/10.3390/ma11050766>
- [37] G. Socrates, *Infrared and Raman Characteristic Group Frequencies: Tables and Charts*, 3rd ed., John Wiley & Sons, Ltd, Chichester, NY **2001**.
- [38] J. E. Bateman, R. D. Eagling, B. R. Horrock, A. Houlton, *J. Phys. Chem. B* **2000**, *104*, 5557. <https://doi.org/10.1021/jp000080t>
- [39] C. A. Canaria, I. N. Lees, A. W. Wun, G. M. Miskelly, M. J. Sailor, *Inorg. Chem. Commun.* **2002**, *5*, 560. [https://doi.org/10.1016/S1387-7003\(02\)00465-3](https://doi.org/10.1016/S1387-7003(02)00465-3)
- [40] L. M. Wheeler, N. C. Anderson, P. K. B. Palomaki, J. L. Blackburn, J. C. Johnson, N. R. Neale, *Chem. Mater.* **2015**, *27*, 6869. <https://doi.org/10.1021/acs.chemmater.5b03309>
- [41] K. Kůsová, L. Ondič, E. Klimešová, K. Herynková, I. Pelant, S. Daniš, J. Valenta, M. Gallart, M. Ziegler, B. Hönerlage, P. Gilliot, *Appl. Phys. Lett.* **2012**, *101*, 143101. <https://doi.org/10.1063/1.4756696>
- [42] S. G. Sridhara, T. J. Eperjesi, R. P. Devaty, W. J. Choyke, *Mater. Sci. Eng. B* **1999**, *61–62*, 229. [https://doi.org/10.1016/S0921-5107\(98\)00508-X](https://doi.org/10.1016/S0921-5107(98)00508-X)
- [43] J. Valenta, M. Greben, Z. Remeš, S. Gutsch, D. Hiller, M. Zacharias, *Appl. Phys. Lett.* **2016**, *108*, 023102. <http://scitation.aip.org/content/aip/journal/apl/108/2/10.1063/1.4939699>
- [44] T. Kimoto, J. A. Cooper, *Appendix C: Major Physical Properties of Common SiC Polytypes*, John Wiley & Sons, Ltd, **2014**, pp. 521–524. <https://doi.org/10.1002/9781118313534.app3>
- [45] A. Kassiba, M. Makowska-Janusik, J. Bouclé, J. F. Bardeau, A. Bulou, N. Herlin-Boime, *Phys. Rev. B* **2002**, *66*, 155317. <https://doi.org/10.1103/PhysRevB.66.155317>
- [46] S. Mandal, *RSC Adv.* **2021**, *11*, 10159. <https://doi.org/10.1039/D1RA00397F>
- [47] B. A. Sawrey, H. E. O'Neal, M. A. Ring, D. Coffey Jr., *Int. J. Chem. Kinet.* **1984**, *16*, 7. <https://doi.org/10.1002/kin.550160104>

SUPPORTING INFORMATION

Additional supporting information may be found in the online version of the article at the publisher's website.

How to cite this article: P. Galář, J. Stuchlík, M. Müller, J. Kočka, K. Kůsová. Highly spherical SiC nanoparticles grown in nonthermal plasma. *Plasma Processes Polym.* **2022**;19:e2100127. <https://doi.org/10.1002/ppap.202100127>



Cite this: *Green Chem.*, 2021, **23**, 898

Non-thermal pulsed plasma activated water: environmentally friendly way for efficient surface modification of semiconductor nanoparticles†

Pavel Galář, *^a Josef Khun, ^b Anna Fučíková, ^c Kateřina Dohnalová, ^d Tomáš Popelář, ^a Irena Matulková, ^e Jan Valenta, ^c Vladimír Scholtz^b and Kateřina Kůsová ^a

Semiconductor nanoparticles proved to be an important material in the composition of modern technologies. The most important properties which shape these nanoparticles include not only their atomic composition and size, but also surface chemistry. Here, we present an environmentally friendly method of their surface modification. The proposed method does not require any possibly toxic chemicals, it relies solely on the use of water and air and an inexpensive plasma-generating system. Water treated by discharge is known to produce the so-called plasma-activated water, containing a complex mixture of water- and air-originating reactive species. We show that water treated by transient spark discharge in a vessel with restricted air flow leads to a novel chemical composition of plasma activated water, beneficial for the modification of the surface of nanoparticles. After the treatment of silicon nanoparticles with our plasma activated water, their photoluminescence quantum yield increases several times and their dispersibility in water is significantly improved. The modification is stable at laboratory conditions for at least several weeks and when the liquid is dried out from the sample. We demonstrate that the modification is caused by surface incorporation of nitrate-water complexes, which subsequently leads to a change of surface-oxide-related strain affecting the charge carrier radiative rates. The general applicability of the method is confirmed using commercial MgO and ZnO nanoparticles. Thus, the proposed method enables chemicals-free surface modification of nanoparticles and opens the door for a wide range of variations based on different liquids and discharge parameters.

Received 30th July 2020,
Accepted 16th December 2020

DOI: 10.1039/d0gc02619k
rsc.li/greenchem

Introduction

Semiconductor nanoparticles are an important class of materials, whose properties can be tailored for various uses.^{1–4} The modification of the surface of these nanoparticles can, to

a great extent, influence their reactivity, dispersibility in various solvents, biocompatibility and biodegradability, optical properties, electrical and thermal conductivity, *etc.*^{3–5} This is why cheap and easy surface modification methods are constantly being sought both by the industry and the research community.

A class of nanoparticles which are of special interest are those based on non-toxic, biodegradable and abundant resources, such as silicon or carbon.^{6,7} In addition to the above mentioned qualities, silicon is known to emit relatively efficient photoluminescence in the quantum-confined state, *i.e.* in the form of silicon nanocrystals (Si-NCs), which makes these nanoparticles interesting candidates for lightning or bio-imaging applications.^{1,4,8–10} The exploitation of Si-NCs in opto-electronics is also enforced by the fact that their luminescence properties can be significantly tailored by the modification of their surface chemistry.^{11,12} This effect is a result of the covalent bonds between the core atoms of a Si-NC, which implies a higher degree of electron sharing than in the more traditional nanoparticles with stronger ionic bonds such as

^aInstitute of Physics, Czech Academy of Sciences, Cukrovarnická 10, Prague 6, Czech Republic. E-mail: Galar@fzu.cz

^bUniversity of Chemistry and Technology, Technická 3, Prague, Czech Republic

^cDepartment of Chemical Physics and Optics, Faculty of Mathematics and Physics, Charles University, Ke Karlovu 3, Prague 2, Czech Republic

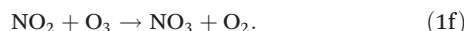
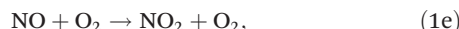
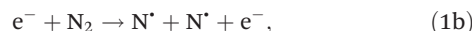
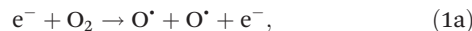
^dInstitute of Physics, University of Amsterdam, Science Park 904, 1098 XH Amsterdam, The Netherlands

^eDepartment of Inorganic Chemistry, Faculty of Science, Charles University, Hlavova 8, Prague 2, Czech Republic

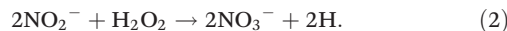
†Electronic supplementary information (ESI) available: Chapter related to *Influence of specific atmospheres on PL change of PAW modified Si-NCs*, *Modification of fresh Si-NCs using corona discharge pre-treatment* and *Influence of PAW environment on the PL properties of modified Si-NCs*. Moreover, these can be found Tables S1 and S2 and Fig. S1–S11 that supplement figures. See DOI: 10.1039/d0gc02619k

CdSe.^{11,13} Unfortunately, the surface modifications of these nanoparticles, be it a classical chemical reaction or a treatment in plasma, are traditionally carried out under strictly controlled conditions (atmosphere, temperature, necessity of carrying gas), which makes such modifications complicated and expensive to use.^{3,11,14–17}

Plasma activated water (PAW), sometimes called “dead water” or plasma treated water, was described as a curious phenomenon found during the investigation of the microbicidal effects of non-thermal plasma, where the persistent microbicidal effect in water after its exposure to plasma was observed.^{18,19} During that time, significant effort was aimed at the elucidation of the chemical and physical properties of PAW as well as its range of applications.²⁰ In general, as a result of the high variability of parameters and methods used to generate the treating plasma, it is impossible to make a definitive list of the chemical species present in PAW. Usually, the most important components are nitrate NO_3^- and nitrite NO_2^- ions, hydrogen peroxide H_2O_2 and ozone O_3 .²⁰ For air atmosphere, the following reactions are considered the main ones determining the contents of PAW:



However, their specific concentrations strictly depend on the nature of the used discharge. For example, the formed NO_3^- and NO_2^- can dissociate all the present O_3 , leading to practically no ozone content. Whereas in a low-energy discharge such as a glow discharge, the energy of electrons is insufficient for the dissociation of water molecules to hydroxyl radicals HO^\cdot , in a higher-energy discharge (during the pulse) such as spark discharge, this process is possible.²¹ Thus, the concentration of H_2O_2 in PAW generated using a spark discharge is often very high. However, its content can be again lowered through an oxidation reaction:²⁰



Despite being relatively simple and very cheap, the treatment of nanoparticles with PAW is still a not very wide-spread method.²² One possible reason for the limited use of PAW in the surface modification of Si-NCs in particular is their potentially destructive interaction with hydrogen peroxide and the controversial effect of nitrogen-containing species,²³ which, however, might not be as straightforward as previously thought.^{24,25} Moreover, the complex chemistry of PAW would most probably prevent the identification of the precise chemical pathways leading to nanoparticles surface modification.

In this contribution, we show that a very simple adjustment of the traditional methods of the preparation of PAW, *i.e.* its activation in a closed-space container with a limited air flow, produces PAW with composition favorable for the surface modification of surface-oxidized Si-NCs. The treatment of Si-NCs in the closed-space-treated PAW leads to the incorporation of water-nitrate complexes into the surface of Si-NCs. By effectively reducing the number of oxygen bridges the incorporation alleviates some of the strain which the original oxide shell exerts on the Si-NC core and which is known to lead to surface trapping of excited carriers and limited bandgap tuneability.²⁶ Also, nitrate complexes significantly improve the dispersibility of Si-NCs in water, and lead to a significant improvement in photoluminescence efficiency and stability. The modification procedure can be easily generalized also to other types of semiconductor nanoparticles as is shown using ZnO and MgO nanoparticles. Even though the treatment of water dispersions of nanoparticles by non-thermal plasma requires only basic equipment and can be carried out at ambient conditions, the same, albeit somewhat smaller effect can be achieved even utilizing only the supplied PAW without any need for a plasma-treatment setup. Thus, we demonstrate the possibility of surface modification of nanoparticles without the need for any chemicals, with all the reactive species originating solely in air or water.

Results and discussion

Optimal plasma generation system: transient spark discharge

The easiest way to surface-modify a nanostructured sample by a plasma activated liquid is to use long-term stable activated water (PAW)²² at ambient conditions and without any need of a continuous flow of a working gas. Corona discharge is the simplest and standard technique of non-thermal plasma liquid modification under these conditions (Fig. S1a and b†).²⁰ However, the energy of the plasma electrons is low, which results in a limited spectrum of the generated reactive species in the air, as demonstrated by the emission spectrum of the discharge containing only molecular peaks (Fig. 1c). The weak effect of the corona discharge on water activation was also verified by the chemical analysis of the resulting PAW (30 minutes modification treatment, Table 1). Thus, we proposed an alternative apparatus for the generation of PAW, as shown in Fig. 1a and b. It is composed of a standard high voltage source and stabilizing ballast impedance that transforms the continuous discharge into a pulse transient spark discharge (a pulsed version of the corona discharge) of a 50 ns pulse length and the frequency of 2 kHz with peak pulse current passing between the electrodes ranging from 5 to 10 A (for more details see Experimental section). Such high energy pulses generate in air not only high energy electrons, but also other charged particles, UV light photons, ozone and a wide spectrum of oxygen- and nitrogen-related species all directed against the water level (see the discharge emission spectrum in Fig. 1c).²⁰ Thus, the resulting PAW then contains: (a) air related species; (b) the reactive species related to the inter-

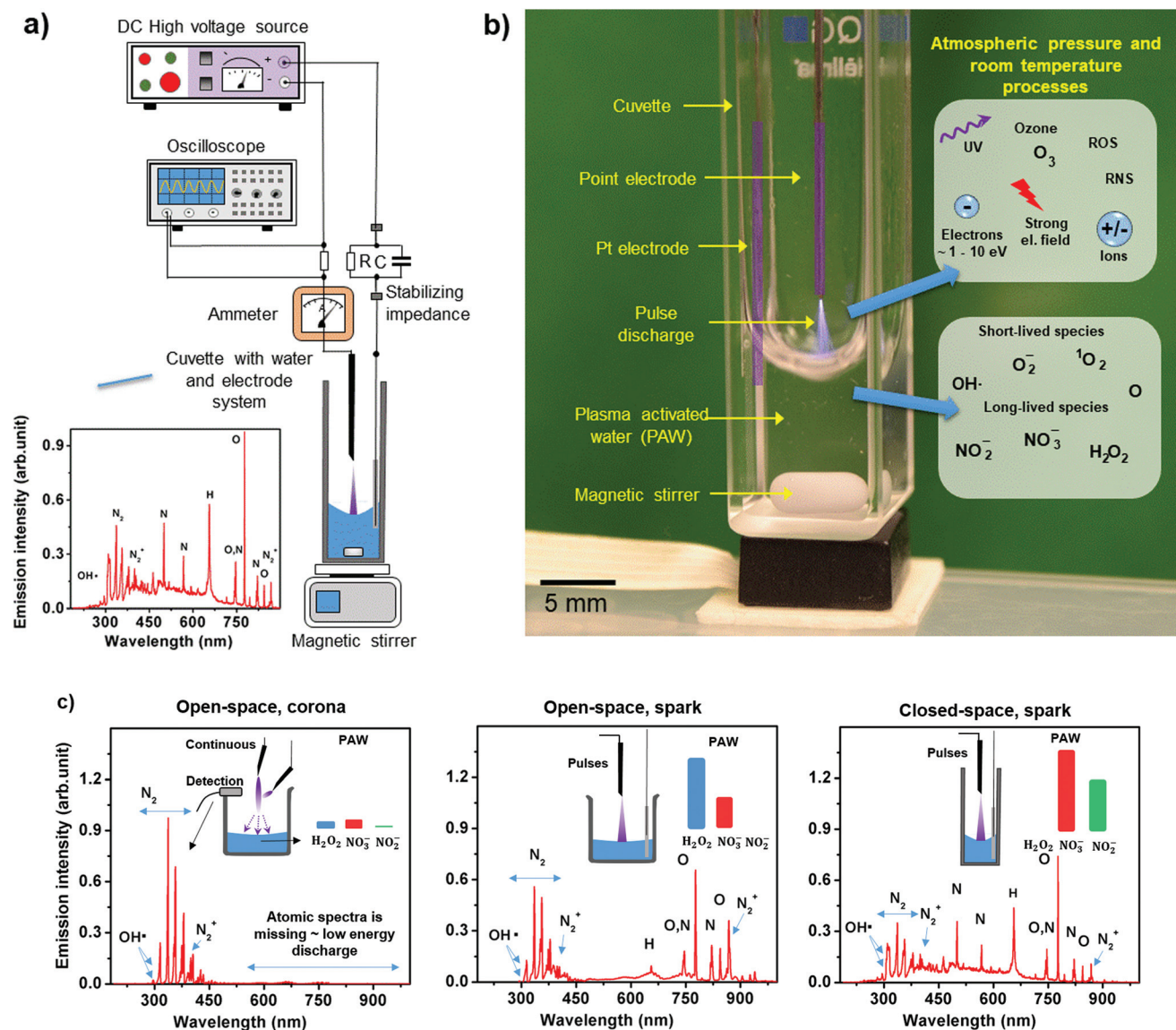


Fig. 1 (a) Apparatus for the generation of the transient spark discharge and for the activation of water with a representative emission spectrum of the discharge. (b) Detailed picture of the water activation area by non-thermal plasma. The representative elements related to generation of plasma in air and in water by the transient spark are presented. (c) Comparison of the emission spectra of the corona discharge (left) and the transient spark discharge (middle) generated in the standard laboratory beaker (referred as open-space setting). These spectra are compared to the one of transient spark discharge generated (right) in open tall quartz cuvette (referred as close-space setting). Graphs are supplemented by a schemes of used modification settings and color bars reflecting the concentration of basic reactive species of generated PAW.

action of high energy electrons and water molecules and (c) species resulting from the mutual reactions of (a) and (b).²⁰ In particular, the PAW treated using transient spark in an open beaker contained zero concentrations of nitrite ions and a very high concentration of hydrogen peroxide (4 mM) and nitrate ions (8 mM), see Table 1 and Fig. S2.[†] These concentrations are significantly higher than the ones detected in PAWs prepared using corona discharge and even a few times higher than in PAWs activated by a barrier dielectric barrier discharge and other techniques as published in the literature.^{27,28} The lack of nitrite ions is caused by their oxidation through the reaction with hydrogen peroxide to nitrate ions (eqn (2)).²⁹

Optimization of PAW composition

While the high concentration of nitrate ions can be potentially beneficial for nanoparticle surface modification, the high concentration of hydrogen peroxide can etch and significantly damage surface of several types of nanoparticles (e.g. silicon) and limits their surface modification by other species; therefore, it is desirable to lower the H₂O₂ concentration. Whereas changing the discharge properties, the volume of the modified liquid and the time of the modification did not lead to a sufficient change in the composition of PAW, surprisingly, we observed sensitivity of the discharge to the restriction of the

Table 1 Chemical analysis of PAW prepared by different plasma settings

PAW property	Open-space	Open-space	Closed-space
Discharge	Corona	Spark	Spark
pH	4	3	1–2
NO_2^- (μM)	40	0	1100
NO_3^- (μM)	740	8000	80 000
H_2O_2 (μM)	240	4000	0
Si PL increase	No	No	Yes

Chemical analysis of the corona and the transient-spark-discharge plasma activated water using an open- and closed-space setting (ambient conditions, after 30 minutes of plasma treatment). The pH of the PAW and concentration of nitrite and nitrate ions and hydrogen peroxide were monitored. The properties of PAW were analyzed after reaching a stable state (approximately 5 minutes after the modification). The effect of the PAW on the PL of dispersed Si-NCs is also displayed.

surrounding air flow, that is if the PAW generation was realized in a sealed container (a hermetically sealed cuvette, referred to as the “sealed setting”) in contrast to the water activation in an open beaker (referred to as the “open-space setting”, results presented in the previous text).

To understand these effects, the emission spectra and the chemical composition of PAW generated under oxygen, nitrogen and standard air atmosphere in a sealed setting were studied (Fig. S3 and Table S1†). The emission spectrum of the discharge in an oxygen atmosphere is, as expected, dominated by the peaks related to atomic oxygen. The composition of PAW generated under oxygen atmosphere was comparable to the one obtained using an open-spaced setting, documenting the importance of oxygen in the generation of PAW at ambient conditions. Discharge generated under nitrogen atmosphere showed mainly atomic and molecular emission from nitrogen, however, the intensity of the molecular part of the spectrum (the UV region) was significantly lower, implying that the composition of form (state) of the nitrogen atoms in the discharge in the sealed atmosphere is different from the open one (Fig. S1c† and Fig. 1c). This difference was manifested also in the chemical composition of PAW. In the PAW generated in a sealed container with nitrogen environment the concentration of NO_3^- increased almost ten times when compared to the open-space one, hydrogen peroxide decreased more than ten times and we detected the concentration of NO_2^- of 1.1 mM. The observed concentrations of NO_3^- and NO_2^- are significantly higher than values commonly presented in the literature that, based on the used technique, range from 0.5 to 6 mM and 0.02 to 0.1 mM, respectively.²⁸ The high concentration of these ions also decreased the pH of the PAW from 3 to 1–2 (Table S1†). Surprisingly, even a better PAW composition was obtained using a sealed container with standard air atmosphere: no presence of hydrogen peroxide, and 1.8 and 85 mM concentration of NO_2^- and NO_3^- , respectively. Similarly to the previous case, the intensity of molecular emission of the discharge decreased fast after turning on of the discharge, changing the sealed air atmosphere to an atomic one. Thus, the presence of both gases

(oxygen and nitrogen) in combination with CO_2 at closed conditions is beneficial for the build-up of a high concentration of reactive nitrogen species (RNS) at the expense of the reactive oxygen species (ROS). Moreover, all the discharges generated in the sealed atmosphere contain an intense peak of H-alpha, which also proves the atomic character of the plasma atmosphere and effective radicalization of the plasma.

Most interestingly, in order to obtain PAW of these exceptional properties, there is no need to have a completely sealed container, which could complicate the electrode setting and discharge generation in general. Comparable results can be achieved using a container which only limits the free air flow during the plasma activation procedure, such as a tall cuvette with water level below half of its height (Fig. 1b). A transient spark discharge generated in this setting (referred to as the “closed-space setting”) showed an emission spectrum comparable to the case of a sealed container with air (Fig. S1d†), as did the chemical composition of the resulting PAW (Fig. S2,† and Table 1). Using the closed space setting showed a compromise in the efficiency of PAW generation and the complexity of the used apparatus, thus this experimental setting was employed in all the following modification procedures.

Modification of Si-NCs by pre-treated PAW

The modification effect of PAW was tested on silicon nanocrystals (Si-NCs). We used ambient-conditions oxidized electrochemically etched Si-NCs, before treatment exhibiting moderate photoluminescence (PL, QY ~ 6%, size ~ 3 nm, for PL and HRTEM characterization please see Fig. S4†),³⁰ whose PL quickly quenches in water without any additional treatment (as shown later). These Si-NCs were simply mixed with PAW previously generated in the closed-space setting (method M1, see Experimental section) and analyzed using steady-state PL spectroscopy afterwards (Fig. 2a). As can be seen, no blue shift of the PL spectrum or a decrease in its intensity, possibly signalizing oxidation, was observed. On the contrary, the PL intensity increased 1.65 times and red-shifted by about 12 nm (~32 meV) (Fig. 2a). The dynamics of these changes show an exponential behavior with the time constants of about 6.2 and 14.7 minutes, respectively (Fig. 2b). Moreover, the dispersibility of the nanoparticles improved significantly, indicating better wettability of the Si-NCs surface. This PL modification was stable in the range of weeks (see below). Since the long-living reactive species persist in PAW even after several weeks,¹⁸ this finding implies that this modification procedure can be applied even using only PAW pre-treated elsewhere, that is even in laboratories not equipped with a plasma charge device.

Effect of the direct plasma treatment on Si-NCs surface chemistry

Whereas only the long-lived species are present in the pre-treated PAW, to study the influence of the short-living reactive species, the nanoparticles in water need to be treated by the discharge directly. Thus, we dispersed Si-NCs in water even before its plasma activation and monitored their photoluminescence during the presence of the discharge (method M2). We used two sets of Si-NCs labelled as A and B (Fig. S4†)

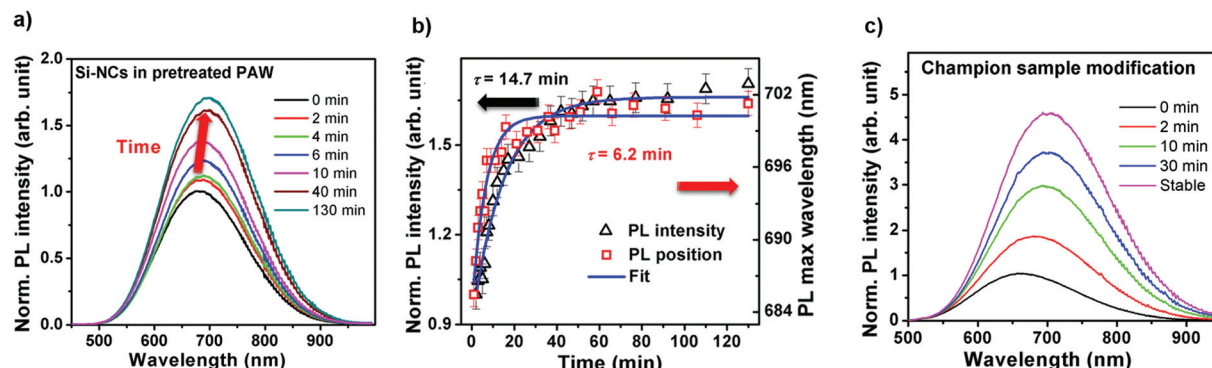


Fig. 2 (a) Temporal evolution of Si-NCs photoluminescence spectra after their dispersion in plasma activated water prepared for 30 minutes at ambient conditions using a closed-space setting (method M1). (b) Temporal evolution of the photoluminescence maximal intensity and the spectral position of the PL band maxima. Data are approximated by a single exponential curve. The resulting time constants are displayed. (c) Photoluminescence spectra of the sample Si-NCs A showing the maximal increase in PL intensity (labelled as the champion sample) before and after PAW modification (method M2). Photoluminescence was excited at 442 nm by a continuous beam of 2.7 mW. All spectra were corrected for the sensitivity of the whole detection system.

differing by size and thus also the position of their PL spectra. Moreover, according to the sample preparation procedure (see Experimental section) it is expected that the sample B is composed of larger nanoparticle agglomerates. The original PL maxima of sample A and B were located at approximately 670 and 700 nm, respectively. In accordance with the previous modification, after starting the transient spark discharge, the PL intensity of both samples started to rise and red shift (Fig. 2c and Fig. S5a, b†). Also in this case, the red shift followed an exponential curve, which approaches almost the same value for both samples (~700–710 nm) with the time constant ranging from 4 to 5 min (Fig. S5c†). In contrast to Si-NCs modified by pre-treated PAW, the PL intensity of these samples showed a much steeper rise during the initial modification period (a few minutes) (Fig. S5d†). This rise was followed by a further gradual increase, which was comparable to the behavior of the Si-NCs in pre-treated water. Interestingly, the secondary rise continued also after turning off of the discharge (Fig. S5a and d†). The time intervals necessary to reach a maximal saturated PL intensity somewhat varied between the two samples and in the following experiments, ranging from 25 to 60 minutes, and so did the overall PL improvement. The most common PL increase was 2.5 times, with the best sample reaching 4.5× of its original PL (Fig. 2c). Thus, the direct contact of the Si-NCs with the discharge and the short-living species causes a steep initial PL rise and improves the resulting increase of PL intensity, but is not a necessary condition for the observed effects. The necessity of a high concentration of RNS and a low concentration of hydrogen peroxide for the efficient increase of Si-NCs PL was also confirmed by the Si-NCs modifications by PAW generated under various protective atmospheres (Fig. S6†). Details of these measurements are described in ESI.†

During our experiments and the optimization process, we also observed that not all Si-NCs samples are sensitive to the PAW modification process described above, namely, only a

minor effect of PAW on the PL properties was observed on not fully oxidized (“fresh”) Si-NCs. This phenomenon can be interpreted taking into account the wide range of reactive species in PAW and the high reactivity of fresh Si-NCs.^{20,31,32} While only some of the modification pathways can be take place during the modification of stable, fully oxidized Si-NCs, in the case of the fresh Si-NCs, more diverse and often mutually competitive and even detrimental processes can be involved, which results in only a negligible improvement of the sample passivation and the associated QY.³¹ To verify and solve this problem, we propose a two-step modification process including a pre-treatment of the originally insensitive samples by corona discharge in air, followed by the standard PAW modification (method M3). Using this procedure, we were able to increase the PL intensity of the Si-NCs by more than 6 times, which is almost twice as much as was observed with the standard fully oxidized Si-NCs (Fig. S7†). Moreover, the PL spectra of the two-step-modified samples shifted to the same spectral position as the PL of the samples modified in the standard way, even though the initial PL maximum of the fresh Si-NCs spectra was located approximately at 750 nm. Surprisingly, the pre-treatment step did not improve the PAW modification of the fully oxidized, surface stable samples (Fig. S7†). For more detail see Experimental section and ESI.†

For clarity, we compared the intensity and the spectral change for all 3 described PAW modification procedures (M1–M3) applied on stable and fresh Si-NCs as was described above, see Fig. 3. Although we presented three different modification methods, each with its own application in a different situation, nanocrystals modified using only the M2 method were selected for the study of physical, chemical and structural properties of the treated samples.

Effect of PAW modification on physical properties of Si-NCs

These modifications are much more stable (within weeks) under standard laboratory conditions (ambient atmosphere) in

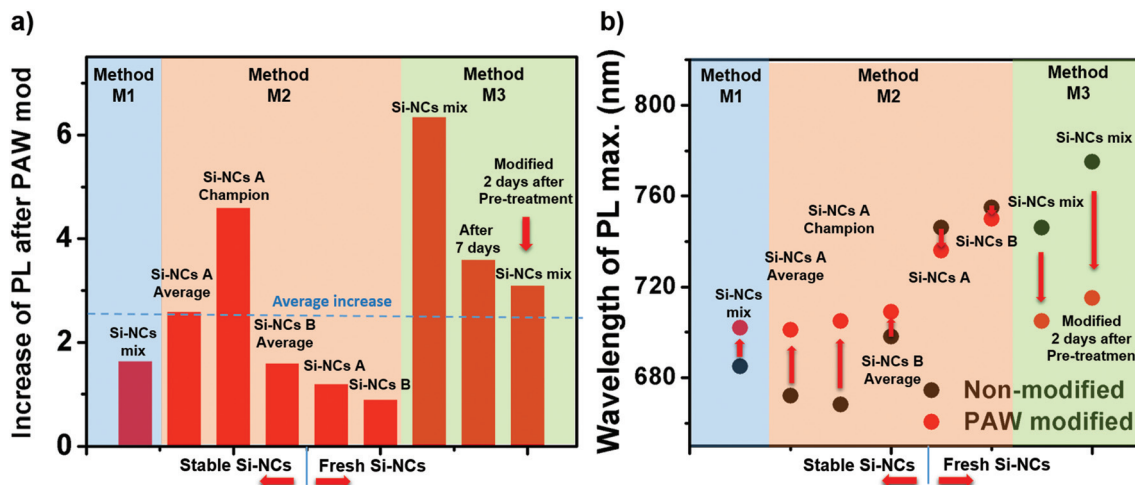


Fig. 3 Comparison of Si-NCs (a) PL intensity and (b) position of the spectral maximum before and after the different variations of PAW modification: (i) M1 (the blue region); (ii) M2 (the red region); (iii) M3 (the green region). The figure presents the modification results of the Si-NCs supernatant and the sediment labelled as A and B, respectively (for more information see Experimental section). When the modification method does not allow for the separation of these parts, the samples were labelled as Si-NCs mix. For clarity, we present results of not only the average modification, but also the best modification attempt labelled as average and champion, respectively. To show the effect of the surface reactivity of Si-NCs on the modification process, we present results observed on reactive fresh and surface stabilized (oxidized) Si-NCs labelled as Fresh and Stable, respectively. Only using the modification procedure M3, we observed a decrease of PL intensity with time after modification. This ageing process is therefore also presented. Photoluminescence was excited at 442 nm by a continuous beam of 2.7 mW.

contrast to non-treated samples in water. As can be seen from Fig. 4a, the decrease of PL intensity of all the PAW modified samples while still in water was not higher than 10% after 2 weeks, in contrast to a 70% decrease of non-modified Si-NCs in deionized water. Even though the modification is closely related to the PAW, the samples keep their improved properties also after drying. Fig. S8b[†] compares the normalized spectra of Si-NCs before modification, after modification, after drying and after 1 more day. It is not easy to compare the absolute PL intensity of the Si-NCs in a liquid and after drying, but it is evident that the red spectral shift caused by the PAW modification is kept unchanged. Because the PL of Si-NCs can be affected also solely by pH of the colloidal solution,³³ which is

low in our modified sample, we also performed filtration dialysis of the modified sample. After this procedure, the purified colloid had pH of about 6, while keeping its PL properties (Fig. S9[†]). The long-term stability of such purified water-dispersed Si-NCs is a topic for further research. For more detail, see ESI.[†]

To elucidate the physical meaning of the observed PL changes, we further characterized the photophysical properties of the Si-NCs A sample before and after the modification (treated using M2). The external QY of the Si-NCs increased about 3 times after the modification (from 6.8% to 21.2%) using the excitation wavelength at 440 nm, proving that the PL increase is related to the processes of charge carrier recombination.

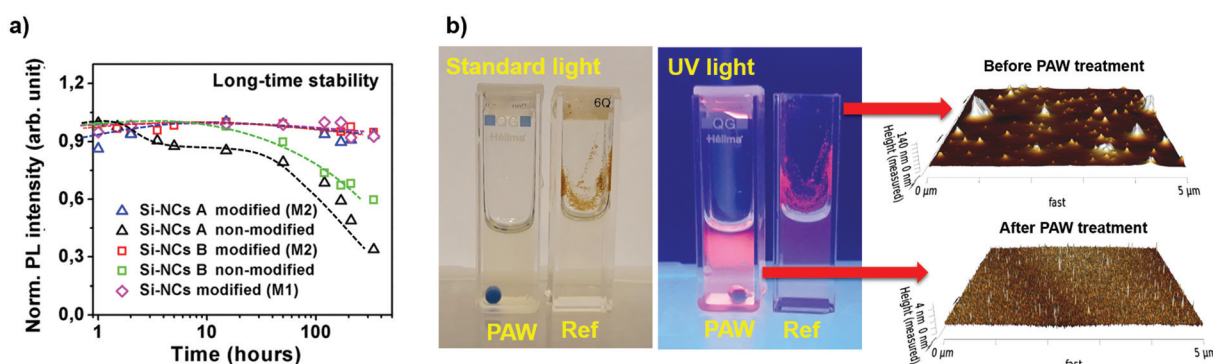


Fig. 4 (a) Study of long-time stability of the PL intensity of Si-NCs modified by methods M1 and M2 at the band maximum normalized with respect to the beginning of the experiment. Solid lines are only to guide the eye. (b) Photos of Si-NCs B dispersed in distilled water (labelled as ref) and PAW-treated (M2 method) ones under standard light (left) and UV illumination (right). The photos are supplemented by 3D picture of the Si-NCs after drying obtained using atomic force microscopy.

tion, and not only to the ones changing the amount of the absorbed excitation or emitted light such as scattering on the Si-NCs ensembles *etc.* (Fig. 5a). Interestingly, in contrast to the non-modified Si-NCs which have an approximately a constant 5–7% QY at the excitation wavelengths between 400 and 500 nm, the QY of the modified Si-NCs decreases with the increasing excitation wavelength from 28% to 14%. Such behavior is in apparent violation of the Kasha–Vavilov rule, basically stating that the quantum yield should be excitation-wavelength independent.³⁴ However, this rule strictly applies only to very simple systems with uncomplicated carrier relaxation processes and cannot be generalized to semiconductor nanocrystals, among other things due to the presence of trap states.³⁴ In our case, the excitation-wavelength dependent QY change only signifies that the modification procedure works better for smaller Si-NCs with the absorption edge shifted to the blue part of the spectrum, most possibly as a result of a higher surface-to-volume ratio of smaller Si-NCs and a larger (detrimental) effect of surface trap states before the modification.

Furthermore, we observed that the PL decays (Fig. S10†) of the modified and the non-modified samples could be with a good precision approximated by the stretch-exponential curve, whose PL average time constant τ_{av} increased about 1.3 times within the whole range of detected wavelengths (Fig. 5b). While this result proves the positive effect of PAW on the radiative recombination rates of Si-NCs, its value is smaller than the corresponding increase in the PL intensity and the external QY. This, together with the wavelength-dependent change in the external QY, suggests that the modification procedure positively influences not only the radiative rates, but also other properties influencing the external QY, *e.g.* by lowering the number of non-emissive (“dark”) Si-NCs. Moreover, the insensitivity of the stretch-exponential parameter β to the PAW modification of the nanocrystal confirms that the surface treatment changes only the surface chemistry of the Si-NCs and does not influence their size, which is in agreement with AFM measurements and the absence of hydrogen peroxide in the PAW (Fig. 4a and Fig. S8b†).

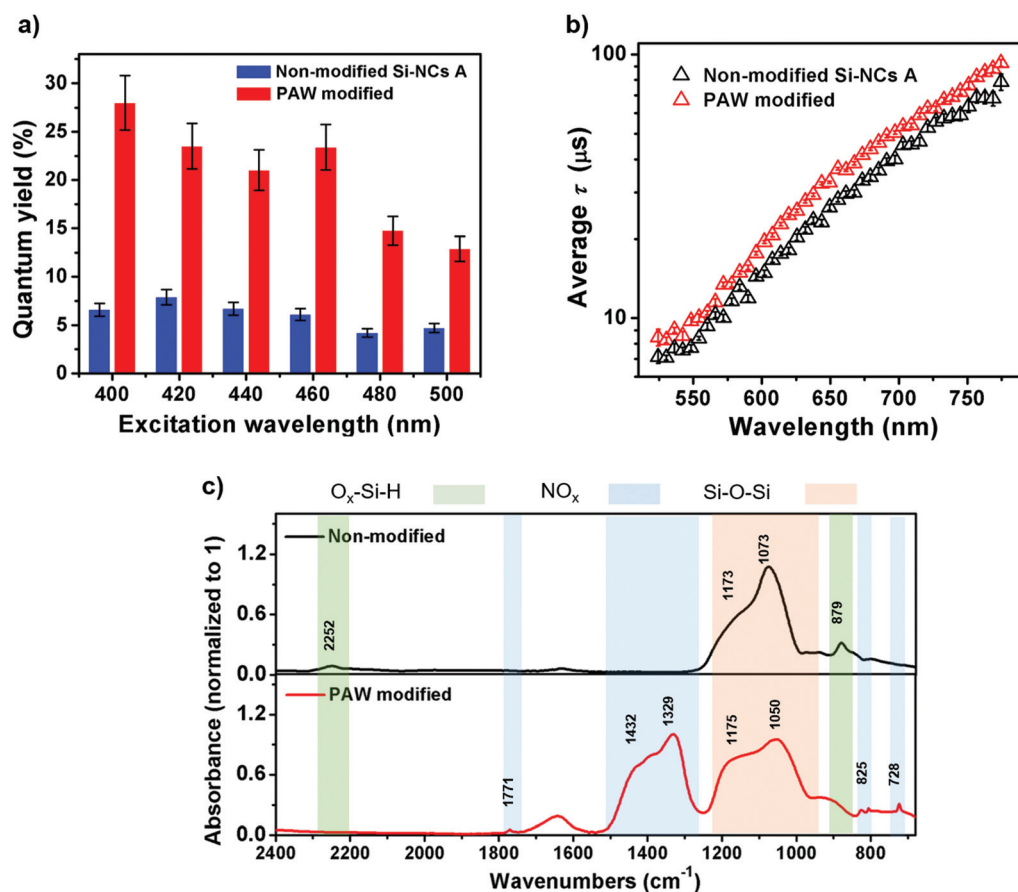


Fig. 5 (a) Comparison of the photoluminescence quantum yield of Si-NCs A non-modified and PAW modified, measured at several excitation wavelengths. (b) Spectral dependence of the fitted average lifetime τ_{av} (displayed in log-lin scale), which was used to describe the photoluminescence decay of samples Si-NCs A before and after PAW modification. Error bars corresponding to the uncertainty of τ_{av} calculation are displayed. The PL was excited by the laser pulses at 343 nm. The repetition frequency of the pulses was 1 kHz and the time duration of the pulses was approximately 200 fs. (c) FTIR-ATR measurements of the Si-NCs before and after PAW modification. Positions of the main bands and peaks are displayed and interpreted. The NO_x^- presence can be also detected as a week band around 1050 cm^{-1} . This band would be however hidden under the strong $\text{Si}-\text{O}-\text{Si}$ band.³⁵ Samples were modified using method M2.

Surface chemistry and DFT simulations

The dispersibility of Si-NCs in water was significantly improved after the surface-modification treatment, which is obvious by a simple naked-eye observation (Fig. 4b). This improved dispersibility is corroborated by the AFM-based structural study of both the non-treated and the treated sample, which confirmed that the PAW modification lowered the number of nanocrystal agglomerates (Fig. 4b and Fig. S8†). Such a marked change in dispersibility clearly points to a change of the chemical composition of the surface of the modified Si-NCs.

To elucidate the origin of the observed changes, the Si-NCs A (treated by M2) were characterized by Fourier transform infrared spectroscopy before and after the PAW modification with the direct presence of the discharge (Fig. 5c). The modification procedure causes surface-chemistry changes. Specifically, the generally less stable O_x–Si–H_y bonds are diminished and the characteristic band of the Si–O–Si bonds (the interval between approximately 1050 and 1200 cm⁻¹) changes.^{30,36} Moreover, a completely new band appears

between 1300 and 1500 cm⁻¹. Based on its shape and spectral position, this band can be interpreted as the incorporation of nitrate–water complexes into the surface layer of the Si-NCs, possibly *via* weak bonding interactions.³⁷ Details of the surface chemistry characterization were published elsewhere.²⁵ The incorporation of nitrites to the Si-NC shell is also in good agreement with the chemical composition of the used PAW.

The effects of the surface-bonded nitrate complexes on the PL of Si-NCs were simulated using DFT calculations, see Fig. S11† (detailed description is presented in Experimental section). The non-modified Si-NCs were modelled as a Si-NC with 100% surface coverage by –OH species, while the replacement of about 50% of the surface sites with the –O–NO₂ groups represented the effects of the modification procedure. The computed radiative rates were thermally averaged in order to obtain a more meaningful comparison with the experiment (carried out at room temperature, Fig. 6). To visualize which of the Si-NC states contribute to the light emission, we apply a violin-plot representation¹³ to the thermally averaged radiative rates, which allows us to better understand the PL-related behavior of a NC.

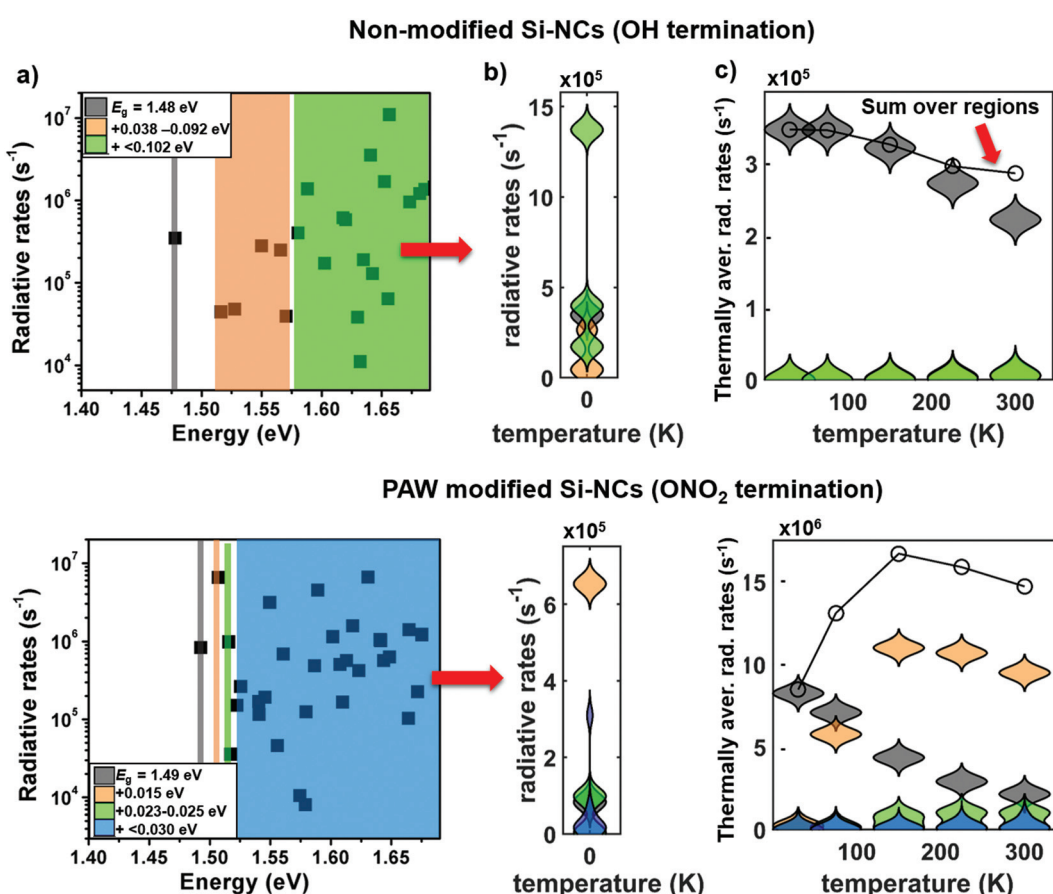


Fig. 6 (a) Calculated zero-temperature radiative rates corresponding to the first (black) and higher excited states (orange and green) of non-modified and PAW modified Si-NCs A. (b) Radiative rates from column (a) can be plotted using the violin-plot representation, where color coding designates the states lying within the corresponding energy intervals in (a) and the shaded areas indicate the number of states reaching a given radiative rate value (an analogy to a histogram). Without considering the effect of temperature (thermal population of higher-lying states), only the energetically lowest transition (the gray one) is possible. (c) The thermal evolution of energetically resolved thermally averaged radiative rates ($\langle R_{\text{rad}}^{i \rightarrow j} \rangle_T$) from eqn (4) (Experimental section). The solid line connecting the circles presents the total thermally averaged radiative rates ($\langle R_{\text{rad}} \rangle_T$).

In this representation (see Fig. 6b), the energetic position of the states is color coded and all the values of the calculated radiative rates are plotted in a single column. After the application of thermal averaging (eqn (4)), as is shown in Fig. 6c, it becomes clear that according to the calculations, the light emission of the non-modified oxidized Si-NCs is dominated by the transitions from a single level, which has a high degree of spatial localization on the surface oxide (see Fig. S11[†]). Such behavior is typical for oxidized Si-NCs.³⁸ On the other hand, the incorporation of nitrites to the surface causes more states to participate in the emission and the corresponding wave function is much more core-localized (Fig. S11[†]), which indicates a much larger participation of the Si core in light emission.

When considering strictly only the lowest computed transition, the radiative rate enhancement is about 2.5×. However, taking into account also the effect of temperature, the calculations predict an even higher 5× increase in the total radiative rates. The corresponding measured changes in the decay lifetime (1.3×) are in good agreement with these numbers, even though they are slightly smaller. The lower experimentally observed enhancement is to be expected, since the simplicity of

our modification procedure clearly prevents a perfect surface coverage, it only leads to the amelioration of the original state.

The mechanisms through which the radiative rates are enhanced very probably include also the alleviation of surface-oxide-related strain. Fig. S11a[†] plots the distribution of Si-Si bond lengths in the modified and non-modified Si-NCs. The much narrower distribution for the nitrate-containing Si-NC suggests that the presence of the modified surface leads to a much lower occurrence of highly strained areas in the NC, which improves the radiative rates. An independent corroboration of the reduced strain in the NC was also provided by our previous optical measurements published elsewhere, which showed that SiO_2 -related defects are strongly suppressed after the modification.²⁵ Moreover, fitting of the Si-O band of the FTIR measurements (Fig. 5c) also yields higher wavenumbers (1052 a 1090 cm^{-1} vs. 1042 and 1072 cm^{-1}) and larger FWHMs (the difference is 9 and 6 cm^{-1} , respectively) for the modified sample, suggesting lower interfacial Si/ SiO_2 strain.³⁹ Lower strain levels lead to less trap states, which might imply a smaller proportion of “dark”, non-emitting Si-NCs, an effect suggested also experimentally by our optical characterization presented above.

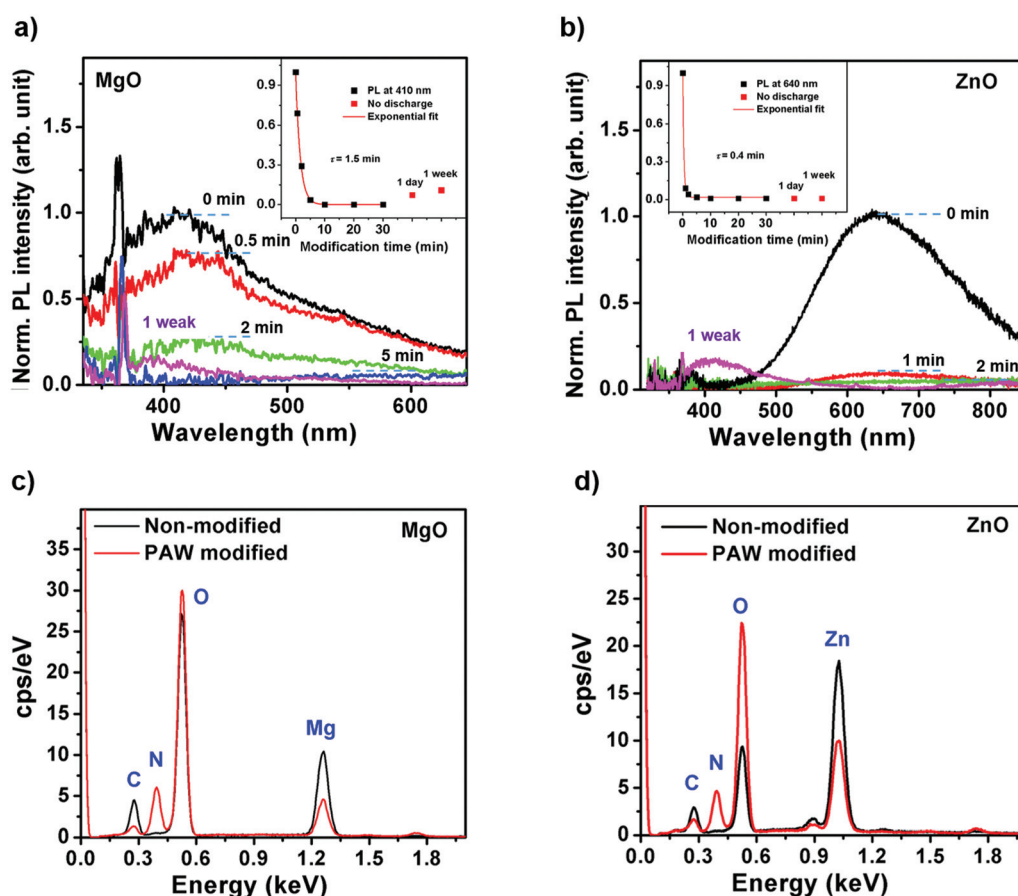


Fig. 7 (a) Temporal evolution of (a) MgO and (b) ZnO nanoparticles photoluminescence spectra during the first few minutes of PAW modification. PL spectra of the samples after 1 week in PAW are also displayed. Inset: Evolution of both samples PL at maxima of the spectra during 30 minutes modification by PAW. Ageing of the PL intensity after 1 week is displayed. Photoluminescence was excited at 325 nm by continuous beam of 3.4 mW. All spectra are corrected to sensitivity of whole detection system. Elemental analysis of (c) MgO and (d) ZnO using energy – dispersive X-ray spectroscopy before and after modification by PAW (method M2).

Effect of PAW modification of zinc oxide and magnesium oxide nanoparticles

The general applicability of the described surface modification method was tested on other semiconductor nanoparticles, namely using commercial ZnO and MgO nanoparticles. These nanoparticles were selected for their similar surface chemistry to Si-NCs (silicon nanocrystals possess an oxide based shell) and the typical surface related photoluminescence which should be sensitive to the modification of surface chemistry.^{40–42}

MgO nanoparticles were dispersed under the same conditions as Si-NCs and modified for 30 minutes in PAW with the presence of a closed-space transient spark discharge (treatment method M2). The PL evolution of the suspension is presented in Fig. 7a. As can be seen, the original-defect related PL at 410 nm (band gap of nano-MgO 5.0–6.2 eV) is quickly quenched.⁴³ In this case, the PL intensity can also be well-approximated using an exponential fit (Fig. 7a inset) with the time constant of 1.5 min. The modification was stable, only a small re-increase of the intensity of 10% was observed after 1 week in PAW. These results are in good agreement with our previous observations in Si-NCs: as the blue PL of MgO nanoparticles does not originate from the quantum confinement effect, but from surface defects, the PAW modification effectively quenched them. The elemental composition of the modified and pure samples was analyzed using energy – dispersive X-ray spectroscopy (Fig. 7c and Table S2†), confirming the presence of nitrogen and an increase in oxygen in the modified MgO samples. The obtained ratio of nitrogen and oxygen (after subtracting the original value) was (2.02 ± 0.08) , in good agreement with the surface modification being a result of nitrate-water complexes.

A similar modification was realized also using ZnO nanoparticles (band gap 3.3 eV).^{40,41} The PL evolution of the ZnO nanoparticles in water during the PAW modification is presented in Fig. 7b (treatment method M2). The initial PL band located at 650 nm, commonly interpreted as due to oxygen-related surface defects,⁴¹ was again quickly quenched (Fig. 7b inset). The intensity evolution was approximated by an exponential curve showing time constant of 0.4 min. While the modification was stable within several days, a new PL band with the maximum at approximately 420 nm emerged. This band is related to the over-the-bandgap radiative recombination, which can be red-shifted in ZnO in nanostructured samples in water, proving a significant improvement of the surface passivation of the nanoparticle.⁴⁰ Also in the case of ZnO the change of the elementary composition was studied by EDS showing a significant rise of nitrogen and oxygen atoms (Fig. 7d). The ratio of nitrogen and oxygen atoms obtained by the PAW modification was 2.61 ± 0.09 , proving presence of mixture of nitrate and nitrite-water complexes.

Conclusions

In conclusion, we show that a very simple alteration of the typical procedures used to generate plasma activated water,

namely plasma activation in a closed-space vessel with restricted air flow, leads to a novel chemical composition of plasma activated water beneficial for the modification of the surface of nanoparticles. The modification procedure is carried out at ambient conditions (no need of controlling the atmosphere or temperature) and in its simplest form it involves only the dispersion of nanoparticles in plasma activated water pre-treated in a closed-space vessel. Using silicon nanocrystals, the improvement of light emission after this type of modification was $1.8\times$. A direct treatment of Si-NCs by the non-thermal plasma, simply by employing inexpensive and easy-to-operate equipment for the generation of a transient-spark or corona discharge, led to a six-fold improvement of the original PL. The modification is stable at laboratory conditions in water for at least several weeks and when the liquid is dried out from the sample. In addition to PL, also the dispersibility of Si-NCs in water is significantly improved. The modification-related changes were demonstrated to be due to the incorporation of nitrate-water complexes to the surface of Si-NCs. Our DFT calculations and other results indicate that the alleviation of surface-oxide-related strain could be responsible for the improvement of PL, which results from both the enhancement of radiative rates and the brightening of non-emissive Si-NCs. Even though the modification procedure is demonstrated here using Si-NCs as the studied nanoparticles, its application can be easily generalized also to other types of water-tolerating nanoparticles, which we confirm using commercial MgO and ZnO nanoparticles. The described procedures prove the feasibility of chemicals-free surface modification of nanoparticles, opening the door a broad range of surface modification chemistries using other environmentally friendly and abundant liquids.

Experimental

Samples

The Si-NCs were prepared by a standard electro-chemical etching followed by ambient-conditions oxidation of the surface.⁴⁴ Briefly, the B-doped wafers of crystalline silicon was electrochemically etched in a solution of HF/EtOH for 2 hours. The resulting thin layer was washed with Ethanol and kept in controlled condition (ambient atmosphere and humidity of approximately 50%) for a few days. The thin layer of oxidized Si-NCs was treated by mechanical pulverization yielding a few mg of freestanding Si-NCs powder afterwards. The commercially available ZnO (average size of 14 nm, specific surface $30 \pm 5 \text{ m}^2 \text{ g}^{-1}$ and purity >99%) and MgO (average size of 20 nm, specific area $50 \text{ m}^2 \text{ g}^{-1}$ and purity >99%) nanoparticles were manufactured by PlasmaChem GmbH.

Non-thermal plasma systems

Plasma is generated by two following systems of corona discharge:

- (a) Continuous corona discharge system, previously described in Scholtz V. *et al.*,⁴⁵ burned at atmospheric con-

ditions and consisted of 2 electrodes generating a plasma jet directed through a scattering grating onto the dry powder sample using a commercial 5 kV source (Fig. S1a†). The passing current was approximately 0.2 mA. To improve the effect of the active atmosphere, the system is encapsulated, limiting the free flow of air.

(b) Pulsed corona discharge system referred as to the transient spark discharge system consisted of a commercial high voltage source, oscilloscope, ammeter, a stabilizing ballast impedance with a parallel connection of a $10\text{ M}\Omega$ resistor and a capacitor of 500 pF and two electrodes.²⁷ The electrodes were nested in a glass beaker or a quartz cuvette with 1 ml of deionized water (optionally with dispersed nanoparticles), when one electrode is above and the other one under the water level, so the discharge burned between the upper electrode and the water level (Fig. 1a and b). The properties of the resulting discharge are: 50 ns pulse length, frequency of 2 kHz and peak pulse current ranges from 5–10 A depending on the distance of the first electrode and water level. The pulse duration and the repetition rate are set to reach the optimal combination of high impact energy and low heating of the modified system. The transient spark burned in open air atmosphere or in closed atmosphere of O_2 or N_2 .

Surface modification procedures

In all the procedures detailed below, the volume ratio of the deionized water to the air in the cuvette was 1:3.5. The internal size of the cuvette was $1 \times 1 \times 4.5\text{ cm}^3$. The area of the water level was 1 cm^2 . These conditions ensure that stable atomic plasma is generated above the water level, which is an essential condition for these modification procedures to proceed as required.

(a) *Modification of the nanoparticles by pre-treated PAW* (labelled in the text as method M1): PAW was prepared by a direct treatment of 1 ml of deionized water in a quartz cuvette using transient spark discharge for 30 minutes and kept for 2 h to eliminate the short-living species. Afterwards, 1 mg of nanocrystals was mixed with 2 ml of the PAW.

(b) *Modification of nanoparticles by PAW with the direct presence of discharge* (labelled in the text as method M2): 2 mg of nanoparticles were suspended in 2 ml of deionized water and treated in an ultrasonic pulse homogenizer (Bandelin Sonoplus) for 1 hour (total delivered energy of 60 kJ). The Si-NCs sample was additionally let to sediment for 1 hour and the supernatant (sample A) and the sediment (sample B) were used as two different samples. Both samples were refilled by deionized water to the volume of 2 ml. A half of each sample was kept as a reference afterwards. The MgO and ZnO samples were prepared with the same procedure omitting the separation of the supernatant and sediment. The samples were then put into a quartz cuvette and treated by the transient spark discharge for 30 minutes (unless otherwise stated). To ensure the homogeneity of the modifications of the samples in PAW, nanoparticles are magnetically stirred during the plasma treatment.

(c) *Modification of nanoparticles by PAW and discharge with additional plasma pre-treatment* (labelled in the text as method

M3): this method is an extension to method M2. In contrast to M2, this procedure is preceded by a pre-treatment of the dry nanoparticles by continuous corona discharge for 4 hours at ambient conditions before their mixing with water. To avoid the degradation of the new surface chemistry of the nanoparticles, this method intentionally omits their ultrasound treatment before the PAW modification.

Filtration dialysis purification

The sample was purified using dialysis tubing (Sigma-Aldrich, cellulose tubing, 23 mm, MWCO 12 400). The volume of 0.5 ml of the modified sample stirred in 100 ml of deionized water for 2 days, after which the Si-NCs luminescent sample was transferred from the tubing to a cuvette and characterized. Neither the tubing nor the deionized water exhibited the characteristic Si-NC PL after the purification procedure.

Steady-state luminescence and plasma emission measurements

The emission spectra of discharges and photoluminescence (PL) spectra of the nanoparticles were obtained using the imaging spectrograph Shamrock 300i (Andor, Oxford Instruments) coupled with an EMCCD camera (Newton 971, Andor, Oxford Instruments). The PL spectra were excited using a continuous wave (cw) HeCd laser at 442 and 325 nm of intensity $\sim 2.55\text{ mW}$ (decrease by ND filters from original $\sim 17\text{ mW}$) and 3.40 mW, respectively.

Time-resolved luminescence measurements

The time-resolved PL measurements were realized using a system consisting of a pulsed femtosecond laser Pharos SP – 1.5 mJ (pulse width 150 fs), harmonic generator HiRo (both Light Conversion) and a streak camera (Hamamatsu) coupled with an imaging spectrometer. The PL signal was excited by pulses at 343 nm having a 1 kHz repetition rate and intensity of $65\text{ }\mu\text{J cm}^{-2}$, which corresponds to approximately 1.2×10^{14} photons per cm^2 . The angle between the detection and the excitation paths was 90 degree. To ensure that the sample is not modified by the pulse energy during the measurements, the suspensions are magnetically stirred during the measurements and their response before and after the laser exposition were compared. The temporally and spectrally resolved PL data were analyzed using the procedure published by Kůsová and Popelář.⁴⁶ In brief, PL time-dependence rising edge, caused by the finite pulse duration, was effectively deconvolved using a convolution of a best fitting decay function and the known systems response (laser pulse shape). To improve the signal-to-noise ratio four spectrally neighboring PL decays were averaged. Fitting in the temporal domain was performed through all the averaged PL decays (~ 130 decays per a single spectrum). First, to evaluate the signal onset, decay was fitted using only a single exponential function to describe the PL decay and onset rise-time was deconvolved. Then, the final and more precise fit was realized using a stretched-exponential function $I = I_0 \exp[-(t/\tau)^\beta]$ to describe the PL decay, using a

fixed onset time obtained previously. The final average decay is obtained using:⁴⁷

$$\tau_{av}(\lambda) = \frac{\Gamma\left(\frac{2}{\beta(\lambda)}\right)}{\Gamma\left(\frac{1}{\beta(\lambda)}\right)} \tau(\lambda). \quad (3)$$

Quantum yield measurements

Absolute quantum yield (QY) was measured using a home-built set-up with tunable Laser-Driven Light-Source LDLS (Energetiq EQ-99) coupled to a 15 cm focal length long monochromator (Acton SP-2150i). The detection part consisted of a 30 cm focal length long imaging spectrograph (Acton SP-2300i) coupled to a liquid nitrogen (LN) cooled back-illuminated CCD camera (Spec-10 : 400B, Princeton Instruments). The sample (nanoparticles dispersed in PAW inside a quartz cuvette) was placed in an integrating sphere (Sphere Optics). Both the excitation and the emission signals were coupled and guided using silica fiber bundles connecting the sphere, excitation source and detector. Set-up was absolutely calibrated using calibrated black-body radiation source (45 W tungsten-halogen lamp, Newport Oriel). For more details, see ref. 48.

Material analysis

The Fourier Transform Infrared (FTIR) absorption analysis was measured using the attenuated total reflectance (ATR) technique (on Ge crystal) using Nicolet iN10 FTIR microscope (Thermo Scientific) with a resolution of 4 cm⁻¹ and the Norton-Beer strong apodization function in the range from 675 to 4000 cm⁻¹. Homogeneity of the sample was verified through measurements on several spots on each sample. Energy dispersive X-ray spectroscopy (EDX) measurements were performed using Bruker Quantax 200 with 6|10 XFlash detector with acceleration voltage of 15 kV. Transmission electron microscopy (TEM) images were obtained using Jeol 2200 FS (200 kV). As a support for the nanoparticles, holey carbon 300 mesh copper grids were used for the TEM. Chemical analysis of the PAW was realized using commercial pH and NO₂⁻ and NO₃⁻ indication strips (Quantofix).

Simulations

The technique used to calculate the radiative rates of non-modified and PAW modified Si-NCs was described in detail elsewhere.^{13,25} In brief, for the density functional theory (DFT) ground state simulations, we used the cp2k code and Quickstep implementation of the GPW basis set.⁴⁹ In particular, the Gaussian basis set was chosen as the short-range double-zeta polarized basis DVZP-MOLOPT-SR. Plane wave cutoff was set to 400 Ry. Self-consistency convergence was set to 10⁻⁶. Simulations are done using the generalized gradient approximation (GGA) functional Perdew Burke Ernzerh (PBE).⁵⁰

Si crystalline core of ~2 nm diameter was built in the Vesta editor by making a cutoff from a bulk crystal along

the (100), (110) and (111) crystal planes resulting in a spherical Si-NCs. The surface is composed of facets with -SiX₂ and -SiX binding sites (-SiX₃ species are chemically unstable and thus were removed prior to simulations). The resulting Si-NCs were covered 100% by hydrogen and serve as a starting structure. The final Si core contains 235 Si atoms with approximately 2 nm in diameter. This size is ideal, as it is reasonably close to the experimentally studied material, it is not too large for the simulation and the role of the surface capping is expected to play a strong role, because about 50% of atoms are positioned on the NC surface. A 100%-OH coverage was used to model the oxidized sample (before modification) and an Si-NC containing mixed passivation with OH group on half of the surface sites (55 sites) and -O-NO₂ at the remaining ones models the ‘modified sample’. First, Si-NC structures are pre-relaxed with -H capping and then again with the ligands. Molecular orbitals and energies are then simulated using the fully optimized (relaxed) structures.

Thermally averaged photon-less radiative rate $\langle R_{rad} \rangle_T$ were calculated from the obtained photon-less radiative rates $R_{rad}^{i \rightarrow j}$ using a formula:^{13,51}

$$\langle R_{rad} \rangle_T = \sum_{i,j} \langle R_{rad}^{i \rightarrow j} \rangle_T = \sum_{i,j} \frac{R_{rad}^{i \rightarrow j} \exp\left(\frac{E^{i \rightarrow j}}{kT}\right)}{\sum_{i,j} \exp\left(\frac{E^{i \rightarrow j}}{kT}\right)}, \quad (4)$$

where $E^{i \rightarrow j}$ stands for the energy difference between the participating energy levels, k is the Boltzmann constant and T is temperature. Energy-resolved thermally averaged radiative rates $\langle R_{rad}^{i \rightarrow j} \rangle_T$ are plotted as violin plots following a procedure outlined in ref. 13. In brief, radiative rates are grouped into intervals based on their oscillator strengths and energy difference and then are plotted as a single-column violin plot using Matlab 2015. States above a certain energy threshold have basically zero influence at room temperature, and therefore do not need to be considered.

Conflicts of interest

The authors declare no conflict of interest.

Acknowledgements

The Czech Science Foundation funding, Grant No. 18-05552S (PG, TP, KK) and 18-07977Y (AF), the Operational Programme Research, Development and Education financed by European Structural and Investment Funds and the Czech Ministry of Education, Youth and Sports (Project No. SOLID21 CZ.02.1.01/0.0/0.0/16_019/0000760, KK), the CUCAM Centre of Excellence (OP VVV “Excellent Research Teams” project No. CZ.02.1.01/0.0/15_003/0000417, IM), NWO funding (FOM Projectruimte No. 15PR3230, KDN) and the PPLZ program of the Czech Academy of Science (PG), are gratefully acknowledged.

References

- 1 M. V. Kovalenko, L. Manna, A. Cabot, *et al.*, Prospects of Nanoscience with Nanocrystals, *ACS Nano*, 2015, **9**(2), 1012–1057, DOI: 10.1021/nn506223h.
- 2 S. Chen, W. Li, J. Wu, *et al.*, Electrically pumped continuous-wave III-V quantum dot lasers on silicon, *Nat. Photonics*, 2016, **10**(5), 307–311, DOI: 10.1038/nphoton.2016.21.
- 3 V. I. Klimov, *Semiconductor and Metal Nanocrystals: Synthesis and Electronic and Optical Properties*, CRC Press, New York, 2003, 500 p.
- 4 V. Kumar, *Nanosilicon*, Elsevier, Amsterdam, 2008, pp. 388.
- 5 C. Tupei and L. Yang, *Semiconductor Nanocrystals and Metal Nanoparticles*, CRC Press, Boca Raton (US), 2016.
- 6 J.-H. Park, L. Gu, G. von Maltzahn, *et al.*, Biodegradable luminescent porous silicon nanoparticles for in vivo applications, *Nat. Mater.*, 2009, **8**(4), 331–336, DOI: 10.1038/nmat2398.
- 7 J.-H. Liu, Y. Wang, G.-H. Yan, *et al.*, Systematic Toxicity Evaluations of High-Performance Carbon “Quantum” Dots, *J. Nanosci. Nanotechnol.*, 2019, **19**(4), 2130–2137, DOI: 10.1166/jnn.2019.15807.
- 8 B. Ghosh and N. Shirahata, Colloidal silicon quantum dots: synthesis and luminescence tuning from the near-UV to the near-IR range, *Sci. Technol. Adv. Mater.*, 2014, **15**(1), 014207, DOI: 10.1088/1468-6996/15/1/014207.
- 9 Z. Kang, Y. Liu and S.-T. Lee, Small-sized silicon nanoparticles: new nanolights and nanocatalysts, *Nanoscale*, 2011, **3**(3), 777–791, DOI: 10.1039/C0NR00559B.
- 10 X. Ji, H. Wang, B. Song, *et al.*, Silicon Nanomaterials for Biosensing and Bioimaging Analysis, *Front. Chem.*, 2018, **6**(38), 1–9, DOI: 10.3389/fchem.2018.00038.
- 11 K. Dohnalová, T. Gregorkiewicz and K. Kůsová, Silicon quantum dots: surface matters, *J. Phys.: Condens. Matter*, 2014, **26**(17), 173201, DOI: 10.1088/0953-8984/26/17/173201.
- 12 T. A. Pringle, K. I. Hunter, A. Brumberg, *et al.*, Bright Silicon Nanocrystals from a Liquid Precursor: Quasi-Direct Recombination with High Quantum Yield, *ACS Nano*, 2020, **14**(4), 3858–3867, DOI: 10.1021/acsnano.9b09614.
- 13 K. Dohnalova, P. Hapala, K. Kůsová, *et al.*, Electronic structure engineering achieved via organic ligands in silicon nanocrystals, *Chem. Mater.*, 2020, **32**(15), 6326–6337, DOI: 10.1021/acs.chemmater.0c00443.
- 14 X. Cheng, S. B. Lowe, P. J. Reece, *et al.*, Colloidal silicon quantum dots: from preparation to the modification of self-assembled monolayers (SAMs) for bio-applications, *Chem. Soc. Rev.*, 2014, **43**(8), 2680–2700, DOI: 10.1039/C3CS60353A.
- 15 U. R. Kortshagen, R. M. Sankaran, R. N. Pereira, *et al.*, Nonthermal Plasma Synthesis of Nanocrystals: Fundamental Principles, Materials, and Applications, *Chem. Rev.*, 2016, **116**(18), 11061–11127, DOI: 10.1021/acs.chemrev.6b00039.
- 16 M. H. Mobarok, T. K. Purkait, M. A. Islam, *et al.*, Instantaneous Functionalization of Chemically Etched Silicon Nanocrystal Surfaces, *Angew. Chem., Int. Ed.*, 2017, **56**(22), 6073–6077, DOI: 10.1002/anie.201609651.
- 17 A. F. J. van den Boom, S. P. Pujari, F. Bannani, *et al.*, Fast room-temperature functionalization of silicon nanoparticles using alkyl silanols, *Faraday Discuss.*, 2020, **222**, 82–94, DOI: 10.1039/C9FD00102F.
- 18 J. Julák, V. Scholtz, S. Kotúčová, *et al.*, The persistent microbicidal effect in water exposed to the corona discharge, *Phys. Med.*, 2012, **28**(3), 230–239, DOI: 10.1016/j.ejmp.2011.08.001.
- 19 K. Oehmigen, M. Hähnel, R. Brandenburg, *et al.*, The Role of Acidification for Antimicrobial Activity of Atmospheric Pressure Plasma in Liquids, *Plasma Processes Polym.*, 2010, **7**(3–4), 250–257, DOI: 10.1002/ppap.200900077.
- 20 P. J. Bruggeman, M. J. Kushner, B. R. Locke, *et al.*, Plasma-liquid interactions: a review and roadmap, *Plasma Sources Sci. Technol.*, 2016, **25**(5), 053002, DOI: 10.1088/0963-0252/25/5/053002.
- 21 P. Lu, D. Boehm, P. Bourke, *et al.*, Achieving reactive species specificity within plasma-activated water through selective generation using air spark and glow discharges, *Plasma Processes Polym.*, 2017, **14**(8), 1600207, DOI: 10.1002/ppap.201600207.
- 22 D. Mariotti, V. Švrček, J. W. J. Hamilton, *et al.*, Silicon Nanocrystals in Liquid Media: Optical Properties and Surface Stabilization by Microplasma-Induced Non-Equilibrium Liquid Chemistry, *Adv. Funct. Mater.*, 2012, **22**(5), 954–964, DOI: 10.1002/adfm.201102120.
- 23 M. Dasog, Z. Yang, S. Regli, *et al.*, Chemical Insight into the Origin of Red and Blue Photoluminescence Arising from Freestanding Silicon Nanocrystals, *ACS Nano*, 2013, **7**(3), 2676–2685, DOI: 10.1021/nn4000644.
- 24 G. Morselli, F. Romano and P. Ceroni, Amine functionalised silicon nanocrystals with bright red and long-lived emission, *Faraday Discuss.*, 2020, **222**, 108–121, DOI: 10.1039/C9FD00089E.
- 25 P. Galář, T. Popelář, J. Khun, *et al.*, The red and blue luminescence in silicon nanocrystals with an oxidized, nitrogen-containing shell, *Faraday Discuss.*, 2020, **222**, 240–257, DOI: 10.1039/C9FD00092E.
- 26 K. Kůsová, P. Hapala, J. Valenta, *et al.*, Direct Bandgap Silicon: Tensile-Strained Silicon Nanocrystals, *Adv. Mater. Interfaces*, 2014, **1**(2), 1300042, DOI: 10.1002/admi.201300042.
- 27 J. Julák, A. Hujacová, V. Scholtz, *et al.*, Contribution to the Chemistry of Plasma-Activated Water, *Plasma Phys. Rep.*, 2018, **44**(1), 125–136, DOI: 10.1134/S1063780X18010075.
- 28 P. S. G. Subramanian, R. Harsha, D. K. Manju, *et al.*, Characterization of Plasma Activated Water for Medical Applications, *Adv. Mater. Lett.*, 2019, **10**(12), 4, DOI: 10.5185/amlett.2019.0041.
- 29 B. J. Tyler, Reaction of Hydrogen Peroxide and Nitric Oxide, *Nature*, 1962, **195**(4838), 279–280, DOI: 10.1038/195279a0.

- Published on 22 December 2020. Downloaded by Institute of Physics of the Czech Academy of Sciences on 8/18/2023 1:21:34 PM.
- 30 K. Kůsová, O. Cibulka, K. Dohnalová, *et al.*, Brightly Luminescent Organically Capped Silicon Nanocrystals Fabricated at Room Temperature and Atmospheric Pressure, *ACS Nano*, 2010, **4**(8), 4495–4504, DOI: 10.1021/nn1005182.
- 31 M. J. Sailor and E. J. Lee, Surface chemistry of Luminescent Silicon Nanocrystallites, *Adv. Mater.*, 1997, **9**(10), 783–793, DOI: 10.1002/adma.19970091004.
- 32 K. Dohnalová, K. Kůsová and I. Pelant, Time-resolved photoluminescence spectroscopy of the initial oxidation stage of small silicon nanocrystals, *Appl. Phys. Lett.*, 2009, **94**(21), 211903, DOI: 10.1063/1.3141481.
- 33 M. Cannas, P. Camarda, L. Vaccaro, F. Amato, F. Messina, T. Fiore and M. Li Vigni, Enhancing the luminescence efficiency of silicon-nanocrystals by interaction with H⁺ ions, *Phys. Chem. Chem. Phys.*, 2018, **20**, 10445–10449, DOI: 10.1039/c8cp00616d.
- 34 B. Li, P. J. Brosseau, D. P. Strandell, *et al.*, Photophysical Action Spectra of Emission from Semiconductor Nanocrystals Reveal Violations to the Vavilov Rule Behavior from Hot Carrier Effects, *J. Phys. Chem. C*, 2019, **123**(8), 5092–5098, DOI: 10.1021/acs.jpcc.8b11218.
- 35 J. Koktan, H. Sedláčková, I. Osante, *et al.*, Chiral supramolecular nanoparticles: The study of chiral surface modification of silver nanoparticles by cysteine and its derivatives, *Colloids Surf., A*, 2015, **470**, 142–148, DOI: 10.1016/j.colsurfa.2015.01.079.
- 36 D. B. Mawhinney, J. A. Glass and J. T. Yates, FTIR Study of the Oxidation of Porous Silicon, *J. Phys. Chem. B*, 1997, **101**(7), 1202–1206, DOI: 10.1021/jp963322r.
- 37 S. G. Moussa, A. C. Stern, J. D. Raff, *et al.*, Experimental and theoretical studies of the interaction of gas phase nitric acid and water with a self-assembled monolayer, *Phys. Chem. Chem. Phys.*, 2013, **15**(2), 448–458, DOI: 10.1039/C2CP42405C.
- 38 M. V. Wolkin, J. Jorne, P. M. Fauchet, *et al.*, Electronic States and Luminescence in Porous Silicon Quantum Dots: The Role of Oxygen, *Phys. Rev. Lett.*, 1999, **82**(1), 197–200, DOI: 10.1103/PhysRevLett.82.197.
- 39 K.-S. Chang-Liao and L.-Ch. Chen, Silicon dioxide/silicon interfacial strain analyzed by infrared spectroscopy, *Surf. Coat. Technol.*, 1997, **94**–**95**, 379–382, DOI: 10.1016/S0257-8972(97)00442-8.
- 40 R. Raji and K. G. Gopchandran, ZnO nanostructures with tunable visible luminescence: Effects of kinetics of chemical reduction and annealing, *J. Sci. Adv. Mater. Devices*, 2017, **2**(1), 51–58, DOI: 10.1016/j.jsamrd.2017.02.002.
- 41 L. Hongjun, Z. Zang and X. Tang, Synthesis mechanism and, optical properties of well nanoflower-shaped ZnO fabricated by a facile method, *Opt. Mater. Express*, 2014, **4**(9), 8, DOI: 10.1364/OME.4.0001762.
- 42 H. R. Moon, J. J. Urban and D. J. Milliron, Size-Controlled Synthesis and Optical Properties of Monodisperse Colloidal Magnesium Oxide Nanocrystals, *Angew. Chem., Int. Ed.*, 2009, **48**(34), 6278–6281, DOI: 10.1002/anie.200902056.
- 43 A. Kumar and J. Kumar, On the synthesis and optical absorption studies of nano-size magnesium oxide powder, *J. Phys. Chem. Solids*, 2008, **69**(11), 2764–2772, DOI: 10.1016/j.jpcs.2008.06.143.
- 44 K. Dohnalová, L. Ondič, K. Kůsová, *et al.*, White-emitting oxidized silicon nanocrystals: Discontinuity in spectral development with reducing size, *J. Appl. Phys.*, 2010, **107**(5), 053102, DOI: 10.1063/1.3289719.
- 45 V. Scholtz, E. Vaňková and J. Julák, Microbial Inactivation by Electric Discharge with Metallic Grid, *Acta Phys. Pol., A*, 2013, **124**, 62–65, DOI: 10.12693/APhysPolA.124.62.
- 46 K. Kůsová and T. Popelář, On the importance of onset times and multiple-wavelength analysis of photoluminescence decays, *J. Appl. Phys.*, 2019, **125**(19), 193103, DOI: 10.1063/1.5097065.
- 47 M. Greben, P. Khoroshyy, I. Sychugov, *et al.*, Non-exponential decay kinetics: correct assessment and description illustrated by slow luminescence of Si nanostructures, *Appl. Spectrosc. Rev.*, 2019, **54**(9), 758–801, DOI: 10.1080/05704928.2018.1517263.
- 48 J. Valenta, Determination of absolute quantum yields of luminescing nanomaterials over a broad spectral range: from the integrating sphere theory to the correct methodology, *Nanosci. Methods*, 2014, **3**(1), 11–27, DOI: 10.1080/21642311.2014.884288.
- 49 Homepage of the cp2k open source package for molecular dynamics simulations. <http://www.cp2k.org>.
- 50 J. P. Perdew, Density functional theory and the band gap problem, *Int. J. Quantum Chem.*, 1985, **28**(S19), 497–523, DOI: 10.1002/qua.560280846.
- 51 C. Delerue, G. Allan and M. Lannoo, Theoretical aspects of the luminescence of porous silicon, *Phys. Rev. B: Condens. Matter Mater. Phys.*, 1993, **48**(15), 11024–11036, DOI: 10.1103/PhysRevB.48.11024.

The red and blue luminescence in silicon nanocrystals with an oxidized, nitrogen-containing shell[†]

Pavel Galář,^a Tomáš Popelář,^a Josef Khun,^b Irena Matulková,^c Ivan Němec,^c Kateřina Dohnalova Newell,^d Alena Michalcová,^b Vladimír Scholtz^b and Kateřina Kůsová^a  

Received 27th September 2019, Accepted 22nd October 2019

DOI: 10.1039/c9fd00092e

Traditionally, two classes of silicon nanocrystals (SiNCs) are recognized with respect to their light-emission properties. These are usually referred to as the "red" and the "blue" emitting SiNCs, based on the spectral region in which the larger part of their luminescence is concentrated. The origin of the "blue" luminescence is still disputed and is very probably different in different systems. One of the important contributions to the discussion about the origin of the "blue" luminescence was the finding that the exposure of SiNCs to even trace amounts of nitrogen in the presence of oxygen induces the "blue" emission, even in originally "red"-emitting SiNCs. Here, we obtained a different result. We show that the treatment of "red" emitting, already oxidized SiNCs in a water-based environment containing air-related radicals including nitrogen-containing species as well as oxygen, diminishes, rather than induces the "blue" luminescence.

1 Introduction

Silicon nanocrystals (SiNCs) are an efficient light-emitting material with prospective applications ranging from biological imaging through light-emitting devices to photovoltaics.^{2–5} As is expected in a quantum-dot-based system, their optical properties are tunable with size. However, it is not only the maximum of the photoluminescence (PL) which changes with size as a result of the bandgap opening.^{6–13} Unlike in other quantum-dot-based systems, the decay lifetimes also

^aInstitute of Physics, Czech Academy of Sciences, Cukrovarnická 10, Prague 6, 162 00, Czech Republic. E-mail: kusova@fzu.cz

^bUniversity of Chemistry and Technology, Technická 3, Prague, 166 28, Czech Republic

^cDepartment of Inorganic Chemistry, Faculty of Science, Charles University, Hlavova 8, Prague 2, 128 43, Czech Republic

^dInstitute of Physics, University of Amsterdam, Science Park 904, 1098 XH Amsterdam, The Netherlands

† Electronic supplementary information (ESI) available. See DOI: 10.1039/c9fd00092e

depend on the size of the SiNCs^{12,14–17} as the efficiency of the emission is tuned by a changing level of confinement. Naturally, the quantum yield also changes.^{12,18}

“Bare” H-terminated SiNCs are strongly prone to oxidation under an ambient atmosphere,¹⁹ implying that their surface always needs to be terminated with a non-silicon-based chemical species. In addition to the size, the type of surface termination also strongly affects the optical properties.^{20–23} Probably the most typical surface chemistries include natural or intentional oxidation^{6,10,24} and long-alkyl-chain attachment *via* hydrosilylation,^{9,11,25,26} exhibiting emission in the red and near-infrared spectral region with radiative lifetimes on the order of 10–100 μ s. However, a wide range of other types of surface terminations are possible.

The optical properties introduced so far apply only to one class of SiNCs. It is generally recognized that in addition to the “red” emitting SiNCs described above, a second class of SiNCs exists: the “blue” emitting ones with much faster emission rates. The blue PL band can either co-exist with the red band,^{27,28} or it can stand completely on its own.^{1,29} Since fast emission in the blue spectral region under UV illumination is quite a common occurrence, there are as many models explaining the physical origin of the blue band as there are proposed mechanisms for the switch between the red and the blue types of emission. Given the prevalence of the blue emission across various materials, it is actually quite possible that different explanations are valid for different samples and more than one of the proposed models are necessary to explain the wealth of the observed types of behavior.

Starting with oxidized SiNCs, the blue band has been proposed to be connected with the crystalline core of the SiNCs,³⁰ possibly with the non-thermalized direct $\Gamma_{15}-\Gamma'_{25}$ transition^{31–33} (see Fig. 1a), whereas other studies see it completely as a result of oxidation and SiO_2 defects in the surface oxide.^{28,34} The blue-green emission of organically capped SiNCs was attributed to the crystalline core,³⁵ but a different study saw its origin in a surface defect or impurity.¹ As for the switch from the red to the blue PL, a discontinuity in the spectral tunability with decreasing size starting from the “red” emission is usually observed,^{1,8,13,17,28} even though here an exception to the rule can be found.⁷

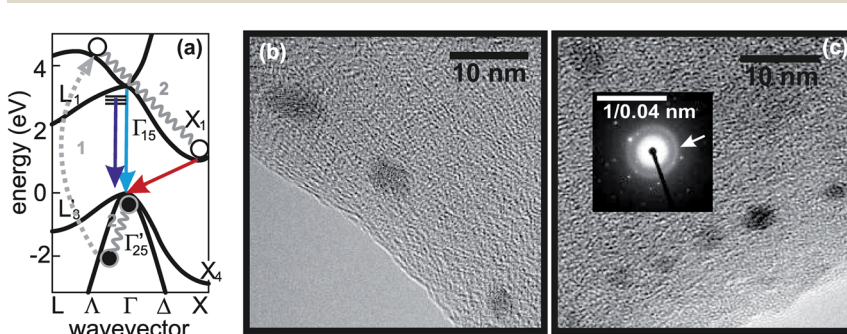


Fig. 1 (a) The band structure of bulk silicon with the transitions discussed in the text highlighted. Number (1) designates the excitation and number (2) the thermalization event. (b and c) Bright-field TEM images of SiNCs before (b) and after (c) surface modification. Individual NCs can be easily discerned. The corresponding selected-area electron diffraction pattern of the surface-modified SiNCs in (c) confirms the presence of randomly oriented NCs in the investigated spot.

Apart from the effect of oxidation,²⁸ an induced switch between red and blue emission has been ascribed to the presence of nitrogen “impurities”.¹ In that work, SiNCs were prepared by a top-down approach (annealing of an Si-rich material, HSQ) and using bottom-up syntheses (Na₄Si₄/NH₄Br reaction and SiCl₄ reduction). Even though all of the samples had basically the same size and the same surface termination, the emitted PL was the “red” type and the “blue” type of emission for the top-down and bottom-up approaches, respectively. The incorporation of nitrogen and oxygen “impurities” was identified as the process responsible for this difference; the mixing of the “red-emitting” SiNCs with nitrogen-containing compounds even induced them to have “blue” PL. As a result of that work, nitrogen is seen as an undesirable element, which can always induce “blue” PL in SiNCs.

There is some evidence in the literature, though, showing that this is not necessarily always true. One body of work constitutes SiNCs prepared *via* the reduction of SiCl₄, surface-terminated using N-linked aromatic compounds (*e.g.* diphenylamine, aniline), where high quantum yields were achieved.²⁹ The maximum PL of the surface-terminated SiNCs could be tuned using different types of surface termination, with aniline-terminated SiNCs emitting in the orange spectral region.²⁹ Fast PL lifetimes were reported, with no information on a possible long component. Similarly, the attachment of N-containing porphyrin molecules active as antennae on “red-emitting” dodecyl-capped SiNCs did not induce a switch of the red PL to blue PL either.³⁶ Looking at older publications, films of SiNCs treated in N₂ plasma, resulting in nitride-terminated SiNC films, were also investigated. The presence of the nitrogen in the nitride-rich SiNC films, just at the surface of the SiNCs, did not induce blue PL.^{37,38} Of particular interest is the comparison of such nitride-terminated SiNCs with oxidized ones,³⁸ which hints at the co-existence of a blue and a red PL band in the oxidized SiNCs, but also at its complete absence of the blue PL band in the nitride-terminated SiNCs. However, the optical experiments performed in that study were a bit rudimentary.

In this contribution, we study the effect of the treatment of oxidized SiNCs in a nitrogen-rich environment, focusing on the blue emission. The original, untreated oxidized SiNCs exhibit a weak blue PL band in addition to the standard red band. Despite the fact that nitrogen builds into the surface passivation layer of the SiNCs in the form of nitrites and/or nitrates, it is observed to cause the disappearance rather than the emergence of the blue band. This finding confirms that the presence of nitrogen close to SiNCs does not necessarily induce blue PL in SiNCs.

2 Methods

The studied SiNCs were prepared by a standardized electrochemical etching treatment followed by oxidation of the surface under ambient-conditions.¹⁷ In brief, crystalline silicon wafers were exposed to a solution of HF/EtOH in an electrochemical cell while current was passed through the etching solution (please note that HF can cause serious burns to the skin with significant complications due to fluoride toxicity). After two hours of etching, the resulting thin layer was washed with ethanol and let to dry in an ambient atmosphere at slightly elevated humidity ($\approx 50\%$). Mechanical pulverization of the electro-

etched layer yielded a powder of oxidized SiNCs, which had already been characterized in great detail.^{17,32,39,40}

In order to carry out the surface-modification treatment, SiNC powder was suspended in deionized water at a concentration of about 1 mg SiNCs/2 ml water and was treated in an ultrasonic pulse homogenizer for 1 hour. Then, the sample was placed in a quartz cuvette. The surface-modification treatment was performed in water using non-thermal plasma generated by electrical discharge in the point-to-plane arrangement and in the regime of transient spark. Transient spark discharge is described in ref. 41, and specific details will be published elsewhere. In brief, an electrode was inserted into the cuvette so that a discharge was generated between the electrode and the water surface under passing current. Processes induced by non-thermal plasma are related to the presence of high energy electrons. Their collisions with air molecules surrounding the water level produce reactive oxygen and nitrogen species, charged molecules and UV and visible photons under the conditions of the experiment. The radical species are dissolved in the water and the high energy molecules/atoms cause the radicalization of the surface part of the water. Moreover, the radicals from the air and the water induce secondary chemical processes in the water medium. This procedure yields the so-called plasma-activated water (PAW, for the details of PAW preparation and analysis see our previous studies^{42,43}), in our case, rich in nitrates NO₃ and nitrites NO₂. Although in many cases PAW is also rich in peroxide, H₂O₂, under the conditions of our experiment, peroxides are not present. The surface of the SiNCs was modified in PAW under the plasma discharge while the suspension was magnetically stirred for about 30 min. The resulting suspension of modified SiNCs was characterized by the methods detailed below. The samples used for EDS and FTIR measurements were washed additionally with deionized water to remove the remaining radicals. PAW for the luminescence measurements was separated from the modified sample using filtration with centrifuge filtration units. The PAW was checked for the absence of red PL to confirm that no SiNCs were present.

The microstructure of the samples and the EDS spectra were observed using a TEM Jeol 2200FS (200 kV) equipped with an Oxford Instruments EDS detector. As a support for the nanoparticles, holey carbon 300 mesh copper grids were used.

For FTIR measurements, the samples were deposited onto an Al plate and dried for three and half days in air, which guaranteed that all volatile substances had already evaporated. The FTIR spectra were recorded using the ATR (Ge crystal) technique using a ThermoScientific Nicolet iN10 FTIR Microscope with a resolution of 4 cm⁻¹ and the Norton-Beer strong apodization function in the spectral region of 675–4000 cm⁻¹, where the average spot size was 100 × 100 μm². Several different spots of each of the evaporated deposits were measured to confirm the homogeneity of samples.

For temporally resolved PL measurement, an optical setup composed of a femtosecond pulsed laser, Pharos SP – 1.5 mJ – 200 (150 fs), a harmonics generator HiRO (Light Conversion) and a streak camera (Hamamatsu) coupled with an imaging spectrospectrometer was employed. An excitation wavelength of 343 nm and a repetition rate of 1 kHz were used, and the impinging excitation intensity was 65 μJ cm⁻² (1.2 × 10¹⁴ photons per cm²). The suspensions of SiNCs were placed in (luminescence-free) quartz cuvettes and were magnetically stirred during the measurements, and we verified that the PL properties of both the

samples were not influenced by the laser beam. The angle between the excitation beam and the detection path was 90° . The PL of the second, modified sample was measured just after that of the unmodified one with minimal delay between the two and under the same excitation/detection conditions. We have also thoroughly verified that the intensity readings of our apparatus are well-repeatable, which implies that the PL intensities reported here are fully comparable across the two samples. The acquired PL maps were analyzed following a dedicated procedure outlined in ref. 44, ensuring high-quality fits. In brief, both the PL onset edge and the decay itself were taken into account using a convolution of a decay function (single-exponential, stretched-exponential) and the (known) shape of the incoming laser pulse. Four spectrally neighboring PL decays (that is a spectral region of about 1.5 nm) were averaged to increase the signal-to-noise ratio and the fitting in the temporal domain was performed for all of these averaged PL decays (≈ 130 decays per one spectrum). The background level (I_0 from eqn (1) introduced later) was determined as the mean of the values before the onset of PL and its homogeneity was checked in order to accurately discriminate possible weak signals from the background. At first, the data were fitted assuming only a simple single-exponential decay to find out the position of the onset edge, and in a second run, a more precise decay function was selected while the onset times were fixed to the values obtained from the first run. Spectrally uncorrected data were used for the fitting procedure, and a spectral correction was applied to the spectral part (decay amplitudes) after the fitting.

The transmittance spectra were collected using a Libra Biochrom S60 spectrophotometer.

For the calculations of the phononless radiative rates, the Si crystalline cores were built using the Vesta editor by making a cut-off from a bulk crystal along the (100) (110) and (111) crystal planes. In this way, approximately spherical SiNCs were obtained. All SiNCs had crystalline cores. The surface of the SiNCs had different types of facets with $-SiX_3$, $-SiX_2$ and $-SiX$ binding sites. The $-SiX_3$ species were not chemically stable and were removed. The (100) facets were reconstructed. The resulting SiNCs were slightly tetrahedral and were 100% covered by hydrogen. OH passivation was 100%, and the mixed $-OH$ and $-O-NO_2$ -capped nanoparticle had $-O-NO_2$ attached to 49 surface sites and OH to the remaining 55 sites. Calculations were performed using density functional theory (DFT) as implemented in the CP2K package Quickstep,⁴⁵ with the generalized gradient approximation functional of Perdew–Burke–Ernzerhof.⁴⁶ The core was approximated by the Goedecker–Teter–Hutter pseudopotential potential.⁴⁷ For the basis set, we used the short-range Gaussian double-zeta valence polarized basis set DVZP-MOLOPT.⁴⁵ Plane wave cutoff of the integration grid was set to 400 Ry and the self-consistency convergence to 10^{-6} . The bandgap energies appeared to be shifted by a constant value of 0.5 eV, which is a known issue of ground state DFT.⁴⁸

3 Results

3.1 Surface modification and changes in chemistry

In our study, we used porous-silicon-based SiNCs oxidized under an ambient atmosphere at slightly elevated humidity, which had already been studied in great detail. In brief, the size of the crystalline core of the light-emitting SiNCs was around 2.5–3 nm,³⁹ and the prevailing surface species was oxide.³⁹ The PL

characteristics were dominated by a broad red PL band positioned around 650 nm with microsecond decay times, even though a fast blue band was also present.^{17,32} The porous-silicon origin of the SiNCs, on the one hand, causes the presence of a broad distribution of sizes of NCs and crystallites in the samples, including crystallites with sizes of ≈ 50 nm.⁴⁰ On the other hand, it ensures that the small light-emitting SiNCs have crystalline cores, since they originate from a single-crystalline Si wafer. It might not be so straightforward to achieve such high concentration of particles with crystalline cores in bottom-up preparation approaches, such as in various types of chemical syntheses.

The water-based suspension of the oxidized SiNCs underwent surface modification by the application of non-thermal plasma under ambient conditions (atmosphere and temperature). The non-thermal plasma discharge ionizes the air surrounding the SiNC suspension and causes the generation of water-related reactive species. The air-originating radicals dissolve in the water and might react with the water-related species. The complex series of chemical reactions leads to a cocktail of reactive species dissolved in water, resulting in the so-called plasma-activated water (PAW). The type and the concentration of the reactive species in the PAW depend on the conditions of the plasma discharge; in our case, the prevailing species are NO_2^- ($\approx 30 \text{ mg l}^{-1}$) and NO_3^- ($\approx 5 \text{ g l}^{-1}$), but H_2O_2 is not present. High concentrations of these radicals caused very low pH values (1–2) in the PAW in our experiment. The details of the modification procedure are beyond the scope of the current contribution.

As can easily be expected from the absence of peroxides the PAW treatment does not affect the crystalline cores of the original SiNCs because the treatment conditions are too mild to possibly destroy a crystalline core. The presence of small crystalline particles in both the original sample and in the sample after the surface modification are documented *via* the TEM measurements in Fig. 1b and c. The SAED diffraction pattern of the surface-modified sample in the inset of Fig. 1c shows a clearly defined circle, typical of very small randomly oriented crystalline nanoparticles.^{24,49} However, the already mentioned presence of larger crystallites originating from the etching preparation procedure causes residual diffraction of the silicon lattice.

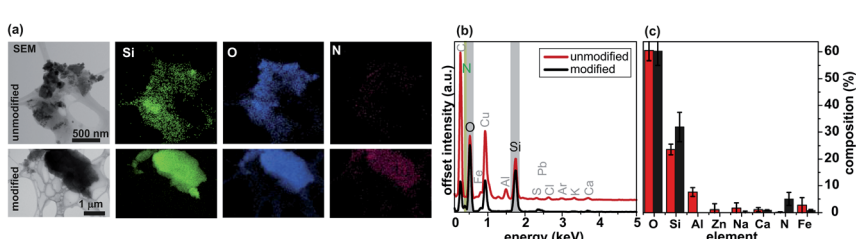


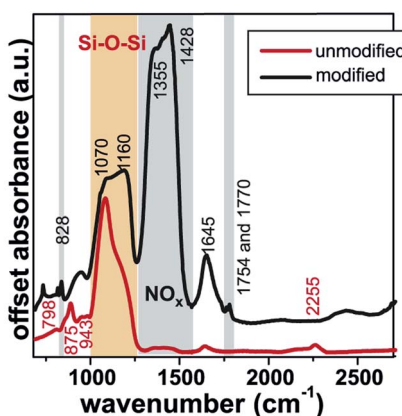
Fig. 2 (a) Elemental analysis of the unmodified (top row) and surface-modified (bottom row) SiNCs. The four pairs of images correspond to the electron-microscopy image (left), and the EDS maps of the Si, O and N content (right). Before the modification, the nitrogen content in the sample was very low, and after the modification, the N content significantly rose in the areas containing Si. (b) Examples of two EDS spectra. (c) Elemental composition averaged over several samples and spots and compensated for the signal of the substrate. The error bars represent the standard deviations of the average values. Color coding is the same as in (b).

The non-thermal plasma treatment of the oxidized SiNCs results in a change in the surface-passivation layer of the SiNCs. Fig. 2 compares electron micrographs and the energy dispersive X-ray spectroscopy (EDS) elemental maps of the original and surface-modified SiNCs, respectively. As expected, the most important elements present in the sample before the treatment were silicon and oxygen (see also the EDS spectra in Fig. 2b). When probed, trace amounts of nitrogen could also be detected. After treatment in the nitrite- and nitrate-rich PAW, silicon and oxygen still remained the most important elements in the modified sample, however, the amount of incorporated nitrogen dramatically increased (Fig. 2a).

Since the acquired EDS spectra from Fig. 2a tend to contain “flakes” of impurity material (such as Cu from the grids, see Fig. S1 in the ESI†), EDS spectra from two different samples were averaged over several spots and compensated for the signal of the carbon substrates. The resulting elemental composition is shown in Fig. 2c. Considering the sizes of the SiNCs under study, a rough estimate of 0.4 surface bonds to be passivated per one silicon atom in the crystalline core can be made.⁵⁶ The different observed silicon-to-oxygen ratio in the unmodified sample was a result of CO₂ being adsorbed by the sample during the measurement. The other elements present in trace amounts are residual impurities originating from the preparation procedure (Al – from the duralumin substrate of the electrochemical etching cell, Fe from the stainless steel scalpel used for mechanical pulverization, and Na from NaOH used for cleaning of the etched wafers). The concentration of all of these impurities decreased after the modification, implying that they are clearly washed out during the radical-removal procedure after the modification treatment and thus not involved in the modifications presented in this study.

The important changes in the elemental composition of the modified sample are a small increase in the silicon-to-oxygen content ratio accompanied by a large increase in nitrogen content, implying that part of the oxidized surface of the unmodified SiNCs is replaced with a nitrogen-containing compound. The increase in the nitrogen content is significant, and it rises from (0.2 ± 0.2)% to as much as (5.0 ± 2.5)%. Just to give an idea of what this means, we can imagine a “model” SiNC composed of about 700 Si core atoms (3 nm in diameter), which has about 250 surface bonds to be passivated.⁵⁶ Presuming a simple case of a 1 : 1 passivation of these surface bonds with bridging oxygen bonds Si–O–Si and with hydroxyl groups –OH, the hypothetical NC has 160 surface oxygen atoms. If 5% of this NC is supposed to be made up of nitrogen, about 40 of these surface oxygen atoms would have to be replaced with nitrogen atoms.

The chemical nature of the incorporated nitrogen was revealed by FTIR measurements in ATR mode, as shown in Fig. 3. The oxidized unmodified SiNC sample has already been studied in detail.³⁹ The prominent surface features are bridging Si–O–Si bonds at 1000–1250 cm⁻¹ and 798 cm⁻¹ accompanied by silanol Si–OH (846 and 943 cm⁻¹) and back-oxidized hydride O_x–SiH_y (875 and 2255 cm⁻¹) groups. The PAW treatment led to the disappearance of the back-oxidized hydride groups whereas silanol groups were preserved. More importantly, some changes in the bridging-oxygen region are observed, suggesting reorganization in the surface oxides. However, the most marked feature of the SiNCs after the treatment was the emergence of a new FTIR band between 1250 and 1560 cm⁻¹. In accordance with the studies of the interactions of HNO₃ with SiO₂ and an organic self-assembled layer-coated Ge crystal under dry and humid



Bond	Wavenumber	Ref
ν_s Si–O–Si	$\approx 795\text{ cm}^{-1}$	50,51
ν_a Si–O–Si	$\approx 975\text{--}1130\text{ cm}^{-1}$	50–52
ν'_a Si–O–Si	$\approx 1130\text{--}1260\text{ cm}^{-1}$	50,52
δ O _x –SiH _y	875 cm^{-1}	51,52
ν O _x –SiH _y	2262 cm^{-1}	51,52
ν Si–OH	$\approx 940\text{ cm}^{-1}$	53
ν_2 NO ₃ ⁻	828 cm^{-1}	54
ν_3 NO ₃ ⁻	$1300\text{--}1500\text{ cm}^{-1}$	55
($\nu_1 + \nu_4$) NO ₃ ⁻	$1750\text{--}1770\text{ cm}^{-1}$	54
δ H ₂ O	1641 cm^{-1}	55
ν H ₂ O	3400 cm^{-1}	55

Fig. 3 FTIR-ATR measurements of the unmodified and modified samples and the assignments of the observed FTIR peaks (ν stands for stretching, δ for deformation, s for symmetric, and a for antisymmetric) with the corresponding references used for the assignments noted.

N₂ flow,⁵⁵ these peaks result from the presence of nitrate/nitrite ions. The shape of this nitrate peak, which is asymmetric but exhibits minimal levels of splitting, indicates that the trigonal symmetry of the nitrate anions is almost retained on the SiNC surface. This fact could be explained by a set of weak bonding interactions \cdots O–NO₂ to the SiNC surface (probably also including a weak bidentate bonding mode of nitrates), which induce only a minimal distortion of symmetry. Additionally, the splitting of the combination band ($\nu_1 + \nu_4$) of the nitrate anions into two bands at 1770 and 1754 cm⁻¹ can also confirm the existence of a weak bonding interaction of NO₃⁻ with the surface of the SiNCs. The separation of the combination band of 24 cm⁻¹ represents the border of the monodentate and chelating bidentate interactions of nitrate ions according to the literature.⁵⁴ The band recorded at 828 cm⁻¹, overlapped by the vibrational motion of silanol, can be also assigned to the ν_2 NO₃⁻ vibration. An alternative explanation of the shape of the 1250–1560 cm⁻¹ FTIR band could be also related to the formation of nitrate–water complexes (discussed in ref. 55 and references therein) bound to the SiNC surface. The presence of water molecules is indicated by the H₂O bending mode recorded at 1645 cm⁻¹. Thus, FTIR not only confirms the increase in

nitrogen content, it also shows that the changes are due to the PAW modification and the incorporation of nitrate–water complexes into the surface layer of the SiNCs.

3.2 The blue photoluminescence band

The incorporation of nitrogen-containing complexes into the shells of the modified SiNCs influences the emitted PL. Even though the “red” PL band is affected by the treatment to some extent (see Fig. 5a), contrary to the results of ref. 1, it does not disappear. Thus, it is not of special interest here.

In order to study the “blue” PL band, we carried out time-resolved PL spectroscopy of both the unmodified and modified samples. The excitation wavelength of 343 nm was chosen for a direct comparison of the blue bands of the two samples, since it lies just outside the absorption range of PAW, see Fig. S2 in the ESI.[†] Even a single look at the measured temporally and wavelength-resolved dependencies of the PL intensity presented in Fig. 4a and d reveals that there is a marked difference between the blue PL bands of the two samples. Interestingly, in accordance with the results presented in ref. 38, the band is observed to diminish rather than increase in intensity following the nitrogen-enriching treatment, see also Fig. 5d.

More insights into the dynamics of the blue PL bands can be gained using a proper analysis, which is unavoidable considering that nearly any material has some blue PL when excited in the UV region. Here, we employ a procedure put forward in ref. 44, which takes into account the whole PL decay including the

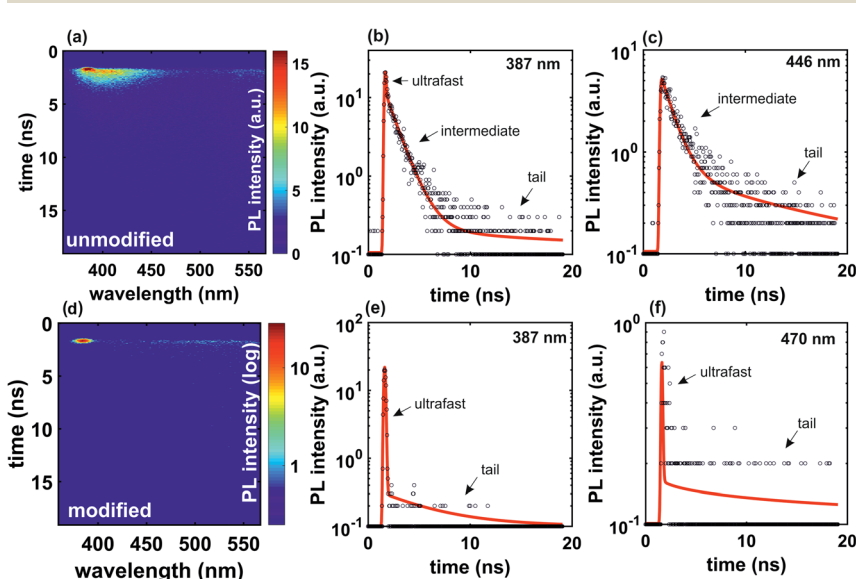


Fig. 4 Time-resolved PL measurements of the unmodified (top row) and surface-modified (bottom row) SiNCs (ultrafast pulsed excitation at 343 nm). The left columns show the measured PL maps (PL as a function of time and wavelength, please note that the PL intensity scale of the modified sample is logarithmic), the remaining two columns display examples of data fits: the measured data (black circles) and the corresponding fits (red curves) are plotted in a shifted logarithmic scale for two selected emission wavelengths.

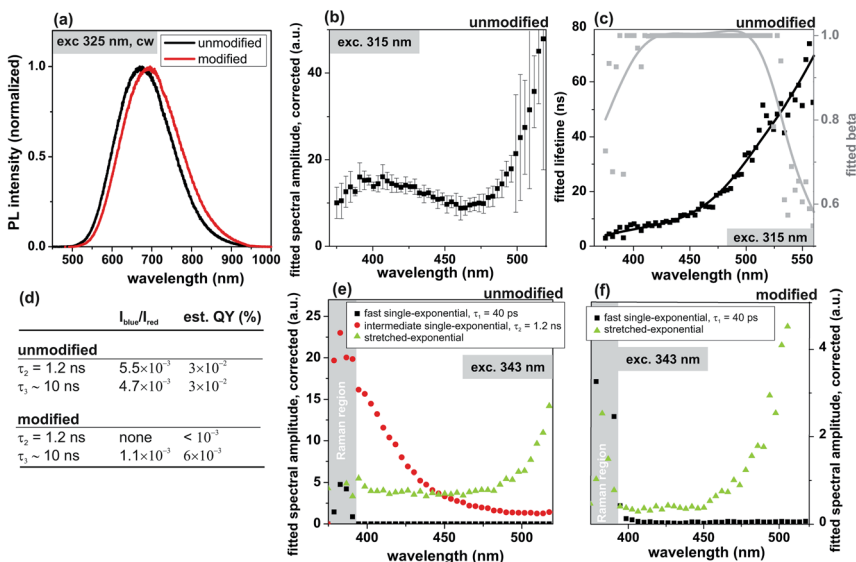


Fig. 5 (a) Comparison of normalized PL spectra of the red bands of the unmodified and modified SiNCs using 325 nm CW excitation. (b and c) Results of the fits of the PL of the unmodified SiNCs using pulsed 315 nm excitation (for the fits, see Fig. S3 in the ES†). The curves represent spline-smoothing of the presented data to serve as guides-for-the-eye. (d) Integrated PL intensities for the second and third component and the corresponding rough estimates of quantum yields (see text for more details). (e and f) Spectral amplitudes of the fitted components of the PL of the unmodified and modified samples under pulsed 343 nm excitation, respectively. The corresponding PL maps are shown in Fig. 4.

onset edge. To do so, a convolution (\star) of a (known) instrument response function $i_{\text{irf}}(t; \sigma)$ with the PL decay function (a single- or stretched-exponential characterized by lifetime τ and stretched parameter β including a proper normalization factor $\text{norm}(\tau, \beta)$) is used as a fitting function:

$$i_{\text{meas}}(t, \lambda; \sigma, \tau_0, I_0, A(\lambda), \tau(\lambda), \beta(\lambda)) = \frac{A(\lambda)}{\text{norm}(\tau(\lambda), \beta(\lambda))} \exp \left\{ - \left(\frac{t - \tau_0(\lambda)}{\tau(\lambda)} \right)^{\beta(\lambda)} \right\} \star i_{\text{irf}}(t; \sigma) + I_0, \quad (1)$$

where $A(\lambda)$ is the amplitude of the corresponding decay component, σ is the apparent width of the laser pulse in the chosen temporal window and I_0 is the background. The fitting was performed over the individual measured wavelength-resolved PL decays and the extracted characteristics $A(\lambda)$, $\tau(\lambda)$ and $\beta(\lambda)$ were checked for any underlying spectral dependencies. In contrast to simply focusing on the PL decay at a single wavelength or on the spectrally unresolved PL, this approach helps one determine if more than a single dynamic component is present and the additional information on its spectral dependence is beneficial for the identification of the underlying physical process.

Starting with the oxidized unmodified SiNCs, three different components were identified. The clear presence of these three components can be visualized when the measured PL decays are plotted on the offset logarithmic scale⁴⁴ (so that the smallest-PL-intensity data points, representing the measured zero, are also

visible), as seen in the fit-and-data plots in Fig. 4b and c. The first component is ultrafast and it was fitted assuming a single-exponential decay with a lifetime set to the temporal difference between two consecutive datapoints ($\tau_1 = 40$ ps in the chosen temporal window), implying that the corresponding lifetime is ≤ 40 ps. The second component is also single-exponential, and was found to be emission-wavelength-independent with⁵⁷ $\tau_2 = 1.2$ ns. A weaker third component produced a slower-than-single-exponentially decaying tail and it was approximated with a stretched-exponential.

In order to suppress the ultrafast PL component, the two samples were also measured using the excitation wavelength of 315 nm. Examples of data-and-fit plots are given in Fig. S3 in the ESI† and the deduced amplitudes, lifetimes and β 's are shown in Fig. 5b and c. This analysis confirms that the slower, stretched-exponential component is excitation wavelength independent and it also allows one to better characterize its spectral evolution, which peaks at ≈ 400 nm. Unfortunately, the properties of the intermediate component could not be accurately analyzed using the shorter excitation wavelength, because the blue-shift of the excitation wavelength causes a much more efficient excitation of the solvent, whose PL characteristics are far too similar to those of the SiNCs to allow for an accurate analysis.

As for the nitrogen-containing modified SiNCs, the PL intensity of their blue PL band is clearly diminished when compared to the unmodified sample. The intermediate $\tau_2 = 1.2$ ns component is completely missing, but a weak stretched-exponential tail persists, as seen in Fig. 4e and f. Despite what it might seem at first sight, the red curves in these plots fit the measured data very well. It is important to realize here that the plot is shown, contrary to standard representation, in a logarithmic vertical scale shifted by a small value to also include the zero values.⁴⁴ This representation provides a better visual cue as to how the signal approaches zero as opposed to a traditional logarithmic plot where the zero (or negative) values are simply omitted as a result of applying the logarithm. As the signal yielded by our apparatus is intrinsically digital, a tail of any PL decay, and that of a slower stretched-exponential one in particular, is made up by increasingly scarce photon-detection events one “level” above the zero. Such photon-detection events are exactly what can be seen in Fig. 4e and f. For a more in-depth discussion, readers should refer to ref. 44. As the signal of this third component is too weak to allow for meaningful fitting by itself, it was assumed to be characterized by the same lifetimes as those of the unmodified sample (the spline curve in Fig. 5c) and only the β parameter and the amplitude were fitted. The deduced spectral amplitudes are plotted in Fig. 5f. The reasonable agreement between the fitted β parameters in the modified (see Fig. S4 in the ESI†) and unmodified samples, respectively, justifies this approach.⁵⁸

In order to get a quantitative comparison of the intensities of the blue bands of the unmodified and modified samples, integrals of the individual spectral components were calculated. Only the spectral region between 400 and 500 nm was considered to avoid the influence of the ultrafast component. Extreme care was taken to ensure that the samples were measured under the same excitation, collection and detection conditions, which enables a direct (relative) comparison of the measured PL intensities. The concentration of the SiNCs in the unmodified and modified suspensions were also roughly the same, which is evidenced by the transmittance spectra in Fig. S2 in the ESI:† the SiNCs cause scattering, resulting

in the decreased transmittance in the 500–700 nm spectral region, which is the same in the two samples. Below 340 nm, the absorption of PAW sets in. Thus, the chosen excitation wavelength of 343 nm seems to ensure optimal conditions for the comparison of the two samples.

The red spectral component of the unmodified sample was also measured and spectrally integrated under the same conditions (not shown). The integrated intensities of the blue components are listed with respect to the integrated intensity of the red PL, see Fig. 5d. Since the quantum yield of the red component is known ($\approx 6\%$), rough estimates of the quantum yields of the blue components under the excitation conditions of this study can be made. They are on the order of 0.01% and are listed in Fig. 5d.

3.3 Computational study of the electronic states

In order to theoretically assess the influence of surface-present nitrogen on the SiNC states, we performed DFT calculations of the electronic states. In particular, the structure of a reasonably sized nanoparticle (Si_{235}H , corresponding to a diameter of about 2.0 nm) was relaxed, including two types of covalently bonded surfaces: (i) full passivation by $-\text{OH}$ groups to simulate surface oxide and (ii) the replacement of some of the $-\text{OH}$ groups with $-\text{O}-\text{NO}_2$ groups ($\approx 50\%$), emulating the surface-modified SiNCs. Importantly, the structure of the nanoparticle does not allow for full surface coverage with $-\text{O}-\text{NO}_2$ groups due to spatial constraints, suggesting that the partial surface chemistry change is a plausible scenario.

As is evident from the results of these calculations presented in Fig. 6, the surface-bonded nitrogen in the form of $-\text{O}-\text{NO}_2$ induces some changes in the density of states in the SiNC. First, low-density-of-states in-gap states close to the edges of both the valence and conduction bands appear. Secondly, disregarding these in-gap states, a small redshift in the bandgap energy (from 1.517 eV in the fully oxidized to 1.493 eV in the partly nitrated SiNC model) occurs. Thirdly, some degree of real-space localization at surface sites, mostly at O and N atoms, occurs for the states at the edge of the conduction band of the partly nitrated particle, as also evidenced by the 3D images in Fig. 6. However, if the radiative rates corresponding to these states are calculated, only an increase of several times is obtained when compared to the fully oxidized SiNC model.

The fact that nitrogen in the shell of the NC does not necessarily lead to an impurity state causing short PL decay is illustrated also in the calculations of the density of states of a partly $-\text{O}-\text{NH}_2$ -terminated Si nanoparticle in Fig. S5 in the ESI,[†] where conduction-band states are much more influenced by the presence of nitrogen than the valence-band states.

4 Discussion

Both the results of our theoretical calculations and experiments confirm that, in the case of the SiNCs studied, the incorporation of non-negligible amounts of nitrogen in the form of nitrate–water complexes does not induce blue PL in the sample. The first-excited-state indirect-bandgap $\Gamma_{15}-\text{X}$ transition is still observable, it is not dramatically affected and the presence of nitrogen in the shell does not give rise to localized in-gap “impurity-like” states.

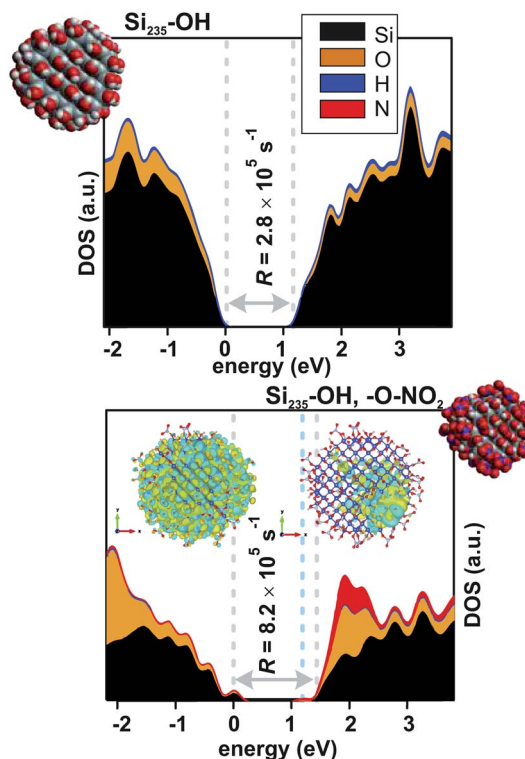


Fig. 6 Calculated real-space density of states as a function of energy for two Si nanoparticles with the same crystalline core (approx. 2.0 nm in diameter) but different surface passivations, showing real-space localization on the corresponding atoms. The insets in the nitrogen-containing Si nanoparticle show 3D real-space localizations of the two energy states as designated by the grey and light blue dashed lines on the left and right, respectively. R values are the calculated radiative rates of the first-excited-state transitions, shown by the grey dashed lines.

Focusing on the blue PL band as observed in the unmodified, oxidized SiNCs, it was made up by three components, two single-exponentials (exp) and one stretched-exponential (SE):

$$I_{\text{PL}}(t, \lambda) = \exp(\tau_1 = 40 \text{ ps}) + \exp(\tau_2 = 1.2 \text{ ns}) + \text{SE}(\tau_3(\lambda) \approx 10 \text{ ns}). \quad (2)$$

Clearly, the ultrafast component ($\tau_1 = 40 \text{ ps}$) can be identified with the Raman signal of the solvent (water) since its spectrum is mostly situated in one peak (see Fig. 5b) (although some ultrafast signals can also be found in other parts of the spectrum). The difference between the excitation and emission wavelengths (343 and 384 nm, respectively) is $\approx 3000 \text{ cm}^{-1}$, implying the assignment of this peak to the typical vibrations of OH groups. Such Raman signal would be expected to shift under shorter-wavelength excitation of 315 nm to 348 nm, *i.e.* out of the collection spectral window, which we verified experimentally, see Fig. S4 in the ESI.†

The origin of the intermediate PL component $\exp(\tau_2 = 1.2 \text{ ns})$, considering the spectral independence of its lifetime τ_2 , most likely lies in the defect states of

SiO_2 , as was suggested by previous studies.³⁴ The third component, then, is stretched-exponential in nature and despite being weak, its characteristics $\tau_3(\lambda)$ and $\beta_3(\lambda)$ were observed to depend on the emission wavelength (see Fig. 5c). Moreover, spectrally speaking, it seems to be a direct continuation of the “red” (stretched-exponentially decaying) PL band towards the shorter emission wavelengths. This trend was also confirmed when using a shorter excitation wavelength to avoid the influence of the Raman component, see Fig. 5b and c. Consequently, this third PL component can be assigned to the non-thermalized, direct $\Gamma_{15}-\Gamma'_{25}$ transition, as discussed earlier.³²

Interestingly, the presence of nitrates in the shells of the SiNCs dramatically decreases the PL intensity of the blue band in the modified SiNCs. This difference is quantified in Fig. 5d, where the integrated PL signals emitted between 400 and 500 nm are listed. Obviously, the observed blue PL band is relatively weak in all cases. The most important change, however, is the complete disappearance of the SiO_2 -defect-related intermediate $\exp(\tau_2 = 1.2 \text{ ns})$ peak. The absence of this peak in the modified sample implies that the PAW treatment radically improves the quality of the surface oxide shell of the SiNCs.

The stretched-exponential component related to the non-thermalized direct $\Gamma_{15}-\Gamma'_{25}$ emission also decreases in intensity by about five times. However, it is important to realize that the decrease in the intensity of this spectral component as a result of the change in the chemical composition of the surface shell of a NC does not automatically imply that this band originates in surface-related states, which might be the first intuitive conclusion. Being connected with non-thermalized (hot) carriers, this band is governed by both the radiative rates of the corresponding transition and the thermalization rates, which are generally very fast. Thus, it is plausible to deduce that the SiO_2 -related defects enhanced the intensity of this non-thermalized emission in the unmodified sample by slowing down the thermalization rates. In the modified sample, the removal of these states clearly increased the thermalization rates and in turn decreased the intensity of the corresponding emission.

The most intriguing result here is clearly the completely different response of SiNCs to the exposure to a nitrogen- and oxygen-rich environment observed in this study (and previously also by Chen *et al.*³⁸) and by Dasog *et al.*¹ Let us briefly review the existing evidence. Dasog *et al.*¹ prepare their SiNCs by three solution-based methods (thermally induced disproportionation of HSQ, the $\text{Na}_4\text{Si}_4/\text{NH}_4\text{Br}$ reaction and the SiCl_4 reduction). In all cases, the surface was terminated with dodecene groups using thermal hydrosilylation. The Si core sizes were reported to be (3.5 ± 0.4) , (6 ± 2) and (2.7 ± 0.6) nm, respectively, based on TEM analysis. Whereas the HSQ-based SiNCs exhibited slow red PL, the SiNC prepared by the other two methods emitted immediately fast blue PL, according to the authors because of trace amounts of nitrogen being incorporated as optically active impurities. Moreover, the exposure of the “red” emitting SiNCs (with H-terminated surfaces) caused a switch to the “blue” PL. Next, in the early work by Chen *et al.*,³⁸ the nitride-terminated SiNCs were prepared by plasma enhanced chemical vapor deposition using SiH_4 and N_2 as source gases with TEM-derived mean sized of 4.6 and 3.1 nm, exhibiting size-dependent slow PL (with no fast signal). A reference oxidized SiNC sample prepared by annealing of an amorphous Si layer in Ar at 1100 °C emitted slow red PL with hints of a fast bluer band. In this study, the exposure of electrochemically etched SiNCs, with mean core sizes of 2.5–3 nm, to

nitrogen-rich PAW quenched the SiO₂-defect-related blue PL and dramatically decreased the core-related blue PL while not quenching the red PL.

Thus, it is very difficult, if not impossible, to formulate a hypothesis encompassing all of these reported results since they are contradictory. The differences between the samples seem to be neither the size (samples with comparable sizes behave differently) nor the surface (H-terminated SiNCs were exposed to nitrogen yielding both “red”³⁸ and “blue”¹ PL, even though during the preparation of the “red” SiNCs there was conceivably no oxygen present). We do not want to form unsubstantiated hypotheses here, which is why such an all-explaining hypothesis is beyond the scope of the current work and is a topic for further research. However, we want to highlight three observations which might help one find the solution to this problem:

(i) The SiNCs in this study are electrochemically etched and as such they are embedded in relatively thick layers of SiO₂. It is plausible to assume that these SiO₂ layers might make it more difficult for the nitrogen to get to the core of the SiNC and form a defect site inside it. Were this the case, the “red”-emitting SiNCs yielded by the plasma deposition in the presence of nitrogen³⁸ could be a result of the absence of oxygen, as suggested by Dasog *et al.*¹

(ii) The “blue” PL as reported by Dasog *et al.*¹ is not by any means evocative of defect PL (it is very broad and excitation-wavelength dependent). Thus, one might hypothesize that nitrogen only quenches the PL of SiNCs and the source of the reported “blue” PL is a completely different material. Were this the case, nitrogen would have to bind differently to SiNCs in this study than in the other two discussed studies. Also, a thorough quantification of quenching of the “red” band would be helpful along with a more detailed analysis of the blue PL emitted by those samples.

(iii) There has also been an ongoing discussion about low- and high-temperature preparation methods yielding the “blue”- and “red”-emitting SiNCs,² respectively. Interestingly, in this regard, Dasog *et al.*¹ actually showed that “blue” PL was emitted by SiNCs prepared by a high-temperature method after their exposure to nitrogen, because HSQ disproportionation constitutes a high-temperature method due to the temperatures involved in the annealing step.

5 Conclusion

The influence of the exposure of oxidized SiNCs to a nitrogen- and oxygen-rich environment of plasma activated water was studied. The plasma-activated-water treatment resulted in the incorporation of nitrate/nitrite complexes onto the surface of the SiNCs and it affected the surface oxide layer, as evidenced by EDS and FTIR measurements. Primary focus was put on the blue PL emission band, which is present, but not dominant, in the unmodified oxidized SiNCs. Temporally and spectrally resolved PL measurements of this blue band analyzed in detail confirm that the blue PL emission is quenched after the intake of nitrogen into the SiNC. These results indicate that the exposure to a nitrogen-rich environment does not necessarily imply a switch to blue PL in all types of SiNCs, as was suggested by previous studies.

Conflicts of interest

There are no conflicts to declare.

Acknowledgements

The Czech Science Foundation funding, Grant No. 18-05552S (PG, TP, KK), the Operational Programme Research, Development and Education financed by European Structural and Investment Funds and the Czech Ministry of Education, Youth and Sports (Project No. SOLID21 CZ.02.1.01/0.0/0.0/16_019/0000760, KK), the CUCAM Centre of Excellence (OP VVV “Excellent Research Teams” project No. CZ.02.1.01/0.0/0.0/15_003/0000417, IM, IN) and NWO funding (FOM Project-ruimte No. 15PR3230, KDN) are gratefully acknowledged.

Notes and references

- 1 M. Dasog, Z. Yang, S. Regli, T. M. Atkins, A. Faramus, M. P. Singh, E. Muthuswamy, S. M. Kauzlarich, R. D. Tilley and J. G. C. Veinot, *ACS Nano*, 2013, **7**, 2676–2685.
- 2 B. Ghosh and N. Shirahata, *Sci. Technol. Adv. Mater.*, 2014, **15**, 014207.
- 3 B. F. P. McVey and R. D. Tilley, *Acc. Chem. Res.*, 2014, **47**, 3045–3051.
- 4 M. Dasog, J. Kehrle, B. Rieger and J. G. C. Veinot, *Angew. Chem., Int. Ed.*, 2016, **55**, 2322–2339.
- 5 K. Kůsová and K. Dohnalová, in *Silicon Nanomaterials Sourcebook: Low-Dimensional Structures, Quantum Dots, and Nanowires, Volume One*, ed. K. D. Sattler, Taylor&Francis Publisher, CRC Press, Boca Raton, Florida, USA, 2017, pp. 367–397.
- 6 M. V. Wolkin, J. Jorne, P. M. Fauchet, G. Allan and C. Delerue, *Phys. Rev. Lett.*, 1999, **82**, 197–200.
- 7 Z. Kang, Y. Liu, C. H. A. Tsang, D. D. D. Ma, X. Fan, N.-B. Wong and S.-T. Lee, *Adv. Mater.*, 2009, **21**, 661–664.
- 8 J. Choi, N. S. Wang and V. Reipa, *Langmuir*, 2007, **23**, 3388–3394.
- 9 C. M. Hessel, D. Reid, M. G. Panthani, M. R. Rasch, B. W. Goodfellow, J. Wei, H. Fujii, V. Akhavan and B. A. Korgel, *Chem. Mater.*, 2012, **24**, 393–401.
- 10 K. Kůsová, L. Ondič, E. Klimešová, K. Herynková, I. Pelant, S. Daniš, J. Valenta, M. Gallart, M. Ziegler, B. Hönerlage and P. Gilliot, *Appl. Phys. Lett.*, 2012, **101**, 143101.
- 11 J. R. Rodriguez Nunez, J. a. Kelly, E. J. Henderson, J. G. C. Veinot, J. R. Rodríguez Núñez, J. a. Kelly, E. J. Henderson and J. G. C. Veinot, *Chem. Mater.*, 2012, **24**, 346–352.
- 12 M. L. Mastronardi, F. Maier-Flaig, D. Faulkner, E. J. Henderson, C. Kübel, U. Lemmer and G. A. Ozin, *Nano Lett.*, 2012, **12**, 337–342.
- 13 S. P. Pujari, H. Driss, F. Bannani, B. van Lagen and H. Zuilhof, *Chem. Mater.*, 2018, **30**, 6503–6512.
- 14 F. Sangghaleh, I. Sychugov, Z. Yang, J. G. C. Veinot and J. Linnros, *ACS Nano*, 2015, **9**, 7097–7104.
- 15 M. Greben, P. Khoroshyy, X. Liu, X. Pi and J. Valenta, *J. Appl. Phys.*, 2017, **122**, 034304.
- 16 S. L. Brown, R. Krishnan, A. Elbaradei, J. Sivaguru, M. P. Sibi and E. K. Hobbie, *AIP Adv.*, 2017, **7**, 055314.
- 17 K. Dohnalová, L. Ondič, K. Kůsová, I. Pelant, J. L. Rehspringer and R.-R. Mafouana, *J. Appl. Phys.*, 2010, **107**, 053102.

- Published on 22 October 2019. Downloaded by Institute of Physics of the Czech Academy of Sciences on 8/18/2023 1:24:14 PM.
- 18 K. Dohnalová, T. Gregorkiewicz and K. Kúsová, *J. Phys.: Condens. Matter*, 2014, **26**, 173201.
 - 19 M. J. Sailor and E. J. Lee, *Adv. Mater.*, 1997, **9**, 783–793.
 - 20 K. Dohnalová, K. Kúsová and I. Pelant, *Appl. Phys. Lett.*, 2009, **94**, 211903.
 - 21 M. Dasog, G. B. D. los Reyes, L. V. Titova, F. A. Hegmann and J. G. C. Veinot, *ACS Nano*, 2014, **8**, 9636–9648.
 - 22 T. Zhou, R. T. Anderson, H. Li, J. Bell, Y. Yang, B. P. Gorman, S. Pylypenko, M. T. Lusk and A. Sellinger, *Nano Lett.*, 2015, **15**, 3657–3663.
 - 23 G. M. Carroll, R. Limpens and N. R. Neale, *Nano Lett.*, 2018, **18**, 3118–3124.
 - 24 R. Anthony and U. Kortshagen, *Phys. Rev. B: Condens. Matter Mater. Phys.*, 2009, **80**, 115407.
 - 25 J. M. Buriak, *Chem. Mater.*, 2014, **26**, 763–772.
 - 26 D. Jurbergs, E. Rogojina, L. Mangolini and U. Kortshagen, *Appl. Phys. Lett.*, 2006, **88**, 233116–233118.
 - 27 K. Dohnalová, K. Žídek, L. Ondič, K. Kúsová, O. Cibulka and I. Pelant, *J. Phys. D: Appl. Phys.*, 2009, **42**, 135102.
 - 28 W. J. I. DeBenedetti, S.-K. Chiu, C. M. Radlinger, R. J. Ellison, B. A. Manhat, J. Z. Zhang, J. Shi and A. M. Goforth, *J. Phys. Chem. C*, 2015, **119**, 9595–9608.
 - 29 L. Wang, Q. Li, H.-Y. Wang, J.-C. Huang, R. Zhang, Q.-D. Chen, H.-L. Xu, W. Han, Z.-Z. Shao and H.-B. Sun, *Light: Sci. Appl.*, 2015, **4**, e245.
 - 30 J. Valenta, A. Fučíková, I. Pelant, K. Kúsová, K. Dohnalová, A. Aleknavičius, O. Cibulka, A. Fojtík and G. Kada, *New J. Phys.*, 2008, **10**, 073022.
 - 31 W. D. A. M. de Boer, D. Timmerman, K. Dohnalova, I. N. Yassievich, H. Zhang, W. J. Buma and T. Gregorkiewicz, *Nat. Nanotechnol.*, 2010, **5**, 878–884.
 - 32 L. Ondič, K. Kúsová, M. Ziegler, L. Fekete, V. Gärtnerová, V. Cháb, V. Holý, O. Cibulka, K. Herynková, M. Gallart, P. Gilliot, B. Hönerlage and I. Pelant, *Nanoscale*, 2014, **6**, 3837–3845.
 - 33 A. A. Prokofiev, A. S. Moskalenko, I. N. Yassievich, W. D. A. M. de Boer, D. Timmerman, H. Zhang, W. J. Buma and T. Gregorkiewicz, *JETP Lett.*, 2009, **90**, 758–762.
 - 34 B. Bruhn, B. J. Brenny, S. Dekker, İ. Doğan, P. Schall and K. Dohnalová, *Light: Sci. Appl.*, 2017, **6**, e17007.
 - 35 K. Dohnalová, A. N. Poddubny, A. A. Prokofiev, W. D. A. M. de Boer, C. P. Umesh, J. M. J. Paulusse, H. Zuilhof and T. Gregorkiewicz, *Light: Sci. Appl.*, 2013, **2**, e47.
 - 36 A. Fermi, M. Locritani, G. Di Carlo, M. Pizzotti, S. Caramori, Y. Yu, B. A. Korgel, G. Bergamini and P. Ceroni, *Faraday Discuss.*, 2015, **185**, 481–495.
 - 37 G. Uchida, K. Yamamoto, M. Sato, Y. Kawashima, K. Nakahara, K. Kamataki, N. Itagaki, K. Koga and M. Shiratani, *Jpn. J. Appl. Phys.*, 2012, **51**, 01AD01.
 - 38 H. Chen, J. H. Shin and P. M. Fauchet, *Appl. Phys. Lett.*, 2007, **91**, 173121.
 - 39 K. Dohnalová, I. Pelant, K. Kúsová, P. Gilliot, M. Gallart, O. Crégut, J.-L. Rehspringer, B. Hönerlage, T. Ostatnický and S. Bakardjieva, *New J. Phys.*, 2008, **10**, 063014.
 - 40 V. Zajac, H. Němec, C. Kadlec, K. Kúsová, I. Pelant and P. Kužel, *New J. Phys.*, 2014, **16**, 093013.
 - 41 J. Khun, V. Scholtz, P. Hozák, P. Fitl and J. Julák, *Plasma Sources Sci. Technol.*, 2018, **27**, 065002.
 - 42 J. Julák, A. Hujacová, V. Scholtz, J. Khun and K. Holada, *Plasma Phys. Rep.*, 2018, **44**, 125–136.

- 43 P. Hozák, V. Scholtz, J. Khun, D. Mertová, E. Vaňková and J. Julák, *Plasma Phys. Rep.*, 2018, **44**, 799–804.
- 44 K. Kúsová and T. Popelář, *J. Appl. Phys.*, 2019, **125**, 193103.
- 45 *Homepage of the CP2K open source package for molecular dynamics simulations*, <http://www.cp2k.org>.
- 46 J. P. Perdew, K. Burke and M. Ernzerhof, *Phys. Rev. Lett.*, 1996, **77**, 3865–3868.
- 47 S. Goedecker, M. Teter and J. Hutter, *Phys. Rev. B: Condens. Matter Mater. Phys.*, 1996, **54**, 1703–1710.
- 48 J. P. Perdew, *Int. J. Quantum Chem.*, 1985, **28**, 497–523.
- 49 G. Viera, M. Mikikian, E. Bertran, P. R. i. Cabarrocas and L. Boufendi, *J. Appl. Phys.*, 2002, **92**, 4684–4694.
- 50 C. T. Kirk, *Phys. Rev. B: Condens. Matter Mater. Phys.*, 1988, **38**, 1255–1273.
- 51 S. Gardelis, A. G. Nassiopoulou, M. Mahdouani, R. Bourguiga and S. Jaziri, *Phys. E*, 2009, **41**, 986–989.
- 52 D. Mawhinney, J. J. A. Glass and J. J. T. Yates, *J. Phys. Chem. B*, 1997, **101**, 1202–1206.
- 53 A. Burneau and C. Carterer, *Phys. Chem. Chem. Phys.*, 2000, **2**, 3217–3226.
- 54 K. Nakamoto, *Infrared and Raman Spectra of Inorganic and Coordination Compounds, Part B: Applications in Coordination, Organometallic, and Bioinorganic Chemistry*, John Wiley & Sons, Inc., New York, 1997.
- 55 S. G. Moussa, A. C. Stern, J. D. Raff, C. W. Dilbeck, D. J. Tobias and B. J. Finlayson-Pitts, *Phys. Chem. Chem. Phys.*, 2013, **15**, 448–458.
- 56 D. König, *AIP Adv.*, 2016, **6**, 085306.
- 57 The lifetime value of $\tau_2 = 1.2$ ns was obtained by performing a fit over all the wavelengths, computing a weighted mean of the fitted lifetimes and fixing the lifetime to this mean value in the next run.
- 58 As a result of the increased absorption of PAW under 340 nm and its consequent luminescence, see Fig. S6,† the PL of the modified sample under 315 nm excitation could not be accurately analyzed and separated into individual spectral components.

PAPER • OPEN ACCESS

Mechanisms leading to plasma activated water high in nitrogen oxides

To cite this article: F Matějka *et al* 2023 *Phys. Scr.* **98** 045619

View the [article online](#) for updates and enhancements.

You may also like

- [Reactive nitrogen species in plasma-activated water: generation, chemistry and application in agriculture](#)

Corina Bradu, Kinga Kutasi, Monica Magureanu et al.

- [Effects of the ground-electrode temperature on the plasma physicochemical processes and biological inactivation functions involved in surface dielectric barrier discharge](#)

Han Xu, Fan Zhu, Yan Liu et al.

- [Development of poly \(1,8 octanediol-co-citrate\) and poly \(acrylic acid\) nanofibrous scaffolds for wound healing applications](#)

Allison Goins, Vidhya Ramaswamy, Elliott Dirr et al.



OPEN ACCESS

PAPER

Mechanisms leading to plasma activated water high in nitrogen oxides

RECEIVED
24 October 2022**REVISED**
14 January 2023**ACCEPTED FOR PUBLICATION**
15 March 2023**PUBLISHED**
28 March 2023F Matějka^{1,2}, P Galář^{2,*}, J Khun¹, V Scholtz¹ and K Kůsova²¹ University of Chemistry and Technology, Technická 3, Prague, Czech Republic² Institute of Physics, Czech Academy of Sciences, Cukrovarnická 10, Prague 6, Czech Republic

* Author to whom any correspondence should be addressed.

E-mail: galar@fzu.cz**Keywords:** plasma activated water, non-thermal plasma, mechanisms of nanoparticles surface modifications, plasma-liquid phase interaction

Original content from this work may be used under the terms of the Creative Commons Attribution 4.0 licence.

Any further distribution of this work must maintain attribution to the author(s) and the title of the work, journal citation and DOI.

**Abstract**

Plasma activated water (PAW) is a unique highly reactive medium, traditionally used in medicine and agriculture because of its decontamination and disinfection abilities. Recently, we have shown that this medium can also be beneficial for tailoring the surface chemistry of semiconductor nanostructures if its composition is tuned to contain a high concentration of nitrogen-related species (HiN:PAW). However, pathways leading to the production of HiN:PAW remained unclear, which we address in this article. By monitoring the composition of the produced PAW and the concentration of selected species in the discharge under different activation geometries and discharge conditions, we identify the activation geometries favourable for the production of HiN:PAW using two phenomenological factors, a barrier parameter P and a maximum effective radius of the vessel r_{\max} . A key point is the presence of a barrier area in the discharge reactor, which forms as a result of the favourable activation geometry and a discharge with prevailing more reactive atomic species. This area acts as a partial barrier between the discharge and the surrounding air atmosphere, limiting, but still allowing a flow of source N₂ molecules from the surrounding atmosphere. The minimal and ideal build-up times of 10 and 30 min, respectively, for the discharge to stabilize are also reported. Using the reported experimental settings, we were able to produce HiN:PAW containing a mixture of various reactive species beneficial for the surface modification of nanoparticles, with the NO₃⁻ to H₂O₂ ratio of at least 20 × 10³: 1, in contrast to approximately 1:1 under more traditional conditions.

1. Introduction

Non-thermal plasma (NTP) is a cutting-edge technology which has been gaining momentum during the last decade due to the simple design of the necessary apparatus, its ease of use, cost-effective operation and a general lack of toxic effects. NTP is generated under specific conditions, when the energy from the plasma source is transferred mainly to electrons in the discharge [1, 2], which then turns electrons into high-energy charge carriers (several eV, ~10 kK), while the positive ions and neutral molecules making up most of the mass are kept at almost ambient temperature. Thus, in contrast to other types of treatment, the interaction with NTP does not cause thermal damage, even though it still can affect materials through a wide range of reactive species originating in the atmosphere where the discharge burns. Many different ways to generate NTP by electric discharges were introduced in the last decades [3], mainly with the aim of treating bio-objects [4–8]. They vary in the structure of electrodes, the type of power sources, a pulse/continual regime and the composition of the used atmosphere. Thanks to these techniques, NTP was successfully employed in a wide range of applications, starting from rendering surfaces hydrophilic [9], their decontamination [10], antifungal and conservation treatment of food and seeds causing extension of their shelf life [8, 11–13] and green technology [14] for the effective disinfection of respirators and other medical equipment [15, 16].

An important example of the use of NTP are plasma activated liquids [1, 17]. In plasma activated liquids, the interaction of reactive species and high-energy electrons in NTP with the liquid results in a specific chemical composition of the NTP-treated, so-called activated liquid [18–20]. Naturally, the most common activated liquid is water [1, 17, 21]. Plasma activated water (PAW) contains many short-lived and long-lived reactive species. A few hundreds of possible chemical pathways related to NTP and PAW generation were described [1, 17, 22]. The typical most abundant short-lived species are ozone O_3 , nitric oxide (NO) or peroxy nitrous acid (ONOOH), long-lived species are most commonly represented by hydrogen peroxide (H_2O_2), followed by nitrates and nitrites (NO_2^- and NO_3^-) [23]. However, the real relevance of the reactions depends on many parameters such as the used NTP system, surrounding conditions, continual/pulsed excitation regime, etc [20, 21, 23]. As a result of its composition, PAW is an environment very hostile to microorganisms, making it an ideal material for the above-mentioned decontamination and disinfection applications.

The plasma activation of water is based on the interaction of molecules and other particles from the surrounding gas and plasma burning in the gas with the liquid phase. Usually, the discharge is located in the gas phase and at the gas-liquid interface. High-speed electrons from the discharge react with molecules of the gas causing theirs dissociation, when it burns in air, the discharge creates mainly oxygen (dissociation energy of O_2 - 5.2 eV molecule $^{-1}$) and nitrogen radicals (N_2 , 9.8 eV molecule $^{-1}$) [23]:



Due to high dissociation energy of the nitrogen molecule, nitrogen radicals can be effectively created also through the reaction of nitrogen molecule with oxygen radicals [23]:



In the discharge area, further reactions leading to radicals and other species are in progress, yielding mostly H_2O_2 , nitrogen-related species (NO, HNO_2 , NO_2) and ozone [24]:



In the liquid phase, the produced H_2O_2 can then be consumed by [24]:



More detailed list of chemical reactions related to discharge burning at ambient conditions, at the air/liquid interface and inside the liquid can be found elsewhere [23–25].

In nanomaterials, surface chemistry plays an important role in their physical and chemical properties, such as light generation efficiency, surface reactivity, dispersibility, toxicity, etc [26–28]. Countless surface-modification techniques are currently available [29–31]. Among these techniques, the surface modification in NTP and by plasma activated liquids is new and attractive due to its simplicity and low cost [18]. In one example, PAW was successfully applied to a nanostructured conductive polymer causing its homogenous oxidation [32]. The treated polymer then showed good stability and good conductive properties. The role of the surface is even more profound in semiconductor nanoparticles. The first pioneering works using PAW and plasma-activated ethanol applied to silicon nanocrystals showed a slight increase of their light generation efficiency and stability [18]. The limitation for further PAW applications to semiconductor nanocrystals was mainly the presence of H_2O_2 , which easily degrades them and also neutralizes the prospective air-originating nitrogen reactive species [23, 33], which can be advantageous surface passivating agents.

In our previous work [34], we introduced a simple technique producing PAW with a high concentration of NO_x (HiN:PAW). This PAW has a novel and unique chemical composition, having only a marginal concentration of H_2O_2 and, at the same time, extraordinarily high concentrations of nitrates and nitrites (NO_3^- : 80 000 μM), suitable for the surface passivation of semiconductor nanoparticles. The key for the generation of HiN:PAW was a combination of a particular NTP generation system (transient spark discharge) and the use of a closed or semi-closed container. In that work [34], the application of HiN:PAW to several types of semiconductor nanoparticles resulted in the enrichment of their surface layer with nitrogen-related species. Especially in the case of Si-NCs, this new termination caused a significant increase in their light generation efficiency and dispersibility and stability in water. Despite being clearly beneficial as a surface-modification agent, the detailed mechanisms leading to a PAW composition favourable for the surface modification of nanoparticles still remains unclear. Therefore, in this contribution, we focus on an in-depth study of the mechanisms leading to the production of HiN:PAW. We monitor the dynamics of the chemical composition of NTP and HiN:PAW under specific conditions (discharge properties, enclosure of the surrounding atmosphere

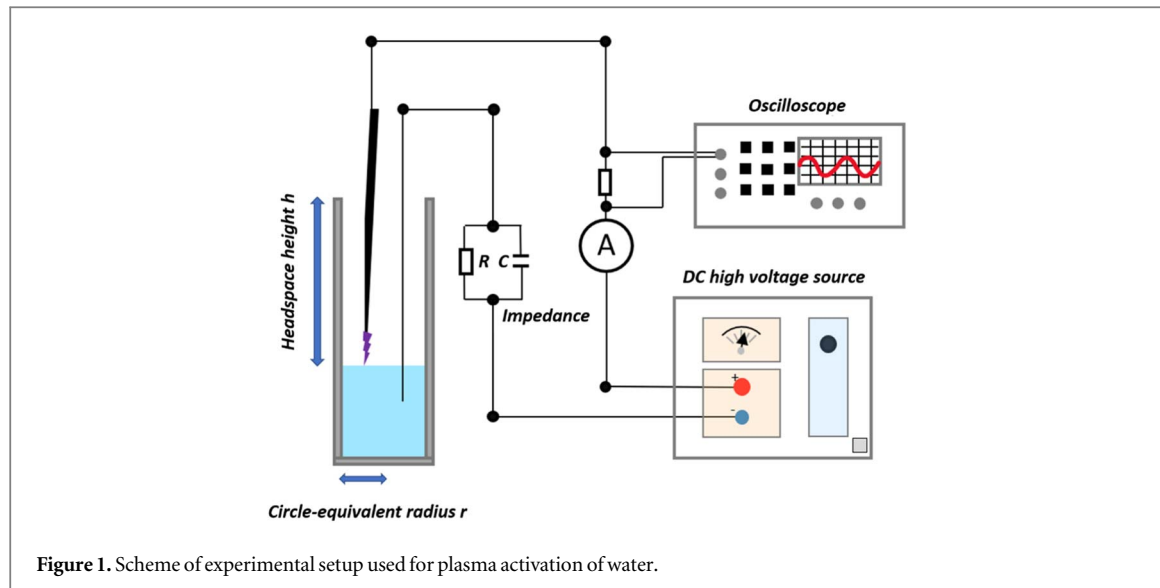


Figure 1. Scheme of experimental setup used for plasma activation of water.

etc.). Based on these results and chemical reactions in atmospheric NTP, the NTP/water interface and the HiN:PAW itself, we propose a reaction model of conditions favourable for the generation of HiN:PAW. We highlight that the shape of the container, the amount of water, the discharge properties, dissociation of air related molecules and high humidity all play a significant role in the activation process. These results can be used not only for the further development of HiN:PAW generation systems, but can also serve as a guide in activation processes of other prospective liquids, whose application is as of now extremely rare.

2. Experimental

2.1. Transient spark discharge apparatus

The transient spark discharge in point-to-plane geometry is generated by a system consisted of a commercial high-voltage source (Utes Brno, DC source HT 2103) (max. voltage 10 kV), oscilloscope (Tektronix 2465, 300 MHz Oscilloscope), ammeter (analog, METRA BLANSKO DU 20), a stabilizing ballast impedance and two electrodes (figure 1). The point electrode is represented by a commercial surgical needle (Medoject, 0.7×40 mm) and is connected to the positive pole of the power supply. The planar electrode is represented by the surface of the treated water which is connected by a platinum wire to the negative pole. The point electrode was localized 2.5 mm above the water surface. Therefore, the discharge burned between the upper electrode and the water level. The ballast impedance contains parallel connection of a $10 \text{ M}\Omega$ resistor and capacitor system of adjustable overall capacity (0.05, 0.1, 0.25, 2.0 and 95.0 nF). The variation of the capacitance affected mainly the pulse peak current and pulse period, which varied from about 9 to 13 A and 300 to 500 μs , respectively. The pulse duration was determined of approx. 30–50 ns. The discharge burnt in ambient conditions (room temperature, no humidity or atmosphere control was applied). Approximate average value of the discharge current measured by analogous ammeter was 500 μA and supply voltage 9 kV. The current and voltage waveforms were published elsewhere [35]. The electrodes were inserted into various reactors. Three main ones were labelled as *Narrow*, *Medium* and *Wide*. The *Narrow* reactor was realized by a quartz cuvette of a $1 \times 1 \times 4.3 \text{ cm}^3$ (without the airtight stopper wedge on the top), the *Medium* reactor by a 5 ml glass beaker of a 2.3 cm diameter and 3 cm tall, and the *Wide* reactor by a glass Petri dish of 4.3 cm diameter and 1 cm tall. The reactors were characterized using two parameters: headspace height h that defines the distance between edge of the reactor and the water level and the circle-equivalent radius r (effective radius) defined as $r = (S/\pi)^{1/2}$, where the S is area of reactor base (figure 1). To study the threshold conditions of HiN:PAW generations we also used standard glass vials of radius 0.65, 1.0 and 1.25 cm.

2.2. Plasma activation of water

Sufficient volume (1–3 ml) of deionized water was pipetted into the used reactors, the electrode system was adjusted and the water surface was exposed to the transient spark discharge for 30 min using ballast impedances of parameters as described above (figure 1). The properties of the discharge were monitored during the whole activation process. Even though evaporation was minimal during the activation, the water level was kept at the same position by adding water to the reactor (~ 0.1 ml during the whole activation process).

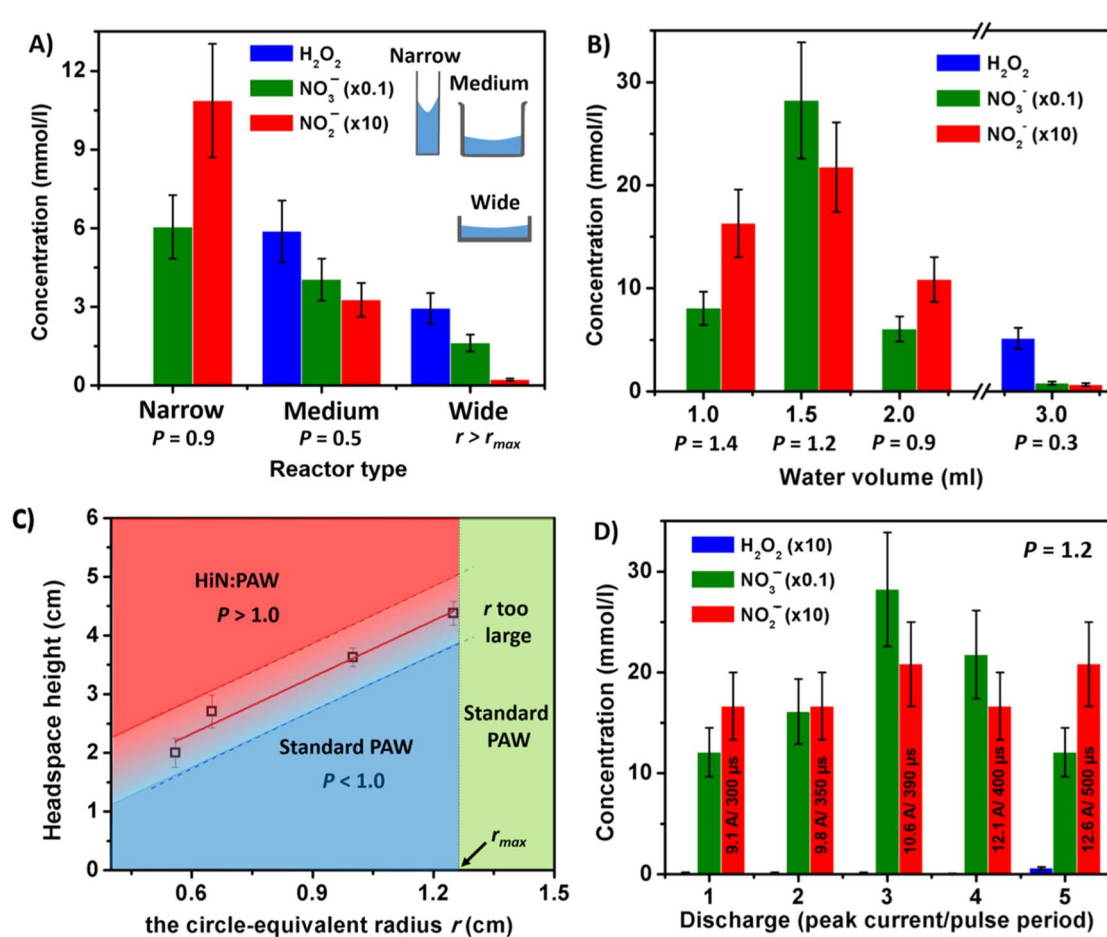


Figure 2. Concentration of H_2O_2 , NO_3^- and NO_2^- generated using transient spark discharge of $10.6 \text{ A} / 390 \mu\text{s}$ (peak current/pulse period) in 2 ml of deionized water after 30 min of treatment placed in a quartz cuvette (narrow container). One of the experimental conditions was varied in each panel, the other parameters are kept the same. The variation of (A) the used reactor, (B) volume of water in the Narrow reactor - cuvette (headspace height h is 3.3, 2.8, 2.3 and 1.3 cm, respectively) and (D) the discharge properties are presented. Please note that the concentrations are multiplied by a suitable constant for clarity. The error bars are given by combined standard deviation of concentration measurements. (C) The summary of how the vessel geometry determines if HiN:PAW is produced using barrier parameters P (equation 4) and r_{max} . The data points and the fit represent the threshold of the minimal h and circle-equivalent radius r of the vessel for HiN:PAW to be produced. In the red $P > 1$ zone, HiN:PAW is produced, blue and green zones lead to standard PAW. The mixed coloured zone represents the precision of the linear fit used to calculate P .

2.3. Characterization of PAW concentration and discharge properties

Within the PAW composition, the H_2O_2 , NO_2^- , NO_3^- species were monitored. The measurements were realized 5 min after finishing of the activation. The concentration of nitrates and nitrites were obtained using standard test strips Quantofix Nitrate/Nitrite (ref no. 91313), showing gradation as follows: 0, 10, 25, 50, 100, 250, 500 mg l⁻¹ for nitrates and 0, 1, 5, 10, 20, 40, 80 mg l⁻¹ for nitrites. To extend the concentration range beyond these values, PAW was diluted with distilled water from 10 to 1000 times. The concentration of hydrogen peroxide was characterized by test strips Quantofix Peroxide 25 (ref no. 91319) having gradation as follows: 0, 0.5, 2, 5, 10, 25 mg l⁻¹. The concentration error was calculated based on the combined standard deviation composed of precision of used test strips and statistical error of repeated measurements. Ozone was not monitored, because its production is not significant while using the transient spark discharge system [36].

The linear fit in figure 2(C) was performed using Matlab 2015 b. Due to the small number of data points, the robust linear least-squares fitting method using bisquare weights was applied. The presented uncertainty gives the prediction observational bounds for one observation (non-simultaneous) for the 67% confidence level.

The NO and NO_2 concentrations in discharge area were measured by Serinus 40H NO_x analyser, ACOEM Ecotech (NO and NO_2 range up to 1000 ppm, measurement accuracy $\pm 1\%$, gas flow rate 0.16 slm) using chemiluminescence detection. Gas mixture for analysis was taken by Teflon tube of inner diameter 3 mm introduced into the cuvette or 5 ml beaker from two different positions. The first position was immediately at the suspension surface (ca 2 mm above the suspension surface), the second position was upper edge of the vessel (ca 13 mm above the suspension surface).

The emission spectra of the discharges were acquired using the Shamrock 300i spectrograph (Andor, Oxford Instruments) with an EMCCD camera (Newton 971, Andor, Oxford Instruments). The emission spectra at

specific times were not measured in the whole spectral range at once, but stepwise. The spectra were combined afterwards. The spectra were corrected for the sensitivity of the whole spectroscopic system. The discharge frequency and peak current were obtained from the oscilloscope as described elsewhere [35].

3. Results

In order to understand the mechanism of the generation of HiN:PAW, we first focus on how the experimental conditions influence the outcome of the activation processes in the liquid phase and then we move on to the gas phase and the properties of the discharge. The processes taking place above the water level and the chemical reactions in the water while it is being activated are closely interconnected and specific conditions need to be met in both these phases for HiN:PAW to be the product of the activation process.

3.1. Influence of activation conditions on the reaction products in the liquid phase

Deionized water was plasma activated using pulsed transient spark discharge, the used apparatus and experimental conditions are described in detail in *Experimental section* and in figure 1. In order to understand the mechanism of the generation of HiN:PAW, the system used in our previous work [34] was employed. In particular, as a starting setting we used a narrow quartz cuvette containing 2 ml of distilled water, discharge conditions of $10.6 \text{ A}/390 \mu\text{s}$ (peak current/pulse period, $R = 10 \text{ M}\Omega$, $C = 0.25 \text{ nF}$) and the modification was realized for 30 min. We varied the reactor shape, the amount of the treated water and the properties of the discharge. To determine the composition of the produced PAW rather than focusing on the short-lived reactive, the measurements of H_2O_2 , NO_2^- , NO_3^- concentrations were made 5 min after finishing the activation.

The geometry of the reactor can have a considerable impact on the local atmosphere around the discharge, therefore, on the reactants and on the rates in which reactions listed in equations (2a–2e) proceed. We used three different types of reactors with a significantly different degree of the separation of the discharge from the non-ionized surrounding atmosphere: (A) Narrow (quartz cuvette), (B) Medium (glass beaker) and (C) Wide (Petri dish). The reactors contained the same amount of water, 2.0 ml. The concentrations of the most important reactants in PAW (H_2O_2 , NO_2^- , NO_3^-) produced in reactors with different geometries are bar-plotted in figure 2(A). Clearly, only the Narrow reactor produced HiN:PAW because it yields the intended high concentration of nitrates and nitrites and at the same time a negligible amount of hydrogen when compared to the more open types of reactors. Thus, the more open space around the discharge clearly leads to the production of more H_2O_2 and a decrease in the concentration of nitrogen-related radicals.

Using the reactor yielding the lowest concentration of hydrogen peroxide (the Narrow reactor), the next key parameter which alters the settings of the system is the volume of water in the reactor. On the one hand, an increase in the amount of water should decrease the concentration of plasma-generated reactive species after the 30-minute treatment, but, on the other hand, an opposite effect can also be expected. The more air (less water) is present in the reactor, the weaker the exchange of the reactive species from the discharge with the atmosphere outside the reactor is, impacting the discharge conditions and thus the generated reactive species in PAW. To investigate this trade-off, the volume of water in the cuvette was varied in the range between 1 ml (minimal possible amount) and 3 ml. Under these conditions, the distance of water surface from the cuvette edge (labelled as headspace height h) varied from 3.3 to 1.3 cm. The composition of the PAW produced under these conditions was monitored, see figure 2(B). Settings with cuvettes holding a smaller volume of water led to the production of HiN:PAW, but the volume of 1.5 ml ($h = 2.8 \text{ cm}$) was found to be optimal in terms of the produced composition. When the headspace height decreased to 1.3 cm (3 ml of water) during the plasma activation process, high concentration of H_2O_2 was produced, yielding PAW of a traditional chemical composition rather than HiN:PAW.

In order to generalize these findings, we repeated the experiment from figure 2(B) using another set of reaction vessels with different geometries. We carried out the water activation procedure with the volume of water in each vessel increased in steps and noted the critical volume above which the produced PAW reverted to high H_2O_2 content. The results are presented as the dependence of headspace height h on the circle-equivalent radius of the vessel r , which well follows a linear dependence, see figure 2(C). Linear fit of this dependence allows us to phenomenologically formulate a dimensionless effective barrier parameter P , which characterizes how limited the exchange of the reactive species between the atmosphere and the discharge is. The barrier parameter P reads:

$$P = \frac{h \text{ (cm)} - 0.3823}{3.225r \text{ (cm)}} \quad (4)$$

where the prediction band for Δh is $\Delta h = 0.555\sqrt{0.7354r^2 - 1.333r + 1.657}$. For the experiment geometry to produce HiN:PAW, it is necessary that $P > 1$. We also observed that any vessel with the circle-equivalent radius

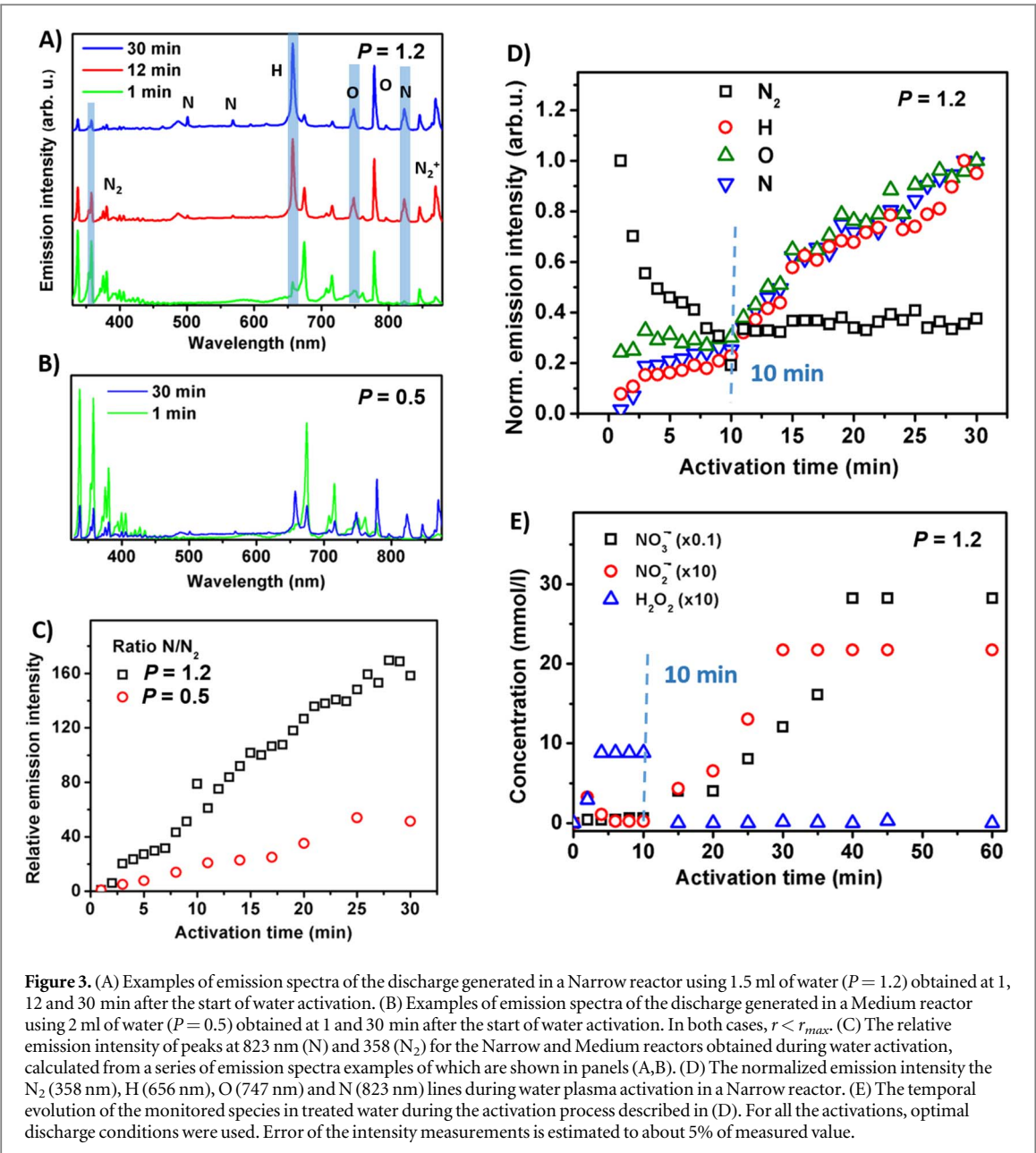


Figure 3. (A) Examples of emission spectra of the discharge generated in a Narrow reactor using 1.5 ml of water ($P = 1.2$) obtained at 1, 12 and 30 min after the start of water activation. (B) Examples of emission spectra of the discharge generated in a Medium reactor using 2 ml of water ($P = 0.5$) obtained at 1 and 30 min after the start of water activation. In both cases, $r < r_{max}$. (C) The relative emission intensity of peaks at 823 nm (N) and 358 nm (N_2) for the Narrow and Medium reactors obtained during water activation, calculated from a series of emission spectra examples of which are shown in panels (A,B). (D) The normalized emission intensity the N_2 (358 nm), H (656 nm), O (747 nm) and N (823 nm) lines during water plasma activation in a Narrow reactor. (E) The temporal evolution of the monitored species in treated water during the activation process described in (D). For all the activations, optimal discharge conditions were used. Error of the intensity measurements is estimated to about 5% of measured value.

wider than 1.25 cm (labelled as r_{max}) did not lead to HiN:PAW no matter what the headspace height was. Therefore, we separated the area of figure 3(c) to three zones: the red zone passing both necessarily conditions ($P > 1$ and $r < r_{max}$) for HiN:PAW generation, the blue one violating the first condition ($P < 1$) and the green one violating the second condition (and $r > r_{max}$). The multicolor overlap zones depict the uncertainties of the zone boarders. The underlying physical mechanism behind these constraints is clearly the need for the discharge to burn in a limited (the $r > r_{max}$ condition) and relatively isolated (the condition for h through the P parameter) volume to be able to produce local conditions favourable for the generation of HiN:PAW and act as an effective barrier. Thus, the barrier parameters P and r_{max} characterize the geometry of the experiment favourable for the production of HiN:PAW, and therefore, its value is included at each experiment in the text of this article (on one occasion in figure 2(A), PAW lacking hydrogen peroxide, but containing not ideal concentration of nitrides was detected even for $P = 0.9$, but this value is close enough to the $P = 1$ threshold considering the experimental error). The value of r_{max} very likely depends on the radius of the discharge (r_d). Using broader discharge while keeping its other properties the same can result in an increase in the r_{max} value. However, a change of r_d cannot be, in the case of transient spark, easily realized, therefore such a study is not included. To be complete, we present the value of a dimensionless parameter r_{max}/r_d which was about 23 in our experimental system, where the lateral size of the discharge (1.1 mm) was estimated using a long-exposure photograph.

The next relevant parameter is the characteristics of the transient spark itself. The delivery of energy is critical for the generation of radical species from molecules present in normal atmosphere, which affects the whole process of water activation. Figure 2(D) presents the concentrations of the species of interest as a function of a

variety of discharge conditions. In this activation process, the narrow reactor filled with 1.5 ml of water was used and the capacitance of the stabilizing ballast was possessed values of: 0.05, 0.1, 0.25, 2.0 and 95.0 nF, which resulted in changes in pulse peak current and period (9.1–12.6 A and 300–500 μ s, respectively). As shown in figure 2(D), the prolongation of the period of pulses leads mostly to changes in the concentrations of NO_3^- in the produced HiN:PAW. These concentrations first rise, but then start to decline for pulses longer than 390 μ s. At even longer pulse duration of more than 500 μ s, the concentration of H_2O_2 starts to rise, marking the end of the range of conditions suitable for the production of HiN:PAW.

3.2. Influence of activation conditions on the reactive species in the discharge

Following from equations (1a–1c) and (2a–2c), the composition of the plasma also influences the final product. Thus, the composition of the plasma discharge was investigated for optimal conditions for the production of HiN:PAW, as detailed above. To fulfil this task, we selected a combination of emission spectroscopy and a direct chemical analysis using NO_x analyser. The former method allows us in a simple but precise way to compare how the ratios related to specific molecules/atoms evolve in time *in situ* when the discharge burns without affecting the conditions inside the reactor. However, it does not provide any quantification of the gas chemical composition during the activation, which is where the direct chemical analysis comes in. The disadvantage of the latter method is the fact that a part of the gas need to be extracted from the reactor area for the analysis, thus affecting the conditions in the reactor by effectively decreasing the barrier factor P . To compare the discharge leading to HiN:PAW and that producing the more traditional composition, we analysed the discharge in the Narrow reactor keeping $P > 1$ ($P = 1.2$) and the Medium reactor with $P < 1$ ($P = 0.5$) with $r < r_{\max}$ in both cases.

The emission spectra were acquired at various times during the activation process and, simultaneously, the composition of the water while it was being activated was characterized, see figure 3. As expected from the activation process being carried out at ambient atmosphere, the species detected in the discharge under the $P > 1$ condition include air-originating molecules and atoms N₂, N, H, O (figure 3(A)). During the first few minutes of the activation process, the molecular N₂ signal decreased, which was accompanied by only a weak rise in the atomic signal (figure 3(D)). However, about 10–12 min after the discharge was switched on, there is clearly a qualitative instead of a simple quantitative change in the discharge, when it transforms from discharge containing mainly ionized molecules into the more energetic discharge containing their dissociated parts, implying more reactive species. Later in the activation process, the atomic peaks further rise and the molecular peaks are almost vanquished. The discharge stabilizes after about 30 min, which gives the timeframe necessary for the activation process of HiN:PAW to be completed. When $P < 1$, we also detected a decrease of the molecular N₂ signal with time, but it was accompanied by only a mild rise of the atomic emission signal, which was insufficient for the discharge to significantly dissociate the air molecules. This difference is evident from figure 3(C), where we compared the dynamics of the ratio between the emission intensity of the N and N₂ peaks for these two sets of experimental conditions.

In addition to the discharge, the composition of the produced PAW was monitored simultaneously with the emission spectroscopy ($P > 1$) and the measured dynamics are compared in figures 3(D) and (E). Clearly, after the discharge was switched on, the gradual decrease in the molecular N₂ signal in the emission spectrum is accompanied by an increase in H_2O_2 and low of NO_3^- and NO_2^- content in the activated water, leading to the traditional high- H_2O_2 content. However, at later stages of the activation process, as the discharge stabilized and dissociated species (N) prevailed in the emission spectra, the rise of NO_3^- and NO_2^- in water was accompanied by a decrease in H_2O_2 and further increase of the atomic N signal in the emission spectrum of the discharge. The transition between these two modes of operation occurred approximately 10 min after the discharge was switched on, giving the timeframe necessary for the discharge to stabilize. The dissociation of the air molecules in the discharge area is thus in correlation with the changes in the concentration of the monitored species in PAW and the presence of atoms in the discharge is clearly a necessary condition for the production of HiN:PAW.

A further corroboration of the presented findings was supported by direct *in situ* analysis of NO and NO_2 concentration during plasma activation of water using the same two sets of experimental conditions (figure 4). As can be seen in figure 4(A) ($P = 1.2$), the concentration of NO_x rose fast within the first approximately 10 min and, in case of the NO_2 , then kept slowly increasing for the next 20 min in the discharge area. Qualitatively comparable results with somewhat lower concentrations and a higher spread between values were obtained at the edge of the vessel. These dynamics are in correlation with the one observed for the emission intensity of N using emission spectroscopy (figure 3), only the secondary rise at $t > 10$ min is weaker. This difference is easily understandable, because during the analysis the discharge is disrupted by the gas extraction to the analyser, which effectively lowers the P parameter and prevents the ideal conditions for the production of HiN:PAW from stabilizing, effectively lowering the P parameter. Under the $P = 0.5$ conditions (Medium vessel, figure 4(B)), the initial rise of the NO_x concentration in the discharge area within the first approximately 10 min also occurred. However, the concentration of both NO and NO_2 was about 2 times lower and the initial rise is followed by

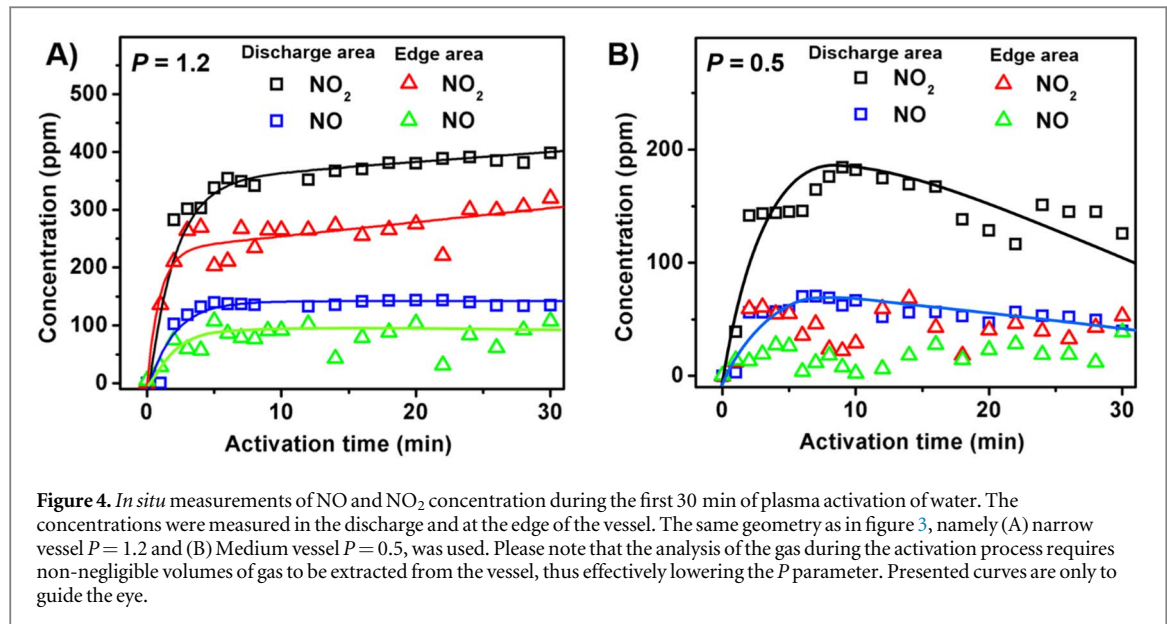


Figure 4. *In situ* measurements of NO and NO₂ concentration during the first 30 min of plasma activation of water. The concentrations were measured in the discharge and at the edge of the vessel. The same geometry as in figure 3, namely (A) narrow vessel $P = 1.2$ and (B) Medium vessel $P = 0.5$, was used. Please note that the analysis of the gas during the activation process requires non-negligible volumes of gas to be extracted from the vessel, thus effectively lowering the P parameter. Presented curves are only to guide the eye.

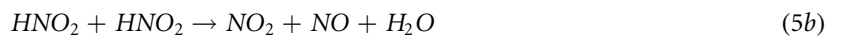
secondary decrease instead of a rise. Moreover, the concentration of both NO_x was low and highly unstable at the edge of the vessel. Thus, it is evident that inside the vessel with $P > 1$, the generation of NO_x is more effective and the conditions are favourable for a secondary rise of their concentration after the first 10 min during water activation in contrast to the vessel of $P < 1$, even though this quantitative method by design prevents the reaching of ideal conditions for the experiment. It is noteworthy that the P factor and the radius of the vessel did not affect the time period of initial rise, in both cases the initial rise was realized within about first 10 min.

4. Discussion

The chemical reactions from equations (1)–(3) are in progress in every PAW system and they represent the basic framework explaining the formation of nitrites/nitrates and hydrogen peroxide in PAW. However, by setting up certain conditions of the generating system, the rate at which the individual reactions happen will change significantly [23]. In this way, the final composition of PAW can be altered. As will be discussed in detail below, we propose that there are two key features of our system which lead to the production of HiN:PAW. These features are (*i*) the formation of a gas-discharge transition area, which governs the conditions of the discharge, and (*ii*) the discharge properties with prevailing atomic species and the existence of a higher-humidity area possibly with water microdroplets close to the water/discharge interface, which is favorable for the generation of nitrogen-related species. Both these processes clearly strongly depend on the geometry of the reaction vessel and the volume of the vessel occupied by water as well as on the discharge itself, as studied in figures 2 and 4.

4.1. High-humidity environment

Despite serving as a general framework, equations (2a)–(2e) do not provide the mechanism of the high content of nitrogen-related species in HiN:PAW. Here, the detailed electrospraying experiments of transient spark discharge by Janda *et al* [20] have already demonstrated the importance of water humidity and HNO₂ in the process of producing PAW with high concentrations of NO_x. They show that production of HNO₂ in the gas phase:



is an important chemical pathway. Henry's law coefficients k_H of HNO₂, representing the solubility in water, of 50 mol kg⁻¹ atm⁻¹ at 300 K is four and five orders of magnitude higher than $k_H^{\text{NO}_2} = 7 \times 10^{-3}$ mol kg⁻¹ atm⁻¹ and $k_H^{\text{NO}} = 1.8 \times 10^{-3}$ mol kg⁻¹ atm⁻¹, respectively. As a result of a much higher solubility of HNO₂ in water, HNO₂ itself is a significant source of nitrogen in HiN:PAW. Despite its lower concentration in the discharge area when compared to NO and NO₂, HNO₂ can be quickly transferred into water in the form of NO₂, either directly or by its solvation into potential microdroplets formed round the water/discharge interface [20]. HNO₂ and NO₂ are then the main sources of NO₂⁻ and NO₃⁻ in PAW:



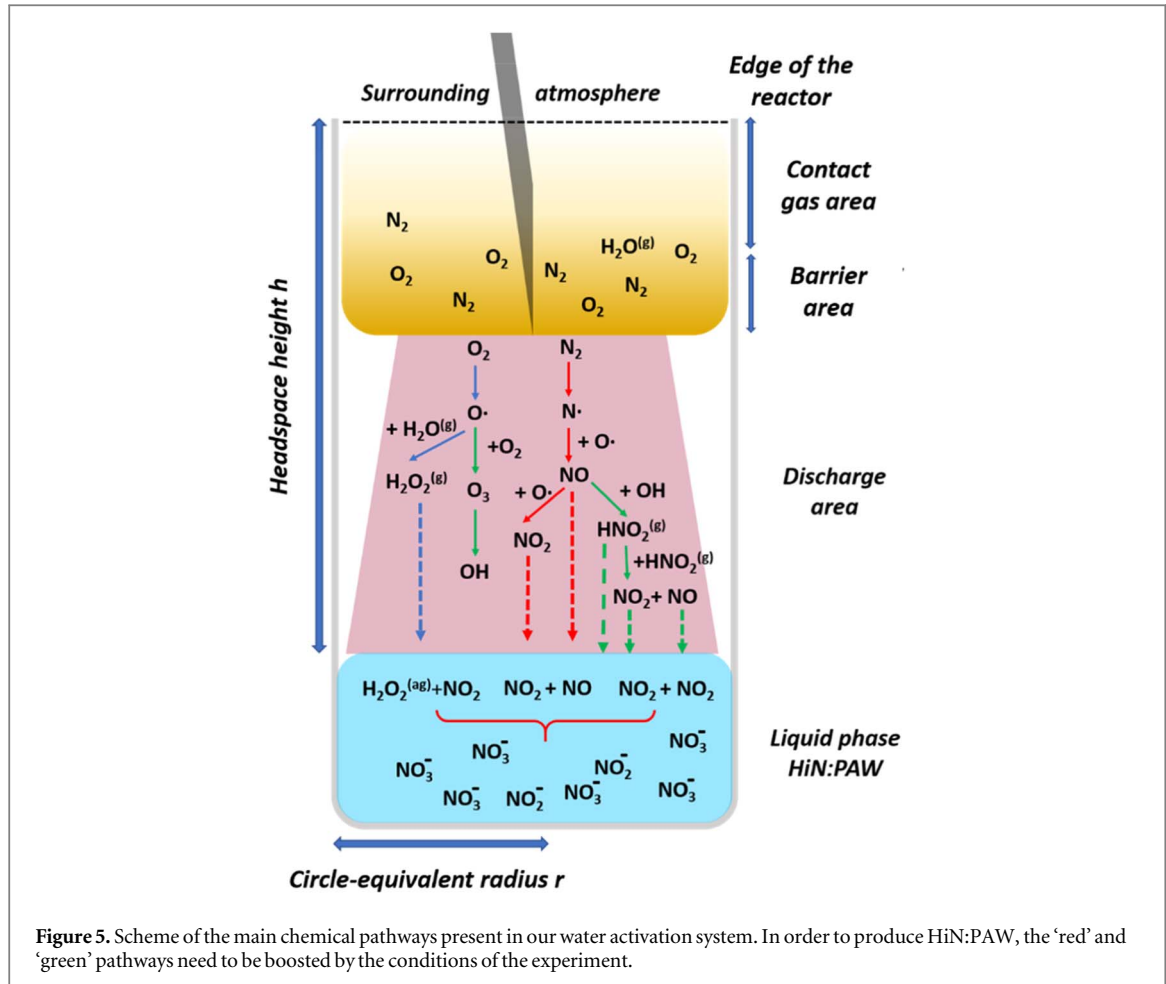
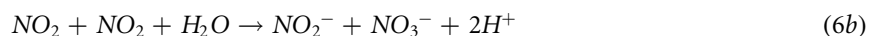


Figure 5. Scheme of the main chemical pathways present in our water activation system. In order to produce HiN:PAW, the ‘red’ and ‘green’ pathways need to be boosted by the conditions of the experiment.



Even though the mechanism of how the nitrogen-related species become dissolved in water are the same in our experiments, we are able to achieve analogical results using a much simpler setup than Janda *et al* [20]. Moreover, we reach much higher nitrogen to hydrogen peroxide ratios. Whereas in Janda *et al* the NO₂ to H₂O₂ ratio is around 40:1 in favour of NO₂, we obtained an even higher ratio of 140:1 and our HiN:PAW also contains high concentrations of NO₃⁻, in the ratio of 20 × 10³ : 1 when compared to H₂O₂. Here, we have even improved on our previous results: [34] using the 1.5 ml volume of water in the Narrow container, the concentration of NO₃⁻ in PAW reached 300 mmol l⁻¹, which is more than 3 times higher than we obtained previously [34].

4.2. Discharge conditions

Discharge properties also have a significant impact on the formation of HiN:PAW. The inability of non-pulse discharge to produce HiN:PAW even under otherwise favorable conditions had already been documented elsewhere [34]. Here, we showed that the effective dissociation of air molecules in the discharge is crucial. In particular, high concentrations of nitrogen and oxygen radicals need to be present (equations (2)). Based on our results (figure 3(D)), there are two opposite influences affecting the concentration of radicals: (*i*) the generation of the radicals in the discharge and (*ii*) their subsequent consumption by chemical reactions (reactions not leading to the formation of NO or NO₂, e.g. equation (2d)). While the increase of the peak current increases the concentration of the radicals, the prolongation of the pulse period gives the radicals more time to produce H₂O₂. As the increase of the ballast capacitance affects the two discharge parameters in an opposite way, there is an optimal combination (10.6 A and 390 μs).

Within the discharge area, we highlight three chemical pathways, as shown in figure 5: (*i*) the one resulting in H₂O₂ (the blue path, equations (1b) and (2d)), (*ii*) NO and NO₂ without OH (the red path, equations (1a), (2a), (2c)) and (*iii*) NO and NO₂ through OH and HNO₂ (the green path, equations (2b), (2e) and, (5a, 5b)). In standard PAW generation systems, the red and green pathways are significantly suppressed, resulting in PAW with high H₂O₂ and a low amount of nitrogen-related radicals. In our system, it is just the opposite. To significantly increase the efficiency of red and green pathways, there needs to be a high concentration of nitrogen radicals. The concentration of N₂ in air is clearly much higher than that of O₂, but N₂ possesses a much higher

bond-dissociation energy (9.8 eV), in contrast to O₂ (5.2 eV). Therefore, high-energy pulse discharge is necessary to effectively dissociate nitrogen molecules (optimized transient spark) and they need to be kept in the discharge region for some time to effectively accumulate - 10 min in our case (figures 3(C), (D) and 4(A)). Under such conditions, the oxygen radicals are consumed mainly in the red and green pathways, causing a decrease of H₂O₂ and a high concentration of NO₂ and NO. This scheme agrees with the observations presented in figure 3(E). The NO₂, NO and HNO₂ species are afterwards a source of an exceptionally high concentration of NO₂⁻ and NO₃⁻ in the resulting HiN:PAW, as described in section 4.1. Residual hydrogen peroxide in PAW is neutralized through equation (3).

4.3. Gas-discharge intermediary phase

The discharge conditions favorable for the production of HiN:PAW are achieved only under certain reaction vessel geometries and volumes of water in the vessel, as reflected in the P and r_{max} parameters (figure 2(C)). To explain these results, we propose a model in which, in addition to the obvious liquid and discharge areas, the gas phase at the top part of the reactor is divided into two areas. While the upper one can effectively exchange molecules with the surrounding atmosphere (labelled as the *Contact gas area*), the lower part the gradient of the concentration of the relevant species effectively acts as a partial barrier between the surrounding atmosphere and the discharge area (labelled as the *Barrier area*). The presence of the barrier area limits the exchange of air molecules from the surrounding air with the discharge area and thus it allows the discharge to effectively dissociate the air molecules, especially N₂.

The importance of the formation of the gas-discharge intermediary area is illustrated by our experiments using different geometries in figures 2(A) and (C). Using a wide open vessel larger than the discharge itself $r > r_{max}$, the outer atmosphere can to a large extent interfere with the discharge, bringing in more of the initial air-originating reactants (N₂ and O₂). Thus, the unrestricted air flow leads to the decrease in the concentration of reactive species above the water-discharge interface (equations (2a, 2c)). A higher but still not sufficient level of nitrogen-related species can be reached using a narrower ($r < r_{max}$) reactor, see the $P = 0.5$ conditions for the Medium vessel in figure 2(A). However, the best conditions were provided when the reaction vessel was 'tall', signifying that the vessel walls are high enough to form a semi-closed space for the plasma discharge, which leads to a more reactive environment. This situation occurs for higher barrier parameter values $P > 1$. Importantly, some air flow delivering the source N₂ and O₂ molecules is still necessary for the reactions to take place (see equations (1)), as we have already pointed out in our previous work [34]. Thus, a trade-off between the flow of the new source molecules and the formation of a highly reactive environment needs to be reached. Based on the results presented in figure 2(B), we propose that such a trade-off is reached for geometries close to, but above $P = 1$ in figure 2(C).

Based on the analysis of the discharge presented in figures 3 and 4, the geometry of the activation process described by the P parameter influences not only the composition of the activated water, but also the concentration of NO_x in the discharge area. These experiments also give the timeframe, about 10 min, after which the composition of the activated water changes into the low H₂O₂/high nitrites and nitrates mode, in correspondence to the discharge with a high concentration of O and N atoms instead of the molecular signal. The same build-up time in the dynamics of the produced reactive species was observed for vessels with two different geometries, suggesting that in this case it is the geometry of the discharge itself which governs the dynamics of the activation process.

Our experiments confirm that a wide variety of parameters influence the production of HiN:PAW. Clearly, PAW is an extremely complex mixture of reactive species and possible reaction pathways, which need to be determined experimentally rather than predicted by theoretical calculations. Thus, for the time being, we formulate the conditions favorable for the production of HiN:PAW phenomenologically based on our experiments, without the quantification of the rates of the corresponding chemical equations, which are beyond the scope of the current work and topic for further research.

5. Conclusion

Based on the monitoring of the chemical composition of HiN:PAW, the emission spectroscopy of the used discharge and the chemical composition of discharge zone, we showed that a crucial condition for the production of HiN:PAW was an increase of air-originating atomic radicals in the discharge area, which was, in our experimental geometry, obtained after 10 min of the discharge burning. This condition of the discharge was enabled by the generation of a gradient of the concentration of the relevant species in the reaction vessel above the discharge, which effectively acts as a partial barrier limiting, but not completely preventing the air flow between the discharge area and the surrounding atmosphere. The formation of this barrier area and its influence on the outcome of the activation process can be very simply adjusted by the geometry of the activation process.

We describe this influence phenomenologically, using a barrier parameter P dependent on headspace height h and the effective radius of the vessel, while also noting the maximal effective vessel radius r_{\max} for the activation process to lead to HiN:PAW. The high concentration of atomic air radicals in the discharge resulting from an optimized P parameter subsequently boosted the chemical pathways leading to the increase in the concentration of nitrogen related species. In addition to NO_2 , the production of HNO_2 was an important pathway, because it readily solvates in water. The combination of these factors allowed us to reach PAW with the NO_3^- to H_2O_2 ratio at least $20 \times 10^3 : 1$, in contrast to approximately 1:1 under more traditional conditions. These results thus show a way to robustly and reliably tune the dominant chemical pathways in a complex system of interconnected individual pathways taking place in plasma activated liquids by controlling a simple parameter of the overall geometry of the activation setup.

Acknowledgments

This research was supported by the Czech Science Foundation Project GAČR GF21-39019L (JK, VS), GF23-05784S (FM, PG, KK).

Data availability statement

The data generated and/or analysed during the current study are not publicly available for legal/ethical reasons but are available from the corresponding author on reasonable request.

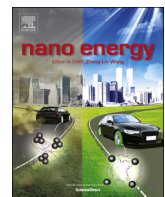
ORCID iDs

F Matějka  <https://orcid.org/0000-0003-3291-2242>
P Galář  <https://orcid.org/0000-0003-2220-2976>
V Scholtz  <https://orcid.org/0000-0002-6981-6169>
K Kůsová  <https://orcid.org/0000-0002-8545-5965>

References

- [1] Bruggeman P J *et al* 2016 Plasma–liquid interactions: a review and roadmap *Plasma Sources Sci. Technol.* **25** 053002
- [2] Tendero C *et al* 2006 Atmospheric pressure plasmas: a review *Spectrochim. Acta, Part B* **61** 2–30
- [3] Ehlbeck J *et al* 2011 Low temperature atmospheric pressure plasma sources for microbial decontamination *J. Phys. D* **44** 13002
- [4] Fridman A, Gutsol A and Cho Y I 2007 Non-thermal atmospheric pressure plasma *Advances in Heat Transfer*. ed A Fridman *et al* (USA: Elsevier) 40, 1–142
- [5] Sonawane S K, T M and Patil S 2020 Non-thermal plasma: an advanced technology for food industry *Food Science and Technology International* **26** 727–40
- [6] Magureanu M *et al* 2021 A review on non-thermal plasma treatment of water contaminated with antibiotics *J. Hazard. Mater.* **417** 125481
- [7] Šerá B *et al* 2021 Effects of non-thermal plasma treatment on seed germination and early growth of leguminous plants—a review *10* 1616
- [8] López M *et al* 2019 A review on non-thermal atmospheric plasma for food preservation: mode of action, determinants of effectiveness, and applications *Front. Microbiol.* **10** 622
- [9] Jeong W-S *et al* 2018 The effects of non-thermal atmospheric pressure plasma treated titanium surface on behaviors of oral soft tissue cells *Sci. Rep.* **8** 15963
- [10] Scholtz V *et al* 2015 Nonthermal plasma—a tool for decontamination and disinfection *Biotechnol. Adv.* **33** 1108–19
- [11] Randeniya L K and de Groot G J J B 2015 Non-thermal plasma treatment of agricultural seeds for stimulation of germination, removal of surface contamination and other benefits: a review *12* 608–23
- [12] Julák J *et al* 2018 Contribution to the chemistry of plasma-activated water *Plasma Phys. Rep.* **44** 125–36
- [13] Thirumdas R *et al* 2018 Plasma activated water (PAW): chemistry, physico-chemical properties, applications in food and agriculture *Trends in Food Science and Technology* **77** 21–31
- [14] Ashford B and Tu X 2017 Non-thermal plasma technology for the conversion of CO₂ *Current Opinion in Green and Sustainable Chemistry* **3** 45–9
- [15] Geyer N D and Morent R 2012 Nonthermal plasma sterilization of living and nonliving surfaces 14255–74 *Annual Review of Biomedical Engineering* **14** 255–74
- [16] Obrová K *et al* 2022 Decontamination of high-efficiency mask filters from respiratory pathogens including SARS-CoV-2 by non-thermal plasma *Front. Bioeng. Biotechnol.* **10** 815393
- [17] Kovačević V V *et al* 2022 Low-temperature plasmas in contact with liquids—a review of recent progress and challenges *J. Phys. D* **55** 473002
- [18] Mariotti D *et al* 2012 Silicon nanocrystals in liquid media: optical properties and surface stabilization by microplasma-induced non-equilibrium liquid chemistry *Advanced Functional Materials* **22** 954–64
- [19] Magureanu M *et al* 2013 Toluene oxidation by non-thermal plasma combined with palladium catalysts *Front. Chem.* **1** 7
- [20] Janda M *et al* 2021 The role of HNO₂ in the generation of plasma-activated water by air transient spark discharge *11* 7053
- [21] Ganesh Subramanian P S *et al* 2019 Characterization of plasma activated water for medical applications *Adv. Mater. Res.* **10** 919–23

- [22] Zhou R *et al* 2020 Plasma-activated water: generation, origin of reactive species and biological applications *J. Phys. D* **53** 303001
- [23] Bradu C *et al* 2020 Reactive nitrogen species in plasma-activated water: generation, chemistry and application in agriculture *J. Phys. D* **53** 223001
- [24] Machala Z *et al* 2013 Formation of ROS and RNS in water electro-sprayed through transient spark discharge in air and their bactericidal effects *Plasma Process. Polym.* **10** 649–59
- [25] Cheng H *et al* 2022 On the dose of plasma medicine: plasma-activated medium (PAM) and its effect on cell viability *Phys. Plasmas* **29** 063506
- [26] Mazzaro R, Romano F and Ceroni P 2017 Long-lived luminescence of silicon nanocrystals: from principles to applications *Phys. Chem. Chem. Phys.* **19** 26507–26
- [27] Kovalenko M V *et al* 2015 Prospects of nanoscience with nanocrystals *ACS Nano* **9** 1012–57
- [28] Dohnalová K, Gregorkiewicz T and Kůsová K 2014 Silicon quantum dots: surface matters *J. Phys. Condens. Matter* **26** 173201
- [29] Mobarok M H *et al* 2017 Instantaneous functionalization of chemically etched silicon nanocrystal surfaces *Angewandte Chemie - International Edition* **56** 6073–7
- [30] van den Boom A F J *et al* 2020 Fast room-temperature functionalization of silicon nanoparticles using alkyl silanols *Faraday Discuss.* **222** 82–94
- [31] Yu Y *et al* 2013 Room temperature hydrosilylation of silicon nanocrystals with bifunctional terminal alkenes *Langmuir* **29** 1533–40
- [32] Galář P *et al* 2017 Influence of non-thermal plasma on structural and electrical properties of globular and nanostructured conductive polymer polypyrrole in water suspension *Sci. Rep.* **7** 15068
- [33] Tyler B J 1962 Reaction of hydrogen peroxide and nitric oxide *Nature* **195** 279–80
- [34] Galář P *et al* 2021 Non-thermal pulsed plasma activated water: environmentally friendly way for efficient surface modification of semiconductor nanoparticles *Green Chem.* **23** 898–911
- [35] Khun J *et al* 2018 Various DC-driven point-to-plain discharges as non-thermal plasma sources and their bactericidal effects *Plasma Sources Sci. Technol.* **27** 065002
- [36] Hozák P *et al* 2018 Further contribution to the chemistry of plasma-activated water: influence on bacteria in planktonic and biofilm forms *Plasma Phys. Rep.* **44** 799–804



Full paper

Perovskite-quantum dots interface: Deciphering its ultrafast charge carrier dynamics



Pavel Galar^{a,1}, Piotr Piatkowski^{a,1,2}, Thi Tuyen Ngo^b, Mario Gutiérrez^a, Iván Mora-Seró^{b,*}, Abderrazzak Douhal^{a,*}

^a Departamento de Química Física, Facultad de Ciencias Ambientales y Bioquímica, y INAMOL, Avenida Carlos III, S/N, Universidad de Castilla-La Mancha (UCLM), 45071 Toledo, Spain

^b Institute of Advanced Materials, Av. de Vicent Sos Baynat, S/N, Universitat Jaume I, 12006 Castelló de la Plana, Spain

ARTICLE INFO

Keywords:

Perovskite
Quantum dots
LEDs
Lighting
Hybrid nanostructures
Electron and hole dynamics

ABSTRACT

Understanding electron and hole (e,h) transport at semiconductor interfaces is paramount to developing efficient optoelectronic devices. Halide perovskite/semiconductor quantum dots (QDs) have emerged as smart hybrid systems with a huge potential for light emission and energy conversion. However, the dynamics of generated e-h pairs are not fully understood. Ultrafast UV-VIS transient absorption and THz spectroscopies have enabled us to unravel the processes of the e-h recombination within a hybrid film of methylammonium lead triiodide (MAPbI₃) interacting with different amount of PbS/CdS core/shell QDs. To accurately analyze the complex behavior, we applied a new model for e-h events in this hybrid material. The results obtained with sample having a high concentration of QDs (7.3 mass percentage) indicate: (i) a large population (92%) of the photogenerated charge carriers are affected by QDs presence. The main part of these carriers (85% of the total) in perovskite domain diffuse towards QDs, where they transfer to the interface (electrons) and QD's valence bands (holes) with rate constants of $1.2 \times 10^{10} \text{ s}^{-1}$ and $4.6 \times 10^{10} \text{ s}^{-1}$, respectively. 7% of these affected charged entities are excitons in the perovskite domain in close vicinity of the interface, and show a recombination rate constant of $3.7 \times 10^{10} \text{ s}^{-1}$. (ii) The carriers not affected by QDs presence (8%) recombine through known perovskite deactivation channels. Lowering the QDs mass percentage to 0.24 causes a decrease of electron and hole effective transfer rate constants, and disappearance of excitons. These results provide clues to improve the performance of perovskite/QD based devices.

1. Introduction

Over the past few years semiconductor colloidal quantum dots (QDs) and trihalide perovskites have been intensively studied [1–6]. The outstanding properties of semiconductor QDs, such as the tunability of the optical band gap across a wide range of energies and their high light absorption coefficient, make them attractive for heterojunction solar cells, light-emitting diodes (LEDs) and lasers [1–3,7,8]. Halide perovskites solar cells have achieved photoconversion efficiencies (PCE) higher than 22% [9], and the performance of LEDs, photo-detectors and lasers based on halide perovskites has improved continuously over the past few years [4,10–17]. Beyond this scenario, a combination of materials with different natures could provide

interesting synergistic interactions that would produce advanced configurations enhancing the performance of related optoelectronic devices. In this sense, the composites of perovskite and semiconductor QDs have shown strong potential in lighting and photovoltaic conversion [18–27]. QDs solar cells showed a significant but lower efficiency than that of other photovoltaic devices due to the low charge carrier mobilities and high surface trap density [28–31]. By combining the efficient charge generation in QDs and the e-h high mobility in the perovskite, efficient colloidal QDs solar cells were fabricated [20–22].

The use of perovskite as a passivating agent for QDs surfaces led to materials that can act as a highly conductive matrix to increase the power conversion efficiency (PCE) of photovoltaic devices based on lead trihalides [19,27], as well as the efficiency of IR LEDs [25] and

Abbreviations: THz, terahertz; TRTS, time-resolved terahertz spectroscopy;; TAS, time-resolved transient absorption spectroscopy;; IRF, instrumental response function;; wt%, mass percentage; ph/cm², photons per cm²

* Corresponding authors.

E-mail addresses: sero@uji.es (I. Mora-Seró), abderrazzak.douhal@uclm.es (A. Douhal).

¹ Equal contribution.

² Current address: Faculty of Chemistry, University of Warsaw, Pasteura 1, 02-093, Warsaw, Poland.

photodetectors [26]. Perovskite and small core/shell QDs have been combined to prepare voltage tunable LEDs that exhibit exciplex emission, which could be used for developing advanced solar cell configurations, such as intermediate band gap ones [23]. In addition to that PbS QDs have been used as seeds to grow perovskite solar cells with larger grain sizes, significantly increasing the performance of the solar cells [19,24]. These results clearly show the enormous potential of combining perovskite and QD materials to develop highly efficient advanced optoelectronic devices. However, detailed studies of the photoinduced processes that occur in these composites are lacking. Understanding the ultrafast events in perovskite/QDs interfaces, such as charge carrier transfer and recombination dynamics, is paramount to improving the overall efficiency of optoelectronic devices based on these materials. However, the real-time observation of the interfacial processes remains unexplored.

Herein, we report on photodynamics studies of thin polycrystalline films of methylammonium lead triiodide (MAPbI_3) matrix embedded with different concentrations of PbS/CdS (core/shell) QDs, using ultrafast time-resolved transient visible-NIR absorption and terahertz (THz) spectroscopies (TAS and TRTS, respectively). By photogenerating charge carriers over the band gap of MAPbI_3 (~1.55 eV) in the MAPbI_3 /QDs hybrid material, we observed fast and efficient charge carrier deactivation due to their transfer to the QDs. The initial (< 1 ps) population and mobility of electrons and holes in the perovskite domain are not affected by the presence of QDs. To accurately elucidate the complex electrons and hole events within the material, we propose a new kinetic model. We found that: (i) the majority (~90%) of photoexcited electrons and holes diffuse towards QDs and is afterwards transferred to the interface and QDs, respectively, (ii) few percent of them fast recombine as excitons in the close vicinity of the interface, and (iii) a small part of the photoexcited charges is not affected by the presence of QDs, and therefore follows the typical perovskite deactivation channels. Lowering the QDs concentration increases the carrier diffusion time, and thus slows down their effective transfer to the interface and QDs, and decreases the concentration of excitons. These results show high collection efficiency of electrons and holes by these QDs in this hybrid material, and the relevance of MAPbI_3 /QDs interface states in charge carrier transition/trapping processes. We propose that further optimization of perovskite/QD system requires a reduction of the interface traps. Not of less importance, the proposed kinetic model can be used to characterize the electron-hole events in other complex hybrid structures.

2. Materials and methods

2.1. synthesis of PbS/CdS core-shell QDs

Core/shell quantum dots (QDs) were synthesized according to a previously reported procedure [24,32]. Briefly, a mixture of 0.9 g (4 mmol) of PbO , 2.7 g (9.6 mmol) of oleic acid (OA) and 36 ml of 1-octadecene (ODE) in a three-necked round-bottom flask was heated to 150 °C under N_2 to form Pb-oleate moieties. The solution was degassed for 30 min under vacuum, then opened to N_2 , and 3 ml (6.7 mmol) of trioctylphosphine (90%) was injected. A mixture of 0.42 ml (2 mmol) of hexamethyldisilathiane (HMDS) and 4 ml of ODE was quickly injected to the flask when the temperature dropped to 110 °C. The solution was left to cool to room temperature. The reaction product was cleaned three times with ethanol/acetone (1:1, v/v), centrifuged (3000 rpm for 10 min) and dispersed in toluene (100 mg/ml).

For the growth of the CdS shell, a flask containing 0.34 g (2.6 mmol) of CdO , 1.85 g (6.5 mmol) of OA and 40 ml of ODE was heated to 220 °C in air to dissolve CdO , cooled to 150 °C and then degassed for 1 h under vacuum. After that, the temperature was reduced to 70 °C. 5 ml of the as-prepared PbS QD suspension (100 mg/ml in toluene) was rapidly injected to the flask. The reaction was kept at 70 °C for 5 min then stopped by adding the non-solvent mixture (ethanol/acetone, 1:1, v/v).

The product was washed following the same procedure used for PbS nanocrystals and dispersed in octane for the ligand exchange. We got PbS/CdS QDs of 3.0 ± 0.3 nm in size, and which distribution was characterized by TEM (Fig. S1).

2.2. Ligand exchange and perovskite, perovskite/QDs solution preparation

1.5 ml (10 mg/ml) of PbS/CdS core-shell QDs in octane was mixed with 0.5 ml of dimethylformamide (DMF) containing 58.3 mg of PbI_2 and 25 mg of methylammonium iodide (MAI). The as-mixed solution separated into 2 phases: at the top, QDs in octane (brown) and ($\text{PbI}_2 + \text{MAI}$) in DMF at the bottom (yellow). After stirring for 30 min, the QDs transferred from the top octane phase to the bottom DMF phase, resulting in a color change: transparent at the top and dark at the bottom. The octane solution was removed and the QD solution was washed three more times using the same solution to remove the organic residue. Subsequently, the QDs were precipitated adding toluene. After removing all the liquids, the QDs were dried under vacuum and dispersed in perovskite solution (0.4 M) to form a MAPbI_3 /QDs solution. The amount of C_{QDs} was varied from 2 to 200 mg/ml. The 0.4 M MAPbI_3 reference solution (without QDs) was prepared by dissolving 0.438 mmol of PbI_2 and 0.438 mmol of MAI in a mixture of 1 ml of DMF and 95 µl of dimethyl sulfoxide (DMSO). Further details have been published elsewhere [24].

2.3. Perovskite and perovskite/QDs film preparation

Glass substrates were cleaned with soap, sonicated in distilled water, ethanol and isopropanol for 15 min and then treated with an UV-O₃ lamp for 15 min. MAPbI_3 or MAPbI_3 /QD films were spin coated at 9000 rpm from 50 µl of MAPbI_3 or MAPbI_3 /QD solution, respectively. Diethyl ether was poured on a film after the spin coater was running for 4 s. The films were annealed for 1 min at 65 °C, then for 2 min at 100 °C. The deposition was carried out inside a glovebox filled with N_2 .

2.4. SEM and XRD measurement

The morphology and structural properties of the films were analyzed using a field emission scanning electron microscope (JSM7001F, JEOL) and a Bruker AXS D4 X-ray diffractometer using Cu K α radiation.

2.5. UV–VIS–NIR absorption spectroscopy

The UV–VIS–NIR absorption spectra of the MAPbI_3 , MAPbI_3 /QDs and QDs were measured using a standard spectrophotometer (JASCO V-670). To eliminate the contribution of the scattered light, we carried out diffuse reflectance measurements using a 60-mm integration sphere (ISN-723).

2.6. Femtosecond transient absorption spectroscopy

The used femtosecond (fs) transient UV–VIS–NIR absorption setup has been described elsewhere [33]. Briefly, it consists of a Ti:sapphire oscillator (TISSA 50, CDP Systems) pumped by a 5 W diode-laser (Verdi 5, Coherent). The oscillator output pulses (30 fs, 480 mW at 86 MHz) centered at 800 nm were guided to a regenerative amplifier (Legend-USP, Coherent) and used as a seeding signal. The amplified fundamental beam (50 fs, 1 W at 1 kHz) was then directed through an optical parametric amplifier (OPA, CDP Systems) for wavelength conversion and an additional 1-mm BBO crystal for frequency doubling to obtain 400, 600, 700 and 740 nm pulses. The pump intensities ranged from ~40–250 µW. The transient absorption measurements were performed in the spectral ranges of 450–780 nm. All the spectra analyzed in the visible-NIR region were corrected for the chirp of the white light continuum. To avoid sample degradation, the samples were moved during the measurement using the XY translational stage. The instrument

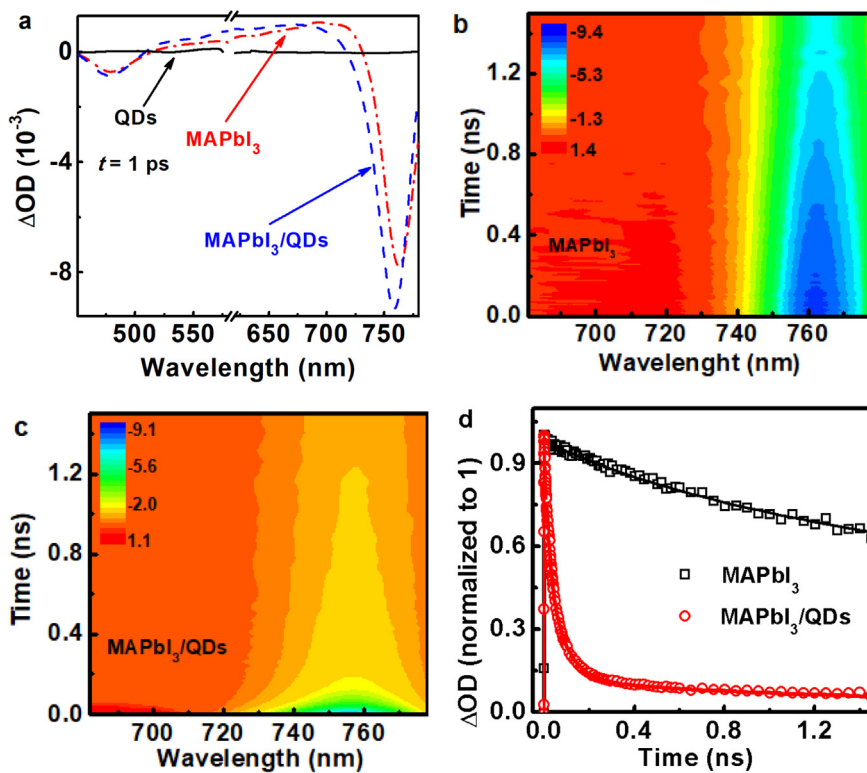


Fig. 1. (a) Transient absorption spectra of MAPbI₃ (red dashed-dotted line), MAPbI₃/QDs (blue dashed line, 6.3 wt%) and neat QDs (black solid line) films at 1 ps pump-probe delay time. Two-dimensional pseudo-color ΔOD map of (b) MAPbI₃ and (c) MAPbI₃/QDs films (6.3 wt%) as a function of both observation wavelengths and pump-probe delay time. (d) Normalized transient absorption decays of MAPbI₃ and MAPbI₃/QDs observed at 760 nm. Data were obtained upon excitation at 600 nm. Used fluence of the absorbed photons was $8.2 \times 10^{12} \text{ ph/cm}^2$. The solid lines in (d) are from the best fits using the kinetic models described in the text.

response function (IRF) of the setup was ~ 70 fs. All the experiments were performed at 293 K [34].

2.7. Sub-picosecond time-resolved terahertz spectroscopy

The terahertz (THz) experiments were done using the same laser setup described in the previous paragraph (Legend-USP regenerative amplifier seeded by the Ti:sapphire oscillator). The amplified fundamental beam centered at 800 nm (50 fs, 1 W, 1 kHz) was divided into three parts. The first one (~ 700 mW) was directed through an OPA and additional 1-mm BBO crystal for frequency doubling to obtain 600 nm pulses. The resulting beam is sent through a long (up to 10 ns) delay line (H2W Technologies) to pump the sample in the time-resolved THz experiment. The second part of the amplified output beam (~ 200 mW) generates the THz probe in a ZnTe crystal by optical rectification. The third part (~ 1 mW) is used for electro-optic detection of the THz signal in another ZnTe crystal. During the measurements, the setup was continuously purged with dry nitrogen gas. The experiments are performed without any additional illumination and at 273 K. The IRF of the setup is < 1 ps [34].

2.8. Flash photolysis spectroscopy

The nanosecond (ns) flash photolysis experimental setup was described previously [35]. Briefly, it consists of an LKS.60 laser flash photolysis spectrometer (Applied Photophysics) and a Vibrant (HE) 355 II laser (Opotek). Pulses from Vibrant are used as an input of light for an optical parametric oscillator (OPO) pumped by a Q-switched Nd:YAG laser (Brilliant, Quantel) generating excitation pulses at 460 nm. The probing light source is a 150 W xenon arc lamp. The light transmitted through the sample is dispersed by a monochromator and detected by visible photomultipliers (Applied Photophysics R928) coupled to a digital oscilloscope (Agilent Infiniium DS08064A, 600 MHz, 4 GSa/s). The measured IRF of the system is ~ 8 ns.

3. Results and discussion

3.1. Morphology, structure and absorption spectra

The morphology and structure of MAPbI₃ and MAPbI₃/QDs (6.3 wt %, QDs size ~ 3 nm) films were characterized by SEM (Fig. S2, for wt% calculation, see Eq. S1). Both samples show comparable fine polycrystalline structure (grains size ~ 30 –100 nm). The thicknesses of MAPbI₃ and MAPbI₃/QDs films are 80 ± 10 and 120 ± 10 nm, respectively. Proper perovskite crystalline structure of both samples was proved also using XRD technique (Fig. S3a). Signal peaks at 14°, 28° and 32° detected on MAPbI₃ and MAPbI₃/QDs correspond to {110}, {220} and {310} atomic planes of MAPbI₃, respectively [19,27,36]. Steady-state absorption spectra of MAPbI₃, MAPbI₃/QDs (6.3 wt%) and QDs not attached to perovskite matrix are presented in Fig. S3b. The spectra of MAPbI₃ and MAPbI₃/QD are comparable and very similar to those already published on this type of perovskite [24,37]. The presence of QDs is mainly manifested by differences in the absorption of MAPbI₃ and MAPbI₃/QDs films in the spectral region > 800 nm.

3.2. Femtosecond time-resolved transient absorption spectroscopy

Time-resolved transient absorption (TA) spectroscopy in the UV–VIS–NIR range was used to characterize and elucidate the charge carrier processes in excited MAPbI₃/QDs films. To obtain a clear picture of the involved events, we have studied MAPbI₃/QDs materials containing various QD concentrations (C_{QDs}): 0, 0.12, 0.18, 0.24, 0.30, 0.59, 1.2, 2.6, 4.6, 6.3 and 7.3 wt%. Samples were excited at different excitation wavelengths: 400, 600, 700 and 740 nm, using the constant fluence of the absorbed photons 8.2×10^{12} photons per cm^2 (ph/cm^2 , for more detail, see Supplementary information). The fluence dependences of TA decays observed for MAPbI₃/QDs (6.3 and 0.3 wt%) are also presented (600 nm, 1.5 – 16×10^{12} ph/cm^2).

3.2.1. Transient spectra and decays

To begin with, we first show and discuss the results of neat

perovskite and MAPbI₃/QDs film containing 6.3 wt% of the QDs upon excitation at 600 nm, using fluence of the absorbed photons 8.2×10^{12} ph/cm². The TA spectrum of MAPbI₃ film consists of two photo-bleaching bands (PB) with intensity maxima located at approximately 480 nm (PB1) and ~ 763 nm (PB2), and positive band (photoinduced absorption, PIA) in the region 520–700 nm (Fig. 1a). This result is in agreement with previous reports on neat perovskite films [38–40]. The initial negative signal at 760 nm (PB2) shifts slightly towards longer wavelengths upon increasing pump-probe delay time (up to 700 fs) due to the band filling process (Fig. S4a) [41–43]. No further spectral changes of PB2 were recorded. The TA spectra of the MAPbI₃/QDs and MAPbI₃ films exhibit the same features (Fig. 1a and S4a,b). The only difference is a blue-shift (5 nm) of MAPbI₃/QDs PB2 when compared to that of MAPbI₃ one. The excitation of neat QDs film (under the same experimental conditions) does not lead to the appearance of a significant TA signal in the 450–780 nm region (Fig. 1a). However, it results in recording of a weak and positive signal ($\sim 0.1 \times 10^{-3}$ ΔOD, in the limit of the sensitivity of the setup) in the range of 850–1100 nm (Fig. S5a). Moreover, the intensity of this signal is constant within the ns-gating time window, contrary to the observed decays of the signals from MAPbI₃ and MAPbI₃/QDs films at the visible and NIR regions (Figs. S5b and S5c). For these samples, the NIR TA bands have similar shapes and intensities, which suggests that under our experimental conditions (QDs concentration, laser excitation and fluence), the recorded signal for the sample of interest here (MAPbI₃/QDs) does not contain a significant information on the dynamics of charge carriers in QDs structure. Therefore, the observed spectral photobehavior of MAPbI₃/QDs sample originates from excitation of perovskite domain and not from QDs excitation. This statement is also supported by the comparable initial TA signal of MAPbI₃ and MAPbI₃/QDs (Fig. 1a). Consequently, the blue shift in the PB2 band of MAPbI₃/QDs is due to changes in the electronic and/or crystallographic structure of MAPbI₃ in presence of the QDs. Such modifications were observed after passivation by the QDs due to the lattice mismatch between the two materials [18,21,44,45]. The interpretation of the blue shift also agrees with reported band gap expansion of MAPbI₃ related to structural deformation [46].

Fig. 1b and c show the two-dimensional pseudo-color maps of the transient absorption signal of neat perovskite and MAPbI₃/QDs in the visible regime. It can be seen that while the signal of both PIA and PB2 bands in the former sample stays up to the ns regime, those of MAPbI₃/QDs strongly decrease in sub-ns. This clearly shows the influence of fast decaying channels in the transients of MAPbI₃/QDs. The dynamics of PIA and PB2 in the TAS of perovskite film are closely related [38,40,47]. Thus, to analyze the involved photoevents, we focus on PB2 fs-transients of both samples (gating at 760 nm).

Fig. 1d exhibits that the signal of excited MAPbI₃ slowly decays losing approximately 35% of its initial value at 1.5 ns. This behavior is caused by the presence of monomolecular (trap-assisted), bimolecular and Auger charge carrier deactivation processes [34,42,48–50]. It is known that the contribution of each process to the overall decay

depends on perovskite composition and concentration of charge carriers. We have quantified the recombination rate constants of these events adopting a kinetic model applied previously for neat perovskite materials (Eq. S3, for more details see Supplementary information) [40,42,51,52]. The obtained values of the rate constants ($k_{\text{mono}} = 1.6 \times 10^7$ s⁻¹, $k_{\text{bimol}} = 8.1 \times 10^{-11}$ cm³ s⁻¹ and $k_{\text{Auger}} = 2.9 \times 10^{-28}$ cm⁶ s⁻¹) are comparable to previously published ones [51–53].

In contrast to the TA spectra, the decays of excited MAPbI₃/QDs are significantly affected by the presence of QDs (Fig. 1d). Except the long-lasting residual signal $\sim 10\%$ (after 1.2 ns), the decay is being done within the first ~ 200 ps (only 20% of the initial intensity is left after 100 ps). While the origin of this behavior will be discussed in more detail further, we briefly assign it to the following events. The fast decay is mainly caused by diffusion and subsequent transfer of the photoexcited holes from the perovskite valence band (VB) to the one of the QDs, and the electrons from perovskite conductive band (CB) to the MAPbI₃/QDs interface. The residual signal is related to charge carriers in the perovskite domain of MAPbI₃/QDs, not affected by the presence of QDs. It is evident that charge carriers diffusion and transfer from MAPbI₃ to QDs dominates the dynamics in this composite material (Fig. S4c). Remark that the TA decays of MAPbI₃/QDs film at the visible (760 nm) and NIR (970 nm) regions are very similar, but different from the one of QDs recorded in the NIR region (Figs. S5b and S5c). A new kinetic model is necessary to analyze the photoevents, and related electrons and holes dynamics in the excited MAPbI₃/QDs film.

Analyzing the short-time scale (< 1 ps), the TA signals of the MAPbI₃ and MAPbI₃/QDs (6.3 wt%) show ultrafast rising components (Fig. S4d). We were able to fit the rising part using a monoexponential function obtaining a time constant of ~ 150 fs for both MAPbI₃ and MAPbI₃/QDs films. Such behavior of the TA signal during the first 100 fs after excitation is typical for perovskite materials, and it reflects hot charge carrier cooling [41,54,55]. Since we recorded the same risetime and comparable ΔOD changes within 1 ps after excitation of both MAPbI₃/QDs and MAPbI₃ films, we conclude that in the sub-ps regime, the charge carrier dynamics in the perovskite domain is not affected by the presence of QD during the initial cooling phase in the MAPbI₃/QDs film.

3.2.2. Influence of QDs concentration

To elucidate the effect of QDs presence on charge carriers deactivation, we have recorded and analyzed the TA decays of excited MAPbI₃/QDs containing different C_{QDs}. Fig. 2 presents the TA decays (observed at 760 nm) of the samples containing: 0, 0.12, 0.18, 0.24, 0.30, 0.59, 1.2, 2.6, 4.6, 6.3 and 7.3 wt% of QDs, under the same experimental conditions of excitation (600 nm, fluence of the absorbed photons 8.2×10^{12} ph/cm²). The samples were prepared under similar conditions (for more details, see the sample preparation in Section 2). In agreement with the behavior shown in Fig. 1d, the decays become shorter upon increasing C_{QDs}. The most significant change starts from C_{QDs} ~ 0.24 wt%. The TA decays of samples containing C_{QDs} lower than

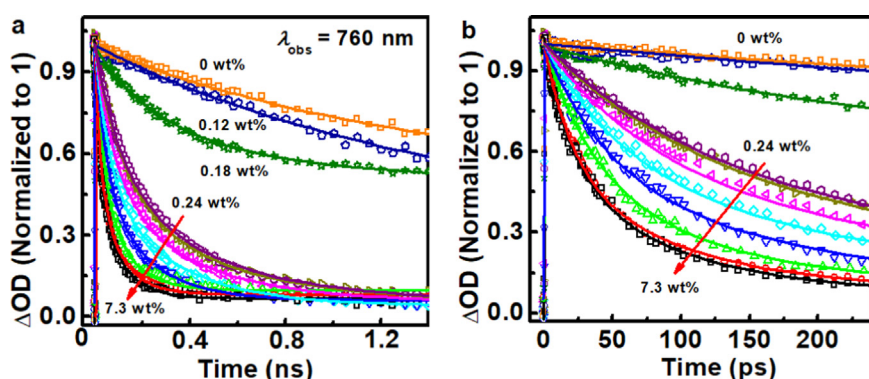
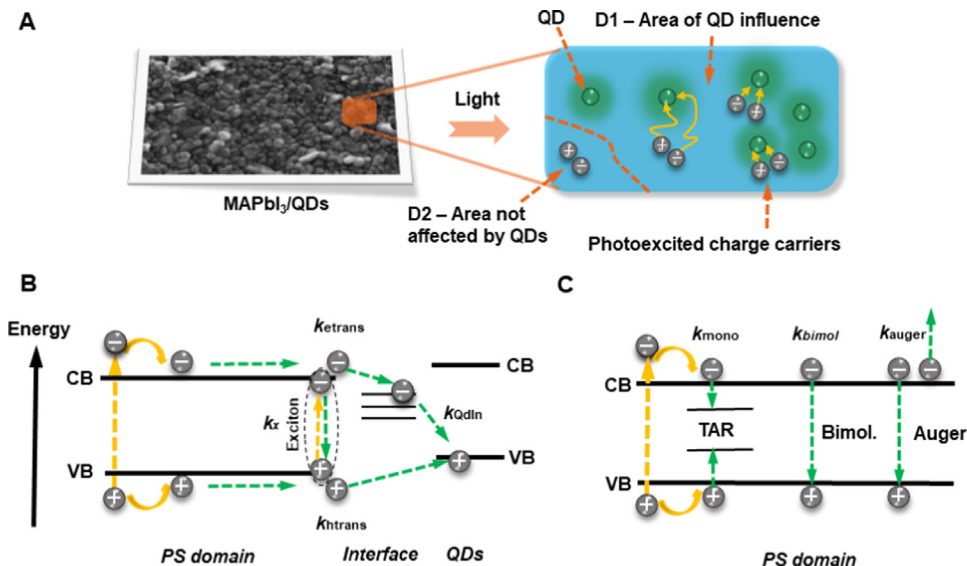


Fig. 2. (a) Normalized transient absorption decays of MAPbI₃/QDs thin polycrystalline films containing QDs of: 0, 0.12, 0.18, 0.24, 0.30, 0.59, 1.2, 2.6, 4.6, 6.3 and 7.3 wt % (mass percentage). Data were observed at 760 nm, upon excitation at 600 nm, and using fluence of the absorbed photons 8.2×10^{12} ph/cm². (b) is a zoom of (a) to show the decays up to 250 ps. Solid lines are from the best fits using the kinetic model described in the text.



0.18 wt% were governed by the behavior of neat perovskite. The dependence of TA decays on C_{QDs} clearly demonstrates that their shortening reflects a charge deactivation processes related to the presence of QDs in the film.

3.3. Kinetic model for MAPbI₃/QDs

3.3.1. Description of the model

To accurately analyze the observed dynamics, we propose the following model (Fig. 3). Because the QDs do not occupy all the perovskite domain, we divided the probed part (width $\sim 100 \mu\text{m}$) in two areas (Fig. 3a): area where the photoexcited charges can be affected by the presence of QDs (domain 1, D1), and area (D2) where these carriers do not interact with the QDs. Fig. 3a,b and c illustrate our concept, and the processes taking place in D1 and D2. Note that for clarity, the scheme in Fig. 3b is simplified, and in D1 the photoexcited population may still follow the dynamics described in Fig. 3c.

To begin with, we describe the events happening in D1: (i) charge carriers transport and transfer from perovskite domain to QDs and MAPbI₃/QDs interface (Fig. 3b), (ii) exciton recombination (Fig. 3b), (iii) electron and hole recombination processes in perovskite (Fig. 3c), and (iv) recombination of transferred charge carriers (Fig. 3b).

- (i) According to the reported energy diagram of MAPbI₃ containing PbS/CdS QDs of 3 nm size, the CB and VB edges of perovskite and QDs are located at -3.93 eV and -5.43 eV , and -3.68 eV and -5.23 eV , respectively [23,37]. Therefore, only holes can be easily transferred from the perovskite domain to QDs. The electrons deactivation can follow several paths. Firstly, because the initial energy of some excited electrons at 600 nm (2.1 eV) in the perovskite domain is higher than the energy difference between the edges of the VB in perovskite and the CB in QDs ($\sim 1.75 \text{ eV}$), the ultrafast transition of these hot charge carriers to the CB of the QDs is possible. However, the occurrence of this process is unlikely due to the presence of highly competitive ultrafast electron cooling in perovskite domain, which has much shorter time ($< 1 \text{ ps}$, Fig. S4d) [38,40] than that of TA decay in MAPbI₃/QDs (~ 200 – 500 ps , Fig. 2). Secondly, the electrons in the CB of perovskite domain may recombine directly with the holes transferred to the QDs VB (via no vertical transitions). However, the presence of such fast recombination process would be in contradiction with long and efficient PL conversion observed from the QDs of this hybrid material, as a result of electron-hole recombination in the PbS/CdS [23]. Remark that a previous work gating the photobehaviour of

Fig. 3. (a) SEM of MAPbI₃/QDs and the cartoon showing the areas of QDs influence (D1) and without their influence (D2) upon excitation over the band gap of perovskite. (b) Energy diagram showing the dynamics of photoexcited charge carriers in MAPbI₃/QDs film in D1 area and (c) D2 area upon excitation over the band gap. For clarity, (b) only shows the processes involving the influence of QDs, while those in (c) representing the classical events in neat perovskite. k_{etrans} and k_{htrans} characterize the effective transfer processes of charge carriers from perovskite to the interface or/and QDs. k_x is the exciton recombination rate constant. k_{Qdn} is the recombination rate constant between trapped electrons and holes in QDs. The positions of the energy levels are taken from references [23,37]. See text for details.

perovskite/PbS QDs (without capping) showed a shortening in the emission decays of the hybrid material [18]. Our results are in full agreement with these previous works, and give details on the dynamics of electrons and holes transport and recombination in the used MAPbI₃/QDs thin films. Moreover, very similar spectral shapes and positions of the PB2 bands in the MAPbI₃ and MAPbI₃/QDs films suggest that the ultrafast electron-hole recombination occurs mostly in the perovskite domain. Thirdly, electrons can be transferred and subsequently trapped in perovskite/QDs interface. Indeed, it has been reported that, in the presence of QDs, the crystallographic structure of the MAPbI₃ lattice might be different inside the crystallite and at the interface with the QDs, thus, new trap states will appear [18,21,44]. The presence of interfacial electron trap states in MAPbI₃/PbS was also proved by the density functional theory calculations [18]. This conclusion is in agreement with our steady-state absorption measurements in the near IR region (the absorption of MAPbI₃/QDs at $> 800 \text{ nm}$, Fig. S3b). It is important to note that before the carriers can be transferred, they need to be transported to MAPbI₃/QDs interface first. Therefore, not only the transfer processes affect the fact deactivation of charges in D1, but also the transport time of charge carriers. We label the combination of both these effects as effective charge carrier transfer. The diagram of energy levels shown in Fig. 3b is based on calculations using QDs of 3 nm in size [23]. Because the population of QDs having size larger than $\sim 3.55 \text{ nm}$ in our sample is very small (Fig. S1a), and which size would correspond to the threshold for switching between type II and I heterostructures for our hybrid material [56], we do not expect direct electron transfer from perovskite CB to the one of QDs. Our QDs size distribution and band gap alignment is therefore preventing effects related to the mixed heterostructure material, contrary to situations observed in other hybrid materials [57,58].

- (ii) It is well known that the binding energy of excitons in MAPbI₃ is below the thermal energy at ambient conditions (25.7 MeV) that should lead to efficient formation of free charge carriers as a result of the photoexcitation [52]. However, the changes in the perovskite lattice in the close vicinity of QDs, can induce and increase localization of photoexcited charges, related excitons bounding energy and Langevin coefficient [59,60]. This may result in an initial formation of excitons able to survive several picoseconds without dissociation in the close vicinity of QD. We believe that this behavior is the origin of the observed initial fast TA decay (first few ps) of excited MAPbI₃/QDs film (Fig. S4c) [34]. Appearance of the interface structural defects in MAPbI₃/QDs films

Table 1

Values of the effective transfer rate constants, k_{htrans} and k_{etrans} , and D1 and D2 population fractions (P_{D1} , P_{D2}) obtained using the kinetic model described in the text to fit the transient absorption decays of MAPbI₃/QDs film, containing the indicated concentration of QDs (Fig. 2). TA data were observed at 760 nm, upon excitation at 600 nm, and using fluence of the absorbed photons 8.2×10^{12} ph/cm². The population fractions of excitons (P_x) in D1 in samples containing C_{QDs} of 7.3, 6.3 and 4.6 wt% are 7%, 6% and 4%, respectively. For these samples, the recombination rate constants of the excitons, k_x , are $\sim 3.5 \times 10^{11}$ s⁻¹. For C_{QDs} lower than 4.6 wt% the $P_x = 0$.

Transient absorption, $\lambda_{\text{pump}} = 600$ nm, $\lambda_{\text{obs}} = 760$ nm				
C_{QDs} (wt%)	k_{htrans} (10^{10} s ⁻¹)	k_{etrans} (10^{10} s ⁻¹)	P_{D1} (%)	P_{D2} (%)
7.3	4.6	1.2	92	8
6.3	4.3	1.04	90	10
4.6	3.0	0.87	90	10
2.6	2.1	0.54	89	11
1.2	1.5	0.37	89	11
0.59	1.2	0.29	89	11
0.30	0.95	0.24	88	12
0.24	0.81	0.22	88	12
0.18	0.39	0.002	85	15
0.12	0.13	0.002	5	95
0	–	–	–	100

were already discussed in Section 3.2.1. The presence of excitons was also verified by the fluence dependence of TA decays and comparison of THz measurements of MAPbI₃/QDs that show the absence of the initial fast signal decrease (*vide intra*, Section 3.7.). This agrees with the reports of TA signal decay in neat PbS/CdS quantum dots, interpreted on the basis of a surface exciton deactivation model [61].

- (iii) For the fast and efficient charge deactivation in MAPbI₃/QDs, the recombination processes (monomolecular trap-assisted, bimolecular and Auger) normally happening in neat perovskite should be significantly suppressed. However, they are still present where the charge carriers are part of perovskite domain.
- (iv) The transferred holes and trapped interfacial electrons can recombine through trap-assisted processes. However, radiative recombination between both types of transferred carriers is more likely. This assumption is in agreement with recent observation of a new NIR luminescence peak when perovskite and PbS/CdS QDs are combined [23]. The energy of the emitted photons corresponds to the difference between positions of shallow electron traps at the MAPbI₃/QDs interface and QDs VB.

Now, we describe the processes in D2 (Fig. 3). The TA decays show a residual signal at times longer than several 100 s ps (Fig. 1d). Because, the signal gated at 760 nm is mainly sensitive to the charges in perovskite, this signal is most probably caused by the photoexcited charges (in D2) not transferred to the interface or QDs interior. Their presence in the perovskite domain might be due to their low mobility (e.g. trapped in shallow states of perovskite band gap) or lack of interaction with QDs [34,46,62]. However, the comparable features of TA and THz signals suggest that these charges keep their mobility during the gating time (up to 1.5 ns). Thus, the latter explanation seems to be the most plausible one (*vide intra*, Sections 3.4. and 3.7.). These charges should follow standard perovskite recombination processes (Eq. S3).

In addition to the discussed processes above, the electron transfer from QDs to MAPbI₃/QDs is also possible. However, taking into account the absence of TA signal of neat QDs layers, and comparable initial TA values of excited neat perovskite and MAPbI₃/QDs at 760 nm, the contribution of such transfer to the signal should be negligible.

3.3.2. Mathematical model

To quantify the processes in D1, we propose a following set of kinetic equations based on previous information [62–64]:

$$\frac{dn_e}{dt} = G_e - n_e k_{\text{mono}} - n_e n_h k_{\text{bimol}} - n_e^2 n_h k_{\text{Auger}} - n_e k_{\text{etrans}}, \quad (1\text{a})$$

$$\frac{dn_h}{dt} = G_h - n_h k_{\text{mono}} - n_e n_h k_{\text{bimol}} - n_h^2 n_e k_{\text{Auger}} - n_h k_{\text{htrans}}, \quad (1\text{b})$$

$$\frac{dn_x}{dt} = G_x - k_x n_x, \quad (1\text{c})$$

$$\frac{dn_{\text{interface}}}{dt} = +n_e k_{\text{etrans}} - n_{\text{interface}} n_{\text{QD}} k_{\text{QDIn}}, \quad (1\text{d})$$

$$\frac{dn_{\text{QD}}}{dt} = +n_h k_{\text{htrans}} - n_{\text{interface}} n_{\text{QD}} k_{\text{QDIn}} \quad (1\text{e})$$

where n_e , n_h and n_x are the concentrations of free electrons and holes in CB and VB of perovskite domains, and excitons in the perovskite domain in close vicinity of the interface, respectively. G_e , G_h and G_x refer to the generation factors of these entities. According to this model, the overall generation factor, G , should be equal to the sum of the generation factors of free charges and excitons. The effective transfer rate constants of holes to QDs and electrons to MAPbI₃/QDs interface are given by k_{htrans} and k_{etrans} , respectively; while the recombination rate constant of excitons is described by k_x . The $n_{\text{interface}}$ and n_{QD} reflect the concentrations of electrons trapped in the interface and holes transferred to the VB of QDs, respectively. The recombination rate constant of these two carriers is given by k_{QDIn} . However, because the TA signal at 760 nm is only sensitive to the charge carriers in the perovskite domain, and we did not observe any TA signal from QDs, we are not able to determine the value of k_{QDIn} .

The overall decay of observed TA signal should be given by the sum of those in D1 and D2:

$$\text{TA signal} = n_{\text{total}}(t) = P_{\text{D1}}(n_e(t) + n_h(t) + n_x(t)) + P_{\text{D2}}n(t) \quad (2)$$

P_{D1} and P_{D2} characterize the population fractions of charge carriers in D1 and D2 areas. We call $n(t)$ the population of the charge carriers in D2, as described in Eq. S3. To simplify the model, we did not take into account the ultrafast dynamics of charge carrier generation, their thermalization and cooling. These events happening commonly in less than 1 ps [52]. Eq. (2) allows to calculate the initial and excited populations of electrons and holes in D1 and D2 as well as the relative contributions of charge carriers in both domains.

3.3.3. Analysis of the transient absorption decays

Fig. 2 shows the fits of the TA decays using the kinetic model, and Table 1 gives the obtained data from the best fits (for TA decays converted to charge carrier concentration, see Fig. S6). The values of k_{mono} , k_{bimol} and k_{Auger} used in the fits were taken from the analysis of the photobehavior of neat perovskite and related known model (for more information about the of the model, see Supplementary information) [63,64].

Firstly, we discuss the observed dependence of k_{htrans} and k_{etrans} values on C_{QDs} (Table 1). The dependence is visualized in the Fig. S7. It is clear that upon increasing the C_{QDs} (0.24–7.3 wt%) the values of k_{htrans} and k_{etrans} (10^{10} s⁻¹) increase from 0.81 to 4.6 and from 0.22 to 1.2, respectively. While the probability of carrier transfer should be independent on C_{QDs} , the observed dependence can be explained by a change in charge carrier diffusion time before reaching QDs. According to the diffusion theory [65] and Wigner-Seitz radius calculation [66], both effective transfer rate constants should be proportion to $C_{\text{QDs}}^{2/3}$ (see Supplementary information, Eqs. S4–6). Fig. S7 shows the agreement of the observation with the theory. The ratio of the $k_{\text{htrans}}/k_{\text{etrans}}$ is constant and equal to approximately 4 in the wide range of C_{QDs} (7.3–0.24 wt%, Fig. S7 inset). Two remarks: (i) its independence on C_{QDs} is in agreement with the diffusion theory. (ii) Its value reflects a combined effect of higher transfer efficiency of holes to QDs VB, in contrast to the electrons transfer to interface states and small differences in charge carriers mobilities (see Supplementary information).

k_{trans} and k_{etra} rate constants behavior for $C_{\text{QDs}} < 0.24 \text{ wt\%}$ is not discussed because of the strong signal from the neat perovskite.

Secondly, the fitting parameters (Table 1) suggest that 92% of all charge carriers in $\text{MAPbI}_3/\text{QDs}$ (7.3 wt%) film should be generated in D1. This value slightly decreases to 88% for sample containing 0.24 wt % of QDs. This result suggests that no ultrafast and fast interaction of photoexcited charges with traps or dark carriers is present in $\text{MAPbI}_3/\text{QDs}$ films. The sample with low C_{QDs} (< 0.18 wt%) showed only weak contribution of D1 region causing a weak acceleration of perovskite-like TA decay.

The analysis also shows that the population fraction of the excitons (P_x) in D1 depends on C_{QDs} . The P_x is 7% for the sample with the highest QDs concentration and vanishes at C_{QDs} lower than 4.6 wt%. Considering that the excitonic states are located in close vicinity of QDs, this result is in agreement with our model. The value of k_x is almost constant in all samples ($\sim 3.5 \times 10^{11} \text{ s}^{-1}$).

3.4. Transient absorption: fluence dependence

To support the kinetic model, we measured the TA decays of $\text{MAPbI}_3/\text{QDs}$ films containing high (6.3 wt%) and low (0.3 wt%) concentration of QDs, using different fluences of the absorbed photons. Fig. 4a shows the decay of TA signal converted to the concentration of charge carriers of $\text{MAPbI}_3/\text{QDs}$ (6.3 wt%) upon excitation at 600 nm, using fluences of the absorbed photons: 1.5×10^{12} , 8.2×10^{12} and $16 \times 10^{12} \text{ ph/cm}^2$. The similarity of the decays proves that non-monomolecular deactivation channels are significantly closed, and the electron/hole deactivation processes should be primarily driven by the interaction between the perovskite and QDs (Fig. S8a). In fact, bimolecular and especially the Auger processes are fluence dependent, and thus their contribution would cause significant shortening of the TA decays at a higher fluence of the excitation [48]. It is noteworthy that the amount of charge carriers responsible for the TA residual signal at longer times ($> 400 \text{ ps}$) increases almost linearly with the fluence, and does not saturate even at the used highest fluences of the absorbed photons. Thus, these carriers should not be related to the localized states in perovskite domain, but they are more likely free charge carriers not affected by QDs. In fact, concentration of trap states in perovskite domain was reported to be lower than photons absorbed per laser pulse using highest pump fluence [52]. The only difference between the recorded decays is their small shortening within the first $\sim 5 \text{ ps}$, when decreasing the fluence of the absorbed photons (Fig. 4a, inset). While the influence of bimolecular or Auger processes would have exactly opposite effect, this behavior is also suggesting the suppression of higher order processes in $\text{MAPbI}_3/\text{QDs}$ [48]. We interpret this behavior in terms of rapid deactivation of charges related to limited amount of states that show saturation under stronger excitation. This is in agreement with our suggestion of excitonic states presence in perovskite domain of D1 in close vicinity to the $\text{MAPbI}_3/\text{QDs}$ interface. All the decays in Fig. 4a were successfully fitted using the proposed kinetic

model. The obtained data are shown in Table S1. Taking into account that doubling the fluence of the absorbed photons from 8.2×10^{12} to $16 \times 10^{12} \text{ ph/cm}^2$ causes only small increase of exciton amount in $\text{MAPbI}_3/\text{QDs}$ (6.3 wt%), the concentration of excitonic states in this sample can be estimated as $\sim 5 \times 10^{16} \text{ cm}^{-3}$.

Comparable results were observed for $\text{MAPbI}_3/\text{QDs}$ containing low C_{QDs} (0.30 wt%) (Fig. 4b, S8b and Table S1). However, as the inset of Fig. 4b shows, there is no variation of the decays with excitation fluence at short time regime indicating a lack of excitons (low C_{QDs}).

The risetimes of the $\text{MAPbI}_3/\text{QDs}$ (6.3 wt%) TA signal increases from 110 to 230 fs (longer than the IRF $\sim 70 \text{ fs}$) when the fluence of the absorbed photons varies from 1.5×10^{12} to $16 \times 10^{12} \text{ ph/cm}^2$ (Fig. S8c, Table S2). The observed behavior is not caused by QDs presence, but it is the result of state saturation and the phonon bottleneck processes happening in perovskite as it has been previously reported [41,54,55]. This explanation is also supported by the very similar behavior of the neat perovskite film (Fig. S8d, Table S2).

3.5. Transient absorption: excess energy of excitation

To elucidate the role of the excess energy of the photogenerated charge carriers on their transport and recombination mechanisms in $\text{MAPbI}_3/\text{QDs}$, we have analyzed the TA decays of $\text{MAPbI}_3/\text{QDs}$ (6.3 wt %) upon excitation at 400 (3.1 eV), 600 (2.1 eV), 700 (1.8 eV), and 740 nm (1.7 eV) (all over band gap excitations). The TA signal was observed at 760 nm. The fluence of the absorbed photons was fixed at $8.2 \times 10^{12} \text{ ph/cm}^2$, and the result is shown in Fig. S9. In contrast to the excitation with the lowest energy (740 nm), the first three excitations are able to create hot electrons with energy higher than that of QDs CB ($\sim 1.75 \text{ eV}$). The TA decays show similar behaviors independently on the excess energy, suggesting no apparent transfer of hot electrons from perovskite domain to QDs CB within the temporal resolution of our experiments (Table S3). In addition to that, we observed an increase in the TA rising time from 70 to 420 fs when increasing the excess energy of the charge carriers (Fig. S9 inset and Table S4). This effect is due to cooling of hot charge carriers in perovskite, and it is not caused by the presence of QDs, as we explained above [38,40].

3.6. Flash photolysis

To get information on the longer-lived species, we used the nanosecond-millisecond flash photolysis technique. We excited the films at 460 nm and observed the decays at 580 nm. For the MAPbI_3 film, the fit of the decays requires two exponential components showing time constants of $\tau_{p1} = 50 \text{ ns}$ and $\tau_{p2} = 560 \text{ ns}$, which are attributed to the recombination of the trapped charge carriers from the surface and the internal trap states of perovskite crystals, respectively (Fig. S10). These results are in agreements with previous reports [12,40,52,67]. However, accurate multi-exponential fit of the $\text{MAPbI}_3/\text{QDs}$ (6.3 wt%) decay needs four components: two of them are similar to those of neat

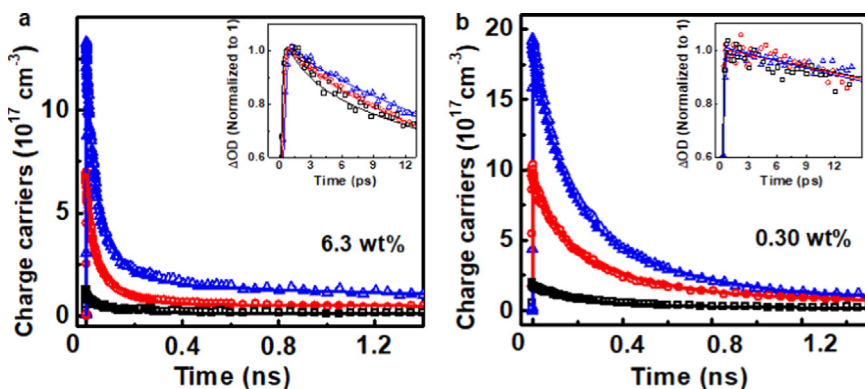


Fig. 4. Decays of transient absorption signal converted to charge carrier concentration of $\text{MAPbI}_3/\text{QDs}$ thin films containing (a) 6.3 wt% and (b) 0.30 wt% of QDs. Data were observed at 760, upon excitation at 600 nm. Used fluences of the absorbed photons were: 1.5×10^{12} (black squares), 8.2×10^{12} (red circles) and 16×10^{12} (blue triangles) ph/cm^2 . The insets are the normalized zooms of (a) and (b) to show the short-time behavior. The solid lines are from the best fit using the kinetic model described in the text.

perovskite ($\tau_{p1} = 50$ ns and $\tau_{p2} = 560$ ns), and two others in the microsecond regime ($\tau_{p3} = 3.8$ μ s and $\tau_{p4} = 45$ μ s). The appearance of these additional components is a result of the interactions between both materials, allowing longer deactivation processes which could be attributed to the transitions involving the electrons states on the interface, holes in QDs and exciplex states [23]. The presence of long lived interface states is also in good agreement with proposed mechanisms of photoexcited electron transfer.

3.7. Time-resolved terahertz spectroscopy

The charge carrier mobility and its time evolution are key parameters shaping the efficiency of optoelectronic devices. Therefore, we used ultrafast time-resolved THz spectroscopy to explore the dynamics of photoconductivity in neat MAPbI₃ and MAPbI₃/QDs (IRF < 1 ps). To begin with, Fig. S11a presents the photoconductivity decays of the MAPbI₃ film upon excitation at 600 nm, using a fluence of the absorbed photons of 8.2×10^{12} ph/cm². The initial mobility has a value of $16.5 \text{ cm}^2 \text{ V}^{-1} \text{ s}^{-1}$, which is in the range of previously reported results for this material (for mobility calculation, see *Supplementary information*, Eq. S7) [68–70]. The THz decays show similar temporal evolution as the TA signal of neat perovskite in the 1.5 ns time window (Fig. S11a). This result indicates that only a change in charge carrier population is responsible for the photoconductivity decrease [34]. Thus, we converted the THz signal to charge carrier concentration, and fitted the decay using the known kinetic model for perovskite (Eq. S3) obtaining, $k_{\text{mono}} = 1.6 \times 10^7 \text{ s}^{-1}$, $k_{\text{bimol}} = 1 \times 10^{-10} \text{ cm}^3 \text{ s}^{-1}$ and $k_{\text{Auger}} = 2.9 \times 10^{-28} \text{ cm}^6 \text{ s}^{-1}$.

Fig. 5a shows the fluence dependence of the photoconductivity decays in the MAPbI₃/QDs film (6.3 wt%) under experimental conditions similar to those used for neat perovskite film. The excitation of neat PbS/CdS QD layer under conditions similar to those used for MAPbI₃/QDs does not lead to a detectable photoconductivity, which indicates that the measured photoresponse of the latter is due to the photoconductivity signal in the perovskite. The values of the initial charge carrier mobilities using different fluences of the absorbed photons ($1.5\text{--}16 \times 10^{12}$ ph/cm²) are similar to that in the neat perovskite and ranges from 15 to $21 \text{ cm}^2 \text{ V}^{-1} \text{ s}^{-1}$. These results reflect the limited influence of QDs on the initial concentration and properties of the electrons and holes, in agreement with the TA data (Fig. 1a, S4d). The only difference between the TA and THz decays of MAPbI₃/QDs (Fig. 5b) is the absence of the 3-ps decaying component in the THz signal (Fig. 5b inset). This absence cannot be caused by the different risetimes of TA and THz signal that are also related to the IRFs of both techniques (TA \sim 70 fs, THz \leq 1 ps), because similar behavior was not observed in the case of neat perovskite film (Fig. S11a inset). While, charge carriers in excitonic form show negligible photoconductivity, also these measurements suggest the presence of fast dissociating excitons in MAPbI₃/QDs film. Comparable difference between decays of TA and THz signals was previously observed in formamidinium lead

triiodide, and also interpreted in terms of excitons presence [48,71]. Moreover, comparable magnitude of the normalized TA and THz residual signals suggests high mobility of charge carriers even at the later stage of the decays and supports the concept of D2 area within MAPbI₃/QDs. We also converted the photoconductivity decay of MAPbI₃/QDs to charge carrier concentration, and analyzed it using our kinetic model (Fig. 5a, S11b, Table S1). The obtained parameters are similar to those using the TA technique, only lacking the ultrafast excitonic component.

The obtained values of charge carrier mobilities in neat perovskite and MAPbI₃/QDs, and related rate constants of charge deactivation processes, using TA results, were used to calculate the diffusion lengths L_D of these carriers (for more information, see *Supplementary information*, Eqs. S8–9). The results are in Table S5, where the L_D increases from 38 to 87 nm, when C_{QDs} in MAPbI₃/QDs decreases from 7.3 to 0.24 wt%. The values of L_D are significantly lower than that of neat perovskite film (318 nm). This result is in full agreement with the presence of additional deactivation sites (QDs) in the hybrid material. The L_D in neat perovskite film is within the range of reported values (105–460 nm) [38,72,73].

Optimization of any kind of optoelectronic device demands the reduction or suppression of non-radiative recombination processes. We have shown that ultrafast characterization of promising perovskite/QD systems for new LEDs fabrication provides key information on the electron and hole dynamics. Further development of perovskite/QD hybrid materials requires reduction of non-radiative recombination at the perovskite grains and the perovskite/QDs interfaces. This optimization will require the control of interfacial defects at the surfaces of both perovskite and QDs. Different methods could be explored to attain this objective, including the passivation of defects using chemical surface engineering, photon curing control and a further development of the methods to embed the QDs within the perovskite material.

4. Conclusions

In summary, we have characterized the ultrafast dynamics of photoexcited charge carrier transfer and recombination processes in a MAPbI₃ thin polycrystalline film containing PbS/CdS (core/shell) QDs using ultrafast time-resolved transient visible-NIR absorption and terahertz spectroscopies. We used a kinetic model to analyze the complex behavior of this promising hybrid material for electro-optical devices. We observed that 85–89% of both electrons and holes were transferred to the perovskite/QDs interface trap states, and to the valence band (VB) of the QDs with effective transfer rate constants of $0.22\text{--}1.2 \times 10^{10} \text{ s}^{-1}$ (83–455 ps) and $0.81\text{--}4.6 \times 10^{10} \text{ s}^{-1}$ (22–123 ps), respectively. Up to 7% charges formed excitons in perovskite domain in the close vicinity of interface showing recombination rate constant of $3.7 \times 10^{11} \text{ s}^{-1}$ (3 ps). A small fraction of photoexcited charges (8–15%) were not affected by the presence of QDs, and thus, their deactivation followed the standard processes of neat perovskite. The changes in the values are related to the QDs concentration of the matrix. We observed

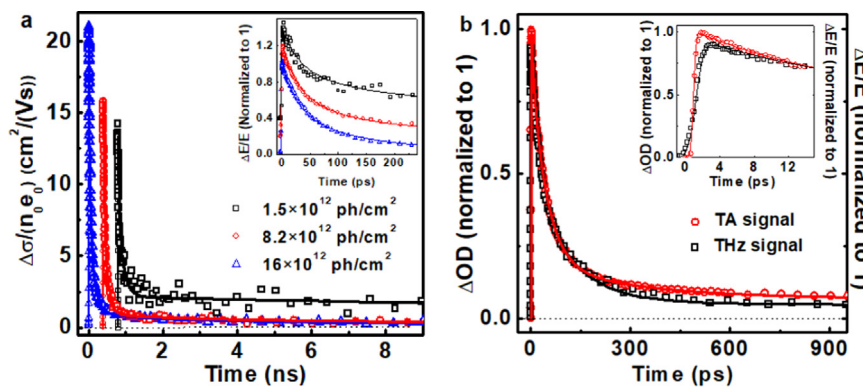


Fig. 5. (a) Photoconductivity decays of MAPbI₃/QDs film (6.3 wt%) excited at 600 nm and using fluences of the absorbed photons: 1.5×10^{12} (black squares), 8.2×10^{12} (red circles) and 16×10^{12} ph/cm² (blue triangles). (b) Normalized photoconductivity and transient absorption decays of MAPbI₃/QDs film (6.3 wt%), excited at 600 nm and using a fluence of the absorbed photons of 8.2×10^{12} ph/cm². The insets are zooms to show the short-time behavior. The TA signal was observed at 760 nm. The solid lines are from the best fits using the kinetic model described in the text.

that lowering the QDs concentration from 7.3 to 0.24 wt% increases the carrier decrease the values of charge carrier effective transfer rate constants to the interface and QDs, and the concentration of excitons. No significant variation in the charge carrier dynamics upon excitation at different energy levels was detected. While the initial (< 1 ps) mobility of charge carriers was not affected by the addition of embedded QDs, the photoconductivity decay was remarkably faster in contrast to the behavior in neat perovskite. The analysis of the data shows the important role of trap states and gives clues for the further improvement of this hybrid system. In addition to that the observation of the preservation of the initial charge carrier mobility like in perovskite film is a very important result highlighting the potentiality of this system in different applications of energy saving. The results here provide clear hints to improve the performance of electronic devices (solar cells, LEDs, photodetectors, etc.) by optimization of QDs concentration and by the passivation of the perovskite/QD interface.

Acknowledgements

This work was supported by Ministry of Economy and Competitiveness in Spain [MAT2014-57646-P, MAT2016-76892-C3-1-R], Junta de Comunidades de Castilla-La Mancha in Spain [PEII-2014-003-P], and European Research Council (ERC) via Consolidator Grant (724424 - No-LIMIT).

Appendix A. Supplementary material

Supplementary data associated with this article can be found in the online version at <http://dx.doi.org/10.1016/j.nanoen.2018.04.069>.

References

- [1] J. Tang, H. Liu, D. Zhitomirsky, S. Hoogland, X. Wang, M. Furukawa, L. Levina, E.H. Sargent, *Nano Lett.* 12 (9) (2012) 4889–4894.
- [2] C.-H.M. Chuang, P.R. Brown, V. Bulovic, M.G. Bawendi, *Nat. Mater.* 13 (8) (2014) 796–801.
- [3] S.V. Kershaw, L. Jing, X. Huang, M. Gao, A.L. Rogach, *Mater. Horiz.* 4 (2) (2017) 155–205.
- [4] S.A. Veldhuis, P.P. Boix, N. Yantara, M. Li, T.C. Sum, N. Mathews, S.G. Mhaisalkar, *Adv. Mater.* 28 (32) (2016) 6804–6834.
- [5] C. Zuo, H.J. Bolink, H. Han, J. Huang, D. Cahen, L. Ding, *Adv. Sci.* 3 (7) (2016) 1500324.
- [6] D. Huber, M. Reindl, Y. Huo, H. Huang, J.S. Wildmann, O.G. Schmidt, A. Rastelli, R. Trotta, *Nat. Commun.* 8 (2017) 15506.
- [7] H. Wang, T. Kubo, J. Nakazaki, T. Kinoshita, H. Segawa, *J. Phys. Chem. Lett.* 4 (15) (2013) 2455–2460.
- [8] F. Fan, O. Voznyy, R.P. Sabatini, K.T. Bicanic, M.M. Adachi, J.R. McBride, K.R. Reid, Y.-S. Park, X. Li, A. Jain, R. Quintero-Bermudez, M. Saravanapavanantham, M. Liu, M. Korkusinski, P. Hawrylak, V.I. Klimov, S.J. Rosenthal, S. Hoogland, E.H. Sargent, *Nature* 544 (7648) (2017) 75–79.
- [9] N.R.E. Laboratory. <https://www.nrel.gov/pv/assets/images/efficiency-chart.png>.
- [10] N. Wang, L. Cheng, R. Ge, S. Zhang, Y. Miao, W. Zou, C. Yi, Y. Sun, Y. Cao, R. Yang, Y. Wei, Q. Guo, Y. Ke, M. Yu, Y. Jin, Y. Liu, Q. Ding, D. Di, L. Yang, G. Xing, H. Tian, C. Jin, F. Gao, R.H. Friend, J. Wang, W. Huang, *Nat. Photon.* 10 (11) (2016) 699–704.
- [11] Z. Xiao, R.A. Kerner, L. Zhao, N.L. Tran, K.M. Lee, T.-W. Koh, G.D. Scholes, B.P. Rand, *Nat. Photon.* 11 (2) (2017) 108–115.
- [12] H. Zhu, Y. Fu, F. Meng, X. Wu, Z. Gong, Q. Ding, M.V. Gustafsson, M.T. Trinh, S. Jin, X.Y. Zhu, *Nat. Mater.* 14 (6) (2015) 636–642.
- [13] S. Shrestha, R. Fischer, G.J. Matt, P. Feldner, T. Michel, A. Osvet, I. Levchuk, B. Merle, S. Golkar, H. Chen, S.F. Tedde, O. Schmidt, R. Hock, M. Rührig, M. Göken, W. Heiss, G. Anton, C. Brabec, J. Nat. Photon. 11 (7) (2017) 436–440.
- [14] L. Zhang, X. Yang, Q. Jiang, P. Wang, Z. Yin, X. Zhang, H. Tan, Y. Yang, M. Wei, B.R. Sutherland, E.H. Sargent, J. You, *Nat. Commun.* 8 (2017) 15640.
- [15] R. Su, C. Diederichs, J. Wang, T.C.H. Liew, J. Zhao, S. Liu, W. Xu, Z. Chen, Q. Xiong, *Nano Lett.* 17 (6) (2017) 3982–3988.
- [16] P. Liu, X. He, J. Ren, Q. Liao, J. Yao, H. Fu, *ACS Nano* 11 (6) (2017) 5766–5773.
- [17] P. Odenthal, W. Talmadge, N. Gundlach, R. Wang, C. Zhang, D. Sun, Z.-G. Yu, Z. Valy Vardeny, Y.S. Li, *Nat. Phys.* 13 (9) (2017) 894–899.
- [18] Z.J. Ning, X.W. Gong, R. Comin, G. Walters, F.J. Fan, O. Voznyy, E. Yassitepe, A. Buin, S. Hoogland, E.H. Sargent, *Nature* 523 (7560) (2015) 324–328.
- [19] S.-S. Li, C.-H. Chang, Y.-C. Wang, C.-W. Lin, D.-Y. Wang, J.-C. Lin, C.-C. Chen, H.-S. Sheu, H.-C. Chia, W.-R. Wu, U.S. Jeng, C.-T. Liang, R. Sankar, F.-C. Chou, C.-W. Chen, *Energy Environ. Sci.* 9 (4) (2016) 1282–1289.
- [20] G. Seo, J. Seo, S. Ryu, W. Yin, T.K. Ahn, S.I. Seok, *J. Phys. Chem. Lett.* 5 (11) (2014) 2015–2020.
- [21] Z.Y. Yang, A. Janmohamed, X.Z. Lan, F.P.G. de Arquer, O. Voznyy, E. Yassitepe, G.H. Kim, Z.J. Ning, X.W. Gong, R. Comin, E.H. Sargent, *Nano Lett.* 15 (11) (2015) 7539–7543.
- [22] X. Lan, O. Voznyy, F.P. García de Arquer, M. Liu, J. Xu, A.H. Proppe, G. Walters, F. Fan, H. Tan, M. Liu, Z. Yang, S. Hoogland, E.H. Sargent, *Nano Lett.* 16 (7) (2016) 4630–4634.
- [23] R.S. Sanchez, M.S. de la Fuente, I. Suarez, G. Munoz-Matutano, J.P. Martinez-Pastor, I. Mora-Sero, *Sci. Adv.* 2 (1) (2016) 1501104.
- [24] T.T. Ngo, I. Suarez, R.S. Sanchez, J.P. Martinez-Pastor, I. Mora-Sero, *Nanoscale* 8 (30) (2016) 14379–14383.
- [25] X. Gong, Z. Yang, G. Walters, R. Comin, Z. Ning, E. Beauregard, V. Adinolfi, O. Voznyy, E.H. Sargent, *Nat. Photon.* 10 (4) (2016) 253–257.
- [26] F.P. García de Arquer, X. Gong, R.P. Sabatini, M. Liu, G.-H. Kim, B.R. Sutherland, O. Voznyy, J. Xu, Y. Pang, S. Hoogland, D. Sinton, E. Sargent, *Nat. Comm.* 8 (2017) 14757.
- [27] Y. Yang, W.Y. Wang, *J. Power Sources* 293 (2015) 577–584.
- [28] C.R. Kagan, C.B. Murray, *Nat. Nanotechnol.* 10 (12) (2015) 1013–1026.
- [29] M.V. Kovalenko, M. Scheele, D.V. Talapin, *Science* 324 (5933) (2009) 1417–1420.
- [30] M.S. Kang, A. Sahu, D.J. Norris, C.D. Frisbie, *Nano Lett.* 10 (9) (2010) 3727–3732.
- [31] D. Yu, B.L. Wehrenberg, P. Jha, J. Ma, P. Guyot-Sionnest, *J. Appl. Phys.* 99 (2006) 10.
- [32] R.S. Sanchez, E. Binetti, J.A. Torre, G. Garcia-Belmonte, M. Striccoli, I. Mora-Sero, *Nanoscale* 6 (15) (2014) 8551–8555.
- [33] M. Ziolek, I. Tacchini, M.T. Martinez, X. Yang, L. Sun, A. Douhal, *Phys. Chem. Chem. Phys.* 13 (9) (2011) 4032–4044.
- [34] P. Piatkowski, B. Cohen, C.S. Ponseca Jr., M. Salado, S. Kazim, S. Ahmad, V. Sundstrom, A. Douhal, *J. Phys. Chem. Lett.* 7 (1) (2016) 204–210.
- [35] M. Ziolek, C. Martín, L. Sun, A. Douhal, *J. Phys. Chem. C* 116 (50) (2012) 26227–26238.
- [36] T. Baikie, Y. Fang, J.M. Kadro, M. Schreyer, F. Wei, S.G. Mhaisalkar, M. Graetzel, T.J. White, *J. Mater. Chem. A* 1 (18) (2013) 5628–5641.
- [37] H.-S. Kim, C.-R. Lee, J.-H. Im, K.-B. Lee, T. Moehl, A. Marchioro, S.-J. Moon, R. Humphry-Baker, J.-H. Yum, J.E. Moser, M. Graetzel, N.-G. Park, *Sci. Rep.* (2012) 2.
- [38] G. Xing, N. Mathews, S. Sun, S.S. Lim, Y.M. Lam, M. Graetzel, S. Mhaisalkar, T.C. Sum, *Science* 342 (6156) (2013) 344–347.
- [39] H.-Y. Hsu, C.-Y. Wang, A. Fathi, J.-W. Shiu, C.-C. Chung, P.-S. Shen, T.-F. Guo, P. Chen, Y.-P. Lee, E.W.-G. Diau, *Angew. Chem. Int. Ed.* 53 (35) (2014) 9339–9342.
- [40] P. Piatkowski, B. Cohen, F.J. Ramos, M. Di Nunzio, M.K. Nazeeruddin, M. Graetzel, S. Ahmad, A. Douhal, *Phys. Chem. Chem. Phys.* 17 (22) (2015) 14674–14684.
- [41] T.C. Sum, N. Mathews, G.C. Xing, S.S. Lim, W.K. Chong, D. Giovanni, H.A. Dewi, *Acc. Chem. Res.* 49 (2) (2016) 294–302.
- [42] J.S. Manser, P.V. Kamat, *Nat. Photon.* 8 (9) (2014) 737–743.
- [43] O. Flender, J.R. Klein, T. Lenzer, K. Oum, *Phys. Chem. Chem. Phys.* 17 (29) (2015) 19238–19246.
- [44] L.L. Hu, Z.Y. Yang, A. Mandelis, A. Melnikov, X.Z. Lan, G. Walters, S. Hoogland, E.H. Sargent, *J. Phys. Chem. C* 120 (26) (2016) 14416–14427.
- [45] D.W. de Quilettes, S.M. Vorpahl, S.D. Stranks, H. Nagaoka, G.E. Eperon, M.E. Ziffer, H.J. Snaith, D.S. Ginger, *Science* 348 (6235) (2015) 683–686.
- [46] B. Kang, K. Biswas, *Phys. Chem. Chem. Phys.* 19 (40) (2017) 27184–27190.
- [47] J.A. Christians, P.A. Miranda Herrera, P.V. Kamat, *J. Am. Chem. Soc.* 137 (4) (2015) 1530–1538.
- [48] P. Piatkowski, B. Cohen, S. Kazim, S. Ahmad, A. Douhal, *Phys. Chem. Chem. Phys.* 18 (39) (2016) 27090–27101.
- [49] Z. Guo, J.S. Manser, Y. Wan, P.V. Kamat, L. Huang, *Nat. Commun.* (2015) 6.
- [50] J.A. Christians, J.S. Manser, P.V. Kamat, *J. Phys. Chem. Lett.* 6 (11) (2015) 2086–2095.
- [51] M.B. Johnston, L.M. Herz, *Acc. Chem. Res.* 49 (1) (2016) 146–154.
- [52] L.M. Herz, *Annu. Rev. Phys. Chem.* 67 (1) (2016) 65–89.
- [53] J. Huang, Y. Yuan, Y. Shao, Y. Yan, *Nat. Rev. Mater.* 2 (2017) 17042.
- [54] Y. Yang, D.P. Ostrowski, R.M. France, K. Zhu, J. van de Lagemaat, J.M. Luther, M.C. Beard, *Nat. Photon.* 10 (1) (2016) 53–59.
- [55] M.B. Price, J. Butkus, T.C. Jellicoe, A. Sadhanala, A. Briane, J.E. Halpert, K. Broch, J.M. Hodgkiss, R.H. Friend, F. Deschler, *Nat. Commun.* 6 (2015) 8420.
- [56] I. Moreels, K. Lambert, D. Smeets, D. De Muynck, T. Nollet, J.C. Martins, F. Vanhaecke, A. Vantomme, C. Delerue, G. Allan, Z. Hens, *ACS Nano* 3 (10) (2009) 3023–3030.
- [57] A.O. El-Ballouli, E. Alarousu, M. Bernardi, S.M. Aly, A.P. Lagrow, O.M. Bakr, O.F. Mohammed, *J. Am. Chem. Soc.* 136 (19) (2014) 6952–6959.
- [58] A.O. El-Ballouli, E. Alarousu, A.R. Kirmani, A. Amassian, O.M. Bakr, O.F. Mohammed, *Adv. Funct. Mater.* 25 (48) (2015) 7435–7441.
- [59] V. Sarritzu, N. Sestu, D. Marongiu, X. Chang, Q. Wang, M.A. Loi, F. Quochi, M. Saba, A. Mura, G. Bongiovanni, *Adv. Opt. Mater.* (2017) 1700839.
- [60] H. Cho, S.-H. Jeong, M.-H. Park, Y.-H. Kim, C. Wolf, C.-L. Lee, J.H. Heo, A. Sadhanala, N. Myoung, S. Yoo, S.H. Im, R.H. Friend, T.-W. Lee, *Science* 350 (6265) (2015) 1222–1225.
- [61] D.A. Wheeler, B.C. Fitzmorris, H. Zhao, D. Ma, J. Zhang, *Sci. China Chem.* 54 (12) (2011) 2009–2015.
- [62] S.D. Stranks, V.M. Burlakov, T. Leijtens, J.M. Ball, A. Goriely, H.J. Snaith, *Phys. Rev. Appl.* 2 (3) (2014).
- [63] E.M. Hutter, J.-J. Hofman, M.L. Petrus, M. Moes, R.D. Abellón, P. Docampo, T.J. Savenije, *Adv. Energy Mater.* 7 (13) (2017) 1602349 (n/a).
- [64] E.M. Hutter, G.E. Eperon, S.D. Stranks, T.J. Savenije, *J. Phys. Chem. Lett.* 6 (15) (2015) 3082–3090.
- [65] A. Einstein, *Ann. Phys.* 322 (8) (1905) 549–560.

- [66] E. Lipparini, Modern Many-particle Physics: Atomic Gases, Quantum Dots and Quantum Fluids, World Scientific Publishing Co, Singapore, 2003.
- [67] Y. Yamada, T. Nakamura, M. Endo, A. Wakamiya, Y. Kanemitsu, J. Am. Chem. Soc. 136 (33) (2014) 11610–11613.
- [68] C.S. Poncea Jr., E.M. Hutter, P. Piatkowski, B. Cohen, T. Pascher, A. Douhal, A. Yartsev, V. Sundstrom, T.J. Savenije, J. Am. Chem. Soc. 137 (51) (2015) 16043–16048.
- [69] C.S. Poncea Jr., T.J. Savenije, M. Abdellah, K. Zheng, A. Yartsev, T. Pascher, T. Harlang, P. Chabera, T. Pullerits, A. Stepanov, J.-P. Wolf, V. Sundstrom, J. Am. Chem. Soc. 136 (14) (2014) 5189–5192.
- [70] C. Wehrenfennig, G.E. Eperon, M.B. Johnston, H.J. Snaith, L.M. Herz, Adv. Mater. 26 (10) (2014) 1584–1589.
- [71] H. Wang, L. Whittaker-Brooks, G.R. Fleming, J. Phys. Chem. C 119 (34) (2015) 19590–19595.
- [72] Y. Li, W. Yan, Y. Li, S. Wang, W. Wang, Z. Bian, L. Xiao, Q. Gong, Sci. Rep. 5 (2015) 14485.
- [73] S.D. Stranks, G.E. Eperon, G. Grancini, C. Menelaou, M.J.P. Alcocer, T. Leijtens, L.M. Herz, A. Petrozza, H.J. Snaith, Science 342 (6156) (2013) 341–344.



Dr. Pavel Galář received his Master (2009) and Ph.D. (2016) in Physics (Optics and Optoelectronic) from Charles University in Prague (CUNI, Czech Republic). During his studies (2014–2016) he worked also as assistant at University of Chemistry and Technology in Prague (UCT). His scientific carrier continued by post-doctoral fellowship (2016–2018) in the group of prof. A. Douhal at University of Castilla-La Mancha (UCLM, Spain). Currently is Dr. Galář working as assistant professor at both UCT and Czech Academy of Sciences (CAS). He is specialized in characterization of ultrafast and fast charge carrier processes in nanostructures using time-resolved laser spectroscopies.



Piotr Piatkowski received his Ph.D. degree in Chemistry from University of Warsaw in 2010. From 2013–2016 he was a postdoctoral researcher at the Departamento de Química Física, Universidad de Castilla-La Mancha (UCLM), Toledo, Spain. In 2017 he was hired as an assistant professor in Faculty of Chemistry, University of Warsaw, Poland. His main research interest lie in the area of the ultrafast processes photoinduced in 1-, 2- and 3-dimensional semiconductor materials. In his work he uses mainly ultrafast time-resolved optical spectroscopies.



Thi Tuyen Ngo graduated in Physics from Vietnam National University in 2008. Next year she worked at Institute of Physics, Vietnam Academy Science and Technology as an assistant researcher. Then she got fellowships from University of the Basque Country and Donostia International Physics Center, Spain, where she did her master in Nanoscience 2009–2011. Later on (2011–2013) she worked in the photovoltaic cells at Cidetec-IK4 Research Alliance, Spain, where she learnt about the preparation and characterization of solar cells. She is now a Ph.D. student at the Institute of Advanced Materials (INAM), focusing on perovskite and quantum dots applied for photovoltaics.



0000-0001-9222-3647.

Dr. Mario Gutiérrez received his Bachelor degree in Chemistry (2012) from the University of Castilla-La Mancha (UCLM). He obtained his Master (2014) and Ph.D. (2017) diplomas in Nanoscience and Nanotechnology (Physical Chemistry) from UCLM under the supervision of Prof. Abderrazzak Douhal. Since 2017, he is developing a post-doctoral research work in the same group. His research interests are focused on the application of different time-resolved spectroscopic techniques to unravel ultrafast processes happening in photoexcited proton/charge transfer dyes, and especially in Metal-Organic Framework (MOF) materials, having the latter applications in photocatalysis, fluorescent sensors and light emitting diodes. ORCID:



Highly Cited Researchers of the Web of Science.



COFs, HOFs, and perovskites). Research ID: L-4940-2014; ORCID: 0000-0003-2247-7566.



Cite this: *J. Mater. Chem. C*, 2020, 8, 14834

Deciphering the role of quantum dot size in the ultrafast charge carrier dynamics at the perovskite–quantum dot interface†

Piotr Piatkowski, ^{a,b} Sofia Masi, ^c Pavel Galar, ^{ad} Mario Gutiérrez, ‡^a Thi Tuyen Ngo, ^c Iván Mora-Seró *^c and Abderrazzak Douhal *^a

Deciphering the electron and hole (e, h) dynamics at the interfaces of photoexcited hybrid materials at different densities of photoexcited charge carriers is paramount to the development of efficient optoelectronic devices. Nanocomposites formed by methylammonium lead iodide perovskite (PS) and semiconductor colloidal quantum dots (QDs) are among these hybrid materials under intensive studies. However, the reciprocal influence of the components in the composite on the charge carriers' dynamics is still poorly explored. Armed with femtosecond time-resolved techniques, we unravel the effect of PbS QD size, embedded in the PS matrix, on the e and h diffusion, transfer to the QD phase and recombination. While the decays are dominated by e and h transition from PS to QDs, the increase in the QD size results in an acceleration of the charge carriers' transitions represented by the total transfer rate constants of electrons and holes. We extract the diffusion times and transfer rate constants to the interfaces. Furthermore, pumping with different fs-laser fluences indicates the photoformation of excitonic states, in which acceleration decreases the contribution of undesirable charge carrier trapping and non-radiative recombination within PS. Our results elucidate the importance of the QD size for improving the efficiency of LEDs based on these nanocomposites.

Received 11th August 2020,
Accepted 18th September 2020

DOI: 10.1039/d0tc03835k

rsc.li/materials-c

1. Introduction

Combining smart materials of different natures, like halide perovskites (PS) and semiconductor colloidal quantum dots (QDs), could provide potential synergistic interactions allowing overcoming limitations of each component, and thus, enhancing the performance of the related devices.^{1,2} PS/QD hybrids constitute one interesting example with important optoelectronic applications

that have been successfully used in the fabrication of infrared (IR) LEDs,^{3–6} solar cells^{7–11} and photodetectors.^{12,13} Halide perovskites can passivate the surface of QDs enhancing the performance of colloidal QD solar cells,^{14,15} while PbS QDs can act as seeds in the growth of PS enhancing the properties of the perovskite layer.^{9,16–19}

Potential applications for the development of advanced optoelectronic device configurations of this kind of hybrid material have been demonstrated using the methylammonium lead triiodide (MAPbI₃) perovskite matrix containing PbS/CdS core/shell QDs.⁴ However, due to the complex nature and structure of these hybrid interfaces, the improvement of their electro-optical devices needs a deeper understanding of the involved charge carrier dynamics at their interfaces, which shapes and quantifies their performance. To this end, ultrafast spectroscopic techniques are powerful tools to unveil the interaction between different materials. Recently, we have used UV-VIS transient absorption (TA) and terahertz (THz) spectroscopy to characterize the interaction of MAPbI₃ with embedded PbS/CdS colloidal QDs considering different densities of QDs.¹⁹ This work showed the important role of the QD electronic states, especially trap states, in the deactivation dynamics of the photoexcited charge carriers in the perovskite matrix.

^a Departamento de Química Física, Facultad de Ciencias Ambientales y Bioquímica, INAMOL, Universidad de Castilla-La Mancha, Avenida Carlos III, 45071 Toledo, Spain. E-mail: abderrazzak.douhal@uclm.es

^b Faculty of Chemistry, University of Warsaw, Zwirki i Wigury 101, Warsaw 02-089, Poland

^c Institute of Advanced Materials (INAM), Universitat Jaume I, Av. de Vicent Sos Baynat, S/N, 12006, Castelló de la Plana, Spain. E-mail: sero@uji.es

^d Institute of Physics CAS, v.v.i., Cukrovarnická 10/112, 162 00 Prague 6, Czech Republic

† Electronic supplementary information (ESI) available: Details of sample preparation; description of utilized experimental techniques; calculation of the average distance between PbS QDs in the perovskite matrix; values of monomolecular recombination rate constants; TEM, X-ray, steady state fluorescence and absorption data for the studied samples; and TA spectra and decays of the samples. See DOI: 10.1039/d0tc03835k

‡ Multifunctional Materials & Composites (MMC) Laboratory, Department of Engineering Science, University of Oxford, Parks Road, Oxford OX1, UK.

However, important aspects of the QD versatility such as the effect in the material composite of the QD size remain unexplored. One of the interesting properties of the colloidal QDs is the easy tuning of the bandgap by the control of the QD size.^{20,21} It was reported that the change in the size of PbS QDs in the PS/QD nanocomposite from 2.3 to 3.0 nm results in a strong shift of the electroluminescence band, which demonstrates the tunability of the optical properties in such systems.⁴ Fine tuning of the band gap in QDs is important to achieve efficient transfer of both electrons and holes from PS to QDs followed by light emission in IR-LEDs. Recently, efficient charge transfer from MAPbI_3 to PbS was directly proven using emission spectroscopy.²² Furthermore, the research of PbS QDs embedded in inorganic perovskites (CsPbBr_3 and $\text{MAPbBr}_{x}\text{I}_{3-x}$) also indicates charge transfer between both components of the related composites.^{23,24} The combination of the properties of both materials makes PS/PbS QD systems ideal candidates for their deployment in the fabrication of a new generation of tunable IR-LEDs. The QD bandgap is therefore a key parameter in order to understand the interaction between different materials, as it affects the alignment of the energy bands, and consequently the charge transfer properties. Moreover, the decryption of the influence of the interface between PS and PbS that is a source of electron, hole and excitonic trap states on the overall properties of the nanocomposite allows detailed studies of the composite materials using different densities of the photoexcited charge carriers.¹⁶ However, to date, there has been no systematic study on the interaction of PS with QDs of different sizes.

Herein, we elucidate the influence of the PbS QD size (2.9, 3.2, 4.5 and 5.3 nm), when the QDs are embedded in a PS matrix, and probe the ultrafast dynamics of photoinduced electrons and holes, when migrating and transferring to the interface between both materials. We used fs-time-resolved VIS-NIR transient absorption (TA), terahertz (THz) and nanosecond flash photolysis spectroscopies. The present PbS QDs are different from the ones using core/shell PbS/CdS nanocrystals in our previous work.¹⁶ We have found that the photogenerated electrons and holes in PS are rapidly transferred to PbS QDs independently of the size of nanostructures. Remarkably, the dynamics of these processes are strongly dependent on QD size. Using a kinetic model, we extract the total rate constants of electrons ($k_e(\text{total})$) and holes ($k_h(\text{total})$). We unravel that both $k_h(\text{total})$ and $k_e(\text{total})$ increase from 0.1 to $4.5 \times (10^9 \text{ s}^{-1})$ and from 0.1 to $2.2 \times (10^{10} \text{ s}^{-1})$, respectively, upon increasing the size of QDs. This reflects a more efficient charge carrier transfer from PS to nanostructures. The results indicate that an electron is transferred from PS to PbS QDs faster than the hole, in contrast to a previous report on core/shell PbS/CdS nanocrystals embedded in PS.¹⁶ Based on the total rate constants along with the THz results, we extracted the values of electron and hole diffusion times ($\tau_{\text{ediff}} = 45 \text{ ps}$ and $\tau_{\text{hdiff}} = 90 \text{ ps}$) and transfer rate constants ($k_{et} = 0.1$ to $1.6 \times (10^{10} \text{ s}^{-1})$ and $k_{ht} = 0.1$ to $0.8 \times (10^{10} \text{ s}^{-1})$) within the systems containing different sizes of QDs. The acceleration of charge carrier transfer from PS to QDs upon increasing the QD size decreases the probability of

non-radiative deactivation within PS and thus it could be further exploited for efficient LED devices based on PS/QDs. The spectral analysis of the TA signal at different pump fluences shows the presence of excitons in all studied samples as well as the photoformation of new excitonic states upon increasing the fluence of the absorbed photons in PS and PS/QD samples. Furthermore, the larger contribution of excitonic states in PS/QD films as related to neat PS is of relevance to the development of photovoltaic devices.

2. Experimental

The PbS QDs of different sizes were synthesized and dispersed in an octane solution following the method described in detail in the ESI[†].^{3,4,22} The QDs and QDs embedded in perovskite were characterized by Transmission Electron Microscopy (TEM) and photoluminescence (PL) spectroscopy. The latter was carried out before and after the ligand exchange with the halide perovskite (PS) precursors, MAI and PbI_2 , see Fig. S1 and S2 (ESI[†]).²⁵ As a result of the efficient formation of the perovskite precursor shell (MAI and PbI_2) on the surface of QDs, a red-shifted emission is observed. In order to produce layers with embedded PbS QDs, ligand exchange is necessary to make PbS QDs soluble in DMF solution with the PS precursors used for the preparation of thin films. Fig. S3 (ESI[†]) shows that ligand exchange, where oleic acid capping is substituted by a MAPbI_3 shell, is successfully carried out as the signature of oleic acid disappears from the FTIR spectra.²⁶ The thin films with embedded PbS QDs present a MAPbI_3 tetragonal structure, see Fig. S4 (ESI[†]),²⁷ thus indicating that PS is formed independently of the presence of PbS QDs that in fact have a seeding effect as previously reported.^{3,7,18,19} See the Experimental section in the ESI[†] for more details.

Thin films of MAPbI_3 with embedded PbS QDs have been analyzed with time-integrated absorption, fs-time-resolved Vis-NIR transient absorption, terahertz and nanosecond flash photolysis techniques (described in detail in the Experimental section in the ESI[†]). In order to evaluate the effect of the QD size, four different sizes 2.9, 3.2, 4.5 and 5.3 nm were used at similar concentrations of nanoparticles per cubic centimeter of the PS host matrix.

3. Results and discussion

3.1 Femtosecond transient absorption studies

We first present and discuss the results of TA studies of neat PS and PS films containing PbS QDs. The samples were fs-pumped at 600 nm using a fluence of the absorbed photons of 8.2×10^{12} ph per cm^2 and probed from 640 to 780 nm. Fig. S5 (ESI[†]) shows representative TA spectra of neat PS and PS/QD films gated at 1 ps pump–probe delay time. The MAPbI_3 TA spectrum is composed of a positive signal ranging from 640 to 720 nm, reflecting the absorption of photoexcited electrons and holes (PA), and a photobleaching band (PB) with minimum intensity at 760 nm.^{28,29} Interestingly, the presence of PbS nanocrystals

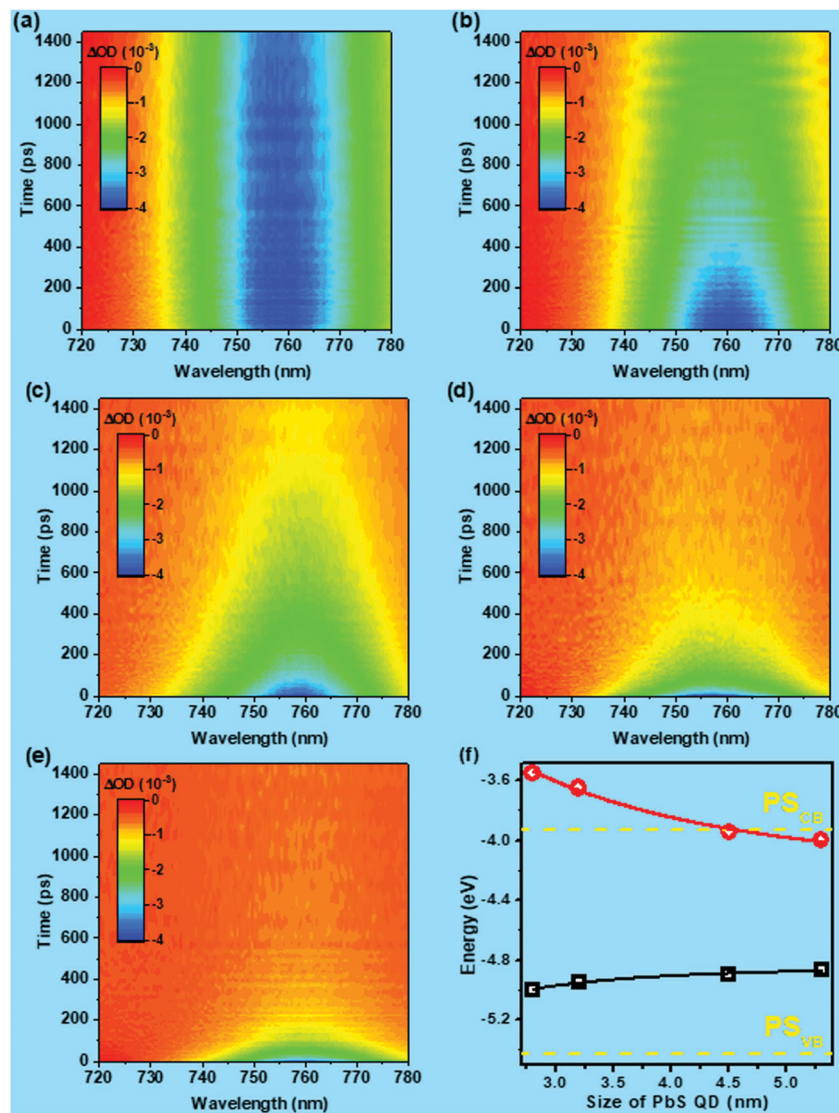


Fig. 1 Two-dimensional pseudo-colour map of (a) PS, (b) PS/QDs 2.9 nm, (c) PS/QDs 3.2 nm, (d) PS/QDs 4.5 nm and (e) PS/QDs 5.3 nm gated at 760 nm in PS and PS/QD samples having QDs of different sizes. (f) Positions of VB (□) and CB (○) for PbS QDs of different sizes. Representative fs-TA decays corresponding to panels (a)–(e) are in the ESI.[†]

does not affect the shape and the position of both TA bands of PS/QD films suggesting that the photoresponse of the system, during the initial charge generation and cooling time period, originates only from the PS host matrix. PbS and MAPbI₃ possess the same six-coordinated Pb atom and they have similar Pb-Pb distances (6.26 and 5.95 Å in the case of MAPbI₃ and PbS, respectively), which gives good structural conditions for minimizing the QD/host matrix interfacial strain, and explains the results presented in Fig. 1.^{3,7,22} In addition to a similar shape, a further monitoring of the TA signals in PS and PS/QD samples shows significant differences, which are discussed below in the analysis of their TA decays at specific wavelength.

Fig. 1a–e show the temporal evolution of the TA spectra upon excitation at 600 nm, while Fig. S6 (ESI[†]) presents single TA decays observed at 760 nm (maximum of PB band). Clearly,

the presence of QDs embedded in the PS film results in faster deactivation of the photoexcited charge carriers in the PS host due to the diffusion and subsequent transfer of electrons and holes from PS to QDs.¹⁶ In addition to that, the decay time becomes shorter upon increasing the size of the PbS nanostuctures. Previous TA experiments on PS/QDs, with a PbS/CdS QD size of 3 nm, clearly showed that the TA of the nanocomposite film is related only to the electrons and holes present within the PS host,¹⁶ and this response was influenced by the concentration of QDs. The comparison of time-integrated absorption spectra of different samples also shows that the photoresponse of the system is mostly due to the presence of PS (Fig. S7 (ESI[†])). Furthermore, the photoexcitation of a thin PbS QD compact layer under the same conditions results in an extremely weak signal in the 400–760 nm region (Fig. S8 (ESI[†])). The signal of a PbS compact layer also appears in the range of

850–1000 nm, and the measurements at longer wavelengths are not possible due to a limitation of our experimental setup. Taking into account the much lower concentration of QDs in the PS/QD film than in a neat compact PbS layer and the strong reabsorption of the emission signal located in the NIR region by free charges located in the PS matrix, it is not surprising that we are not able to directly detect the TA signal of PbS. In the present work, the preparation conditions of the materials were set to obtain similar concentrations of the PbS QDs of different sizes in the different PS/QD films (see the experimental part and Table S1 in the ESI†), and thus, we target the effect of the QD size in the photogenerated dynamics of the hybrid material.

Increasing the QD size can result in higher interfacial defects which act as trap carrier centers.²⁵ In addition to that, there is also a shape evolution from the octahedron for small size QDs (1–3 nm) having surfaces of (111) to the cuboctahedron shape for QDs with size larger than ~4 nm of surfaces with both (111) and (100) orientations.³¹ Hence, increasing the size of embedded PbS QDs might induce a higher concentration of interfacial trap states at PS/QD interfaces. On the other hand, as shown in Fig. 1f, increasing the QD size leads to a change of valence (VB) and conduction (CB) bands of PbS QDs, due to a reduction of quantum confinement. Thus, the occurrence of charge carrier's migration from PS results in faster TA signal decays. For all the used nanocomposite systems, the VB in PS is located below in the one of the QDs (Fig. 1f). Thus, the holes from the PS VB are most probably transferred to the VB in the nanostructure (Scheme 1).^{4,32–34} In the case of photogenerated electrons, the nature of processes of the electron transition differs in function of the QD size. For the systems which contain QDs of 2.9 and 3.2 nm, the CB of PS is located lower than that in the PbS nanostructure, and thus the photoexcited electrons in the PS cannot move into the CB of the QDs (Scheme 1a). However, our previous report suggests that in such a situation, the electrons are efficiently transferred to interfacial electronic states formed between PS and PbS QDs.¹⁶ In the case of nanocomposites which contain bigger QDs (4.5 nm, 5.3 nm), the CB of PS is located slightly below that of PbS, allowing electron transition into the CB of QDs (Scheme 1b).

From Fig. 1 and Fig. S6 (ESI†), it is evident that the TA signals of different nanocomposites (QDs of 3.2–5.3 nm

diameter) decay to small values in 1.5 ns. While the effective masses of electrons and holes in PS are comparable, the photoresponse in the TA experiment should be caused by both charge carriers within the 1.5 ns time window.^{30,35,36} Hence, the observed dynamics suggests that both electrons and holes are transferred from the PS host independently of the size of the QDs. Considering the TA decay of neat PS depicted in Fig. S6 (ESI†), where small changes are observed within the 1.5 ns time range, the contribution of charge carrier recombination within the PS host matrix on observed dynamics in PS/QD should be marginal.

3.2 Kinetic model of PS/QD

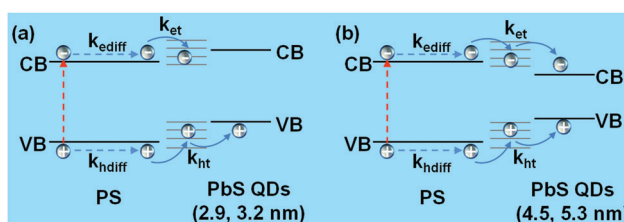
To quantify the dynamics related to the photoevents observed in the nanocomposites, we have used the model described in our previous work,¹⁶ where the TA dynamics are dominated by free charge carriers that are formed directly after photoexcitation of PS.^{37–39} The differential equations were solved by using the 4th order Runge–Kutta (RK) method. The numerical results of RK solutions were fitted to the experimental data by the Levenberg–Marquardt algorithm. Accordingly, the interrogated sample can be effectively separated into two regions where photoexcited charges (i) are affected by the presence of QDs (region A₁) and (ii) behave like in neat PS (region A₂). We assume that the recombination processes within the PS host are characterized by rate constants similar to those for neat MAPbI₃. Hence, we have used eqn (1) to calculate the second (k_{bimol}) and third (k_{Auger}) order rate constants in neat PS and the resulting values were used in the model describing nanocomposite materials:^{28,40,41}

$$\frac{dn}{dt} = -k_{\text{mono}}n - k_{\text{bimol}}n^2 - k_{\text{Auger}}n^3 \quad (1)$$

where n is the excited charge carrier's concentration. The first order rate constants (k_{mono}) of neat PS and PS/QD samples were extracted from multiexponential fits of the flash photolysis results (Fig. S9 and Table S2 (ESI†)). The fit of the experimental data of PS gives the following values: $k_{\text{mono}} = 1.6 \times 10^7 \text{ s}^{-1}$, $k_{\text{bimol}} = 1.28 \times 10^{-11} \text{ cm}^3 \text{ s}^{-1}$ and $k_{\text{Auger}} = 2.75 \times 10^{-29} \text{ cm}^6 \text{ s}^{-1}$. The obtained rate constants are in good agreement with previous reports.^{1,28,38,42}

Obviously, in the presence of QDs new processes appear and the photoexcited charge carriers are deactivated much faster.¹⁶ As we mentioned, the acceleration of the decay is due to efficient and fast electron and hole transfer from PS to QDs. Furthermore, the presence of QDs favors the formation of interfacial excitonic levels, and thus the contribution of excitons to the decay of the TA signal is considered. The equations of the kinetic model for recombination processes in the PS/QD system are given below:¹⁶

$$\frac{dn_e}{dt} = G_e - n_e k_{\text{mono}} - n_e n_h k_{\text{bimol}} - n_e^2 n_h k_{\text{Auger}} - n_e k_e (\text{total}), \quad (2a)$$



Scheme 1 Scenarios of photoinduced hole and electron diffusion and transfer to QDs of different sizes. (a) The electron transfer to the CB in QDs of 2.9 and 3.2 nm is precluded. (b) The electron transfer to the CB of QDs of 4.5 and 5.3 nm is allowed. In both scenarios the hole can be transferred from the PS VB to the QD one.

$$\frac{dn_h}{dt} = G_e - n_h k_{\text{mono}} - n_e n_h k_{\text{bimol}} - n_h^2 n_e k_{\text{Auger}} - n_h k_h(\text{total}), \quad (2b)$$

$$\frac{dn_{\text{ex}}}{dt} = G_x - n_{\text{ex}} k_{\text{ex}}, \quad (2c)$$

$$\frac{dn_{\text{interface}}}{dt} = n_e k_e - n_{\text{interface}} n_{\text{QD}} k_{\text{QDIn}}, \quad (2d)$$

$$\frac{dn_{\text{QD}}}{dt} = n_h k_h - n_{\text{interface}} n_{\text{QD}} k_{\text{QDIn}}, \quad (2e)$$

where n_e , n_h and n_x are the concentrations of electrons and holes in the CB and VB of PS, and excitons close to the PS/QD interface. G_e , G_h and G_{ex} describe the generation factors of these populations. The electron and hole transfer processes from PS to PbS QDs are described by the first order total rate constants $k_e(\text{total})$ and $k_h(\text{total})$, respectively.^{16,43} These rate constants are related to transfers to the CB/interface and to the VB, respectively. In the case PS/QD (2.9 and 3.2 nm), for energetic conditions, the migration of electrons from PS's CB to that of QDs is impossible, and the electrons are trapped at the interface between the two materials (Scheme 1a).¹⁶ However, if the transition of charge carriers between VBs and CBs of the two components in PS/QD systems is favored, the occurrence of simultaneous processes of electron and hole trapping cannot be excluded. The migration of charge carriers to internal electronic states of QDs dominates the TA signal. Furthermore, due to the confined nature of excitons they do not effectively migrate to QDs but recombine within PS which is described by k_{ex} . Finally, in eqn (2d) and (2e), $n_{\text{interface}}$ refers to the concentration of electrons transferred to the interface or to the CB of QDs, while n_{QDIn} reflects the hole transition to the VB of PbS. The recombination rate constant of these carriers is given by k_{QDIn} . Because the TA decays were gated at 760 nm (the signal originates only from processes occurring in PS), the last two equations (eqn (2d) and (2e)) are not considered in the calculations.

The recorded TA signals are given by the sum of the recombination processes in regions A_1 and A_2 :

$$\Delta \text{OD} = P_1(n_e(t) + n_h(t) + n_{\text{ex}}(t)) + P_2(n(t)), \quad (3)$$

where P_1 and P_2 are fractions of populations within areas affected (A_1) and non-affected (A_2) by the presence of QDs and $n(t)$ is the charge carriers' concentrations in the area not affected by QDs.

3.3 Results of the fits to TA decays

Table 1 gives the extracted values of the rate constants for electrons, holes and excitons as well as their relative amplitudes in the TA signals of the studied composite materials having QDs of different sizes. Firstly, the contribution of exciton population (n_{ex}) to the total signal is negligible in all the decays. This reflects a faster and more efficient transition of the charge carriers diffusing towards the surface of the nanostructures. As a result, the contribution of charge carriers (P_1) recombining in the area affected by the presence of PbS (A_1)

Table 1 Values of rate constants for holes, electrons, and excitons, and population fractions within areas affected (P_1) and not affected (P_2) by the presence of QDs. The data are obtained using the kinetic model described in the text to fit the transient absorption decays of the MAPbI_3/QD film, containing PbS crystals of different sizes

QD size (nm)	$k_h(\text{total}) (10^9 \text{ s}^{-1})$	$k_e(\text{total}) (10^{10} \text{ s}^{-1})$	$k_{\text{ex}} (10^{13} \text{ s}^{-1})$	$P_1 (\%)$	$P_2 (\%)$	$n_{\text{ex}} (\%)$
2.9	0.95	0.10	2.48	77	23	—
3.2	1.59	0.89	1.94	91	9	—
4.5	3.52	2.17	0.85	92	8	1
5.3	4.48	2.18	1.77	97	2	1

increases with the size of QDs. It is worth noting that because the mean distance between the QDs remains constant in all the samples (~25 nm), see the ESI† for more details on the estimation, only the size of QDs will have an impact on the observed behavior.

The electrons and holes in the PS matrix are, in fact, generated at different distances from QDs, and thus they must diffuse towards the surface of the nanostructures before being transferred to the PS/QD interface or to VBs/CBs of QDs. Hence, the observed temporal evolution of the TA signal in PS/QD films represented by $k_e(\text{total})$ and $k_h(\text{total})$ in eqn (2) is due to both processes (Scheme 1). The total decay time of electrons ($\tau_e = 1/k_e(\text{total})$) and holes ($\tau_h = 1/k_h(\text{total})$) is a sum of diffusion and transfer times of electrons (τ_{ediff} , τ_{et}) and holes (τ_{hdiff} , τ_{ht}), and it is given by:

$$\tau_e(\text{total}) = \tau_{\text{ediff}} + \tau_{\text{et}}, \quad (4a)$$

$$\tau_h(\text{total}) = \tau_{\text{hdiff}} + \tau_{\text{ht}}, \quad (4b)$$

Our analysis clearly shows a significant increase in the values of the rate constants, $k_e(\text{total})$ and $k_h(\text{total})$, with the size of QDs (Table 1 and Fig. 2). As the mean distances between QDs in the studied nanocomposites are similar (21–25 nm, Table S1, ESI†), the observed differences between the values of $k_e(\text{total})$, $k_h(\text{total})$ are mostly due to the increasing velocity of electron and hole transfer processes at the interface (k_{et} and k_{ht}). Only the values of $k_e (2.17 \times 10^{10} \text{ s}^{-1})$ are the same for QDs of 4.5 and 5.3 nm. The increase in the size of the PbS nanocrystals results in a larger concentration and different energies of available electronic states,⁴⁴ and therefore in an acceleration of deactivation processes related to the speed of the charge carrier transition between PS and QDs. Thus, the observed changes in the values of $k_e(\text{total})$ and $k_h(\text{total})$ should

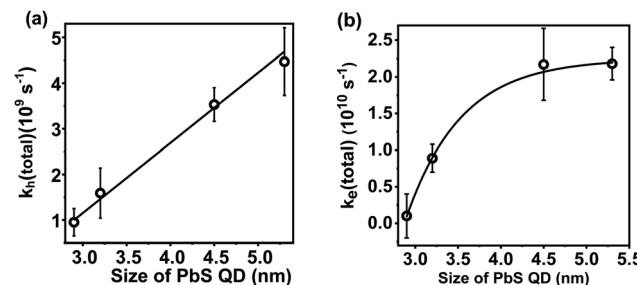


Fig. 2 Experimental values of (a) hole and (b) electron total rate constants in PS/PbS QD samples. The curve is a guide to the eye.

depend on k_{et} and k_{ht} at the PS/QD interface. The probability of the charge carrier transition to QDs also depends on the relative position of the energy states and their energy difference between PS and PbS. For the used QDs, the VB is located above that of PS and the energy difference increases with the size of QDs (Scheme 1). As the driving force of charge carrier transition increases with the difference in energy between the two partners, the time of hole transition into PbS becomes shorter (Fig. 1 and Fig. S6, ESI†).^{45–47} For 2.9 nm and 3.2 nm QDs, the CB is located above that of the PS, and as a result, the electrons can be transferred only to the interfacial trap states (Scheme 1a). However, when the size of QDs is 4.5 and 5.3 nm, the energy of the CB in the QDs is lower than that of PS CB, and thus the electrons are also transferred to the CB of the QDs (Scheme 1b).

Because the equations related to the electron and hole recombination in our model have the same structure, the model cannot give an answer to the question of which value is related to which carrier (eqn (2a) and (2b)). However, as the VB in PS is located significantly below that in PbS nanocrystals, the holes can be efficiently transferred to QDs in all studied samples, see Fig. 1f.¹⁶ Previously, we have shown that when the CB in PS is below that of QDs, the electron could not migrate to this band.¹⁶ However, the decay of the TA signal indicated that both charge carriers in the presence of PbS/CdS leave the CB/VB of PS in a faster way. We concluded that the electrons are trapped at the PS/QD interface and the hole transition was expected to be faster than that of electrons due to larger driving force.¹⁶ Nonetheless, the photobehaviour of the systems studied in the present report suggests that in all the cases, the electron transfer is much faster than the hole one. Direct comparison of the results using the present PS/QD films with those of PbS/CdS QDs is difficult, because of the core/shell structure in the latter. In such a situation the charge carrier transfer is mediated by energy states introduced by a broad energy band of the CdS shell. It was reported that depending on the thickness, the presence of the CdS core strongly influences the processes of charge carrier transfer between PbS and its surrounding, and it strongly affects the trap states on the surface of PbS NCs.^{1,48,49}

Table 1 and Fig. 2 show that the increase of the k_h value with the size of the QDs is almost linear while the dependence of $k_e(\text{total})$ strongly deviates from linearity. The change in the size of QDs from 2.9 to 4.5 nm leads to an increase of $k_e(\text{total})$ from $0.1 \times 10^{10} \text{ s}^{-1}$ to $2.17 \times 10^{10} \text{ s}^{-1}$, which remains the same for QDs with a diameter of 5.3 nm. This behavior points out the occurrence of a different change in the PS/QD systems that significantly influences one kind of recombining charge carrier. Fig. 1f shows that the change of the QD diameter results in the appearance of a new deactivation channel for electrons. The CB energy level in QDs becomes lower than that of PS (Scheme 1b). For QDs of 4.5 nm and 5.3 nm, the transition between the CBs of PS and of PbS becomes possible speeding up the process of electron transfer. Surprisingly, the results show that $k_e(\text{total}) > k_h(\text{total})$ even for the systems where the electron transfer to the CB of QDs is not possible (size: 2.9 and

3.2 nm), and in which the driving force for the hole transfer should be smaller than that for electrons. This result indicates that both electron and hole transfers might be mediated by the interface trap states. A possible explanation is that the density of electron trap states at the PS/QD interface is much larger than that of hole trap states, hence the transition of electrons to QDs is faster than the process for holes. If the density of surface transition channels is lower for holes, these charge carriers might be accumulated at the interface, and slowly transferred to the VB of QDs. A strong effect of trap-states on the dynamics of charge carrier transfer in the systems containing semiconductor materials has been previously reported.^{47,50,51}

As we have already discussed, the $k_e(\text{total})$ and $k_h(\text{total})$ components reflect two processes: charge carriers' diffusion within the PS domain, and transfer at the interface of both materials. Fig. 2b shows that the electron transfer rate constant is the same for the systems which contain QDs of 4.5 and 5.3 nm. As the distance between the nanostructures in these two systems is similar ($\sim 25 \text{ nm}$), the contribution of electron diffusion ($\tau_{e\text{diff}}$) to the processes of electron deactivation is the same in both samples. However, for the systems containing QDs of different sizes the velocity of electron transfer at the interfaces should be different, due to different numbers and reduced energies of the electronic states in the nanostructures. This is in agreement with the hole behavior in all PS/QD systems and with the electron behavior in the PS containing QDs of smaller sizes. The increasing difference between the energies of CBs in PS and QDs should speed up the process of electron transfer at the interface, due to faster depopulation of the initially populated trap states in PbS QDs. As a result, we should see a larger value of $k_e(\text{total})$ for the sample containing QDs of 5.3 nm as compared to the system with QDs of 4.5 nm. Similar values of $k_e(\text{total})$ in both systems suggest that the electron transfer (k_{et}) time is (i) the same in both cases, or (ii) it is different but shorter than the temporal resolution of the experiment ($\sim 70 \text{ fs}$). The first possibility is in contradiction with the observed correlation between k_h for all PS/QD systems and $k_e(\text{total})$ for smaller QDs as well as with our previous results.¹⁶ Therefore, the second option has to be taken into account. From the experimental point of view, similar values of $k_e(\text{total})$ in both systems mean that the times of electron transfer (τ_{et}) at the interface are different for both samples, but they are below the temporal resolution of the setup. In this situation, eqn (4a) reduces to $\tau_e = \tau_{e\text{diff}}$, which means that the fits of the TA decays in the systems containing QDs of 4.5 and 5.3 nm will give the same values of $k_e(\text{total}) = 1/\tau_{e\text{diff}} = 2.17 \times 10^{10} \text{ s}^{-1}$.

This information, in combination with the knowledge of the electron and hole mobilities in PS and PS/QDs, allows us to estimate the values of charge carrier's diffusion time constants in the PS films that contain QDs of different diameters (Table 2). Recent reports indicate balanced electron ($12.5 \text{ cm}^2 \text{ V}^{-1} \text{ s}^{-1}$) and hole mobilities ($7.5 \text{ cm}^2 \text{ V}^{-1} \text{ s}^{-1}$) in MAPbI₃ thin polycrystalline films, in agreement with theoretical predictions, giving similar effective masses of those charges ($m_e = 0.23m_0$ and $m_h = 0.29m_0$).^{52–54} The THz measurements of

Table 2 Values of rate constants of electron and hole diffusion and transfer in PS/QD samples having PbS of the indicated size

QD size (nm)	$k_{\text{ht}} (10^9 \text{ s}^{-1})$	$k_{\text{et}} (10^{10} \text{ s}^{-1})$	$L (\text{nm})$
2.9	1.04	0.11	39
3.2	1.86	1.56	39
4.5	5.32	>1430 ^a	39
5.3	7.81	>1430 ^a	39

^a Estimated based on our time resolution of 70 fs ($k_{\text{et}} > (70 \times 10^{-15} \text{ s}^{-1})$).

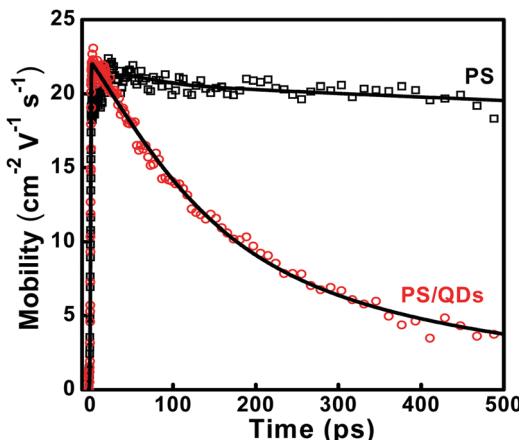


Fig. 3 Femtosecond THz transient decays in neat PS and PS/QD (4.5 nm) films. The samples were fs-excited at 600 nm with a fluence of the absorbed photons of $8.2 \times 10^{12} \text{ ph per cm}^2$.

charge carrier mobilities (μ) in MAPbI_3 have given the values $\mu_e = 2\mu_h$.^{54,55} If the mobility of charge carriers within PS is not affected by the presence of QDs, the diffusion times of the electrons (τ_{ediff}) would be two times larger than that of the holes (τ_{hdiff}). In fact, the comparison of THz signals in neat PS and PS/QD indicates similar initial mobilities ($20 \text{ cm}^2 \text{ V}^{-1} \text{ s}^{-1}$), and thus the diffusion in all samples depends mainly on the PS nature (Fig. 3). As the distances between the QDs in the nanocomposites are similar (21–25 nm), the electron and hole diffusion constants of all samples should be the same independently of the size of QDs. Hence, the value of τ_{ediff} (45 ps) in the PS domain containing QDs of 4.5 and 5.3 nm is similar to those of all PS/QD systems. Because $\mu_e = 2\mu_h$, the value of τ_{hdiff} (90 ps) will be two times smaller than τ_{ediff} .

Next, the above extracted diffusion time constants of electrons and holes allow calculation of the values of transition time constants of charge carriers (k_{et} and k_{ht}), and thus their rate constants in all studied PS/QD hybrid films (Table 2). Their values show that the transition of holes is much slower than that of electrons. Moreover, the total transfer rate constants of holes are dominated by components ascribed to transition to the CB of PbS QDs. Using τ_{ediff} and τ_{hdiff} (Table 2) along with the total mobility ($\mu = \mu_e + \mu_h$), the total diffusion length of charge carriers can also be calculated using the equation:²⁹

$$L = \sqrt{\frac{\mu k_b T}{e}} (\tau_{\text{ediff}} + \tau_{\text{hdiff}}), \quad (5)$$

where k_b is the Boltzmann constant, T is the temperature of the sample and e is related to the elemental charge. The calculated L is equal to 39 nm (Table 2) and it is approximately two times longer than the mean distance between QDs of different sizes embedded in PS (21–25 nm). The difference is because the calculated value is related to the diffusion length of both electrons and holes.

3.4 Fluence dependent TA of PS/QD systems

Important information on charge carrier generation, cooling as well as recombination/transfer processes, can be extracted by exploring charge carrier dynamics upon increasing the pump fluence. Firstly, we discuss the results of the dependence of photoinduced TA signals on the fluence of the absorbed photons ranging from 8.2×10^{12} to $1.23 \times 10^{15} \text{ ph per cm}^2$ for neat PS and PbS NCs of 3.2 nm embedded in the PS film at 2 ps pump-probe delay (Fig. 4a and b). Clearly, the increase in the pump fluence results in a broadening of the PB band with a maximum intensity at 755 nm, and the appearance of a new sub-band at 730/740 nm for both samples. Moreover, in the case of PS/QD, the new band (at 740 nm) shows a stronger TA signal than the one in the neat film of PS (755 nm). Recent TA experiments on PS films indicated the broadening of the bleach band and its small shift at early times upon increasing the fluence of the pump due to a band filling.^{40,56,57} However, the appearance of an additional band was not observed, and thus one can distrust the observed behavior. Previous experiments on perovskite films were carried out at different lower fluences ($1\text{--}100 \mu\text{J cm}^{-2}$).^{40,56,57} In the present work, we used fluences between 2.7 and $410 \mu\text{J cm}^{-2}$. As shown in Fig. 4a, the bleach band at 760 nm for the PS film in the range of used fluences in previous reports is characterized by one band. The change is only a spectral broadening of the bleach band and a small shift of its minimum, which agrees with the state filling model. New bands in PS appear upon pumping with fluences significantly higher than $100 \mu\text{J cm}^{-2}$. Under these experimental conditions, periodic features appear in the TA spectra of both PS and PS/QD (Fig. 4a and b).

One possible reason for such behavior is an interference of the probe light in the thin PS layer. However, we checked that the change of the relative angle between the probe beam and surface of the samples does not affect the observed features, and thus the modulation by the interference has to be excluded. Additionally, the TA spectra of PS and PS/QDs recorded at the lowest fluence do not show any periodic modulations (Fig. S10 (ESI†)). The comparison of the TA spectra of PS and PS/QD films at higher energies clearly shows the existence of additional bands which disappear at approximately 20 ps pump-probe delay time (Fig. S11 (ESI†)). Furthermore, the periodic structure is absent in the TA spectra at longer pump-probe delays, excluding interferences in the thin layer as the origin of the periodicities: in such a case, we expect the modulation of a weak positive signal visible at shorter wavelengths for pump-probe delays longer than 20 ps. The presence of new sub-bands reflects the appearance of new electronic transitions in the studied systems, and it is consistent with the

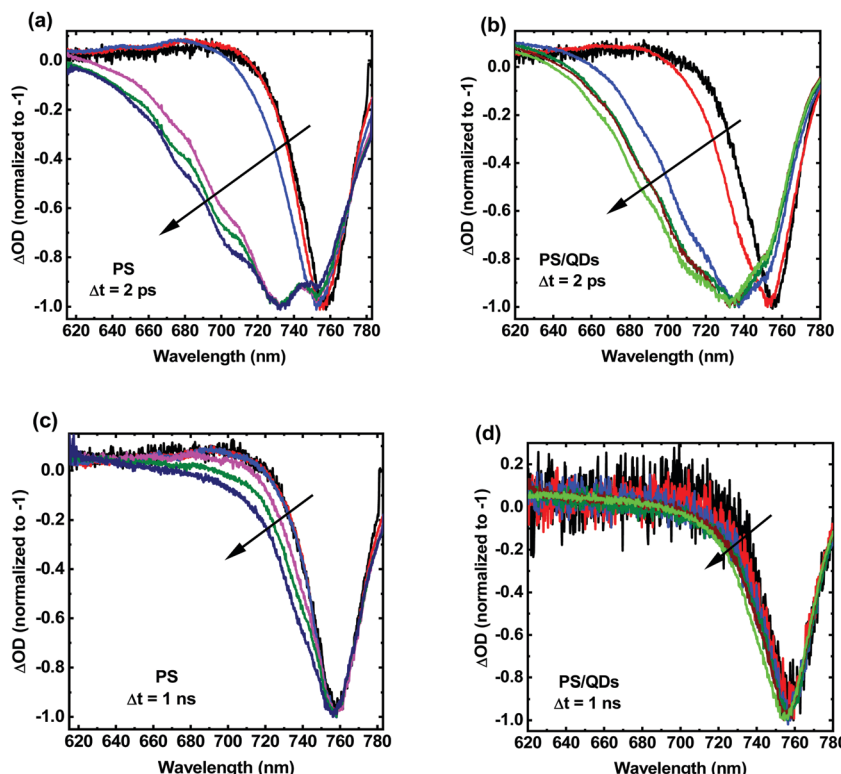


Fig. 4 (a and b) TA spectra of neat PS and PS/QD (3.2 nm) at 2 ps and (c and d) 1 ns pump–probe delay times upon excitation at 600 nm with fluences of absorbed photons ($10^{12} \text{ ph per cm}^2$): 8.2, 41, 82, 410, 820, 1230 for PS and 8.2, 82, 410, 820, 1030, 1230 for PS/QD films. The arrows indicate the direction of the increase of the pump fluence.

results reported for neat PS upon excitation with high fluences.³⁰ The absorption of a high density of photons leads to the saturation of the excited energy states, and to bleaching of the interband optical transition. The excited charge carriers become a source of new local electric field which, in turn, tends to shift the optical transitions and changes their oscillator strengths.^{28,58} Additionally, high initial charge carrier concentration may result in the generation of new transitions at energies spectrally shifted with respect to the low-excitation transitions.⁵⁹ Moreover, the increase in the density of the initially photoexcited charge carriers results in more efficient formation of excitons.

Recently, efficient formation of electron–hole couples bound by Coulomb forces was reported for FAPbI₃.³⁰ Opposite to free charge carriers, the ultrafast decay of the exciton population was observed ($\sim 5 \text{ ps}$).^{30,60,61} Fig. S12 (ESI†) shows TA decays in neat PS and PS/QD systems at representative observation wavelengths within the bleaching band. The new sub-bands decay within the first 20 ps. Unfortunately, due to the complex nature of transitions induced by the high density of photons in the pump beam, we could not apply our model to fit this decay. However, the observed temporal characteristic of the TA decay is similar to that reported for FAPbI₃, and thus it is more probably attributed to exciton population.³⁰ Interestingly, upon excitation at higher pump fluences, the bleaching bands of both samples at 1 ns pump–probe delay time shows that the band with the maximum intensity at 730/740 nm still exists (Fig. S13 (ESI†)). Not all populations observed at shorter

wavelengths decay within 20 ps. As the density of the excited charge carriers in PS is much lower due to the processes of recombination, diffusion and additionally transition to QDs (in the case of PS/QD), the observed feature cannot be related to the interactions between high densities of electrons and holes. This suggests that a high fluence of the absorbed photons may result in the formation and population of excitonic traps within PS and at the PS/QD interface. The presence of the additional signal might be related to the degradation of the sample due to a high density of the absorbed photons. In order to exclude this possibility, the sample was moved during the measurement. Moreover, the experiments were repeated several times giving similar results.

To check the formation efficiency of new transitions, we fitted the bleaching bands of neat PS and PS/QD films by Lorentz functions (Fig. 5 and Fig. S13, S14 (ESI†)). Homogeneous spectral broadening in PS, due to strong phonon coupling of charge carriers arising from their polaronic properties was reported.^{62,63} We have two observations. Firstly, the results indicate that the maximum positions of photogenerated sub-bands in both samples do not depend on the fluence of the absorbed photons. Secondly, the comparison of the integral intensities of the two sub-bands with intensity maxima at 755 nm and 730/740 nm (neat PS and PS/QDs, respectively) at 2 ps pump–probe delay time indicates different dependence of peak intensities on the pump fluences (Fig. 5 and Fig. S13, S14 (ESI†)).

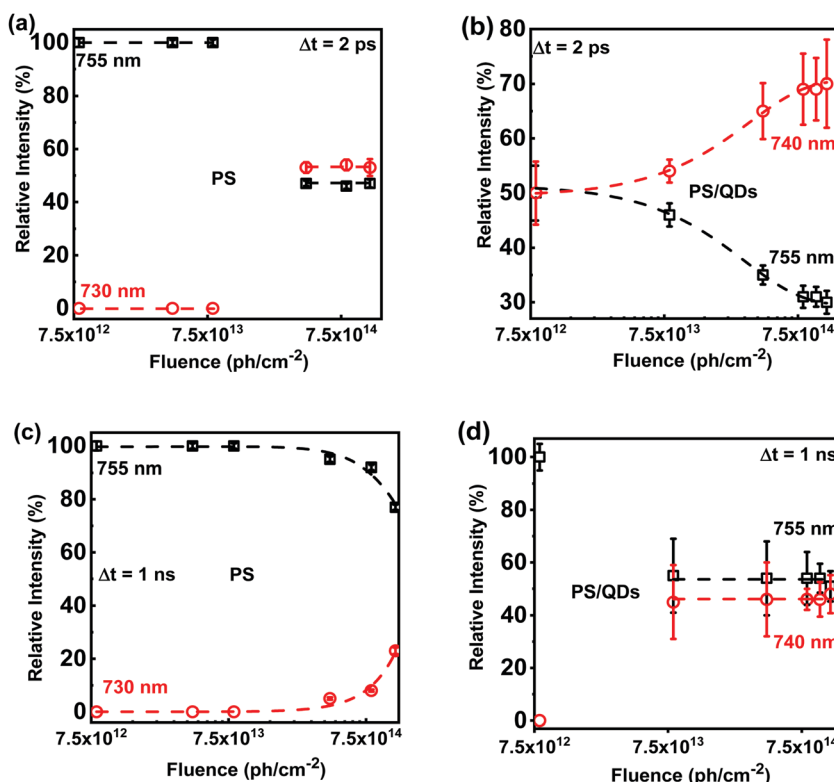


Fig. 5 (a and b) Relative integral intensities of the sub-bands at 730/740 and 755 of neat PS and PS/QD (3.2 nm) upon excitation at 600 nm with different fluences of absorbed photons at 2 ps and (c and d) 1 ns pump–probe delay-times. The sub-bands were obtained as a result of the deconvolution of the bleach band using Lorentz functions. The dashed curves are a guide to the eye.

For the few first fluences, only the band at 755 nm in PS is present, while the 730 nm one appears at a fluence of $4.1 \times 10^{14} \text{ ph per cm}^2$, and it does not change its relative intensity. For the PS/QD film, the 740 nm band is absent only at the lowest pump fluence and its relative intensity rises with increasing fluence of the absorbed photons. Moreover, the intensity of the signal at 740 nm is much higher than that at 755 nm. The 730 nm sub-band in neat PS is still present at 1 ns pump–probe delay time upon excitation at the highest energies, but its intensity is weak (Fig. 5c and Fig. S7, S8 (ESI[†])). On the other hand, in the PS/QD film the integral intensities of the signals at 740 and at 755 nm at 1 ns have comparable values (Fig. S14 (ESI[†])). For the origin of PB upon excitation at high fluences, we assign the signal at 730/740 nm to excitons, and point out that these populations decay within the first 20 ps which is apparently incompatible with the presence of these features at 1 ns pump–probe delay time. As we mentioned above, increasing the density of photoexcited charge carriers leads to higher concentration of excitons, and thus the probability of excitonic trap population increases.^{30,64} Trapped excitons can survive for a relatively long time, contributing to the TA signal. Previous reports on MAPbI_3 indicated the presence of both bulk and surface excitonic traps and the occurrence of exciton trapping within picoseconds.^{65,66} The QDs embedded in the PS matrix might result in an increase of excitonic trap density formed at the PS/QD interface.¹⁶ As a result, the probability of rapid trapping of initially photoexcited excitons rises, and thus the presence and the high intensity of the signal at 740 nm in PS/QD.

Application of photovoltaic materials in commercial devices such as LEDs requires low non-radiative recombination and efficient charge carrier transport. Consequently, to fulfill these requirements the processes of electron and hole trapping must be reduced. In this report, we show a clear PbS QD size effect on the ultrafast dynamics of electrons and holes in PS/QD materials applicable to NIR-LEDs. Our results show ultrafast and efficient charge carrier transfer from the perovskite matrix to PbS, which speeds up with the size of QDs. The acceleration of such processes decreases the contribution of undesirable charge carrier trapping and non-radiative recombination within PS. Owing to this fact, our result shows a way to increase the efficiency of perovskite/PbS QD film-based LEDs.

4. Conclusions

For the first time, we demonstrate a strong correlation between deactivation processes of photoexcited charge carriers in PS and the size of PbS QDs embedded in its matrix. The increase of the QD size results in an acceleration of electron and hole transition from PS to the QDs. Our kinetic model allows extracting the total transfer rate constants of electrons ($k_e(\text{total})$) and holes ($k_h(\text{total})$) in the studied systems. The values of $k_e(\text{total})$ and $k_h(\text{total})$ increase from 0.1 s^{-1} and $1 \times 10^9 \text{ s}^{-1}$ to 4.5 s^{-1} and $22 \times 10^9 \text{ s}^{-1}$ with the size of QDs increasing from 2.9 nm to 5.3 nm, respectively. This is due to

the increasing concentration and changes in the energies of the QD electronic states. Moreover, taking into account the fact that the charge carrier diffusion in the PS matrix does not depend on the presence of QDs, we show that the processes of electron and hole transfer to QDs are mediated by PS/QD interfacial trap states. The analysis of the correlation between the size of QDs and the resulting electron and hole recombination rate constants along with the value of charge carrier's mobility in PS and PS/QD systems allow estimation of the electron and hole diffusion rate constants ($\tau_{\text{ediff}} = 45$ ps and $\tau_{\text{hdiff}} = 90$ ps, respectively). Due to a similar distance between QDs within the PS matrix regardless of the different QD sizes analyzed, these values are similar for all PS/QD nanocomposites. The transfer rate constants of electrons (k_{et}) and holes (k_{ht}) increase with the size of QDs (0.1 to $1.6 \times (10^{10} \text{ s}^{-1})$) and (0.1 to $0.8 \times (10^{10} \text{ s}^{-1})$), respectively. In the case of 4.5 and 5.3 nm QDs, the time of the electron transfer at the interface is shorter than 70 fs, the temporal resolution of the setup. The power-dependent spectral behavior of PS and PS/QD systems suggests the increasing contribution of excitons in the photo-induced dynamics upon pumping with higher pump fluences. We also show that the survival probability of the excitonic state is higher in the case of PS/QD systems than in neat PS which proves a higher concentration of excitonic states at the PS/QD interface than in the PS matrix. This fact could have important implications in the performance of optoelectronic devices based on this kind of hybrid material. The results shown here provide new insights into the ultrafast processes occurring in PS/PbS QD systems and the relevance of the QD size in the electron, hole and exciton dynamics. These results could have important implications to increase the efficiency of nanocomposite-based LEDs.

Conflicts of interest

The authors declare no competing financial interests.

Acknowledgements

This work was supported by the MINECO (Spain) through project MAT-2017-8653-R, Generalitat Valenciana *via* Prometeo Grant Q-Devices (Prometeo/2018/098), and the European Research Council (ERC) *via* Consolidator Grant (724424—No-LIMIT). PP acknowledges the support from the National Science Centre (Poland) through project No. 2017/26/D/ST3/00910.

References

- Z. Huang, Z. Xu, M. Mahboub, X. Li, J. W. Taylor, W. H. Harman, T. Lian and M. L. Tang, *Angew. Chem., Int. Ed.*, 2017, **56**, 16583–16587.
- T. T. Ngo and I. Mora-Seró, *J. Phys. Chem. Lett.*, 2019, **10**, 1099–1108.
- T. T. Ngo, I. Suarez, R. S. Sanchez, J. P. Martinez-Pastor and I. Mora-Seró, *Nanoscale*, 2016, **8**, 14379–14383.
- R. S. Sanchez, M. S. de la Fuente, I. Suarez, G. Muñoz-Matutano, J. P. Martinez-Pastor and I. Mora-Seró, *Sci. Adv.*, 2016, **2**, e1501104.
- X. Gong, Z. Yang, G. Walters, R. Comin, Z. Ning, E. Beauregard, V. Adinolfi, O. Voznyy and E. H. Sargent, *Nat. Photonics*, 2016, **10**, 253–257.
- Z. Yang, O. Voznyy, G. Walters, J. Z. Fan, M. Liu, S. Kinge, S. Hoogland and E. H. Sargent, *ACS Photonics*, 2017, **4**, 830–836.
- S.-S. Li, C.-H. Chang, Y.-C. Wang, C.-W. Lin, D.-Y. Wang, J.-C. Lin, C.-C. Chen, H.-S. Sheu, H.-C. Chia, W.-R. Wu, U. S. Jeng, C.-T. Liang, R. Sankar, F.-C. Chou and C.-W. Chen, *Energy Environ. Sci.*, 2016, **9**, 1282–1289.
- J. Han, S. Luo, X. Yin, Y. Zhou, H. Nan, J. Li, X. Li, D. Oron, H. Shen and H. Lin, *Small*, 2018, **14**, 1801016.
- T. T. Ngo, S. Masi, P. F. Mendez, M. Kazes, D. Oron and I. M. Seró, *Nanoscale Adv.*, 2019, **1**, 4109–4118.
- X. Zheng, J. Troughton, N. Gasparini, Y. Lin, M. Wei, Y. Hou, J. Liu, K. Song, Z. Chen, C. Yang, B. Turedi, A. Y. Alsalloum, J. Pan, J. Chen, A. A. Zhumekenov, T. D. Anthopoulos, Y. Han, D. Baran, O. F. Mohammed, E. H. Sargent and O. M. Bakr, *Joule*, 2019, **3**, 1963–1976.
- J. Z. Fan, N. T. Andersen, M. Biondi, P. Todorović, B. Sun, O. Ouellette, J. Abed, L. K. Sagar, M.-J. Choi, S. Hoogland, F. P. G. de Arquer and E. H. Sargent, *Adv. Mater.*, 2019, **31**, 1904304.
- Z. Moradi, H. Fallah and M. Hajimahmoodzadeh, *Sens. Actuators, A*, 2018, **280**, 47–51.
- C. Liu, H. Peng, K. Wang, C. Wei, Z. Wang and X. Gong, *Nano Energy*, 2016, **30**, 27–35.
- Z. Yang, A. Jammohamed, X. Lan, F. P. García de Arquer, O. Voznyy, E. Yassitepe, G.-H. Kim, Z. Ning, X. Gong, R. Comin and E. H. Sargent, *Nano Lett.*, 2015, **15**, 7539–7543.
- M. Liu, O. Voznyy, R. Sabatini, F. P. García de Arquer, R. Munir, A. H. Balawi, X. Lan, F. Fan, G. Walters, A. R. Kirmani, S. Hoogland, F. Laquai, A. Amassian and E. H. Sargent, *Nat. Mater.*, 2017, **16**, 258–263.
- P. Galar, P. Piatkowski, T. T. Ngo, M. Gutiérrez, I. Mora-Seró and A. Douhal, *Nano Energy*, 2018, **49**, 471–480.
- R. S. Sanchez, E. Binetti, J. A. Torre, G. Garcia-Belmonte, M. Striccoli and I. Mora-Seró, *Nanoscale*, 2014, **6**, 8551–8555.
- C.-Y. Lin, S.-S. Li, J.-W. Chang, H.-C. Chia, Y.-Y. Hsiao, C.-J. Su, B.-J. Lian, C.-Y. Wen, S.-K. Huang, W.-R. Wu, D.-Y. Wang, A.-C. Su, C.-W. Chen and U.-S. Jeng, *Adv. Funct. Mater.*, 2019, **29**, 1902582.
- S. Masi, C. Echeverría-Arrondo, K. M. M. Salim, T. T. Ngo, P. F. Mendez, E. López-Fraguas, D. F. Macias-Pinilla, J. Planelles, J. I. Climente and I. Mora-Seró, *ACS Energy Lett.*, 2020, **5**, 418–427.
- A. P. Alivisatos, *Science*, 1996, **271**, 933–937.
- M.-J. Choi, Y. Kim, H. Lim, E. Alarousu, A. Adhikari, B. S. Shaheen, Y. H. Kim, O. F. Mohammed, E. H. Sargent, J. Y. Kim and Y. S. Jung, *Adv. Mater.*, 2019, **31**, 1805886.
- Z. Ning, X. Gong, R. Comin, G. Walters, F. Fan, O. Voznyy, E. Yassitepe, A. Buin, S. Hoogland and E. H. Sargent, *Nature*, 2015, **523**, 324–328.

- Published on 19 September 2020. Downloaded by Institute of Physics of the Czech Academy of Sciences on 8/18/2023 1:23:38 PM.
- 23 M. X. Liu, Y. L. Chen, C. S. Tan, R. Quintero-Bermudez, A. H. Proppe, R. Munir, H. R. Tan, O. Voznyy, B. Scheffel, G. Walters, A. P. T. Kam, B. Sun, M. J. Choi, S. Hoogland, A. Amassian, S. O. Kelley, F. P. G. de Arquer and E. H. Sargent, *Nature*, 2019, **570**, 96–101.
- 24 X. J. Zhang, X. X. Wu, X. Y. Liu, G. Y. Chen, Y. K. Wang, J. C. Bao, X. X. Xu, X. F. Liu, Q. Zhang, K. H. Yu, W. Wei, J. J. Liu, J. Xu, H. Jiang, P. Wang and X. Wang, *J. Am. Chem. Soc.*, 2020, **142**, 4464–4471.
- 25 I. Moreels, K. Lambert, D. Smeets, D. De Muynck, T. Nollet, J. C. Martins, F. Vanhaecke, A. Vantomme, C. Delerue, G. Allan and Z. Hens, *ACS Nano*, 2009, **3**, 3023–3030.
- 26 D. Zhrebetskyy, M. Scheele, Y. Zhang, N. Bronstein, C. Thompson, D. Britt, M. Salmeron, P. Alivisatos and L.-W. Wang, *Science*, 2014, **344**, 1380–1384.
- 27 N. J. Jeon, J. H. Noh, Y. C. Kim, W. S. Yang, S. Ryu and S. I. Seok, *Nat. Mater.*, 2014, **13**, 897–903.
- 28 P. Piatkowski, B. Cohen, F. Javier Ramos, M. Di Nunzio, M. K. Nazeeruddin, M. Grätzel, S. Ahmad and A. Douhal, *Phys. Chem. Chem. Phys.*, 2015, **17**, 14674–14684.
- 29 P. Piatkowski, B. Cohen, C. S. Ponseca, M. Salado, S. Kazim, S. Ahmad, V. Sundström and A. Douhal, *J. Phys. Chem. Lett.*, 2016, **7**, 204–210.
- 30 P. Piatkowski, B. Cohen, S. Kazim, S. Ahmad and A. Douhal, *Phys. Chem. Chem. Phys.*, 2016, **18**, 27090–27101.
- 31 H. Beygi, S. A. Sajjadi, A. Babakhani, J. F. Young and F. C. J. M. van Veggel, *Appl. Surf. Sci.*, 2018, **457**, 1–10.
- 32 H.-S. Kim, C.-R. Lee, J.-H. Im, K.-B. Lee, T. Moehl, A. Marchioro, S.-J. Moon, R. Humphry-Baker, J.-H. Yum, J. E. Moser, M. Grätzel and N.-G. Park, *Sci. Rep.*, 2012, **2**, 591.
- 33 J. Jasieniak, M. Califano and S. E. Watkins, *ACS Nano*, 2011, **5**, 5888–5902.
- 34 B.-R. Hyun, Y.-W. Zhong, A. C. Bartnik, L. Sun, H. D. Abruña, F. W. Wise, J. D. Goodreau, J. R. Matthews, T. M. Leslie and N. F. Borrelli, *ACS Nano*, 2008, **2**, 2206–2212.
- 35 G. Xing, N. Mathews, S. Sun, S. S. Lim, Y. M. Lam, M. Grätzel, S. Mhaisalkar and T. C. Sum, *Science*, 2013, **342**, 344–347.
- 36 H.-Y. Hsu, C.-Y. Wang, A. Fathi, J.-W. Shiu, C.-C. Chung, P.-S. Shen, T.-F. Guo, P. Chen, Y.-P. Lee and E. W.-G. Diau, *Angew. Chem., Int. Ed.*, 2014, **53**, 9339–9342.
- 37 C. Wehrenfennig, G. E. Eperon, M. B. Johnston, H. J. Snaith and L. M. Herz, *Adv. Mater.*, 2014, **26**, 1584–1589.
- 38 L. M. Herz, *Annu. Rev. Phys. Chem.*, 2016, **67**, 65–89.
- 39 Z. Guo, J. S. Manser, Y. Wan, P. V. Kamat and L. Huang, *Nat. Commun.*, 2015, **6**, 7471.
- 40 J. S. Manser and P. V. Kamat, *Nat. Photonics*, 2014, **8**, 737–743.
- 41 M. B. Johnston and L. M. Herz, *Acc. Chem. Res.*, 2016, **49**, 146–154.
- 42 J. Huang, Y. Yuan, Y. Shao and Y. Yan, *Nat. Rev. Mater.*, 2017, **2**, 17042.
- 43 E. M. Hutter, J.-J. Hofman, M. L. Petrus, M. Moes, R. D. Abellón, P. Docampo and T. J. Savenije, *Adv. Energy Mater.*, 2017, **7**, 1602349.
- 44 G. H. Carey, A. L. Abdelhady, Z. Ning, S. M. Thon, O. M. Bakr and E. H. Sargent, *Chem. Rev.*, 2015, **115**, 12732–12763.
- 45 K. Tvrdy, P. A. Frantsuzov and P. V. Kamat, *Proc. Natl. Acad. Sci. U. S. A.*, 2011, **108**, 29–34.
- 46 A. J. Ward, A. Ruseckas, M. M. Kareem, B. Ebenhoch, L. A. Serrano, M. Al-Eid, B. Fitzpatrick, V. M. Rotello, G. Cooke and I. D. W. Samuel, *Adv. Mater.*, 2015, **27**, 2496–2500.
- 47 J. H. Olshansky, A. D. Balan, T. X. Ding, X. Fu, Y. V. Lee and A. P. Alivisatos, *ACS Nano*, 2017, **11**, 8346–8355.
- 48 H. Zhao, Z. Fan, H. Liang, G. S. Selopal, B. A. Gonfa, L. Jin, A. Soudi, D. Cui, F. Enrichi, M. M. Natile, I. Concina, D. Ma, A. O. Govorov, F. Rosei and A. Vomiero, *Nanoscale*, 2014, **6**, 7004–7011.
- 49 H. Zang, P. K. Routh, Q. Meng and M. Cotlet, *Nanoscale*, 2017, **9**, 14664–14671.
- 50 A. J. Harvie, C. T. Smith, R. Ahumada-Lazo, L. J. C. Jeuken, M. Califano, R. S. Bon, S. J. O. Hardman, D. J. Binks and K. Critchley, *J. Phys. Chem. C*, 2018, **122**, 10173–10180.
- 51 A. Pal, S. Srivastava, R. Gupta and S. Sapra, *Phys. Chem. Chem. Phys.*, 2013, **15**, 15888–15895.
- 52 Y. H. Chang, C. H. Park and K. Matsuishi, *J. Korean Phys. Soc.*, 2004, **44**, 889–893.
- 53 G. Giorgi, J.-I. Fujisawa, H. Segawa and K. Yamashita, *J. Phys. Chem. Lett.*, 2013, **4**, 4213–4216.
- 54 C. S. Ponseca, T. J. Savenije, M. Abdellah, K. Zheng, A. Yartsev, T. Pascher, T. Harlang, P. Chabera, T. Pullerits, A. Stepanov, J.-P. Wolf and V. Sundström, *J. Am. Chem. Soc.*, 2014, **136**, 5189–5192.
- 55 C. S. Ponseca, E. M. Hutter, P. Piatkowski, B. Cohen, T. Pascher, A. Douhal, A. Yartsev, V. Sundström and T. J. Savenije, *J. Am. Chem. Soc.*, 2015, **137**, 16043–16048.
- 56 K. Pydžińska-Białek, J. Szeremeta, K. Wojciechowski and M. Ziółek, *J. Phys. Chem. C*, 2019, **123**, 110–119.
- 57 T. C. Sum, N. Mathews, G. Xing, S. S. Lim, W. K. Chong, D. Giovanni and H. A. Dewi, *Acc. Chem. Res.*, 2016, **49**, 294–302.
- 58 A. A. Mikhailovsky, A. V. Malko, J. A. Hollingsworth, M. G. Bawendi and V. I. Klimov, *Appl. Phys. Lett.*, 2002, **80**, 2380–2382.
- 59 V. I. Klimov, in *Semiconductor and Metal Nanocrystals*, ed. V. I. Klimov, Taylor & Francis, New York, 2005, ch. 5, pp. 200–208.
- 60 H. Wang, L. Whittaker-Brooks and G. R. Fleming, *J. Phys. Chem. C*, 2015, **119**, 19590–19595.
- 61 C. Sheng, C. Zhang, Y. Zhai, K. Mielczarek, W. Wang, W. Ma, A. Zakhidov and Z. V. Vardeny, *Phys. Rev. Lett.*, 2015, **114**, 116601.
- 62 C. Wehrenfennig, M. Liu, H. J. Snaith, M. B. Johnston and L. M. Herz, *J. Phys. Chem. Lett.*, 2014, **5**, 1300–1306.
- 63 D. B. Straus, S. Hurtado Parra, N. Iotov, J. Gebhardt, A. M. Rappe, J. E. Subotnik, J. M. Kilkawa and C. R. Kagan, *J. Am. Chem. Soc.*, 2016, **138**, 13798–13801.
- 64 M. Saba, M. Cadelano, D. Marongiu, F. Chen, V. Sarritzu, N. Sestu, C. Figus, M. Aresti, R. Piras, A. Geddo Lehmann, C. Cannas, A. Musinu, F. Quochi, A. Mura and G. Bongiovanni, *Nat. Commun.*, 2014, **5**, 5049.
- 65 J. Peng, Y. Chen, K. Zheng, T. Pullerits and Z. Liang, *Chem. Soc. Rev.*, 2017, **46**, 5714–5729.
- 66 X. Wu, M. T. Trinh, D. Niesner, H. Zhu, Z. Norman, J. S. Owen, O. Yaffe, B. J. Kudisch and X. Y. Zhu, *J. Am. Chem. Soc.*, 2015, **137**, 2089–2096.

Influence of non-diamond carbon phase on recombination mechanisms of photoexcited charge carriers in microcrystalline and nanocrystalline diamond studied by time resolved photoluminescence spectroscopy

Pavel Galář,^{1,*} Branislav Dzurňák,¹ Marian Varga,^{2,3} Marian Marton,³ Alexander Kromka² and Petr Malý¹

¹Faculty of Mathematics and Physics, Charles University in Prague, Ke Karlovu 3, Prague 2, 121 16, Czech Republic

²Institute of Physics of the ASCR v.v.i., Cukrovarnická 10, Prague 6, 162 00, Czech Republic

³Institute of Electronics and Photonics, FEI STU, Ilkovičova 3, Bratislava, 812 19, Slovakia

*pavel.galar@mff.cuni.cz

Abstract: Recombination processes of photoexcited charge carriers in as-grown micro/nanocrystalline diamond films containing various amounts of non-diamond carbon phase were studied by time resolved photoluminescence spectroscopy. The photoluminescence was found to be strongly sensitive to diamond morphology and concentration of non-diamond carbon phase. We found two photoluminescence components differing in decay rates (nano/microsecond time scales) and in response to ambient air pressure, temperature and excitation light parameters. Experimental data form the basis for interpretation of recombination paths of photoexcited charge carriers in micro/nanocrystalline diamond films in dependence on their morphology and non-diamond carbon phase content.

©2014 Optical Society of America

OCIS codes: (300.6500) Spectroscopy, time-resolved; (160.4236) Nanomaterials; (260.3800) Luminescence; (320.4240) Nanosecond phenomena; (180.5655) Raman microscopy;

References and links

1. J. de Sanoit, E. Vanhove, P. Mailley, and P. Bergonzo, "Electrochemical diamond sensors for TNT detection in water," *Electrochim. Acta* **54**(24), 5688–5693 (2009).
2. S. Stehlík, T. Ižák, A. Kromka, B. Dolenský, M. Havlík, and B. Rezek, "Sensitivity of Diamond-Capped Impedance Transducer to Tröger's Base Derivative," *ACS Appl. Mater. Interfaces* **4**(8), 3860–3865 (2012).
3. M. Davydova, M. Stuchlík, B. Rezek, K. Larsson, and A. Kromka, "Sensing of phosgene by a porous-like nanocrystalline diamond layer with buried metallic electrodes," *Sens. Actuators B Chem.* **188**, 675–680 (2013).
4. B. Rezek, M. Krátká, A. Kromka, and M. Kalbáčová, "Effects of protein inter-layers on cell-diamond FET characteristics," *Biosens. Bioelectron.* **26**(4), 1307–1312 (2010).
5. M. Krátká, A. Kromka, E. Ukrainstev, M. Ledinský, A. Brož, M. Kalbáčová, and B. Rezek, "Function of thin film nanocrystalline diamond-protein SGFET independent of grain size," *Sens. Actuators B Chem.* **166–167**, 239–245 (2012).
6. A. Härtl, E. Schmich, J. A. Garrido, J. Hernando, S. C. Catharino, S. Walter, P. Feulner, A. Kromka, D. Steinmüller, and M. Stutzmann, "Protein-modified nanocrystalline diamond thin films for biosensor applications," *Nat. Mater.* **3**(10), 736–742 (2004).
7. J. Čermák, B. Rezek, P. Hubík, J. J. Mareš, A. Kromka, and A. Fejfar, "Photo-conductivity and Hall mobility of holes at polypyrrole-diamond interface," *Diamond Related Materials* **19**(2–3), 174–177 (2010).
8. V. Prajzler, M. Varga, P. Nekvindová, Z. Remeš, and A. Kromka, "Design and investigation of properties of nanocrystalline diamond optical planar waveguides," *Opt. Express* **21**(7), 8417–8425 (2013).
9. L. Ondič, O. Babchenko, M. Varga, A. Kromka, J. Cyroký, and I. Pelant, "Diamond photonic crystal slab: Leaky modes and modified photoluminescence emission of surface-deposited quantum dots," *Sci Rep* **2**, 914 (2012).
10. A. M. Zaitsev, *Optical Properties of Diamond* (Springer, 2001), Chap.5.
11. M. Vaněček, J. Rosa, M. Nesládek, and L. M. Stals, "Evidence for the principal defect states in CVD diamond films: Optical study," *Diamond Related Materials* **5**(9), 952–957 (1996).

12. P. Achatz, J. A. Garrido, M. Stutzmann, O. A. Williams, D. M. Gruen, A. Kromka, and D. Steinmüller, "Optical properties of nanocrystalline diamond thin films," *Appl. Phys. Lett.* **88**(10), 101908 (2006).
13. B. Dzurňák, F. Trojánek, J. Preclíková, A. Kromka, B. Rezek, and P. Malý, "Ultrafast photoluminescence spectroscopy of H- and O-terminated nanocrystalline diamond films," *Diamond Related Materials* **20**(8), 1155–1159 (2011).
14. P. Němec, J. Preclíková, A. Kromka, B. Rezek, and P. Malý, "Ultrafast dynamics of photoexcited charge carriers in nanocrystalline diamond," *Appl. Phys. Lett.* **93**(8), 083102 (2008).
15. B. R. Smith, D. Gruber, and T. Plakhotnik, "The effects of surface oxidation on luminescence of nano diamonds," *Diamond Related Materials* **19**(4), 314–318 (2010).
16. T. Ikeda, K. Teii, C. Casiraghi, J. Robertson, and A. C. Ferrari, "Effect of the sp^2 carbon phase on n-type conduction in nanodiamond films," *J. Appl. Phys.* **104**(7), 073720 (2008).
17. J. Preclíková, F. Trojánek, B. Dzurňák, P. Malý, A. Kromka, and B. Rezek, "Light-assisted adsorption processes in nanocrystalline diamond membranes studied by femtosecond laser spectroscopy," *Diamond Related Materials* **19**(7-9), 918–922 (2010).
18. M. Varga, T. Ižák, A. Kromka, M. Veselý, K. Hruška, and M. Michalka, "Study of diamond film nucleation by ultrasonic seeding in different solutions," *Cent. Eur. J. Phys.* **10**(1), 218–224 (2012).
19. T. Ižák, M. Marton, M. Varga, M. Vojs, M. Veselý, R. Redhammer, and M. Michalka, "Bias enhanced nucleation of diamond thin films in a modified HFCVD reactor," *Vacuum* **84**(1), 49–52 (2009).
20. W. Fortunato, A. J. Chiquito, J. C. Galceran, and J. R. Moro, "Crystalline quality and phase purity of CVD diamond films studied by Raman spectroscopy," *J. Mater. Sci.* **42**(17), 7331–7336 (2007).
21. B. Dzurňák, F. Trojánek, J. Preclíková, A. Kromka, B. Rezek, and P. Malý, "Subgap photoluminescence spectroscopy of nanocrystalline diamond films," *Diamond Related Materials* **18**(5-8), 776–778 (2009).
22. M. Varga, Z. Remeš, O. Babchenko, and A. Kromka, "Optical study of defects in nano-diamond films grown in linear antenna microwave plasma CVD from $H_2/CH_4/CO_2$ gas mixture," *Phys. Status Solidi, B Basic Res.* **249**(12), 2635–2639 (2012).
23. K. Dunn, J. Derr, T. Johnston, M. Chaker, and F. Rosei, "Multiexponential photoluminescence decay of blinking nanocrystal ensembles," *Phys. Rev. B* **80**(3), 035330 (2009).
24. L. Pavesi and M. Ceschini, "Stretched-exponential decay of the luminescence in porous silicon," *Phys. Rev. B Condens. Matter* **48**(23), 17625–17628 (1993).
25. J. Bisquert, "Interpretation of a fractional diffusion equation with nonconserved probability density in terms of experimental systems with trapping or recombination," *Phys. Rev. E Stat. Nonlin. Soft Matter Phys.* **72**(1), 011109 (2005).
26. P. H. Sher, J. M. Smith, P. A. Dalgarno, R. J. Warburton, X. Chen, P. J. Dobson, S. M. Daniels, N. L. Pickett, and P. O'Brien, "Power law carrier dynamics in semiconductor nanocrystals at nanosecond timescales," *Appl. Phys. Lett.* **92**(10), 101111 (2008).
27. J. Klafter and M. F. Shlesinger, "On the relationship among three theories of relaxation in disordered systems," *Proc. Natl. Acad. Sci. U.S.A.* **83**(4), 848–851 (1986).
28. M. Nesládek, K. Meykens, L. M. Stals, M. Vaněček, and J. Rosa, "Origin of characteristic subgap optical absorption in CVD diamond films," *Phys. Rev. B Condens. Matter* **54**(8), 5552–5561 (1996).
29. D. J. Huntley, "An explanation of the power-law decay of luminescence," *J. Phys. Condens. Matter* **18**(4), 1359–1365 (2006).
30. A. K. Jonscher and A. de Polignac, "The time dependence of luminescence in solids," *J. Phys. C Solid State Phys.* **17**(35), 6493–6519 (1984).
31. J. Preclíková, F. Trojánek, A. Kromka, B. Rezek, B. Dzurňák, and P. Malý, "Ultrafast photoluminescence of nanocrystalline diamond films," *Phys. Status Solidi., A Appl. Mater. Sci.* **205**(9), 2154–2157 (2008).
32. J. Robertson, "Gap states in diamond-like amorphous carbon," *Philos. Mag. B* **76**(3), 335–350 (1997).
33. Z. Remeš, T. Ižák, A. Kromka, and M. Vaněček, "High optical quality nanocrystalline diamond with reduced non-diamond contamination," *Diamond Related Materials* **19**(5-6), 453–456 (2010).
34. P. Hubík, J. J. Mareš, H. Kozák, A. Kromka, B. Rezek, J. Kristofik, and D. Kindl, "Transport properties of hydrogen-terminated nanocrystalline diamond films," *Diamond Related Materials* **24**, 63–68 (2012).

1. Introduction

Nanocrystalline diamond (NCD) and microcrystalline diamond (MCD) are unique materials unifying properties of bulk diamond with modifications caused by the presence of the diamond grain boundaries and by the non-diamond carbon phase located between the grains. This combination of bulk and nano-scale properties makes MCD/NCD perspective for a wide spectrum of applications in chemical [1–3] and biological sensing [4–6] as well as in optical and opto-electronical devices [7–9]. However, the complex structure and nano-character of MCD/NCD gives rise to a complicated system of sub-gap energetic states [10]. This makes rather difficult to describe processes such as transport and recombination of charge carriers that are essential for optimization of preparation methods and further extension of MCD/NCD possible applications. To elucidate these characteristics a lot of effort has been made during

last two decades [11–14]. It has been shown that major effect on the properties of NDC has the sp^2 carbon phase localized between the grains, and the composition and concentration of non-diamond carbon phase in general, even if the ratio of non-diamond to diamond carbon phase is usually low [15,16]. Just the differences in non-diamond phase composition and its interaction with the sp^3 carbon on the diamond grain interface could be the reason of fundamental differences in the published results on MCD/NCD by many groups. Although various models have been proposed, proper interpretation of the influence of sp^2 on MCD/NCD subsurface processes and interaction between the diamond and non-diamond carbon phase is still missing [12].

We address this issue and present a comprehensive study of recombination processes of photoexcited charge carriers in MCD/NCD sub-gap states. In this work, we aim to clarify the origin of recombination processes of excited carriers in MCD/NCD not only in terms of sub-gap energy states, but also in morphological structures. For this purpose, the research was carried out on a series of well-defined samples with different structure and ratio of non-diamond phase. Raman spectroscopy and SEM were used to monitor the structure and composition of diamond films. Properties of our samples were studied by time resolved photoluminescence (PL) on a broad picosecond-to-millisecond scale under various conditions (vacuum, low temperature). This method has been successfully used for investigation of electronic recombination processes in solid state physics for a long time, nevertheless only few papers on polycrystalline diamond [13, 17] have been published.

2. Samples and Experimental

Mirror-polished n-type (phosphorus doped) (100) oriented Si substrates ($10 \times 10 \text{ mm}^2$) were used for the diamond thin film deposition. First, the samples were cleaned by ultrasonication in acetone for 10 min and in pure isopropyl alcohol for 1 minute. Immediately afterwards, the substrates were mechanically seeded, applying ultrasonic agitation in water based diamond powder suspension (diamond powder from Sigma-Aldrich with an average grains size of 10 nm). The typical seeds density after such process is in range up to 10^{11} cm^{-2} [18]. Diamond films were grown in a modified hot filament chemical vapor deposition (HFCVD) system [19] from a CH_4/H_2 gas mixture at the total gas pressure of 3 kPa and substrate temperature in the range of 600 - 700 °C. The samples labeled as A, B and C were deposited at various CH_4 concentration, i.e. 1, 5 and 10% of CH_4 , respectively. The diamond film surfaces of the prepared samples remained as-grown. Finally, to obtain transparent diamond membranes the middle parts of the silicon substrates were etched by NHA solution ($\text{HF} + \text{HNO}_3 + \text{CH}_3\text{COOH} = 50:3:8$) through a piceine mask. Preparation conditions and basic characterization of all samples are summarized in Table 1. The quality factor f_q , which reflects the ratio of diamond and non-diamond carbon phase was calculated using the formula [20]:

$$f_q = \frac{75S_D}{75S_D + \sum_{ND} S_{ND}} \cdot 100, \quad (1)$$

where S_D characterizes the area under the D-peak in Raman spectra and $\sum_{ND} S_{ND}$ describes areas under all other bands of the Raman spectrum. Ideal monocrystalline diamond sample would have f_q value of 100. Thickness of the prepared diamond films was determined from cross-section SEM measurements and verified by evaluation of the interference fringes in the reflectance spectra measured in visible and near infrared region with use of commercial software for modeling the optical properties of thin films (FilmWizard).

Table 1. Preparation conditions, thickness and quality of samples A, B and C

Sample	A	B	C
CH ₄ conc. [%]	1	5	10
Deposition time [hours]	7	8	4
Thickness [μm]	1.3	7.5	2.1
Quality factor - <i>fq</i>	99	59	40

In the time resolved PL measurements femtosecond light pulses of the Ti-sapphire femtosecond laser (Tsunami 3960, Newport/Spectra-Physics) with the regenerative amplifier Spitfire Pro-F1KXP (Newport/Spectra-Physics) were used for excitation. The second (400 nm) and fourth (200 nm) harmonics of the amplifier output was used. Pulses at 325 nm were generated by parametric amplifier TOPAS (Newport/Spectra-Physics). The parameters of femtosecond pulses were: repetition rate 1 kHz, pulse duration 100 fs, wavelength 400, 325 and 200 nm and fluence 1.3, 0.3 and 0.04 mJ/cm², respectively. It was found that the threshold of photoinduced changes of samples was wavelength dependent so that was not possible to find a common magnitude of pump fluence for all excitation wavelengths leading to a sufficient PL signal and not causing the modification of samples. That is why the magnitude of the pump fluence was chosen as the maximum value not exceeding the photo-modification threshold [21]. The time decay of PL was measured by the streak camera C5680 (Hamamatsu) with a spectral sensitivity range of 200 – 900 nm in the time range of 0.1 ns – 1 ms. We used a cryostat chamber with closed helium circulation system and a cascade of oil and turbomolecular pump for the low pressure (pressure approx. 10⁻³ Pa) and low temperature (to 15K) measurements.

Morphology of the samples was characterized by scanning electron microscope (Zeiss FE SEM Leo 1 550) and the sample composition was studied by Raman spectroscopy (Renishaw In Via Reflex) with the excitation wavelength of 442 nm.

3. Results

3.1. SEM and Raman spectroscopy

Structural characterization and Raman spectra of all three samples are presented in Fig. 1. It is obvious that the samples substantially differ in morphology. Sample A, labeled as microcrystalline diamond (MCD), contains large (~500 nm) randomly oriented diamond grains. Diamond film of sample B has a columnar structure where the height is given by the thickness of the film (7.5 μm). The pores between columns are clearly apparent. Sample C, labeled as nanocrystalline diamond (NCD), reveals a fine structure made of small (≤ 10 nm) nanocrystals. Above mentioned morphologies agree well with the measured Raman spectra. The spectra of all the samples contain a narrow peak at 1 332 cm⁻¹ (D-peak related to sp³ bonds) despite various CH₄ concentration during the deposition. Of course, in comparison with sample A, the characteristic D-peak is strongly reduced in intensity in the spectra of the samples B and C whereas the domination of D-band (1350 cm⁻¹) and G-band (1530 cm⁻¹) features is evident. This effect is characteristic for fine-crystalline/amorphous carbon phases. The signal originating from G- and D- band is usually associated with carbon in sp² phase in any structural formation and situated in ring structural compositions, respectively [16]. Narrow band at 1 150 cm⁻¹ (samples B and C) is related to trans-polyacetylene-like fragments, and is observed with other peaks/bands at 1 332, 1 350 and 1 530 cm⁻¹ in the spectra of a NCD films [22]. Fairly high signal from sp² phase (G-band) observed in the Raman spectra of sample C is caused by using very high CH₄ concentration during the CVD deposition along with a limited etching rate of sp² bonded carbon by atomic hydrogen. Despite these effects it is evident that higher methane concentration in gas mixture during the sample preparation leads to a larger fraction of non-diamond carbon phase and smaller diamond grain sizes due to higher renucleation.

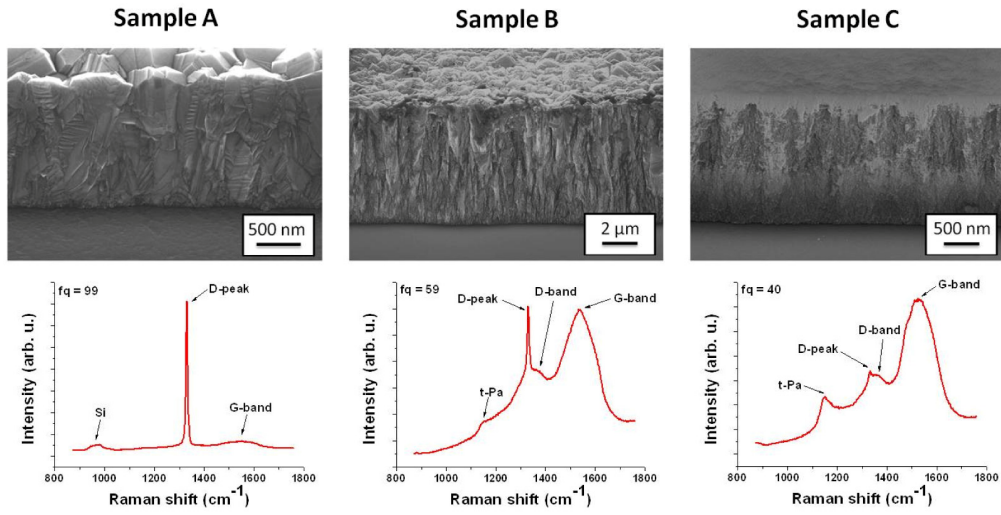


Fig. 1. Cross-section SEM images and corresponding Raman spectra of the diamond films deposited at various methane concentrations (1, 5 and 10% for the samples A, B and C, respectively).

3.2. Time-resolved photoluminescence at room ambient conditions

The PL decays of all samples are shown on log-log scales in Fig. 2. We display the PL dynamics at 460 nm for all three samples at room temperature and atmospheric pressure in Fig. 2(a). PL was excited by femtosecond laser pulses at 325 nm with energy fluence 0.3 mJ/cm². Each decay curve is composed of the data measured piecewise to ensure the best time resolution that is limited by the streak camera response on each time scale. The PL dynamics of the samples are different to each other. The PL signal of sample A is strong in sub/nanosecond time interval and contains an additional slow decay stretching up to 1 ms as shown in Fig. 2(b). The PL signals of other two samples are weaker and much faster and their microsecond signals were at (sample B) or below (sample C) the resolution of the streak camera. The PL decay is non-exponential for all samples. We have found that it can be reproduced well by the stretch-exponential ($c \cdot \exp[-(t/\tau)^{\delta}]$) and power-law ($c \cdot t^{-n}$) functions for

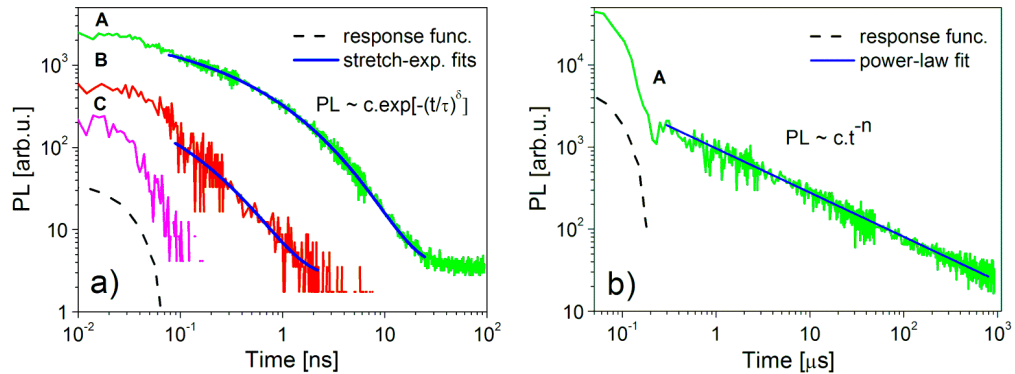


Fig. 2. a) PL decay of samples A, B and C at 460 nm on the sub and nanosecond time scales (nanosecond PL component) b) PL decay of sample A at 550 nm on the microsecond scale (microsecond PL component). Excitation laser pulse parameters: 325 nm, 0.3 mJ/cm². Decays were measured piecewise and for clarity are presented on log-log scale. Dashed curves - streak camera response function (resolution limit). Blue curves - fits of stretch-exponential and power-law functions.

the nanosecond (all samples) and microsecond (sample A) time scales, respectively. The latter appears as a straight-line in the log-log plot (Fig. 2(b)).

Time integrated PL spectra of our samples are displayed in Fig. 3(a). The PL intensities follow the trend discussed in connection with Fig. 2(a) and the spectra differ also in shape. Sample C shows a broad spectral band from approx. 360 to 700 nm (3.44 – 1.77 eV) with maximum at 450 nm (2.75 eV). The spectrum of sample B is located in similar interval. Only the peak is red shifted to approx. 505 nm (2.46 eV). PL spectrum of sample A is about 45 nm red-shifted and approx. 30 times more intense than that of sample B. The maximum is located at 550 nm (2.26 eV). A weak spectrum modulation of sample A is caused by light interference in the diamond membrane as was verified by transmittance measurement (not shown here). The time evolution of PL spectrum of sample A is presented in Fig. 3(b). The spectra were obtained by integrating the signal over the successive time intervals ≤ 0.1 ns, 1-10 ns and 0.1-1 ms. Spectra in Fig. 3(b) clearly show a gradual spectral shift towards the longer wavelengths with increasing time. We can see a good agreement between the spectra of samples B and C (Fig. 3(a)) and time resolved spectra of sample A (Fig. 3(b)) in corresponding time windows. PL of sample C decays very fast and can be detected only during the initial sub nanosecond time interval which results in its spectrum corresponding well to that of sample A in the same time window. This analysis shows that although the PL nanosecond component of sample A is stronger than those of the other samples, its time integrated spectrum is dominated by the microsecond component. This example clearly demonstrates benefits of time resolved PL in wide time interval, when simple comparison of standard PL for our samples could lead to rather confusing interpretations.

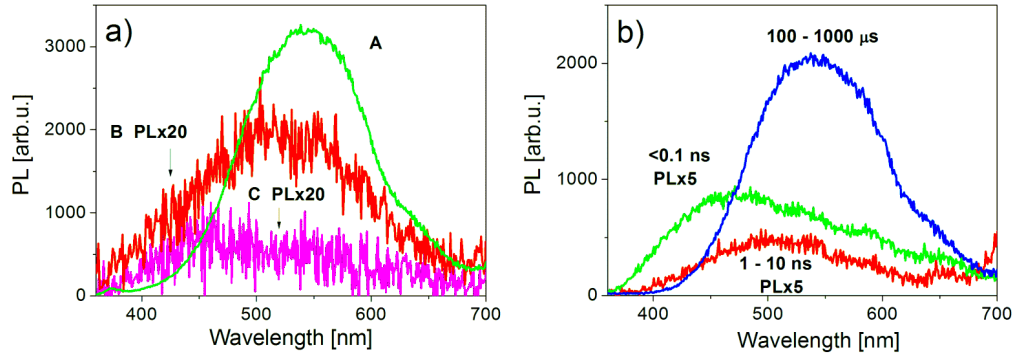


Fig. 3. a) Time integrated spectra of samples A, B and C. b) Time resolved spectra of sample A. For clarity were selected PL spectra multiplied by appropriate constant. Parameters of excitation laser pulses: 325 nm, 0.3 mJ/cm².

We measured also the PL dynamics at different wavelengths within the PL spectrum of sample A which has the most intense PL. We have found that the nanosecond PL decay does not depend on the wavelength in the interval from approx. 400 to 660 nm as shown in Fig. 4(a). The PL decays measured at the lower wavelengths (≤ 400 nm) showed intensity increase in time interval ≤ 0.1 ns that could be caused by the presence of additional radiative recombination mechanism with time constant under the camera resolution. On the other hand, the microsecond PL decay was spectrally dependent in the whole spectral interval being faster at shorter wavelengths. This decay can be fitted well by the power-law decay function for all wavelengths (see Fig. 2(b) for the data fit at 550 nm). The obtained values of the power-law coefficient n in dependence on PL photon energy are shown in Fig. 4(b). The spectral dependence of the coefficient can be approximated very well by an exponential function $n \sim \exp(E/E_0)$ with $E_0 = 0.90$ eV. This spectral dependence is nearly the same as that found in ultrafast initial decay in NCD membranes [13, Fig. 5].

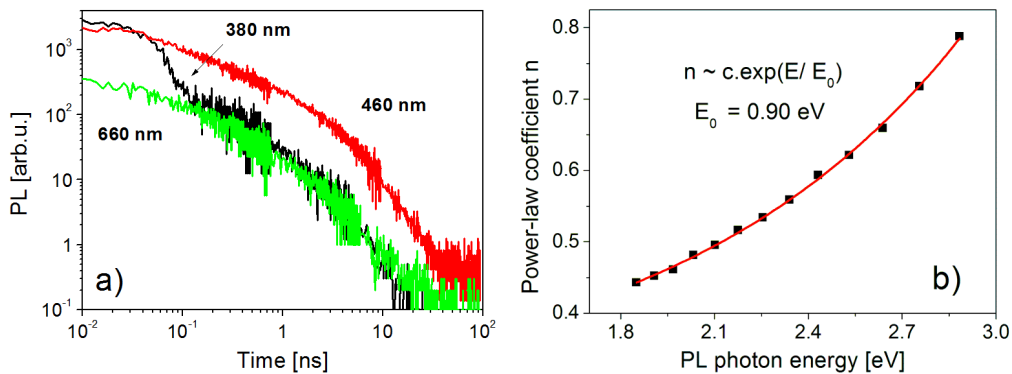


Fig. 4. a) Spectral dependence of sample A PL decay (nanosecond component). b) Spectral dependence of power-law coefficient n of sample A (microsecond component). Parameters of excitation laser pulses: 325 nm, 0.3 mJ/cm².

3.3. Time-resolved photoluminescence - temperature and pressure dependence

To obtain complete information about carrier dynamics the temperature dependence of PL decay on sample A was studied. The PL decay was measured in the interval of 15 K – 300 K. PL was excited by femtosecond pulses at the wavelength of 325 nm. The results are shown in Fig. 5 on the log-log scale. We have observed that the nanosecond decay is slowing down with cooling the sample from room temperature down to approx. 240 K (Fig. 5(a)). The dynamics are not changing with further cooling. The microsecond part of PL decay maintains its power-law shape with nearly unchanged coefficient n in the whole interval of temperatures (Fig. 5b).

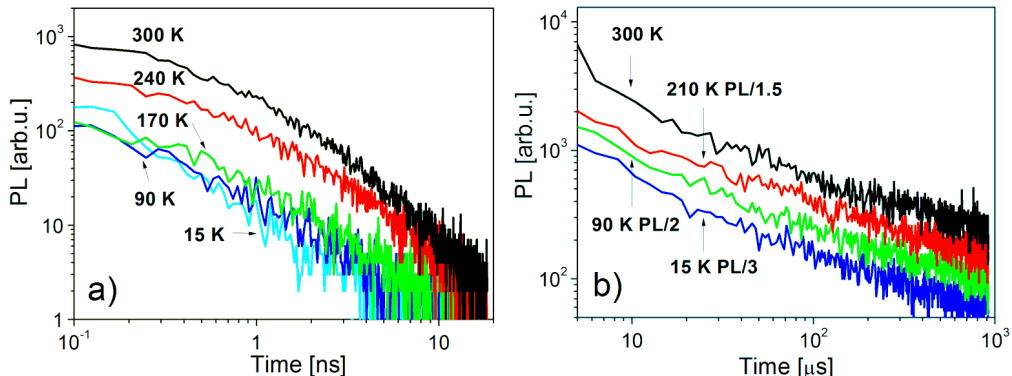


Fig. 5. a) Temperature dependence of sample A PL decay in nanosecond time interval measured at 500 nm (maximal intensity). b) Temperature dependence of sample A PL decay in microsecond time interval measured at 550 nm. Parameters of excitation laser pulses: 325 nm, 0.3 mJ/cm². For clarity specific PL spectra were divided by appropriate constant.

The time integrated PL signals of the nanosecond and microsecond PL parts display different temperature behavior (Fig. 6). The PL signal integrated over the initial time interval to 20 ns decreases strongly with decreasing temperature down to 200 K, which correlates with the temperature dependence of PL dynamics. On the other hand the signal integrated from 0.05 to 1 ms changes only weakly in the whole range of temperatures.

We carried out also the PL measurements under low pressure of about 0.001 Pa. We observed apparently no effect of ambient pressure on the PL decay shapes for all samples. The only PL property that was affected by the pressure was the time integrated intensity as shown in Fig. 7. While the magnitude of the microsecond PL component increased only by units of percent (Fig. 7(b)), the amplitude of the nanosecond PL component almost doubled

for sample A after the pressure reduction (Fig. 7(a)). On the other hand, only small or even no PL intensity change was observed in the case of sample C.

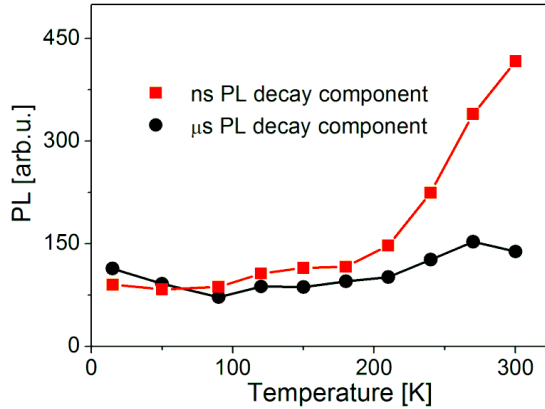


Fig. 6. Temperature dependence of time integrated PL spectra of nanosecond and microsecond components of sample A at 500 and 550 nm, respectively. Parameters of excitation laser pulses: 325 nm, 0.3 mJ/cm². For clarity the microsecond component was rescaled to match the nanosecond component at low temperatures.

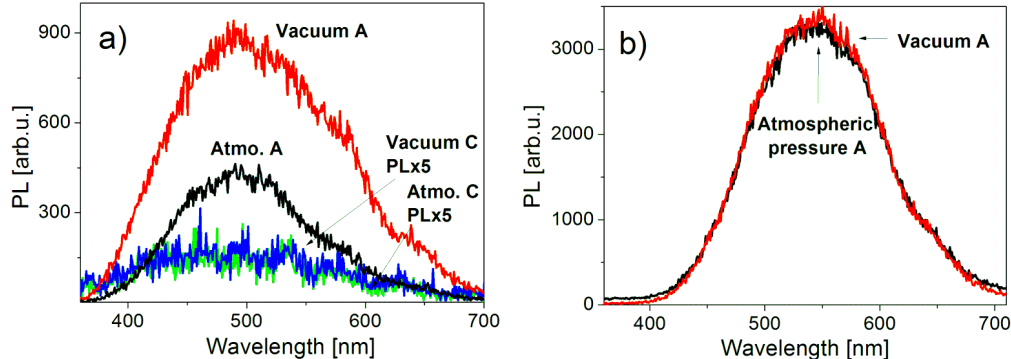


Fig. 7. a) Influence of air pressure to time integrated spectra of nanosecond PL component of the samples A and C. b) Influence of air pressure to time integrated spectra of microsecond PL component of sample A. Label “vacuum” corresponds to the pressure 0.001 Pa. Parameters of excitation laser pulses: 325 nm, 0.3 mJ/cm².

3.4. Time-resolved photoluminescence - excitation wavelength and fluence dependence

We have also investigated the behavior of PL in dependence on the excitation wavelength. In Fig. 8 we compare the PL spectra of the nanosecond and the microsecond PL of sample A under different excitation wavelengths, namely 200 nm (6.2 eV), 325 nm (3.8 eV), and 400 nm (3.1 eV). The spectrum of the nanosecond PL component shown in Fig. 8(a) was obtained by integration of the spectrally resolved PL signal over the initial time interval to 20 ns. In Fig. 8(b) we display the spectrum of the microsecond PL component that was integrated over the time interval from 0.05 to 1 ms. In these measurements, the excitation intensity was smaller for shorter wavelengths (about 30 times) and the absorption of sample increases for shorter wavelengths. That is why one cannot correctly compare the PL scaling for different wavelengths of excitation. However, there is a striking difference between the behaviors of both PL parts. The spectrum of the nanosecond component decreases in a magnitude and shifts towards shorter wavelengths with decreasing excitation wavelength whereas the spectrum of the microsecond PL component increases in the magnitude and neither changes

its spectral position nor PL decay. The comparison of spectra in Fig. 8(a) and Fig. 8(b) indicates unambiguously different origin of both PL components.

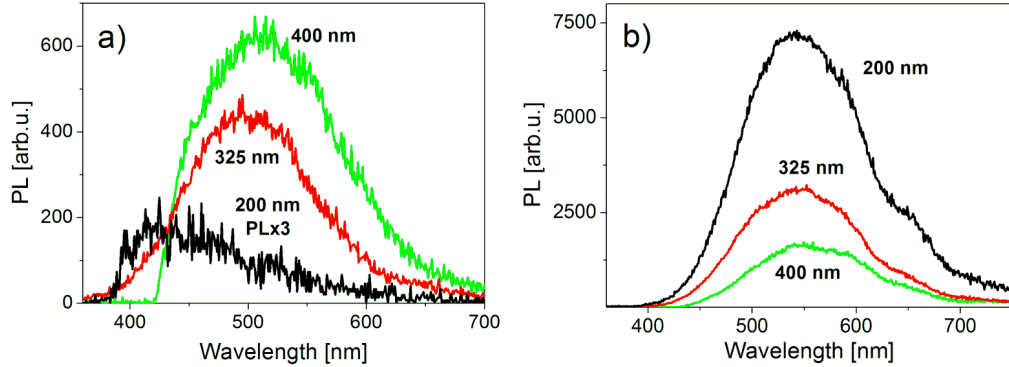


Fig. 8. a) Time integrated spectra of nanosecond PL component of sample A (time interval to 20 ns). b) Time integrated spectra of microsecond PL component of sample A (time interval from 0.05 to 1 ms). Excitation wavelengths were 400 nm, 325 nm and 200 nm with fluence of 1.3 mJ/cm², 0.3 mJ/cm² and 0.04 mJ/cm², respectively.

To confirm this conclusion we have also studied the influence of the excitation fluence on PL for above and below the diamond band gap energy (approx. 5.5 eV). We used excitation wavelengths 325 and 200 nm with the pulse fluencies 0.05 – 0.62 mJ/cm² and 0.001 – 0.1 mJ/cm², respectively. Unlike in the previous experiments, the nanosecond PL component is integrated over the time interval from 1 to 20 ns in order to ensure equal detection conditions on all excitation fluencies. Results for sample A are shown in Fig. 9. We observed that the PL decay and the associated shape of the time integrated spectrum of nanosecond component was not affected by the fluence changes at 325 nm (Fig. 9(a), inset), and the time integrated PL intensity was increasing linearly with the fluence (Fig. 9(a)). The nanosecond part of the measured PL under 200 nm excitation wavelength was rather weak and the measurement of fluence dependency was not possible. The microsecond PL component scaled also linearly with the pump fluence under the excitation at 325 nm while it exhibited saturation for fluences above approximately 0.02 mJ/cm² in the case of 200 nm excitation. The

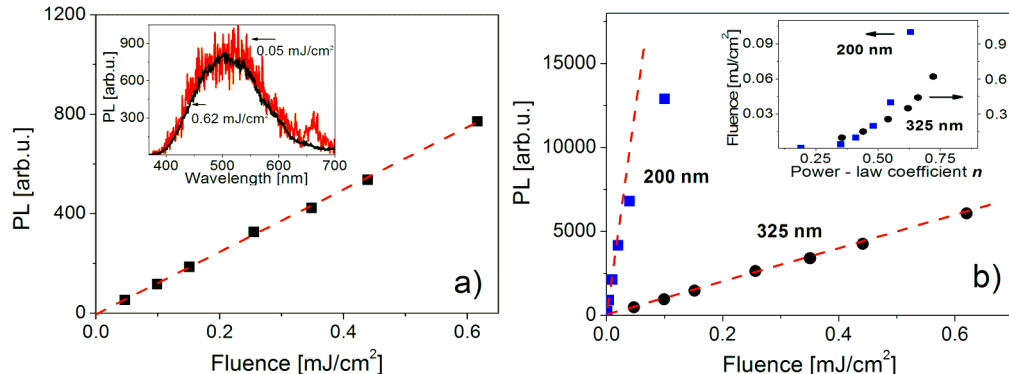


Fig. 9. a) Dependence of pulse fluence on PL intensity of sample A nanosecond component at 500 nm. PL was excited at 325 nm. Inset: time integrated PL spectrum of sample A nanosecond component excited by fluence of 0.62 mJ/cm² and 0.05 mJ/cm² (normalized). b) Dependence of excitation intensity on PL intensity of sample A microsecond component at 550 nm. PL was excited at 325 and 200 nm. Inset: fluence dependence of the power-law coefficient *n*.

microsecond decay rate was also affected by excitation fluence speeding up for a stronger pumping. However, the shape of the decay was still of the power-law type for both excitations

at 200 nm and 325 nm. The power-law coefficient n was thus found to be a function of excitation fluence as shown in the inset of Fig. 9(b). The spectral shape of time integrated spectra of microsecond PL component was also independent of excitation fluence at both excitation wavelengths (data are not presented).

4. Discussion

Our results indicate that the behavior of initial nanosecond PL of studied MCD/NCD samples differs from that observed in microsecond time region. Therefore the underlying microscopic origin and/or energy states seem to be different. The overall PL decay is nonexponential. The nanosecond decay can be described well by the stretched-exponential function (Fig. 2(a)) and the microsecond decay can be fitted by the power-law decay function (Fig. 2(b)). The PL evolution described by stretched-exponential function is usually interpreted as a multiexponential decay and is being observed when one PL source is changing its lifetime in time [23] or when there are similar sources with different lifetimes [24]. The physical meaning of stretch-exponential coefficient τ is then the mean decay time. The power-law decay is well-known from the dynamics of carriers in disordered systems (amorphous or nanocrystalline materials) where the carriers separation occurs [25, 26]. The carrier survival probability in a site due to the trapping process into randomly distributed traps can be indeed described by the power-law function, see [27]. The power-law coefficient n should scale with the separation of the traps, i.e. with the relevant density of states. This means that the values of n for PL decay curves at various photon energies reflect the energy dependence of number of the states. This indicates that the sites responsible for microsecond PL component are exponentially distributed in energy (see Fig. 4(b)) with density increasing with increasing energy (“exponential tail”). The time integrated spectra of nanosecond and microsecond components do not differ substantially (Fig. 3), but the red spectral time evolution is clearly apparent in accord with nanosecond PL decay at shorter wavelengths. The maximum photon energy of nanosecond PL (about 3.4 eV) corresponds to the energetic distance between $\pi-\pi^*$ states of carbon sp² phase as measured on NCD by photothermal deflection spectroscopy [11, 22, 28]. Moreover, the time coefficient τ of sample A (~ 0.19 ns) agrees well with the results published by Plakhotnik et al. [15] that interpreted PL with lifetime ≥ 0.5 ns as a radiative recombination in non-diamond carbon content around diamond grains. The presence of additional radiative recombination mechanism with fast time constant (≤ 100 ps) in nanosecond PL at short wavelengths can be also interpreted as over band gap recombination between $\pi-\pi^*$ states of carbon sp² phase (Fig. 4a).

The process related to the nanosecond decay is thermally activated (see Fig. 6). The thermal activation leads to releasing of the trapped carriers which can in turn radiatively recombine as indicated by an intensity increase and decay acceleration of the nanosecond PL component for higher temperatures (Fig. 5(a)). Very weak temperature dependence of the microsecond power-law-like decay suggests a negligible role of thermal activation (higher energy barriers or another process) between the carrier sites (Fig. 5(b)). The negligible thermal effect, power-law shape of PL decay realized also over 1 milisecond and coefficient $n < 1$ indicate that the tunneling of trapped carriers could be the recombination mechanism responsible for microsecond PL [29, 30]. Based on this assumption the fluence dependence of power-law coefficient presented in the inset of Fig. 9b can be interpreted as follows. Increasing pulse fluence results in a higher occupation of trap sites and consequently to an increased overlap of wavefunctions of trapped carriers. This would cause an acceleration of tunneling process that is for power-law decaying PL expressed by increasing a magnitude of coefficient n . Different change of time integrated PL intensity of both PL components in response to the change of excitation wavelength indicates a different way of filling the energy states corresponding to the appropriate PL components (Figs. 8(a), and 8(b)). The energy states related to the microsecond component seem to be accessible well by photocarriers from bulk diamond created during over band gap excitation (a large increase in intensity between 325

nm and 200 nm that exceeds the bulk diamond band gap) that is in the contrast to results observed for nanosecond PL component. The energy sites responsible for microsecond PL are also shielded from the ambient atmosphere (Fig. 7(b)) or are not sensitive to the influence of adsorbates [13, 31]. For these reasons these states can be likely situated on the surface of diamond grains or directly inside the grains. The latter option, however, seems unlikely according to the results presented in Fig. 9(b), i.e. the PL intensity saturation of microsecond PL with relevant n value about 0.5 for the excitation at 200 nm. If we interpret the PL intensity saturation in terms of trap site filling, the traps are getting full while the overlap of carriers wavefunctions is not as high as in the case of excitation at 325 nm ($n \sim 0.7$ and no PL intensity saturation). This implies that not all trap sites are easily accessible for the carriers from the bulk diamond and therefore will be unlikely located inside the diamond grains. Despite all the differences we expect that the origin of states responsible for microsecond PL component should be similar to the states connected with the nanosecond PL due to the similar PL spectrum (Fig. 3).

4.1 Structural and energy states model for high f_{q} diamond

Based on these results and reported data on polycrystalline diamond and amorphous carbon we introduce a simplified structural model and a scheme of energy states of microcrystalline diamond with high f_{q} (Fig. 10). Our three studied samples were prepared at various CH_4 concentrations in order to obtain MCD/NCD films of different fraction of non-diamond carbon phase and different morphology as can be seen in Fig. 1.

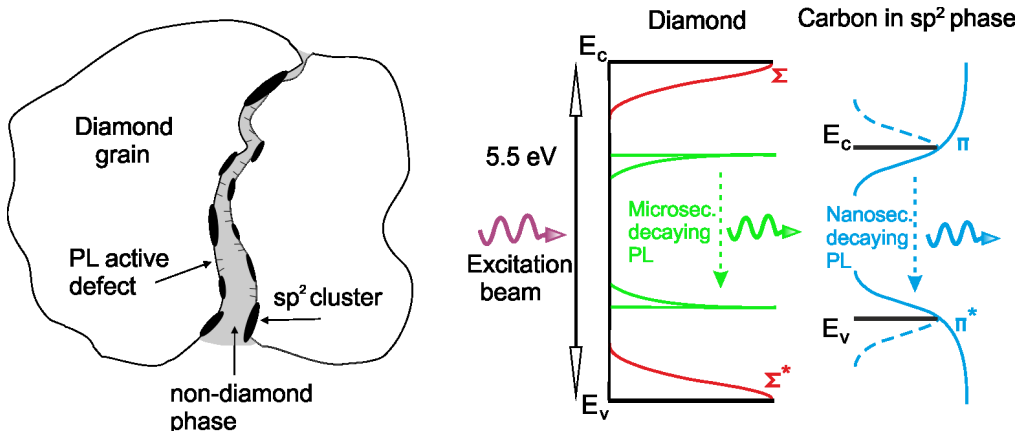


Fig. 10. a) Schematic model of NCD structure for high f_{q} . b) Simplified model of energy states in microcrystalline diamond for high f_{q} .

For small concentration of CH_4 the sample contains large diamond grains and small amount of non-diamond matter. The latter is supposed to consist of the sp^2 clusters [32], structures of graphitic origin localized at the grain surface and other unspecified form of carbon in non-diamond phase filling the space between diamond grains (Fig. 10(a)). Similar structure of NCD was also proposed by Dzurňák et al. [21]. The localization of carbon in sp^2 phase responsible for nanosecond PL in differently sized clusters (various lifetimes of PL) is in good agreement with the stretch-exponential shape of the decay.

The scheme of energy states is composed of the bulk diamond band of diamond grains (volume states), diamond Σ states that are generally accepted as a diamond tail states caused by carbon atoms in sp^3 phase deformed on grain surface, the exponentially decaying trap states on diamond surface (microsecond PL) and separated sp^2 carbon phase located in clusters presented by $\pi-\pi^*$ states that we assume should be responsible for nanosecond PL (Fig. 10(b)). In fact, the NCD is a composite material and as discussed the interaction of sp^2 and diamond grains is questionable so we have spatially separated the states linked to sp^2

carbon phase from bulk diamond. In the scheme we have neglected the presence of unspecified form of carbon in non-diamond filling the space between diamond grains, because it should not be source of intense PL [32]. We are aware that this carbon will absorb incident light and therefore might play role in filling of energetic states in sp^2 clusters and in the charge transport between the clusters, but this effect is clearly not apparent from any measurement we have made. Unlike the other authors we are not expecting that the $\pi - \pi^*$ states would have only Gaussian shape of density of states (DOS) [28]. We assume that the density of states continue increasing after crossing the gap about 3.4 eV (Fig. 10(b) – Full blue curve). This energetic structure is in good agreement with results gained by photothermal deflection spectroscopy [28] and photoconductivity measurements [33] on NCD. These measurements commonly fit perfectly to Gaussian density of π states till the value about 3 eV, but the absorption or photoconductivity signal never decrease when the energy of incident light cross the π states gap. This discontinuity is usually explained by the presence of diamond $\Sigma - \Sigma^*$ tail states transition at higher energies that compensate the decrease of π DOS. However these states should be spatially separated from sp^2 carbon and therefore the intensive filling of $sp^2 \pi$ states by electrons and holes from Σ tail that would be necessary for interpretation of Fig. 8(a) is based on our previous discussion rather questionable. Moreover we did not observe any PL signal in the interval of wavelengths from 350 nm to diamond band gap (3.4 – 5.5 eV) after excitation at 200 nm so we cannot confirm an influence of sigma states to presented phenomena. Moreover, the density of π states presented in our model could easily interpret the lack of PL in UV region (fast relaxation of photoexcited charge carriers in the region of continuous density of states to gap energies and tail) as well as properties of nanosecond PL part excited by different excitation wavelengths. Laser pulses at 400 nm (3.1 eV) can excite charge carriers only to tail of π states where they are well localized what results in PL maximum around 510 nm. Excitation at 325 nm (3.8 eV) has enough energy to excite carriers over the π state band gap. The carriers are free after excitation, but are limited by the size of sp^2 clusters as observed in recent conductivity measurements [34]. However these carriers have a higher probability to be spatially separated that will cause accelerating of PL decay. This effect is further amplified when the excitation at 200 nm is used. We interpreted already our previous results on picosecond PL decay in nanocrystalline diamond in terms of the spatial separation of the electron and hole of a photoexcited electron-hole pair by trapping of one of the carrier by a surface trap [14].

4.2 Structural and energy states model for low f_q diamond

According to this discussion and our results, we propose following structural model and model of energy states also for samples with lower f_q (Fig. 11). A higher CH_4 concentration in the gas mixture during the preparation results in an increase of fraction of non-diamond carbon phase and in a decrease of diamond grain size, i.e. the growth of NCD (Fig. 1 – sample C). Both effects could cause increasing size of sp^2 clusters, higher probability of their mutual penetration and a further distortion of clusters by other forms of non-diamond phase (Fig. 11(a)). It is also evident that the creation of specific defects that are sources of microsecond PL requires the CVD process at low methane concentration (Fig. 2(b) and Table 1). This could be interpreted in the term of specific preparation conditions for their formation or higher covering of grain surface by sp^2 clusters that would limit the creation of mentioned defects on the diamond grain surface. Considerable decrease of microsecond PL at samples B and C in contrast to A could be also linked to its recombination mechanism. Tunneling effect is significantly dependent on a distance of the closest carriers and therefore the amount of trap size could scale greatly with the total PL intensity.

Although the concentration of sp^2 is increasing (decrease of f_q) the intensity of nanosecond PL decreases (Fig. 11(b)) and its decay gets faster: $\tau \sim 0.19$ and 0.05 for sample A and B, respectively. (Figs. 1, 2(a) and 3(a)). This phenomenon can be explained by the increased number of non-radiative decay channels in the low quality samples. An important

role in the PL acceleration would play the change of sp^2 cluster shape and their mutual connection with decreasing quality of NCD that would decrease localization of trapped charge carriers and allow their easier spatial separation. Also the increasing concentration of non-diamond phase in NCD could cause shielding of sp^2 clusters from ambient (Fig. 7(a)) that would result in insensitivity to change of air pressure of nanosecond PL in contrast to the microcrystalline diamond, i.e. the sample with high f_q (Fig. 7(a)).

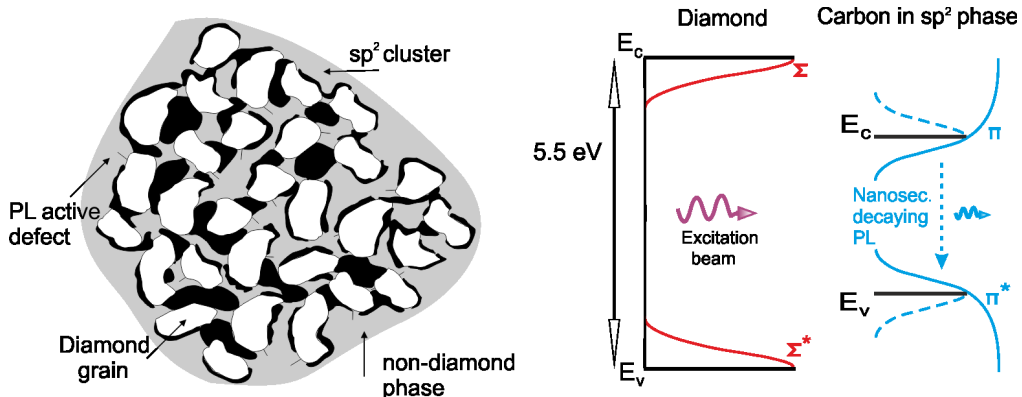


Fig. 11. a) Schematic model of NCD structure for low f_q . b) Simplified model of energy states in nano-crystalline diamond for low f_q .

In our model, we have not included explicitly the role of color centers the presence of which in the samples cannot be excluded. However, our experimental results do not seem to reflect the known features of dopant-related centers (spectral shape, lifetime, dependence to experimental parameters).

5. Conclusion

MCD/NCD diamond films containing various amount of non-diamond phase were studied by time resolved PL, Raman spectroscopy and SEM. We have presented that increase of CH₄ in gas mixture during preparation cause increase of non-diamond phase and decrease of diamond grains. We have showed that PL of microcrystalline diamond (sample A) with low concentration of non-diamond carbon phase is composed of two independent PL components. PL decay of these components was observed in sub nanosecond and microsecond time scales and followed the stretch-exponential and power-law dependence, respectively. Properties of both PL components were studied at different stages of decay, with a wide range of excitation wavelengths and fluencies, at ambient conditions, as well as at low pressure and temperatures. We have also demonstrated that increasing concentration of non-diamond carbon phase and structural changes in MCD/NCD are causing a quenching of microsecond PL and acceleration of nanosecond PL decay. Characterization of PL decay by power-law and stretched-exponential laws and establishing dependence of relevant coefficients on experimental parameters made it possible to map the MCD/NCD carrier dynamics in a fairly complex parameter space. Based on these results we have proposed the structural model and model of energetic states for diamond films with high and low quality factor f_q . We interpret the nanosecond PL in terms of radiative recombination between $\pi - \pi^*$ states of sp^2 carbon phase localized in clusters between diamond grains. The microsecond PL is most probable caused by tunneling between sites of non-diamond carbon origin on the diamond grain surface. The change of preparation conditions leading to lower quality factor of NCD is preventing the formation of the tunneling sites and causing structural changes of sp^2 clusters that result in easier spatial separation of photo-generated carriers in sp^2 . Presented comprehensive model of structural and energy states of MCD/NCD describing well the influence of non-diamond carbon phase on photoluminescence and recombination properties of diamond contributes to

understanding a manifold of often apparently contradictory published results of measurements of MCD/NCD prepared by different preparation methods.

Acknowledgments

Authors would like to acknowledge the kind assistance of M. Michalka for SEM and B. Rezek for theoretical consultations about presented phenomenon. This work was supported by Charles University in Prague grant SVV-2013-265306, by GAUK 151910/2012, GAČR projects no. 13-12386S, P108/12/G108, and Slovak Research and Development Agency under the contract No. APVV-0365-12.

RESEARCH ARTICLE | DECEMBER 11 2014

Electrochemically grafted polypyrrole changes photoluminescence of electronic states inside nanocrystalline diamond

P. Galář ; J. Čermák; P. Malý; A. Kromka; B. Rezek 



Journal of Applied Physics 116, 223103 (2014)

<https://doi.org/10.1063/1.4903937>



CrossMark

Articles You May Be Interested In

Distribution of NCDS datasets on CD-ROM

AIP Conference Proceedings (August 1993)

Synthesis of novel Ag@NG-PPy nanocomposite by *in-situ* oxidative polymerization method

AIP Conference Proceedings (April 2019)

Electrical properties of covalently linked silicon/polypyrrole junctions

Appl. Phys. Lett. (June 1999)

500 kHz or 8.5 GHz?
And all the ranges in between.

Lock-in Amplifiers for your periodic signal measurements



[Find out more](#)



Electrochemically grafted polypyrrole changes photoluminescence of electronic states inside nanocrystalline diamond

P. Galář,^{1,a)} J. Čermák,² P. Malý,¹ A. Kromka,² and B. Rezek²

¹Faculty of Mathematics and Physics, Charles University in Prague, Ke Karlovu 3, Prague 121 16, Czech Republic

²Institute of Physics ASCR v.v.i., Cukrovarnická 10, Prague 160 00, Czech Republic

(Received 1 September 2014; accepted 22 November 2014; published online 11 December 2014)

Hybrid diamond-organic interfaces are considered attractive for diverse applications ranging from electronics and energy conversion to medicine. Here we use time-resolved and time-integrated photoluminescence spectroscopy in visible spectral range (380–700 nm) to study electronic processes in H-terminated nanocrystalline diamond films (NCD) with 150 nm thin, electrochemically deposited polypyrrole (PPy) layer. We observe changes in dynamics of NCD photoluminescence as well as in its time-integrated spectra after polymer deposition. The effect is reversible. We propose a model where the PPy layer on the NCD surface promotes spatial separation of photo-generated charge carriers both in non-diamond carbon phase and in bulk diamond. By comparing different NCD thicknesses we show that the effect goes as much as 200 nm deep inside the NCD film.

© 2014 AIP Publishing LLC. [<http://dx.doi.org/10.1063/1.4903937>]

I. INTRODUCTION

NCD has many unique properties of the bulk diamond which can be in addition affected by the presence of the grain boundaries and of the non-diamond carbon phase between the diamond grains.^{1,2} This leads to creation of new energy states inside diamond band gap (5.5 eV) that among others contribute to optical absorption and luminescence of NCD in visible spectral range. Unlike monocrystalline diamonds the NCD can be deposited in thin films also over large area and on almost arbitrary substrates. This extends wide spectrum of synthetic diamond applications in chemical sensing,^{3,4} biological sensing^{2,5} as well as opto-electronic devices.^{6,7} Hybrid NCD-organic interfaces are beneficial and often fundamental for many of these applications.^{5,8} Promising category of such hybrid interfaces is diamond modified by optically and electronically active macromolecules or conjugated polymers.^{6,7,9} Typical example is PPy that also exhibits good biocompatibility, chemical sensitivity and good stability under ambient conditions. PPy can be electrochemically deposited on diamond substrates in layers of few to hundreds of nanometers thickness. Unlike on oxidized diamond surfaces¹⁰ the electrochemical deposition on H-terminated diamond creates covalent bond between the PPy and diamond substrate.⁶ This provides strong binding and is beneficial for opto-electronic interactions. These interactions were already evidenced by photocurrent, photovoltage, and Hall effect measurements.⁶ However, direct optical evidence of charge separation in such system was not yet reported.¹¹

Optical and especially time-resolved photoluminescence (PL) spectroscopies are one of the most suitable techniques to provide insight into the mechanism of charge generation, recombination, and transport inside the nanostructured and

composite materials.^{12,13} In this work we build upon our previous study¹³ where we showed that NCD membrane PL dynamics are composed of two time separated parts (μ s and ns time range) regardless of the excitation wavelength. We focused on the interpretation of the PL origin and characterization of NCD sub-gap states in general. By using the time-resolved PL measurements we show here that these optical and opto-electronic properties of NCD can be significantly and reversibly modified by a thin PPy layer grafted on top of the NCD film. We take advantage of the electrochemically prepared PPy that has negligible own photoluminescence in spite of strong light absorption in the whole visible spectrum.¹⁴ We present structural and energy models of NCD modified by PPy layer and discuss potential implications of these results for energy conversion and electrical control of diamond color centers.

II. EXPERIMENTAL

Two NCD films labeled as A and B were prepared in AIXTRON reactor (P6) by microwave plasma enhanced chemical vapor deposition (PECVD) technique on fused silica substrate (Suprasil 2000). Prior to diamond film growth the substrates (10 mm × 10 mm) were treated by the seeding procedure applying ultrasound agitation in diamond powder suspension (5–10 nm, NanoAmindo, New Metals and Chemicals Corp. Ltd., Kyobashi).¹⁵ Our study confirmed that at optimal process conditions this technique can result in the seeding density as high as 10^{11} cm^{-2} . Preparation conditions for samples A/B were – 1% methane diluted in hydrogen (300 sccm), microwave power 2500/1500 W, gas pressure 50 mbar, substrate temperature 450 °C and deposition time 2/8 h. Samples were subsequently terminated by hydrogen in the same reactor for 10 min at 500 °C. Average thickness of the NCD layers A/B was $(170 \pm 11) \text{ nm}/(920 \pm 56) \text{ nm}$ and the layer roughness was $(14 \pm 1) \text{ nm}/(47 \pm 1) \text{ nm}$, respectively. The thickness of the samples was

^{a)}Author to whom correspondence should be addressed. Electronic mail: pavel.galar@mff.cuni.cz

determined by scanning electron microscopy (SEM-Maia 3, Tescan Ltd.) and the roughness was determined by atomic force microscopy (AFM-Ntegra, NT-MDT), see Figs. 1(a) and 1(c). SEM was equipped with a Schottky field emission gun, 60° immersion objective lens and beam deceleration technology. AFM was working in semicontact mode using a silicon cantilever with Al reflective coating (BSTap300Al-G, BudgetSensors). NCD quality factors f_q that reflect the ratio of diamond and non-diamond carbon phase inside diamond samples were calculated from Raman spectra¹⁶ (excitation wavelength 325 nm/3.8 eV) by using the formula¹⁷

$$f_q = \frac{75S_D}{75S_D + \sum_{ND}S_{ND}} \times 100, \quad (1)$$

where S_D characterizes the area under the D-peak in Raman spectra and $\sum_{ND}S_{ND}$ describes areas under all other bands of the Raman spectrum. f_q of sample A and B were 95 and 97, respectively (f_q of monocrystalline diamond would be 100). PPy was electrochemically synthesized on the NCD films from solution of pyrrole (240 mM; Aldrich) and NaCl (100 mM) in deionised water. The electrochemical deposition was performed in the area of 2 mm² in galvanostatic regime by applying the current of 2 μA for 150 s between the substrate and the counter electrode (Pt) using a potentiostat/galvanostat (Autolab PGSTAT302). Volume of the solution was 0.3 μl. After the PPy deposition the sample was rinsed by deionised water and dried by compressed air. Average thickness of the PPy layers on sample A and B were (163 ± 20) nm and (141 ± 26) nm, respectively, as was determined by SEM (Figs. 1(b) and 1(d)).

For the time-resolved PL measurements the Ti-sapphire femtosecond laser (Tsunami 3960, Spectra-Physics) with the regenerative amplifier (Spitfire Pro-F1KXP, Spectra-Physics) was used. The parameters of femtosecond pulses were: repetition rate 1 kHz, pulse duration 100 fs, wavelength 200 and 400 nm and fluence 0.04 and 1.3 mJ/cm², respectively. The samples were excited by the second (400 nm ∼ 3.1 eV) and fourth (200 nm ∼ 6.2 eV) harmonics of the amplifier in order to characterize the dynamics of

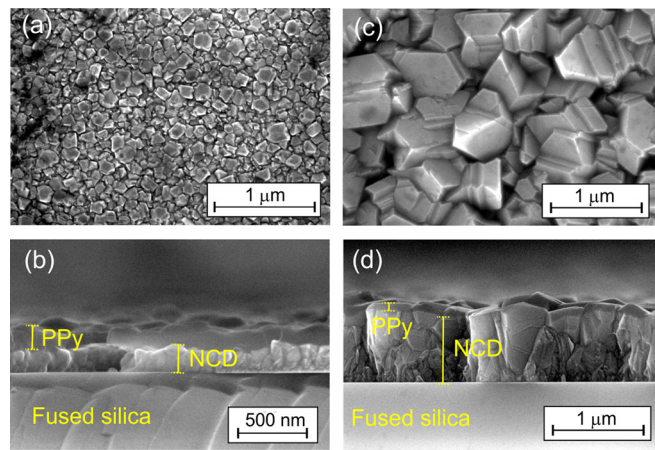


FIG. 1. (a) Top view of NCD sample A (170 nm thickness) without PPy; (b) Cross-section of the sample A with deposited PPy layer; (c) Top view of NCD sample B (920 nm thickness) without PPy; (d) Cross-section of the sample B with deposited PPy layer.

charge carriers photogenerated in both bulk diamond and sub-gap states. The pump fluence values were chosen as the maximal values that do not cause photoinduced changes of the NCD and PPy on the appropriate wavelength. Because of the high absorption of visible light in PPy the NCD film was excited from the substrate side. The PL was measured also from that side of the substrate. Decay of PL was measured by the streak camera C5680 (Hamamatsu) that allows signal detection in spectral range from 200 (6.2 eV) to 900 nm (1.38 eV) and in the time range from 0.1 ns to 1 ms with the highest time resolution of approximately 100 ps.

III. RESULTS

To evaluate the influence of PPy presence on NCD PL properties we have focused on monitoring the change of PL decay shape and intensity/shape of time-integrated PL spectra after PPy deposition. We have studied these changes separately for microsecond and nanosecond PL decay components on basis of our previous results.

Fig. 2 shows the PL time decay measurements of pristine and functionalized NCD of both samples at room temperature and atmospheric pressure in nanosecond time range. Decays of PL and time-integrated spectra (inset) of sample A excited by 400 nm laser pulses are presented on log-log scale in Fig. 2(a). While the decay of pristine sample A can be reproduced well by the stretch-exponential function ($c \cdot \exp[-(t/\tau)^{\delta}]$) the functionalized part of the NCD shows the power-law decay ($c \cdot t^{-n}$) that is linear in log-log scale. The NCD functionalization by PPy causes also blue spectral shift (~20 nm) and intensity decrease (about 3.5 times) of the time-integrated PL spectrum, see Fig. 2(a) inset. Similar behavior of PL was observed also after excitation by 200 nm laser pulses, although the changes are not that pronounced due to the weaker signal (Fig. 2(b)). PL of electrochemically deposited PPy is negligible¹⁴ at both excitation wavelengths and time range and it is not visible in these spectra.

Figs. 2(c) and 2(d) show PL decay and time-integrated spectra (inset) measured on sample B. The PL decay of pristine sample B excited by 200 and 400 nm laser pulses can be approximated with a good accuracy by a stretch-exponential function similarly as for sample A. However, in the case of sample B we did not observe noticeable effect of PPy on the PL decay. This can be clearly seen after normalization with respect to the beginning of the decay (Figs. 2(c) and 2(d)). We have also not detected any change of spectral shape of time-integrated spectra for both excitation wavelengths. The only change of time integrated spectra of sample B in nanosecond range was about 2.5 times decrease in the PL intensity for both excitation wavelengths (Figs. 2(c) and 2(d), inset).

The PL decay measurements of pristine and functionalized NCD of both samples at room temperature and atmospheric pressure in microsecond time range are presented in Fig. 3. In this case, the shape of PL decays and time-integrated spectra of pristine and functionalized NCD do not significantly differ for both samples and at both excitations (200 and 400 nm). All observed PL decays are non-exponential and can be approximated well by power-law

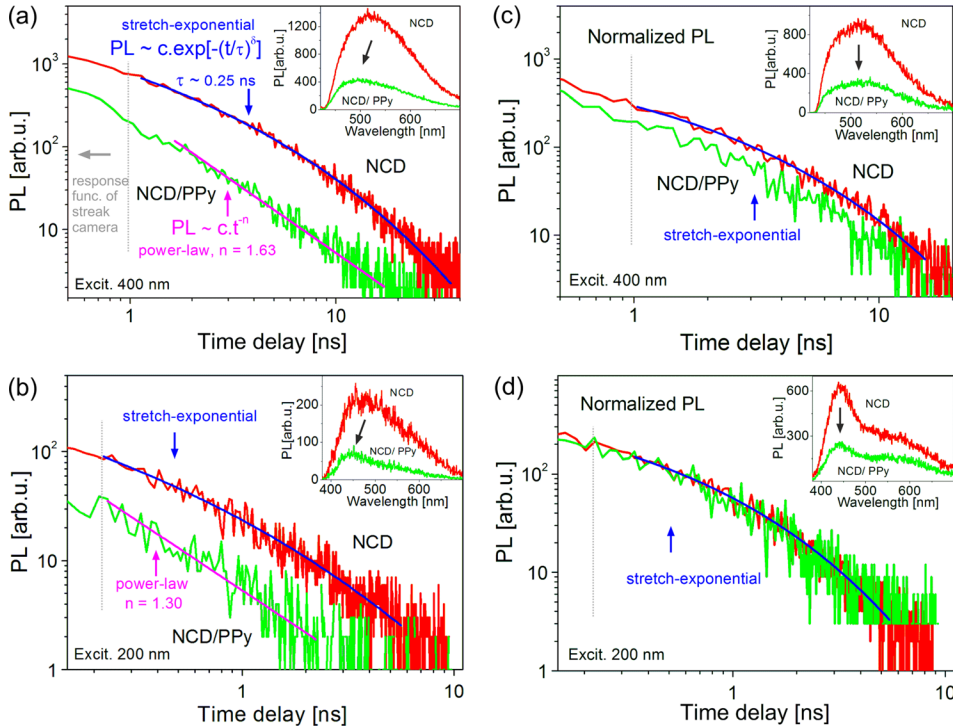


FIG. 2. Comparison of PL decays of pristine and PPy-modified NCD of sample A and B on nanosecond time range excited by 200 and 400 nm laser pulses with the fluence of 0.04 and 1.3 mJ/cm^2 , respectively. (a) PL decays of sample A at 500 nm (2.5 eV) when excited by 400 nm; (b) PL decays of sample A at 460 nm (2.7 eV) when excited by 200 nm; (c) Normalized PL decays of sample B at 500 nm when excited by 400 nm; (d) Normalized PL decays of sample B at 460 nm when excited by 200 nm. The PL decays are approximated by power-law (magenta line) and stretch-exponential (blue line) functions. The insets show time-integrated PL spectra of pristine (red) and PPy-modified NCD (green). The PL spectra were integrated for the initial time range to 40 ns.

functions. The only influence of PPy on NCD PL decay is a small increase (about 10%) of power-law parameter n that was detected mainly on sample A. On the other hand, the intensity of time-integrated PL spectra changed differently. While the PL intensity of sample A excited by 200 nm pulses decreased almost 7 times after PPy deposition, measurements carried out at all other conditions on both samples showed decrease of about 2.5 times (Figs. 3(a) and 3(b), inset). The degree of intensity decrease of both PL components for sample A and B after PPy deposition is for better clarity summarized in Table I. It should be noted that PL excited by 200 and 400 nm laser pulses has comparable shape and intensity even though the UV excitation intensity was more than 30 times lower.

For the deeper insight into the role of PPy in the changes of PL of NCD sub-gap states we have compared PL decays

of pristine sample A, functionalized sample A after mechanical PPy removal, and pristine sample A with a small drop of immersion mineral oil for fluorescence microscopy (Cargille Laboratories, Cat. No. 16424), see Fig. 4. PPy layer was mechanically peeled away by tweezers when rinsed in deionized water. The PL was excited by 400 nm laser pulses. In contrast to the results presented in Fig. 2(a) all three decays have similar stretch-exponential shape. Only the intensity of NCD PL decreased after the polymer removal (by about 10%) or oil deposition (about 2 times).

IV. DISCUSSION

As indicated in Table I, the time-integrated PL intensity decreased typically about 2.5 times (and as much as 7 times) on both samples after PPy deposition. We assume that the

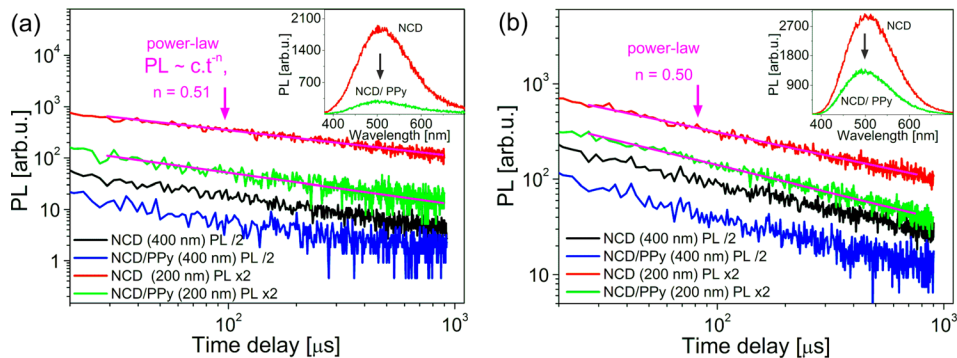


FIG. 3. Comparison of PL decays of pristine and PPy-modified NCD of sample A and B on microsecond time range excited by 200 and 400 nm laser pulses with the fluence of 0.04 and 1.3 mJ/cm^2 , respectively. (a) PL decays of sample A studied at 510 nm. Values of power-law parameter for NCD and NCD/PPy excited by 200 nm and for NCD and NCD/PPy excited by 400 nm were 0.51, 0.56, 0.58, and 0.61, respectively. (b) PL decays of sample B studied at 510 nm. Values of power-law parameter for NCD and NCD/PPy excited by 200 nm and for NCD and NCD/PPy excited by 400 nm were 0.50, 0.54, 0.51, and 0.53, respectively. PL decays are multiplied by appropriate factors for better clarity. The PL decays are approximated by power-law (magenta line) functions. The integration range was from 10 μs to 1 ms.

TABLE I. Overview of the decrease of time-integrated photoluminescence intensity after PPy deposition. PL of samples A and B was excited by 200 and 400 nm laser pulses and detected on nanosecond and microsecond time range.

Sample	Excitation wavelength [nm]	PL component	Factor of decrease
A	400	ns	3.5
		μs	2.5
	200	ns	4.0
		μs	6.7
B	400	ns	2.5
		μs	2.7
	200	ns	2.4
		μs	2.3

PL intensity decrease is not of electronic origin and that it is caused by the change of effective refractive index on the NCD surface by PPy deposition¹⁸ and by reduction of multiple reflections and scattering (i.e., light absorption) of excitation beam and PL in the NCD film due to high imaginary part of PPy refractive index.¹⁹ More detailed presentation and discussion of the optical effects is beyond the scope of this article. Here we focus on differences in the PL decay.

The PL decay of pristine sample A and B excited at 200 and 400 nm are composed of two separated time components that is in a good agreement with our previous results on NCD membranes.¹³ Both PL components were observed in almost similar spectral range, but they exhibited different decay shape and response to the PPy presence (Figs. 2 and 3). The microsecond PL decay always followed power-law dependence with negligible differences in the coefficient n . The power-law decay is well-known from the dynamics of carriers in disordered systems (amorphous or nanocrystalline materials) where the carrier separation occurs.²⁰ The type of transport mechanism (tunnelling/drift/diffusion) is characterized by the time range, where the PL occurs and by the value of coefficient n .²¹ The coefficient n around 1 and lower usually indicates tunnelling of charge carriers between trap and recombination centre. On the other hand, carrier hopping or diffusion could be involved for $n \geq 1.5$. Values in between imply that both mechanism could be involved.²² Based on

the long lifetime of microsecond PL and values of the power-law coefficient n (about 0.51 and 0.58 for 200 and 400 nm for both samples, respectively) the PL is most likely caused by tunnelling of charge carriers between traps. The difference in the coefficient n for both excitations can be caused by different efficiency of trap filling by photogenerated carriers. The high PL intensity generated by weaker pulses at 200 nm in contrast to the excitation at 400 nm indicates that these traps are well accessible for the carriers photogenerated in bulk diamond. For more details see.¹³

On the other hand, the nanosecond PL component of sample A changed the original stretch-exponential decay to power-law decay after the PPy deposition when excited by 400 nm pulses ($\tau \sim 0.25$ ns and $n \sim 1.63$). PL decay described by the stretch-exponential function is usually interpreted as a multi-exponential decay. Physical meaning of the coefficient τ is then the mean decay time. Change of nanosecond PL properties cannot be interpreted merely by optical effects. Time dependence of optical effects on the PL intensity is very unlikely. Moreover, intensity of PL in the ns time range decreased about 8 times in average. This is in contrast to the time-integrated PL intensity that decreased 3.5 times after the PPy deposition. This difference is caused by the presence of sub-nanosecond PL (under response function of streak camera) that is also included in the time-integrated PL spectra and that was not significantly affected by the PPy presence (decreased about 2.5 times). Similar behavior was also observed when the sample A was excited by 200 nm pulses, although the NCD PL intensity was lower than under the 400 nm excitation (Fig. 2(b)).

In contrast, we have observed only negligible effect of PPy on sample B nanosecond PL (Figs. 2(c) and 2(d)) in spite of similar internal composition of both samples (common preparation conditions and almost similar f_g) and PPy layers (Fig. 1). The PL decays are similar for pristine and modified NCD. Also the 2.5 times decrease of time-integrated spectra intensity (Table I) is in a good agreement with the value expected from optical effects. According to these results we assume that the thickness of NCD layer determines the degree of PPy influence on NCD PL properties.

The effects of PPy presented in Figs. 2(a) and 2(b) are reversible and cannot be caused just by any material on the NCD surface. The decay profile changed back to stretched-exponential after PPy removal (compare Figs. 2(a) and 4). Deposition of immersion oil decreased PL intensity about 2 times but it did not change the PL decay dynamics. Similarly, decrease of PL intensity but no change of dynamics was observed after deposition of chemically synthesized PPy¹⁴ on the NCD surface. Thus covalent binding between PPy and NCD is most likely fundamental for influencing PL of the NCD sub-gap states on the ns time range.

According to these results and our previous work¹³ we assume that the nanosecond PL could originate from radiative recombination between $\pi - \pi^*$ sub-gap states of non-diamond carbon sp^2 phase. This assumption is supported by the spectral range of time-integrated PL that was observed within the whole visible region down to approx. 380 nm (3.3 eV). This corresponds to the energetic difference between the NCD π states as obtained by photothermal deflection spectroscopy.²³

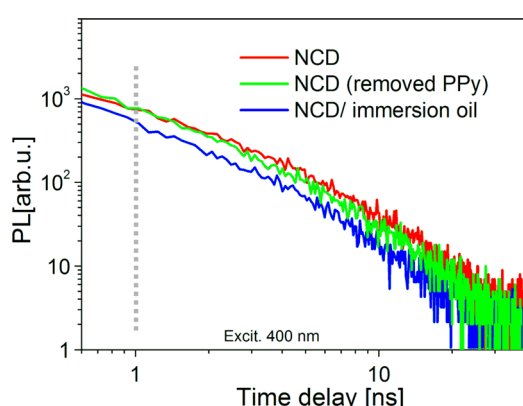


FIG. 4. PL decay of pristine NCD, NCD after PPy removal and NCD with immersion oil at 500 nm. It was excited by 400 nm laser pulses with the fluency of 1.3 mJ/cm².

Moreover, the decay time $\tau = 0.25$ ns is in a good agreement with PL decay ($\tau \leq 0.5$ ns) presented by Plakhotnik *et al.*²⁴ The microsecond PL should originate from defects on the diamond grain surface. This interpretation is in a good agreement with the high intensity of microsecond PL component excited by 200 nm laser pulses. The microsecond PL component can be thus attributed to localized defect states on the diamond grain surface. This slow PL is enhanced by UV excitation that leads to additional generation of carriers in diamond grains (see Figs. 3(a) and 3(b)). The carriers diffuse to the grain surface and recombine there both in radiative (microsecond PL) and non-radiative way on various kinds of surface defects. The negligible influence of PPy presence on the microsecond PL decay shape is then most likely caused by strong localization of charges in these defect states and limited connection of these states with non-diamond carbon between the grains. This assumption is also in a good agreement with negligible effect of PPy on the time-integrated PL spectra when the NCD was excited by 400 nm pulses, because no charge carriers were generated in bulk diamond. On the other hand, based on this theory we could interpret the almost 7 times decrease of microsecond PL intensity after PPy deposition on sample A. If we assume that the main reason for the strong microsecond PL at 200 nm excitation are the photogenerated charge carriers in bulk diamond that diffuse to the grain surface and fill the photoactive diamond surface states the only possibility for decreased PL intensity without change of PL decay is that the photogenerated carriers are affected by PPy so that they do not fill these surface states. The above argument indicates that the PPy on NCD can affect not only charge carriers localized in the non-diamond carbon phase between the diamond grains but it can also influence transport behavior of free carriers in bulk diamond.

The above results and discussion clearly show that the PPy grafting does not affect only immediate vicinity of the NCD-PPy interface or only effective optical properties of the NCD-PPy system but affects even opto-electronic properties of sub-gap states deep inside the NCD film. Based on the measurements of thicker NCD samples we estimate that the affected region should extend up to 200–300 nm inside the NCD film.

We propose following model that explains this behavior. It is schematically shown in Fig. 5. If we take the π states not only as defects in the diamond band gap but as states in a separate matter (spatially separated from the diamond grains) that is connected with PPy via non-diamond carbon phase around grains, there may be charge exchange between these parts. Because the inter-grain phase has lower electrical resistance compared to diamond grains it could mediate the communication between the π states in the NCD volume and PPy on the surface. The influence of non-diamond carbon phase on delocalization of photoexcited charges in the π states was already observed.¹³ In the present situation, holes photoexcited to the π states will not only diffuse through non-diamond carbon phase, get trapped in π tail states and radiatively recombine with electrons from π^* states or recombine non-radiatively like in the pristine NCD. They will also drift to the PPy on the surface. This additional spatial charge separation represents non-radiative channel in $\pi - \pi^*$ transition and, therefore, it will decrease PL intensity

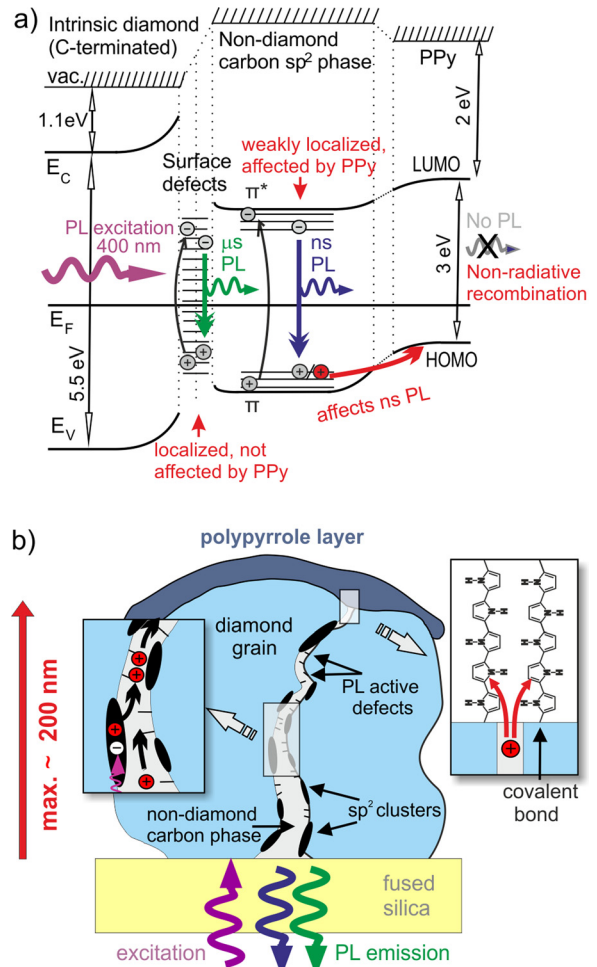


FIG. 5. (a) Schematic energetic model of PPy-NCD interface that depicts recombination and charge separation mechanisms of photoexcited charge carriers generated by sub-gap excitation wavelength (400 nm). PPy influences photoluminescence of NCD $\pi - \pi^*$ sub-gap states, but not long-lived defect states on/in diamond grains. Energy and vacuum levels of diamond, carbon sp² phase and PPy were taken from Refs. 13 and 25–28. (b) Structural model of PPy/NCD excited at 400 nm. Model is focused on description of possible transport mechanism of photogenerated charge carriers generated in sp² carbon clusters to surface PPy layer.

and change the recombination mechanism to the power-law decay in the nanosecond PL. The charge separation is corroborated by the high value of power-law coefficient n (1.63) of the nanosecond PL after PPy deposition. The charge drift could be caused by concentration gradient or internal electric field (depletion region). The latter seems to be more likely option because in case of concentration gradient the charge should be separated also without PPy. The same transport mechanism can be realized also for the super band gap (200 nm) excitation. There would be only additional charges generated in bulk diamond that would be filling mainly defects on the grain surface. These effects are included also in the thicker functionalized NCD sample (920 nm), but the PL is dominated by PL active states outside the influence of PPy on the surface.

The model implies that for the thicker sample B with larger grains, smaller density of grain boundaries within the deduced extraction depth may reduce the hole dissociation and transport when functionalized with PPy. This is indeed

in agreement with different PL decay for functionalized samples A and B on nanosecond scale (see Fig. 2). For the thicker sample B, the volume not affected by PPy dominates the PL signal.

The transfer of holes at PPy-diamond interface can be in principle used also for conversion of energy from light. More specifically, the electron-hole pairs generated by visible light in nanocrystalline diamond are dissociated by covalently bound PPy on the diamond surface. Based on the estimated interaction depth, the system would be in particular, efficient on nanoscale dimensions below 200 nm, e.g., nanowire-based photovoltaic systems. Nanocrystalline and/or nanostructured morphology of the diamond represents here a fundamental feature for absorbing visible light by otherwise wide-band gap diamond material.

V. CONCLUSION

We have shown that PL properties of NCD films are significantly modified by electrochemical grafting of PPy. Main effects were change of PL decay behavior, blue shift of the broad spectral band of the nanosecond PL and PL intensity decrease by as much as 85%. The PL intensity decreases partially due to optical effects (as confirmed also by immersion oil). Yet the fundamental changes are of electronic origin. We proposed the model based on spatial separation of photo-excited charge carriers from non-diamond carbon states that is promoted even deep inside the NCD film (up to approx. few hundreds of nm) by PPy grafted on the surface. We also proved that this effect is reversible and cannot be caused by any permanent modifications of NCD during deposition. There are also indications that the PPy can affect the transport behavior of free carriers inside the bulk diamond. Thus grafting of PPy to diamond may have impact on diverse applications including electrical control of color centers in diamond and energy conversion. It remains to be clarified if other substances can generate similar effect (immersion oil could not) and to what degree is covalent link to diamond necessary.

ACKNOWLEDGMENTS

This work was carried out in the frame of LNSM infrastructure and supported by Charles University in Prague grant SVV-2013-265306, by GAUK 151910/2012 and by GAČR P108/12/G108. I would like to thank to E. Ukrainstev for sample preparation and J. Libertínová for AFM characterization, both from Institute of Physics ASCR.

¹P. Hubík, J. J. Mareš, H. Kozák, A. Kromka, B. Rezek, J. Kristofik, and D. Kindl, "Transport properties of hydrogen-terminated nanocrystalline diamond films," *Diamond Related Mater.* **24**, 63–68 (2012).

²M. Krátká, A. Kromka, E. Ukrainstev, M. Ledinský, A. Brož, M. Kalbačová, and B. Rezek, "Function of thin film nanocrystalline diamond-protein SGFET independent of grain size," *Sens. Actuators B Chem.* **166**, 239–245 (2012).

³J. de Sanoit, E. Vanhove, P. Mailley, and P. Bergonzo, "Electrochemical diamond sensors for TNT detection in water," *Electrochim. Acta* **54**, 5688–5693 (2009).

⁴S. Stehlík, T. Izak, A. Kromka, B. Dolenský, M. Havlík, and B. Rezek, "Sensitivity of diamond-capped impedance transducer to Tröger's base derivatives," *ACS Appl. Mater. Interfaces* **4**, 3860–3865 (2012).

⁵A. Hartl, E. Schmich, J. A. Garrido, J. Hernando, S. C. R. Catharino, S. Walter, P. Feulner, A. Kromka, D. Steinmuller, and M. Stutzmann, "Protein-modified nanocrystalline diamond thin films for biosensor applications," *Nature Mater.* **3**, 736–742 (2004).

⁶B. Rezek, J. Čermák, A. Kromka, M. Ledinský, P. Hubík, J. J. Mareš, A. Purkrat, V. Cimrová, A. Fejfar, and J. Kočka, "Synthesis, structure, and opto-electronic properties of organic-based nanoscale heterojunctions," *Nanoscale Res. Lett.* **6**, 238–1–238–12 (2011).

⁷W. C. Poh, K. P. Loh, W. De Zhang, and S. Tripathy, "Biosensing properties of diamond and carbon nanotubes," *Langmuir* **20**, 5484–5492 (2004).

⁸S. Koizumi, C. H. Nebel, and M. Nesládek, *Physics and Applications of CVD Diamond* (Wiley-VCH, Weinheim, 2000).

⁹P. Strobel, M. Riedel, J. Ristein, and L. Ley, "Surface transfer doping of diamond," *Nature* **430**, 439–441 (2004).

¹⁰E. Ukrainstev, A. Kromka, W. Janssen, K. Haenen, and B. Rezek, "Controlling physical and chemical bonding of polypyrrole to boron doped diamond by surface termination," *Int. J. Electrochem. Sci.* **8**, 17–26 (2013).

¹¹K. Tada, T. Sonoda, Y. Yokota, K. Kobashi, and K. Yoshino, "Hole injection from diamond into conducting polymer," *J. Appl. Phys.* **84**, 5635–5638 (1998).

¹²J. Preclíková, P. Galář, F. Trojánek, B. Rezek, Y. Němcová, and P. Malý, "Photoluminescence of nanocrystalline titanium dioxide films loaded with silver nanoparticles," *J. Appl. Phys.* **109**, 083528 (2011).

¹³P. Galář, B. Dzurňák, M. Varga, A. Kromka, and P. Malý, "Influence of non-diamond carbon phase on recombination mechanisms of photoexcited charge carriers in microcrystalline and nanocrystalline diamond studied by time resolved photoluminescence spectroscopy," *Opt. Mater. Express* **4**, 624–637 (2014).

¹⁴P. Galář, B. Dzurňák, P. Malý, J. Čermák, A. Kromka, and M. Omastová, "Chemical Changes and Photoluminescence Properties of UV Modified Polypyrrole," *Int. J. Electrochem. Sci.* **8**, 57–70 (2013).

¹⁵A. Kromka, B. Rezek, M. Kalbáčová, J. Barešová, J. Zeman, C. Konak, and M. Vaněček, "Diamond seeding and growth of hierarchically structured films for tissue engineering," *Adv. Eng. Mater.* **11**, B71–B76 (2009).

¹⁶See supplemental material at <http://dx.doi.org/10.1063/1.4903937> for getting detail information about Raman spectra of sample A and B excited at 325 nm (3.8 eV).

¹⁷W. Fortunato, A. J. Chiquito, J. C. Galceran, and J. R. Moro, "Crystalline quality and phase purity of CVD diamond films studied by Raman spectroscopy," *J. Mater. Sci.* **42**, 7331–7336 (2007).

¹⁸D. E. Aspnes, "Optical properties of thin films," *Thin Solid Films* **89**, 249–262 (1982).

¹⁹M. Born and E. Wolf, *Principles of Optics* (Cambridge University Press, Cambridge, 1999), pp. 735–790.

²⁰J. Bisquert, "Interpretation of a fractional diffusion equation with nonconserved probability density in terms of experimental systems with trapping or recombination," *Phys. Rev. E* **72**, 011109 (2005).

²¹D. J. Huntley, "An explanation of the power-law decay of luminescence," *J. Phys.: Condens. Matter* **18**, 1359–1365 (2006).

²²A. K. Jonscher and A. De Polignac, "The time dependence of luminescence in solids," *J. Phys. C: Solid State Phys.* **17**, 6493–6519 (1984).

²³M. Vaněček, J. Rosa, M. Nesládek, and L. M. Stals, "Evidence for the principal defect states in CVD diamond films: Optical study," *Diamond Related Mater.* **5**, 952–957 (1996).

²⁴B. R. Smith, D. Gruber, and T. Plakhotnik, "The effects of surface oxidation on luminescence of nano diamonds," *Diamond Related Mater.* **19**, 314–318 (2010).

²⁵J. Robertson, "Diamond-like Amorphous Carbon," *Mater. Sci. Eng. R.* **37**, 129–281 (2002).

²⁶C. Saguy, E. Baskin, and R. Kalish, "Electrical properties of undoped and ion-implanted type IIa diamonds measured by photo-Hall," *Diamond Related Mater.* **14**, 344–349 (2005).

²⁷P. Somani and S. Radhakrishnan, "Sensitization effect in doped and undoped state of polypyrrole by methylene blue in solid state electrochemical cells," *Chem. Phys. Lett.* **379**, 401–405 (2003).

²⁸J. Čermák, A. Kromka, M. Ledinský, and B. Rezek, "Illumination-induced charge transfer in polypyrrole–diamond nanosystem," *Diamond Related Mater.* **18**, 800–803 (2009).